FLOW MODELING OF SCROLL COMPRESSORS AND EXPANDERS

by

George Karagiorgis

A Thesis submitted to
The City University
for the Degree of
Doctor of Philosophy

August 1998

Department of Mechanical Engineering and Aeronautics
The City University
Northampton Square, London EC1V OHB.

To my family

TABLE OF CONTENTS

ACKNOWLEDGEMENTS

I would like to express my sincere appreciation to my parents and family, and especially to my wife Spyroula for her support and understanding during the difficult times of this project.

I also would like to thank Dr. D. N. Papadakos (Imperial College) for allowing me to use his powerful computing facilities without which this project would never have reached this stage.

Finally, I would like to thank my supervisor Prof. I. K. Smith.

DECLARATION

I grant powers of discretion to the University Librarian to allow this thesis to be copied in whole or in part without further reference to me. This permission covers only single copies made for study purposes, subject to normal conditions of acknowledgement.

ABSTRACT

The use of scroll compressors in refrigeration systems is becoming increasing popular. However the development and use of a scroll machine as an expander to replace a throttle valve has never been reported. This thesis describes the work carried out to develop a two phase scroll expander for use in vapour compression refrigeration systems. By this means the power requirements of the system would be decreased and the refrigeration effect increased.

A computer simulation of the geometry of the scroll device was first developed. This was attached to a package of subroutines developed to analyse compressor and expander thermodynamic performance to obtain estimates of both scroll expander and compressor performance.

The results of the expander compressor analyses were used to estimate the performance of a scroll expander driving a second scroll compressor in a sealed unit used in a large industrial chiller of 4MW thermal output.

By this means the power requirement for the main compressor was reduced by approximately 10% while, due to the expansion in the expander being more nearly isentropic than in the throttle valve, the refrigeration effect was simultaneously increased by nearly 2%. This lead to an overall improvement in coefficient of performance of nearly 13.5%. Further investigation of the system and more specially on the scroll device appears to be justified.

A 3D simulation was then performed by the use of a CFD package called CFX4. This gave an excellent understanding on the flow 'inside' the machine. From the flow patterns obtained it is obvious that the scroll device behaviour appears to be excellent as compressor but not so good as an expander. This is mainly due to the huge recirculation during the filling process and due to the significant pressure drop of approximately 2 bar (Max) associated with it.

Chapter 1

Introduction

1.1 Introductory Remarks

Studies in fluid flow analysis are generally conducted using either experimental or numerical-computational approaches. From the theoretical point of view fluid dynamics are highly developed, however the mathematical formulations are highly complex and can only be solved analytically in very few simplified cases. On the other hand advances in numerical analysis and computer hardware/software have made feasible the solution of the relevant equations using numerical techniques. This thesis is concerned with the development of a an efficient scroll expander which can operate with two phase flow, and the modeling of its working conditions.

During the last few years, numerical flow analysis techniques have become more and more important in machine design. A key factor in obtaining a realistic solution is mesh generation, considered as a basic problem requiring a sustained effort. In fact, the interaction between the mesh characteristics and the development of it of the solver calculation are closely linked as far as stability, convergence and definition of the solution are concerned.

The study was carried out using Computational Fluid Dynamics (CFD) techniques. The advantages of successful computational procedures compared with actual experiments are significant. Computational studies are relatively cheap to perform. Furthermore the parameters defining the geometry or the operating conditions of the device can be varied at will and hence the required optimum can be achieved.

Scroll expanders present definite advantages over other machines. In addition, the reduced number of parts, the ability to cope with two phase working fluids and the inherent reliability proven in compressor mode are major reasons for its wider use in energy recovery. The fast growing mass production of such units as compressors is also likely to contribute to a lowering of the production costs for expander applications.

As is the case for all rotary volumetric machines, reverse motion is inherently possible and, therefore the conversion of scroll compressor to scroll expander can be envisaged. Smith's investigation for this type of machine indicated that the machines most applicable for the expansion of a two phase flow are the Lysholm twin screw expander and the scroll expander. As far as the first type is concerned, work was initiated by Smith at the Centre for Compressor Technology, City University London in late 1982.

In order to perform a thermodynamic analysis of the scroll compressor - expander first we have to describe the physical behavior of the machine in terms of mathematical equations. Functions of working volume, sealing lines, touching conditions etc. in terms of crank angle, (i.e. time) form the foundations for the analysis.

1.2 Present Contribution

The objective of this research project was to design and develop a two phase expander to be used as a substitute of the throttle valve in a vapour compression refrigeration system, and to model the thermodynamics and fluid mechanics of this machine when operating in the compression mode. The major contributions of the work presented in this thesis are:

1. A parametric study giving all the mathematical equations needed for the modeling of the scroll compressor-expander. This includes the derivation of mathematical expressions giving the working volumes, the sealing lines, the touching conditions, the thickness and the lengths of the arms, etc. as functions of the various design parameters (such as α and N) and the crank angle θ .
2. Implementation of the geometry developed into a Quasi One Dimensional Flow package called SCORPATH. This gave some estimates of the performance of the scroll compressor and expander operating under different working conditions.
3. Design and development of a grid generation program that can handle the complexity of the working volumes of the scroll device. Aspect ratios, orthogonality, cell distortion and smooth distribution are some of the difficult issues involved in the transient, structured, body fitted grid generation package developed. This is a major contribution to the development and understanding of these type of machines.
4. Coupling of the Transient Grid Generation Code developed with a Computational Fluid Dynamics (CFD) package called CFX4. Implementation

of the resulted executable yielded thermodynamic results, as well as an in depth understanding of the flow patterns within the scroll device. Consequently visualization software tools can be used to improve the overall behavior of the device.

5. Finally a test case was devised and studied in which the scroll expander substituted the throttle valve in a Carnot refrigeration cycle.

1.3 Thesis Layout

The thesis is structured as follows:

In chapter 2 previous efforts to develop two-phase expanders and compressors are examined. Emphasis is placed on the work done on scroll compressors mainly because knowledge on this topic is essential for the design and development of scroll expanders. It is also demonstrated that the scroll device is the most appropriate machine for the requirements of the present study. The existing, very limited amount of work that has been done up to now on scroll expanders, is also presented.

Chapter 3 describes the computation of thermodynamics and flow process in a scroll compressor-expander based on the work of N. Stosic. It also contains a discussion of the results from the Quasi 1-D flow modeling. The importance of the relationship between build-in volume ratio and build-in pressure ratio and the use of the correct pressure ratio is clearly defined. The significant point is that the build-in volume ratio is a constant for any given scroll compressor or expander design but the pressure ratio is not, and is a function of both the gas being handled and the rotational speed. The linking of a scroll expander to a scroll compressor in a sealed 'Expressor' unit is also described in this chapter. This may be used both in new systems and for retrofit applications in place of a throttle valve. The results of computer simulations of Expressor performance in a large industrial chiller are shown.

In the first part of chapter 4 we present the necessary equations needed for the analysis. As will be shown in section 4.4, these equations form the basis for the development of the grid generation code. The derivation of the equations was necessary since it is not based on any publish data, however it is partially based on the patent of the inventor of the machine. Full analysis of the geometry is given in appendix A. Then follows a survey on the different methods of grid generation and finally the design and development of a grid generation program that can handle

the complexity of the working volume of the scroll device is analyzed. Aspect ratio, orthogonality, cell distortion, and smooth distribution, are some of the difficult issues involved in the transient structured body fitted grid generation package developed.

In chapter 5 we give the mathematical basis for a comprehensive general purpose model of fluid flow and heat transfer from the basic principles of conservation of mass, momentum and energy. This leads to the governing equations of fluid flow, the so called Navier - Stokes equations. The governing equations are complex non linear partial differential equations, which can be solved using numerical methods. Discretization methods, advection schemes, time differencing schemes and pressure / velocity coupling algorithms are discussed. Commercially available CFD software packages are reviewed and CFX - FLOW3D is described in detail. Flows inside scroll compressors - expanders are turbulent, time dependent, compressible and for the case of the expander two phase. Furthermore these flows are driven by the wall motion and, therefore, are characterized by moving boundaries. In the last section of this chapter the results of the three dimensional modeling are shown.

Chapter 6 contains some concluding remarks and suggestions for possible future research.

Chapter 2

Literature Survey

2.1 Introduction

Since its invention by Perkins in 1834, there has been no major change in the layout of vapour compression refrigeration plant. However, design aspects such as refrigerating controls, amount of superheating, sub-cooling, etc. have been modified over the years. All these modifications were related to production cost, ambient conditions and other manufacturing related factors. The need to develop more efficient compressors considering all aspects such as noise, vibration, weight, efficiency as well as the losses due to throttling, still exists.

In this chapter we examine previous efforts to develop two-phase expanders and compressors. Emphasis is placed on the work done on the scroll. It is also demonstrated that the scroll device is the most appropriate machine for the requirements of the present study. The existing, very limited amount of work that has been done up to now on scroll expanders, is also presented.

2.2 Compressors

Compressors are generally divided into two different categories or types based on the principle on which they operate. These types are positive displacement and aerodynamic, the latter type is sometimes called dynamic. Figure 2-1 shows a chart of common compressor types separated according to the above categories.

An area where confusion arises surprisingly often is in the specification of the *"**duty**"* required from an industrial compressor. Different industries have different conventions, some call for volume flow, others mass flow, and in the refrigeration industry the *"**duty**"* is rated in the heat units absorbed by the refrigeration plant. Over and above the basic *"**duty**"* specification, there is the question of performance, tolerances and guarantees which can also be a subject of misunderstandings.

The convention for rating compressors in the refrigeration industry is quite

different from the convention used in the case of air, gas or chemical applications. Compressors in the refrigeration industry are rated on the basis of their refrigeration capacity at specific evaporating and condensing temperatures. This is largely a function of mass flow.

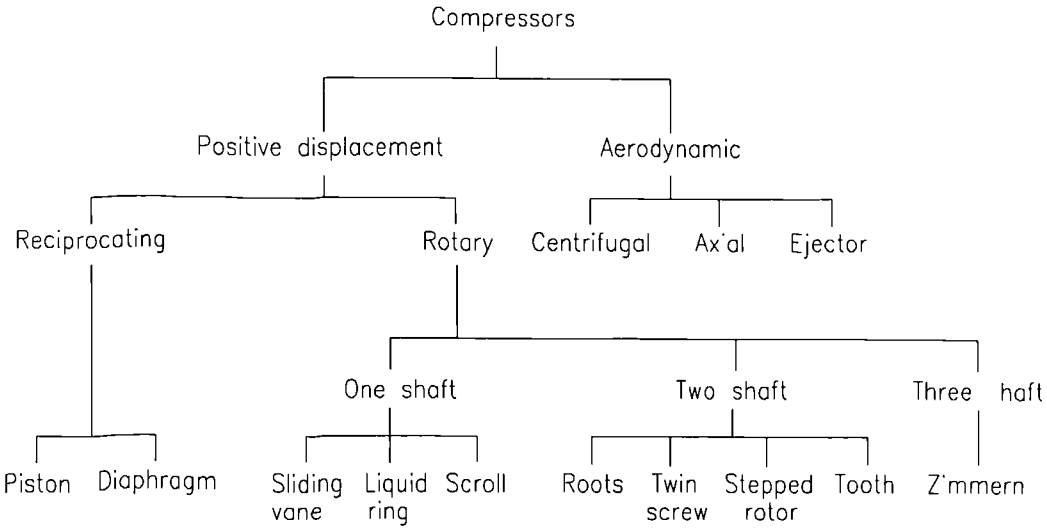

Figure 2.1 Classification of common industrial compressors

2.2.1 Aerodynamic Compressors

In a turbine the working fluid enters at a high pressure and acquires increased kinetic energy as it expands through a ring of fixed nozzles to a lower pressure. The stream of fluid then undergoes a change of momentum as it flows trough passages between blades attached to the rotor, and the component in a direction tangential to the circle of rotation produces the output torque at the shaft.

This series of events is reversed in aerodynamic compressor. Input torque from some external source imparts a change of momentum to the working passage between the rotor blades. Having acquired an increased velocity, the fluid then slows down with an accompanying rise of pressure while flowing through a ring of fixed diffusers.

There are two main types of aerodynamic compressors, distinguished by whether the flow through the machine is in the axial or radial direction. In these machines the fluid undergoes a continuous steady-flow process and the speed of flow is very high. For this reason comparatively small machines can handle large mass flows and large work transfers, and the processes can be assumed to be adiabatic (Rogers

& Mayhew 1980).

2.2.1.1 Centrifugal Compressors

The first commercial centrifugal compressor used in refrigeration service was promoted by Willis Carrier in 1920. Since then the centrifugal compressor has become the dominant type of compressor in large installations.

Centrifugal compressors serve refrigeration systems in the range of 200 to 10,000 kW of refrigeration capacity. Evaporating temperatures in multistage machines may extend downwards to -100^0 C, although one of the major uses of the compressor is the chilling of water to about 6^o C to 8^o C in air conditioning systems.

Centrifugal compressors are similar in construction to centrifugal pumps in that the incoming fluid enters the eye of the spinning impeller and is thrown by centrifugal forces to the periphery of the impeller. Thus the blades of the impeller impart high speed to the gas. From the impeller the gas flows either into diffuser blades or into a volute, where gas momentum is lost and its pressure increases. The centrifugal compressor may be manufactured with only one wheel if the pressure ratio is low, although these kind of compressors are generally multistage. Centrifugal compressors operate with adiabatic efficiencies of 70 to 80 percent.

2.2.2 Positive Displacement Compressors

In this type of machine gas is drawn into the compressor, it is trapped within it and is then positively displaced out of it by the movement of one or more components. The term ***"trapped"*** is used to indicate that the quantity of gas involved in the compression processes, is not affected by either the suction or discharge cycles of the machine. These types of compressor can develop at the discharge port exactly that pressure which is necessary to discharge the gas from the machine, subject of course to the power available and the physical constrains of the compressor design.

2.2.2.1 Reciprocating Compressors

Reciprocating compressors have been in existence for a very long time. The basic principle of a piston or reciprocating compressor is that gas is drawn into a cylinder by the movement of a piston. Originally, the piston's movement leaves a free space and the gas flows into this to fill it. The piston then reverses the direction of its

movement and forces the gas back out of the cylinder. Valves are fitted to both inlet and outlet which ensure that the gas enters and leaves by different ports.

From the action of the piston compressor it is clear that this device belongs to the type of positive displacement machines. The air or gas is sucked in, compressed and then pushed out, that is displaced by the movement of the piston. The higher the pressure of the system into which the gas is to be discharged the greater the force required to move the piston during the compression-discharge cycle and hence the greater the input power of the device. Consequently, the power input to a reciprocating compressor increases with its discharge pressure. The maximum possible discharge pressure of a piston compressor is dictated by the available power, subject to the mechanical and thermal limitations of the design, and is not in any way affected by the speed.

By construction, at the end of the compression/discharge stroke, there is still some space left between the piston and the top of the cylinder. This is the so called clearance volume and the gas trapped in there is at discharge pressure. Due to this pressure, if at the end of the compression/discharge stroke the force at the back of the piston is released the gas in the clearance volume expands pushing the piston backwards some distance until the forces on either sides of the piston become equal. Two points arise from this situation.

Firstly, the expansion of the gas does useful work in moving the piston backwards, so recovering much of the compression work put into the gas in the clearance volume.

Secondly, no additional gas is drawn into the cylinder until the clearance volume gas has expanded down to the suction pressure. After this point is reached, further movement of the piston reduces the pressure in the cylinder below suction pressure and suction flow past the inlet valve commences. Thus the volumetric efficiency of a compressor with clearance volume is directly affected by the clearance volume.

2.2.2.2 Screw Compressors

The so called ***"twin"*** screw compressor is the type of compressor which has been developed for the widest list of applications and has the largest range of available sizes. Compared to some other types, for example piston compressors, the history and therefore technology, of screw compressors is relatively young. The screw

compressor was developed in the 1930s and first became popular for refrigeration service in Europe in the 1960s.

The screw compressor consists essentially of two meshing rotors in a casing. The male rotor drives the female rotor in a stationary housing. The refrigerant enters the one end of the compressor at the top and leaves the other end at the bottom. At the suction position of the compressor a void is created into which the inlet vapor flows. Just before the point where the interlobe space leaves the inlet port, the entire length of the cavity or gully is filled with gas. As the rotation continues the trapped gas is moved circumferentially around the housing of the compressor. Further rotation results in meshing of the male lobe with the female gully, decreasing the volume in the cavity and compressing the gas. At a certain point into the compression process the discharge port is uncovered and the compressed gas is discharged by further meshing of the lobe and the gully. A major feature of this is that there is zero clearance volume.

2.2.2.3 Scroll Compressors

After the 1970's energy crisis, conservation has been the most emphasized topic for air conditioners. The demand for air conditioners with higher efficiency have been required from the distributors to meet the customer's needs concerning energy savings. Under such a situation, there came a strong demand for higher efficiency compressors, because the improvement of the compressor efficiency is the most economical method in spite of technological difficulties. Thus most compressors manufactures have been eagerly improving conventional compressors. However, some of them turned their attention to scroll devices.

The concept of scroll devices goes back to the beginning of this century. The scroll machine was invented by Leon Greux, a French scientist in June 1905 and was patented on 3rd October 1905. It is currently attracting the designers attention because of its high efficiency and smooth operation. One of the main reasons why scroll machines were not fully developed or substantially improved for such a long period, was the lack of precise production techniques needed for the construction of such machines. However designers started looking at these kind of devices again in the early 1970's.

The scroll compressor was not commercially successful until 1976. This was primarily because of sealing and wearing problems which placed severe limitations on the efficiencies, operating life and pressure ratios attainable. Such sealing and

wear problems were of both radial and tangential types. However, since then a lot of work is been done and many problems were overcome.

Scroll compressors have a lower level of noise and vibration, than rolling piston rotary compressors, and because of this, they are used extensively as air conditioner refrigeration compressors.
Compared to the other types of compressors, the inherent advantages of the scroll compressors are :

- fixed build-in volume ratio making it valveless and more reliable as well as adaptable to variable speed,
- large inhaling hole and nearly continuous inhaling making it have small pressure drop,
- high volumetric efficiency,
- low noise.

However, designing and manufacturing this machine is very difficult. The early 1970's, research and development work on the scroll compressor has been carried out steadily until now. Practical application however, was not achieved until recently mainly for the following reasons :

- very high precision tooling is required for the production of the scroll compressor,
- a complicated process is required to assemble the parts involved in the compression mechanism.

2.2.2.3.1 Working Process

The main components of the scroll compressor are shown in Figs. 2.2a and 2.2b. There are the fixed scroll, orbiting scroll, anti-rotation coupling, crankshaft and crankcase. The outside suction port and the outside discharge port are in the fixed scroll. The inside suction ports are located at the vane profile termination, the inside discharge ports are located at the vane profile start. The area of the inside suction ports varies periodically with the crankshaft rotation. The gas is inhaled from the outside suction port then gets into the suction pockets tangentially through the inside suction ports. After compression it leaves the displacement volume tangentially through the inside discharge ports, then enters the central pockets. Finally it leaves the compressor axially through the outside discharge port.

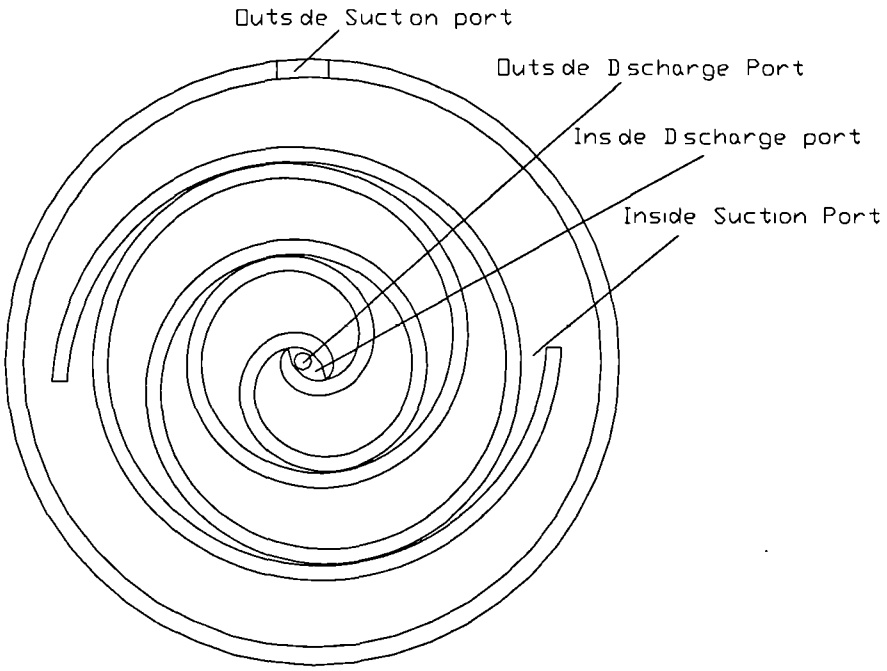

Figure 2.2a The ports

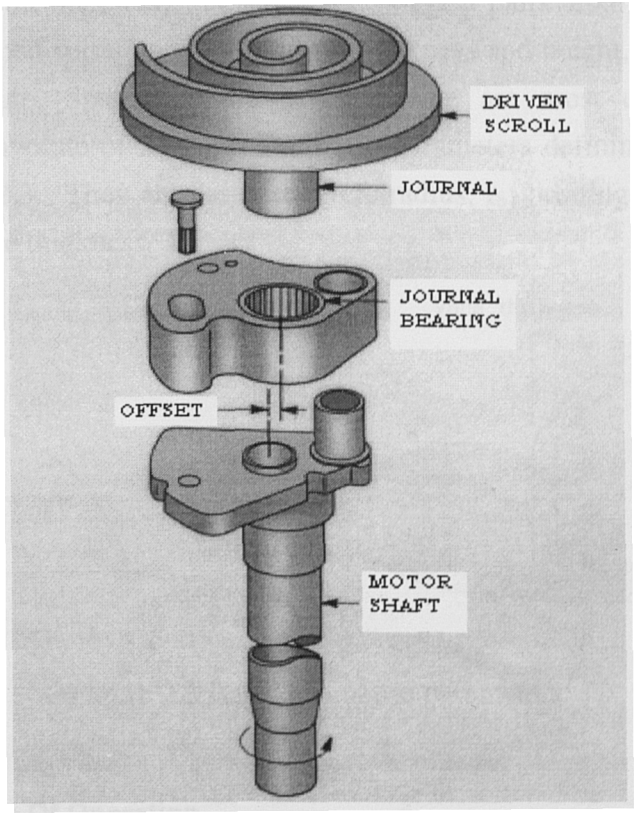

Figure 2.2b Scroll compressor rotating mechanism

The working process can be divided into five stages: steady suction, suction closing, compression, initial discharge, and steady discharge. In the steady suction stage, the displacement volume increases from zero to a maximum, the crank angle range is broad and the suction time is long. In the suction closing stage, the volume begins to decrease gradually, but the inside suction ports are not closed off, so the gas returning phenomenon arises and the pressure of the closed pockets is higher than the nominal suction pressure, this increases the volumetric efficiency. In the compression stage, leakage has the main influence on the compressor efficiency. In the initial discharged stage, the compressor starts to discharge forcibly, the gas scurries through the inside discharge ports when the pocket pressure is different from the central pockets. In the steady discharge stage, the gas leaves the compressor but the effective area of the outside discharge port decreases because of the orbiting scroll interference. So the velocity increases. A detailed survey of scroll compressors follows.

2.2.2.3.2 Scroll Members

Conventional scroll members are mirror imaged pairs comprising a single appropriately shaped spiral vane, of uniform thickness and height, protruding from an end vane plate. Spirals of the involute type are most commonly used, particularly the involute of a circle. The basic parameters defining the scrolls are displayed on fig.2.3. They are the base circle radius, r_b; orbiting radius, r_{or}; vane height, H and vane thickness, T.

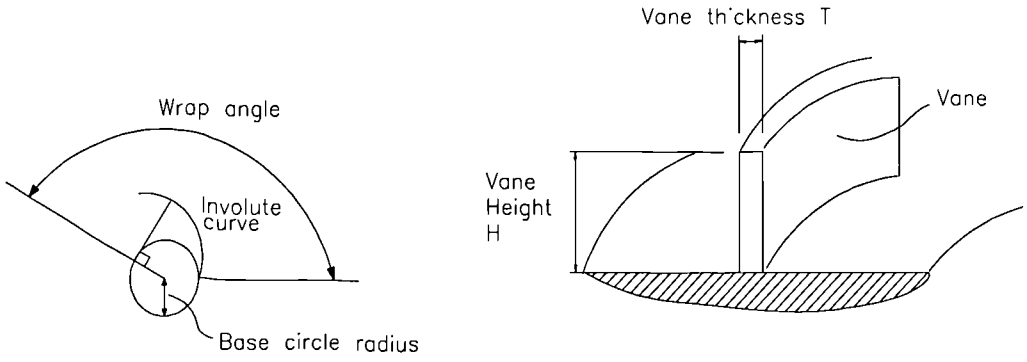

Figure 2.3 Basic geometric parameters

2.2.2.3.3 Principle Of Operation

The members are appropriately phased, and eccentrically mated, so as to form various pockets bounded by the vanes and their respective end plates, as shown in

fig.2.4 Most commonly one scroll is fixed and the other is made to orbit by a crank mechanism. Through relative motion of the members the pockets, initially opened to the surroundings, are first formed, sealed off, progressively moved inwards while reducing in volume, and finally merged into a common discharged volume.

Conversely simultaneous rotation of the members about their respective geometric centre yields an equivalent relative motion of members. However the first scheme only was considered in the present study.

The inherent advantages of such a scroll machine are valveless compression virtually constant volumetric efficiency, nearly continuous suction and discharge flow, smooth operation, low relative velocity and potentially low unbalance.

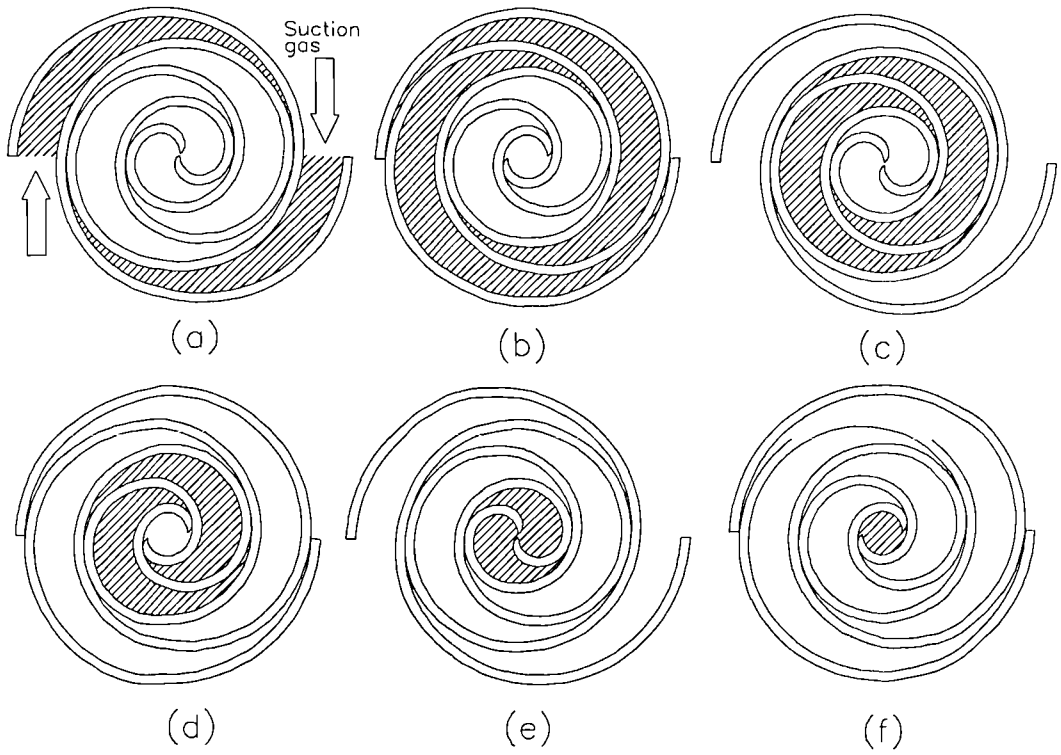

Figure 2.4 Working volumes in a scroll compressor

2.2.2.3.4 Analytical Model

To model the scroll suction compression and discharge process, descriptions of volume in the pair of compression pockets and area open for suction and discharge flow as functions of time are required. These geometric relationships are more conveniently described as functions of scroll orbit angle, or crank angle.

The volume in a pair of scroll pockets for a typical scroll compressor is shown in fig.2.5 from the start of suction (SOS) through the end of discharge (EOD). The process from the start of compression (SOC) to the start of discharge (SOD) is approximately a closed compression process; only leakage or porting for some pneumatic operations such a back chamber, prevent it from being truly sealed.

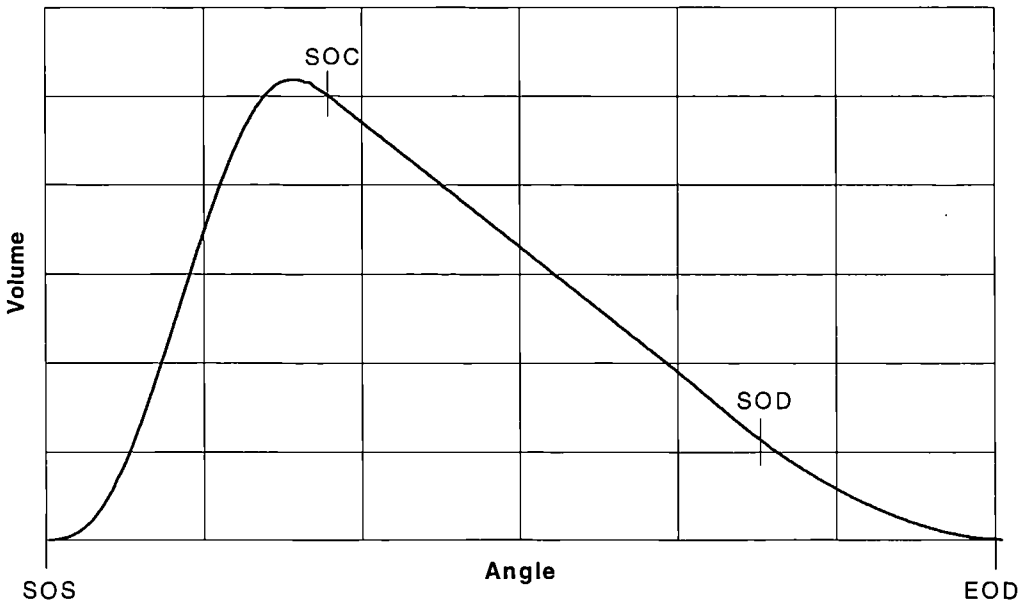

Figure 2.5 Volume in a pair of typical scroll pockets from SOS to EOD.

However as far as the "closed" process is concerned, by the time the inner wrap tips open at SOD, the control volume in the pocket is no longer "closed", and the problem of defining a boundary to the control volume in the open regions must be resolved.

SUCTION PROCESS

The suction gas flow in a scroll compressor is driven by the opening and closing of the pair suction pockets. The pair of suction pockets referred to are shown crosshatched in fig.2.6 for a typical scroll compressor geometry. The volume in the suction pockets, and the inlet cross - sectional area into the pockets varies with the crank angle. During most of a scroll orbit cycle, the volume in the suction pockets increases and causes gas to be pulled into the pockets. But near the end of the orbit cycle, the volume in the pockets begins to decrease until they are abruptly closed off at the end of one complete cycle. (Note that the end of the suction process coincides with the start of the closed compression process)

To adequately model the scroll suction process, the flow dynamics into the control volume of the suction pockets must be considered. The instantaneous mass of suction gas contained within the suction pockets control volume can be defined by the time differential continuity equation.

$$\frac{d}{dt}(m_{cv}) = \dot{m}_{sp} \qquad (2.1)$$

Where : m_{cv} = mass of gas in suction pockets control volume

m_{sp} = mass of gas into or out of suction pockets

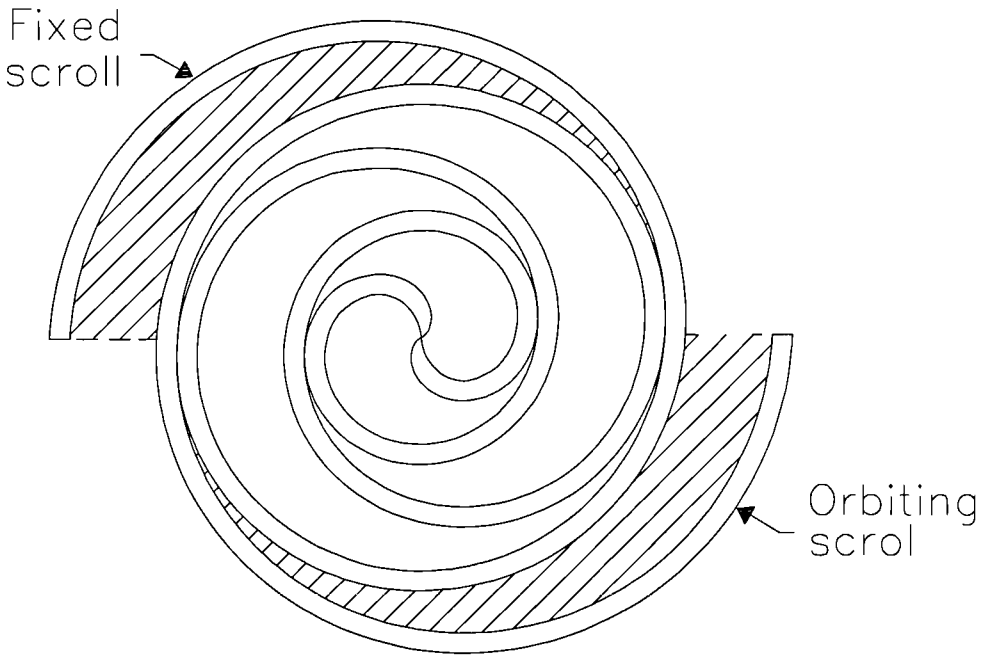

Figure 2.6 Typical pair of scroll suction pockets

The instantaneous mass flow rate of suction gas entering or leaving the control volume can be described using the steady one-dimensional, isentropic flow equation.

$$\dot{m}_{sp} = C_D \rho A_{sp} \sqrt{2(h_{up} - h_{do})} \qquad (2.2)$$

Where : C_D = Discharge coefficient for flow into or out of suction pocket

ρ = Density of gas

A_{sp}= Suction pocket cross sectional area

h_{up} = Enthalpy of gas upstream or suction pocket inlet

h_{do} = Enthalpy of gas downstream

Also, the first law of thermodynamics on a time rate basis is applied to the suction pockets control volume.

$$\frac{d}{dt}(E_{cv}) = \dot{Q} - \dot{W} + \sum \dot{m}_{in}\left[h + \frac{v^2}{2} + gz\right]_{in} - \sum \dot{m}_{out}\left[h + \frac{v^2}{2} + gz\right]_{out} \qquad (2.3)$$

Where: E_{cv} = Energy contain within the control volume

For all equations it is assumed that gas properties are uniform throughout each defined region, e.g. properties are uniform throughout the suction pockets. In applying the above equation it is reasonable to assume that the following terms are negligible and can be eliminated: heat transfer, boundary work and kinetic and potential energies. One might question why the boundary work term can be neglected since the suction pockets volume changes considerably during each cycle.

$$\dot{W} = (P_{SP} - P_{SC})\frac{d}{dt}(V_{SP}) \qquad (2.4)$$

Where: P_{SP} = Pressure in suction pockets
P_{SC} = Pressure in suction chamber
V_{SP} = Volume in pair of suction pockets

The reason is that the pressure difference across the suction pockets control volume boundary is quite small, consequently the product in the work term is negligible compared to the enthalpy terms. What is left then is the classic filling process energy equation where it is assumed the time rate change of energy in the control volume equals the time rate change of internal energy.

$$\frac{d}{dt}(u_{cv}) = \dot{m}_{sp}\, h_{up} \qquad (2.5)$$

Where: u_{cv} = Internal energy of gas in the control volume

To utilise eq. (2.2) for the mass flow rate into or out of the suction pockets the conditions in the suction pockets and the suction chamber surrounding the orbiting scroll must be known. Immediately after the start of the cycle, the volume in the pocket is still quite small. During this early part of the suction process it can be assumed that quasi - static filling of the suction pockets takes place so that at any instant in time the volume in the pockets is completely filled with gas. This assumption allows the analysis to be initiated as conditions in the suction pocket can then be defined. With the conditions in the suction pockets and suction

chamber specified, the mass flow rate into the pockets can be computed. The continuity equation then determines the instantaneous mass in the suction pockets so that the conditions in the pockets can be defined for that time increment. This process is continued until the end of the suction cycle.

What results from using this scroll suction model (Nieter J.F. & Gacne D.P. 1988) is the ability to predict the pressure rise in the suction pockets that occurs as the volume in the pockets is reduced near the end of the suction process. This increase in suction pockets gas pressure indicates that early compression takes place before the displacement volume of gas is sealed off at the start of the actual closed compression process (S.O.C). Besides predicting the early compression of suction gas, this suction process model can also produce a continuous function for instantaneous mass flow rate at suction which is important for accurate prediction of suction pressure pulsations in the manifold system.

COMPRESSION PROCESS

The compression process pertains to *"closed"* compression after the outer wrap tips seal off at SOC and continues until the inner wrap tips open at the SOD. Farther compression effectively continues after SOD, through the discharge process until EOD. Therefore the following relationships that are used to model the compression process are actually applied from SOC to EOD as well. For all process equations, it is assumed that gas properties are uniform through each region, e.g. properties are uniform throughout the compression and discharge pockets.

The instantaneous mass of gas contained within the control volume for a pair of compression pockets can be described by the differential continuity equation.

$$\frac{dm_c}{dt} = \sum (\dot{m}_{in} - \dot{m}_{out}) \qquad (2.6)$$

Where: m_c = Mass flow rate of gas in the volume

Leakage's are also included in the above equation, however a detail analysis about leakage's follows later on in this chapter.

The gas state in the control volume during the compression process normally is modeled by one of two approaches: either using the polytropic process, or using the first law of thermodynamics (energy conservation). The polytropic process model

is quite often a good approximation to employ for displacement compressors. It simply uses the relation :

$$P_c = P_{soc}^{\eta_p}\left[\frac{\rho_c}{\rho_{soc}}\right]^{\eta_p} \qquad (2.7)$$

Where: Subscript c: control volume

The greatest difficulty with this model is obtaining an accurate value for the polytropic exponent η_P , a good approach is to measure η_P in a laboratory experiment. However the first law of thermodynamics on a time rate basis can be applied to the control volume using:

$$\frac{d}{dt}(m_c u_c) = \dot{Q} - \dot{W} + \sum \dot{m}_{in}\left[h + \frac{v^2}{2} + gz\right]_{in} - \sum \dot{m}_{out}\left[h + \frac{v^2}{2} + gz\right]_{out} \qquad (2.8)$$

This approach is more difficult that the polytropic model. The general energy equation given must be reduced to usable form, typically a differential equation of gas temperature in the control volume. Further reduction of the general form involves obtaining a number of partial differentials relating enthalpy and pressure to temperature and specific volume. These are trivial for the ideal gas properties, but for real gas properties are more difficult to compute, in such cases the polytropic approach would be completely inappropriate. Finally, the greatest obstacle using eq.(8) is in obtaining reasonably accurate values of heat transfer Q. Models used for heat transfer in positive displacement compressors have been fairly documented for reciprocating piston types, but much less so for other types, and almost not at all for scroll compressors.

DISCHARGE PROCESS

The instantaneous mass flow rate of discharge gas exiting or back-flowing into the control volume can be described using the steady, one dimensional isentropic flow equation for a nozzle.

$$\dot{m}_D(\theta) = \rho_D A_D C_D \sqrt{2gd(h_{up} - h_{do})} \qquad (2.9)$$

Where: A_D = Discharge port area

C_D = Appropriately chosen flow coefficient

As stated previously, the relationships used to model the state of gas in the control volume during the discharge process are the same as those used during the "closed" compression process.

Gas pulsation's in compressors manifolds have a significant effect upon suction and discharge processes. Modeling this interaction between the discharge flow process and the manifold pressure pulsation's can be accomplished in a number of ways. Probably the most powerful and flexible of these approaches is the transfer matrix which is performed in the frequency domain.

In the transfer matrix approach, pressure pulsation's are modelled by combining the steady state acoustical impedance description of the manifold with an acoustical source: the oscillatory gas flow in or out of the port. Since the mass flow rate through the discharge port is a periodic function of time or crank angle, it can be represented by a finite Fourier series.

LEAKAGES

Minimizing leakage from the compression chamber is a significant subject in any type of compressor.

Compression chambers of the scroll compressor are the spaces configurationaly formed between the fixed scroll wrap and the orbiting scroll wrap, so there occurs clearance through the fine clearances from the higher pressure chamber to the lower pressure chamber, as shown in fig.2.7. There are two kinds of leakage, one is the radial flow through the axial clearance, and the other one is the tangential leakage flow through radial clearance. In the scroll compressor, leakage from the higher to the lower pressure pockets is the largest factor governing both the volumetric and adiabatic efficiencies.

1-D APPROACH

Considering only the leakage between the tips and bases, flow rates that include frictional effects are determined using (Gaillat J. L. 1988):

$$\dot{m} = A_{bt}\sqrt{2\Delta_p \rho_u D_h/(fL)} \qquad (2.10)$$

Where: A_{bt} = Leakage flow area between tips and bases

Δ_P = Inter pocket pressure difference

ρ_u = Upstream density

D_h = Hydraulic diameter

f = Friction factor - Moody

L = Inter pocket tip/base leakage path

To solve this equation iteration is required since the friction factor f, is dependent on the Reynolds's number, which in turn is dependent upon mass.

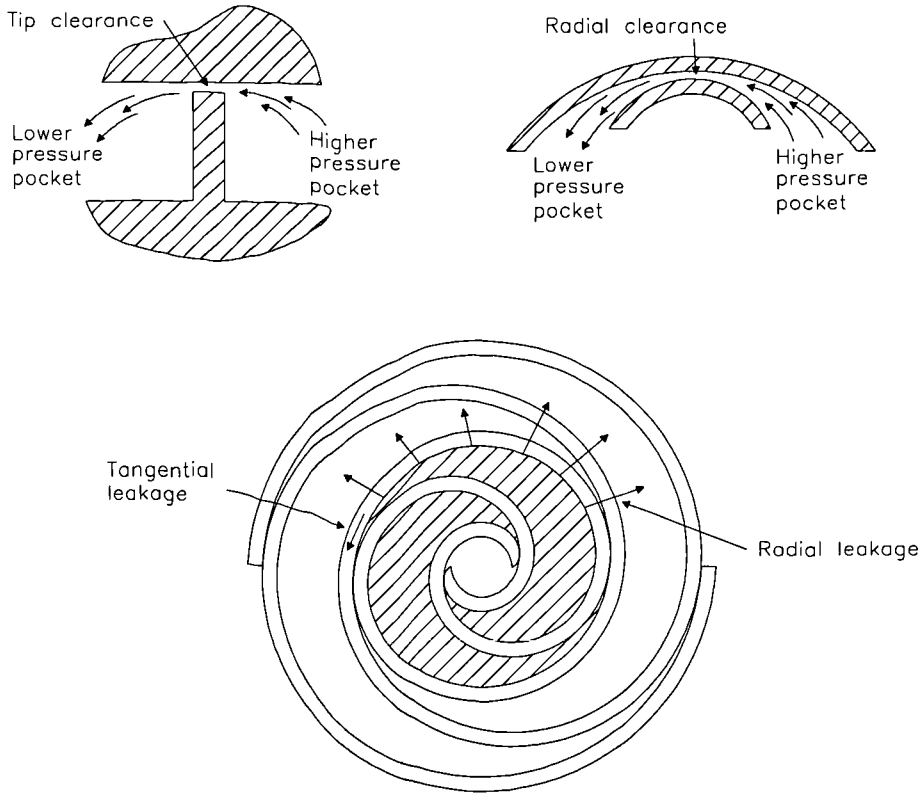

Figure 2.7 Leakages in a scroll machine

Flank leakage is modeled as a converging nozzle. With a known pressure difference and flank clearance, an assumption of isentropic steady-state compressible flow yields.

$$\dot{m} = KA_f\sqrt{P_u\rho_u\,{}^{2}/_{(\gamma-1)}\left[R_p^{\,2/\gamma} - R_p^{\,\gamma+1/\gamma}\right]} \qquad (2.11)$$

Where: K = Contraction coefficient - empirical

A_f = Leakage flow area between vane flank surfaces

P_u = Upstream pressure

R_P = Down stream to upstream pressure ratio

The deficiency of the 1-D inviscid model is that viscous effects, while important, are neglected. On the other hand, purely 1-D viscous flow (stokes flow) ignores the convection effect, which may be significant when the pressure gradient is large.

To fully understand the flow through clearances, an approach based on computational fluid dynamics (CFD), made by Yong H. 1994 is presented here. The aim was to calculate the detailed flow field, including velocity, pressure and mass flow across the clearance and assessing the threshold as to when a quasi 1-D model is sufficient enough to predict the mass flow. The set-up of the problem is illustrated in fig.2.8 One dimensional models or quasi 1-D models can be a good approximation only when the ratio δ/L is very small.

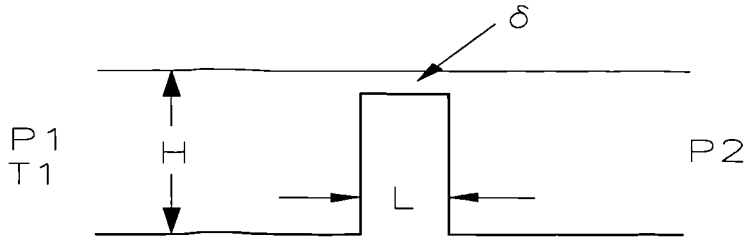

Figure 2.8 Tip clearance geometry

2-D APPROACH

Two dimensional Navier Stokes equations are used to calculate the flow field. The flow is assumed to be compressible, viscous and laminar. The ideal gas law is employed as the equation of state. The system of partial differential equations governing this type of flow is described as follows in non-dimensional form for Cartesian co-ordinate.

$$\frac{\partial Q}{\partial t}+\frac{\partial E}{\partial x}+\frac{\partial F}{\partial y}=\frac{1}{\mathbf{Re}}\left[\frac{\partial Ev}{\partial x}+\frac{\partial Fv}{\partial y}\right],$$
$$P=(\gamma-1)\left[\rho-\frac{1}{2}\rho(u^2+v^2)\right], \quad a^2=\gamma\frac{p}{\rho}. \qquad (2.12)$$

Where: $Q = [\rho, \rho_u, \rho_v, e]^T$

$E = [\rho_u, \rho_u{}^2+P, \rho_{uv}, u(e+p)]^T$

$F = [\rho_v, \rho_{uv}, \rho_v{}^2+p, v(e+p)]^T$

ρ is density, u and v are velocity components, e is total energy, P is pressure, a is the speed of sound and γ is the ratio of specific heats. Reynolds's number Re is defined as: $Re = \rho_1 a_1 H/\mu_1$. The viscous terms are:

$$E_v = \begin{bmatrix} 0 \\ \tau_{xx} \\ \tau_{xy} \\ u\tau_{xx} + v\tau_{xy} + \mu p_r^{-1}(\gamma-1)^{-1}\dfrac{\partial a^2}{\partial x} \end{bmatrix} F_v = \begin{bmatrix} 0 \\ \tau_{yx} \\ \tau_{yy} \\ u\tau_{xx} + v\tau_{xy} + \mu p_r^{-1}(\gamma-1)^{-1}\dfrac{\partial a^2}{\partial x} \end{bmatrix} \quad (2.13)$$

Where shear stress: $\tau_{xy} = \mu\left(\dfrac{\partial u}{\partial y} + \dfrac{\partial v}{\partial x}\right)$, etc.

and Pr is Prandtl number. The viscosity follows Sutherland's law:

$$\frac{\mu}{\mu_\infty} = \left[\frac{T}{T_\infty}\right]^{3/2} \frac{T\infty + 110}{T + 110} \quad (2.14)$$

A finite volume method was used to discretize eq.(12) so that a system of algebraic equations for five unknown variables (ρ, u, v, p, e) were derived. With the appropriate upstream boundary conditions where total pressure and temperature were specified and downstream conditions where static pressure was set, the equations are integrated to steady state using Mac-Cormac method; which is second order accurate. Upstream and downstream locations are defined as some distance up and down the step (about 10 H).

2.3 Two Phase Expanders

A vapour compression refrigeration system is characterised by the direct two-phase expansion of the entire flow, from the exit of the condenser to the entrance of the evaporator. Fig.2.9 illustrates the cycle on a T-S diagram.

With reference to basic fundamental thermodynamic principles it can be stated that this process (expansion) has the ability to produce a specific amount of work. However since the fluid expands entirely in the two phase area, it is necessary to design and develop an expander which could accept a two phase flow of liquid and gas at reasonable efficiency and reliability.

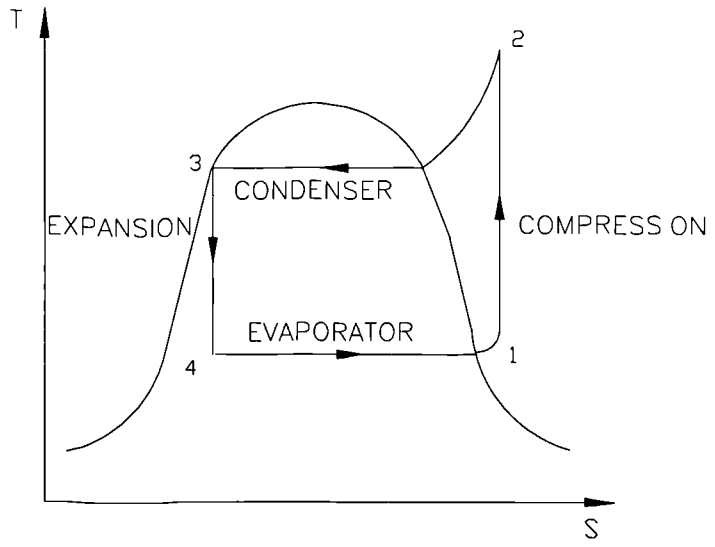

Figure 2.9 Refrigeration cycle with isentropic expansion

Up to date a lot of work is been done to develop two phase expanders that could be used to substitute throttle valve and recover some power from the expansion process in a refrigeration cycle. Two phase expanders such as biphase turbines, and screw expanders have been developed, however efforts to develop and produce scroll expanders started recently, and not much information is available.

Instead of throttling the refrigerant to produce cold liquid, the refrigerant could be expanded in a two phase expander. The work conventionally lost in the irreversible throttling process could be recovered as shaft power, which could in turn assist in driving a second compressor (or the main compressor). The electricity consumption for refrigeration could be reduced by approximately 10% also the coefficient of performance will be increased by 13%. Apart from the above application two phase expanders could be used in low grade heat recovery (Trilateral Flash Cycle).

It is a well known fact that conventional turbines and reciprocators are not suitable for the expansion of hot liquids in this manner since liquid droplets erode turbine blades and reduce the aerodynamic efficiency of the turbine, while they wash the lubricating oil off the cylinder walls of reciprocating expanders and so promote wear and seizure of the mechanism. Therefore some alternative methods have been investigated for this purpose. These are:

1. Scroll expander
2. Lysholm total flow expander
3. Specially designed two phase turbines

2.3.1 Scroll Expander

In recent years, scroll machinery has been put into practice as compressors, taking advantage of their higher efficiency and their low noise/vibration. However the scroll principle can be applied also to the expansion process.

Unfortunately not much work is been done on scroll expanders. However the very small and limited amount of work that has been done is concerning only the single phase flow.

In 1988 Yanagisawa et. al. published a paper (in Japanese) with the title "study on fundamental performance of scroll expander". Equations of volume pressure and output torque were derived. Moreover, practical losses which occur in the scroll expander were analysed theoretically. It was also shown that the leakages through axial clearances increase the flow rate of the expander and decrease the torque greatly. An experimental scroll expander was also developed and showed reasonable performance and recorded its maximum efficiency of 75%.

In 1992 Morishita et. al. used the scroll principle to develop a scroll expander to use it in the Otto cycle spark ignition engine. The theory and experience of the scroll compressor was extended to an engine with a scroll compressor and a scroll expander. The scroll compressor compresses the air fuel mixture, and the scroll expander is used to get power from the heat of the combustion. The flow is continuous and uni-directional. Which is different from that of the reciprocating engine. Although the Brayton cycle engine is possible with a scroll compressor and expander, the temperature of the scroll expander could be extremely high due to the continuous combustion. The requirement of the scroll material was becoming very severe. The spark ignition engine was therefore studied in their report, based on the air standard Otto cycle.

PRINCIPLE

The scroll engine Morishita recommends consists of two main components, the scroll compressor and the scroll expander. The elements were assumed to have the same geometric dimensions and to be synchronised via a proper mechanism. After several degrees of rotation, the compressed air-fuel mixture discharge is to commence. The volume of the combustion chamber (innermost) of the scroll compressor is minimum at this angle, actually is zero. The discharge port of the scroll compressor and the combustion chamber of the scroll expander were

connected via a discharge valve, the compressed air-fuel mixture is transferred to the combustion chamber of the scroll expander. The volume change rate of the two connected chambers is the same during the transfer process. The discharge valve is then closed this corresponds to the end of the compression process.

The air fuel-mixture is ignited in the combustion chamber of the scroll expander. The combustion is assumed to take place instantly. The pressure of the combustion chamber of the scroll expander increases suddenly. The orbiting scroll of the expander is therefore driven by the high pressure of the combustion gas. The gas pressure decreases during expansion. This corresponds to the expansion process. The expansion ends when the gas reaches the outermost chamber. The gas is then exhausted from the expander.

Another paper on the scroll expanders was published by the Swiss Federal Institute of Technology on 1994. That paper describes a 1 to 3.5 kW hermetic scroll expander-generator modified from a standard hermetic scroll compressor, an organic Rankine cycle test facility build to test up to 10 kW, and a set of experimental results using HCF134a in the dry vapour domain. Peak overall isentropic efficiencies in the range of 63% to 65% for speeds of rotation varying 2400 and 3600 rpm were reported.

2.3.2 Lysholm Total Flow Expander

The idea to use a Lysholm twin screw machine as a direct two-phase expander (of geothermal brines) stems from the patents of Sprankle [1973][1976]. The Lysholm design consists of a pair of parallel rotors with meshing helical lobes which form compression or expansion chambers in the casing. This configuration was patented in Sweden by Lysholm in 1934. The design has found its main use as a heavy duty air compressor known for its reliability. The use of the Lysholm design as an engine has been suggested at several times, including the suggestion for its use in geothermal energy conservation. Lysholm [1967] had earlier proposed his machines for dry gas expanders.

The Lysholm twin screw expander is a positive displacement machine which operates by the direct expansion of fluids. With the aid of fig.2.10 the principle of operation of the expander can be described as follows. The pressurized fluid flows through the throttle T and enters the high pressure pocket formed by the meshed rotors, the rotor case bores and the case face. This pocket designated by A in the

figure, is mostly hidden by the rotor lobes, but it can be seen in the plan section view. As the rotors turn, the pocket elongates, splits into a V, and moves away from the inlet port to form the region designated by B. With continued rotation, the V lengthens, expanding successively to C,D and E as the point of meshing of the rotors appears to retreat from the expanding fluid. The expanded fluid at a low pressure is then discharged into the exhaust port. Energy is extracted from the fluid in the process. Engine geometry determines the theoretical volumetric expansion ratio, which is the ratio of the final to the initial chamber volumes.

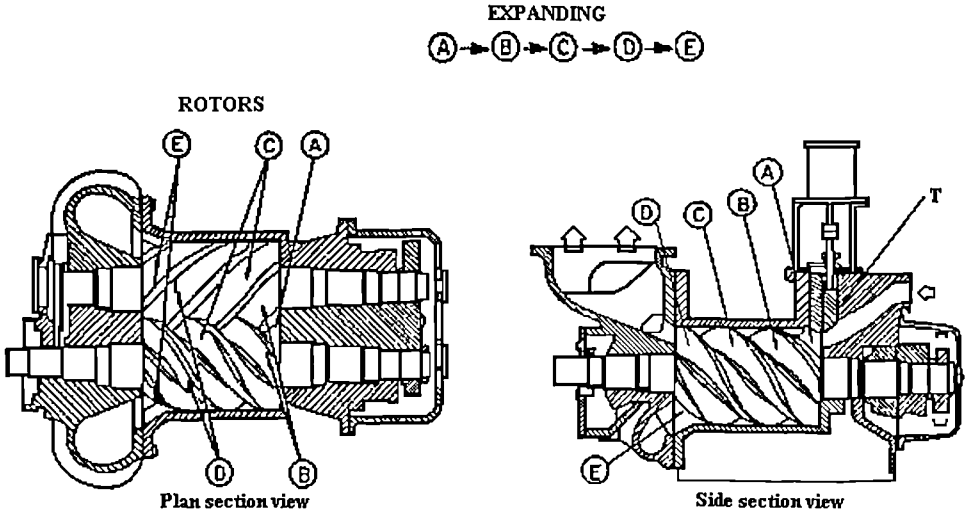

Figure 2.10 Layout of Lysholm screw Expander

Testing of the Lysholm engine has since been conducted by the Lawrence Livermore Laboratory (LLL), by the Jet Propulsion Laboratory (JPL), and by the department of Mechanical Engineering at University of California, Berkely. The unit tested was an air compressor with 152.4 mm rotors modified by Sprankle. A maximum efficiency of 55% was observed for a power output of 30 kW at 5000 rpm. Latterly a smaller version of this (130 mm rotors) was build from which a maximum expander efficiency of 53% was obtained at 47 kWe output (Steidel [1982]). Despite extensive experimental work, there had been a general lack of theoretical analysis on the Lysholm screw expander. Steidel proposed an empirical model using curve fitting. More recently Taniguchi et al [1988] developed an analytical method for estimating the performance of a two phase screw expander. The operation of a screw expander was simulated by the expansion of a fluid between two pistons with appropriate leakage paths. Good agreement was obtained against the experimental results from a prototype machine with a

diameter of 81.6 mm and a length of 135 mm. However, the various frictional losses and the two phase interaction were not accounted in the procedure.

2.3.2.1 City University And Lysholm Expander

Besides the work world wide, a research programme on two phase expanders was initiated by Smith at City University, London beginning in late 1982. This was intended primarily as a means of improving power recovery from geothermal resources. The work concentrated on the development of twin-screw expanders using suitable organic fluids operating in a closed cycle system.

A unique test rig was constructed and on it twin screw expanders attained adiabatic efficiencies of more than 70% at power as low as 25 kW when operating in the two phase mode. In addition to the experimental work, a programme of analytical studies was developed from earlier work on the computer modeling of screw compressor performance carried out at the university of Sarajevo by Stosic.

Smith and Stosic concluded from their investigation that the failure of the earlier investigators to get good results was entirely due to the design of such machines with inappropriate build in volume ratios. However, they also examine the possibility to replace the throttle valve in the refrigeration cycle with a screw expander. They obtained an overall adiabatic efficiency for the expander, including bearing, seal and timing gear losses, to be of the order of 70% over a large range of operating conditions.

2.3.3 Two Phase Turbines

During the same period, work was initiated at JPL and LLL to seek an alternative efficient two phase expander system aimed at overcoming the restrictions imposed by the positive displacement type machines. Austin [1973] and his geothermal group at the LLL proposed a two-phase impulse turbine for geothermal application in which the two phase brine from geothermal wells would be passed though the turbine. It was hoped that the water drops would be small enough for the steam and water to behave as a homogeneous fluid and give these turbines efficiencies comparable to those of vapour turbines. However the detail calculations on drop sizes and trajectory showed that the liquid drops in two phase turbines would be too large to follow the gas phase, and that the liquid would impinge on the blades and form a thin liquid film. The friction drag of this film would be so high that the

efficiency of single-stage impulse turbines would be limited to little more than 50%.

As a result of low efficiencies achieved by two phase impulse turbines a rotary separator turbine was developed by Biphase Energy Systems [1982]. The basic idea was to replace the throttle valve with a separator system in the traditional flashed steam cycle system. In place of the throttle valve, the geothermal fluid is expanded in a two phase nozzle with an adiabatic efficiency of around 90%. The high velocity liquid and vapour so formed are then separated in a rotary drum. The steam is then passed to the steam turbine, while the liquid is either used in a liquid turbine to produce additional power or pressurised in a diffuser to reduce the re injection power. This rotary separator turbine was investigated and tested in the laboratory and at three geothermal resources. The machines were reported to operate well and a power gain of some 20 -25% more than that from a single flash system was achieved. A maximum adiabatic efficiency of the separator system of 35% was measured although it was predicted that improved designs with up to 50% efficiency were attainable in the future. It was thought that the impact and other losses in the rotary separator would limit the turbine efficiency as severely as the liquid friction in blade turbines.

Further work on a specially designed two-phase turbine was attempt by Elliot [1982] at the JPL using either steam for total flow or organic fluids. The two phase turbine utilised a uniform mixture of liquid and gas accelerated in a two-phase nozzle which is similar in design to that used in the rotary separator turbine. The mixture acts directly on an axial flow or tangential impulse turbine. Based on this concept he predicted an upper limit efficiency of about 65% for two phase turbines, and probably only attainable with organic working fluids. This prediction could not be justified by the extensive experimental program carried out on both JPL and LLL, which showed that this efficiency was not attainable and a maximum efficiency of only 55% was achieved using organic fluids. However it was found that the JPL two-phase nozzle study calculated velocities which are within 2 - 4 percent of measured values and the nozzle showed good performance over a wide range of operating conditions.

Carrier [1994] introduced in their chiller plant a device using a high efficiency two phase nozzle, followed by separation of the liquid and vapour components for independent power recovery. This biphase turbine is introduced as a throttle valve replacement. The adiabatic efficiency recorded is 50% and the turbine is linked

directly to the main compressor to reduce the power output to the electric motor. Gains in COP of 3 - 5% are stated to be possible by this means. See figure 2.11.

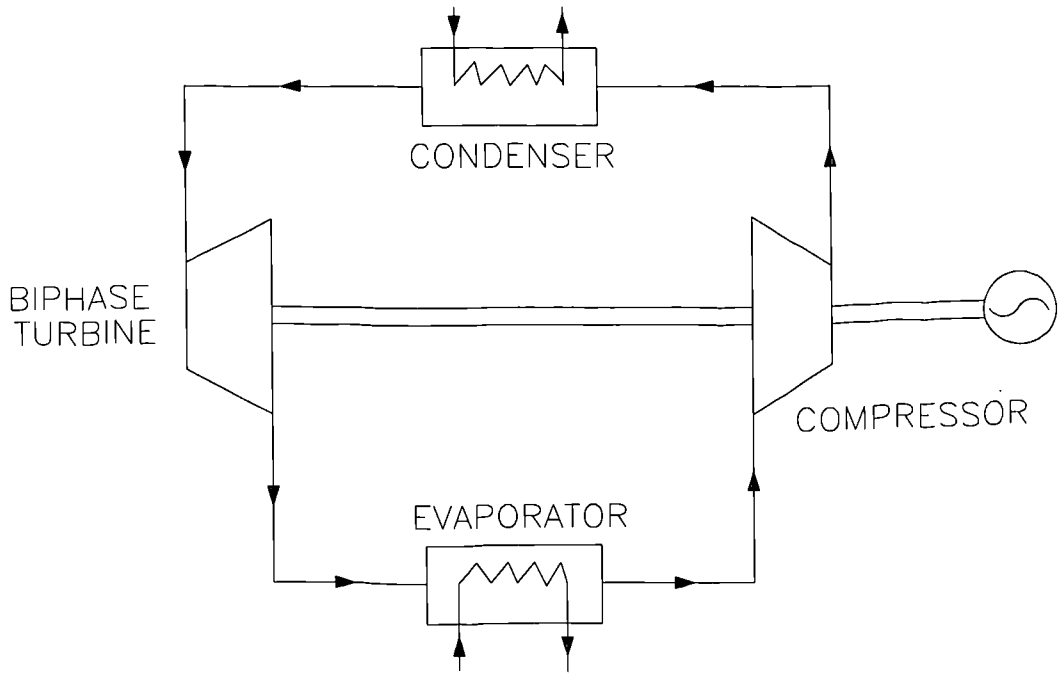

Figure 2.11 Refrigeration cycle, Carrier

As it was said above, Carrier has linked the expander with the compressor and therefore the expander run at the same speed as the compressor. This might result in a not so good working performance of the expander for the case where the system will run at off design conditions. This thesis uses a completely different way to recover the work from the expander.

2.4 Conclusions

Since the expansion process in the vapour compression cycle occurs entirely in the two-phase region, a mechanical expander which can operate with two phase mixtures and operate at high efficiency is the most important part of this study, because the success of the whole project depends upon this. As it can be seen from the literature review the need to design and develop a machine like this still exists.

As is the case for all rotary volumetric principles, reverse motion is inherently possible and, therefore the conversion of scroll compressor to scroll expander can be envisaged. Smith's investigation for this type of machine indicated that the machines most applicable for the expansion of a two phase flow are the Lysholm twin screw expander and the scroll expander.

Scroll expanders present definite advantages over potential volumetric machines. In addition, the reduced number of parts, the ability to cope with two phase working fluids and the inherent reliability proven in compressor mode are major reasons for its wider use in energy recovery. The fast growing mass production of such units as compressors is likely to also contribute to a lowering of the production costs for expander applications.

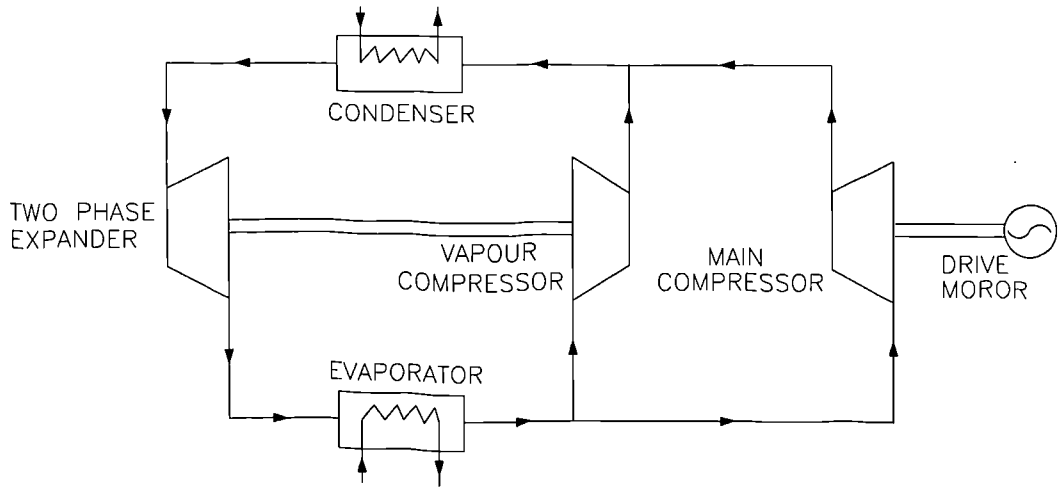

Figure 2.12 The proposed cycle

What is recommended by this project is instead of coupling the expander with the main compressor, introduce a second smaller compressor that will run in parallel with the main one. All the work that will be produced from the expander in terms of shaft power will be used to drive this new compressor which in turn will contribute to the mass flow rate. This design appears to be more complicated than the one Carrier uses, but the main reason is the performance of the expander at off design conditions. The cycle is illustrated above (figure 2.12).

Chapter 3

Quasi One Dimensional Flow Modeling

3.1 Introduction

In this chapter we describe the computation of thermodynamics and flow process in a scroll compressor and a scroll expander with reference to Stosic's work. This chapter discusses also the results from the Quasi 1-D flow modeling. The importance of the relationship between built-in volume ratio and pressure ratio and the use of the correct pressure ratio is clearly defined. The significant point is that the built-in volume ratio is a constant for any given scroll compressor or expander design but the pressure ratio, which is a function of the gas being compressed or expand is not. Speed also affects the relationship between pressure and volume ratios.

Therefore, while it would be convenient to identify a compressor - expander by its build-in pressure ratio since this is the basis of the correct selection for efficiency, it is not practical to do so unless the compressor - expander is always going to operate on only one gas. This is the case with air compressors so that typically these use the pressure ratio for identification, whereas gas or refrigeration compressors normally use the built in volume ratio. The feature of the "built-in volume ratio" has been treated on the basis that it is a constant value in scroll machinery. While this is true in the majority of cases, it is possible to incorporate into the compressor - expander features which enable it to be varied. (such as controlling the opening - closing of the discharge port)

The linking of a scroll expander to a scroll compressor in a sealed 'Expressor' unit is also described in this chapter. This may be used both in new systems and for retrofit applications in place of a throttle valve. The results of computer simulations of Expressor performance in a large industrial chiller are shown.

3.2 Theory

The equation set consists of the conservation equations for energy and mass continuity together with a number of algebraic equations defining various phenomena, which accompany the fluid suction, compression and discharge. The mathematical model employs the differential kinematics relationship which describes the instantaneous operating volume and its change with the rotational angle, as well as the equations of conservation of the mass and the energy for the adopted control volume. These are applied for each phase of the process that the fluid is subjected to: suction, compression and discharge. The solution of the equation set is performed numerically by employing the Runge-Kutta 4^{th} order method.

The model takes also into account the following effects:

- The working fluid can be any ideal or real gas or liquid gas mixture of known properties (internal thermal energy , enthalpy).
- Inevitable leakage of the working medium which occur at any stage of the process through axial or radial clearances is taken into account.
- Account can be taken of the effect of liquid such as oil, water or refrigerant injecting during suction, expansion or discharge for lubricating, sealing or cooling purposes.

3.2.1 Assumptions

Some assumptions need to be made in order to ensure an efficient computation, these are:

- The fluid flow is assumed to be quasi-one dimensional.
- Gas or gas-liquid mixture inflow or outflow through the compressor suction or discharge port was assumed isentropic.
- The leakage of the fluid through the clearances is assumed to be adiabatic.

3.2.2 Conservation Equations

The main difference of this model (comparing with other models) is the use of the non-steady flow rather than the steady flow energy equation. Stosic proved that this practice is computationally beneficial in evaluating the properties of real fluids, as compared with the conventional methods using enthalpy as the dependent variable.

Non-Steady Flow Energy Equation: $$\left(\frac{du}{d\phi}\right)_V = \left(\dot{m}\,h\right)_{in} - \left(\dot{m}\,h\right)_{out} + \dot{Q} + \dot{W} \qquad (3.1)$$

Where: ϕ = Crank angle.

$h = h(\phi)$ Specific enthalpy.

$\dot{m} = \dot{m}(\phi)$ Mass flow rate.

$\dot{Q} = \dot{Q}(\phi)$ Heat transfer between fluid and sarroundings.

$\dot{W} = P\frac{dv}{dt}$ Thermodynamic work supplied to the gas.

ENERGY GAIN DUE TO THE GAS INFLOW $[mh]_{in}$

The energy gain due to the gas inflow into the working chamber is represented by the product of the mass intake, and its average enthalpy. As such the energy inflow varies with the crank angle. During the suction period gas enters the working volume bringing the average gas enthalpy which dominates in the suction chamber. While this process is taking place, a certain amount of the compressed gas leaks into the working chamber through the axial and radial clearances. The mass flow rate of the leaking gas as well as its enthalpy are determined on the basis of the gas leakage equations.

Total inflow enthalpy is also affected by the amount of enthalpy flow into the working chamber in the case of oil injection. Therefore if oil is injected into the working chamber, the oil mass inflow together with its enthalpy must be included in the inflow terms.

The mass inflow rate consists of :

$$\dot{m}_{in} = \dot{m}_{suc} + \dot{m}_{l.g} + \dot{m}_{oil} \qquad (3.2)$$

Where $\dot{m}_{suc}$ = Suction mass flow rate.

$\dot{m}_{lg}$ = Mass flow rate due to leakage gain.

$\dot{m}_{oil}$ = Mass flow rate due to the injection of oil.

The velocity of the oil depends on the amount of oil injected. The velocity of the leaking gas will be analysed later on this chapter. Now as far as the suction fluid velocity is concerned the following equation is used:

$$\omega = \mu\sqrt{2(h_2 - h_1)} \qquad (3.3)$$

Where μ is the suction coefficient, assumed to take a value of μ =0.6 While "1" and "2" denote conditions upstream and downstream of the considered port.

The fluid total inflow component consists of the following components:

$$\left(\dot{\mathbf{m}}\,\mathbf{h}\right)_{in} = \left(\dot{\mathbf{m}}_{suc}\,\mathbf{h}_{suc}\right) + \left(\dot{\mathbf{m}}_{l.g}\,\mathbf{h}_{l.g}\right) + \left(\dot{\mathbf{m}}_{oil}\,\mathbf{h}_{oil_{in}}\right) \qquad (3.4)$$

ENERGY GAIN DUE TO GAS OUTFLOW $[mh]_{in}$

The energy loss due to the gas outflow from the working volume is defined by the product of the mass outflow and its average gas enthalpy. During the compression this is the gas which leaks through the clearances from the working chamber into the neighbouring chambers at a lower pressure, where as in the case of delivery this is the gas entering the discharge plenum.

The mass outflow rate consists of:

$$\dot{\mathbf{m}}_{out} = \dot{\mathbf{m}}_{dis} + \dot{\mathbf{m}}_{l.l} \qquad (3.5)$$

where $\dot{\mathbf{m}}_{dis}$ = Discharge flow rate.

$\dot{\mathbf{m}}_{l.l}$ = Mass flow rate due to leakage loss.

The discharge fluid velocity can be calculated by the use of equation 3.3 but with the appropriate discharge coefficient μ. Therefore the fluid total outflow enthalpy consists of:

$$\left(\dot{\mathbf{m}}\,\mathbf{h}\right)_{out} = \left(\dot{\mathbf{m}}_{dis}\,\mathbf{h}_{dis}\right) + \left(\dot{\mathbf{m}}_{l.l}\,\mathbf{h}_{l.l}\right) \qquad (3.6)$$

Each of the mass flow rates satisfies the continuity equation:

$$\dot{m} = V\rho A \qquad (3.7)$$

Where: V [m/s] denotes fluid velocity

ρ [kg/m^3] fluid density

A [m^2] the flow cross section area and

The mass continuity equation of the model is :

$$\left[\frac{dm}{dt}\right] = \dot{m}_{in} - \dot{m}_{out} \qquad (3.8)$$

HEAT TRANSFER [Q]

The heat exchange between the fluid and the compressor/expander tip and casing (and through it to the surrounding) due to the difference in temperatures of gas and casing and spiral surfaces is accounted for by the heat transfer coefficient evaluated from the expression:

$$\mathbf{Nu} = \mathbf{0.023\,Re^{0.8}} \qquad (3.9)$$

Here the surface over which the heat is exchanged, as well as the wall temperature depend on the crank angle. The characteristic velocity for Re number is computed from the local mass flow and the cross sectional area.

WORK SUPPLIED [W]

The thermodynamic work supplied to the gas during the compression process is represented by:

$$\dot{W} = P\left(\frac{dv}{dt}\right) \qquad (3.10)$$

Where : P = Pressure in control volume
dv/dt = Working volume

3.2.3 Gas Leakage

The leakages in a scroll machine affect the total flow rate and therefore play an important role because they influence the process by affecting the mass flow rate (and therefore the volumetric efficiency), and the work efficiency. Two types of leakages according to their direction with respect to the working chamber exists: gain and loss leakages. The loss leakage leave the working chamber towards neighbouring chamber with lower pressure. On the other hand gain leakages come from the neighbouring working chamber which has a higher pressure.

The fluid flow through the clearance is taken into account for the computation of the leakage velocity. The process is essentially adiabatic (Fanno flow). The present model treats only the gas, no attempt is made to account for leakages of gas-liquid

mixture. The clearance gap is assumed to have a rectangular shape and the mass flow of the leaking fluid is expressed by the continuity equation:

$$\dot{m}_l = \mu_l V_l \rho_l A_g = \mu \gamma_l A_g \qquad (3.11)$$

where: $\gamma_l = V\rho$ -The mass velocity of the leaking gas
$A_g = l_g\ \delta_g$ -The clearance ("gap") cross sectional area
l_g -The leakage clearance length (sealing line)
δ_g -The leakage clearance width ("gap")
μ_l(Re,Ma) -The "discharge" coefficient.

The computation of the leaking gas velocity follows from the momentum equation which accounts for the fluid wall friction:

$$\omega \mathbf{d}\omega_1 + \frac{\mathbf{dp}}{\rho_1} + \mathbf{f}\frac{\omega_1^{\,2}}{2}\frac{\mathbf{dx}}{\mathbf{Deg}} \qquad (3.12)$$

Where: f(Re,Ma) is the friction coefficient (dependent on Re and Mach number)
Deg is the effective diameter of the clearance gas (Deg ≈ 2δg)
dx is the length increment

From the continuity equation (and assuming that T ≈ constant to eliminate gas density in terms of pressure) the equation can be integrated in terms of pressure from high pressure side (position "2") to the lower pressure side (position "1") of the gap to yield:

$$\gamma_1\left[{}^{kg}/_{rad}\right] = \omega_1\rho_1 = \frac{1}{\omega}\sqrt{\frac{\mathbf{P_2}^2 - \mathbf{P_2}^2}{\mathbf{RT_2}\left[\zeta + 2\ln\left({}^{P_2}/_{P_1}\right)\right]}} \qquad (3.13)$$

Where $\zeta = \mathbf{f}\frac{\mathbf{L_g}}{\mathbf{Deg}} + \sum \xi$ characterizes the flow resistance (3.14)

L_g = clearance length in the leaking flow direction
f = friction factor and
ξ = local resistance coefficient

ζ can be evaluated for each clearance gap in function of its dimensions and shape and flow Re and Ma numbers. The full procedure would require incorporation into model of the friction and drug coefficients in terms of Re and Ma number for each

type of clearance. However Stosic recommends a value of $\zeta \approx 0.6$.

3.2.4 Oil Injection

Injection of oil or other liquids for lubrication, or sealing purposes, modifies substantially the thermodynamic process in a scroll machine. A convenient parameter to define the injected oil mass flow is the oil to gas mass ratio, m_{oil}/m_{gas} In addition to lubrication major purpose for injecting oil is the cooling of the gas.

In the present model the heat exchange with the gas is determined from the differential equation for the instantaneous heat transfer between the surrounding gas and an oil droplet. Assuming that the droplets retain a spherical form, with a prescribed Sauter mean diameter ds, the heat exchange between the droplet and gas can be expressed in terms of a simple cooling law:

$$\mathbf{Q_o = h_o A_o\left(T_{gas} - T_o\right)} \qquad (3.15)$$

Where: A_0 is the droplet surface $A_0 = (ds^2\,\pi)$

ds^2 is the mean Sauter diameter of the droplet and
h_0 is the heat transfer coefficient determined from the empirical expression

$$\mathbf{Nu = 2 + 0.6\,Re^{0.6}\,Pr^{0.33}} \qquad (3.16)$$

The exchanged heat must balance the rate of change of heat taken or given away by the droplet in the unit time.

$$\mathbf{Q_o = m_o C_{oil}\frac{dT_o}{dt} = m_o C_{oil}\omega\frac{dT_o}{d\phi}} \qquad (3.17)$$

Where C_{oil} is the oil specific heat and the index "o" denotes oil droplet. The rate of change of oil droplet temperature can be expressed now as:

$$\mathbf{\frac{dT_o}{d\phi} = \frac{h_o A_o\left(T_{gas} - T_o\right)}{m_o C_{oil}\omega}} \qquad (3.18)$$

A simplified integration of the equation between the two time (angle) steps yields the new oil droplet temperature at each new time (angle) step:

$$T_o = \frac{T_{gas} + kT_{ob}}{1+k} \tag{3.19}$$

Where: T_{ob} is the oil droplet temperature at the previous time step k is the non-dimensional time constant of the droplet, $k = \tau\omega / \Delta\phi$ with $\tau = m_o C_{oil} / h_o A_o$ being the real time constant of the droplet. For the given mean Sauter diameter ds the non-dimensional time constant takes a form:

$$k = \frac{m_o C_{oil}\omega}{h_o A_o \Delta\phi} = \frac{ds}{6}\frac{C_{oil}}{h_o}\frac{\omega}{\Delta\phi} \tag{3.20}$$

The obtained droplet temperature is further assumed to represent the average temperature of the oil, i.e. $T_{oil} \approx T_o$, which is further used to compute the enthalpy of the gas-oil mixture.

Because the inclusion of a complete model of droplet dynamics would unnecessarily complicate the computer code, Stosic developed and used the above described simplified approach. The inputs parameters are only the mean Sauter diameter of the oil droplets, ds and oil properties - density, viscosity and specific heat.

3.2.5 Computation Of Fluid Properties

For the ideal gas, the internal (thermal) energy of the gas oil mixture is given by:

$$u = \frac{mRT_{gas}}{\gamma - 1} + (m_{cv}T)_{oil} = \frac{Pv}{\gamma - 1} + (m_{cv}T)_{oil} \tag{3.21}$$

Where R is the gas constant. The pressure and temperature of the fluid in the working chamber can be explicitly calculated by the help of the equation for oil.

$$\text{Temperature: } T = \frac{(\gamma - 1)(1+k)u(m_{cv}T)_{oil}}{(1+k)mR + (m_{cv})_{oil}} \tag{3.22}$$

PROPERTIES OF REAL GASES

For the case of a real gas the situation is more complex. Many gases differ in their properties from ideal gases. The above theory is based on the compression of ideal gases. In the application of industrial compressors allowances have to be made where possible for the differences between real and ideal gases.

Real gases do not behave exactly in the manner of ideal gases, and in some

instances the differences can be quite significant, particularly when the pressure and temperature are in the region of the critical conditions.

Accurate equations of state are inconvenient for everyday calculations because they lead to unwieldy expressions. They are most used for the preparation of tables and diagrams of properties. When tables are not available, and for conditions where the perfect gas laws are too inaccurate, correction factors may be applied to the perfect gas relations. Thus the equation of state, for example, can be written as

$$\mathbf{Z} = \frac{\mathbf{pv}}{\mathbf{RT}} \qquad (3.23)$$

where $\mathbf{Z}$ is the *compressibility factor*. The value of this factor depends upon the gas and it is also a function of the pressure and temperature. The combination of $\mathbf{Z} = \phi(\mathbf{p}, \mathbf{T})$ and the above equation is the complete characteristic equation.

3.3 Results of the 1-D Flow Modeling

As it was stated earlier in this study the Quasi One Dimensional Flow Modeling was performed with the aid of an advance commercial package called *"SCORPATH"*, written by Professor N. Stosic. The performance characteristics over a wide range of speed and other operating conditions have been analysed.

3.3.1 Scroll Compressor

The function of the compressor is to raise the pressure of the vapour leaving the evaporator to a value at which its corresponding saturated vapour pressure is high enough to enable heat to be rejected to its surroundings by means of a condenser.

Because in a scroll compressor the opening of the delivery port is determined entirely by the geometry of the machine, there is a certain build - in volume ratio and a corresponding build in pressure ratio for a particular gas. If the pressure in the working chamber has not reached the pressure in the delivery pipe when the port is uncovered, gas flows back into the working chamber. On the other hand, if the pressure inside the working chamber at the instant of opening exceeds that of the delivery pipe, gas rushes out suddenly at an unresisted expansion. In either event there is a loss of efficiency.

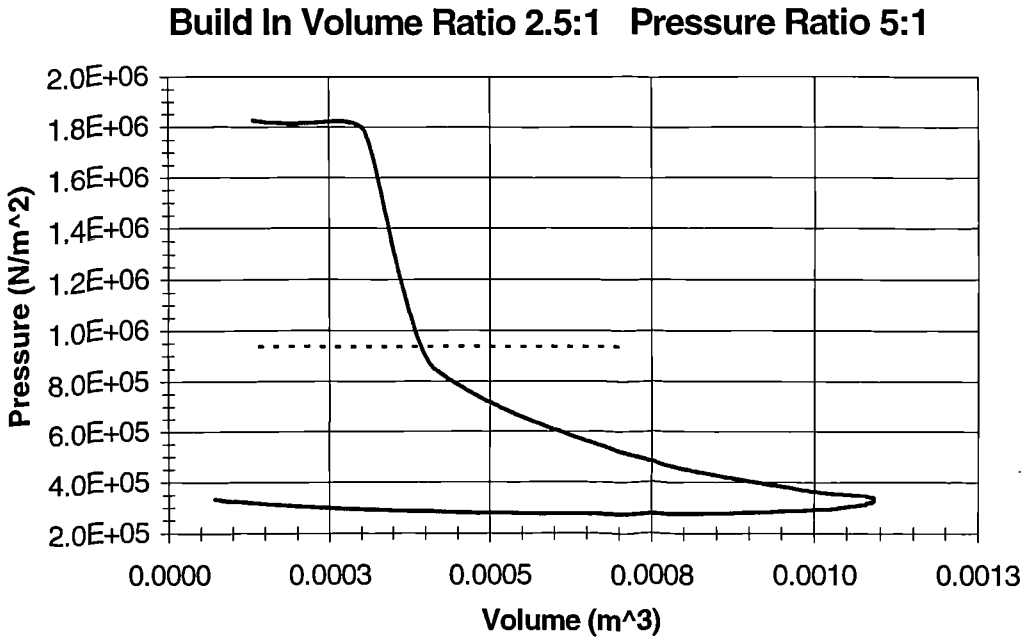

Figure 3.1 Pressure - Volume diagram for condition where system pressure ratio is much greater than build in Volume ratio. Speed 3000 RPM. Working fluid R134A, dry vapour.

Ideally the build - in pressure ratio should match the actual pressure ratio for maximum efficiency but this is not possible in practice because a compressor in any given installation may have to operate at different pressure ratios, depending on the *evaporating and condensing temperatures*. Nevertheless there is usually one pressure ratio which corresponds to average or design conditions and the machine can be designed for this.

In figures 3.1 to 3.4, the pressure-volume and pressure-angle diagrams corresponding to the conditions of greater and smaller pressure ratio, than the build in volume ratio are shown. The dramatic increase in scroll pocket pressure shortly after the start of discharge due to the strong back flow is apparent in figures 3.1 and 3.2. This back-flow effect results in an increase in compressor power over what would be required if the compressor pressure ratio matched the system. The area located under the curve and above the dashed line in figure 3.1 represents this increase in compression power. The total compression power is proportional to the enclosed pressure-volume area.

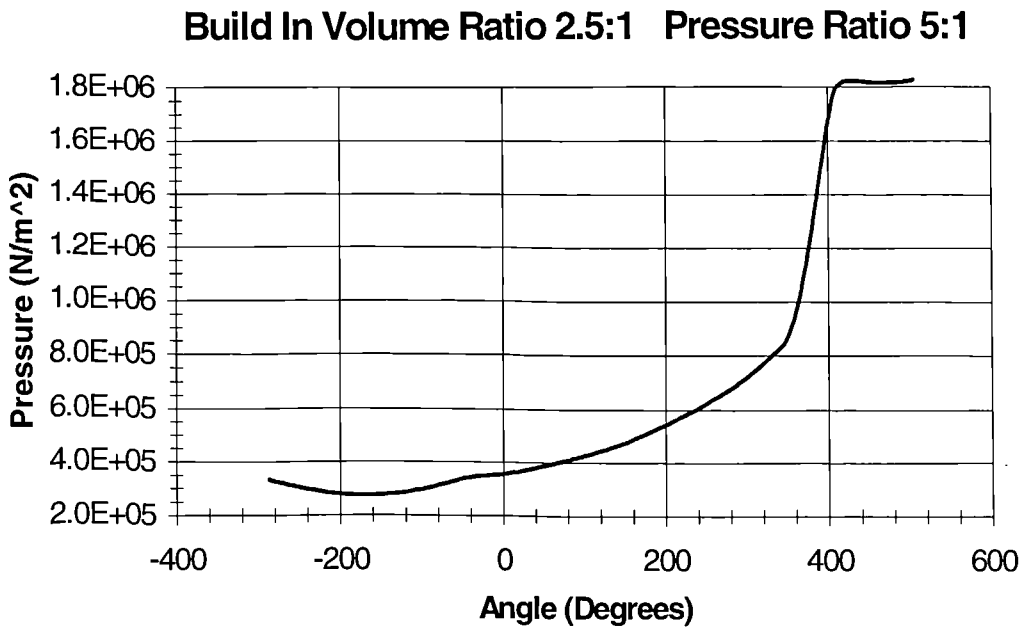

Figure 3.2 Pressure - Angle diagram for condition where system pressure ratio is much greater than build in volume ratio. Speed 3000 RPM. Working fluid R134A dry vapour.

In figures 3.3 and 3.4, the pocket pressure after the start of discharge increases more gradually due to normal flow and over-pressure before peaking and then slowly decreasing back to discharge pressure. There is no increase in power due to back flow, only the increase in power due to over-pressure. Generally speaking the area between the discharge pocket curve and the discharge pressure curve for both cases (greater-lower pressure ratios) represents the increase in compression power due to over-pressure.

As was said above there is an average pressure ratio that corresponds to the build in volume ratio of the machine. Figures 3.5 and 3.6 illustrates this. As it can be seen from these figures there is not any major decrease or increase on the pressure after the discharge port is open. This is because there is more pressure equilibrium between the discharge pipe and the chamber.

During the suction period which is quite long some fluctuations on the pressure were recorded, this is due to the fact that some gas might flow backwards due to the pressure difference caused from the opening of the suction port. Now as far as the compression is concerned figures 3.5 and 3.6 shows that the process which takes long appears to be very smooth. This is because the momentum term ρV^2 is small since gas density is not large.

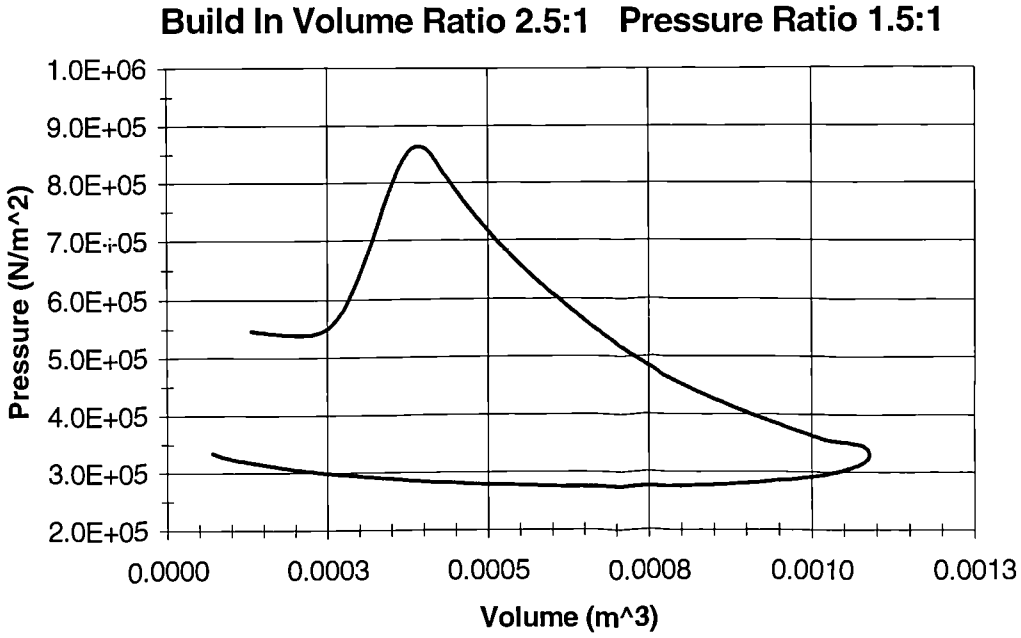

Figure 3.3 Pressure - Volume diagram for condition where system pressure ratio is less than build in Volume ratio. Speed 3000 RPM. Working fluid R134A dry vapour.

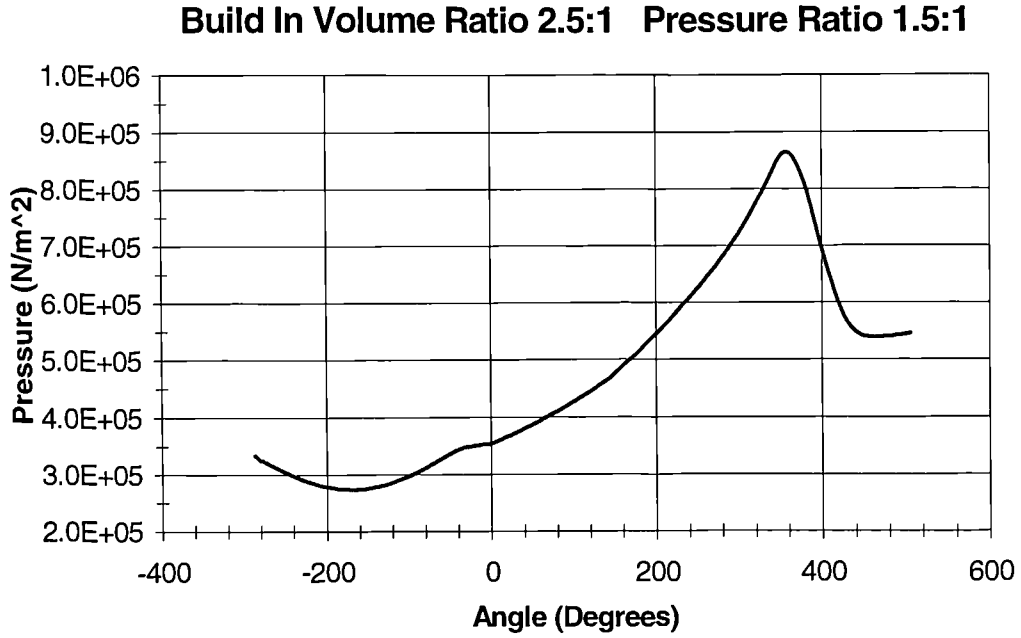

Figure 3.4 Pressure - Angle diagram for condition where system pressure ratio is less than build in Volume ratio. Speed 3000 RPM. Working fluid R134A dry vapour.

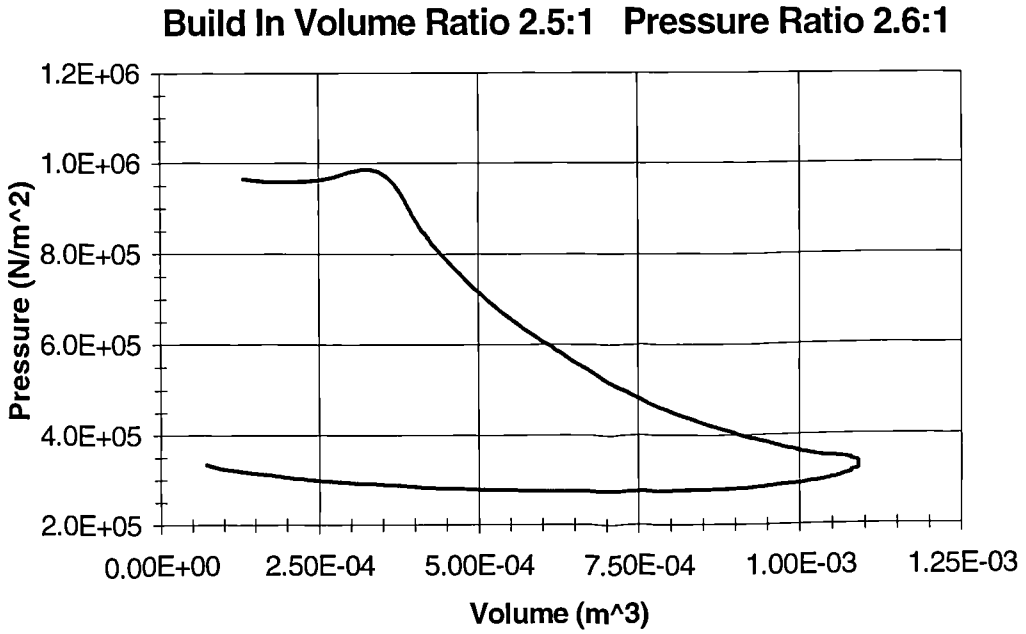

Figure 3.5 Pressure - Volume diagram for condition where system pressure ratio is the same with the build in Volume ratio. Speed 3000 RPM. Working fluid R134A dry vapour.

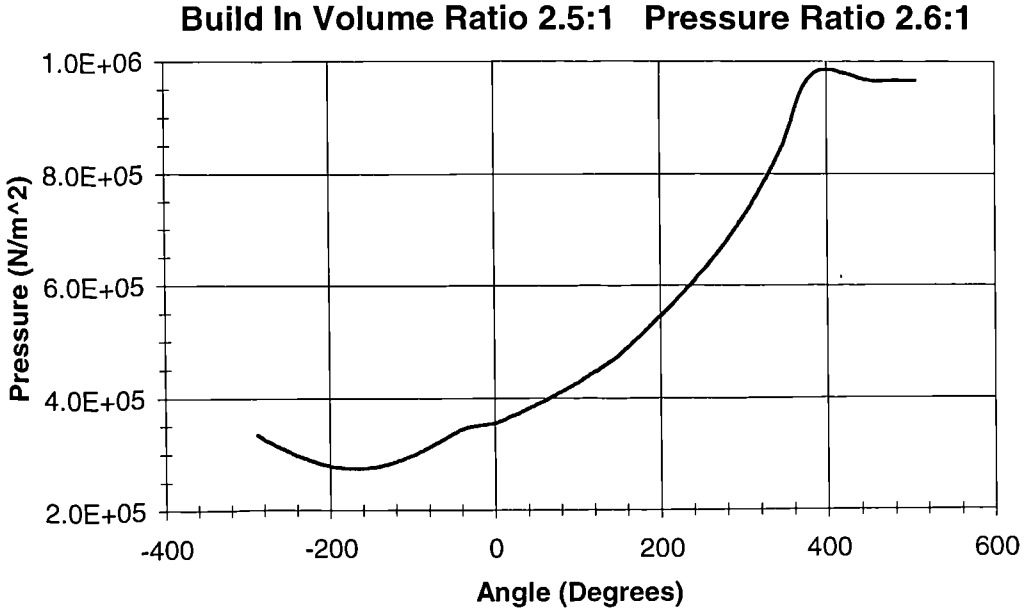

Figure 3.6 Pressure - Angle diagram for condition where system pressure ratio is the same with the build in Volume ratio. Speed 3000 RPM. Working fluid R134A dry vapour.

The relationship between build-in volume ratio and build-in pressure ratio and individual gas properties is also important. The physical situation is that a scroll compressor has a built-in volume ratio. It draws in volume of gas V_1 and reduces this internally to a smaller volume V_2. The build-in volume ratio is therefore the ratio of these, i.e.

$$\mathbf{V_R} = \frac{\mathbf{V_1}}{\mathbf{V_2}}$$

However, we have already seen that the optimum efficiency occurs when the pressure ratio is approximately the same with the built-in volume ratio. The significant point is that the build-in volume ratio is a constant for any given compressor design but pressure ratio is not. **Z** is a function of the gas being handled. For an isentropic compression process we have

$$\frac{\mathbf{P_2}}{\mathbf{P_1}} = \left(\frac{\mathbf{V_1}}{\mathbf{V_2}}\right)^{\gamma}$$

where γ is the isentropic index of the gas concerned, i.e. C_p/C_v. The isentropic index varies quite widely for different gases, typical examples at atmospheric pressure and temperature being: [O'Neill, P. A. 1993 Industrial compressors pp. 309]

Fluid	γ
Propane	1.14
Ammonia	1.29
Air	1.4
Helium	1.63

Thus if a compressor has a build-in volume ratio of 3.5:1 the build in pressure ratio with the above gases would be:

Fluid	Pressure ratio
Propane	4.17
Ammonia	5.03
Air	5.77
Helium	7.71

If however, we are dealing with a polytropic process then the equation will become

$$\frac{\mathbf{P_2}}{\mathbf{P_1}} = \left(\frac{\mathbf{V_1}}{\mathbf{V_2}}\right)^{\eta}$$

and the pressure ratio will depend on the value of η. Raymon, L., et. al. 1988

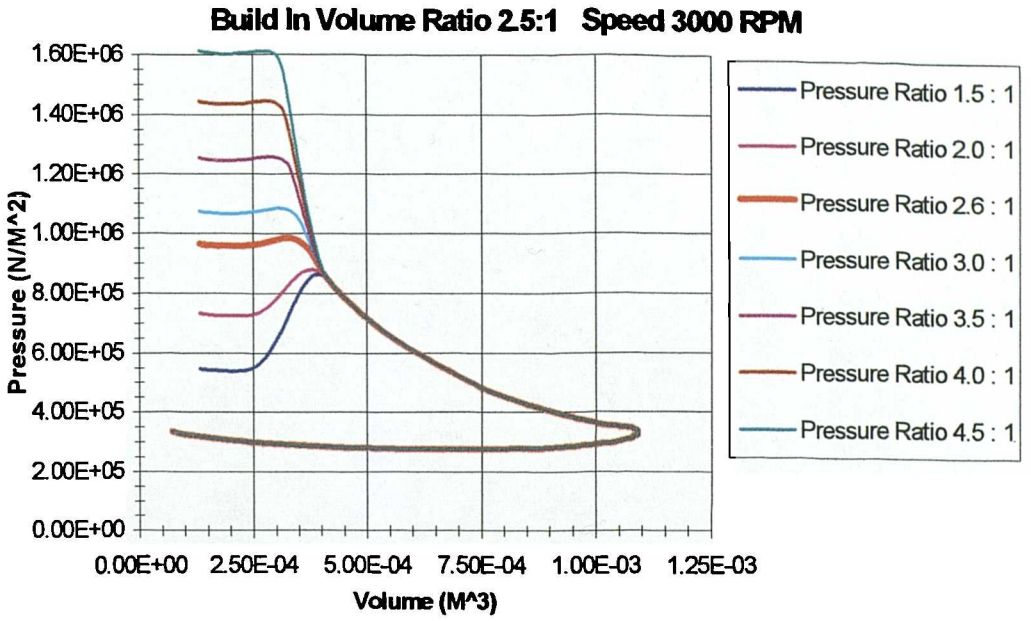

Figure 3.7 Pressure - Volume diagram for different pressure ratios. Working fluid R134A dry vapour.

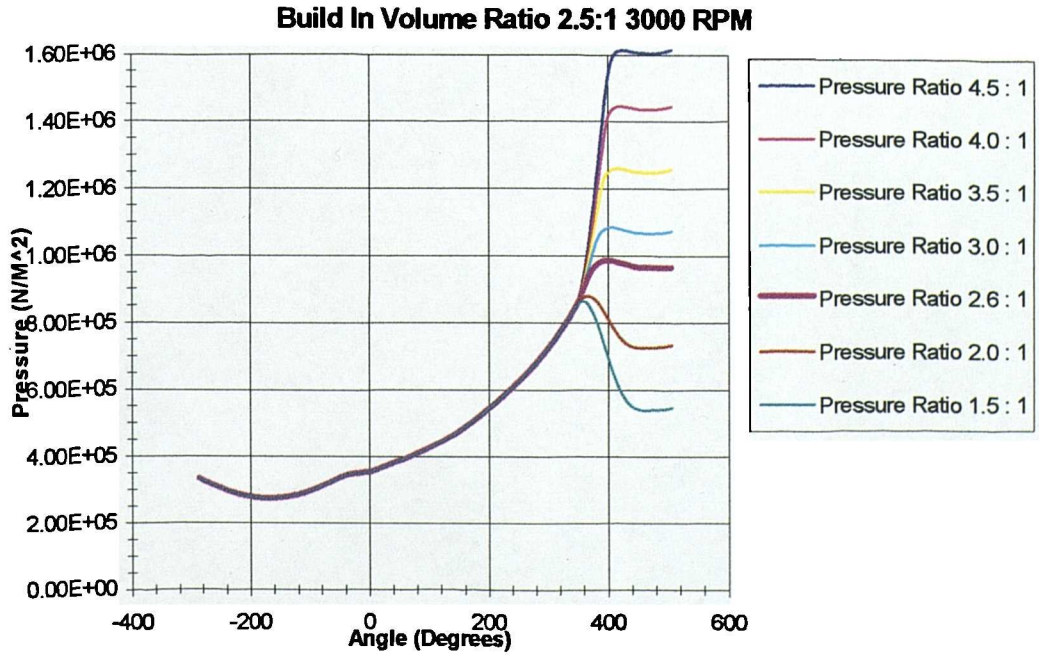

Figure 3.8 Pressure - Angle diagram for different pressure ratios. Working fluid R134A dry vapour.

Figures 3.7 and 3.8 shows influence of operating pressure ratio, on the pressure curve. Under the ideal condition the discharge pressure changes in a stepwise manner at the start of the discharge process. At higher pressure ratio operation, the discharge pressure rises smoothly as an extension of the compression process and the over- compression becomes small as the pressure ratio increases. On the other hand over-compression becomes very large at an operating pressure ratio lower than the build-in pressure ratio.

Figure 3.9 shows relationships between adiabatic and volumetric efficiencies for different pressure ratios. The pressure ratio at which adiabatic efficiency peaks depends on the built-in volume ratio as noted earlier. An optimum operating pressure ratio moves to low pressure ratio with increasing leakage. The reason is that the leakage loss becomes large as the operating ratio increases. The characteristic of volumetric efficiency versus pressure ratio is quite different. The back leakage increases a little with increasing pressure ratio but only to a small degree. There are also leakage and fluid injection effects which greatly affect the choice of volume ratio for a given pressure rise.

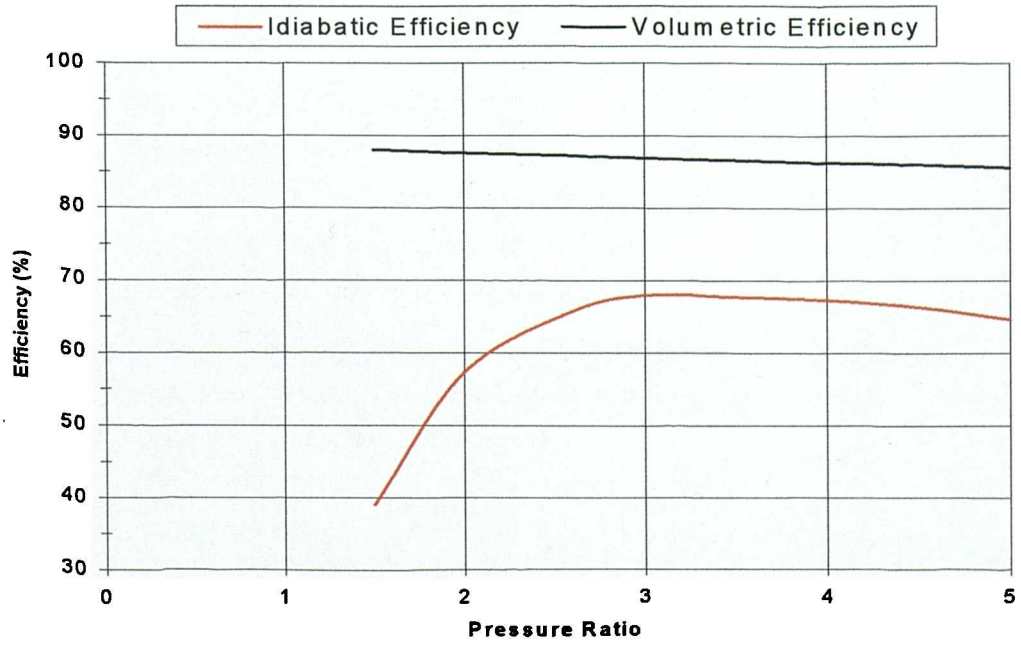

Figure 3.9 Efficiencies - Pressure Ratio. Speed 3000 RPM, Build In Volume Ratio 2.5:1. Working fluid R134A dry vapour.

As the scroll compressor is a positive displacement machine, the discharge pressure is not dependent on compressor speed, however Rotational Speed can be used to control the capacity of the machine. Ideally this would be true only if there is no leakage. Figure 3.10 shows the influence of the rotational speed on the pressure curve. As the rotational speed increases, the discharge pressure increases. On the other hand, pressure during suction process becomes slightly low but pressure during compression is almost the same. This is due to the leakage, which is influenced by the rotational speed. Leakage takes place between the radial (flank) and tangential (tip) clearance. Both kinds of leakage raise the delivery temperature, because the vapour which is throttle back to a lower pressure is subsequently recompressed adiabatically. A sudden rise in delivery temperature is a sign of excessive leakage. The presence of oil is an important factor in achieving good sealing

The influence of leakage on the scroll compressor performance is mainly indicated in the compression power and the volumetric efficiency, which is the ratio of the volume flow rate to the theoretical delivery. The leakage through tip clearance, increase the pressure during the compression process but lessens somewhat the

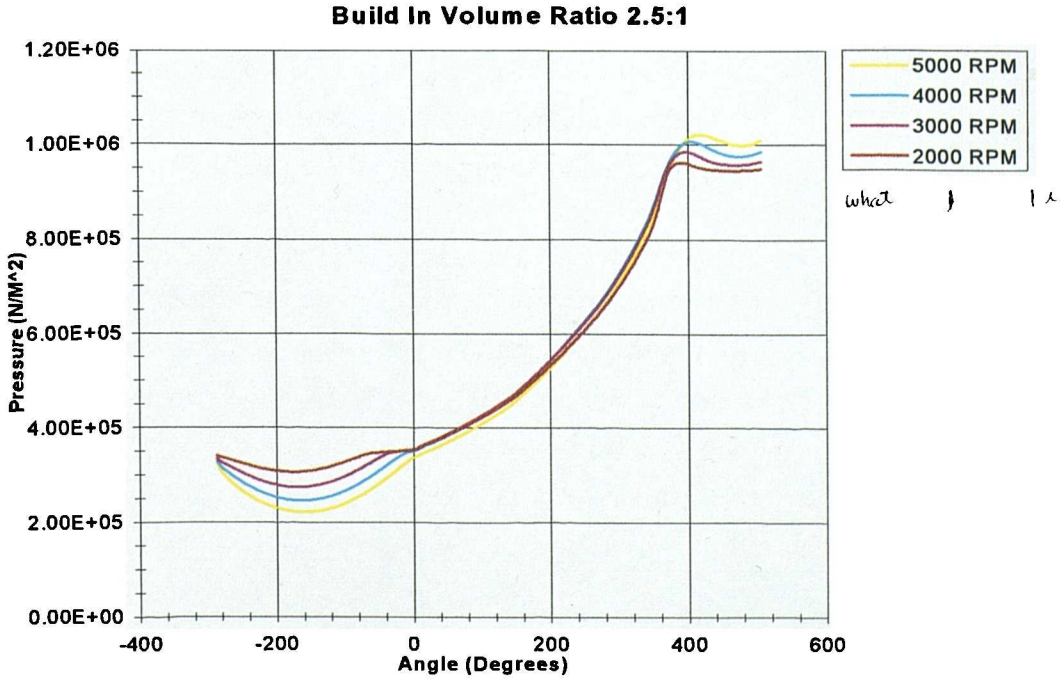

Figure 3.10 Pressure - Angle diagram for different rotational speed. Working fluid R134A dry vapour.

over-compression during the discharge process. On the other hand, the leakage through flank clearance, accelerates the pressure rise during a later part of the compression process and increases the succeeding over-compression. When both the leakages are considered, the compression pressure increases.

Figure 3.11 shows that the volumetric efficiency increases with increasing rotational speed though it decreases at extremely high speed operation. Figure 3.12 shows that power and mass flow rate also increase with speed. Figures 3.13 and 3.14 shows how the mass flow rate and the power of the compressor change when system is working at off design conditions.

Increasing of rotational speed increases an over-compression loss at low pressure ratio operation but moderates an under-compression loss at high pressure ratio operation, which leads to a higher optimum operating pressure ratio. Therefore, dimensions of scroll wrap must be selected such as it has a maximum efficiency at an actual operating pressure condition by taking into account of rotational speed and leakage.

Most refrigeration systems reject heat to the atmosphere, and the ambient conditions change throughout the year. Process refrigeration plants that operate year round are particularly subjected to a wide range of condensing temperatures. The response of a scroll compressor to changes in condensing temperature is analyzed here. Firstly the behavior of the machine was examined by varying the condensation temperature and keeping fixed the evaporating temperature. This forces the compressor to operate at off design conditions, as far as the operating pressure ratio is concern.

Figure 3.15 shows the changes in the adiabatic and volumetric efficiency for a scroll compressor as a function of condensing temperature, for an evaporating temperature of -10^{0}C. As the temperature increases the volumetric efficiency drops off. On the same figure the increase of the pressure ratio due to the increase of the condensation temperature, and therefore pressure is shown. The remaining important characteristic is the power, shown on Figure 3.16. The work of compression in kJ/Kg increases as the condensing temperature increases.

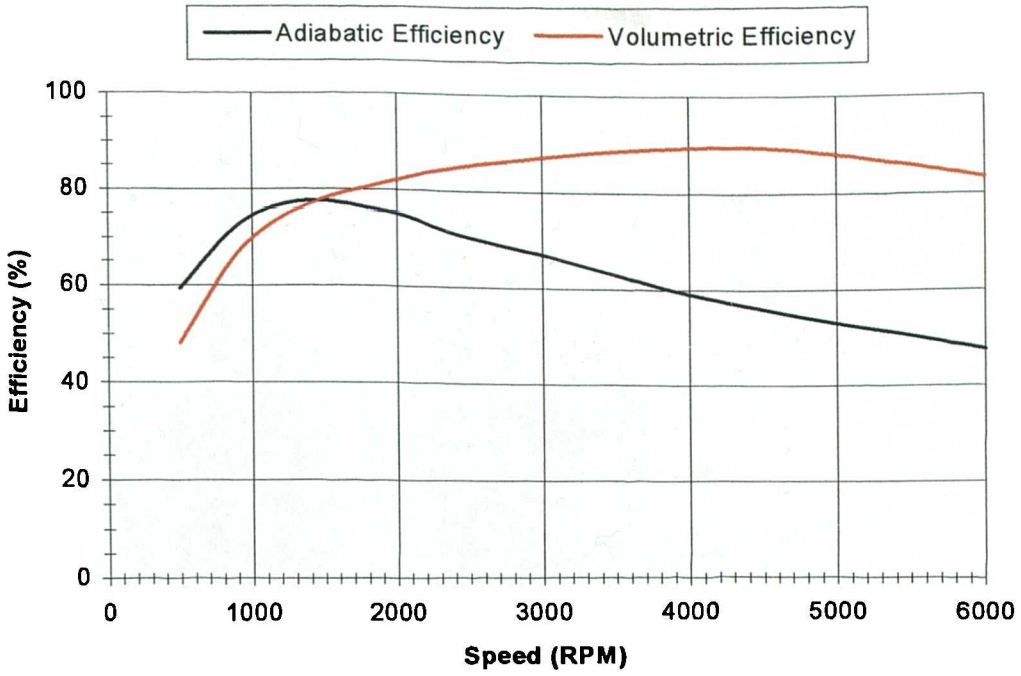

Figure 3.11 Efficiencies - Speed. Working fluid R134A dry vapour.

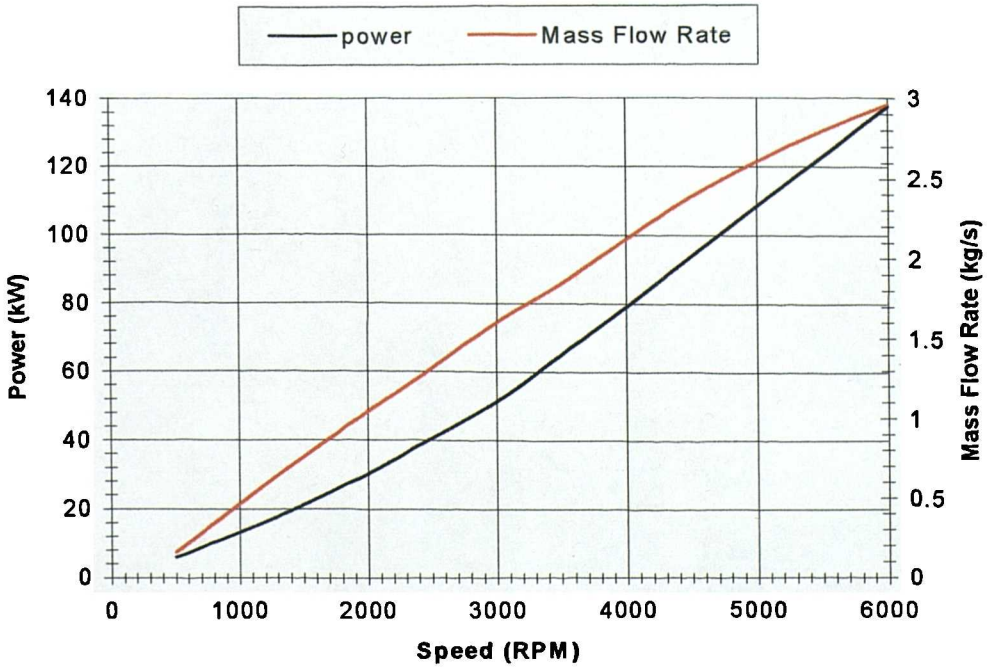

Figure 3.12 Power / Mass Flow Rate - Speed. Working fluid R134A dry vapour.

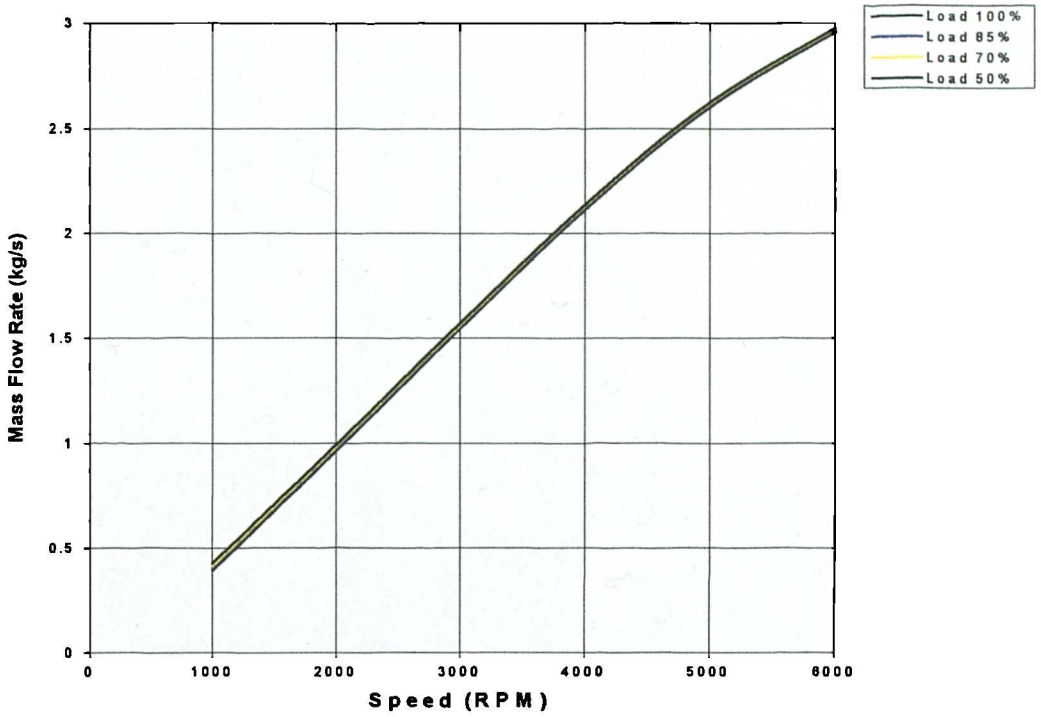

Figure 3.13 Mass Flow/Rate-Speed. Working fluid R134A dry vapour. Different load conditions

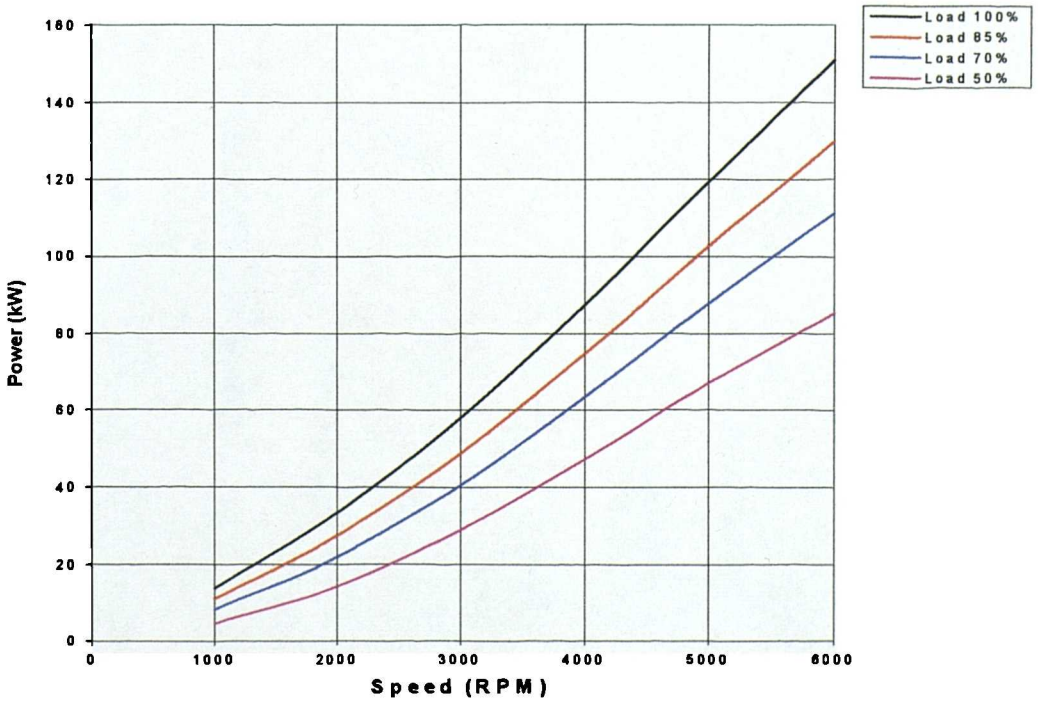

Figure 3.14 Power / Mass Flow Rate - Speed. Working fluid R134A dry vapour. Different Load conditions

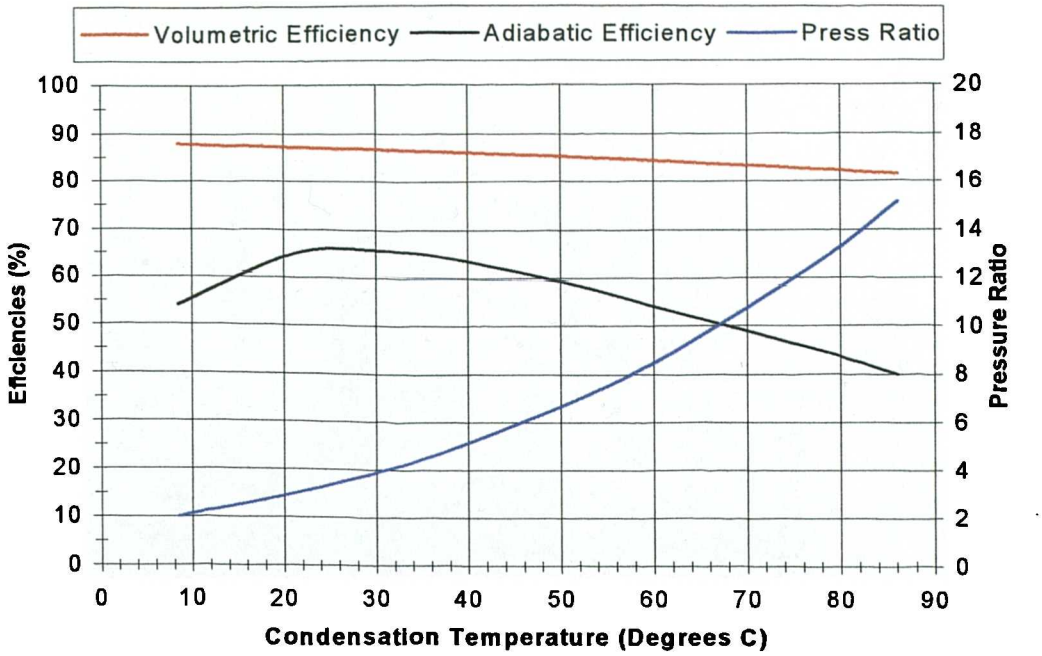

Figure 3.15 Efficiencies / Condensation Temperature. With fixed evaporating Temperatures and therefore varying pressure ratios. Working fluid R134A dry vapour.

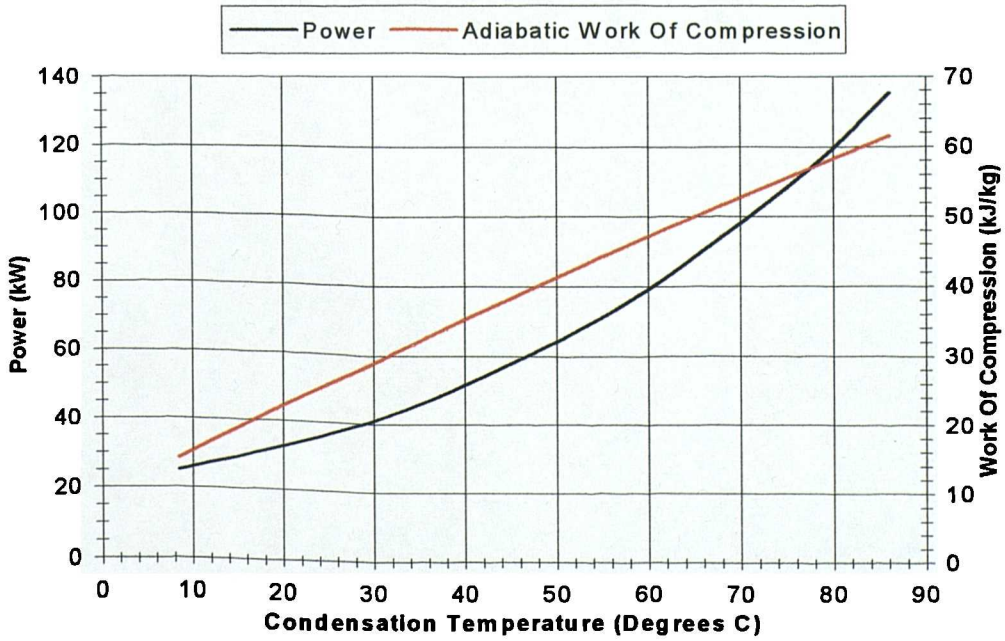

Figure 3.16 Power-Work of Compression / Condensation Temperature. With fixed evaporating Temperatures and therefore varying pressure ratios. Working fluid R134A dry vapour.

Figures 3.17 and 3.18 shows the behavior of the machine for different condensation temperatures but fixed operating pressure ratio. This was achieved by varying both the condensing and evaporating temperatures. As it can be seen from figure 3.17 the volumetric efficiency remains approximately the same, and the adiabatic efficiency appears to be better than the one in figure 3.15. Figure 3.18 shows that the adiabatic work of compression remains approximately the same. The Indicated power curve follows a similar trend to that of figure 3.16 but with match greater range.

A few comments on the significance of the trends in Figs. 3.15 to 3.18 follow. With more moderate differences between the condensing and evaporating temperatures the expectation is that the power required by the compressor will increase with an increase in condensing temperature. The refrigerating capacity always decreases with an increase in condensing temperature. Another important characteristic which is not shown on the graphs is the coefficient of performance, which decreases monotonically as the condensing temperature increases.

From the standpoint of power and efficiency, a low condensing temperature is desirable; thus condensers should use the coldest air or water available.

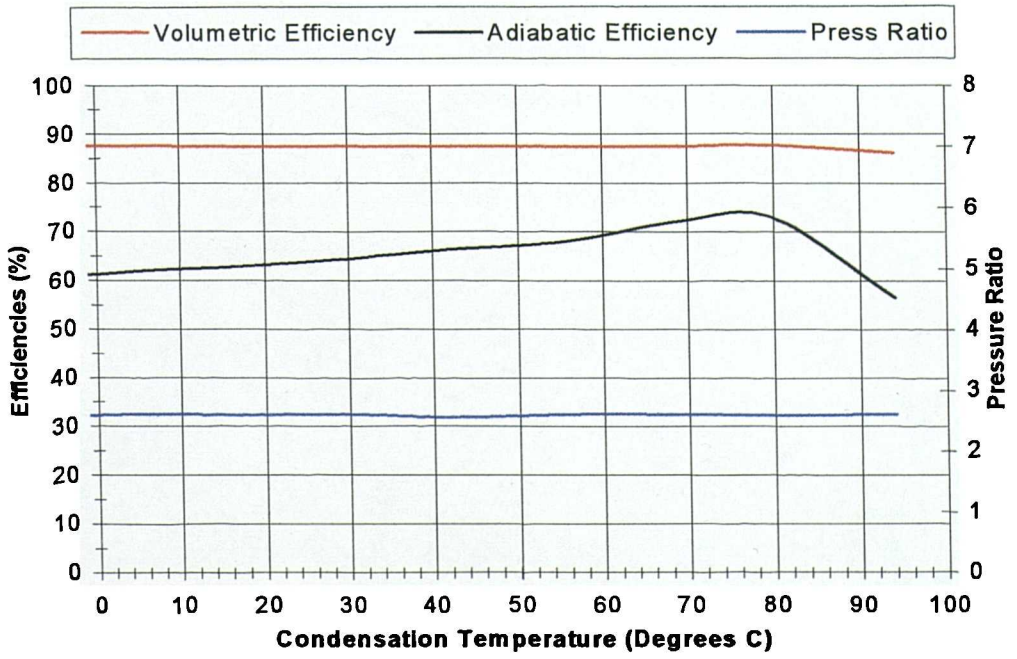

Figure 3.17 Efficiencies / Condensation Temperature. With fixed pressure ratio. Working fluid R134A dry vapour.

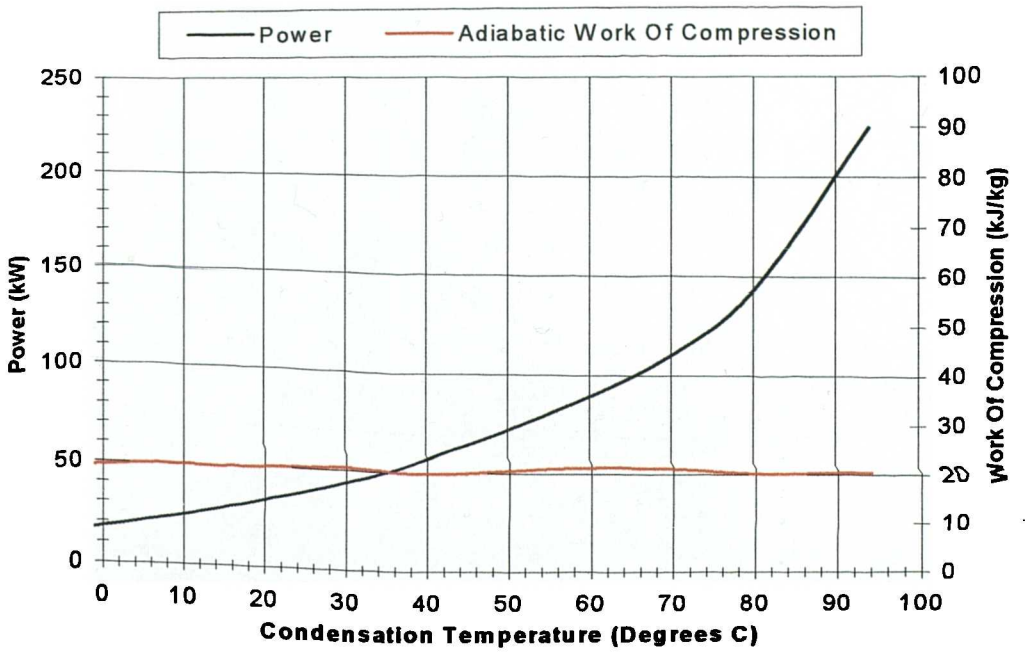

Figure 3.18 Power-Work of Compression / Condensation Temperature. With fixed pressure ratio. Working fluid R134A dry vapour.

3.3.2 Scroll Expander

As was said earlier, the function of a compressor is to admit the fluid from a low pressure region, compress it and deliver it to a high pressure region. An expander carries out the reverse processes with the object of producing work.

In section 3.3.1 the importance of the correct build in volume ratio for a scroll compressor was analyzed. In the case of the expander the build in volume ratio is also extremely important. If the pressure in the working chamber has fallen below the pressure in the delivery pipe, (over-expansion) when the port is uncovered, gas flow back into the working chamber. As can be seen from fig 3.19 the delivery port opens before the pressure in the working chamber has fallen enough, (under-expansion) this results in an unresisted expansion, which in this case corresponds to the waste of a certain amount of energy.

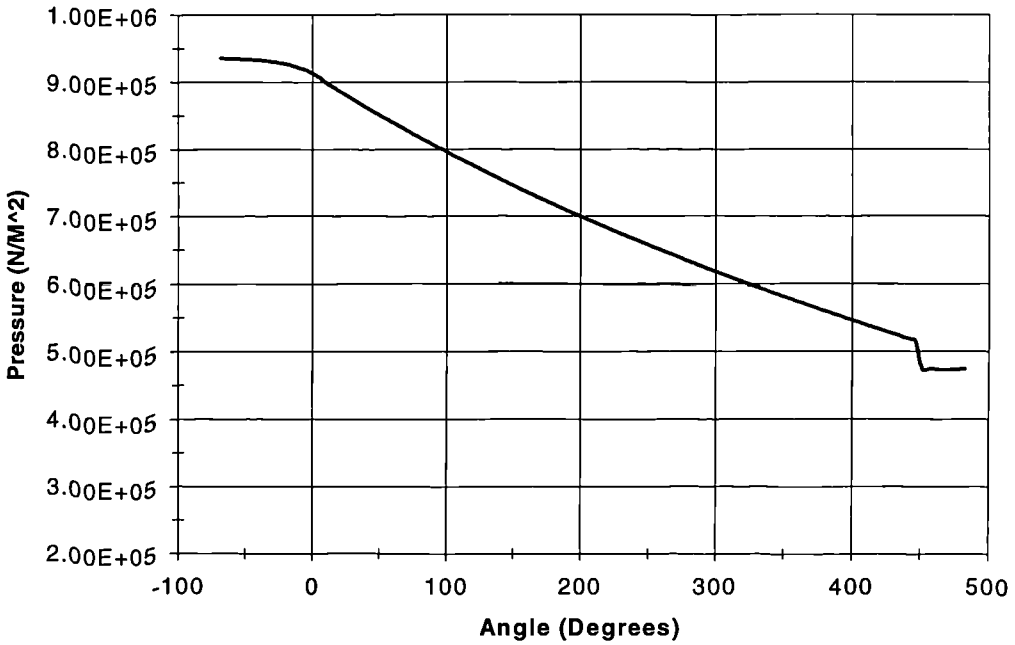

Figure 3.19 Pressure / Angle. Speed 3000 RPM. Working fluid R134A wet vapour.

The most distinctive feature of the results is the shape of the pressure-volume diagram, of which a typical result is shown in figure 3.20. As can be seen the initial filling process, which is normally assumed to take place at approximately constant pressure, is in fact associated with a small pressure drop and therefore some expansion. This pressure drop is due to the acceleration of the fluid as it enters the varying space between the spirals. Theoretically this pressure drop must be larger than the pressure change associated with gas discharge from compressors through the same area in the reverse direction. This is because the fluid entering the suction pocket of the expander has a very high liquid content and therefore a much greater density. However figure 3.20 shows that the pressure drop during the suction process of the expander is smaller than the change of pressure during the discharge process of the compressor.

However it must be noted that the pressure-volume characteristics of wet vapours are different to those of dry vapours and these lead to the need for a larger build-in volume ratio for scroll expanders.

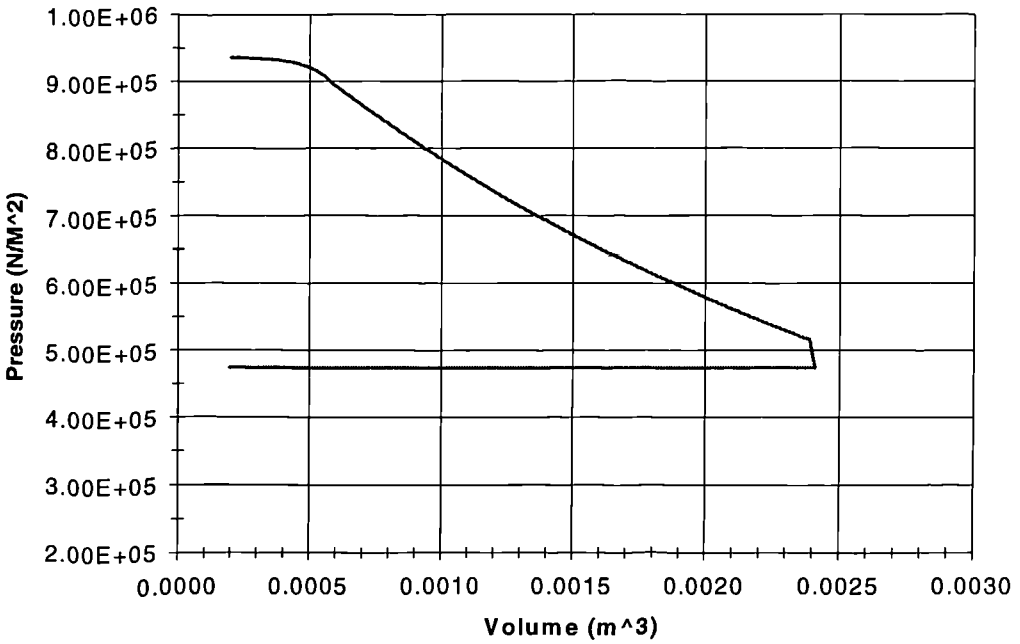

Figure 3.20 Pressure / Volume diagram of a two phase expansion process. Speed 3000 RPM. Working fluid R134A wet vapour.

Figures 3.21 and 3.22 shows some performance characteristics of the expander with respect to rotational speed change. The adiabatic efficiency is shown to increase together with the speed, a similar behaviour is recorded for the mass flow rate and the power. As can be seen adiabatic efficiencies are of the order of 70% over a wide range of operating conditions. The reason for the comparatively high efficiency at low speeds is that leakage, which is then relatively large is in the same direction as the bulk flow and hence its effect on performance is not so adverse. From fig. 3.21 we can see a huge drop of the Volumetric efficiency with speed. This is because the momentum term associated with filling becomes very large at high speeds.

Figures 3.23 and 3.24 shows how mass flow rate and power change, over a wide range of load conditions.

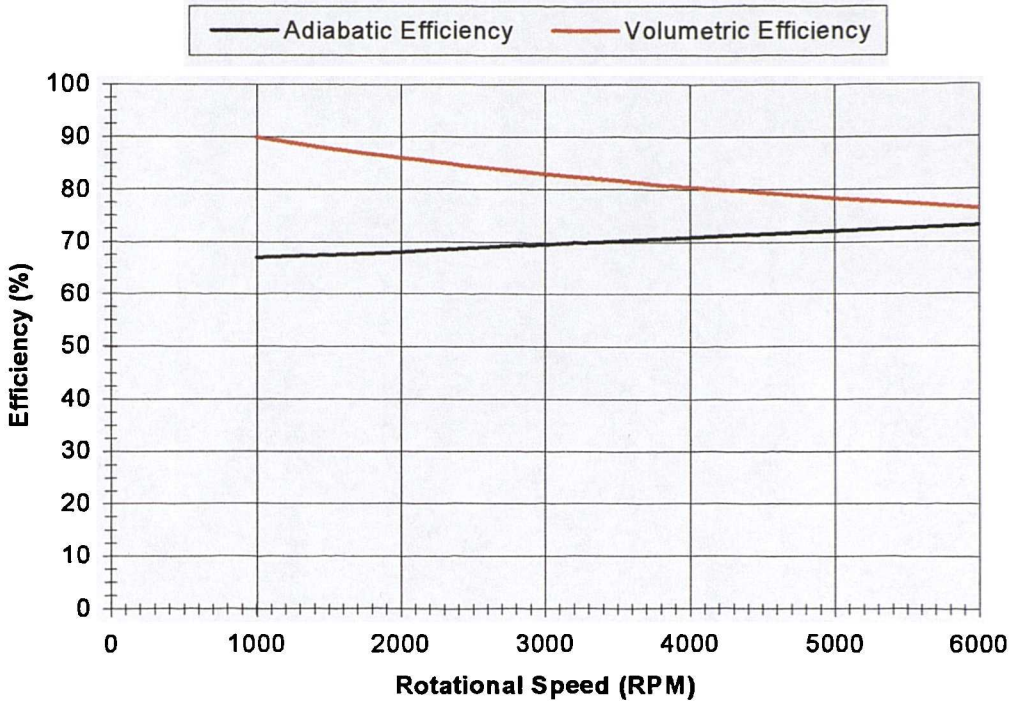

Figure 3.21 Efficiencies / Speed. Working fluid R134A wet vapour.

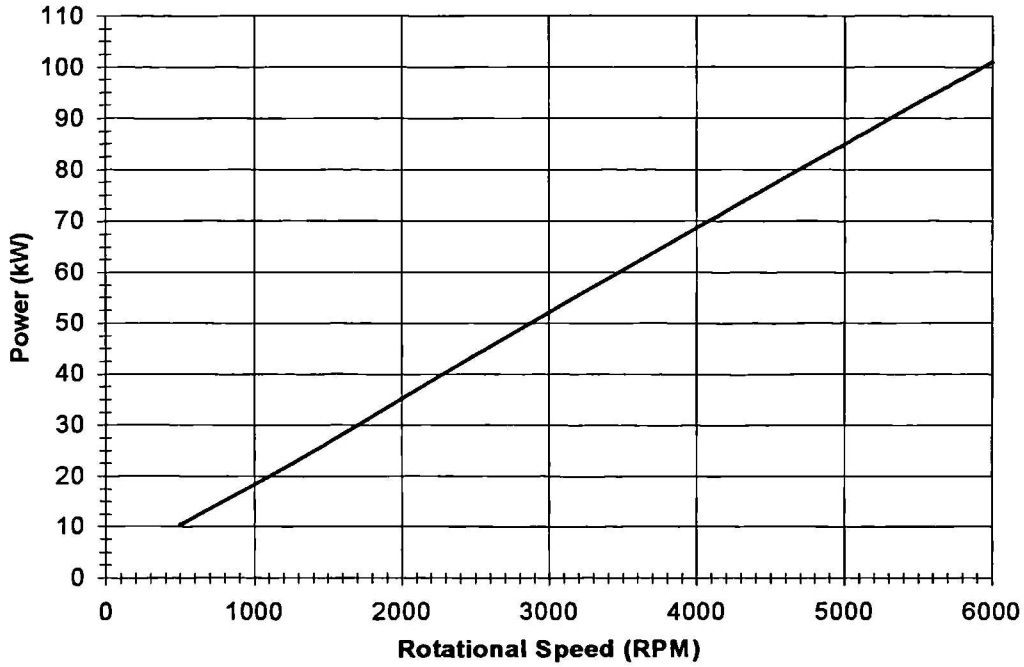

Figure 3.22 Power / Speed. Working fluid R134A wet vapour.

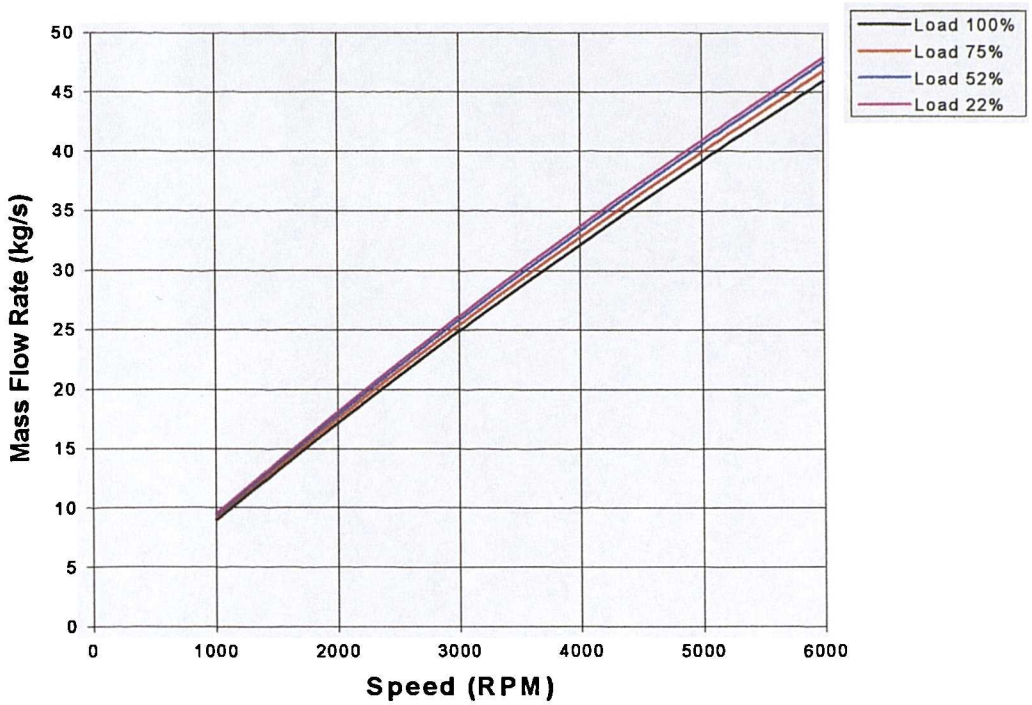

Figure 3.23 Mass Flow Rate/Speed. Working fluid R134A wet vapour. Different Load conditions.

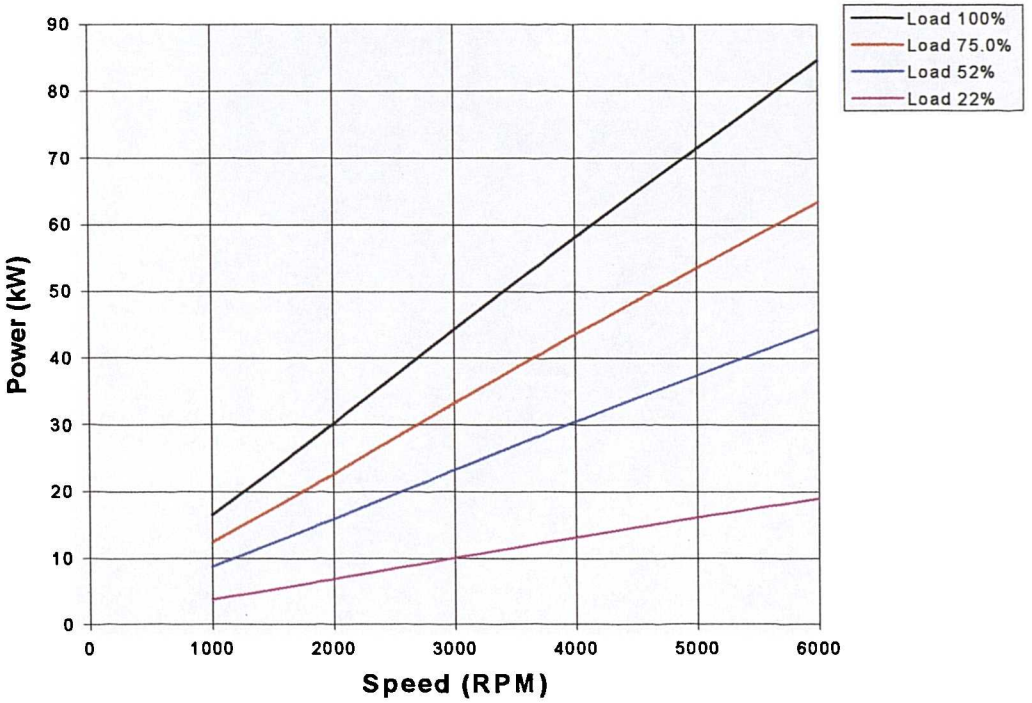

Figure 3.24 Power / Speed. Working fluid R134A wet vapour. Different Load conditions.

3.4 Applications Of the Scroll Compressor - Expander

The concept of improving the coefficient of performance of vapour compression refrigeration cycle systems by utilising the throttle expansion process to generate mechanical power is well known. It has the advantages not only of its potential use to reduce the power requirement to the main compressor but also, by expanding more nearly reversibly, of increasing the refrigeration effect per unit mass of fluid passing through the evaporator. However, until relatively recently its practical embodiment has not been followed with much interest by the refrigeration and air conditioning industry. The main reasons for this lack of interest were:

I) Gains in COP produced by improved compressor performance and reduced heat exchanger temperature differences were more cost effective and significant.

II) Efficient means of recovering power from two-phase expansion were not available.

At present, the situation has changed in that:

a) The continuing gains obtained from improved compressor performance and reduced heat exchanger temperature differences have reached a stage where further advances are diminishing in significance and escalating in cost to the point where such improvements are no longer cost effective.

b) As a result of the relatively high efficiencies in modern compressors, the gains achievable from two-phase expanders, which are relatively constant, have become more significant.

3.4.1 Cycle Proposed

To make use of the work produced from the expander in terms of shaft power and therefore reduce the power requirements of the compressor, the scroll expander needs to be coupled with the compressor. This might create some performance problems with the expander. Since it is well known that the mass flow rate of the refrigerant varies, mainly because it depends on the load, the scroll expander must not be coupled directly to the main compressor because this will force the expander to run at the same speed with the compressor. The result of this will be a not so good working performance for the expander when the system will operate at off design conditions. To overcome this problem and allow the expander to adjust its speed for any instantly mass flow rate (which depends on the load) it was decided to coupled the expander with a second compressor.

The second compressor will work in parallel with the main one, it will be driven

only by the work produced from the expander and it will contribute to the system in terms of mass flow rate, The whole cycle is illustrated below.

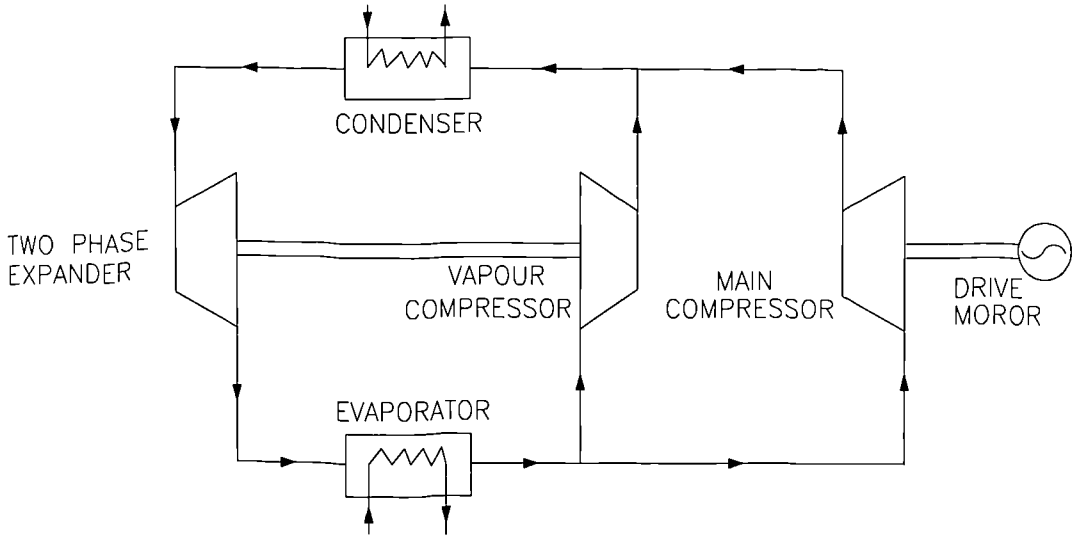

Figure 3.25 The proposed cycle. (*'Expressor'*)

3.4.2 The proposed Model

A study was performed on a standard vapour compression refrigeration cycle using refrigerant R134a. Although several working fluids, as for example R22 or propane etc. could be used for the desired applications, HFC134a was chosen for ease of use, non flammability and mainly because of global environmental acceptance. The cycle was operating on the following conditions:

- Evaporating temperature : 5^0C
- Superheating : 10^0C
- Condensing temperature : 35^0C
- Sub cooling : 0^0C

Parameters	Main compressor	Second compressor	Expander
Width (m)	0.5	0.12	0.1
Height (m)	0.062	0.02	0.0165
Thickness (m)	0.00006	0.00003	0.000025
Speed (RPM)	2200	3000	3000
Mass flow rate (kg/s)	23.44	1.55	25.1

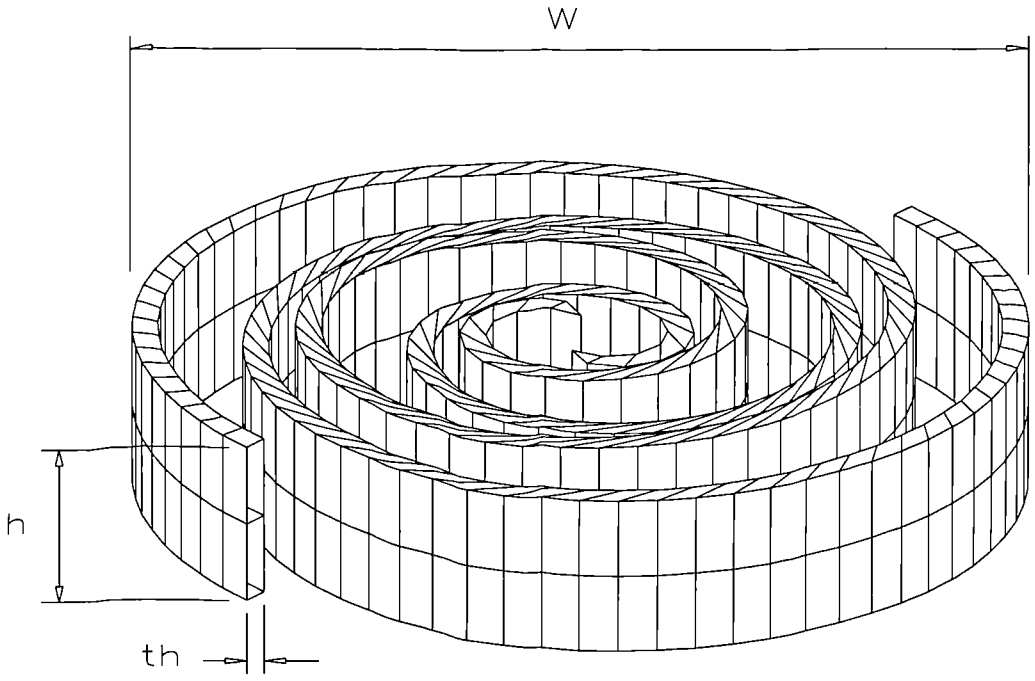

Figure 3.26 Scroll machine.

3.4.3 Expander Characteristics

These are shown in figures 3.21 to 3.24. As may be seen overall adiabatic efficiencies, which include bearing, seal and timing gear losses, are of the order of 70% over a range of operating conditions. For the design conditions of this model the power output of the expander is approximately 52 kW.

3.4.4 Compressor Characteristics

These are shown in figures 3.11 to 3.14. Since leakage in compressors opposes the bulk flow, its effect on idiabatic efficiencies should be greater than in expanders. However as it was said earlier in this Chapter the pressure-volume characteristics of wet vapours are different to those of dry vapours and these lead to the need for a larger build in volume ratio for the expander. The larger build in volume ratio for the expander implies that the leakage flow is relatively larger. Hence the superior compressor efficiency at higher speeds.

3.4.5 Combined Characteristics

The expander and compressor characteristics may be combined to show how the proposed model will perform over different rotational speeds. Figures 3.27 to 3.29 show these performance. Figure 3.27 shows how the mass flow through the second compressor compares with that through the evaporator and hence the main compressor. From figure 3.28 it may be seen that the expander will be able to drive the compressor to produce an increased mass flow rate at speeds above 3000 RPM.

As far as the performance gains are concern, firstly it should be noted that if the scroll expander is used (as proposed) then the mass flow through the expander will be increased by the extra mass flow it induces in the coupled compressor. Secondly, the inclusion of the expander has the additional advantage of making the expansion process more nearly isentropic and hence increases the evaporation effect per unit mass flow.

The refrigeration effect was increased from 157.177 kJ/kg to 160.082 kJ/kg, 1.81% increase. The power requirements of the main compressor were decreased from 923.199 kW to 827.266 kW, 10.39% decrease. Now as far as the coefficient of performance is concern it was increase from 4.29 to 4.87 which corresponds to an increase of approximately 13%. (This is only given as an example at one operating point).

This study has demonstrated that an Expressor unit comprising a scroll expander driving a scroll compressor in a sealed unit is a viable and stable device for use as a throttle valve replacement in large vapour compression chiller systems which can produce improvements in the Coefficient of Performance of the order of 13% at the design operating conditions.

Since it is not connected mechanically to the main compressor, an Expressor may be readily incorporated into a chiller unit even as a retrofit device.

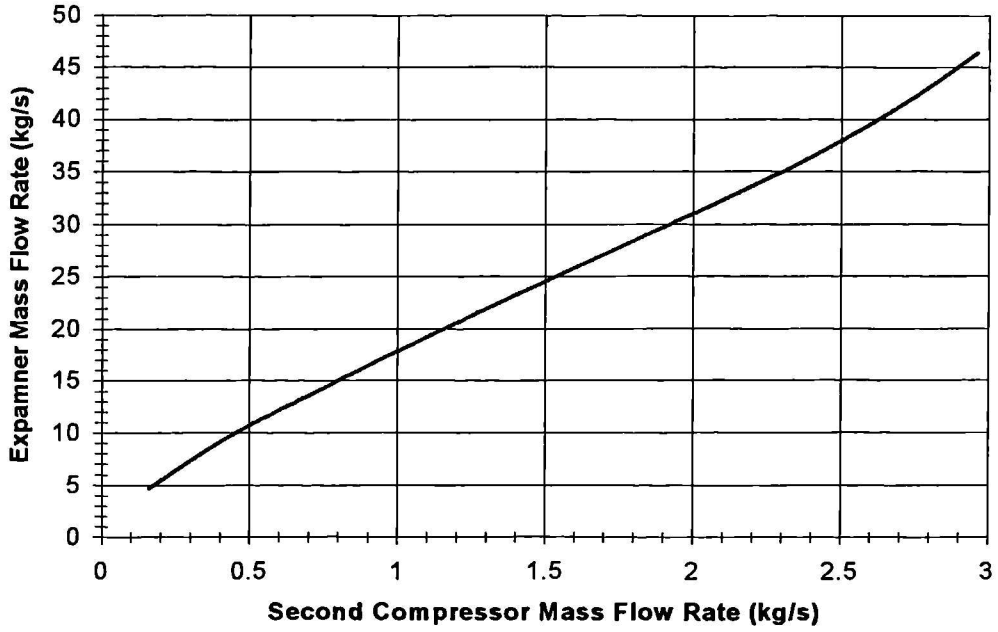

Figure 3.27 Combined Characteristics, Mass Flow Rate.

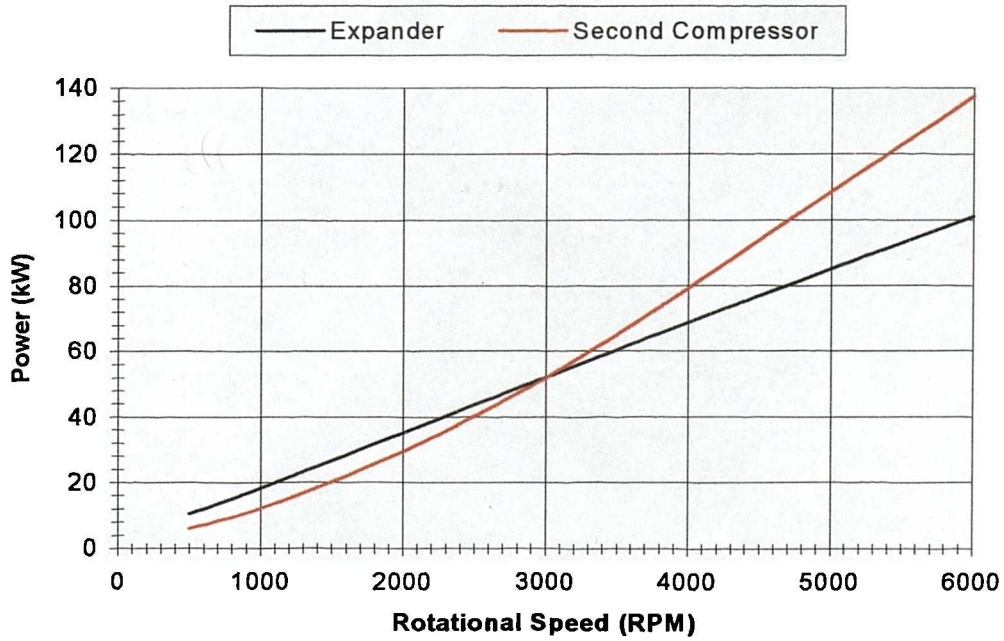

Figure 3.28 Combined Characteristics, Power.

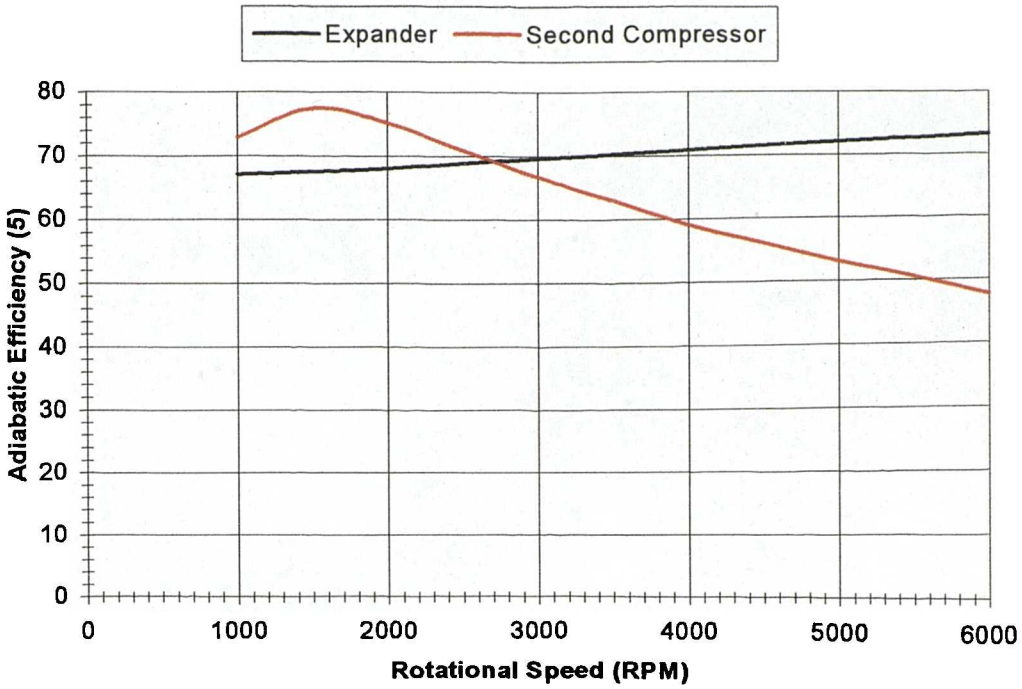

Figure 3.29 Combined Characteristics, Efficiencies.

Chapter 4

Geometry And Grid Generation

4.1 Introduction

In order to perform a thermodynamic analysis of the scroll compressor - expander first we have to describe the physical behavior of the machine in terms of mathematical equations. Functions of working volume, sealing lines, contact conditions etc. in terms of crank angle, (i.e. time) form the foundations of the analysis. In the first part of this chapter we present the necessary equations needed for the analysis. As will be shown in section 4.4 these equations form the basis for the development of the grid generation code. The derivation of the equations was necessary since it is not based on any published data. However it is partially based on the patent of the inventor of the machine. Full analysis of the geometry is given in appendix A

During the last few years, numerical flow analysis techniques have become increasingly important in machine design. A key factor in obtaining a realistic solution is mesh generation, considered as a basic problem requiring a sustained effort. In fact, the interaction between the mesh characteristics and the development of the solver are closely linked as far as stability, convergence and definition of the solution are concerned. Therefore section 4.4 of this chapter deals with the design and development of a grid generation program that can handle the complexity of the working volume of the scroll device. Aspect ratio, orthogonality, cell distortion, and smooth distribution, are some of the difficult issues involved in the transient structured body fitted grid generation package developed.

4.2 Geometry

The basic elements in a scroll compressor are the identical scroll wraps whose quality is vital to the compressor's performance. Geometrically speaking the wraps are usually made on the basis of an involute of a basic circle (IOC).

As can be seen from the literature survey, there is almost nothing published on the geometry of the scroll compressor. However even in the very few papers published so far on this topic, only basic principles are stated. Therefore it was decided to develop our own unique geometry based on the patent of the innovator of the scroll engine Leon Greux [1905]. A detailed analysis of the geometry needed for the design of a scroll machine is shown in appendix A, however some of the basic equations are shown here:

The involute spiral of a circle is an appropriate curve for a scroll compressor because of its simplicity of construction. If one unwraps a string from a circle, keeping the string taut, the end of the string will trace out an involute spiral. The envelope, formed by orbiting (revolving without rotating) an involute about a separate origin, is in itself an involute spiral which differs from the original involute by its starting angle. To build a spiral of this type both the inner and outer curves must be known.

The curves $C_1 \equiv C_{FO}$, $C_2 \equiv C_{FI}$, $C_3 \equiv C_{OO}$ and $C_4 \equiv C_{OI}$, defining the inner and outer surfaces of the fixed and orbiting spirals of the compressor are shown in figure 4.1. The meaning of the subscripts is : FO = Fixed Outer, FI = Fixed Inner, OO = Orbiting Outer, and OI = Orbiting Inner. The analytical expressions describing the curves $C_1=C_{FO}$, $C_2=C_{FI}$, $C_3=C_{OO}$ and $C_4=C_{OI}$. are:,

$$
\begin{aligned}
C_1=C_{FO} \;:\; & \begin{pmatrix} x_1 \\ y_1 \end{pmatrix} = r\begin{pmatrix} \cos(\varphi)+\varphi\sin(\varphi) \\ \sin(\varphi)-\varphi\cos(\varphi) \end{pmatrix}, \\
C_2=C_{FI} \;:\; & \begin{pmatrix} x_2 \\ y_2 \end{pmatrix} = r\begin{pmatrix} \cos(\varphi+\gamma)+\varphi\sin(\varphi+\gamma) \\ \sin(\varphi+\gamma)-\varphi\cos(\varphi+\gamma) \end{pmatrix}, \\
C_3=C_{OO} \;:\; & \begin{pmatrix} x_3 \\ y_3 \end{pmatrix} = -\begin{pmatrix} r(\cos(\varphi)+\varphi\sin(\varphi))+d\cos(\theta) \\ r(\sin(\varphi)-\varphi\cos(\varphi))+d\sin(\theta) \end{pmatrix}, \\
C_4=C_{OI} \;:\; & \begin{pmatrix} x_4 \\ y_4 \end{pmatrix} = -\begin{pmatrix} r(\cos(\varphi+\gamma)+\varphi\sin(\varphi+\gamma))+d\cos(\theta) \\ r(\sin(\varphi+\gamma)-\varphi\cos(\varphi+\gamma))+d\sin(\theta) \end{pmatrix},
\end{aligned}
\qquad (4.1)
$$

It is now assumed that the curves $C_1=C_{FO}$ and $C_4=C_{OI}$ have been constructed in such a way that they never intersect each other, but there exist points at which they are tangent. The same assumptions are also made for the pair of the curves $C_2=C_{FI}$ and $C_3=C_{OO}$. At these touching points the following relations hold

$$\varphi_1 = 2k\pi + \frac{\pi}{2} + \theta, \quad \varphi_3 = 2k\pi + \frac{\pi}{2} + \theta,$$

$$\varphi_4 = \pi + \varphi_1 - \gamma, \quad \varphi_2 = \pi + \varphi_3 - \gamma, \quad \varphi_i \geq 0 \ (i=1,2,3,4), \quad d = r(\pi - \gamma), \qquad (4.2)$$

$$0 < \gamma = \text{constant} < \pi/2, \quad k \in \mathbb{W}, \quad \theta \in \Re.$$

Clearly, the relations between the angles φ_1, φ_4 and θ refer to the contact conditions of the curves $C_1=C_{FO}$ and $C_4=C_{OI}$, while the relations between the angles φ_2, φ_3 and θ refer to the touching conditions of the curves $C_2=C_{FI}$ and $C_3=C_{OO}$.

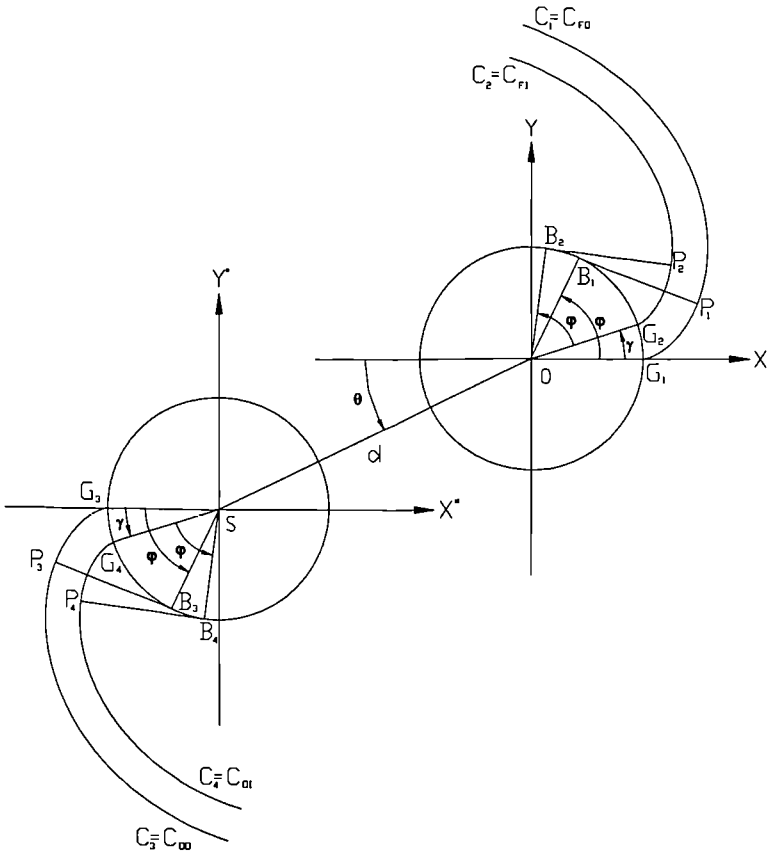

Figure 4.1. Generating circles and involutes.

The derivation of the working volumes leads to a number of formulae. For example the volume of the suction chamber only is described by four different equations depending on the relative position of the spiral walls of the device. Therefore it has been decided not to put all those equations here. As already stated a mathematical analysis is shown in appendix A.

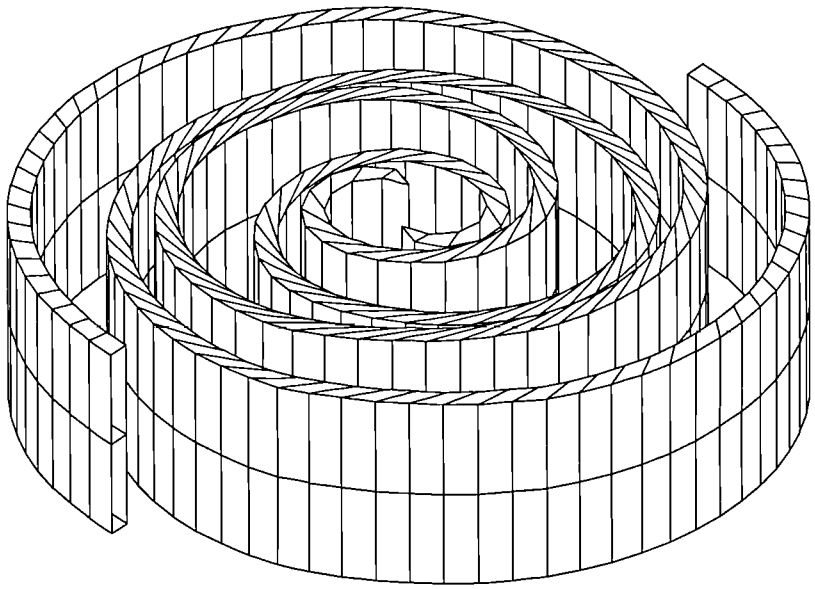

Figure 4.2. 3-D View of the Scroll Machine using the involute of a circle

New types of curves named as *"The Involute of a Basic Square"* and *" The Involute of a Basic Triangle"* have been recently studied [1992] in an attempt to improve or replace the conventional one. The involute of a basic square can be obtained when unwrapping a string from a square as shown in figure 4.3.

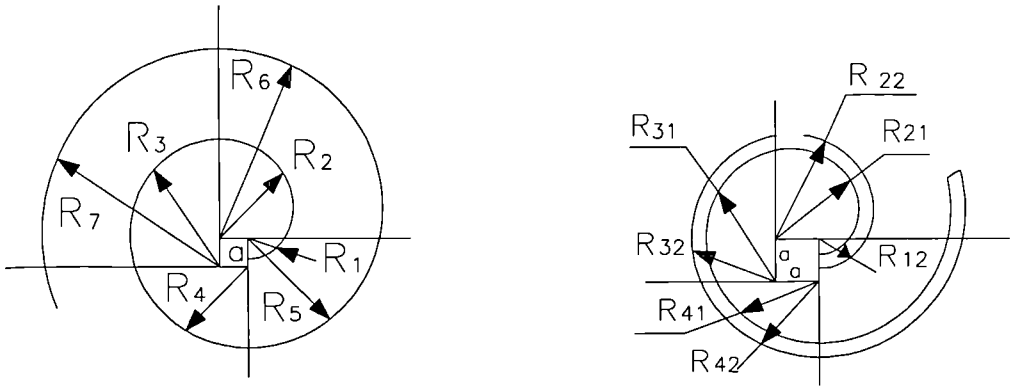

Figure 4.3. Formation of involute of square, wrap design.

It is obvious from the formation process that, the curve consists of several quarter circles, that is, its curvature changes every quarter circle. Something quite similar happens with the involute of the basic triangle.

Besides the types of curve mentioned above an Archimedes spiral can also be used for the design of scroll machinery. However when using this type of curve extreme caution must be taken in order to avoid any problems regarding contact conditions. (i.e. leakages)

4.3 Theory Of Grid Generation

One of the main problems in computing numerical solutions of Partial Differential Equations (PDE) is the generation of the mesh for the solution domain. The grid has to be well-constructed otherwise it may lead to instability or lack of convergence. Numerical grid generation has now become a fairly common tool in the numerical solution of PDE on arbitrarily shaped regions and several commercial packages are available (Thompson, 1988). A comprehensive survey of procedures and applications has been given by Thompson et al. (1982; 1984).

Body-fitted curvilinear coordinate systems, used in modern CFD codes generated to maintain coordinate lines coincident with the boundaries, were introduced to extend the capabilities of Finite Difference Methods (FDMs) to deal with complex geometries and assist in the imposition of boundary conditions without the need for special procedures at the boundaries. Motion of the boundaries is also possible, the coordinate system adjusting to follow variations developing in the evolving physical solution. In any case, the numerically-generated grid allows all computations to be done on a fixed square grid in the computational field which is always rectangular by construction. However, the cost of the greater flexibility afforded by the use of body-fitted grids and general coordinates is an increase in complexity of the equations to be solved, due to the non-linear coordinate transformation.

The first step in the generation of the grid is the transformation of the physical space (complex-geometry domain) into a computational domain (simple-rectangular domain), where all numerical algorithms, finite difference, finite volume or finite element, are implemented. Numerical grid generation techniques may be roughly classified into three categories:

(a) Complex variable methods.
(b) Algebraic methods.
(c) Differential Equation Techniques.

Complex variable methods are restricted to two dimensional problems and so their applicability is very limited. These techniques have the advantage that the transformation used are analytic or partially analytic as opposed to the other methods that are entirely numerical. ***Algebraic and differential equations techniques*** can be used for complicated three-dimensional problems. In the next sections we present the main approaches to the generation of meshes for structured grids. Then, special techniques for gridding complex geometries will be discussed.

4.3.1 Algebraic Methods

Algebraic mesh generation methods determine the coordinate positions by interpolating among boundaries and / or intermediate surfaces using known functions of sets of data points. The main advantages of algebraic mappings are that they are direct and the metrics of the transformation can be computed analytically. However, since inherent smoothing properties are missing, discontinuities can arise in the mesh.

Several interpolation methods are used, and are classified as ***unidirectional*** and ***multidirectional*** methods. In the unidirectional interpolation method, the interpolation, in one curvilinear coordinate direction only, occurs between points. These points can, however lie on boundary (or interior) curves of surfaces, and in this sense the unidirectional interpolation can be considered to be between these curves or surfaces. Several interpolation techniques are available (Lagrange, Hermite, Splines, Tension Splines, B-Splines etc.), the most general procedure being the 'multi-surface procedure (Eiseman. 1979) of which Lagrangian or Hermitian interpolations are special cases. This procedure is constructed from the interpolation of a specified vector field, defined from piecewise-linear curves determined by the boundaries and successive intermediate control surfaces. These vectors are taken to be tangential to the coordinate lines intersecting the surfaces, so that integration of this vector field produces the position vector field for the grid points.

Multi-directional interpolation involves interpolation among functions of curves or surfaces. The most general method used is the 'transfinite', described in detail by Rizzi and Erikson (1981). The interpolation generates the mapping by combining unidirectional interpolation with Boolean sums, and matches the function at any number of points.

4.3.2 Partial Differential Equation Methods

These techniques are the most highly developed for generating grids. The grid points are obtained by the solution of a set of partial differential equations, which can be ***hyperbolic***, ***elliptic*** or ***parabolic***. If the coordinate points are specified on the entire closed boundary of the physical region, the equations must be elliptic, while if the specifications is only a portion of the boundary the equations would be parabolic or hyperbolic.

The use of elliptic PDEs to generate grids has been treated extensively by Thompson (1974). This procedure transforms the physical space into the computational space where the mapping is controlled by general Poisson-type systems. The generation system guarantees a one-to-one mapping for boundary conforming curvilinear coordinate systems on general closed boundaries. The advantages of using this technique are to generate a smooth grid, complex boundaries being easily treated, without overlap of grid lines (extremum principles). However, grid point control on the interior is difficult to achieve, and if boundaries are changing in time, (as in the case of a scroll compressor / expander) since the grid has to be computed for each time step, large amounts of computer time may be consumed.

The most simple elliptic partial differential system is the Laplace equation:

$$\nabla^2 \xi^i = 0 \qquad (i=1,2,3)$$

where ξ^i is the coordinate vector in the computational domain.

This system exhibits an extremum principle and considerable smoothness. Control of the coordinate line distribution in the field can be obtained by generalizing the elliptic generating system for the Poisson equations:

$$\nabla^2 \xi^i = P^i \qquad (i=1,2,3)$$

in which the 'control functions' P^i, can be fashioned to control the spacing and orientation of the coordinate lines. In the absence of the control functions the coordinate lines will tend to be generally equally spaced away from the boundaries regardless of the boundary point distribution. Variations of elliptic systems are noted in Thompson et al. (1982; 1984).

A number of different algorithms have been used for the solution of these equations, including point and line SOR, ADI (Alternating-Direction-Implicit-Technique) (Thompson et al., 1982; Thompson, 1984). The convergence can be accelerated by using multiple grid iteration (Forsey and Billing, 1988). For general configurations, point SOR is certainly the most convenient to code and has been found to be rapid and dependable, using over-relaxation, for a wide variety of configurations. Since the system is nonlinear, convergence depends on the initial guess in iterative solutions. Algebraic grid generation procedures may be used to generate this initial guess. ***Transfinite*** interpolation generally produces a more

reliable initial guess than unidirectional interpolation does because of its reduced skewness.

A fundamental development of the hyperbolic generation system was made by Starius (1977). Hyperbolic systems are applicable to domains in which the inner boundary is specified but the surrounding outer boundary is arbitrary, and therefore of interest only for use in calculation on physically unbounded regions where the precise location of a computational outer boundary is important. The parabolic system can be applied to generate the grid between the two boundaries of a doubly-connected region with each of these boundaries specified. The grid control is generally weak and difficult compared with the elliptic methods. However the weakest method in the grid control is the grid generation method. Both parabolic and hyperbolic grid generation systems have the advantage of being generally faster than elliptic generation systems, but, as noted, are applicable only to certain configurations.

Orthogonality is one of the most desirable properties in grid generation techniques. Orthogonal coordinate systems produce fewer additional terms in transformed partial differential equations, and thus reduce the amount of computation required. This also makes the application of boundary conditions more straightforward, and permit a greater degree of vectorization on supercomputers. A severe departure from orthogonality will introduce truncation error in 'different expressions'. Orthogonality in three dimensions is difficult to achieve, and only exists when the coordinate lines on the bounding surfaces follow lines of curvature, i.e., lines in the direction of maximum or minimum curvature of the surface. It is possible, however, to have the system locally orthogonal at boundaries, and/or to have orthogonality of surface coordinates. Since a part of the truncation error decreases as the grid becomes more orthogonal, it is of interest to generate grids which are 'nearly-orthogonal'. Various generation procedures of orthogonal systems are surveyed in Thompson (1980).

4.3.3 Adaptive Grids

Adaptive grids are generated with the object of directing the distribution of grid points so that a functional relationship on them may represent the physical solution with sufficient accuracy. As the physical solution develops, grid points move, concentrating in regions of large gradients in the solution as they emerge. Movement of grid points is coupled to their neighbours, and cannot be too far or

too fast, otherwise oscillations may occur.

Different techniques for constructing adaptive grids have been proposed. Brackill and Saltzman (1980) have developed a technique for constructing an adaptive grid using a ***variational approach***. It offers a powerful method for constructing computational grids; however, a considerable effort must be expended in solving the equations which govern the grid generation. Many applications of adaptive grids require grid motion along one coordinate. The ***equidistribution scheme*** is a minimization process applied in a one-dimensional form, and the grid points are distributed so that the weight function is equally distributed over the field. A number of applications of the use of one-dimensional equidistribution are cited in the survey on adaptive grids given by Thompson (1984). The ***grid speed scheme*** developed by Hindman and Spencer (1983) also incorporates the idea of equidistribution. The grid speeds are established by differentiating the steady grid equation, and solving the resulting equation. To advance the grid to the next time level the grid speeds are integrated. Several other approaches are discussed by Thompson (1984).

Once adaptivity criteria have been formulated, it is necessary to move points around the domain so that the flow solution has a minimum error. Three basic strategies may be employed to do so: (i) redistribution of a fixed number of points, (ii) local refinement of a fixed set of points, (iii) local increase in algorithm order.

Solutions to PDEs obtained using numerical methods in conjunction with adaptive grids show significant improvements in either accuracy or resolution. Oscillations associated with cell Reynolds number and with shocks in fluid mechanics computations have been shown to be eliminated with adaptive grids. The adaptive grid is most effective when it is dynamically coupled with the solution, so that the solution and grid are solved together in a single continuous problem. The development and application of adaptive grids have been surveyed by Eiseman and Eriebacher (1987).

4.3.4 Moving Boundary Grids

Moving Boundary procedures have recently been developed by a number of research groups and are included in the most advanced commercially available CFD codes. Moving boundaries are a chief feature of the flow in the scroll machine where the fluid flow is driven by the motion of the wall.

Details of the application of moving boundaries procedures to the Navier-Stokes equations are given by Demirdzic and Peric (1990), and Hawkins and Wilkes (1991).

4.3.5 Computational Grids For Complex Geometry Domains

There are three basic types of computational grid in current use:
(i) Single-block, fully structured grids,
(ii) Multi-block grids,
(iii) Unstructured grids.

Single-block fully structured grids, discussed above, are traditionally used in Finite Difference Methods (FDMs). As shown in figure 4.4 they transform the physical space into a rectangular (or hexahedronal in 3-D) computational space. In complex geometry domains, to have accurate solutions of the flow, special techniques are required for gridding, such as multi-block and unstructured grids.

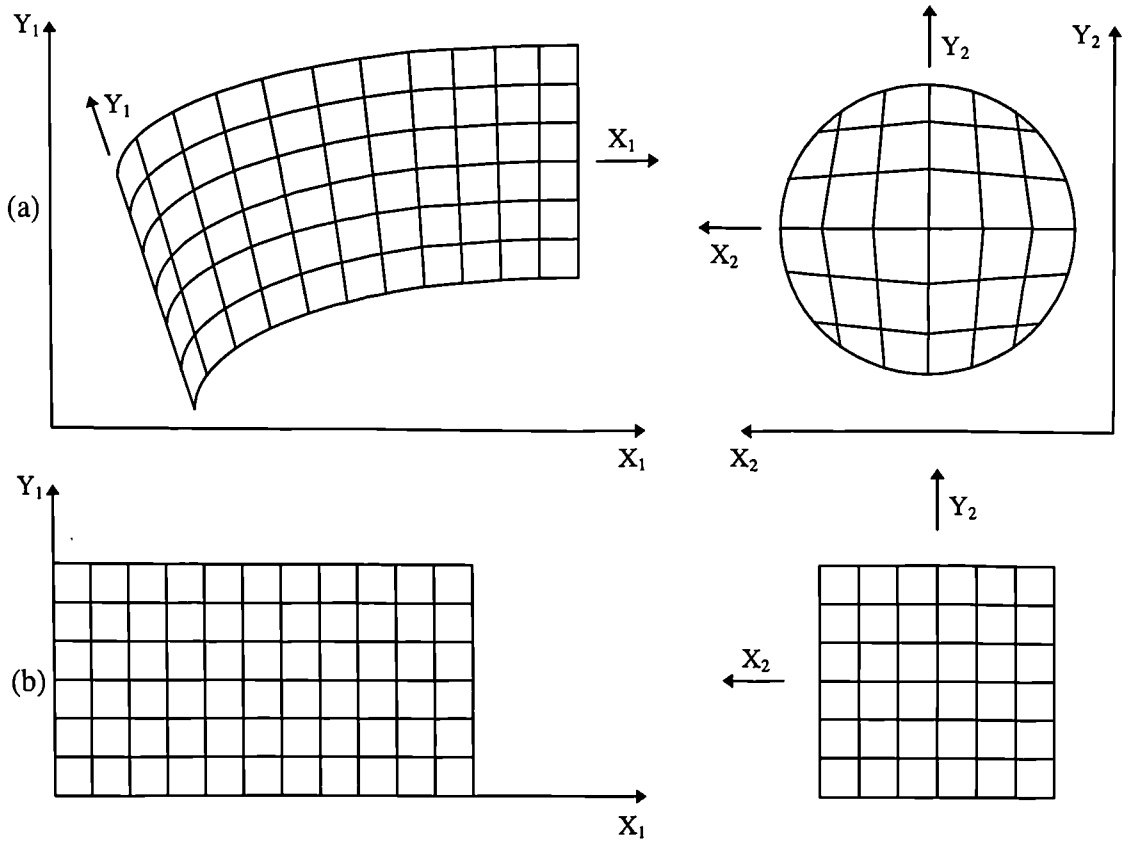

Figure 4.4 Samples of a single-block grid. (a) Physical domain. (b) Computational domain

4.3.5.1 Multi-Block Grids

The multi-block approach is a very popular method of applying structured grids to complex geometrical regions. The physical domain is segmented into sub-regions which constitute contiguous blocks. Each block has to be transformed into a hexahedron, so that several local curvilinear systems are constructed and connected together. However, the global distortion of the grid is relatively less accentuated. Grid points at block interfaces have to be treated so that points at the common edge of any two adjacent blocks are continuous and so that slope continuity may be enforced.

Multi-block grids are very powerful in that they allow the use of a wide range of mesh topology for a given configuration and different coordinate systems are allowed in each block. They are restricted to the grid generation technique - algebraic or partial differential equations. Although the concept of a multi-block mesh is very attractive from a mesh generation point of view, additional complexities are introduced in the solution procedures, that involve a slow-down of the calculation time.

Examples of three-dimensional multi-block grids applied to complex geometry are given in the literature by Weatherill and Forsey (1984), and are noted in the survey given by Thompson and Warsi (1983). Multi-block grids have been implemented in the latest Releases (3.12, 3.2, etc.) of CFX-FLOW3D.

4.3.5.2 Unstructured Grids

Unstructured meshes, traditionally used in FEM, are generally composed of triangles and/or arbitrary quadrilaterals in 2-D, and tetrahedra and /or hexahedra in 3-D. Therefore the number of cells surrounding a typical node of the mesh is not constant. Techniques for the generation of unstructured meshes are discussed in detail by Peraire et. Al. (1990). It was found that to have an adaptive mesh, triangulation is necessary to allow easy transition between small and large elements.

The unstructured nature of the mesh requires a local coordinate system for each element. The resultant mesh, therefore, is poorly ordered and less amenable to the use of vectorization algorithms. Also larger computer time storage is required in comparison with structured grids. However, unstructured meshes are more efficient in complex geometry domains, and offer the possibility of incorporating adaptivity.

In order to minimize computer time requirements, renumbering strategies for unstructured grids have been proposed.

4.4 Development Of Grid Generation Code

In this subsection we analyze the development of the grid generation code, which is used for the requirements of this project . The area for which we need to create the grid, is the working chamber of the machine (see figure2.4). Since this area depends on the boundaries of the working volume, and since these boundaries are changing with time, it can be concluded that we need a technique to move the mesh to its new position with respect to the movement of the boundaries. What we have done is to re-calculate the vertices. At this point we have to make it clear that we are not doing re-meshing, we are using some analytical mathematical equations that we develop to re-calculate the coordinates of the vertices. The topology is maintained the same.

At the beginning we tried to use commercial grid generation packages (Patran, Femgv, Sophia etc.). One of the limitations we found with these packages is their inability to handle complex moving geometries. If the geometry is fixed in space then these packages will produce a good mesh. If however, movement is involved then problems arise.

4.4.1 Two Block Grid Generation Code

After we took the decision to develop our own grid generation code the first step was to describe mathematically the working volumes. As can be seen from figure 2.4, the working volumes are mainly described by two curves each. Equations 4.1 and 4.2 (touching conditions) define these curves. The next step was to decide about the number of blocks. At the first attempt we used a two block grid, the first block was used for the one working chamber and the second one for the other chamber. The first thought was that we would select a certain number of points along each curve and then interpolate between the points to find intermediate vertices. The problem was how to subdivide each curve. One idea was to use uniform distribution. If we used this option then we would not have any idea how the points on the one curve were related to the points on the other. Therefore we thought that since the curves are similar to each other (both are involutes of a circle), maximum orthogonality would be obtained if we found where the curves have the same gradient (parallel) and fit straight lines between them. With this

method we only needed to subdivide the one curve. The idea was that we would select a point on one curve, then calculate the gradient of the curve at that point and then use a numerical technique to find which point on the other curve has a gradient as close as possible to the first one. Note also that there might be more than one point that would satisfy this condition (case of same gradients), therefore a second restriction was imposed. This was that the second point must give the minimum distance between the two curves. Once we knew these two points then we could fit a straight line to connect them, or perform a linear interpolation to calculate intermediate points. The number of the elements would depend on the number of intermediate points and on the number of points selected on the first curve. This logic was supposed to be true for all the different processes of the machine (suction, compression, discharge). A major problem was the point where the two working chambers approached each other (in space). When these two come in contact their vertices should coincide, otherwise errors will occur in the solver. This problem was overcomed by calculating the vertices only on the one site and forcing the vertices of the other block to take the same values.

After spending a considerable amount of time, the program was ready. The grid movement was successful, the user would need to specify the number of subdivisions on the curve, the number of intermediate points, the number of subdivisions on the Z axis, the time, and the rotational speed which is needed for the calculation of the crank angle with respect to time. The grid results were very disappointing the biggest problem was the skewnes of the grid especially on the discharge process. At the end of the discharge process overlapping occurs. This overlapping results in the calculation of negative volumes. The results of this first attempt are shown in figures 4.5 to 4.15

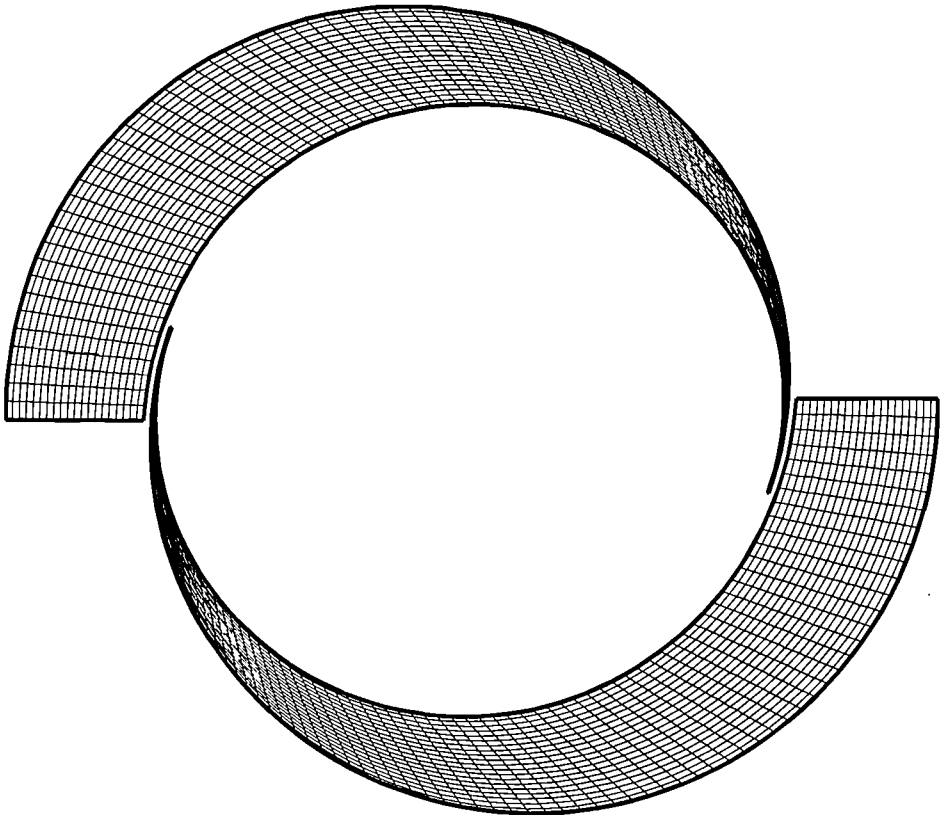

Figure 4.5 Crank angle 200^0

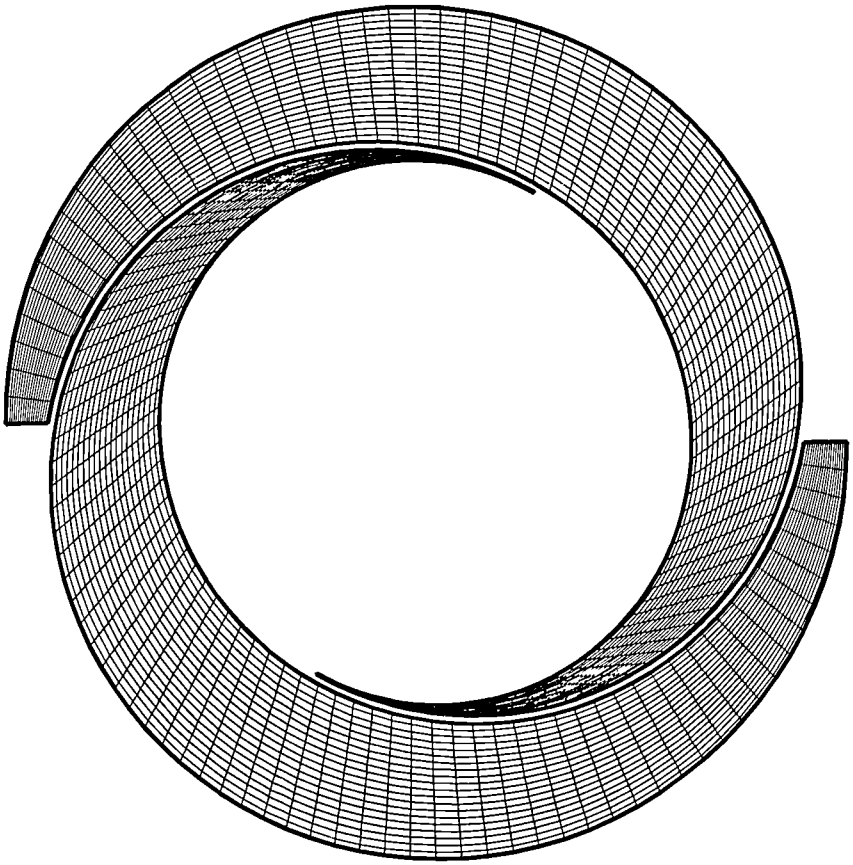

Figure 4.6 Crank angle 300^0

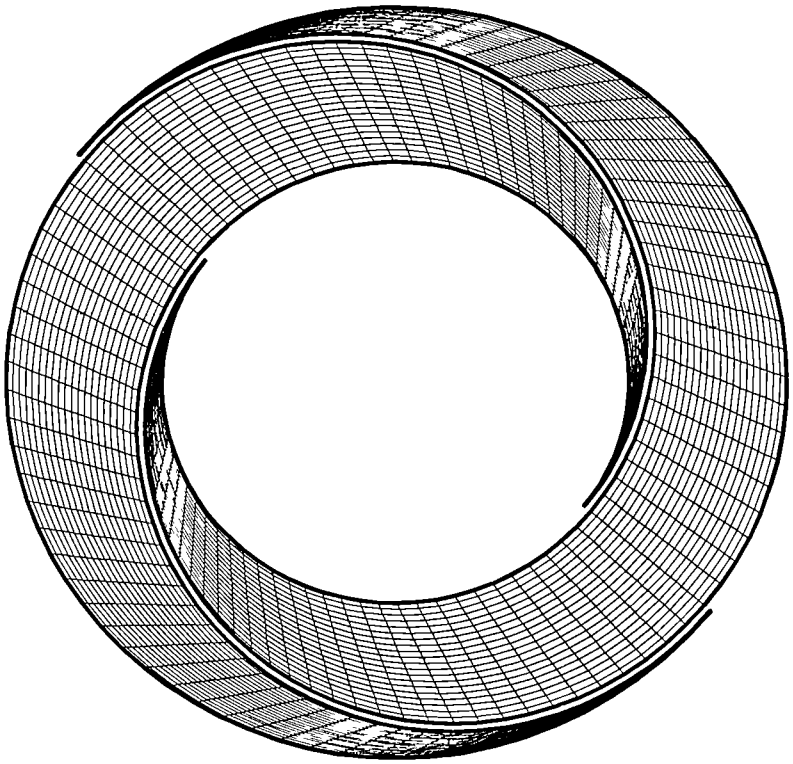

Figure 4.7 Crank angle 400^0

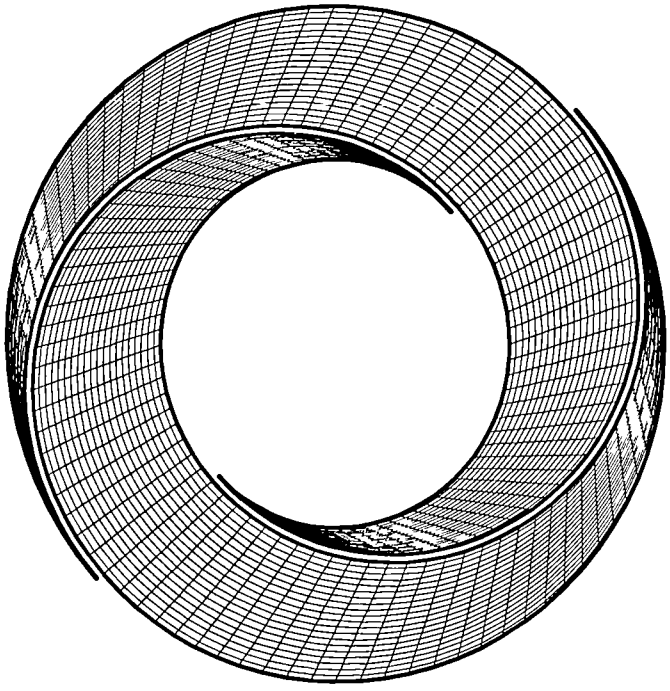

Figure 4.8 Crank angle 500^0

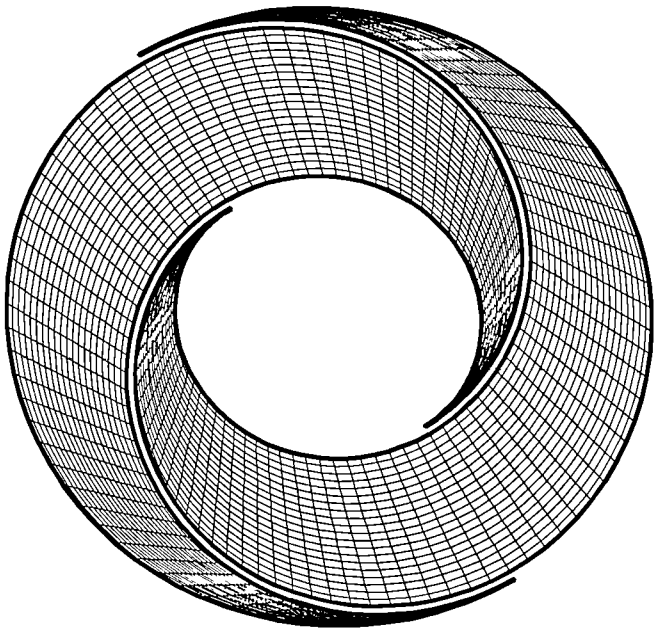

Figure 4.9 Crank angle 600^0

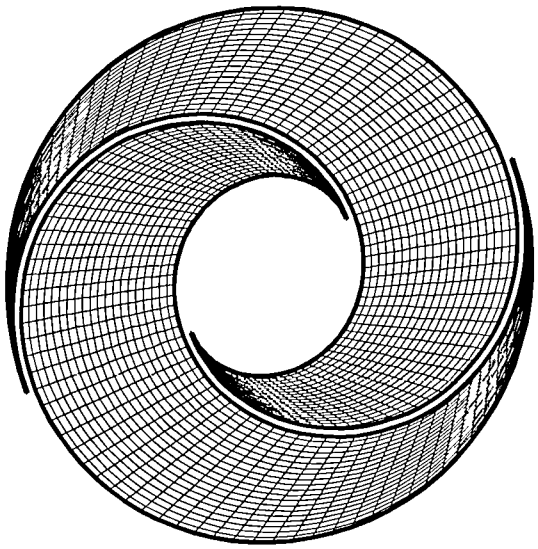

Figure 4.10 Crank angle 700^0

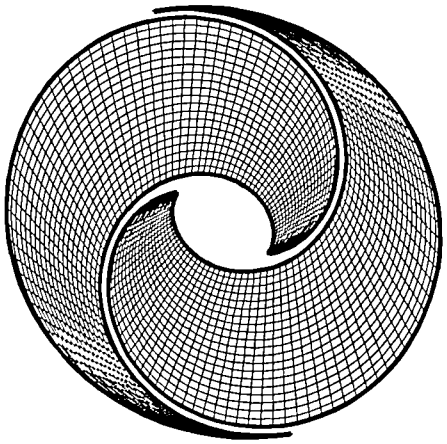

Figure 4.11 Crank angle 800^0

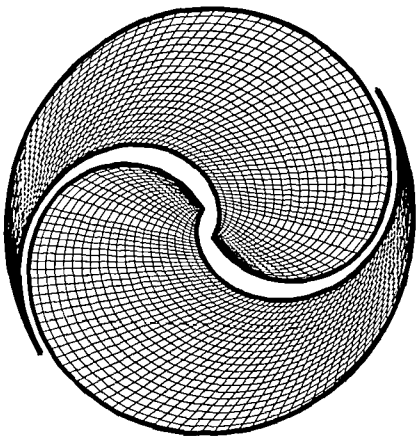

Figure 4.12 Crank angle 860^0

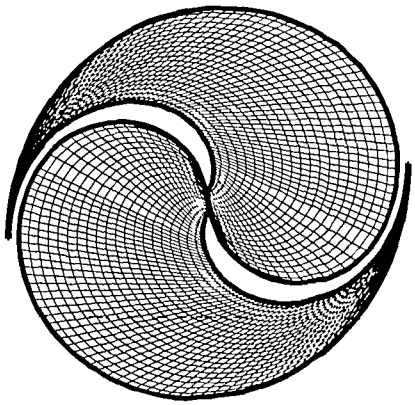

Figure 4.13 Crank angle 900^0

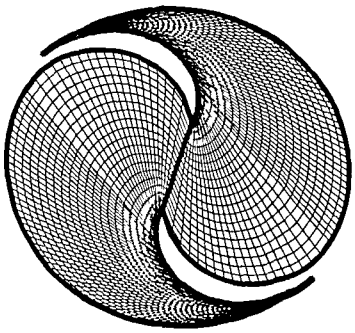

Figure 4.14 Crank angle 950^0

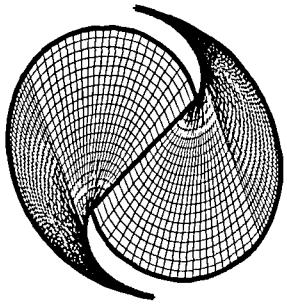

Figure 4.15 Crank angle 1000^0

4.4.2 Four Block Grid Generation Code

Having identified the problems from our first attempt we decided to make some changes. The first was that we would use four blocks instead of two. Initially the two blocks would be more or less equal, but as the domains move inwards the block on the inside begin to expand where as the other one continues its shrinking mode. This coincides with the beginning of discharge as shown in figure 4.24. Then, some elements will be compressed and others will expand. This would give the flexibility needed to control the vertices within the discharge chambers and therefore avoid overlapping (which results in negative volumes). The second and biggest change was the implementation of transfinite interpolation. This would control the case where we do not know the intermediate points and we want the intermediate curvature to be as close as possible to the boundaries i.e. the discharge chamber.

4.4.2.1 Implementation of Transfinite Interpolation

The problem of generating a curvilinear coordinate system can be formulated as a problem of generating values for the Cartesian coordinates in the interior region

from specified values on the boundaries. This, can be done directly by interpolation from the boundaries, and such coordinate generation procedures are referred to as algebraic generation systems. As was mentioned in section 4.3.1, these systems are divided into two major categories, Unidirectional and multidirectional interpolation. Transfinite interpolation falls in the second category.

In two directions we may write a linear Lagrange interpolation function individually in each curvilinear direction:

$$\underset{\sim}{r}(\xi,n)=\sum_{n=1}^{2}\phi_n\left(\frac{\xi}{I}\right)\ \underset{\sim}{r}(\xi_n,n)$$

$$\underset{\sim}{r}(\xi,n)=\sum_{m=1}^{2}\psi_m\left(\frac{n}{J}\right)\ \underset{\sim}{r}(\xi,n_m)$$

This interpolation is now called 'Transfinite' since it matches the function on the entire boundary defined by ξ=0 and ξ=I in the first equation, or by n=0 and n=J in the second. The final form of the transfinite interpolation is shown below:

$$\begin{aligned}\underset{\sim}{r}(\xi,n)=&\sum_{n=1}^{N}\phi_n\left(\frac{\xi}{I}\right)\underset{\sim}{r}(\xi_n,n)+\sum_{m=1}^{M}\psi_m\left(\frac{n}{J}\right)\underset{\sim}{r}(\xi,n_m)\\&-\sum_{n=1}^{N}\sum_{m=1}^{M}\phi_n\left(\frac{\xi}{I}\right)\psi_m\left(\frac{n}{J}\right)\underset{\sim}{r}(\xi_n,n_m)\end{aligned}\qquad (4.3)$$

The transfinite interpolation form above, interpolates the entire set of intersecting arbitrary curves. The interpolation function defined above with N=M=2, using the Langrange interpolation polynomials as the blending functions, is termed the transfinite bilinear interpolant and is the one used in this project. With N=M=3, this form is the transfinite biquadratic interpolant. Other immediate candidates for the blending functions are the Hermite interpolation polynomials and the splines.

The results are shown on figures 4.16 to 4.26 As it can be seen there is some improvement but not to an acceptable level. Initially we thought of subdividing both curves and using a faster distribution on the one curve so that the pairs of points will face each other as closely as possible. This was to be done by implementing a geometric or other series that would control the distribution. Eventually this proposal was abandoned, mainly because this would not guarantee the required orthogonality and it would also need numerical opimisation.

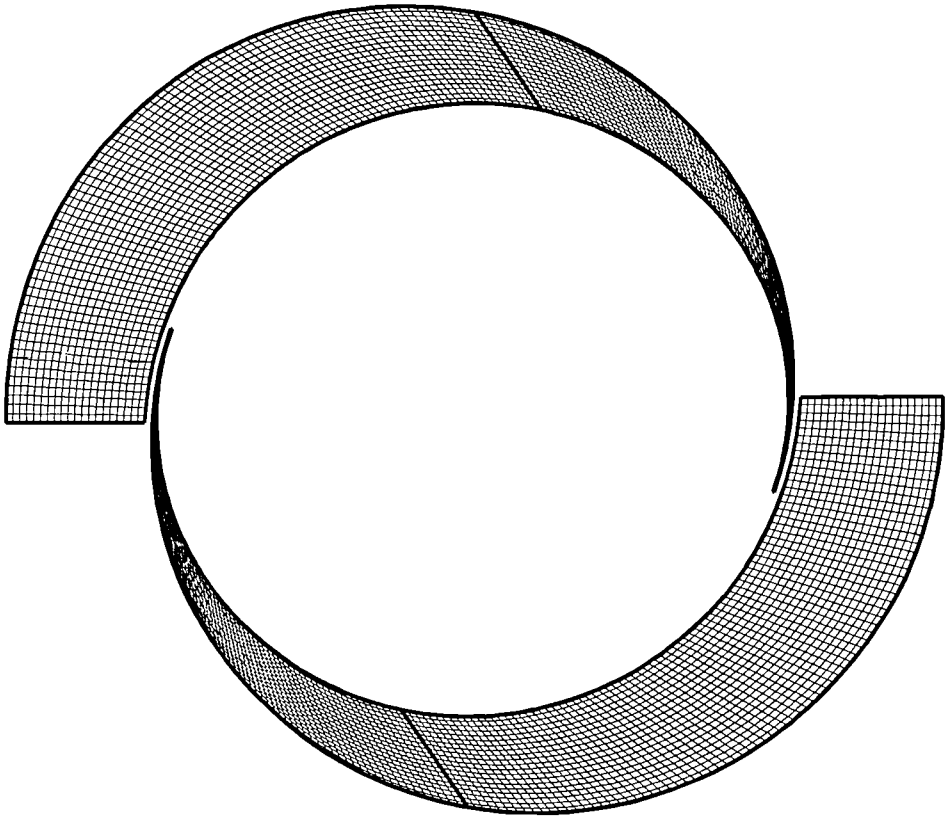

Figure 4.16 Crank angle 200^0

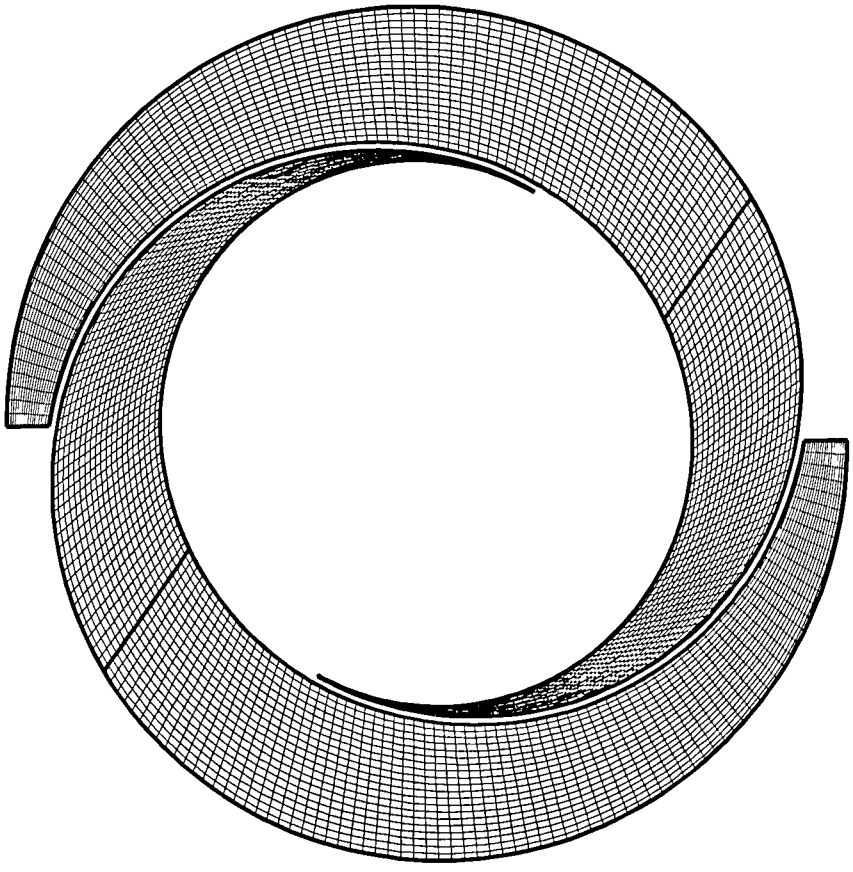

Figure 4.17 Crank angle 300^0

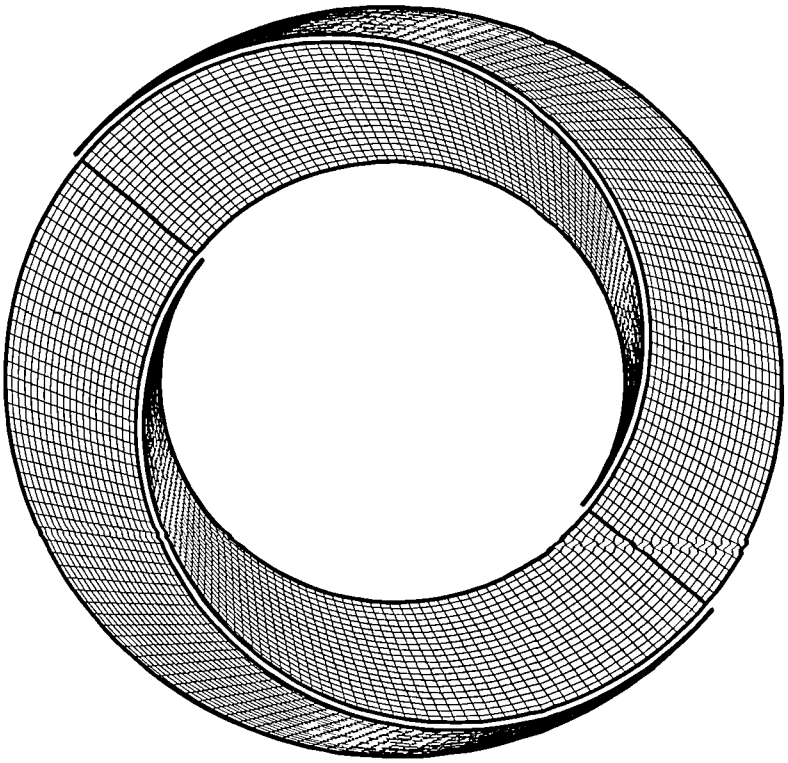

Figure 4.18 Crank angle 400^0

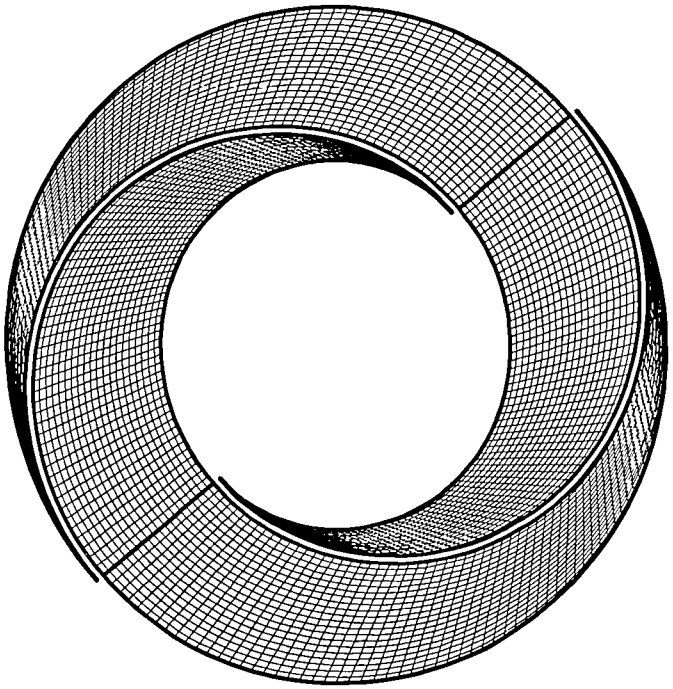

Figure 4.19 Crank angle 500^0

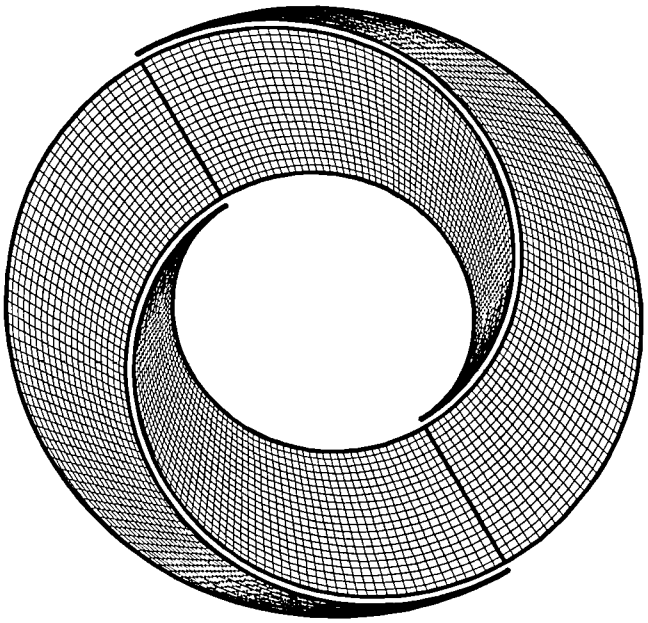

Figure 4.20 Crank angle 600^0

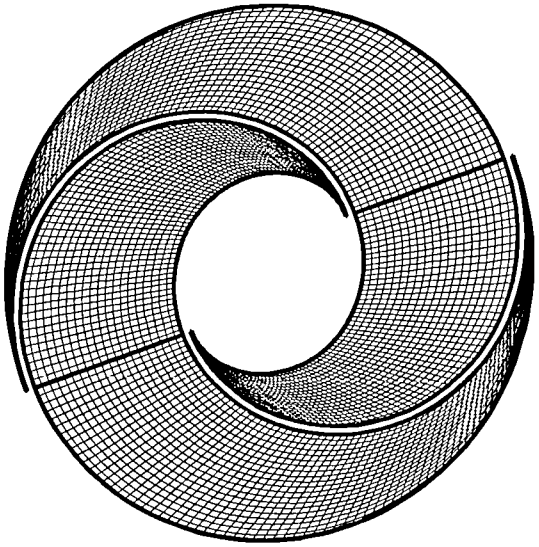

Figure 4.21 Crank angle 700^0

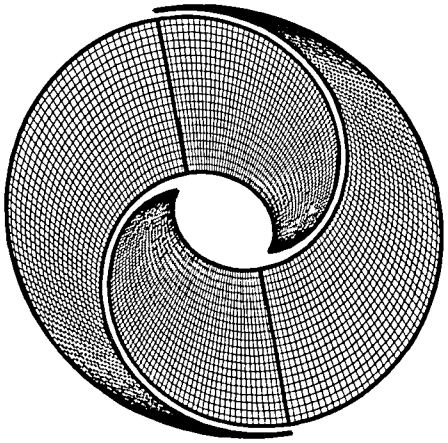

Figure 4.22 Crank angle 800^0

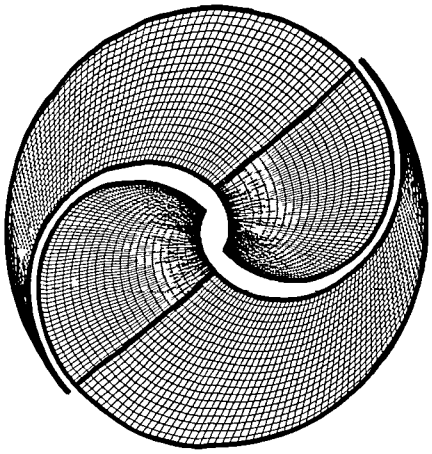

Figure 4.23 Crank angle 860^0

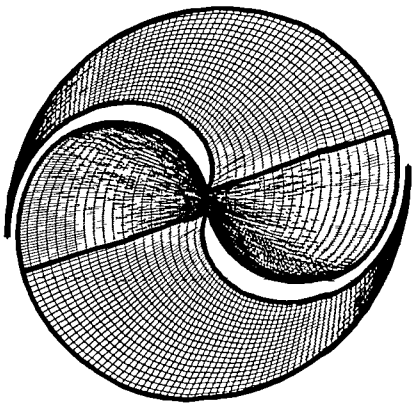

Figure 4.24 Crank angle 900^0

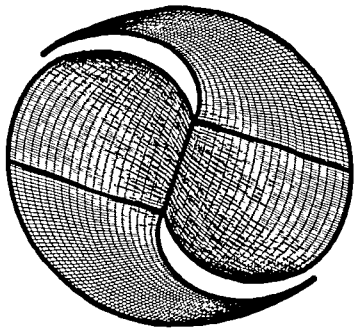

Figure 4.25 Crank angle 950^0

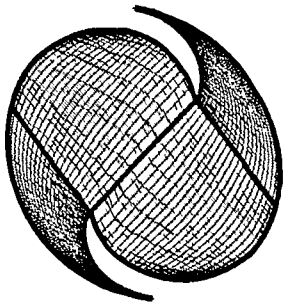

Figure 4.26 Crank angle 1000^0

4.4.3 Mid-Planes Based Grid Generation Code

After careful consideration of the problem it was decided to rewrite the code based on a completely new procedure. The new idea was to find a curve that would be located somewhere in the center of the two boundary curves. This curve would be something like a mid-plane, and instead of subdividing the one or both the boundary edges we would march along this mid-plane (see figures 4.27, 4.28). First we selected a point on the mid plane. Then we drew a straight line that passed from this point and intersected the one curve of the working volume perpendicularly. Then a second line would be drawn, in this case the line passing from the same point on the mid-plane and cutting the other curve of the domain perpendicularly as shown in figure 4.29. By this method we ensured that the elements close to the curves would have maximum orthogonality. Therefore now the objective was firstly to find this mid-plane and secondly to find the points on the curves that would satisfy this condition. After spending some time, two different numerical

techniques were found for the mid-plane and the points on the curves respectively. Eventually, these techniques were not used mainly because they led to excessive computational time. The next step was then to find analytical functions that would satisfy the requirements specified above. After spending a considerable amount of time, some mathematical equations were developed for the mid-plane, and for the points needed for the lines. These are:

$$\begin{pmatrix} \mathbf{XMP\_FO\_OI} \\ \mathbf{YMP\_FO\_OI} \end{pmatrix} = r \begin{pmatrix} \cos\varphi + \left(\varphi + \frac{\pi-\gamma}{2}\right)\sin\varphi - \left(\frac{\pi-\gamma}{2}\right)\cos\theta \\ \sin\varphi - \left(\varphi + \frac{\pi-\gamma}{2}\right)\cos\varphi - \left(\frac{\pi-\gamma}{2}\right)\sin\theta \end{pmatrix},$$

$$\begin{pmatrix} \mathbf{XMP\_OO\_FI} \\ \mathbf{YMP\_OO\_FI} \end{pmatrix} = -r \begin{pmatrix} \cos\varphi + \left(\varphi + \frac{\pi-\gamma}{2}\right)\sin\varphi + \left(\frac{\pi-\gamma}{2}\right)\cos\theta \\ \sin\varphi - \left(\varphi + \frac{\pi-\gamma}{2}\right)\cos\varphi + \left(\frac{\pi-\gamma}{2}\right)\sin\theta \end{pmatrix} \quad (4.4)$$

where MP_FO_OI is the mid plane between the fixed outer and orbiting inner curves, and MP_OO_FI is the mid plane between the orbiting outer and fixed inner curves

Therefore now that we had three points we could either connect them with two lines or, assume that these points are lying in the circumference of a circle, find the center of the circle and then fit a circular arc to connect the points. In this case the interpolation would be performed along the arc as shown in figure 4.30. In the program the user has the option either to use straight lines or circular arcs. The latter appears to produce better grids in terms of smoothness.

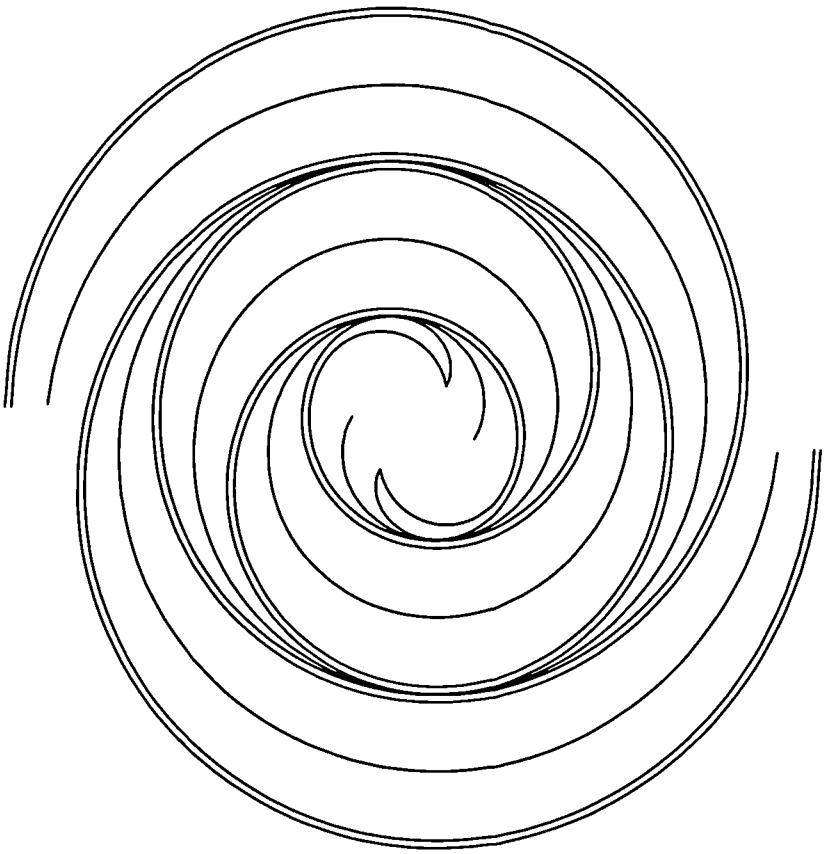

Figure 4.27 Scroll geometry and mid-planes. Crank angle 170^0.

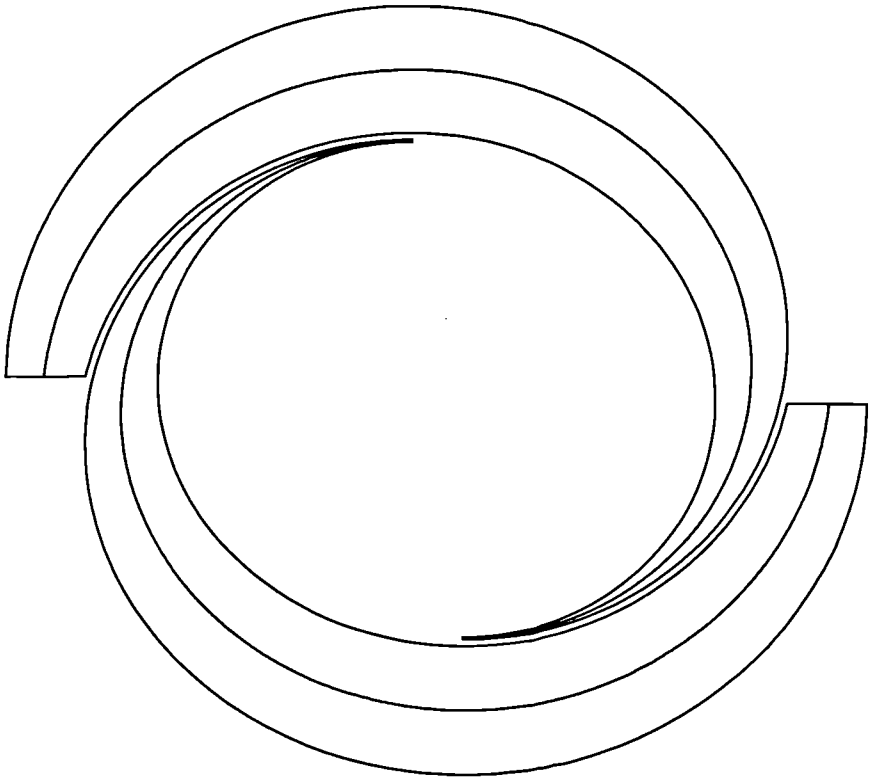

Figure 4.28 Working volumes and mid-planes. Crank angle 170^0.

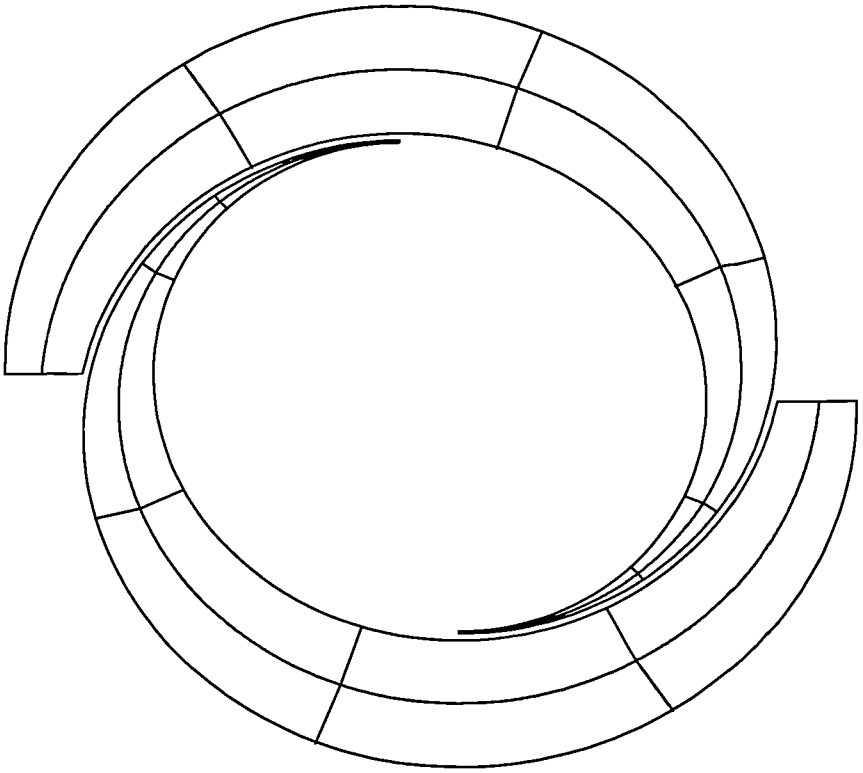

Figure 4.29 Working volumes, mid-planes and samples of lines. starting from points on mid-planes and finishing at the boundary curves forming angles of 90^0. Crank angle 170^0.

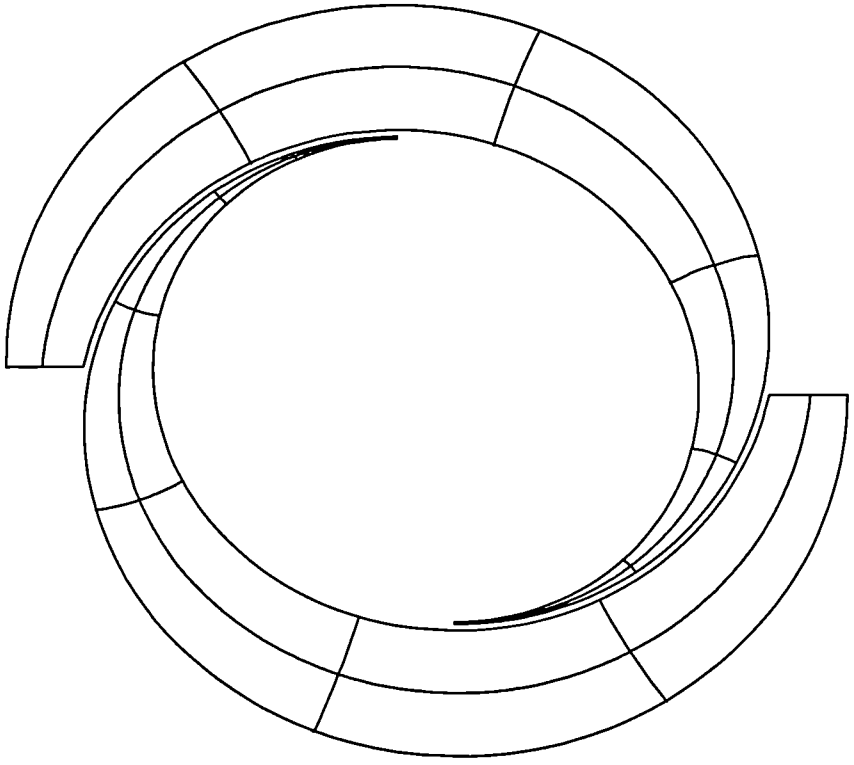

Figure 4.30 Working volumes, mid-planes and samples of circular arcs passing from mid-planes and finishing at the boundary curves forming angles of 90^0. Crank angle 170^0.

Unlike the previous two versions of the program, this method is not the same for all the processes. The general idea is the same but the program is divided into four parts. The first part covers all the suction process of the compressor and a large part of the compression process. It stops at the point where the edges of the spirals start sliding along the circular arcs (see appendix A). The second part covers the rest of the compression process. The third part is for the discharge process and finally the last part is concerned with the inclusion of the discharge pipe in the grid. However before we proceeded to analyze each part of the code, we had to analyze the implementation of a non uniform element distribution. This option together with the transfinite interpolation and the mid-planes are the 'heart' of this final and eventually successful attempt to create a robust, transient, body fitted, structured grid generation package, with maximum orthogonality and aspect ratio within acceptable limits specifically developed for scroll machinery.

4.4.3.1 Implementation of Non Uniform Distribution Functions

With the above approach (mid-planes) the biggest problem i.e. departing from orthogonality was overcome. The next step was to find a way to control the element distribution. Eventually two different mathematical models were implemented. These are, hyperbolic function distribution and circular function distribution (Thompson 1985).

In general, interpolation between $\mathbf{r}_1$ at ξ=0 and $\mathbf{r}_2$ at ξ=**I** can be written as

$$\mathbf{r}(\xi) = \varphi(\xi/\mathbf{I})\mathbf{r}_2 + \left[1 - \varphi(\xi/\mathbf{I})\mathbf{r}_1\right] \qquad (4.5)$$

where φ can be any function such that $\varphi(0)$=0 and $\varphi(1)$=1. The linear polynomial case is obtained here with $\varphi(\xi/\mathbf{I}) = \xi/\mathbf{I}$. The function φ in this form may contain parameters which can be determined so as to match the slope at the boundary, or to match interior points and slopes.

The interpolation function, φ, in this form is often referred to as a 'stretching' function, and the most widely used function is the exponential:

$$\varphi(\xi/\mathbf{I}) = \frac{\exp(\alpha\,\xi/\mathbf{I}) - 1}{\exp(\alpha) - 1} \qquad (4.6)$$

where α is a parameter that can be determined to match the slope at a boundary.

Thus. Since from equation 4.5

$$\mathbf{r}_\xi = \frac{1}{\mathbf{I}}(\mathbf{r}_2 - \mathbf{r}_1)\varphi' \tag{4.7}$$

we can determine α from the equation

$$(\mathbf{r}_\xi)_1 = \frac{\mathbf{r}_2 - \mathbf{r}_1}{\mathbf{I}} \frac{\alpha}{\exp(\alpha) - 1} \tag{4.8}$$

with $(\mathbf{r}_\xi)_1$ specified.

The truncation error is strongly affected by point distribution, and studies of distribution functions have been made in that regard. The exponential, while reasonable, is not the best choice when the variation spacing is large, and polynomials are not suitable in this case. The better choices are the hyperbolic tangent and the hyperbolic sine. The hyperbolic sine gives a more uniform distribution in the immediate vicinity of the minimum spacing, and thus has less error in this region, but the hyperbolic tangent has the better overall distribution. (M. Vinokur, 1983, J.F. Thompson, 1983). These are implemented as follows (following M. Vinokur, 1983), with the spacing specified at either both ends, or a point in the interior, or a point distribution on a curve.

Let the arc length, **s**, vary from 0 to 1 as ξ varies from 0 to **I**: **s**(0)=0, **s**(**I**)=1. Then let the spacing be specified at ξ=0 and ξ=**I** :

$$\mathbf{s}_\xi(0) = \Delta\mathbf{s}_1, \quad \mathbf{s}_\xi(\mathbf{I}) = \Delta\mathbf{s}_2 \tag{4.9}$$

The hyperbolic tangent distribution is then constructed as follows. First,

$$\mathbf{A} = \frac{\sqrt{\Delta\mathbf{s}_2}}{\sqrt{\Delta\mathbf{s}_1}}\Delta\mathbf{s}_1, \quad \mathbf{B} = \sqrt{\Delta\mathbf{s}_1\,\Delta\mathbf{s}_2} \tag{4.10}$$

Then the following nonlinear equation is solved for δ:

$$\frac{\sinh\delta}{\delta} = \frac{1}{\mathbf{B}} \tag{4.11}$$

The arc length distribution then is given by

$$\mathbf{s}(\xi) = \frac{\mathbf{u}(\xi)}{\mathbf{A} + (1 - \mathbf{A})\,\mathbf{u}(\xi)} \tag{4.12}$$

where

$$\mathbf{u}(\xi) = \tfrac{1}{2}\left\{1 + \frac{\tanh\left[\delta\left(\xi/\mathbf{I} - \tfrac{1}{2}\right)\right]}{\tanh\left(\tfrac{1}{2}\delta\right)}\right\} \tag{4.13}$$

If this is applied to a straight line on which $\mathbf{r}$ varies from $\mathbf{r}_0$ to $\mathbf{r}_I$, we have for the point locations:

$$\mathbf{r}(\xi) = \mathbf{r}_0 + (\mathbf{r}_I - \mathbf{r}_0)\mathbf{s}_\xi \tag{4.14}$$

The points are then located by taking integer values of ξ:

$$\xi = 0, 1, 2, \ldots, I$$

Clearly, the arc length distribution, $\mathbf{s}(\xi)$, is here the function of φ of equation 4.5.

Note that $\mathbf{B}$ is essentially the ratio of the specified spacing to the linear spacing, $1/\mathbf{I}$. If $\mathbf{B}$ is greater than unity, i.e. if the specified spacing exceeds the linear spacing, the hyperbolic functions all revert to circular functions in all the relations of this section.

With the spacing $\Delta\mathbf{s}$ specified at only $\xi = 0$, the construction proceeds as follows. First $\mathbf{B}$ is calculated from

$$\mathbf{B} = \mathbf{I}\,\Delta_s \tag{4.15}$$

and eq. 4.11 is solved for δ. The arc length distribution then is given by

$$\mathbf{s}(\xi) = 1 + \frac{\tanh\left[\tfrac{1}{2}\delta\left(\xi/\mathbf{I} - 1\right)\right]}{\tanh\left(\tfrac{1}{2}\delta\right)} \tag{4.16}$$

With the spacing specified only at $\xi = \mathbf{I}$ the procedure is the same, except that relation 4.13 is replaced by

$$\mathbf{s}(\xi) = 1 + \frac{\tanh\left(\tfrac{1}{2}\delta\,\xi/\mathbf{I}\right)}{\tanh\left(\tfrac{1}{2}\delta\right)} \tag{4.17}$$

If the spacing $\Delta\mathbf{s}$ is specified at only an interior point $\mathbf{s} = \sigma$, $\mathbf{B}$ is again calculated

from 4.15, and then δ is determined as the solution of

$$1+\left(\frac{\mathbf{B}}{\sigma\delta}\right)^2=\left(\frac{\cosh\delta-1+1/\sigma}{\sinh\delta}\right)^2 \qquad (4.18)$$

The value of ξ at which $\mathbf{s}=\sigma$ is obtained by solving the nonlinear equation,

$$\mathbf{x}=\frac{\mathbf{I}}{\delta}\tanh^{-1}\left(\frac{\sinh\delta}{1/\sigma+\cosh\delta-1}\right) \qquad (4.19)$$

The arc length distribution then is given by

$$\mathbf{s}(\xi)=\sigma\left\{\frac{1+\sinh\left[\delta(\xi-\mathbf{x})/\mathbf{I}\right]}{\sinh\left(\delta\mathbf{x}/\mathbf{I}\right)}\right\} \qquad (4.20)$$

This last distribution is based on the hyperbolic sine. From this, a distribution based on the hyperbolic sine with the spacing specified at one end can be derived. Here **B** is evaluated from 4.15, and then δ is determined as the solution of,

$$\frac{\sinh\delta}{\delta}=\frac{1}{\mathbf{B}} \qquad (4.21)$$

The arc length distribution then is given by

$$\mathbf{s}(\xi)=\frac{\sinh\left(\delta\xi/\mathbf{I}\right)}{\sinh\delta} \qquad (4.22)$$

if the spacing is specified at ξ=*0*. With the specification at ξ=**I**, the distribution is

$$\mathbf{s}(\xi)=1-\frac{\sinh\left[\delta(1-\xi/\mathbf{I})\right]}{\sinh\delta} \qquad (4.23)$$

In the code, the above method is implemented in such a way that the following three options are available:

I) Both initial and final divisions are specified.

II) Only initial division is specified.

III) Only final division is specified.

However, the program is optimized and there is no need for the user to choose between these options. The only thing that the user has to define is whether the distribution is uniform or non uniform.

It has to be noted at this point that the functionality and the behavior of all the mathematical equations used in this program were first checked using Matlab. Matlab is a mathematical package that offers good graphics. The main reason for using Matlab was the advantage of viewing the behavior of the curves first, and then deciding whether or not to implement them into the code.

4.4.3.2 Suction - Part of Compression

Since the two working volumes are identical we will analyze only the one. In this new approach the grid is made up of four blocks with two blocks in each working chamber. From the figures that follow it can be seen that each working volume appears to have only one block. In fact there is a second block but it is so small it can not be seen at this stage. The importance of this 'hidden' block will become apparent later on. (i.e. for the rest of the compression process). This part of the code is not so complicated as the other parts. First we calculated the grid on the 'hidden' block using transfinite interpolation and then we calculated the grid on the other block using the mid-planes technique. At this point it should be stated that another 'sub-block' was introduced within block 3 as shown in figure 4.31. Actually this is not a block by itself, but forms a part of block 3 and is used to put additional smoothness in the connection between the two blocks.

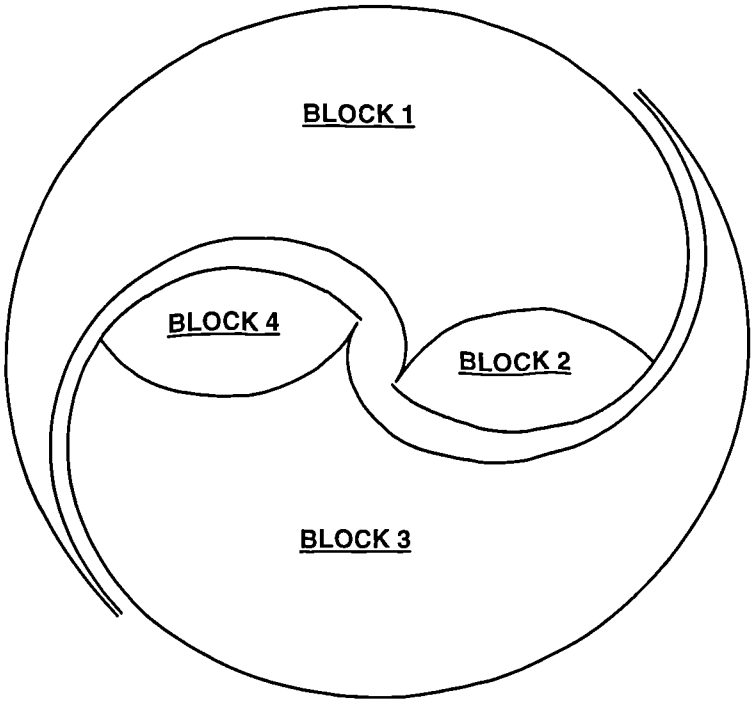

Figure 4.31 Blocks structure during compression process. Crank angle 820^0.

No matter how small are the elements of the 'hidden' block, the use of non-uniform distribution functions discussed above ensures that the increase of the size of the elements on the vicinity will be as smooth as possible. In fact at the edge of contact between the two blocks (block 3 and 4) the elements on each side either have exactly the same size or there is a maximum difference of 1.2 between them. The grid for this process is shown in figures 4.37to 4.50

4.4.3.3 Remainder of Compression

This part of the grid is more complicated than the first one. In this case the so called 'hidden' block begins to expand in a non uniform way. For convenience this 'hidden' block will be called block 4 for the rest of this chapter. The expansion should be as smooth as possible in order to avoid oscillations on the solution. In this case the edges the hidden block 4 are shown in figure 4.32

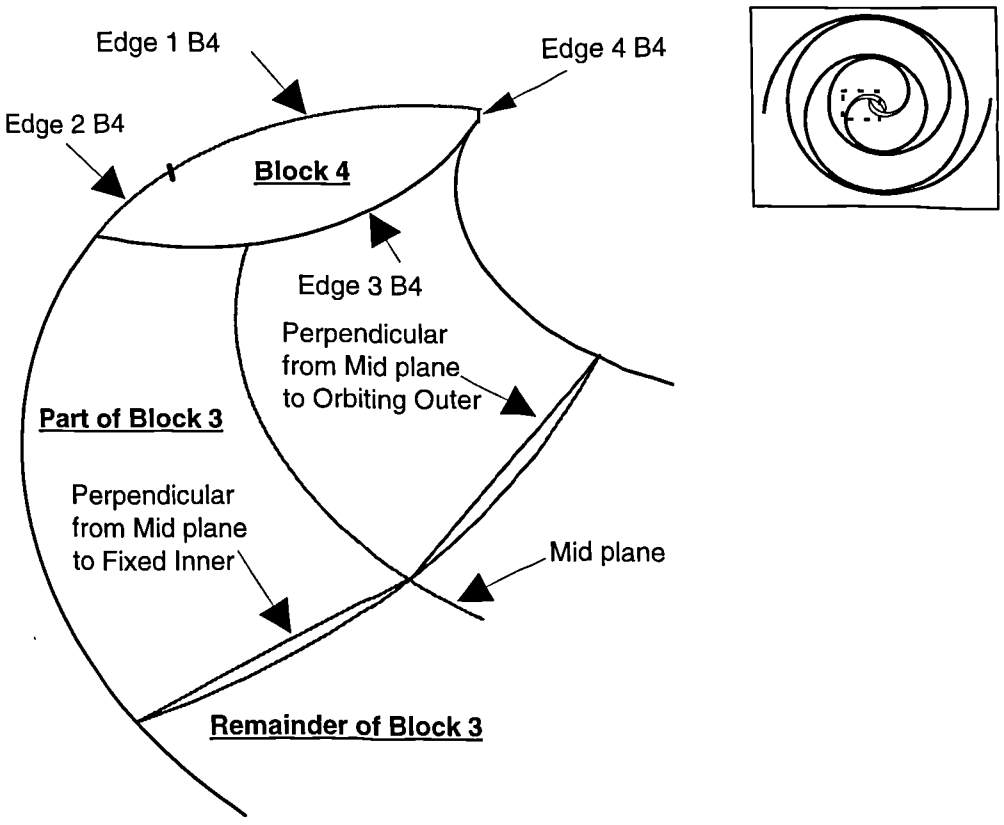

Figure 4.32 Blocks structure during compression process. Crank angle 820^0.

The size of edge 4B4 remains the same until the discharge process. Even though the size remains the same, because it is the clearance between the two curves, the relative position will change according to the crank angle. The sizes of the edges,

1B4, 2B4 and 3B4 were found experimentally. It has to be noted here that this was the most time consuming procedure in the development of the code. This is mainly because without an analytical solution, everything was optimized experimentally.

Once the four edges were clearly identified and their mathematical definition known we continued with the non uniform subdivision of the edges and then used tranfinite interpolation to calculate vertices in the interior of block 4. The next step now was to construct the mesh for part of block 3. In this case the edges were found experimentally and this was also very time consuming. Then the edges were non uniformly subdivided and finally, transfinite interpolation was used to calculate points on the interior. For the remainder of block 3, the non uniform distribution was employed again, and the interior vertices were calculated using the mid plane technique. The grid for this section is shown in figures 4.51 and 4.52.

4.4.3.4 Discharge Process

In this case, edge 4B4 comes in contact with the corresponding edge of block2. In order to avoid any problems, we have to make sure that the vertices in each side match. The way we did this was to calculate the vertices only on the edge 4B4 and then to force the other edge to have these values. This process is more or less the same as the previous one. There are however two main differences. These are: (a) the edge 4B4 is expanding and (b) part of block 3 disappears very slowly and very smoothly. It mast be reemphasised that the size, type, etc. of the edges of block 4 and those of the part of block 3, were found and optimized using the extremely time consuming technique of trial and error. This was the biggest problem we faced. The grid for the case of block 4 and part of block 3, if there is any, are calculated using the transfinite interpolation, and non uniform distribution, where as the grid of the remaining of block 3 was created using the combination of mid plane technique and non uniform distribution. The results for this section are shown in figures 4.53 to 4.55.

4.4.3.5 Inclusion of the Inlet Pipe

The development of this code was the biggest challenge of the project. The next step i.e. the inclusion of a pipe into the grid was also a great challenge. The pipe is located at block 4 and is adjacent to the edge 1B4. The problem here is not how to constrain a pipe into the grid. The main problem in this case is that the pipe is fixed in space. Everything (elements) around the pipe can move but the grid of the pipe

has to remain stationary. This pipe is of great importance, because using this pipe we will specify the boundary conditions needed for the analysis.

In order to do this, Block 4 was divided into four parts. The one part is the pipe, and the other three are the parts around the pipe. Once the user set the flag for the pipe ON then the program is waiting for the diameter of the pipe. Everything is automatic. The user has to specify only the diameter, height and the number of K subdivisions. If the pipe diameter is too big, for the size of the machine then the program returns a warning, requesting a smaller diameter. Once the diameter is within acceptable limits then the code calculates the position of the pipe, and then the number of elements of the pipe. The number of cells for the pipe is not determined by the user. If the grid of the pipe is too coarse then there is an indirect way to add more elements in there. To do this the user can increase the number of the elements of block 4, and this will automatically increase the number of elements in the pipe. The four parts of block 4 are shown below (figures 4.33 to 4.36). The difficult part of this section was once again the specification of the edges. The combination of transfinite interpolation with non uniform distribution was the grid generation tool for this case. The final results for this section are shown in figures 4.56 to 4.64.

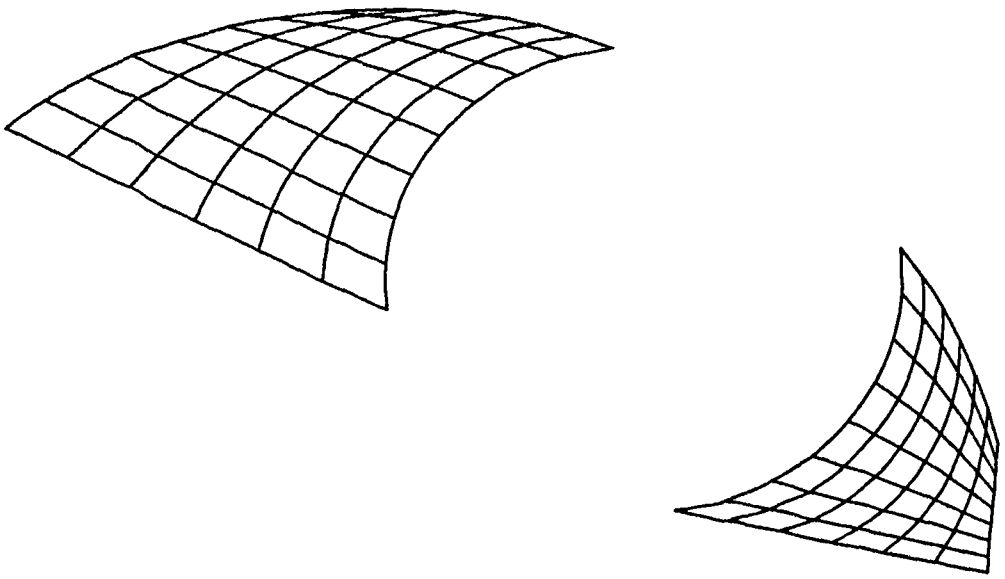

Figure 4.33 Grid of Parts 1 and part 3 of Block4 Crank angle 925^0, Diameter of pipe 0.02 m. (Transfinite interpolation)

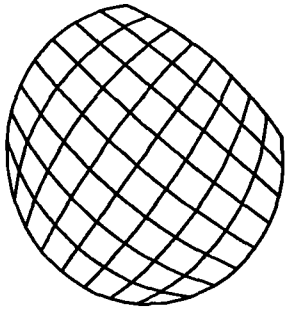

Figure 4.34 Grid of Part 2 of Block4 Crank angle 925^0, Diameter of pipe 0.02 m. (Transfinite interpolation)

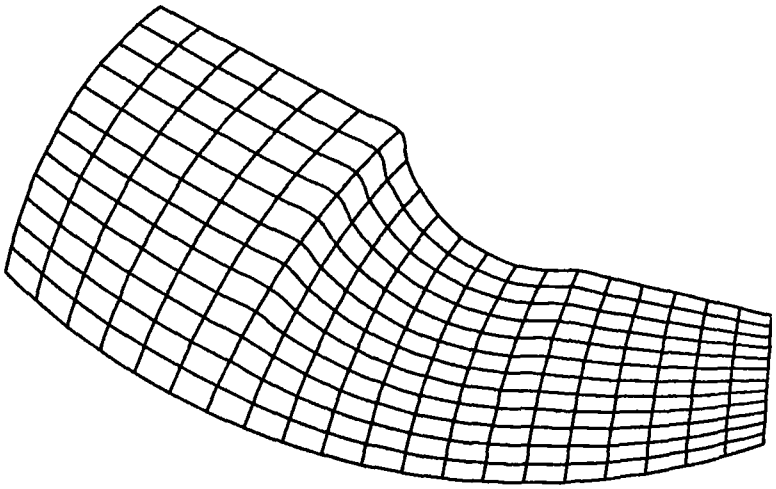

Figure 4.35 Grid of Part 4 of Block4 Crank angle 925^0, Diameter of pipe 0.02 m. (Transfinite interpolation)

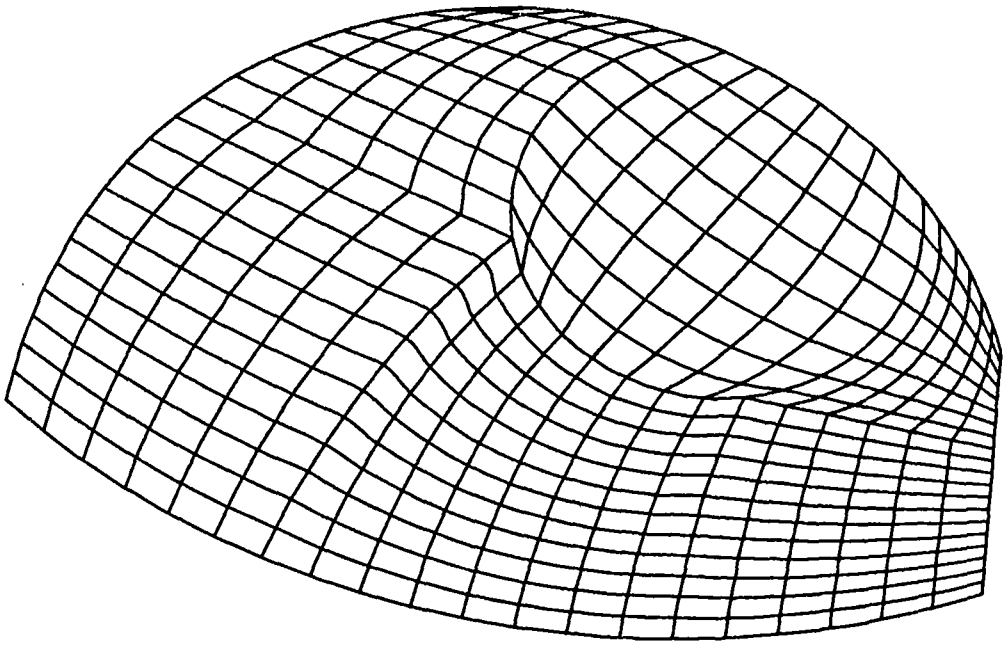

Figure 4.36 Grid of Block4 Crank angle 925^0, Diameter of pipe 0.02 m.

4.4.3.6 Use of the Code

Before we proceed with the final description of how to use the code, we have to say something about how the grid is constructed in three dimensions. As is known, the height of the scroll compressor-expander is constant, therefore the grid constructed in two dimensions (x,y) can be simply extruded in the Z-axis. Please note that the constant height of the machine does not permit us to solve the problem by a two dimensional approach. The reason is because the flow "in" (case of expander) or "out" (case of compressor) is coming from the Z-axis (pipe).

To run the program there are two main options. The first one is to call it from CFX as a sub-routine (the code is implemented into CFX4), and the second one is to run it independently. Let us first analyze the case where the program is running independently. In this case there is an input file in which the user can specify all the parameters needed for the generation of the grid. The first thing the user has to specify is the size of the machine. This is done by giving the base circle radius, the thickness of the walls, the height of the walls, the clearance and the length of the spirals. Then the crank angle must be given. The crank angle is the parameter that will indicate whether the working volumes are in the Suction, Compression, or Discharge stage. The next step is to specify the number of elements in each block. Note that blocks which share the same edge should have the same number of elements along that edge. This is done by specifying the number of subdivisions along each axis (I,J,K).

Once the process of subdivision is completed, the type of interpolation for the interior points has to be specified. There are two options as shown in figs 4.37 to 4.50. These are either the use of linear interpolation along a straight line or interpolation along a circular arc. Next is the decision about the type of distribution. Options are: Uniform distribution or Non uniform distribution. Finally comes the option of the pipe. This option is not available for any crank angle. This is obvious because we cannot have a pipe in the grid during the suction, or compression processes. If, however, the user specifies a pipe by mistake at those conditions, its requirement is ignored. At the end of the run an output file called 'GROUT' is created. The grid calculated and stored into file 'GROUT' is only for that specific crank angle the user defined at the input file. To view the results we have our own post processor Fortran program, using GINO Libraries.

For the case where the program is called from CFX there is only one major change.

That is the crank angle is related to real time and speed. In this case the user has to specify the rotational speed of the machine, the time step (needed for the simulation) and only the initial crank angle, all the other parameters are the same as for the case where we run the program independently. For example if we have ten time steps, the program will be called ten times. Each time the program is called a new crank angle is calculated (because of the increase in time) from the relation between speed and time. As a result of this a new grid for that specific time step is created, and given to the solver. This process continues until the last time step.

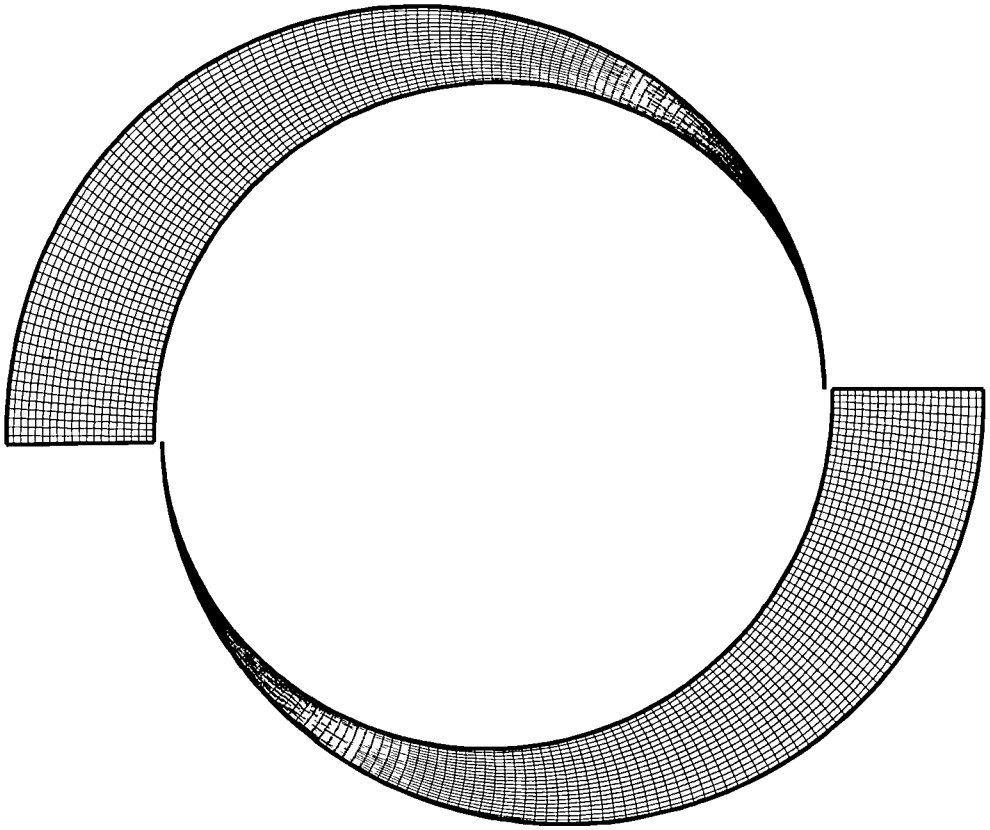

Figure 4.37 Grid 150*20*1. Crank angle 180^0, Non Uniform Distribution, Circular arcs

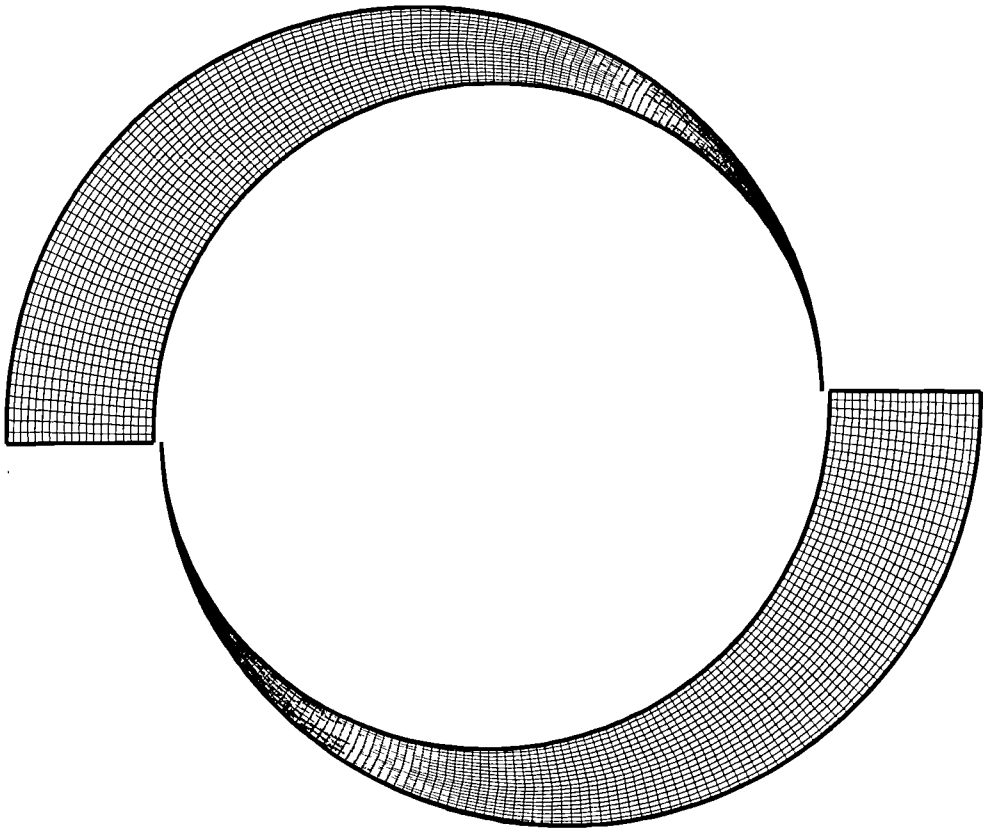

Figure 4.38 Grid 150*20*1. Crank angle 180^0, Uniform Distribution, Straight lines

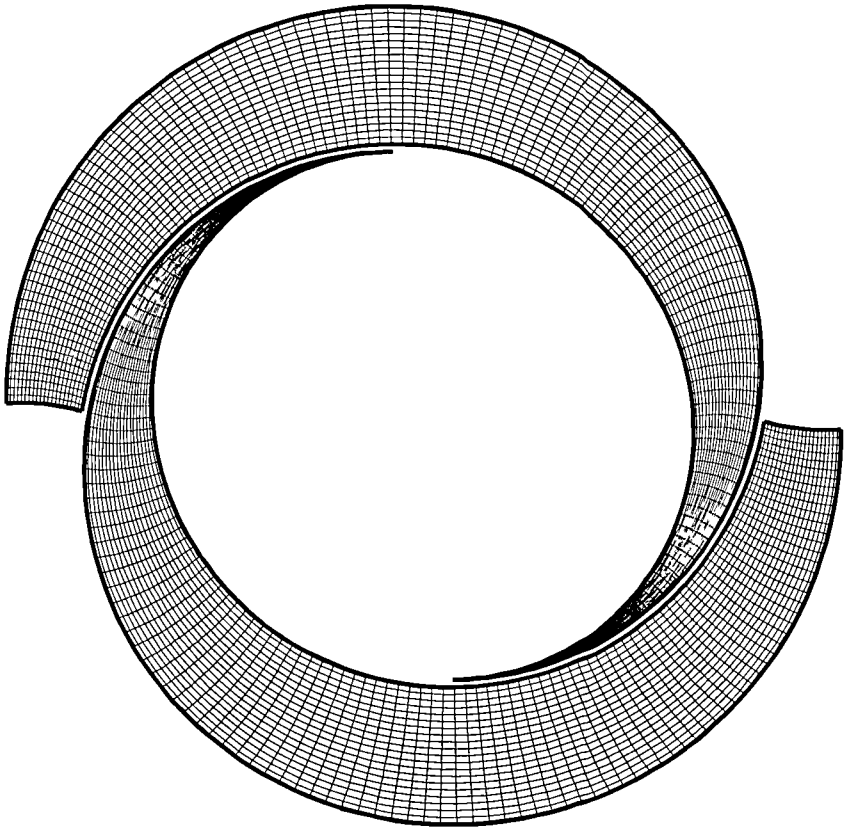

Figure 4.39 Grid 150*20*1. Crank angle 270, Non Uniform Distribution, Circular arcs

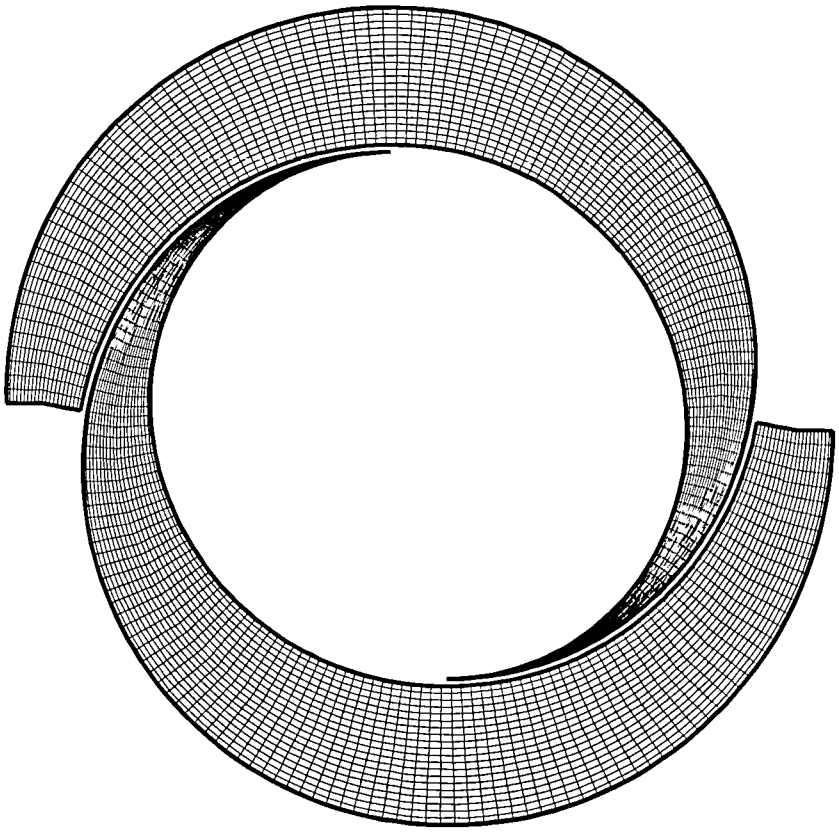

Figure 4.40 Grid 150*20*1. Crank angle 270^0, Uniform Distribution, Straight lines

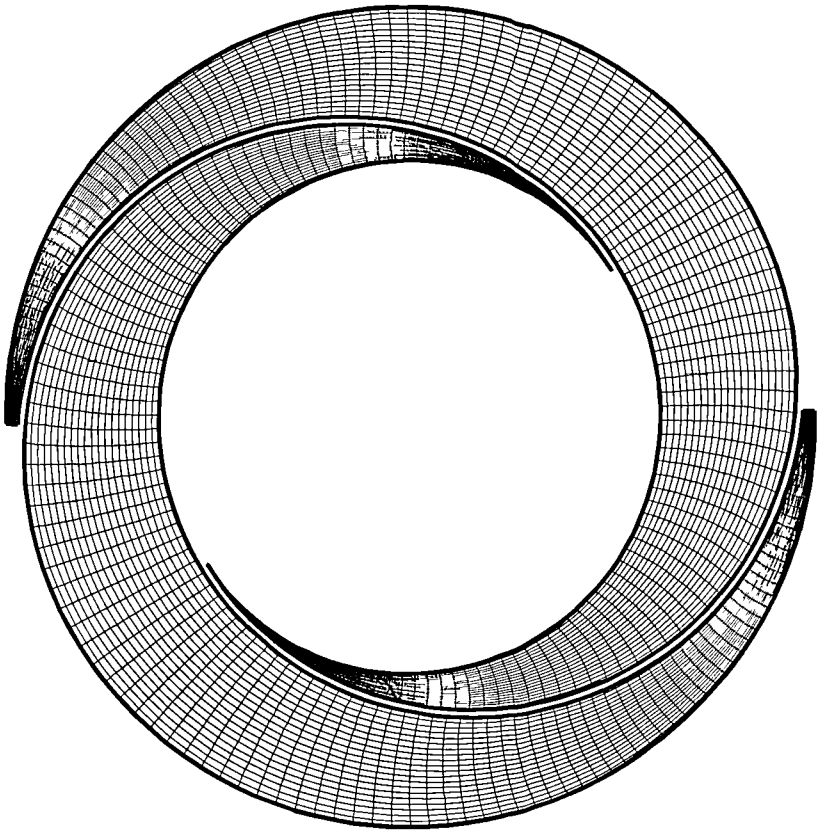

Figure 4.41 Grid 150*20*1. Crank angle 330^0, Non Uniform Distribution, Circular arcs

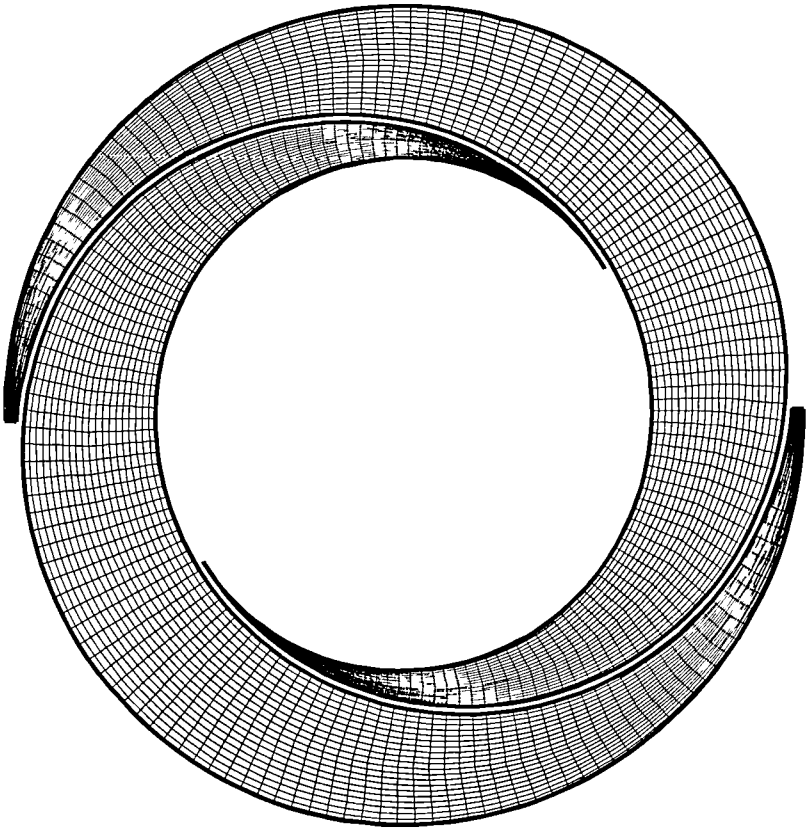

Figure 4.42 Grid 150*20*1. Crank angle 330^0, Uniform Distribution, Straight lines

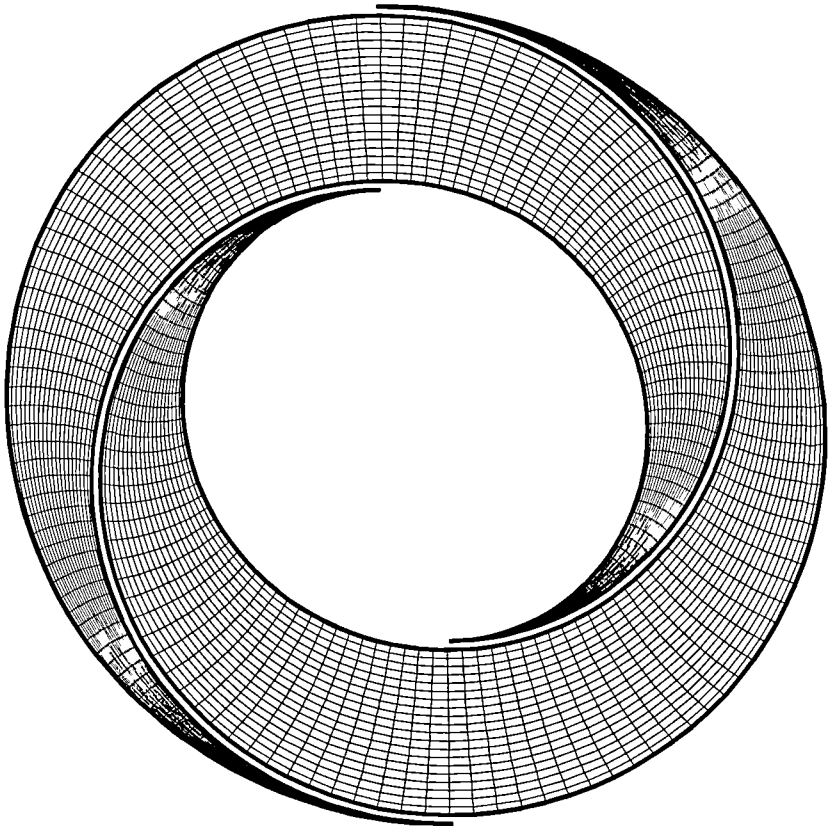

Figure 4.43 Grid 150*20*1. Crank angle 450^0, Non Uniform Distribution, Circular arcs

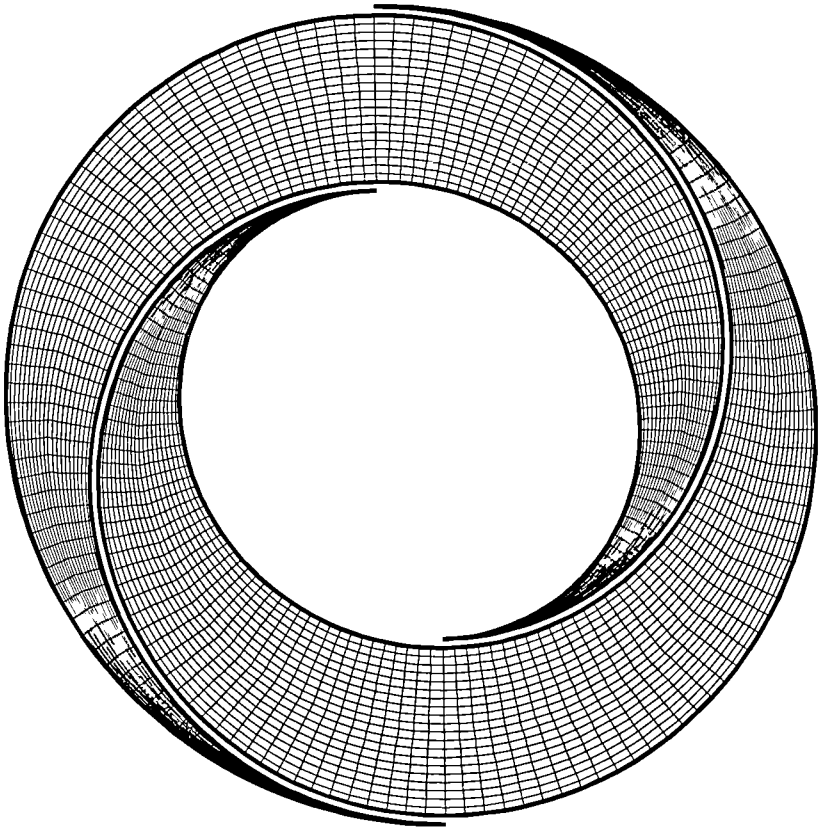

Figure 4.44 Grid 150*20*1. Crank angle 450^0, Uniform Distribution, Straight lines

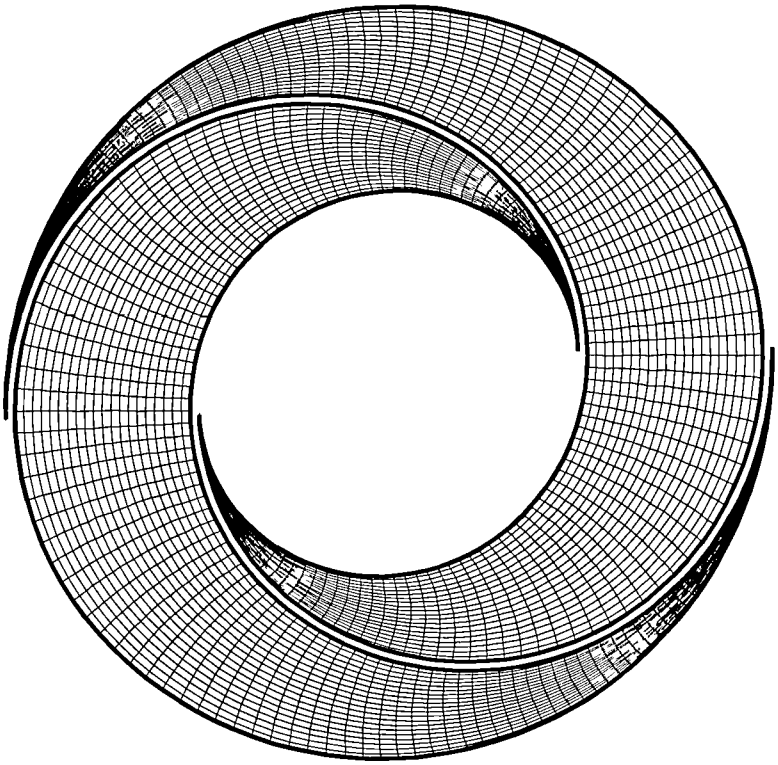

Figure 4.45 Grid 150*20*1. Crank angle 540^0, Non Uniform Distribution, Circular arcs

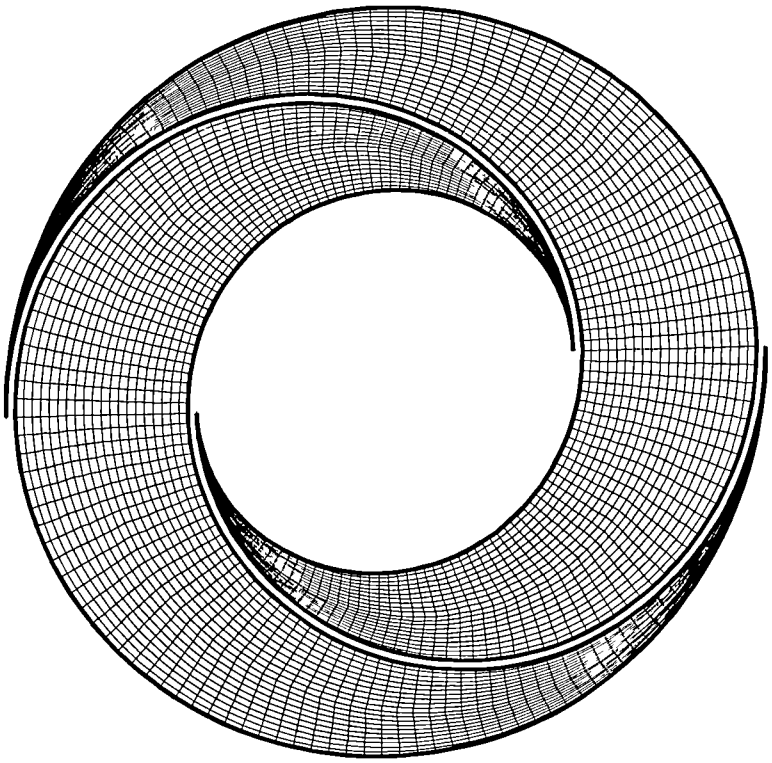

Figure 4.46 Grid 150*20*1. Crank angle 540^0, Uniform Distribution, Straight lines

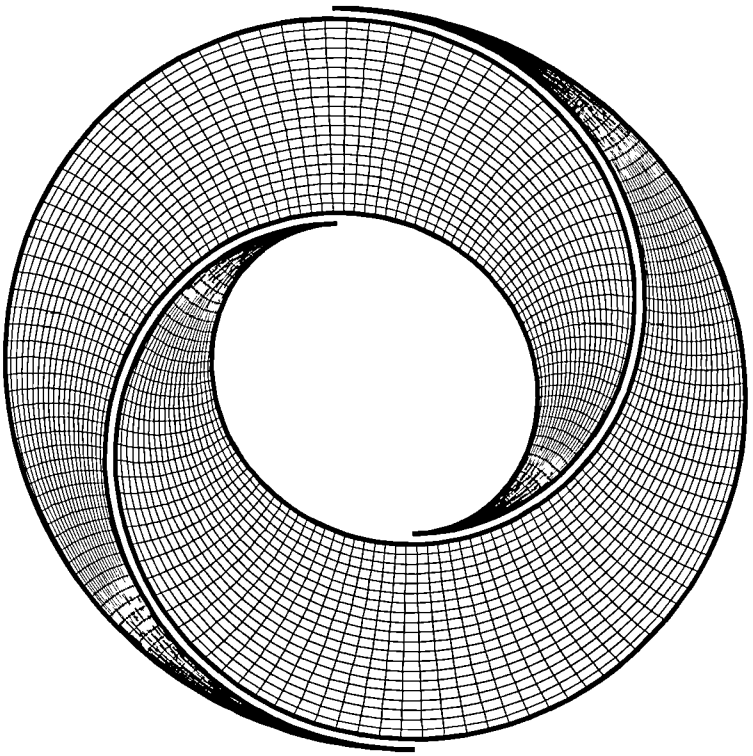

Figure 4.47 Grid 150*20*1. Crank angle 630^0, Non Uniform Distribution, Circular arcs

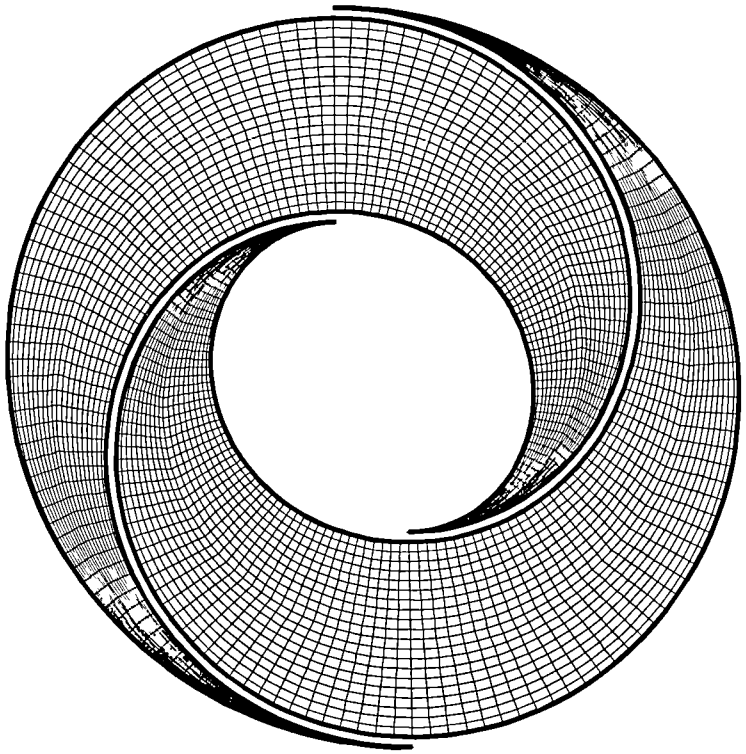

Figure 4.48 Grid 150*20*1. Crank angle 630^0, Uniform Distribution, Straight lines

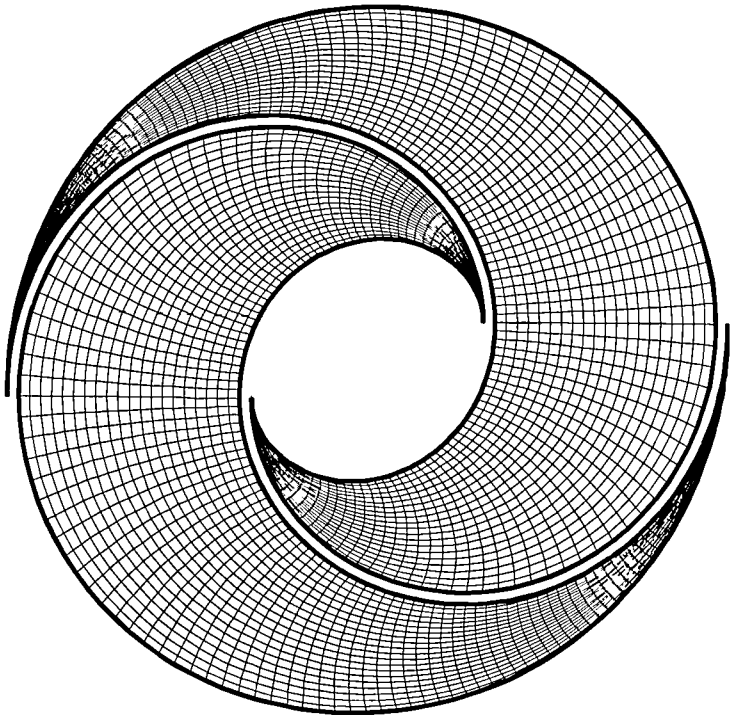

Figure 4.49 Grid 150*20*1. Crank angle 720^0, Non Uniform Distribution, Circular arcs

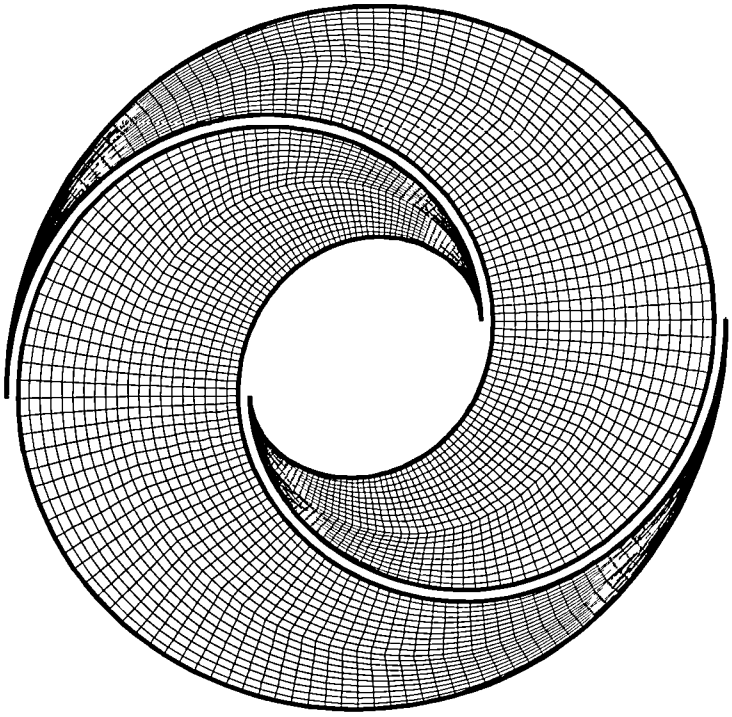

Figure 4.50 Grid 150*20*1. Crank angle 720^0, Uniform Distribution, Straight lines

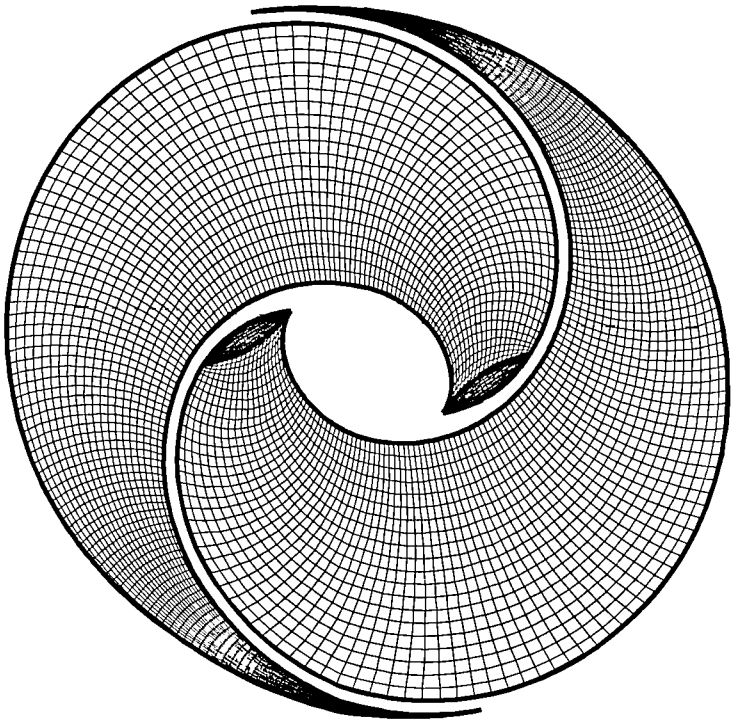

Figure 4.51 Grid 150*20*1. Crank angle 800^0, Non Uniform Distribution, Circular arcs

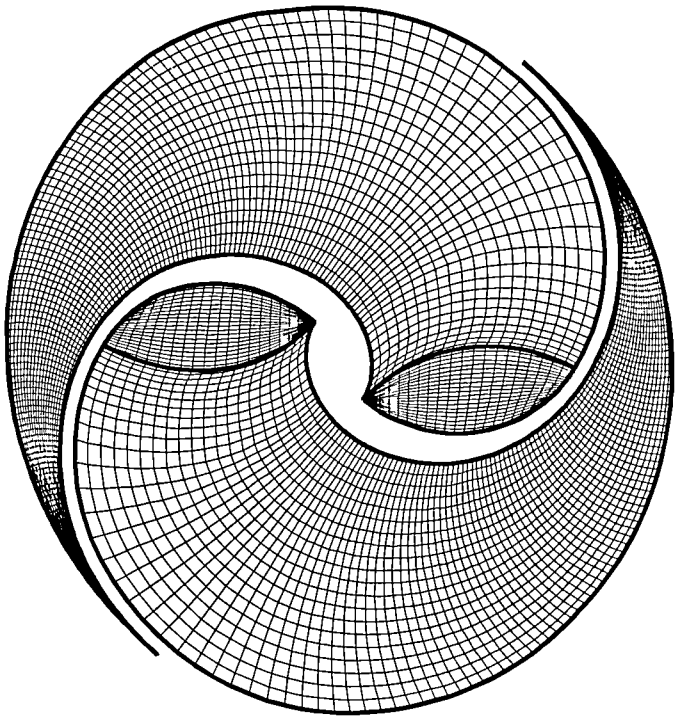

Figure 4.52 Grid 150*20*1. Crank angle 850^0, Non uniform Distribution, Circular Arcs

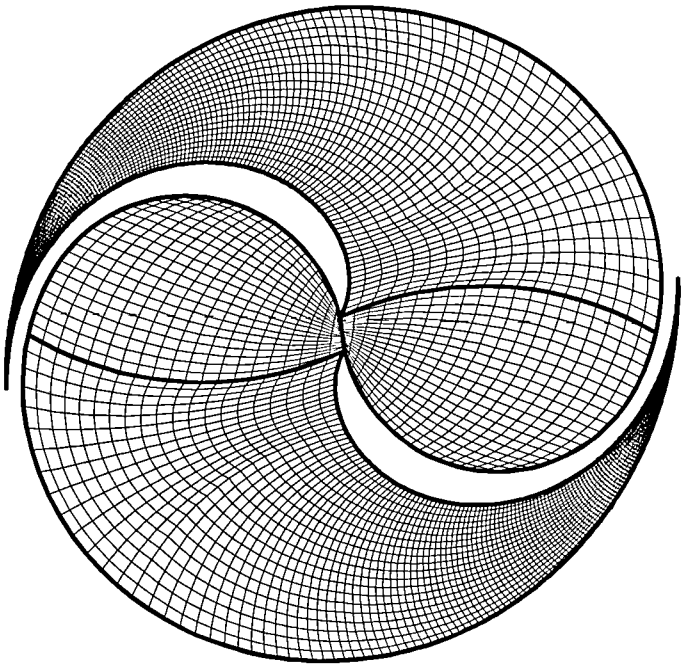

Figure 4.53 Grid 150*20*1. Crank angle 900^0, Non Uniform Distribution, Circular arcs

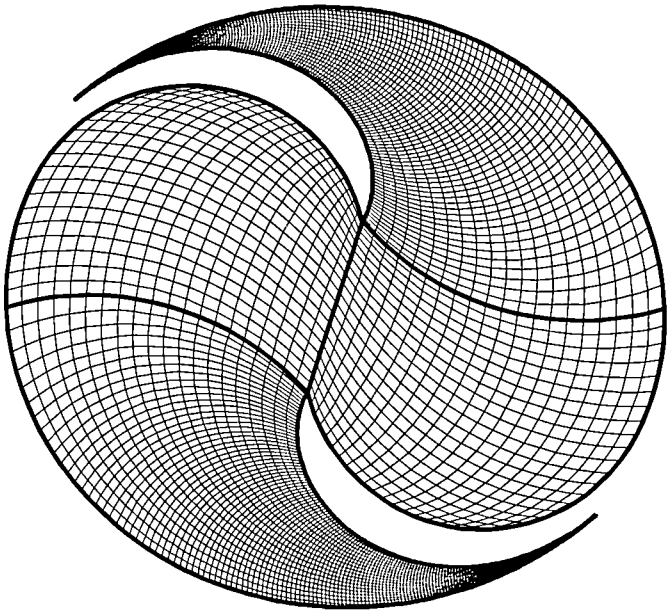

Figure 4.54 Grid 150*20*1. Crank angle 950^0, Non Uniform Distribution, Circular arcs

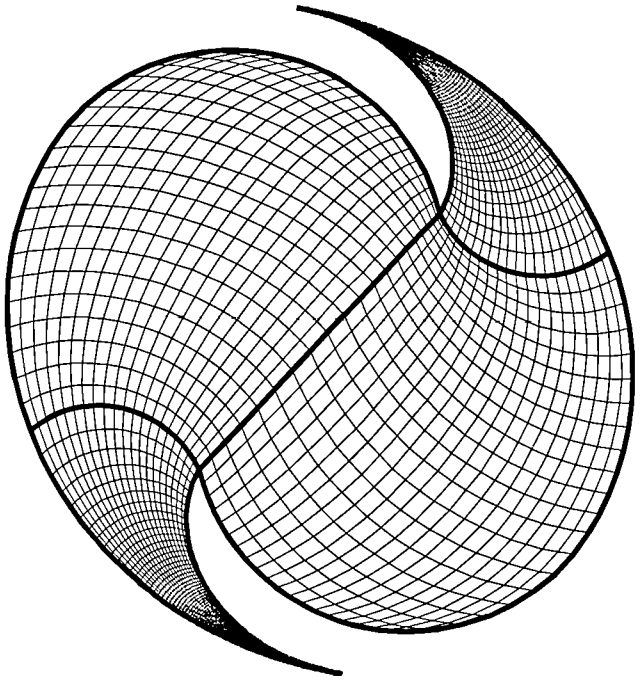

Figure 4.55 Grid 150*20*1. Crank angle 1000^0, Non Uniform Distribution, Circular arcs

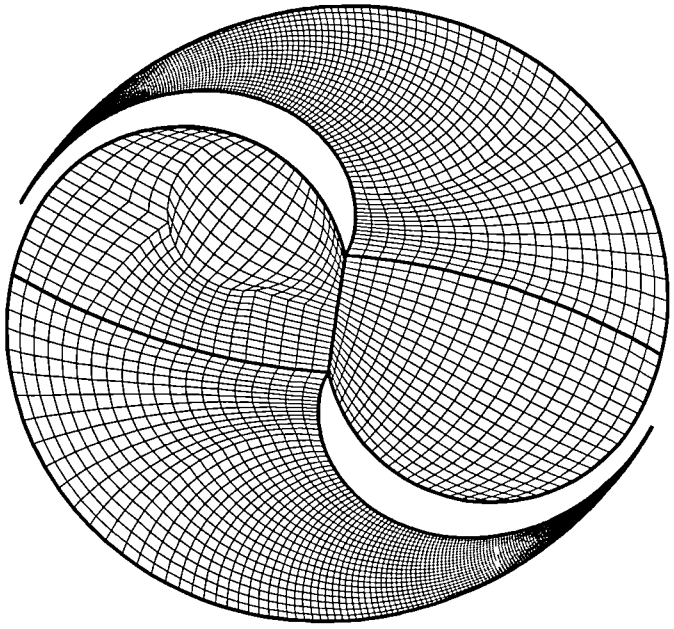

Figure 4.56 Grid 150*20*1. Crank angle 930^0, Non Uniform Distribution, Circular arcs, inlet pipe diameter 0.02m

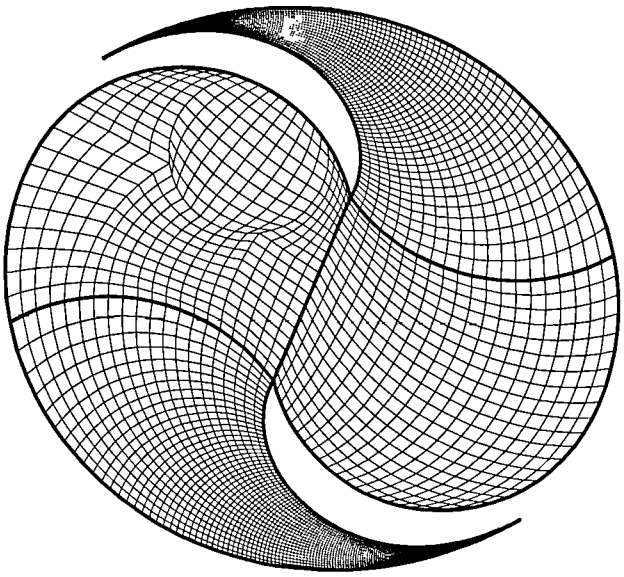

Figure 4.57 Grid 150*20*1. Crank angle 960^0, Non Uniform Distribution, Circular arcs, Inlet pipe diameter 0.02m

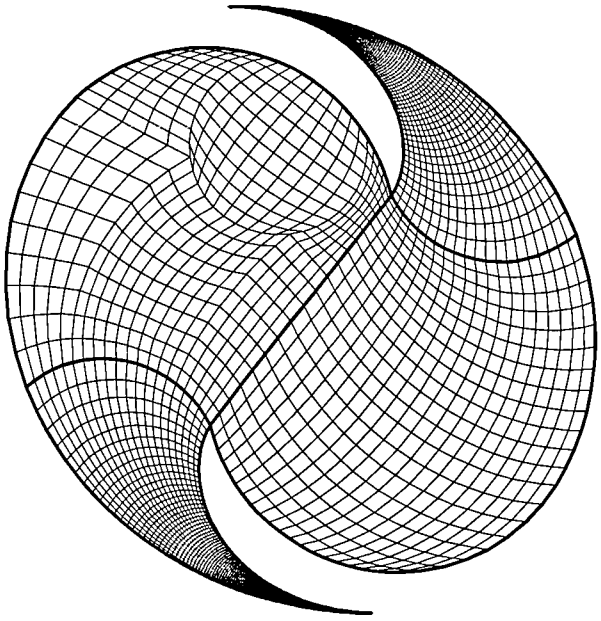

Figure 4.58 Grid 150*20*1. Crank angle 1000^0, Non Uniform Distribution, Circular arcs, Inlet pipe diameter 0.02m

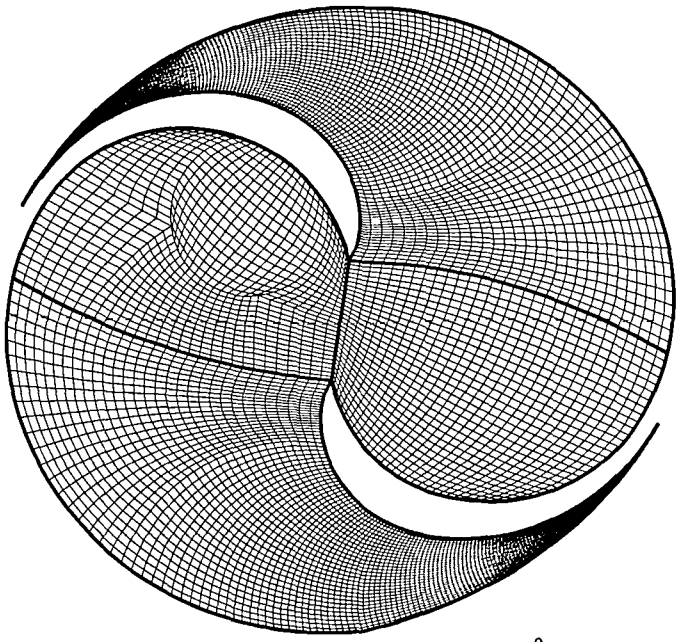

Figure 4.59 Grid 150*30*1. (Refined mesh) Crank angle 930^0, Non Uniform Distribution, Circular arcs, Inlet pipe diameter 0.02m

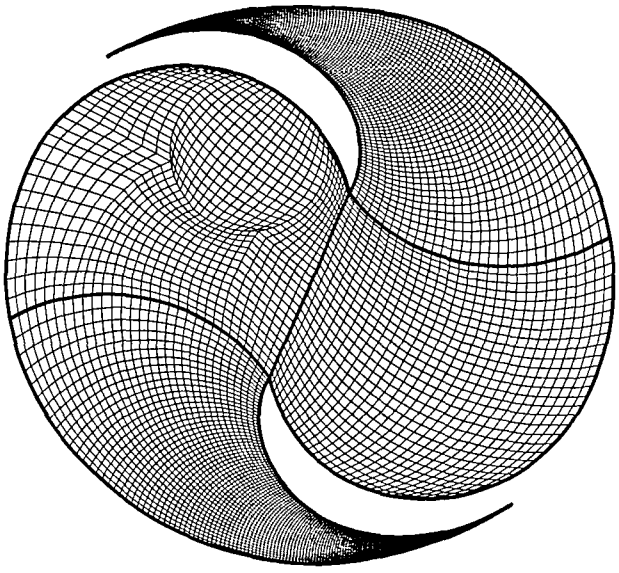

Figure 4.60 Grid 150*30*1. (Refined mesh) Crank angle 960^0, Non Uniform Distribution, Circular arcs, Inlet pipe diameter 0.02m

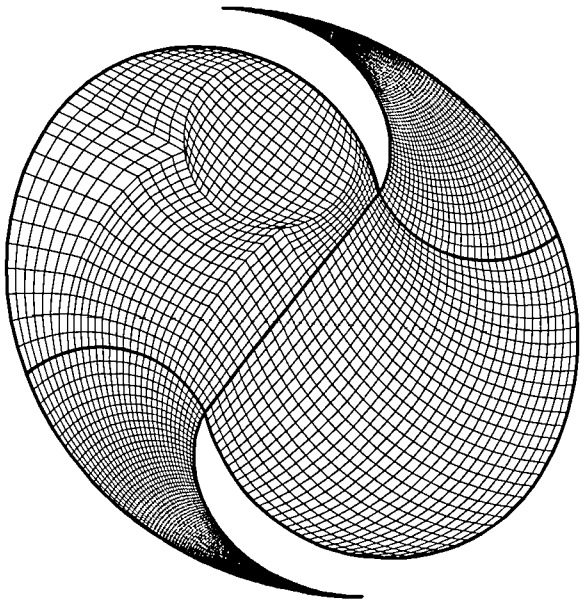

Figure 4.61 Grid 150*30*1. (Refined mesh) Crank angle 990^0, Non Uniform Distribution, Circular arcs, Inlet pipe diameter 0.02m

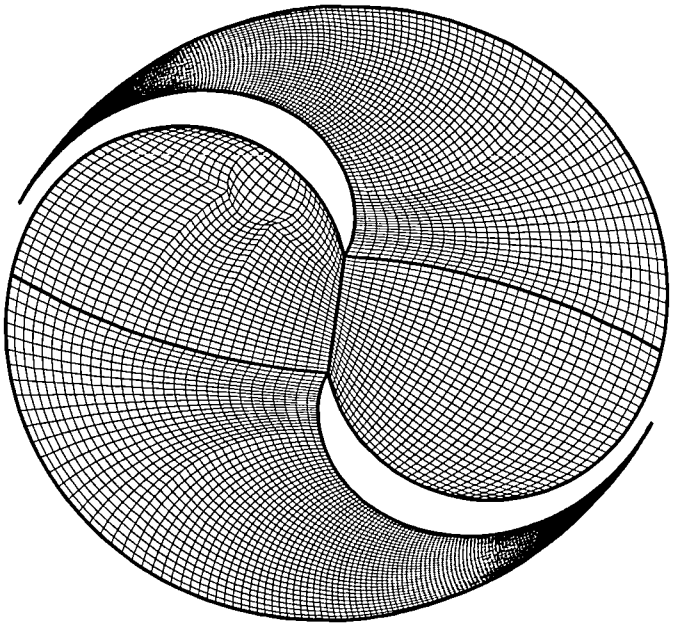

Figure 4.62 Grid 150*30*1. (Refined mesh) Crank angle 930^0, Non Uniform Distribution, Circular arcs, Inlet pipe diameter 0.01 (smaller pipe diameter)

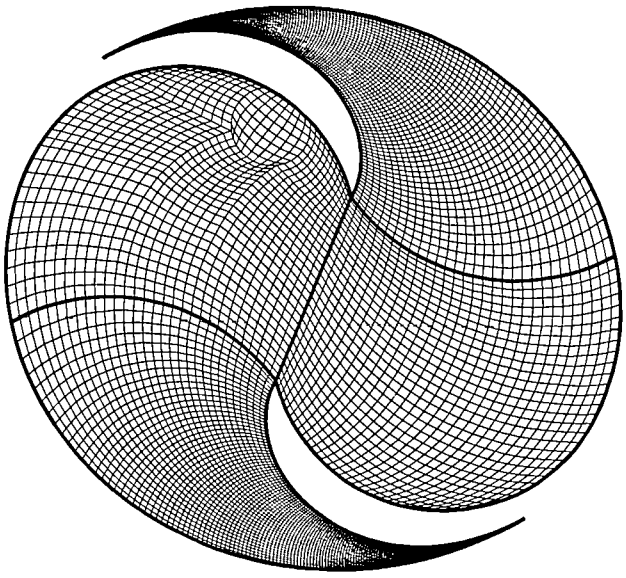

Figure 4.63 Grid 150*30*1. (Refined mesh) Crank angle 960^0, Non Uniform Distribution, Circular arcs, Inlet pipe diameter 0.01 (smaller pipe diameter)

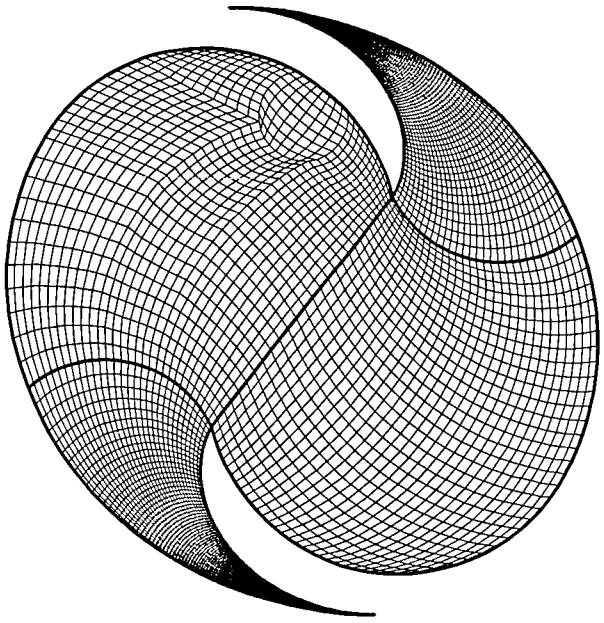

Figure 4.64 Grid 150*30*1. (Refined mesh) Crank angle 990^0, Non Uniform Distribution, Circular arcs, Inlet pipe diameter 0.01 (smaller pipe diameter)

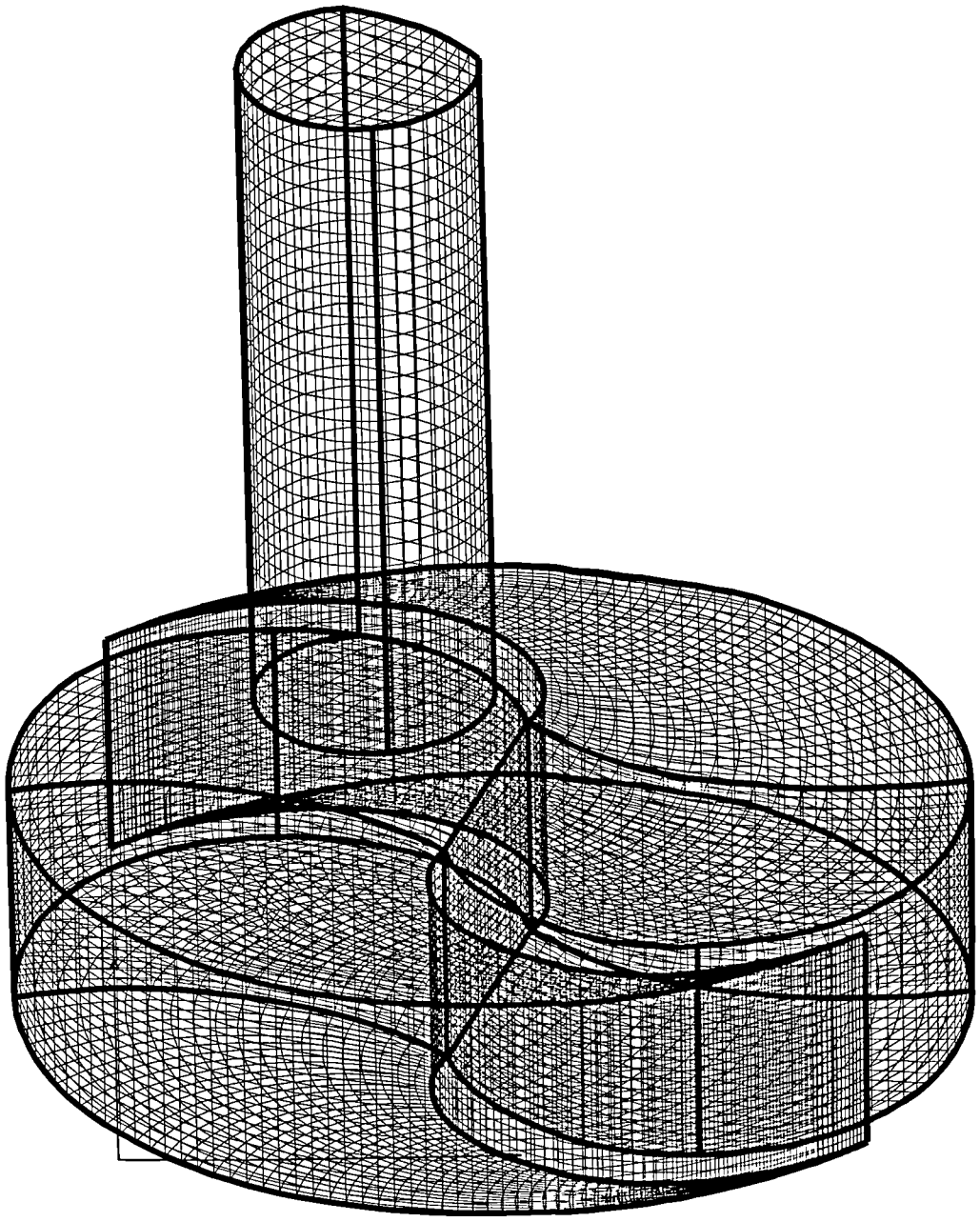

Figure 4.65 Block1 mesh: 150*30*20, Block2 mesh: 30*30*20, Block3 mesh: 150*30*20 Block4 mesh: 30*30*20, Pipe mesh: 10*10*30, Total number of elements 219000. Crank angle 930^0, Non Uniform Distribution, Circular arcs, Inlet pipe diameter 0.02m

Chapter 5

Three Dimensional Flow Modeling

5.1 Introduction

In this chapter we give the mathematical basis for a comprehensive general purpose model of fluid flow and heat transfer from the basic principles of conservation of mass, momentum and energy. This leads to the governing equations of fluid flow, the so called Navier - Stokes equations. The governing equations are complex non linear partial differential equations, which can be solved using numerical methods. Discretization methods, advection schemes, time differencing schemes and pressure / velocity coupling algorithms are discussed. Commercially available CFD software packages are reviewed and CFX - FLOW3D is described in detail.

Flows inside scroll compressors - expanders are turbulent, time dependent, compressible and, for the case of the expander, two phase. Furthermore these flows are driven by the wall motion and, therefore, are characterized by moving boundaries. In the last section of this chapter the results of the three dimensional modeling are shown.

5.2 Theory

All of CFD, in one form or another, is based on the fundamental governing equations of fluid dynamics, the continuity, momentum, and energy equations. These *equations speak physics*. They are the mathematical statements of three fundamental physical principles upon which all of fluid dynamics is based: namely the conservation of mass, momentum and energy.

- Mass is conserved.
- Newton's second law, **F=ma**.
- Energy is conserved.

5.2.1 Governing Equations

The equations that result from applying the Conservation of Mass law to a fluid flow is called the continuity equation. The Conservation of Momentum law is nothing more than Newton's second law (***F= ma***). When this law is applied to a fluid flow, it yields a vector equation known as the momentum equation. The Conservation of Energy law is identical to the First Law of Thermodynamics, and the resulting fluid dynamic equation is named the energy equation. In addition to the equations developed from these universal laws, it is necessary to establish relationships between fluid properties in order to close the system of equations. An example of such relationships is the equation of state, which relates the thermodynamic variables pressure p, density ρ, and temperature T. The derivation of all the above equations is shown in Appendix B.

5.2.1.1 The Continuity Equation

Physical principle: mass is conserved

$$\frac{\partial \rho}{\partial t} + \nabla \cdot (\rho V) = 0 \qquad (5.1)$$

Equation (5.1) is a partial differential equation form of the *continuity equation.* It was derived on the basis of an infinitesimally small element fixed in space. The fact that the element was fixed in space leads to the specific differential form given by equation (5.1), which is called the *conservation form.* The forms of the governing flow equations that are directly obtained from a flow model which is fixed in space are, by definition, called the conservation form.

5.2.1.2 The Momentum Equation

Physical principle: $F= ma$ (Newton's second law)

Equations (5.2a) to (5.2c) are the x, y, and z components respectively, of the momentum equation (in conservation form). They are called the *Navier - Stokes equations* in honor of two men, the Frenchman M.Navier and the Englishman G. Stokes, who independently obtained the equations in the first half of the nineteenth century.

$$\frac{\partial(\rho u)}{\partial t}+\nabla\cdot(\rho uV)=-\frac{\partial p}{\partial x}+\frac{\partial \tau_{xx}}{\partial x}+\frac{\partial \tau_{yx}}{\partial y}+\frac{\partial \tau_{zx}}{\partial z}+\rho f_x \qquad (5.2a)$$

$$\frac{\partial(\rho v)}{\partial t}+\nabla\cdot(\rho vV)=-\frac{\partial p}{\partial x}+\frac{\partial \tau_{xy}}{\partial x}+\frac{\partial \tau_{yy}}{\partial y}+\frac{\partial \tau_{zy}}{\partial z}+\rho f_y \qquad (5.2b)$$

and

$$\frac{\partial(\rho w)}{\partial t}+\nabla\cdot(\rho wV)=-\frac{\partial p}{\partial z}+\frac{\partial \tau_{xz}}{\partial x}+\frac{\partial \tau_{yz}}{\partial y}+\frac{\partial \tau_{zz}}{\partial z}+\rho f_z \qquad (5.2c)$$

5.2.1.3 The Energy Equation

Physical principle: Energy is conserved

Equation (5.3) below is the *conservation* form of the energy equation written in terms of total energy $e+V^2/2$.

$$\begin{aligned}&\frac{\partial}{\partial t}\left[\rho\left(e+\frac{V^2}{2}\right)\right]+\nabla\cdot\left[\rho\left(e+\frac{V^2}{2}\right)V\right]=\rho\dot{q}+\frac{\partial}{\partial x}\left(k\frac{\partial T}{\partial x}\right)+\frac{\partial}{\partial y}\left(k\frac{\partial T}{\partial y}\right)\\&+\frac{\partial}{\partial z}\left(k\frac{\partial T}{\partial z}\right)-\frac{\partial(up)}{\partial x}-\frac{\partial(vp)}{\partial y}-\frac{\partial(wp)}{\partial z}+\frac{\partial(u\tau_{xx})}{\partial x}+\frac{\partial(u\tau_{yx})}{\partial y}+\frac{\partial(u\tau_{zx})}{\partial z}\\&+\frac{\partial(v\tau_{xy})}{\partial x}+\frac{\partial(v\tau_{yy})}{\partial y}+\frac{\partial(v\tau_{zy})}{\partial z}+\frac{\partial(w\tau_{xz})}{\partial x}+\frac{\partial(w\tau_{yz})}{\partial y}+\frac{\partial(w\tau_{zz})}{\partial z}+\rho f\cdot V\end{aligned} \qquad (5.3)$$

5.2.2 Mathematical Behavior Of Partial Differential Equations

The partial differential equations for continuity, momentum, and energy in fluid flow have a certain mathematical behaviour. This behaviour might be different from one case to another, depending, for example, on the local Mach number of the flow. The same equations may have different mathematical behavior depending on whether the flow is locally subsonic or supersonic. The behavior may also be different depending on whether the flow is steady or unsteady. Any differences in mathematical behavior of these equations reflect different physical behavior as well. There are two separate techniques for determining the classification of partial differential equations: Gramer's rule, and the eigenvalue method. Both these methods lead to the same results.

Quasi-linear second order partial differential equations in two independent variables can be classified into three types: hyperbolic, parabolic, and elliptic. This distinction is based on the nature of the characteristics, curves along which information about the solution is carried. Every equation of this type has two sets of characteristics.

In the hyperbolic, the characteristics are real and distinct. This means that information propagates at finite speeds in two sets of directions. In general the information propagates in a particular direction so that one datum needs to be given at an initial point on each characteristic; the two sets of characteristics therefore demand two initial conditions. If there are lateral boundaries, usually only one condition is required at each point because one characteristic is carrying information out of the domain and one is carrying information in. There are however exceptions to this rule.

In parabolic equations the characteristics degenerate to a single real set. Consequently, only one initial condition is required. At lateral boundaries, one condition is needed at each point.

Finally, in the elliptic case, the characteristics are imaginary or complex so there are no special directions of information propagation. Indeed, information travels essentially equally well in all directions. Generally, one boundary condition is required at each point on the boundary and the domain of solution is usually closed although part of the domain may extend to infinity. Unsteady problems are never elliptic.

These differences in the nature of the equations reflect in the methods used to solve them. It is an important general rule that numerical methods should respect the properties of the equations they are solving.

The Navier -Stokes equations are a system of non-linear second order equations in four independent variables. Consequently the classification scheme does not apply directly to them. Nonetheless Navier -Stokes equations do posses many of the properties outline above and many of the ideas used in solving second order equations in two independent variables are applicable to them but care must be exercised.

5.2.2.1 Hyperbolic Flows

To begin, consider the case of unsteady inviscid compressible flow. A compressible fluid can support sound and shock waves and it is not surprising that these equations have an essentially hyperbolic character. Most of the methods used to solve these equations are based on the idea that the equations are hyperbolic and, given sufficient care, they work quite well.

For steady compressible flows, the character depends on the speed of the flow. If the flow is supersonic, the equations are hyperbolic while the equations for subsonic flow are essentially elliptic.

It should be noted however, that the equations for a viscous compressible flow are still more complicated. Their character is a mixture of elements of all of the types mentioned above; they do not fit well into the classification scheme and numerical methods for them are difficult to construct.

In terms of CFD, the computation of flow fields that are governed by hyperbolic equations is set up as "marching" solutions. The algorithm is designed to start with the given initial conditions, say in the y axis, and sequentially calculate the flow field, step by step, marching in the x direction.

5.2.2.2 Parabolic Flows

Information travels only downstream in these equations and they may be solved using methods that are appropriate for parabolic equations. Parabolic equations, like hyperbolic equations, lend themselves to marching solutions.

5.2.2.3 Elliptic Flows

When a flow has a region of recirculation i.e. flow in a sense opposite to the principal direction of flow, information may travel upstream as well as downstream. As a result, one cannot apply conditions only at the upstream end of the flow. The problem then acquires an elliptic character. This situation occurs in subsonic (including incompressible) flows and makes solution of the equations a very difficult task. The major mathematical characteristic of elliptic equations is that a disturbance is felt everywhere throughout the domain, therefore the solution must be carried out simultaneously at all the points of the domain.

It should be noted that unsteady incompressible flows actually have a combination

of elliptic and parabolic character. The former comes from the fact that information travels in both directions in space while the latter results from the fact that the information can only flow forward in time. Problems of these type are called incompletely parabolic.

5.2.3 Numerical Solutions To Partial Differential Equations

We have seen in the sections above that the equations governing the motion of fluids are partial differential equations. The transformation of these equations to what is known as an algebraic equation it is called discretization. In essence discretization is the process by which a closed-form mathematical expression, such as a function or a differential or integral equation involving functions, all of which are viewed as having an infinite continuum of values throughout some domain, is approximated by analogous (but different) expressions which prescribe values at a finite number of discrete points or volumes in the domain.

Analytical solutions of partial differential equations involve closed - form expressions which give the variation of the dependent variables continuously throughout the domain. In contrast, numerical solutions can give answers at only discrete points in the domain, called grid points. The discretization methods fall into three main categories: (a) Finite Difference method, (b) Finite Element method and (c) Finite Volume Method.

5.2.3.1 Finite Difference Method

This is the oldest method for numerical solution of the partial differential equations believed to have been introduced by Euler in the 18^{th} century. It is also the easiest method to use for simple geometries.

The starting point is the conservation equation in differential form. The solution domain is covered by a structured grid. At each grid point, the differential equation is approximated by replacing the partial derivatives by approximations in terms of the nodal values of the functions. The result is one algebraic equation per grid node, in which the variable value at that and at a certain number of neighbor nodes appears as a number of unknowns.

Taylor series expansion or polynomial fitting is used to obtain approximations to the first and second derivatives of the variables with respect to the coordinates. When necessary, these methods are also used to obtain variable values at locations

other than grid nodes (interpolation).

On structured grids, the finite difference method is very simple and effective. It is especially easy to obtain higher - order schemes on regular grids. The restriction of simple geometries is a significant disadvantage.

5.2.3.2 Finite Element Method

The domain is broken into a set of discrete volumes of finite elements that are generally unstructured. The distinguishing feature of finite element methods is that the equations are multiplied by a weight function before they are integrated over the entire domain. In the simplest FE methods, the solution is approximated by a linear shape function within each element in a way that guarantees continuity of the solution across element boundaries. Such a function can be constructed from its values at the corners of the elements. The weight function is usually of the same form.

This approximation is then substituted into the weighted integral of the conservation law and the equations to be solved are derived by requiring the derivative of the integral with respect to each nodal value to be zero; this corresponds to selecting the best solution within the set of allowed functions (the one with a minimum residual). The result is a set of non-linear algebraic equations.

An important advantage of finite element methods is the ability to deal with arbitrary geometries; there is an extensive literature devoted to the construction of grids for finite element methods. The grids are easily refined; each element is simply subdivided. Finite element methods are relatively easy to analyze mathematically and can be shown to have optimal properties for certain type of equations. The principal drawback, which is shared by any method that uses unstructured grids, is that the matrices of the linearized equations are not as well structured as those for regular grids making it more difficult to find efficient solution methods.

A hybrid method called the control-volume-based finite element method should also be mentioned. In it, shape functions are used to describe the variation of the variables over an element. Control volumes are formed around each node by joining the centroids of the elements. The conservation forms in integral form are applied to these control volumes in the same way as in the finite volume method.

The fluxes through control volume boundaries and the source terms (associated with the creation or destruction of ϕ) are calculated element-wise.

5.2.3.3 Finite Volume Method

The third, and probably most popular, numerical discretization method used in CFD is the finite volume method. This method is similar in some ways to the finite difference method, but some implementations of it also draw on features taken from the finite element method. The finite volume method was developed specifically to solve the equations of heat transfer and fluid flow and is described in detail by Patankar (1980).

The finite volume method uses the integral form of the conservation equations as its starting point. The solution domain is subdivided into a finite number of contiguous control volumes (CV), and the conservation equations are applied to each CV. At the center of each CV lies a computational node at which the variable values are to be calculated. Interpolation is used to express variable values at the CV surface in terms of the nodal (CV center) values. Surface and volume integrals are approximated using suitable quadrature formulae. As a result, one obtains an algebraic equation for each CV in which a number of neighbor nodal values appear.

The finite volume method can accommodate any type of grid, so it is suitable for complex geometries (a structural orthogonal grid is recommended, whenever possible). The disadvantage of finite volume methods compared to finite difference schemes is that higher than second order methods are more difficult to develop in 3D. This is due to the fact that the finite volume approach requires two levels of approximation: interpolation and integration.

5.2.3.4 Comparison Of The Discretization Techniques

There are, several differences between the three methods and these include the following:

- the finite difference method and the finite volume method both produce numerical equations at a given point based on the values at neighboring points, whereas the finite element method produces equations for each element independently of all other elements. It is only when the finite element equations are collected together and assembled into the global matrices that the interaction between elements is taken into account.

- the finite element method takes care of derivative boundary conditions when the element equations are formed, and then the fixed values of variables must be applied to the global matrices. This contrasts with the other two methods which can easily apply the fixed-value boundary conditions by inserting the values into the solution, but must modify the equations to take account of any derivative boundary conditions.

There are, however, several common features. These features are that each method:

- produces equations for the values of the variable at a finite number of points in the domain under consideration.
- requires that we know the boundary conditions of the problem.
- can produce explicit or implicit forms

Finite difference methods are based on the substitution of difference equations for the partial derivatives in partial differential equations. These difference equations link the values of variables at a set of points to the derivatives and so a grid of points is used throughout the spatial domain. The finite difference method requires, that the grid points is topologically regular. This means that the grid must look cuboid in a topological sense.

Finite elements produce the numerical equations for each element from data at known points on the element and nowhere else. Consequently, there is no restriction on how the elements are connected as long as the faces of neighboring elements are aligned correctly. This means that the faces between elements should have the same nodes for each of the adjoining elements. This flexibility of element placement allows a group of elements to model very complex geometry.

Algorithms that have been developed using the finite volume method have tended to use a regular grid to take advantage of the efficiency of computation, just like the grids used with finite difference methods. Recently, however, to enable calculations to be carried out in complex geometries, algorithms have been developed with the finite volume method that can utilize irregular finite element-like meshes. Both finite element and irregular mesh finite volume programs pay a computational overhead for this geometrical flexibility. This flexibility slows down the programs considerably.

5.2.4 Pressure / Velocity Coupling Procedures

The process of discretization of the governing differential equations lead to a set of non -linear, coupled algebraic equations, which are solved using iterative methods. One of the most popular early techniques for solving the 2-D incompressible Navier-Stokes equations is the *Vorticity-Stream-Function method* (Gosman et al., 1969). The main attraction of this approach is the fact that pressure does not appear in the formulation; however difficulties in specifying the vorticity at boundary conditions at sharp corners may cause problems in obtaining a converged solution.

A change of variables is made replacing the velocity components with the vorticity ζ and the stream function ψ. Using these new dependent variables, the two momentum equations can be combined to lead to the parabolic vorticity transport equation and an elliptic PDE in the form of a Poisson equation. This allows the separation of the mixed elliptic-parabolic PDE into one parabolic and one elliptic, that can be solved with any standard iterative method such as SOR (Succesive Over-Relaxation). In order to determine the pressure, an additional equation, referred to as a Poisson equation for pressure is solved.

The extension of the vorticity-stream function approach to three-dimensional problems is complicated by the fact that a stream function does not exist for a truly three-dimensional flow. However, using a velocity-potential vector, it is possible to have a vector Poisson equation and a vector vorticity transport equation, which must be separated into three parabolic and three elliptic PDEs. As a result, it does not appear that the vorticity-stream function approach offers any advantage over the *primitive-variable* approach when solving a 3-D problem (Roache, 1972). The latter uses the incompressible Navier-Stokes equations in the primitive-variable form, and then non-dimensionalizes them.

The artificial compressibility method of Chorin (1967) is one of the early techniques proposed for solving the incompressible Navier-Stokes equations in the primitive-variable form. An artificial compressibility is introduced which vanishes when the steady-state solution is reached and makes the differential equations a mixed set of hyperbolic equations which can be solved using a standard time-dependent approach.

The most common primitive-variable approach, however, involves the use of a Poisson equation in place of the continuity equation in order to separate the pressure effects into a single equation. This technique was first used by Harlow and

Welch (1965) in conjunction with their Marker-and-Cell (Mac) method, for solving the incompressible Navier-Stokes equations for transient flows. Approximate initial values are given to the pressure gradients to find velocities from the momentum equation and the pressure from the Poisson equation. This procedure is repeated until the solution converges. The Alternating-Direction-Implicit (ADI) scheme is applied to the momentum equations (Ghia et al., 1981) and a SOR method is used to solve the Poisson pressure equation.

5.2.4.1 Simple Algorithms

All the above methods converge slowly, suffered from stability problems and were very difficult to use in 3-D flows. In the early 1970s a pressure-correction technique referred to as SIMPLE (Semi-Implicit Method for Pressure-Linked Equations) procedure was developed by Patankar and Spalding (1972). The SIMPLE procedure marked a significant improvement and is currently used, in one of its many forms, in all general purpose CFD codes.

This procedure is based on a cyclic series of guess-and-correct operations to solve the governing equations and is, with its variants SIMPLER and SIMPLEC, the most widely used in solving for the pressure field. It was first proposed for parabolic flows, and then was soon adapted to general 3-D elliptic problems. The velocity components are first calculated from the momentum equations using a guessed pressure field. The pressure and the velocities are then corrected so as to satisfy continuity. This process continues until the solution converges. The actual pressure p at the generic iteration step is written as

$$p = p_o + p'$$

where p_o is the estimated (or intermediate) value of pressure and p' is the pressure correction. Similarly in 2-D

$$u = u_o + u' \qquad v = v_o + v'$$

where u_o and v_o are estimated values, and u' and v' are the velocity corrections.

Using these equations and approximate forms of the momentum equations, we obtain a pressure correction which is a Poisson equation in the pressure correction p' and the estimated velocity vector. Once the first guess of the pressure is made and the velocities are then estimated by the momentum equations, the pressure-

correction is solved to find p', then p and finally u, and v using the approximate form of the momentum equations. These new values are then used as estimated values and the process is repeated until the solution converges.

Because the pressure correction equation tends to overestimate the value of p' in certain cases, the rate of convergence was found to be unsatisfactory. Under-relaxation techniques were used to improve the convergence properties. A new technique was then proposed by Patankar (1981), called SIMPLER (SIMPLE Revised), where initially the velocity field is guessed. Velocity corrections are computed in the same manner as in SIMPLE, but a complete Poisson equation is used to compute the pressure. With this procedure the need of under-relaxation is greatly reduced and a convergence solution is obtained in a fewer iterations, although more computational effort is involved per iteration. The original implementation of this scheme required the use of staggered grids in order to prevent a numerical instability known as 'checkerboarding', which occurred on a single grid because the velocities were insensitive to small oscillations in the pressure solution, and vice versa.

The SIMPLEST method (Spalding, 1980) is based on an explicit treatment of convective terms and implicit treatment of diffusive terms in the momentum equations. The SIMPLEC method, proposed by Van Doormal and Raithby (1984), uses consistent under-relaxation for the momentum and pressure corrections. This method has been shown to allow faster convergence in pressure gradient-dominant and drag forces-dominant problems.

5.2.4.2 Piso Algorithms

An alternative pressure-correction scheme was proposed by Issa (1985) as a Pressure-Implicit with Splitting of Operators (PISO) technique. In order to remove completely the need to iterate between pressure and velocity equations, a second pressure-correction equation is solved in each iteration, much like SIMPLER yielding pressure and velocity fields that are second-order accurate in time. This allows its use as a non-iterative method (one cycle per time step), but it requires an accurate solution of the linearized equations.

Although this method appear to be preferentially indicated for problems where conservation of mass and momentum are particularly important, it does require pressure and velocity equations to be solved to tight convergence tolerances, and in

practice the scheme is often implemented in an iteration loop similar to that used for SIMPLE. It was proved to be faster than SIMPLE for transient problems in which the flow field varies markedly at each step, but not for 'smooth' time-dependent flows (Ciofalo and Collins 1988). At last, in the PISOC method similar modifications to SIMPLEC are applied.

A review of pressure-velocity coupling algorithms is given by Latimer and Polland (1985). The SIMPLE-like and PISO-like methods have all been implemented in the previous versions of CFX-FLOW3D (single-block versions). Only SIMPLE and SIMPLEC methods are available in the more recent multi-block versions of CFX-FLOW3D. In fact, these are the only ones that have been proved to be robust for more general purpose applications.

5.2.4.3 Pressure/Velocity Coupling Techniques for FEMs

As in FDM, early calculations using FEM circumvented the pressure/velocity coupling problem by using the vorticity-stream function formulation. Techniques in use to date for handling the coupling between velocity and pressure are the *Penalty Method*, the *Langrange Multiplier Method* or a combination of these, and the *PALM Method* (Smith, 1985). In other cases either the momentum and continuity equations are solved directly or a SIMPLE-like iterative procedure is devised.

The *Penalty Method*, first presented by Zienkiewizc (1977), uses a penalty parameter which, multiplied by the pressure, is introduced in the right-hand side of the continuity equation, and should be zero for the continuity condition. This parameter is very small so that the continuity equation is nearly satisfied. The pressure, given as the ratio of the divergence of the velocity vector and the vanishing penalty parameter, is substituted into the momentum equation, thereby eliminating pressure. A general discussion of the penalty method is given by Reddy (1982), while Baker (1984) has described the use of the penalty method in three-dimensional parabolic flows. In the *Lagrange Multiplier Method*, the pressure is considered as a linear function or piecewise constant over quadratic or linear velocity elements respectively (Gresho et al., 1980). That is, the approximation for pressure has to be of lower degree than that used for the velocity.

Solution existence can be only guaranteed for those velocity/pressure element nodal arrangements that satisfy the Babuska-Brezzi condition (Babuska and Aziz,

1982; Brezzi, 1974). That is, on a triangular element it is required to have velocity on more than each vertex (for example also on the medians), and pressure at more than at the centroid (for example, at three internal point centroids).

5.2.4.4 Rhie-Chow Interpolation Method

In order to prevent a 'checkerboard' pressure field that may develop when velocity components and pressure are located at the same grid point and the FDM are applied, a common approach has been the use of 'staggered grids'. In this case pressures and scalars are defined at the centroids of the control volumes, while the velocities are defined at the centroids of the faces to which are normal. However, this approach may become quite cumbersome in the presence of non-orthogonal, body-fitted grids.

The Rhie-Chow algorithm (Rhie, 1981; Rhie and Chow, 1983) allowed the required components on the cell faces to be computed from the values of velocity and pressure at the cell centroids in non-staggered grids without including checkerboarding. It works on 3-d body fitted grids, and allows a natural application of SIMPLE-like algorithms. The Rhie-Chow algorithm has been incorporated into CFX-FLOW3D since its release 2 version; and it is also implemented into most last-generation computer codes.

An improvement to this algorithm has been carried out within the last versions of CFX-FLOW3D to allow applications to be treated where large pressure gradients occur which balance strongly varying body forces. Details of this formulation are in the user manuals (Anonymous, 1994a; 1994b).

5.2.5 Advective-Term Methods

In recent years, a significant amount of research effort has been directed toward discretization of the combined convection (transport due to fluid flow) and diffusion (transport due to variations of ϕ from point to point) fluxes. Inaccurate modeling of these terms can seriously degrade overall accuracy and stability of the solution. In many cases, it is almost impossible to refine the grid sufficiently so that the numerical errors will reduce to acceptable levels. Thus, it is essential to have a convection-diffusion formulation that leads to a stable and accurate solution with grids of modest fineness. Whereas many methods have been formulated, there exists no clear consensus about a preferred method. The more accurate schemes

tend to be less robust and slower.

In order to help subsequent discussion, some of the more common models will be described. We shall consider a simple situation of steady one-dimensional flow where only convection and diffusion terms are present. If ϕ is the variable advected at a constant velocity u, then, integrating the relevant advection term over the control volume shown in figure 5.1gives

$$\int u\frac{\partial \phi}{\partial x} = u(\phi_e - \phi_w)$$

As values of ϕ are only known at the center of each control volume, a linear profile can be taken to estimate ϕ_e and ϕ_w. The result is the Central Difference Scheme (CDS):

$$\phi_e = \frac{1}{2}(\phi_E - \phi_P) \qquad \text{and} \qquad \phi_w = \frac{1}{2}(\phi_P - \phi_W)$$

The factor ½ arises from the assumption of the interfaces being midway. This scheme is formally second-order accurate, but can lead to spurious spatial oscillation ('wiggles') of the solution (Roache, 1972) or physically non-realistic solutions unless the cell Peclet number ($Pe = \rho u \Delta x/\Gamma$, where Δx is the cell width, and Γ is the diffusion coefficient) is less than 2. There has been some misunderstanding in the literature as to the nature of these oscillations; however, it is now accepted that they are related to an accuracy problem rather than to a stability problem (Vreugdenhil, 1989). It is also relevant that, when CDS is used and the cell Peclet number is high, the linearized governing equations lose diagonal dominance. This makes the CDS algorithm lose its 'robustness', and very small under-relaxation factors, or very small time steps, are needed to obtain convergence.

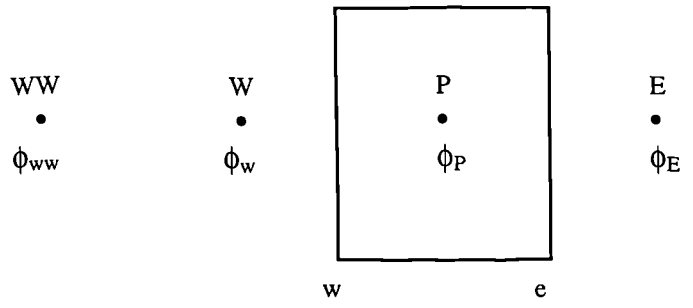

Figure 5.1Typical control Volume

An unconditionally stable but rather 'crude' approximation is to assume that the value at the face is the same as the nodal value upstream of the face. This technique is the basis of the Upwind-Difference Scheme (UDS). It was first put forward by Courant et al. (1952) and subsequently by Gentry et al. (1966). This scheme introduces a false 'numerical diffusion' and produces a result that is actually the solution to a different problem.

The exponential scheme which uses the exact solution profile would give a highly desirable behaviour, but at very high computational cost and without being able to be applicable to more general situations. An easy-to-compute scheme that has the qualitative behavior of the exponential scheme is the Hybrid Difference Scheme (HDS). It was developed by Spalding (1972), and applies a central difference scheme for the Peclet number range $-2 \leq Pe \leq 2$ and an upwind difference outside this range by ignoring diffusion. This advection model is used as a default in many FDM programs. It is again first-order accurate and cannot eliminate false diffusion errors, but it is slightly better than upwind differencing because second-order central difference will be the result across streams and in regions of low flow.

Since it is the grid Peclet number that decides the behavior of the numerical schemes, it is, in principle, possible to refine the grid (i.e., to use smaller Δx) until Pe is small enough (< 2) for the central differencing scheme to yield a reasonable solution. In most practical problems, however, this strategy requires excessively fine grids, which are usually not feasible on economic grounds.

A large number of differencing schemes have been proposed to prevent numerical diffusion while preserving robustness and avoiding 'wiggles'. They include the following approaches:

(a) *Higher-order upwind schemes*, based on the use of more than one grid point value in the finite difference expression of the advective fluxes, such as the second-order upwind, third-order upwind (QUICK), or the related 'power law' schemes (Patankar, 1980) (PLDS), 'Hermitian Polynomial' schemes (Glass and Rodi, 1982), and 'spline' methods (Rubin and Graves, 1975).

(b) *'Skew' schemes*, such as the 'skewed upwind' (SUS) and the 'skewed upwind weighted' (SUWDS) schemes (Raithby, 1976), the 'mass flow weighted' (Hassan et al., 1983), the 'vector upstream' (Lillington. 1981), 'bounded skew upwind' (BSUDS) (Syed and Chiappetta, 1985), and 'flux bending' schemes

(Gosman and Peric, 1985): all take some account of the angle at which the fluid crosses the coordinate lines.

(c) *Methods based on a locally exact solution* of the governing equations, such as the 'finite analytic' method (Chen et al., 1981), and the 'locally analytic' scheme (LOADS) (Wong and Raithby, 1979). These formulations do give stable and accurate results but are rather complex and expensive for regular use.

(d) *Modified-central differencing schemes*, such as CONDIF (Runchal, 1987), and NONDIF (Hedberg,1989).

Among these we give some details of advection schemes available in CFX-FLOW3D. The Higher-order Upwind scheme (HUM) represents a more accurate upwind scheme, which uses an additional nodal value further from the face. Assuming equal spatial increments, ϕ_w is given by:

$$\phi_w = \frac{3}{2}\phi w - \frac{1}{2}\phi w w$$

A formally more accurate scheme than HUV is the quadratic upwinding scheme known as QUICK (Leonard,1979). This is an upwinded scheme which is third-order accurate for the advection and second-order accurate for the diffusion terms. This scheme uses two upstream points and one downstream point, which makes it slightly unstable:

$$\phi_w = \frac{3}{8}\phi p + \frac{3}{4}\phi w - \frac{1}{8}\phi w w$$

The higher order upwinded schemes can suffer non-physical overshoots in their solutions. For example, turbulent kinetic energy can become negative. The CCCT scheme is a modification of the QUICK scheme which is bounded, eliminating these overshoots. The scheme has:

$$\phi_w = \left(\frac{3}{8} - a\right)\phi p + \left(\frac{3}{4} + 2a\right)\phi w - \frac{1}{8}\phi w w$$

where a is a parameter that depends on the curvature of the variable ϕ. Full details for the calculation of a are given by Alderton and Wilkes (1988).

CONDIF is a modification of central differencing in which the coefficients are written in such a way as to be diagonally dominant, and upwind differencing is used at any points at which the solution may have a non-physical overshoot. Again full details are given by Alderton and Wilkes (1988).

A survey of comparative studies on advection schemes is given by Patankar (1988). While some reviews are in favour of the QUICK scheme, others report over- and under-shoots, oscillations and convergence problems, and conclude in favour of HUW or even UDS. Also, higher-order schemes imply a significant increase in computational complexity. Burns and Wilkes (1987) handled this problem using the 'deferred correction approach', that is, they included the extra terms on the right hand side of the equation in the source term (associated with the creation or destruction of ϕ).

Convection-diffusion formulation in *Finite Element* methods have followed a similar pattern, and various comparable upwinding schemes have been proposed. Because of non-linearity of the advection terms, Newton-Raphson or Picard iteration methods are commonly used. A control-volume formulation was introduced by Baliga and Patankar (1980), who used a shape function based on the direction of the local velocity vector. In the Galerkin formulation of the finite-element method, a streamline upwind procedure was employed by Brooks and Hughes (1982).

5.2.6 Time Stepping procedures

In steady-state problems, the generic transport equation for the variable ϕ can be written as:

$$F(\phi) = S_\phi$$

In time-dependent problems this equation becomes:

$$\frac{\partial \phi}{\partial t} + F(\phi) = S_\phi$$

The time derivative of the flow variable ϕ can be discretized with a degree of implicitness χ ($0 < \chi \leq 1$)

$$\frac{1}{\Delta t}\left(\phi^{n+1} - \phi^n\right) + \chi F\left(\phi^{n+1}\right) + (1-\chi)F\left(\phi^n\right) = S$$

which can be written in the same form as the steady-state equation (5.31):

$$F\left(\phi^{n+1}\right) = S_{\phi}$$

Thus the same basic algorithms can be used, though some extra storage is required for the values of the variables at step n. For a degree of implicitness χ =1.0 we have, for example, the fully implicit backward time differencing scheme; for χ =0.5 there is the time-centered scheme of Crank-Nicolson and for χ =0.0 the scheme is fully explicit. The fully implicit and the Crank-Nicolson schemes are unconditionally stable in the mathematical sense, while the explicit method is subjected to the Courant stability criterion, e.g., the Courant number $Cr \leq 1$, (where $Cr = c/(\Delta x/\Delta t)$, with c as celerity of propagation in the analytical solution and Δx the width of the smallest cell).

In Finite Element Methods, Crank-Nicolson or backward Euler time stepping may be used. However, more general time-splitting techniques are becoming popular, some of which have recently been reviewed by Glowinski and Pironneau (1992).

5.2.7 Solution Techniques For The Linearized Equations

The discretization/linearization techniques described above lead, at the generic inner iteration (SIMPLE iteration), to very large systems of linear equations representing either scalar transport equation or the pressure correction equation, having the general form:

$$A\,x = b$$

In the pressure correction case, the coefficient matrix is symmetric. In all cases, if the 'deferred correction technique', described above, is used the matrix A contains only seven non-zero diagonals (in 3-D problems) and is efficiently stored as a $N \times 7$ array, N being the overall number of control volumes in the grid.

To solve such a large system only iterative methods, such Gauss-Seidel and Successive Over-Relaxation (SOR) methods, are applicable. These consist in guessing and solving the equations respectively until the iterative procedure converges.

Whereas the Gauss-Seidel (point-by-point, line-by-line or ADI) methods have been commonly used for the solution of linear algebraic equations, these methods

converge very slowly, especially when a large number of grid points are involved. For large three dimensional problems, it has been found that a more reliable technique is the Strongly Implicit Procedure (SIP) proposed by Stone (1968). This technique has proved to be the best in the solution of the pressure correction equation having a high degree of accuracy. It applies a 'factorization strategy', which consists in replacing the original sparse matrix A by a modified matrix $A+T$, such that it can be decomposed into upper and lower triangular matrices. The matrix T has to be selected so that the ADI procedure can be applied.

Recently, new techniques have been proposed, some of which are extensions of the SIP method. Lin (1985) has proposed the use of three free parameters to accelerate the convergence of Stone's method. In the methods formulated by Schneider and Zedan (1981) and Peric (1987), the five diagonal matrix in Stone's method is replaced by a nine-diagonal matrix. As a result, these modified methods (Modified Strongly-Implicit, MSI) are applicable to the discretization formulations which lead to nine-diagonal matrices. They have also been shown to be more efficient when applied to file-diagonal systems.

5.2.8 Commercially Available Codes

Computational Fluid Dynamics has been used for numerical prediction of fluid flows and heat transfer since the 1960s. With the development of computer hardware, computational techniques have been vigorously proposed, tested and refined to the point that these are recognized as cost-effective and convenient means of obtaining detailed data for complex physical situations. Many powerful CFD programs are available based on the three above mentioned (section 5.2.3) numerical methods with varying degrees of modeling capabilities. Among these, commercially available codes are: CFX-FLOW3D, STAR-CD, PHOENICS, FLUENT, ASTEC, FIRE, FEAT, FIDAP, P/FLOTRAN, NEKTON.

Grid generation and post-processing packages are often included. Pre and post processing are also available from specialized companies and referred to as visualization software, such as CAD, PATRAN, FEMVIEW, UNIRAS and AVS. The power and flexibility of the CFD packages available today are such that there is now little need to develop purpose-build programs for specific problems.

Vector-processing and parallel processing capabilities of new supercomputers have made some impact both on computer programming and on the development of

numerical algorithms that have been specifically designed to achieve a high degree of vectorization and speed up computational time. A recent survey of a number of CFD codes has been presented by Wolfe (1991) and by Collins and Ciofalo (1991).

(a) Finite Volume Codes. TEACH (Gosman and Pun, 1974) can be considered the 'ancestor' of many CFD codes based on FVMs. It was developed in the early 1970s at Imperial College, and could handle problems of 2-D flows; it employed a k-ε turbulent flow model and the SIMPLE algorithm. Several last generation codes, such as PHOENICS, CFX-FLOW3D, STAR-CD and ASTEC, can be considered as 'offsprings' of TEACH. These codes solve 3-D flows in laminar and turbulent regimes, with steady and time dependent conditions, in complex geometries treated by body-fitted grids. PHOENICS and CFX-FLOW3D are based on *structured grids*, while STAR-CD and ASTEC can use *unstructured grids*. Details of CFX-FLOW3D, which was used throughout this research, are given in the next section.

(b) Finite Element Codes. FEAT, developed at the Berkeley Nuclear Laboratories, is a 'classic' finite element code for CFD and heat transfer problems. Also FIDAP is widely used. In addition to these, most general purpose FE packages such as MSC/NASTRAN, ADINA/ANSYS, NISA-II and ABAQUS, include CFD modules although they are less advanced than specialized CFD codes. A review of FE methods for CFD problems is given by Lohner (1987).

5.2.8.1 CFX-FLOW3D: CODE OVERVIEW

CFX-FLOW3D, also known as HARWELL-FLOW3D up to a few years ago, is a general purpose thermofluid-dynamic computer code born, as other computer codes of the same family, in the early seventies and developed from the research work at Imperial College. The original version of FLOW3D was limited to simple staggered and rectilinear grid, Cartesian or cylindrical coordinates, (Wilkes et al. 1985, Jones et al. 1985, 1986). HARWELL-FLOW3D was marketed with the release 2 of the code (Burns et al., 1986, 1987). A body fitted coordinate system was implemented in a structured non-staggered grid, and the Rhie-Chow algorithm (Rhie and Chow, 1983) was used to prevent 'chequerboarding'. The pressure/velocity coupling algorithm was a SIMPLE-family algorithm. Linear equations solvers were used (Kightley and Jones, 1985), and higher order advection treatment schemes (including HUW and QUIVK) (Thompson and Wilkes 1982). Adaptive gridding, combustion models, coupling with radiation codes, some two-

phase flow capabilities, and new advection treatment schemes were introduced, like CCCT and CONDIF.

Description Of The Code

The suite of CFX-FLOW3D programs consists of a number of modules: (a) Pre-Processing Modules, or Geometry and Grid Generators; (b) Interactive Frontend; (c) Solution Module of CFX-FLOW3D; (d) Post-Processing, or Graphics Modules.

The geometry and Grid Generators may be used to define the finite difference grid. The grid coordinates are dumped to disk in a form readable by the frontend. Through the use of a flag in the Frontend, the program is informed that the grid information is to be read from the disk. Use of these modules is optional. The grid can also be defined within the Frontend. The geometry and Grid Generators include the interactive grid generator CFX-BUILD. Body-Fitted Grids are generated using transfinite interpolation.

The Frontend takes the input specification of the problem and converts it from a form convenient for the user into a form designed for efficient execution. Detailed error checking is performed. Facilities are available to provide a database which calculates the physical properties of some common fluids. The problem is specified in a single data file using the Command Language, that is a set of English-like commands, subcommands, and associated keywords. In the Interactive Frontend, this data file is constructed automatically via a series of displays on the screen. User-defined Fortran routines may be included for features that are too complex to be described using the Command Language.

The solution module solves the discretized representation of the problem. It receives the information in a form that permits maximum efficiency to be obtained on different types of computers including vector processors. The solution Module has only a few output facilities- for example, for printing and dumping the solution to disk files.

The Graphics Modules produce the main graphics output, interrogating the disk files written by the solution module. Interfaces to other post-processing packages have been constructed, and there are a number of post-processing options available for various workstations. Use of these modules is optional, and described in the ENVIROMENT User Guide.

In the present work no use was made of the pre-processing facilities such as the interactive grid generator (CFX-BUILD former SOPHIA), since this so far does not allow for transient grids automatically. In fact, it would have been necessary to construct the grid for each time step. Use of the Fortran user subroutine USRGRD was found to be more flexible to define a time dependent grid. Problem specification was made using the Command Language file.

The main features of the code are summarized in table 5.1

Computational Domain

The generic computational domain in 2D is shown in figure 5.2

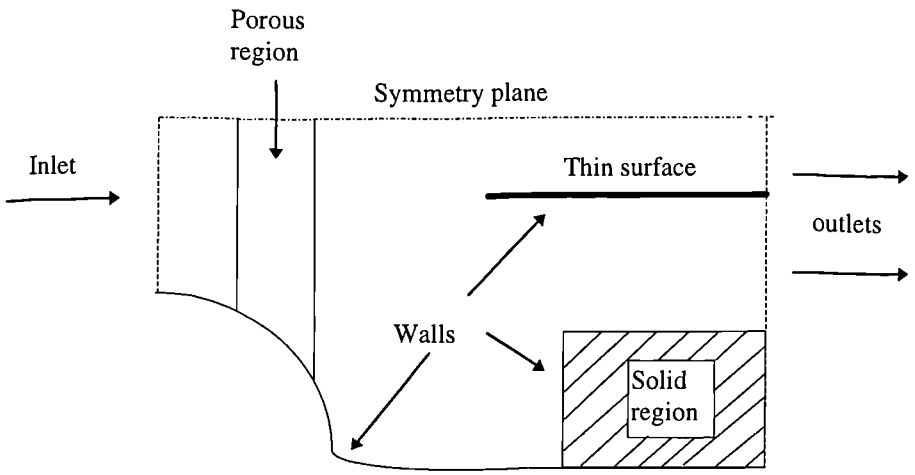

Figure 5.2 Generic CFX-FLOW3D 2-D computational domain and structures which can be defined within it.

Multi-block grids are constructed by patching together a number of simple, rectangular grids to form a grid that is not restricted to be topologically rectangular. Topological features within the domain of each block are described using patches (Boundary condition surfaces and interblock boundaries). The generic block grid include NI, NJ, NK volumes along the 'intrinsic' directions I, J, K respectively. The grid is defined by specifying the coordinates of the grid vertices in physical space, arbitrarily oriented.

The generic control volume, is shown in figure 5.3. The corners of the volume are numbered, and 'intrinsic' directions are indicated following the 'compass rose' convention. In order to invoke boundary conditions the control volumes lying on the perimeter of a grid block, considered outside the solution domain, are added

(automatically) to constitute dummy control volumes. The interior control volumes are called active control volumes. Two dimensional problems are treated as three-dimensional with two symmetry or periodicity planes. If cylindrical coordinates are used, a special treatment is implemented to deal with the singularity created by the fact that the axis is included in the computational domain.

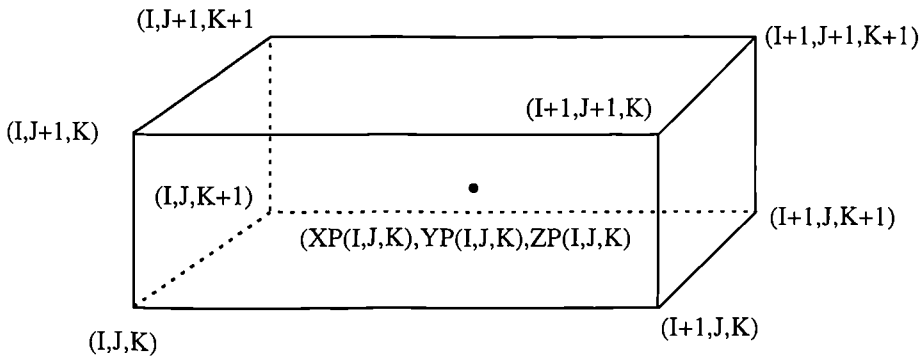

Figure 5.3 Generic control volume. Indices of corners are shown

A summary of CFX-FLOW3D commands and keywords is reported in the manual. The schematic flow chart for the code is shown in figure 5.4. the 'inner' iterations of the linear solvers, are nested in the loop of the 'outer' iterations, which in turn are nested in the time stepping loop. The 'outer' iteration process is stopped either completely or for the current time step of a transient problem, when the chosen convergence criteria are satisfied. The criteria are for example: maximum number of outer iterations, the tolerance on a residual, the CPU limit. In the tolerance on a residual criterion, iterations are stopped when the overall residual mass source ε_m (the sum of the absolute mass source residual in all control volumes) falls below a predicted value SORMAX.

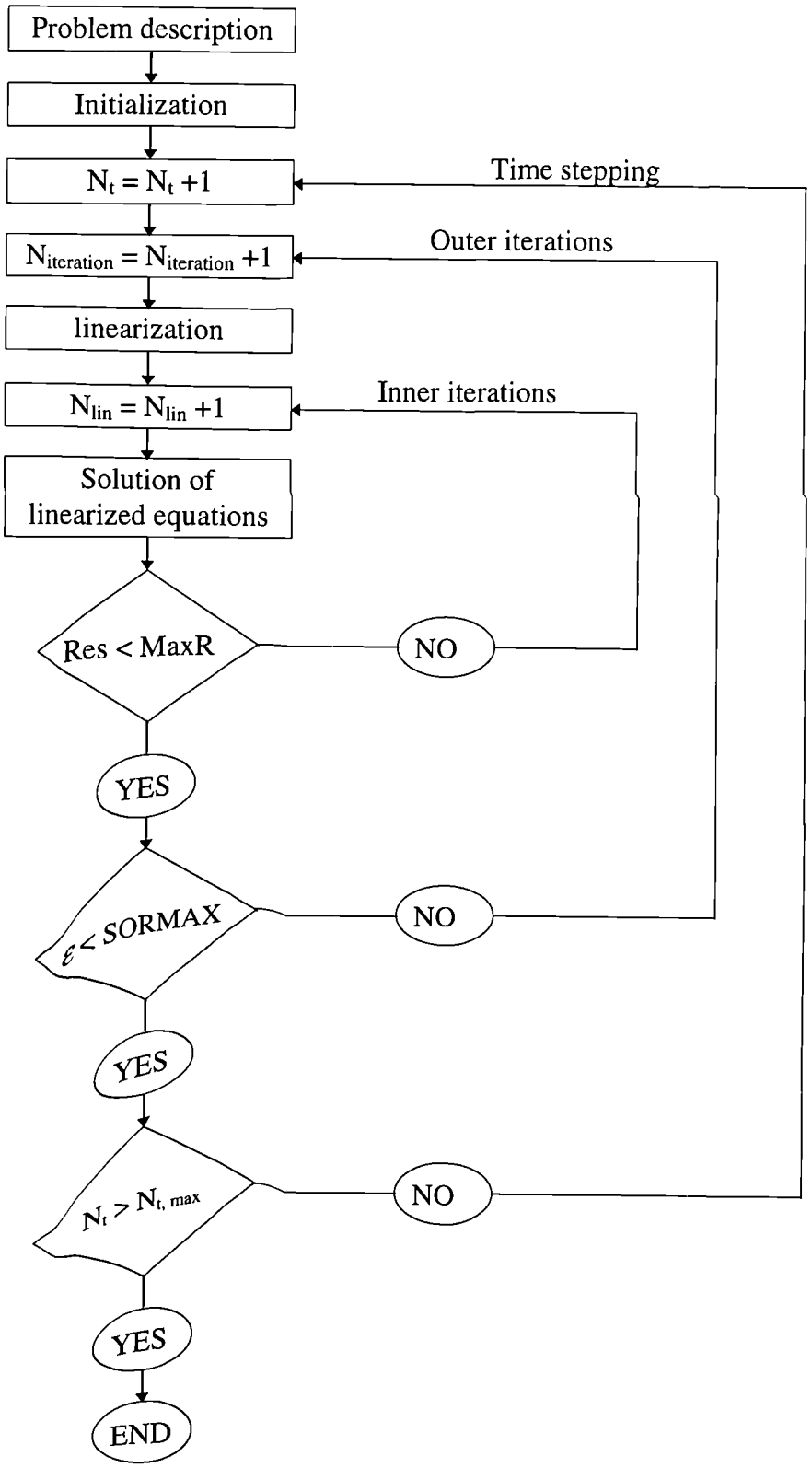

Figure 5.4 Schematic flow chart of CFX-FLOW3D.

Table 5.1
Main features and capabilities of CFX-FLOW3D, Release 4.2

1. Physical Models and Geometry

Physical Space Coordinates:	Cartesian / Cylindrical
Type of Flow:	Laminar / Turbulent Steady / Unsteady 2-Dimensional / Three Dimensional Incompressible / Weakly Compressible, Fully Compressible Isothermal / Non Isothermal Forced / Natural Convection Buoyant: Boussineq approximation of fully compressible Multiphase flow: multi-fluid model / homogeneous model
Boundary Conditions:	Solid Walls Symmetry or Periodicity Surfaces Inlet / Outlet Faces Pressure Boundary Mass Flow Boundary
Turbulence Models:	k-ε for high Reynolds number / Low Reynolds number model Higher order turbulence models: Algebraic Reynolds Stress model (ASM)/ Differential Reynolds Stress model (RSM)/ Differential Reynolds Flux model
Combustion Models:	Two gaseous model s: eddy break-up model / mixed-is-burnt model
Particle Transport Models:	Langrangian
Grid:	Rectangular / body-fitted Multi-block Rotating coordinate system Adaptive Grids
Other Options:	Solids / Thin Walls / Porous Regions Heat Conduction in Solids Radiative Heat Transfer (via RAD3D code) Chemical Kinetics for single-phase chemical reactions Additional Scalar Transport Equations for fluid mixture

2. Numerical Methods

Finite Volume Discretization:	multi-block unstructured, non staggered grid
Time - Differencing:	Fully Implicit Backward Euler Differencing [a] Crank Nicolson (central) differencing
Pressure / Velocity Coupling:	SIMPLE / SIMPLEC [b]
Advection Algorithm Schemes:	Central /Upwind / Hybrid / HUW QUICK / CONDIF / ICCG
Linear Equation Solver:	Line Relaxation / Preconditioned Conjugate Gradient (ICCG) Full field Stone's Method / Block Stone's Method Algebraic Multi-Grid

[a] This option should not be used with transient gridding

[b] PISO and PISOC are available on the new Release

5.3 Results Of The 3D Modeling

In this study the three dimensional flow modeling was performed by the use of a finite volume CFD code known as CFX-FLOW3D. In Chapter four the design and development of a grid generation package, that can handle the complexity of the grid, for a scroll compressor - expander was analyzed. The next step was to implement this transient grid generation package with CFX-FLOW3D. The final stage before running the code was to write the Command Language that described the physics of the problem. The Command Language is shown in Appendix C.

In solving fluid flow problems we need to be aware that the underlying physics are complex, and the user must have skills in a number of areas. Prior to setting up and running a CFD simulation there is a stage of identification and formulation of the flow problem in terms of the physical and chemical phenomena that need to be considered. Typical decisions that might be needed are whether to model a problem in two or three dimensions, to exclude the effects of ambient temperature or pressure variations on the density of an air flow, to choose to solve the turbulent flow equations etc. To make the right choices requires good modeling skills, because in all but the simplest problems we need to make assumptions to reduce the complexity to a manageable level whilst preserving the salient features of the problem in hand.

Flows inside scroll compressors - expanders are turbulent, time dependent, compressible and for the case of the expander two phase. Furthermore these flows are driven by the wall motion

When the solver runs it produces a large amount of data that has to be analyzed. The analysis can be divided into two major categories, (a) CFD analysis, i.e. check to see if the solution is reliable, and (b) Thermodynamic analysis i.e. use CFD as a tool to improve understanding of the behavior of the thermodynamic system under consideration. The following two sub-sections 5.3.1 and 5.3.2 discus the results obtained from the CFD simulation with reference to the above two categories.

5.3.1 CFD Analysis

Three mathematical concepts are useful in determining the success or otherwise of CFD algorithms: convergence, consistency and stability. **Convergence** is the property of a numerical method to produce a solution which approaches the exact solution as the grid spacing, control volume size or element size is reduced to zero.

Consistent numerical schemes produce systems of algebraic equations which can be demonstrated to be equivalent to the original governing equations as the grid spacing tends to zero. **Stability** is associated with damping of errors as the numerical method proceeds. If a technique is not stable even round off errors in the initial data can cause wild oscillations or divergence.

Engineers need CFD codes that produce physically realistic results with good accuracy in simulations with finite (sometimes quite coarse) grids.

Performing the actual CFD computation itself requires operator skills of a different kind. Specification of the domain geometry and grid design are the main tasks at the input stage and subsequently the user needs to obtain a successful simulation result. The two aspects that characterize such a result are convergence of the iterative process and grid independence. The solution algorithm is iterative in nature and in a converged solution the so-called residuals-measures of the overall conservation of the flow properties are very small. Progress towards a converged solution can be greatly assisted by careful selection of the settings of various relaxation factors and acceleration devices. There are no straightforward guidelines for making these choices since they are problem dependent.

Optimization of the solution speed requires considerable experience with the code itself, which can only be acquired by extensive use. There is no formal way of estimating the errors introduced by inadequate grid design for a general flow. Good initial grid design relies largely on an insight into the expected properties of the flow. A background in the fluid dynamics of the particular problem certainly helps and experience with gridding of similar problems is also invaluable. The only way to estimate errors due to the coarseness of a grid is to perform a *grid dependence study*, which is a procedure of successive refinement of an initially coarse grid until certain key results do not change. Then the simulation is grid independent. A systematic search for grid-independent results forms an essential part of all high quality CFD studies.

Figure 5.5 shows how the residuals change with iterations. Figures 5.6 to 5.10 show how residuals, pressure, and velocities (p, u, v, w) change with the number of elements in the domain (grid dependency study). From figure 5.6 it can be seen that the residuals do not change significantly for a number of elements higher than 60000. In figure 5.7 the pressure follows a similar trend to the residuals but in this case the solution is stable for a number of elements higher than 40000. For the case

of u velocity which is shown in figure 5.8 stability appears to be insured for a number of elements higher than 70000. As far as v, and w velocities are concern they appear to be stable earlier, 30000 elements for v and 60000 for w.

As it can be seen from the figures the solution changes when the number of elements is less than 70000 and it appears to be stable for number of elements above that. Figure 5.11 show another important parameter that might affect the solution, namely the length of the time step. It is obvious that the smaller the time step the easier for the code to achieve convergence. However there is no need to use extremely small time steps because then more computational time will be needed. As can be seen from figure 5.11 the solution does not change for time steps less than 5.55E-05 seconds. This is the time step we use for the 3D simulation, it corresponds to a change of half a degree on the crank angle when the rotational speed is 1500 RPM. For higher or lower rotational speeds the time step is adjusted so as to reflect only half a degree change on the crank angle.

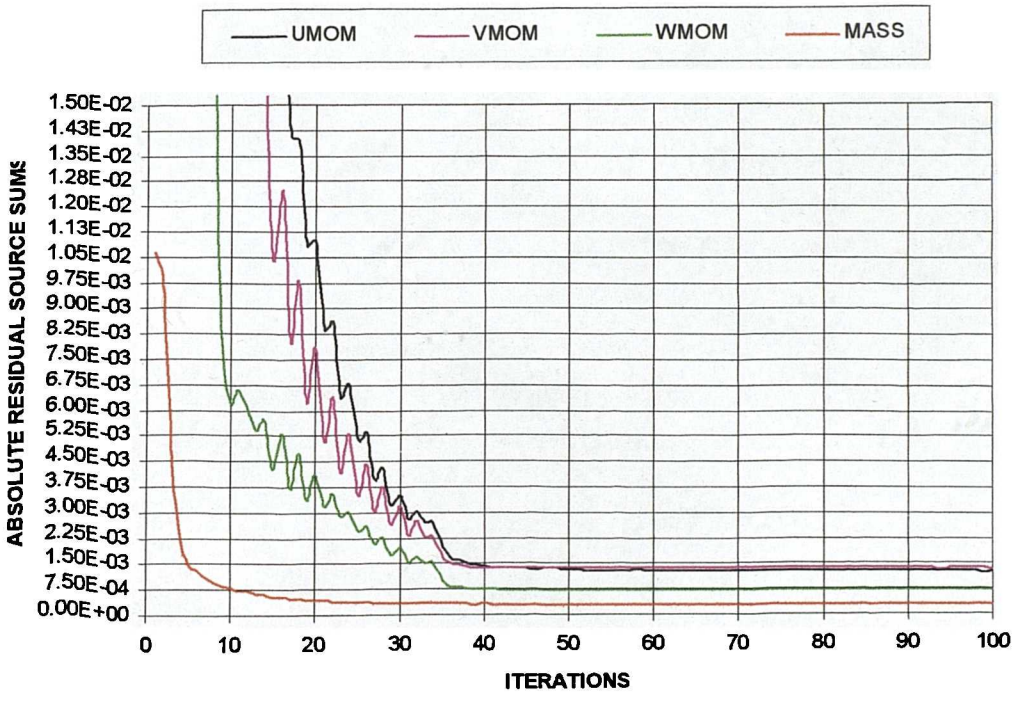

Figure 5.5 Residuals - Iterations. Speed 3000 RPM.

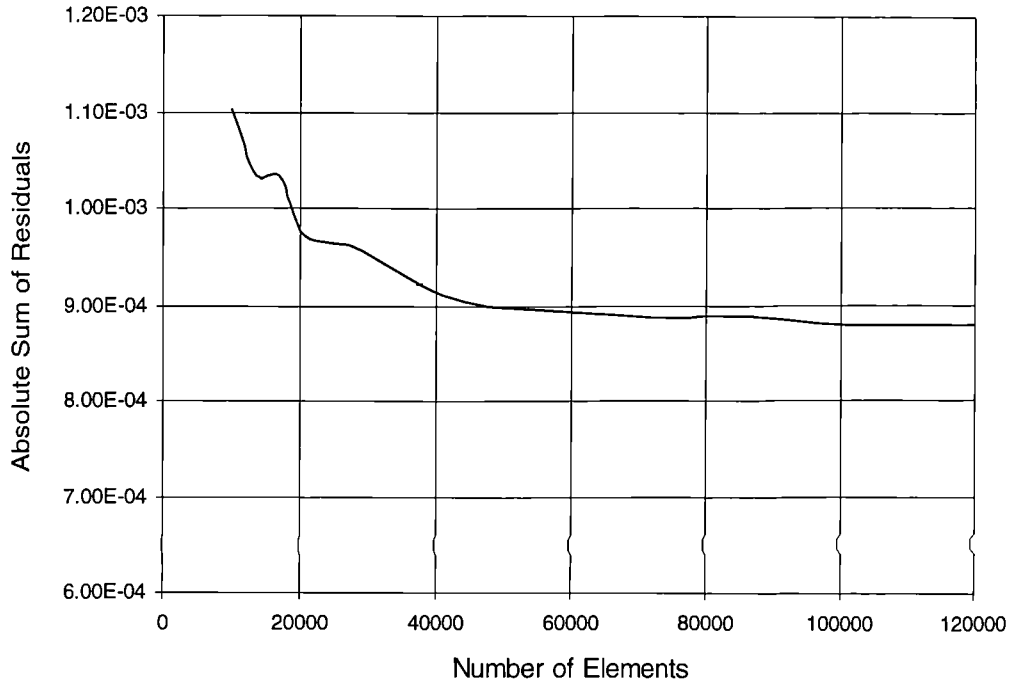

Figure 5.6 Residuals - Number of Elements. Speed 3000 RPM.

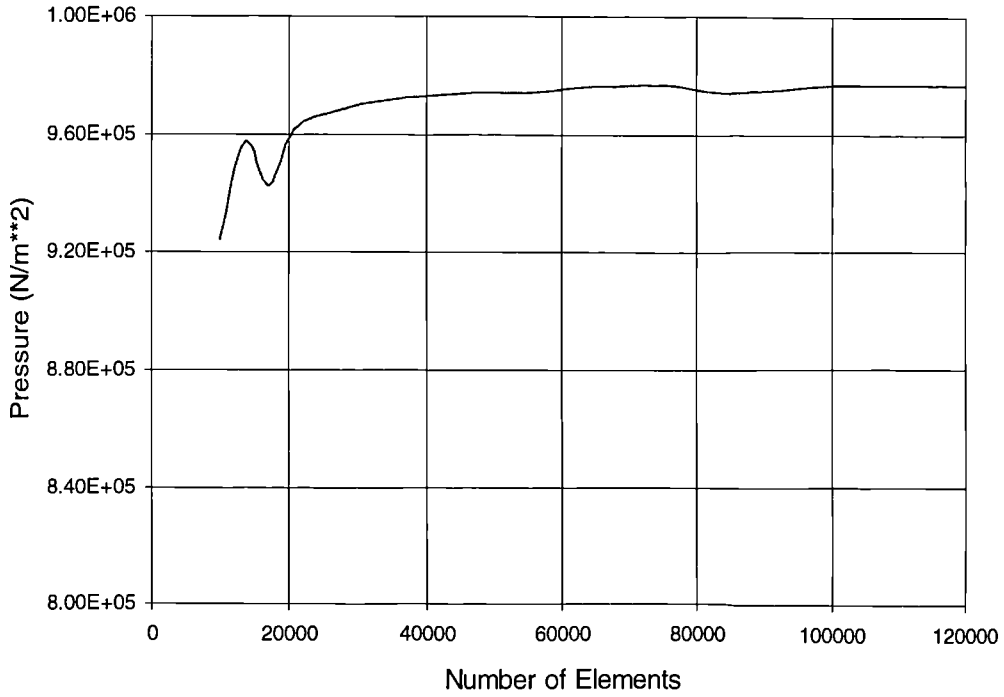

Figure 5.7 Pressure - Number of Elements. Speed 3000 RPM.

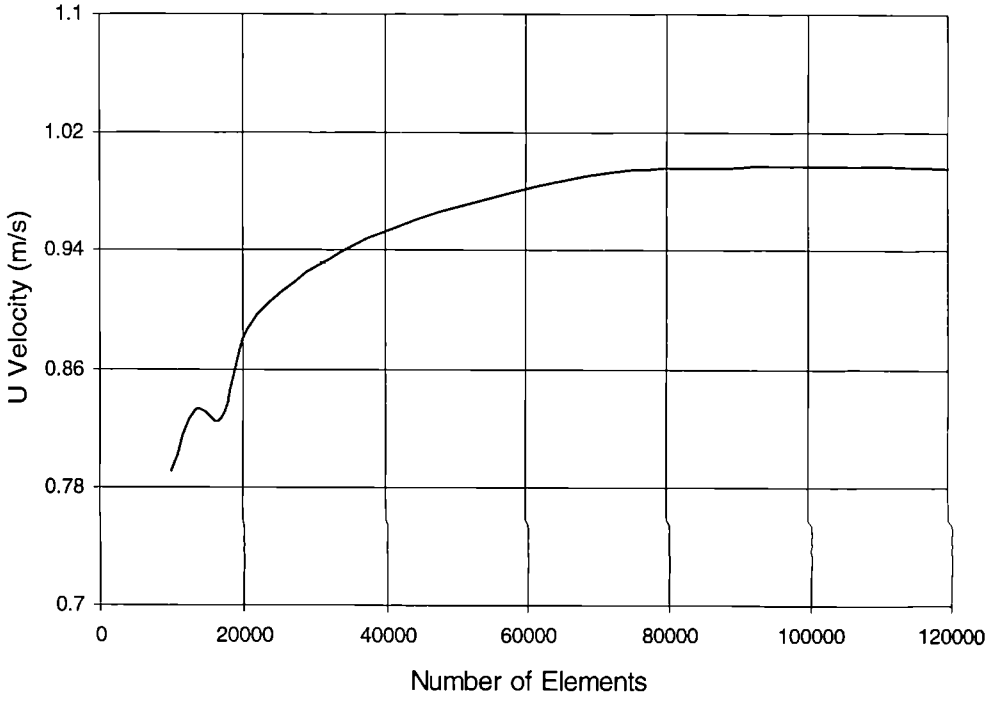

Figure 5.8 ***U*** velocity - Number of Elements. Speed 3000 RPM.

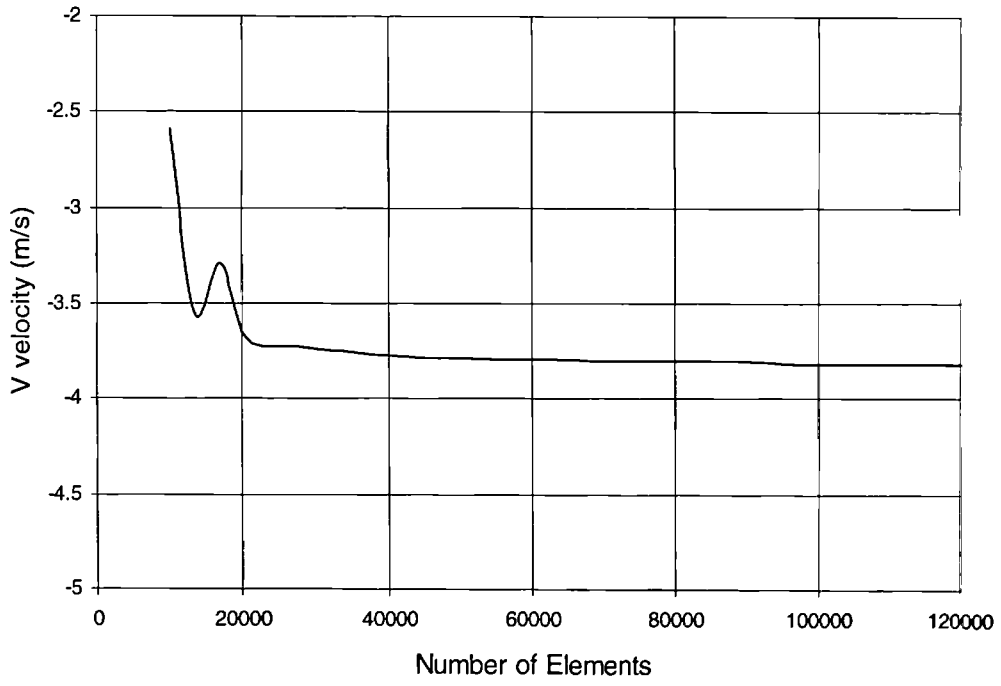

Figure 5.9 ***V*** velocity - Number of Elements. Speed 3000 RPM.

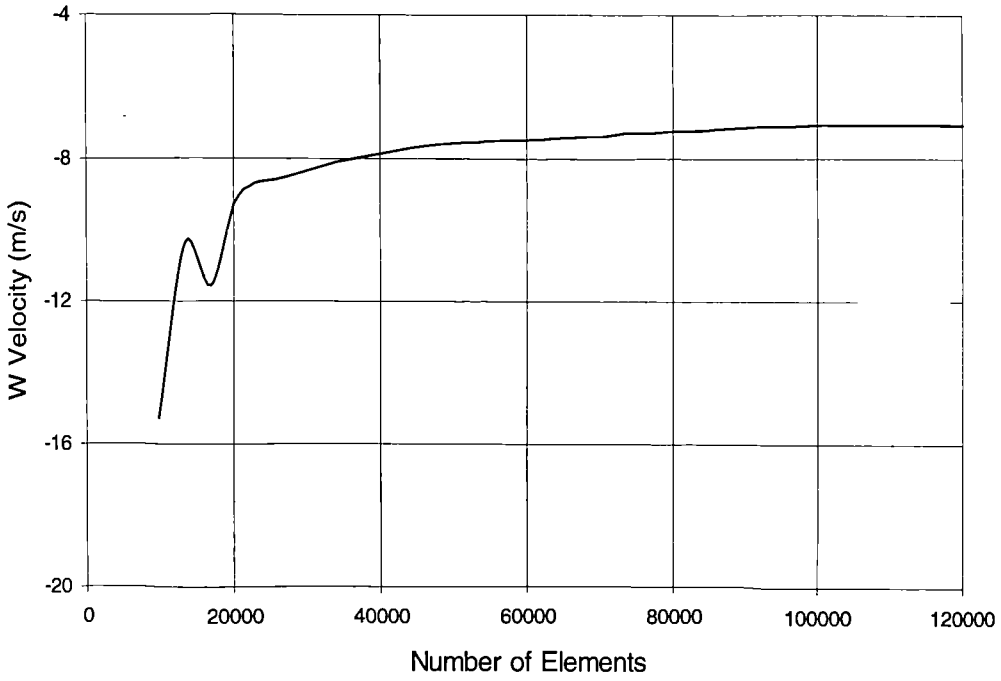

Figure 5.10 *W* velocity - Number of Elements. Speed 3000 RPM.

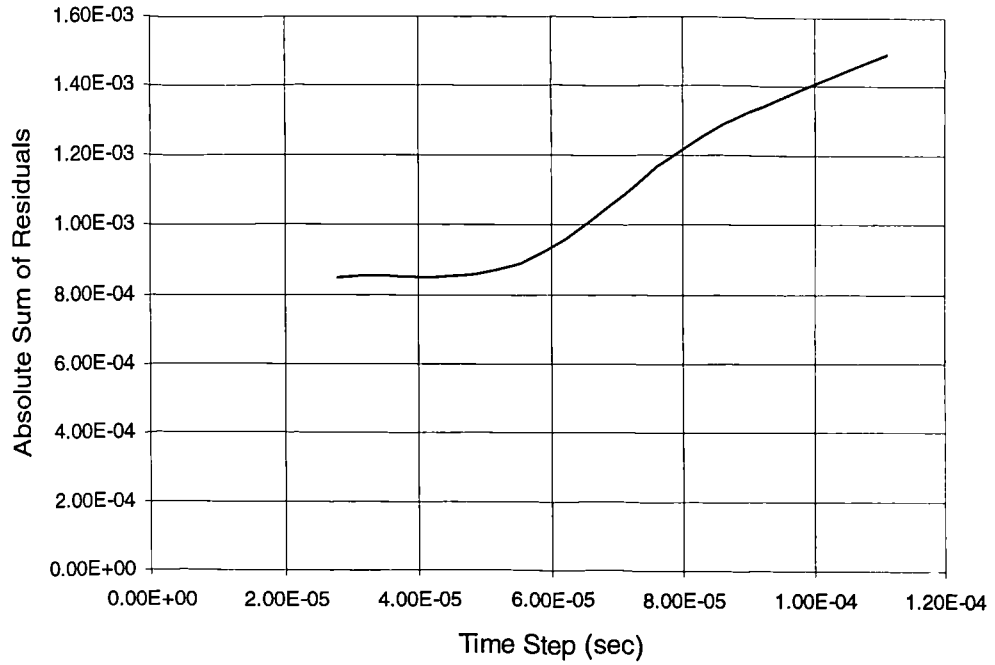

Figure 5.11 Residuals – Time Step. Speed 3000 RPM.

5.3.2 Thermodynamic Analysis

After the CFD analysis is completed the results can be used to improve understanding of the behavior of the suction process of the scroll expander, and discharge process of the scroll compressor. As was shown in section 5.3.1 the system is said to be grid independent for 70000 elements or more. The results shown in the figures of this section are obtained from a grid of 70000 elements.

In this section we use different types of graphic techniques to present the results. These are contour plots, vector plots, and streamlines. The *xy* plots are not used in this section mainly because they represent the variation of one dependent variable versus another independent variable. A disadvantage of *xy* plots is that they usually do not illustrate the global nature of a set of CFD results on one view. On the other hand, contour plots, vector plots, streamlines and particle tracking do provide such a global view.

5.3.2.1 Expander Characteristics

Figures 5.12 to 5.71 give an excellent understanding of the behavior of the suction process of the scroll expander. The results cover rotational speeds from 1000 RPM to 6000 RPM, the entry conditions are defined in section 3.4.2. What it is shown in these figures is the result of the compressible turbulent and transient flow modeling. It has to be noted here that in order to come to this stage the simulation was performed in steps. The first step was an incompressible laminar transient simulation, followed by an incompressible turbulent transient simulation, the model used for the turbulence parameters was the high Reynolds $k\ \varepsilon$. The next step was to calculate changes of density. In this case density changes were calculated from the equation of state but they were only affected by pressure because the temperature was fixed. This simulation was called weakly compressible turbulent transient flow. The final step (which is presented here) allows density calculation to depend on the changes of both pressure and temperature. In all the above models the simulations were performed for the rotational speed range of 1000 RPM to 6000 RPM (every 1000 RPM). It has to be mentioned at this point that the results presented here are only the 1/10 of the total results obtained.

As far as the results are concerned it is very difficult, perhaps impossible, to compare them with the results obtained from the quasi 1-D modeling (chapter 3). In that case the expander show good overall working performance. However the 3-D modeling which is more advanced and much more accurate indicates that this

is not 100% true. A careful examination of the figures that show the pressure contours will show that there are quite significant pressure differences within the flow domain. At higher rotational speeds these pressure differences are higher. The velocity vector graphs show that there are areas of re-circulation both in z and y-planes. If we look at the stream lines figures we will see that the flow pattern is not so good. At the beginning, the flow is coming in from the inlet pipe with a constant velocity, it hits the bottom wall of the expander and as a result there is a build up of pressure at that point. Then the flow goes in all directions hitting the side walls while the velocity begins to decrease. After the flow hits the side walls, the velocity decreases further and there also is re-circulation.

From this simulation it is obvious that the scroll expander will have major problems that will affect its operating behaviour (specially during the suction process). The reason for this is mainly the significant pressure drop that takes place during the filling process. At higher speeds the pressure drop within the working volume is of the order of 2 bar. From this modeling, and with the use of the visualisation packages, we manage to get the feeling of how the fluid will behave in such a machine. To give a better understanding of what we learn let us examine the case of an expansion that takes place in a turbine or in a screw expander, and then compare it with the scroll-expander. The reason for doing this is to identify the major problem of the scroll expander. What happens in those cases is that the flow 'in' is coming in a completely different way, angle of attack, and the machine will also behave in a completely different way. The flow hits the blades of the expander and as a result of this there is a movement of the blades. In our case the fluid is coming from the top but the expected movement of the spirals is horizontal, (90^{o} degrees difference). Unlike the case of the screw expander the flow 'in' in a scroll expander hits first the bottom of the machine (stagnation point occurs there), which results in the build up of pressure there, and then the residual flow moves the wall spirals. This is also the main reason for the fluid to swirl. Please note that all these facts are taking place during the suction process of the scroll expander. It looks like things will improve during the expansion process, but the results are not clear in that case.

5.3.2.2 Compressor Characteristics

As for the case of the expander, the simulation of the discharge process of the scroll compressor was also performed in steps, the same ones as for the case of the expander. However the results in this case, which are shown in figures 5.72 to 5.143 indicate that the scroll compressor is an excellent positive displacement machine. We have approximately uniform pressures within the domain. The velocity vectors shows that there is a small area of re-circulation closed to the outlet pipe, but this is something reasonable for this type of machine. The stream line figures show that some swirling is taking place, mainly in the outlet pipe.

Close to the walls the velocity is relatively low and uniform. As the walls move inwards the fluid velocity near the pipe increases and takes its peak value inside the discharge pipe. The velocities within the pipe are not uniform and are higher on the side of the moving spiral. Almost under the pipe we can see that there is some area of re-circulation. This area increases as the flow approaches the inlet of the discharge pipe. Now as far as the pressures are concerned it can be seen that everywhere in the domain except from the area below the discharge pipe the pressure is at its highest value and is also uniform. As the flow approaches the discharge pipe from all sides small pressure drops begin, these pressure drops continue smoothly until about the middle of the discharge pipe where they stabilize for the rest of the outlet pipe.

The midplane (Z-plane=-0.1) velocity vectors characterize the nature of the flow within the entire volume. The flow vectors indicate the nature of the flow depending upon the location. Three dimensional flow tends to move vertically upwards as it approaches the central section of the volume which is directly below the discharge port. The flow characteristics exhibited here possess a strong axial component combined with an in-plane (horizontal) vortex component occurring in all axial levels. The results show that this basic vortex flow pattern persists in the area below the discharge port throughout the entire axial extent of the flow volume. The calculations indicate that the flow passing through the discharge port is not uniform.

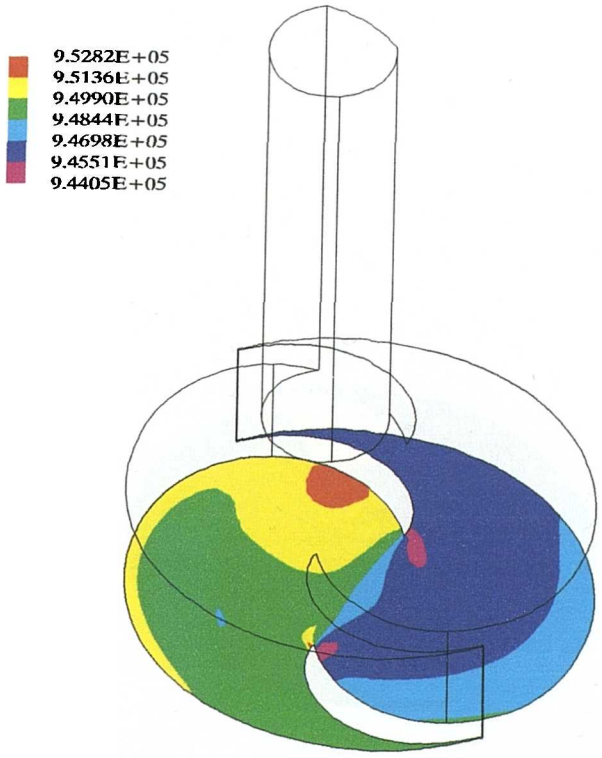

Figure 5.12 Scroll-Expander. Rotational speed 1000 RPM, Pressure contours, Z-plane =-0.2, step=100, 50 degrees (8.333m sec) after suction commences

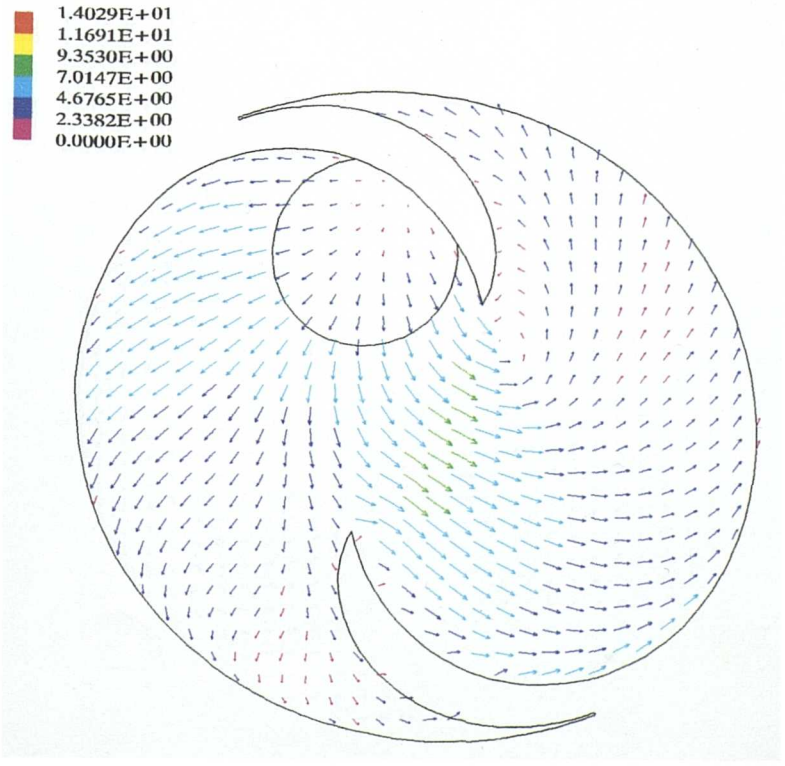

Figure 5.13 Scroll-Expander. Rotational speed 1000 RPM, Speed vectors, Z-plane =-0.018, step=100, 50 degrees (8.333m sec) after suction commences

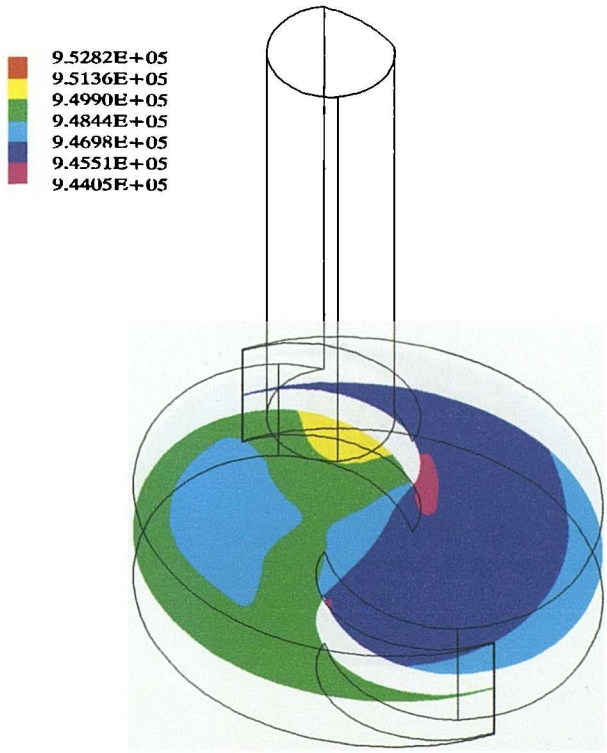

Figure 5.14 Scroll-Expander. Rotational speed 1000 RPM, Pressure contours, Z-plane =-0.1, step=100, 50 degrees (8.333m sec) after suction commences

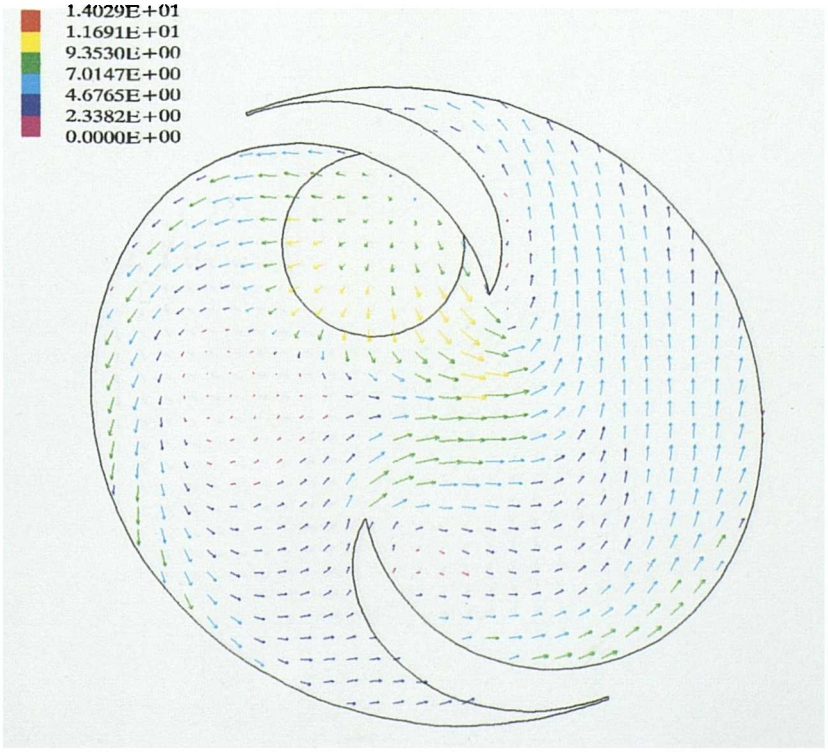

Figure 5.15 Scroll-Expander. Rotational speed 1000 RPM, Speed vectors, Z-plane =-0.1, step=100, 50 degrees (8.333m sec) after suction commences

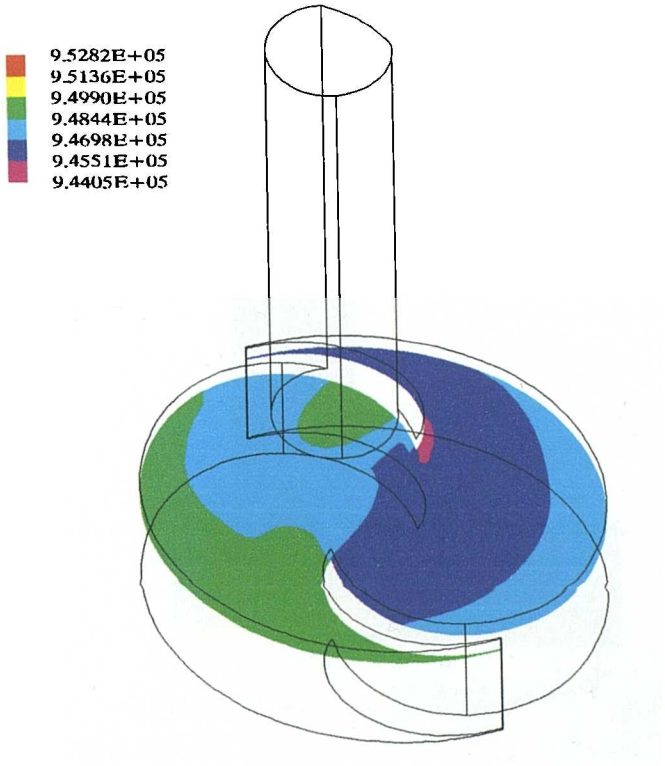

Figure 5.16 Scroll-Expander. Rotational speed 1000 RPM, Pressure contours, Z-plane =-0.0025, step=100, 50 degrees (8.333m sec) after suction commences

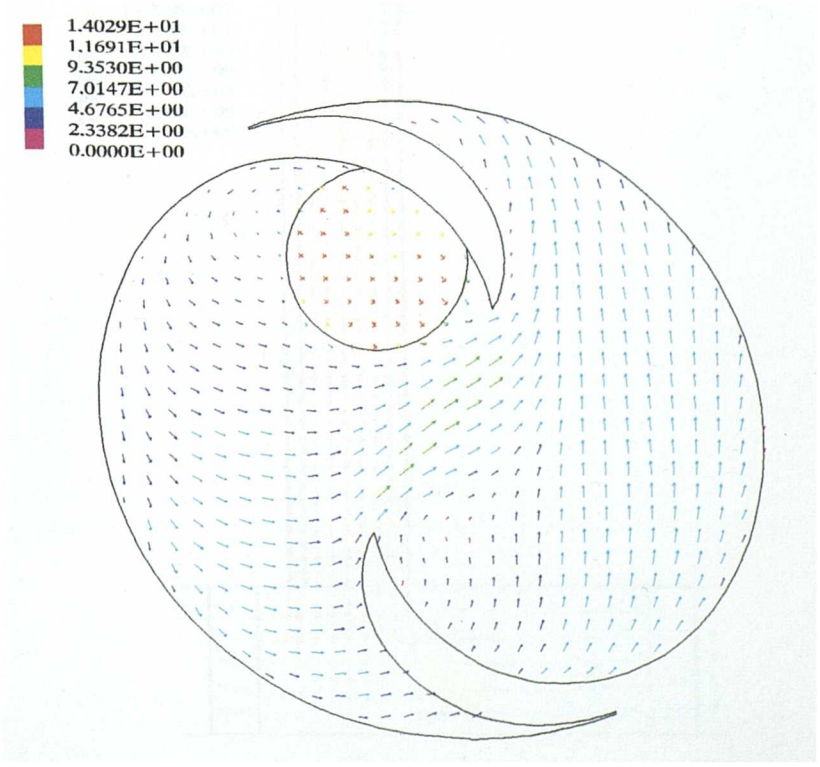

Figure 5.17 Scroll-Expander. Rotational speed 1000 RPM, Speed vectors, Z-plane =-0.0025, step=100, 50 degrees (8.333m sec) after suction commences

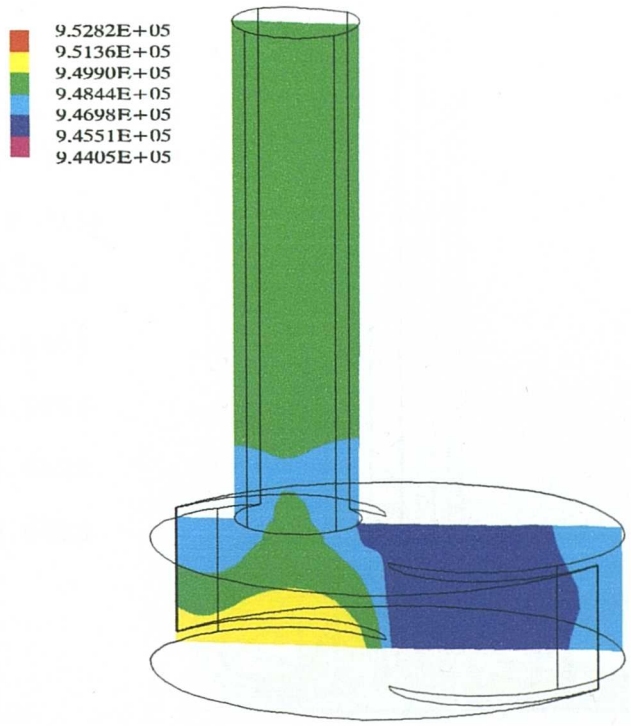

Figure 5.18 Scroll-Expander. Rotational speed 1000 RPM, Pressure contours, Arbitrary plane, step=100, 50 degrees (8.333m sec) after suction commences

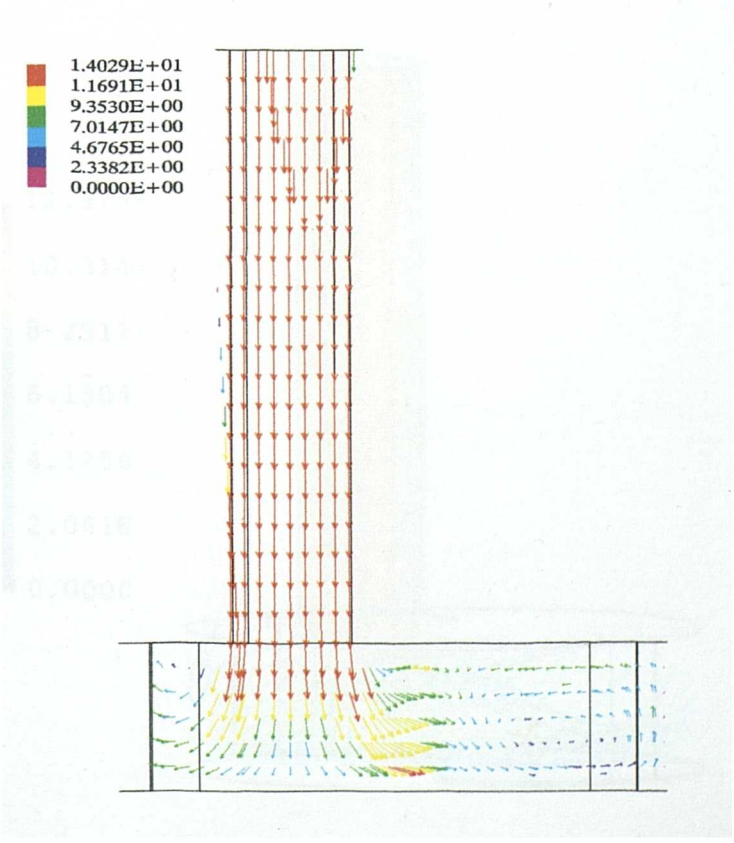

Figure 5.19 Scroll-Expander. Rotational speed 1000 RPM, Speed vectors, Arbitrary plane, step=100, 50 degrees (8.333m sec) after suction commences

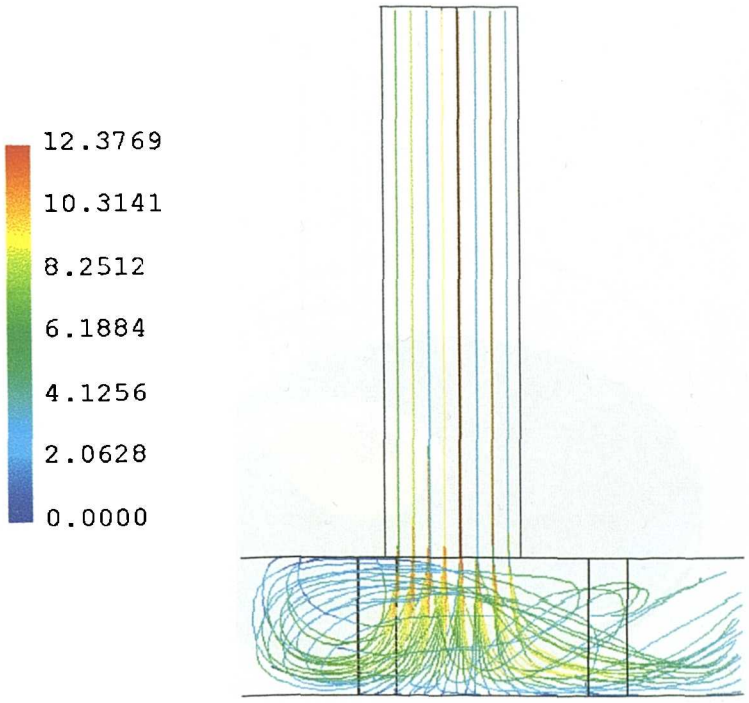

Figure 5.20 Scroll-Expander. Rotational speed 1000 RPM, Stream lines step=100, 50 degrees (8.333m sec) after suction commences

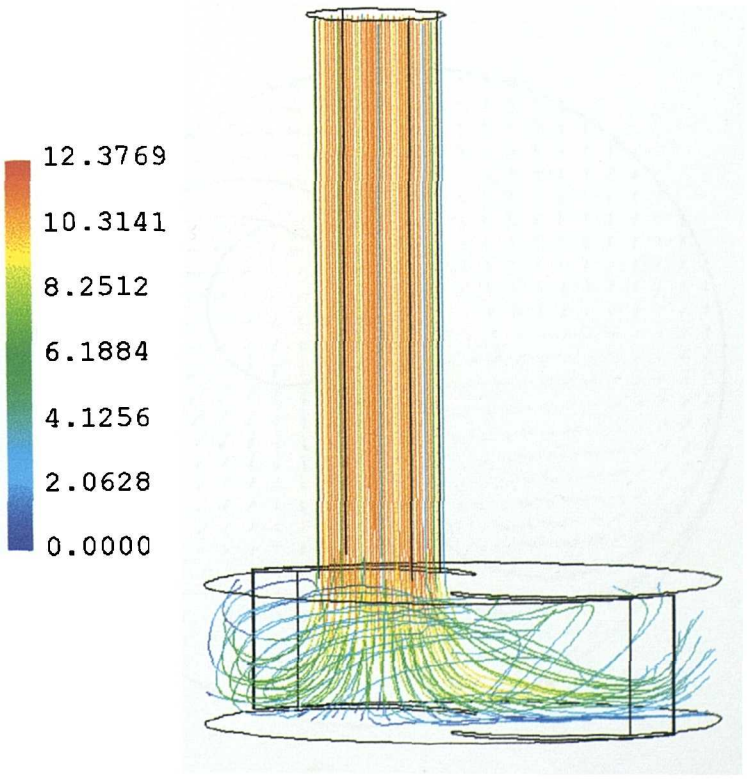

Figure 5.21 Scroll-Expander. Rotational speed 1000 RPM, Stream lines, step=100, 50 degrees (8.333m sec) after suction commences

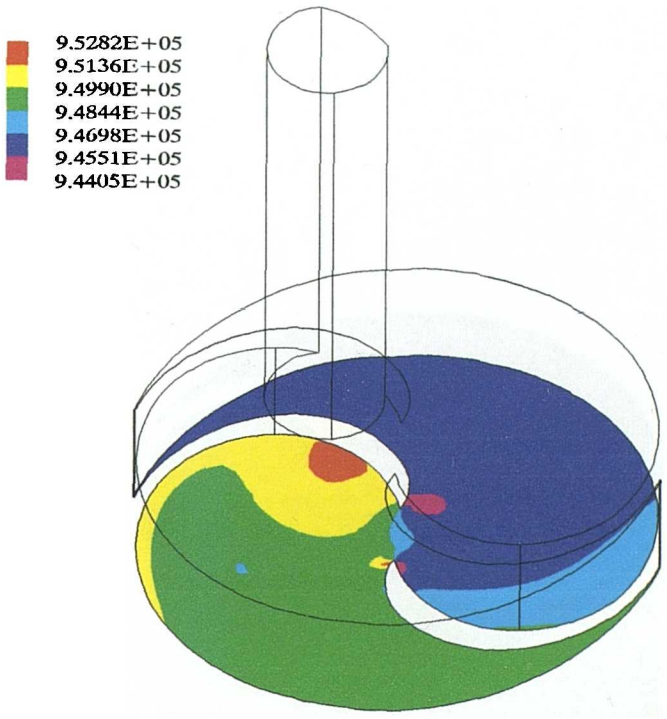

Figure 5.22 Scroll-Expander. Rotational speed 1000 RPM, Pressure contours, Z-plane =-0.2, step=200, 100 degrees (16.66m sec) after suction commences

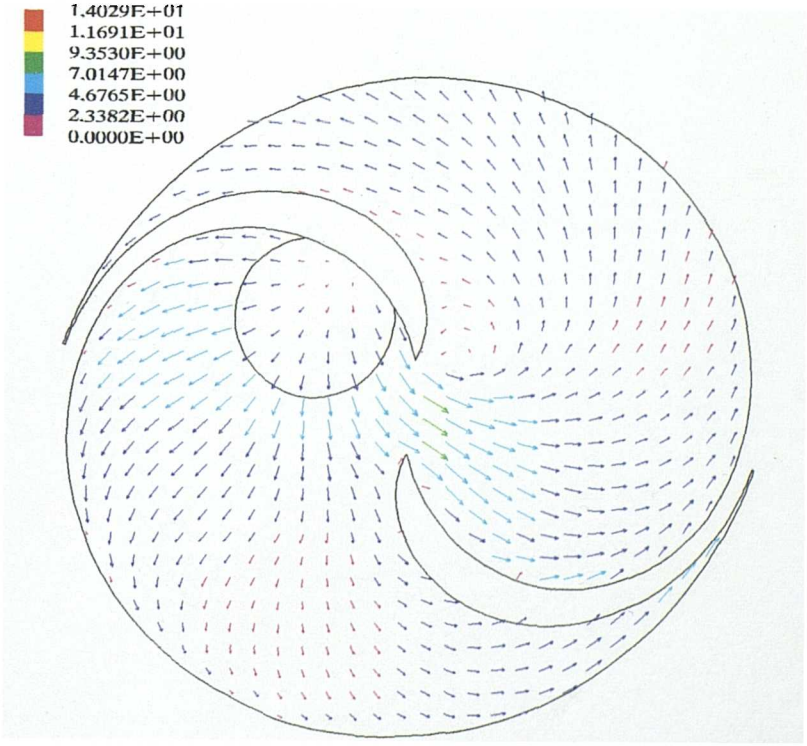

Figure 5.23 Scroll-Expander. Rotational speed 1000 RPM, Speed vectors, Z-plane =-0.018, step=200, 100 degrees (16.66m sec) after suction commences

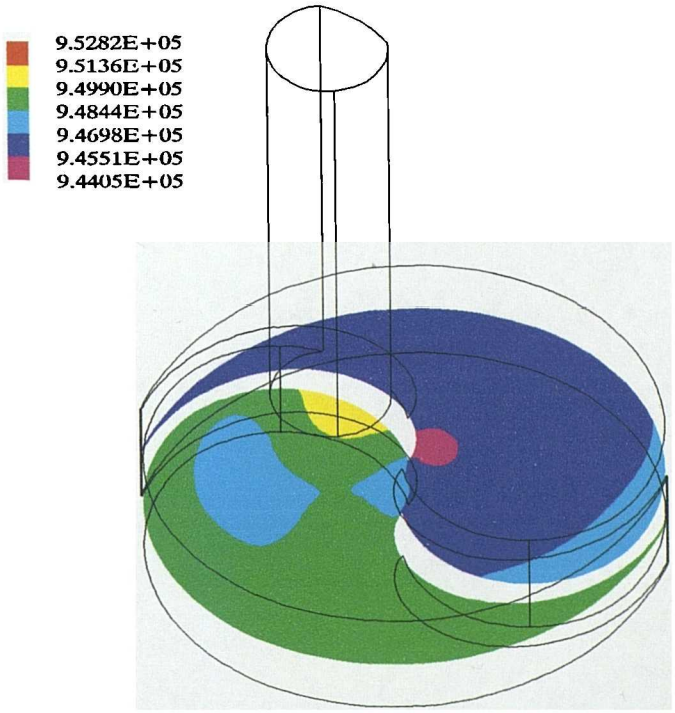

Figure 5.24 Scroll-Expander. Rotational speed 1000 RPM, Pressure contours, Z-plane =-0.1, step=200, 100 degrees (16.66m sec) after suction commences

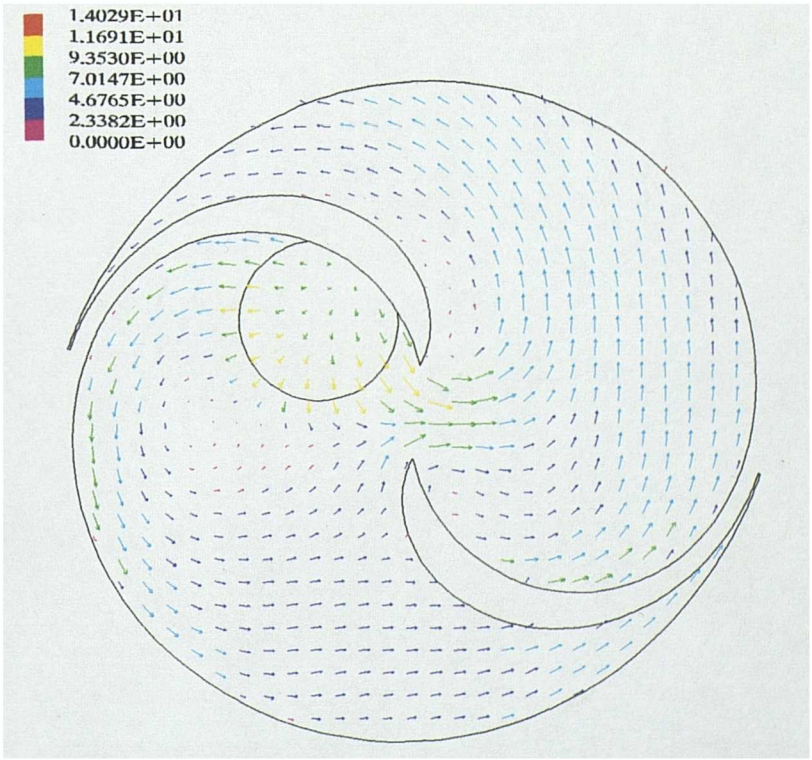

Figure 5.25 Scroll-Expander. Rotational speed 1000 RPM, Speed vectors, Z-plane =-0.1, step=200, 100 degrees (16.66m sec) after suction commences

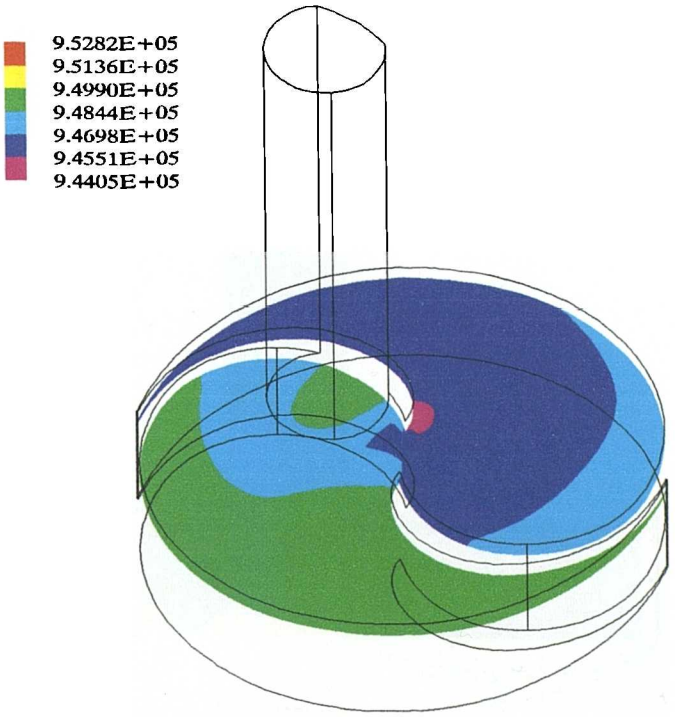

Figure 5.26 Scroll-Expander. Rotational speed 1000 RPM, Pressure contours, Z-plane =-0.0025, step=200, 100 degrees (16.66m sec) after suction commences

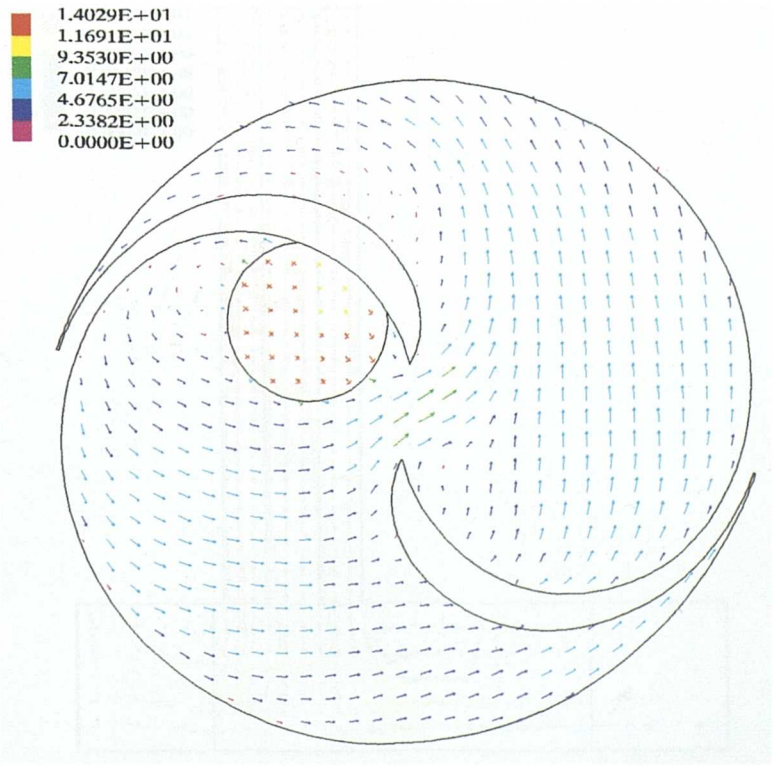

Figure 5.27 Scroll-Expander. Rotational speed 1000 RPM, Speed vectors, Z-plane =-0.0025, step=200, 100 degrees (16.66m sec) after suction commences

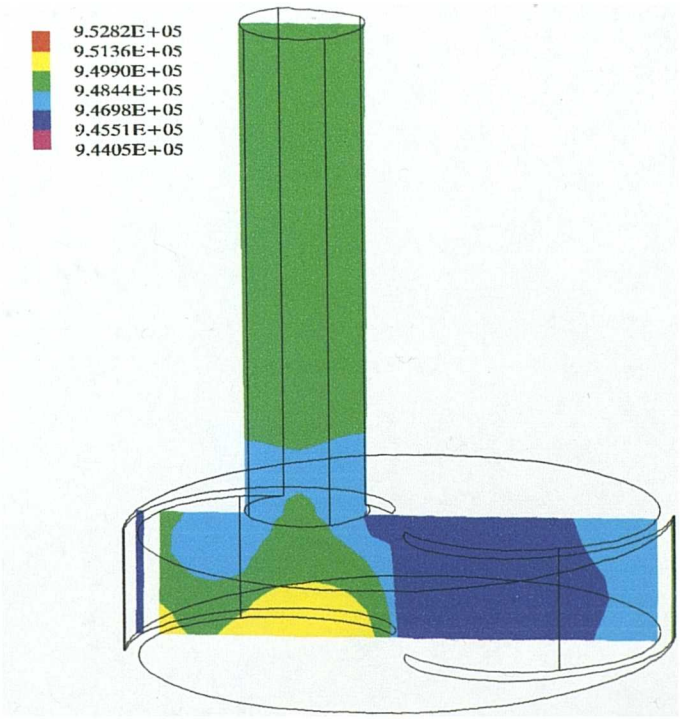

Figure 5.28 Scroll-Expander. Rotational speed 1000 RPM, Pressure contours, Arbitrary plane, step=200, 100 degrees (16.66m sec) after suction commences

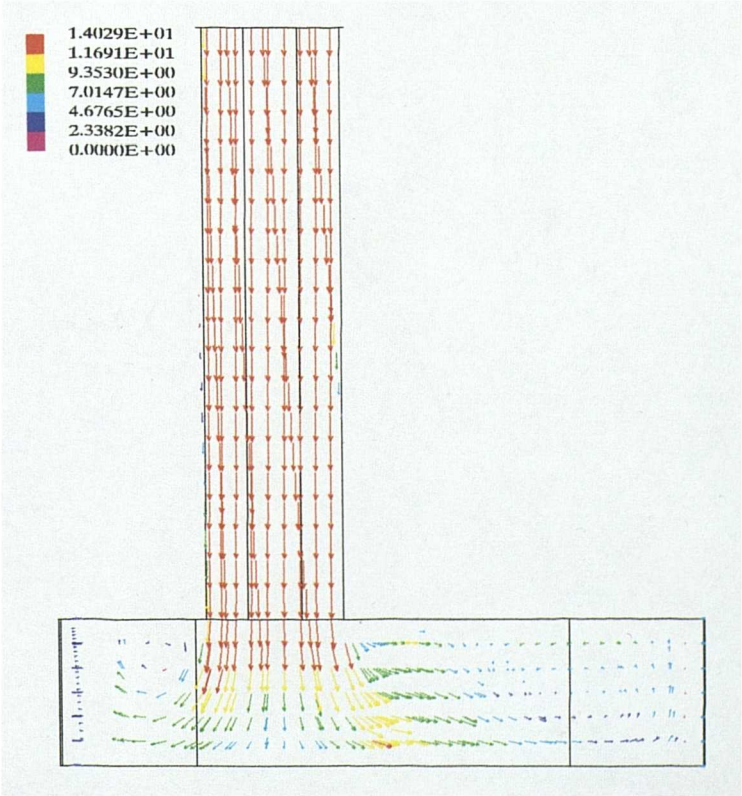

Figure 5.29 Scroll-Expander. Rotational speed 1000 RPM, Speed vectors, Arbitrary plane, step=200, 100 degrees (16.66m sec) after suction commences

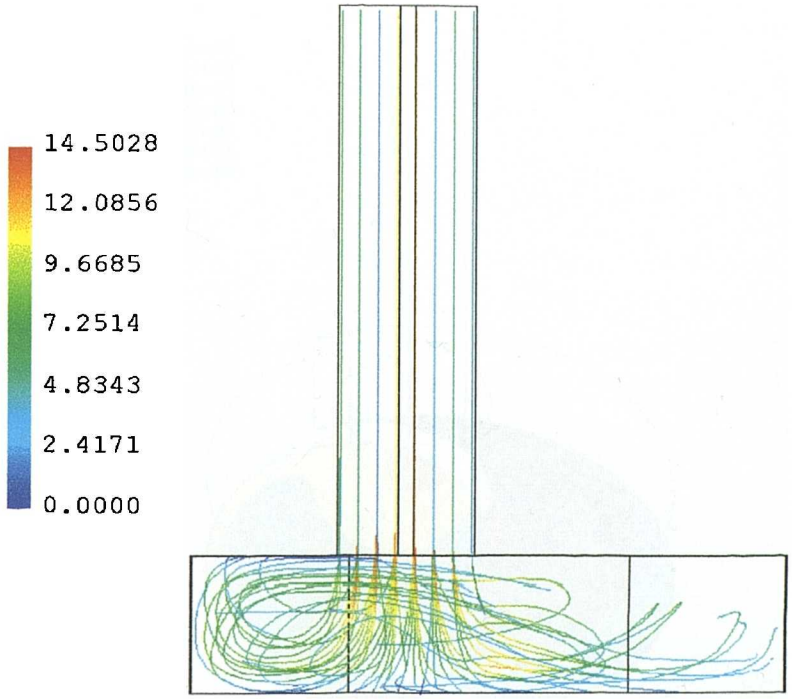

Figure 5.30 Scroll-Expander. Rotational speed 1000 RPM, Stream lines step=200, 100 degrees (16.66m sec) after suction commences

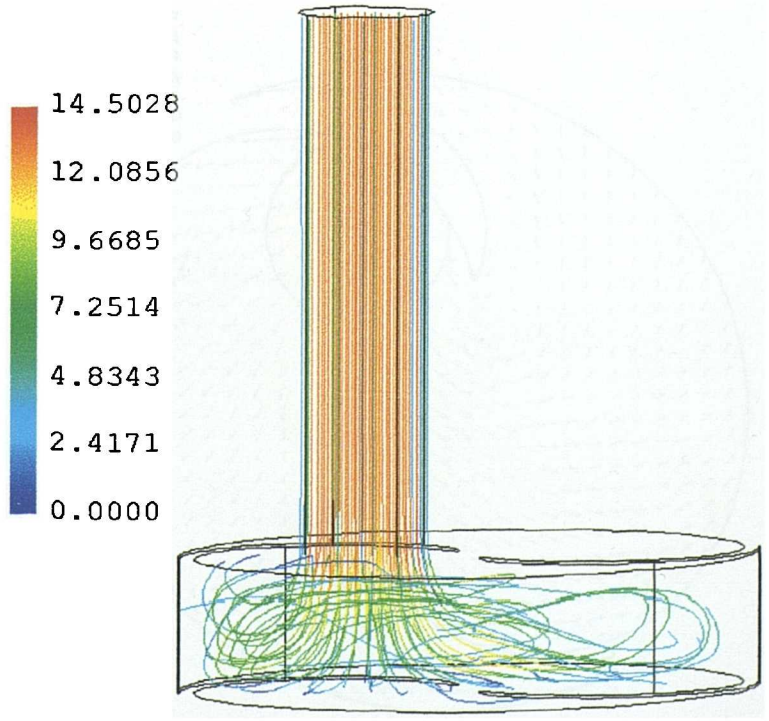

Figure 5.31 Scroll-Expander. Rotational speed 1000 RPM, Stream lines, step=200, 100 degrees (16.66m sec) after suction commences

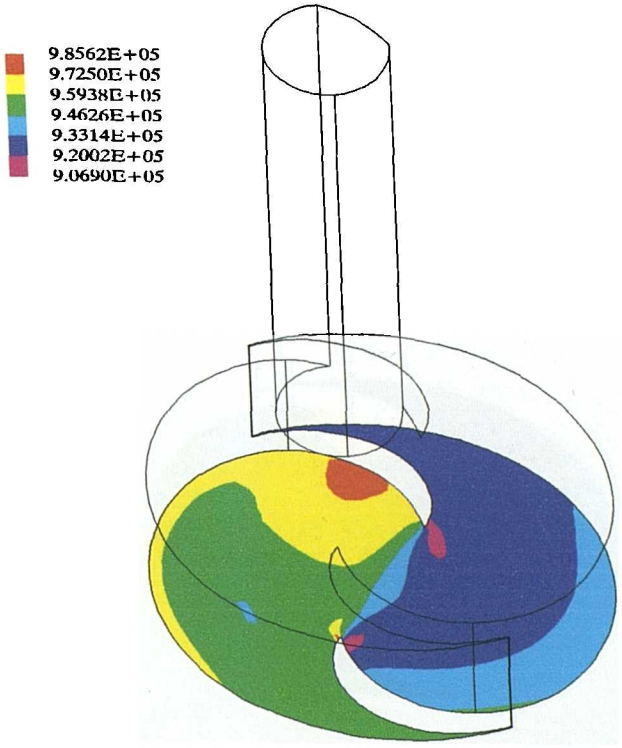

Figure 5.32 Scroll-Expander. Rotational speed 3000 RPM, Pressure contours, Z-plane =-0.2, step=100, 50 degrees (2.777m sec) after suction commences

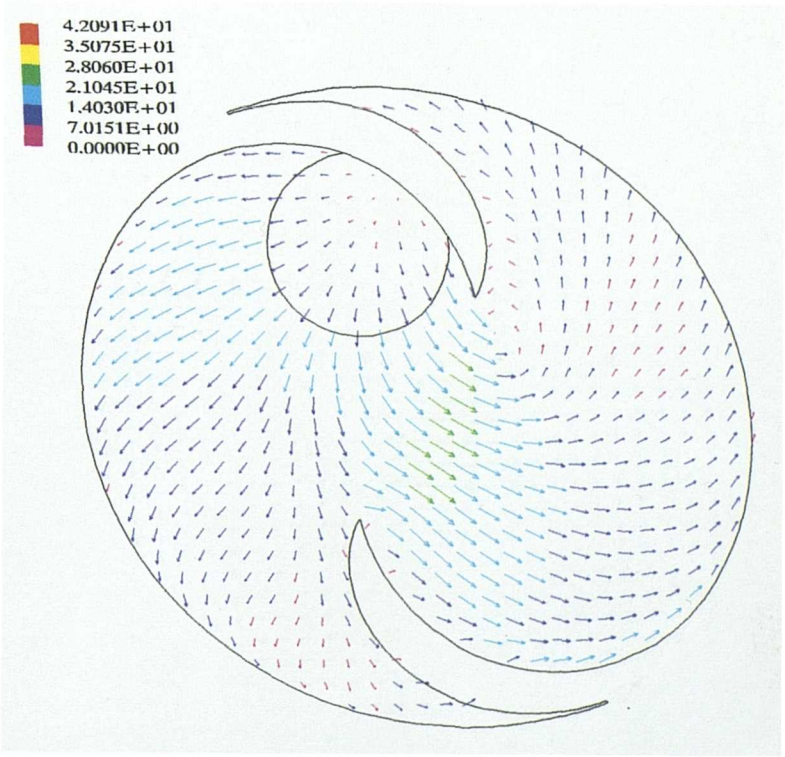

Figure 5.33 Scroll-Expander. Rotational speed 3000 RPM, Speed vectors, Z-plane =-0.018, step=100, 50 degrees (2.777m sec) after suction commences

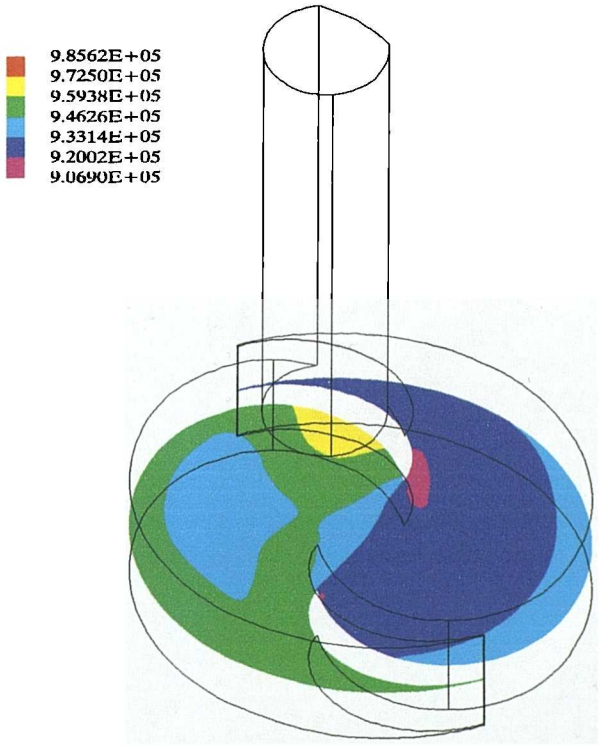

Figure 5.34 Scroll-Expander. Rotational speed 3000 RPM, Pressure contours, Z-plane =-0.1, step=100, 50 degrees (2.777m sec) after suction commences

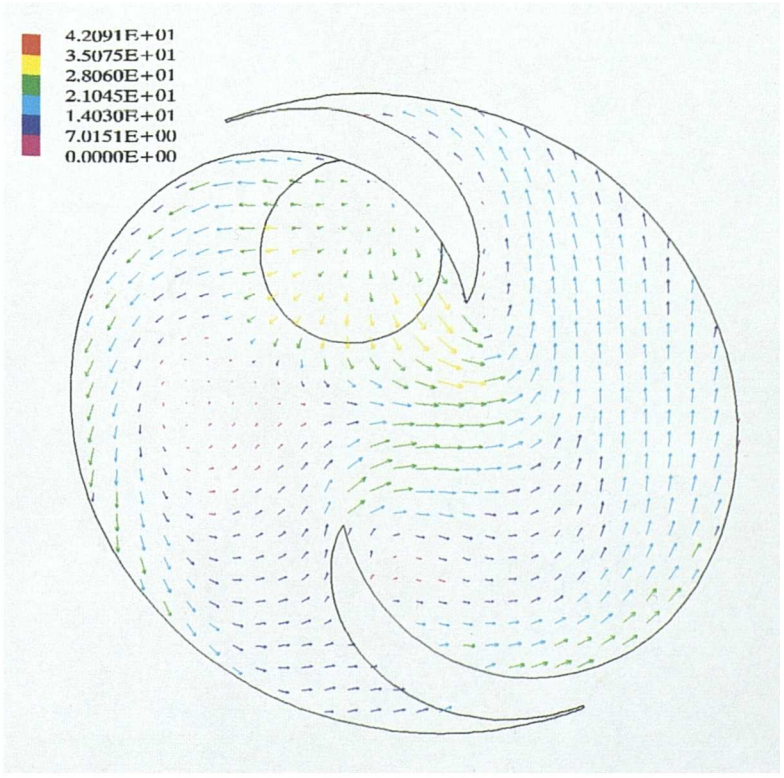

Figure 5.35 Scroll-Expander. Rotational speed 3000 RPM, Speed vectors, Z-plane =-0.1, step=100, 50 degrees (2.777m sec) after suction commences

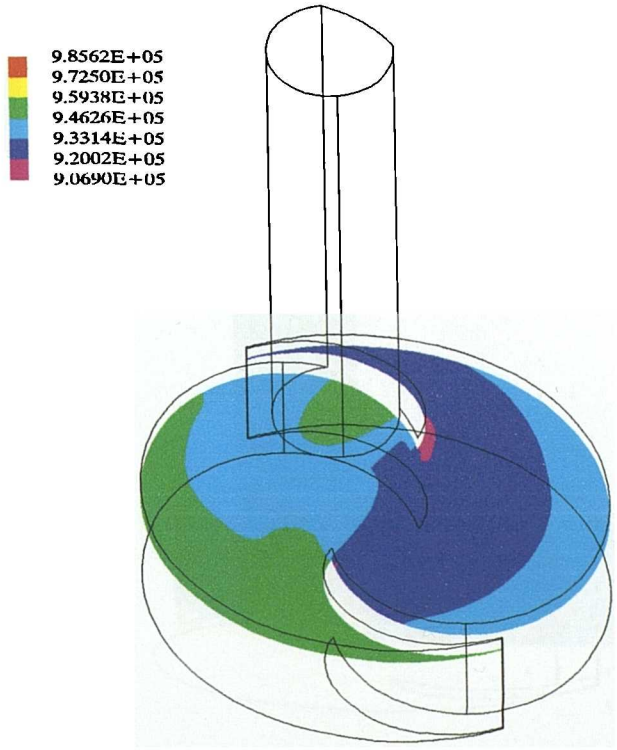

Figure 5.36 Scroll-Expander. Rotational speed 3000 RPM, Pressure contours, Z-plane =-0.0025, step=100, 50 degrees (2.777m sec) after suction commences

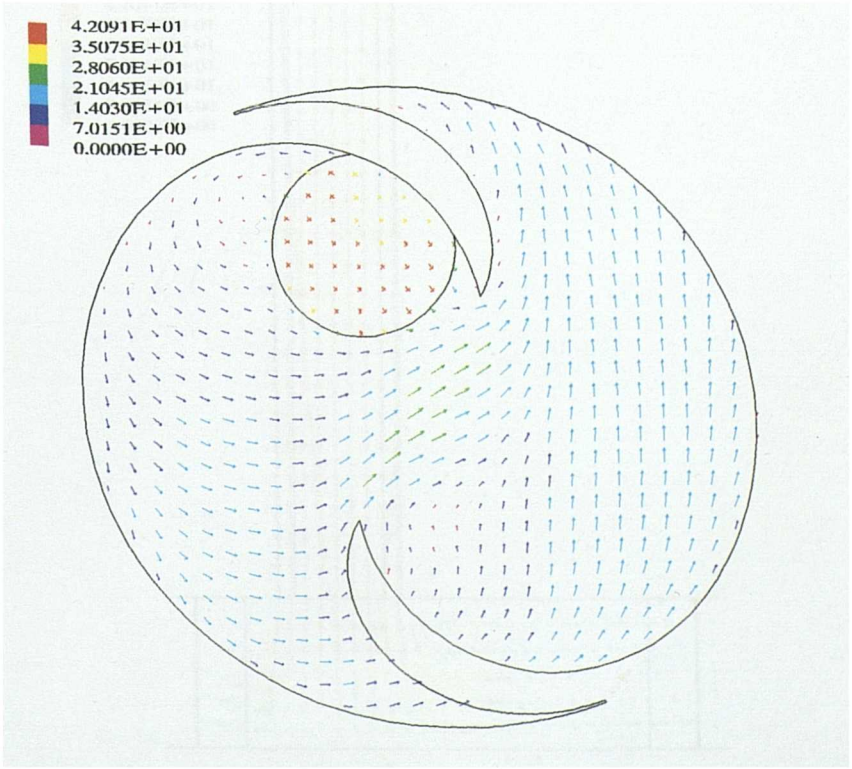

Figure 5.37 Scroll-Expander. Rotational speed 3000 RPM, Speed vectors, Z-plane =-0.0025, step=100, 50 degrees (2.777m sec) after suction commences

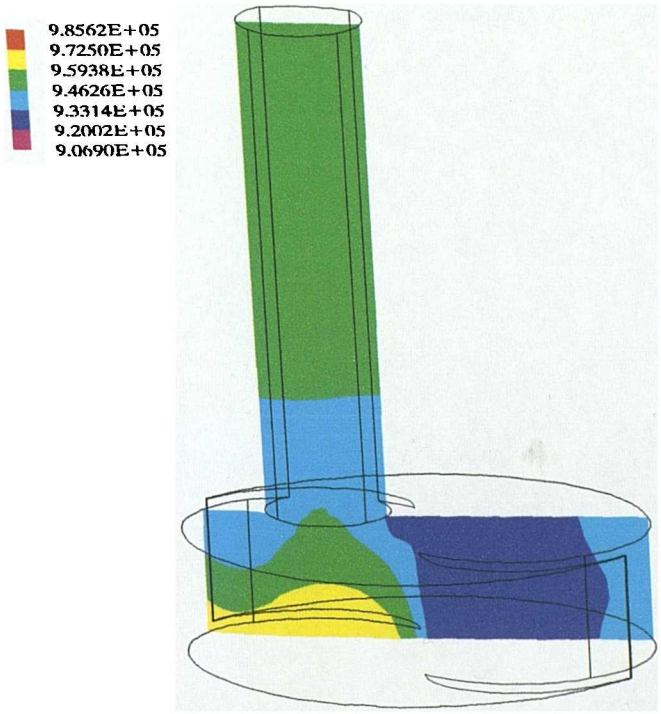

Figure 5.38 Scroll-Expander. Rotational speed 3000 RPM, Pressure contours, Arbitrary plane, step=100, 50 degrees (2.777m sec) after suction commences

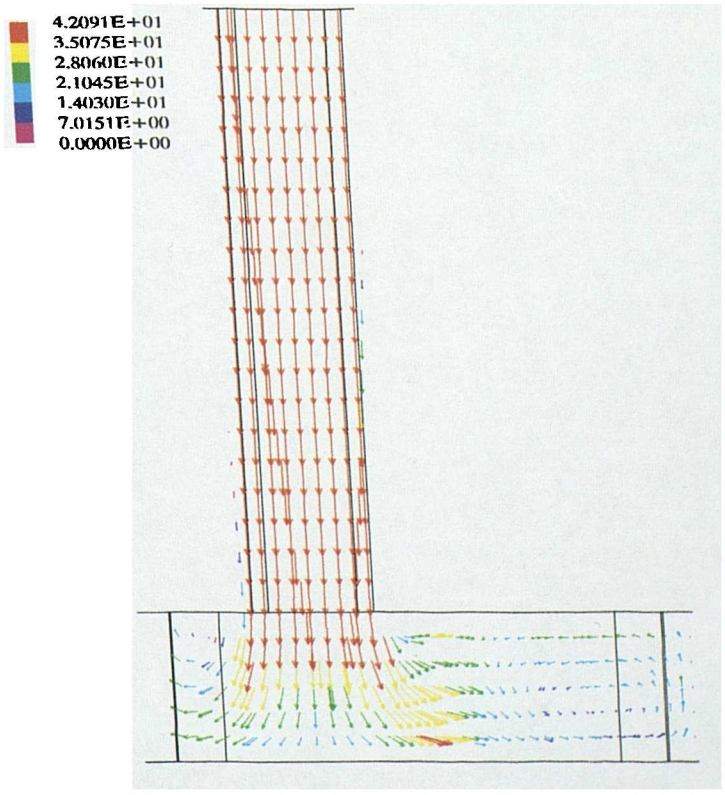

Figure 5.39 Scroll-Expander. Rotational speed 3000 RPM, Speed vectors, Arbitrary plane, step=100, 50 degrees (2.777m sec) after suction commences

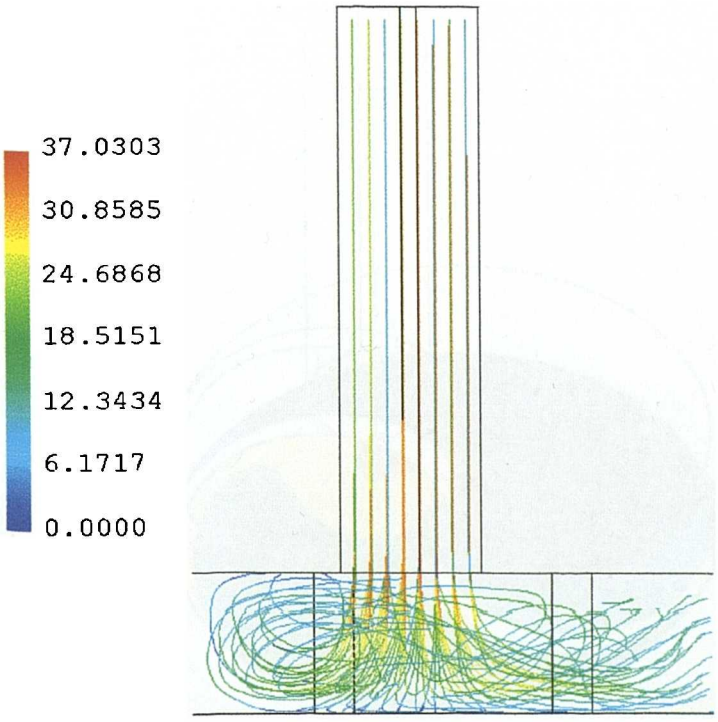

Figure 5.40 Scroll-Expander. Rotational speed 3000 RPM, Stream lines step=100, 50 degrees (2.777m sec) after suction commences

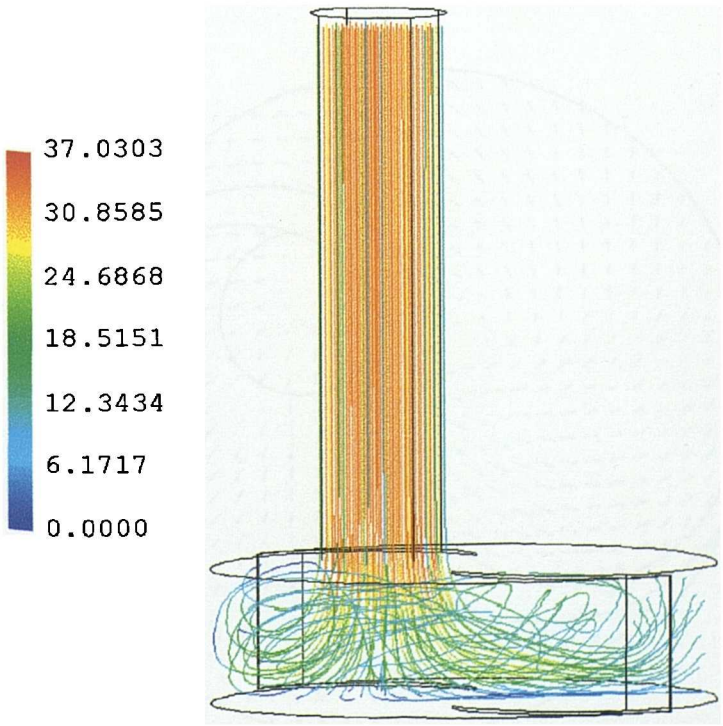

Figure 5.41 Scroll-Expander. Rotational speed 3000 RPM, Stream lines, step=100, 50 degrees (2.777m sec) after suction commences

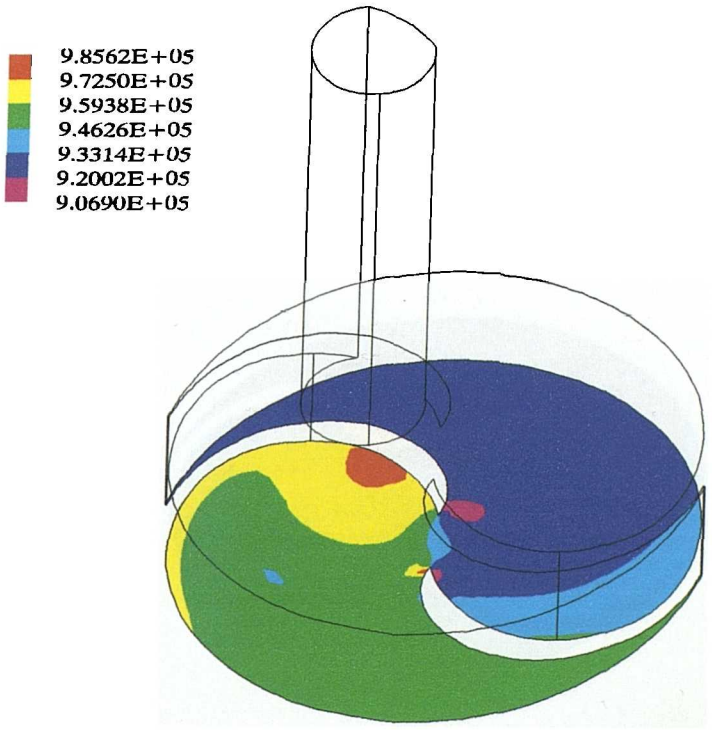

Figure 5.42 Scroll-Expander. Rotational speed 3000 RPM, Pressure contours, Z-plane =-0.2, step=200, 100 degrees (5.54m sec) after suction commences

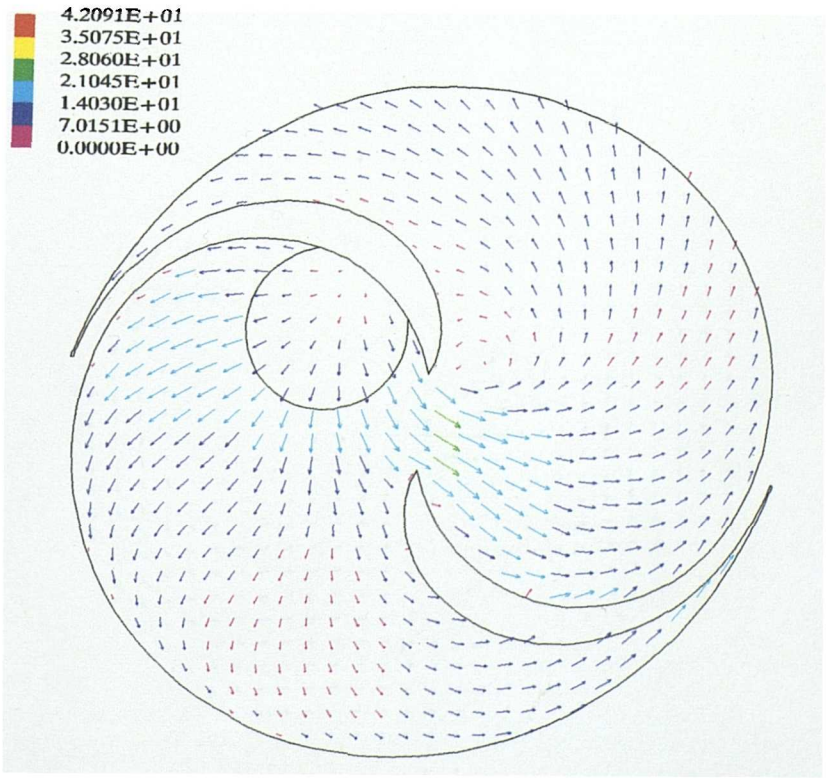

Figure 5.43 Scroll-Expander. Rotational speed 3000 RPM, Speed vectors, Z-plane =-0.018, step=200, 100 degrees (5.54m sec) after suction commences

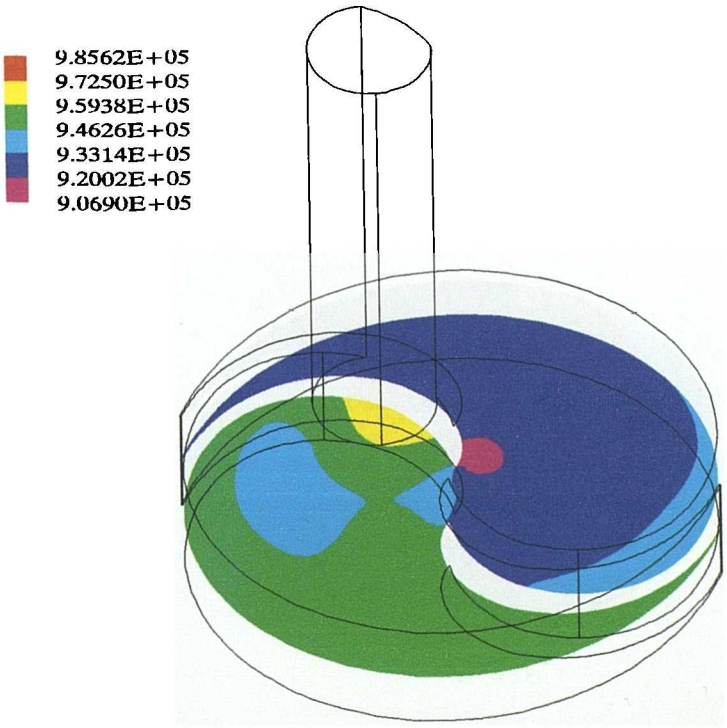

Figure 5.44 Scroll-Expander. Rotational speed 3000 RPM, Pressure contours, Z-plane =-0.1, step=200, 100 degrees (5.54m sec) after suction commences

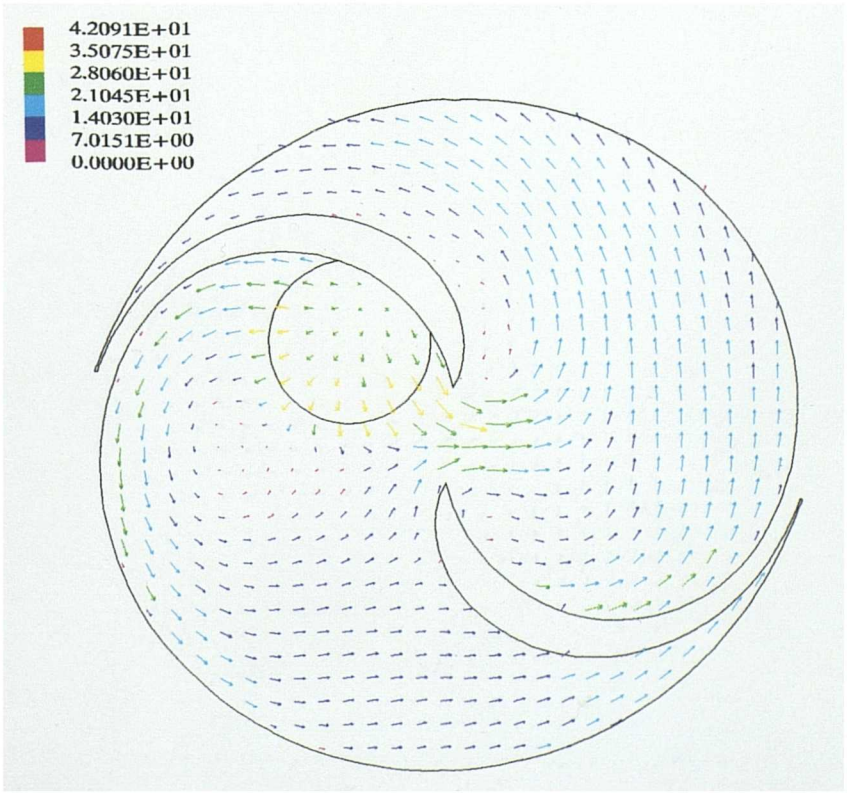

Figure 5.45 Scroll-Expander. Rotational speed 3000 RPM, Speed vectors, Z-plane =-0.1, step=200, 100 degrees (5.54m sec) after suction commences

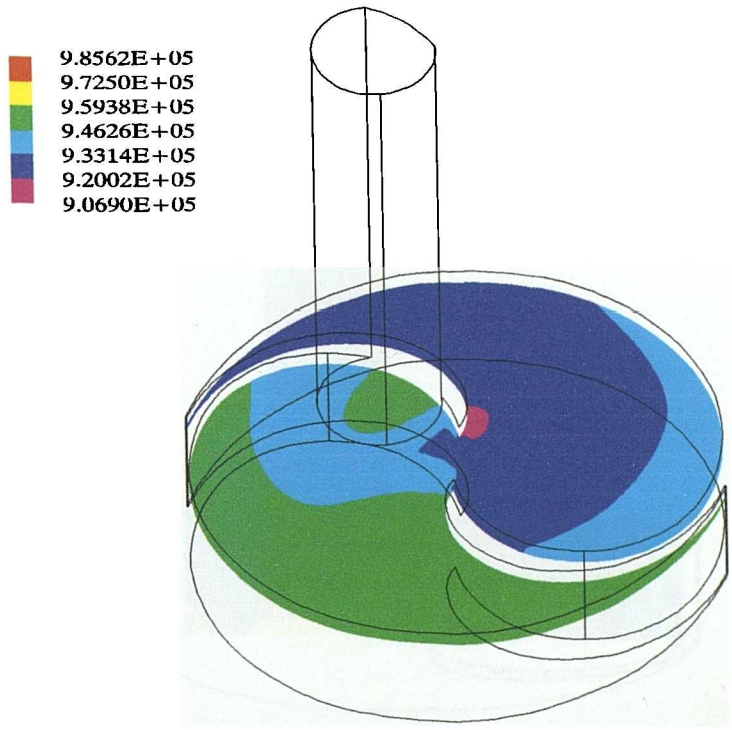

Figure 5.46 Scroll-Expander. Rotational speed 3000 RPM, Pressure contours, Z-plane =-0.0025, step=200, 100 degrees (5.54m sec) after suction commences

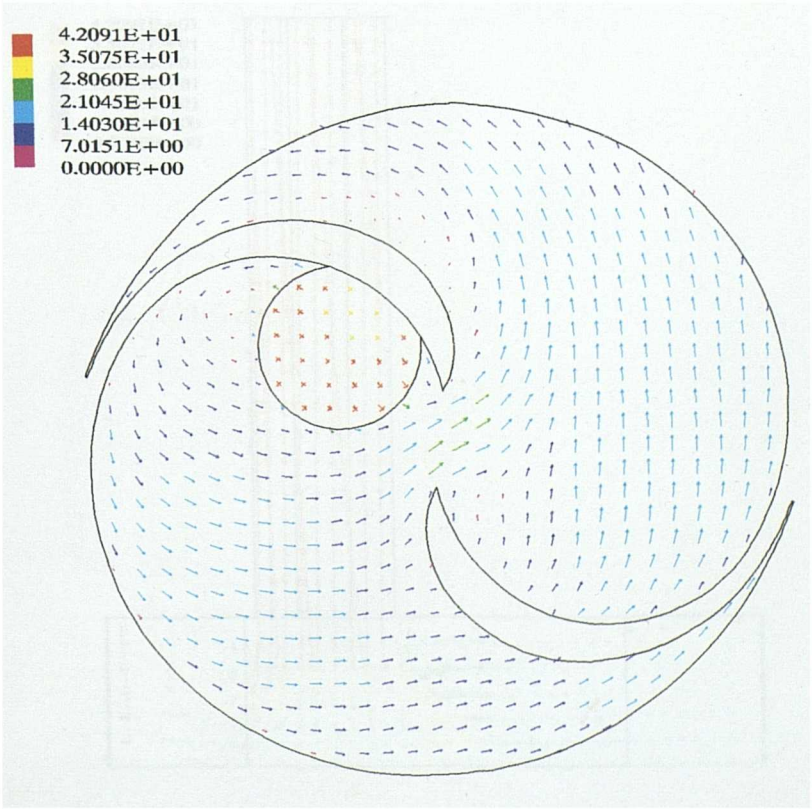

Figure 5.47 Scroll-Expander. Rotational speed 3000 RPM, Speed vectors, Z-plane =-0.0025, step=200, 100 degrees (5.54m sec) after suction commences

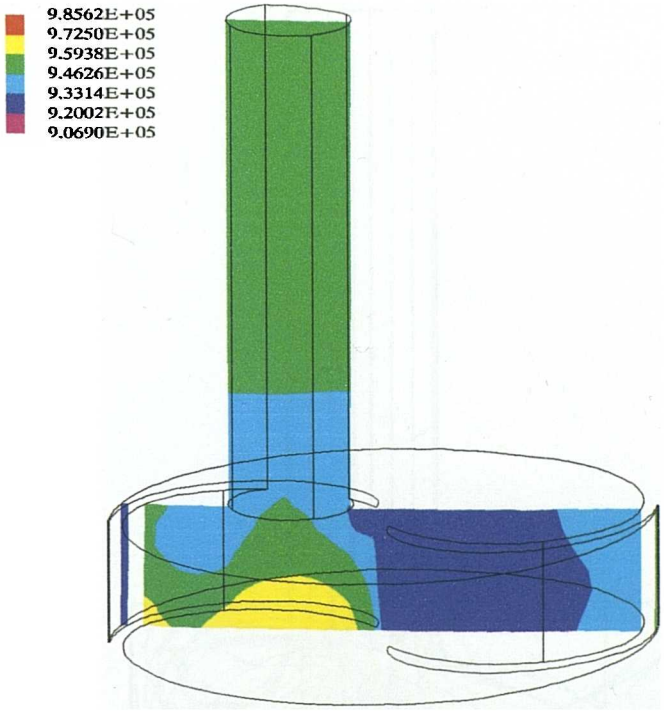

Figure 5.48 Scroll-Expander. Rotational speed 3000 RPM, Pressure contours, Arbitrary plane, step=200, 100 degrees (5.54m sec) after suction commences

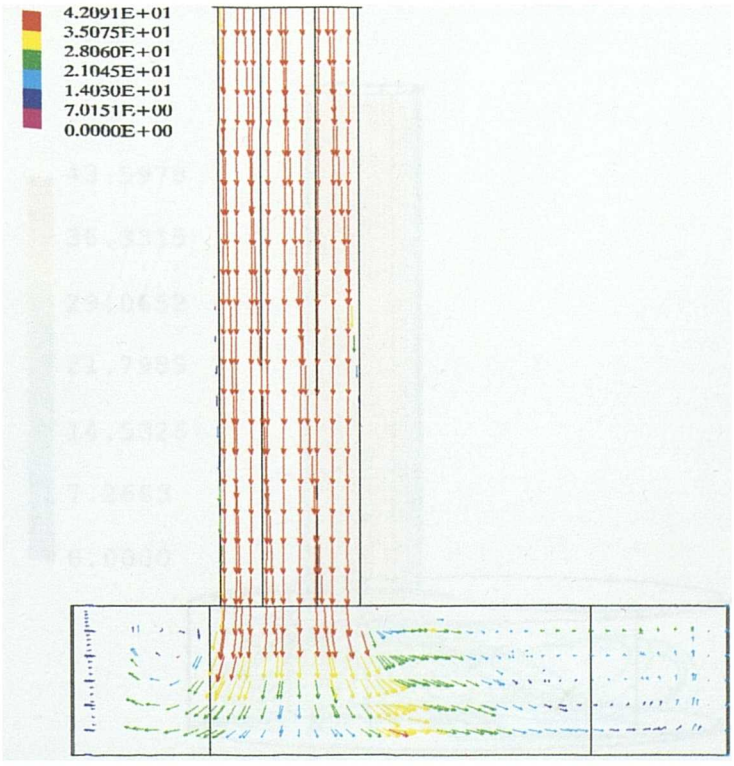

Figure 5.49 Scroll-Expander. Rotational speed 3000 RPM, Speed vectors, Arbitrary plane, step=200, 100 degrees (5.54m sec) after suction commences

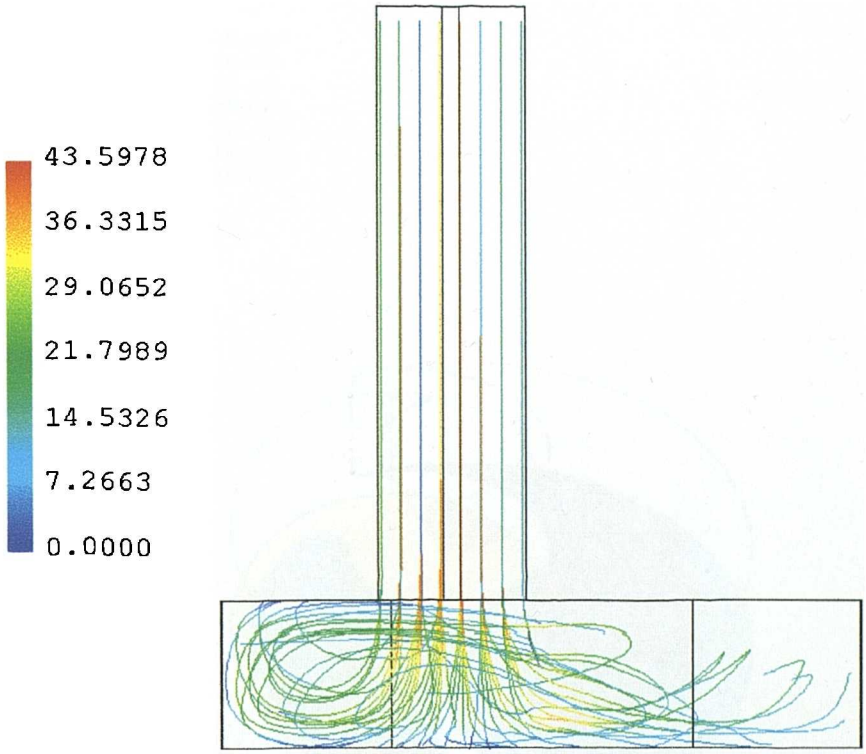

Figure 5.50 Scroll-Expander. Rotational speed 3000 RPM, Stream lines step=200, 100 degrees (5.54m sec) after suction commences

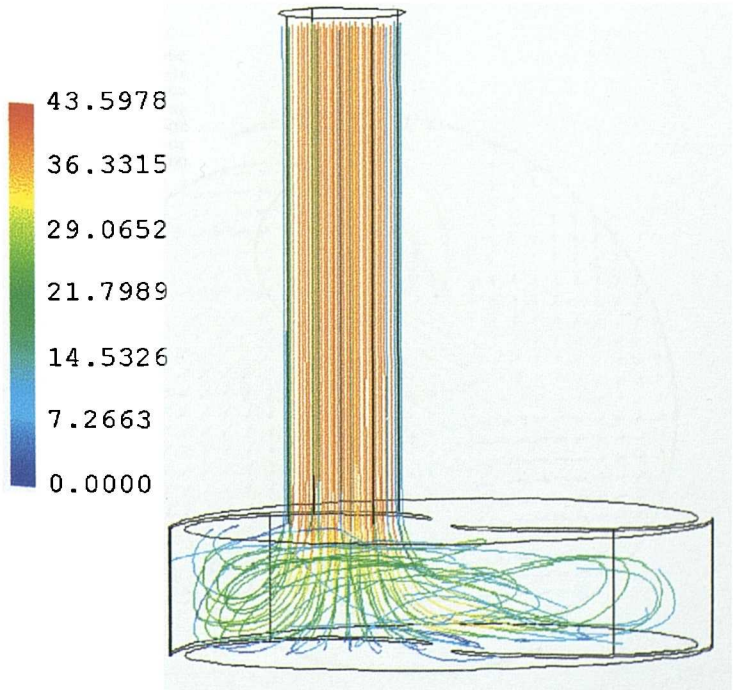

Figure 5.51 Scroll-Expander. Rotational speed 3000 RPM, Stream lines, step=200, 100 degrees (5.54m sec) after suction commences

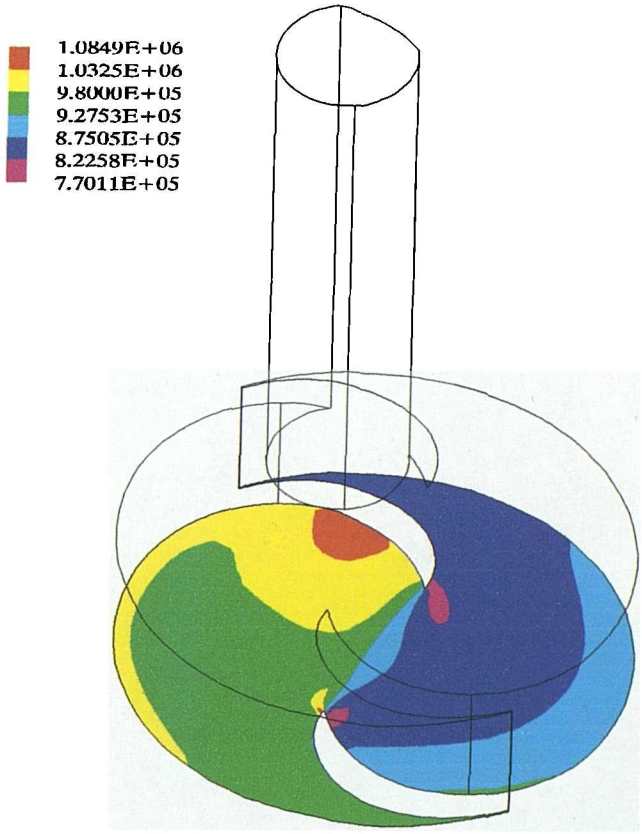

Figure 5.52 Scroll-Expander. Rotational speed 6000 RPM, Pressure contours, Z-plane =-0.2, step=100, 50 degrees (1.389m sec) after suction commences

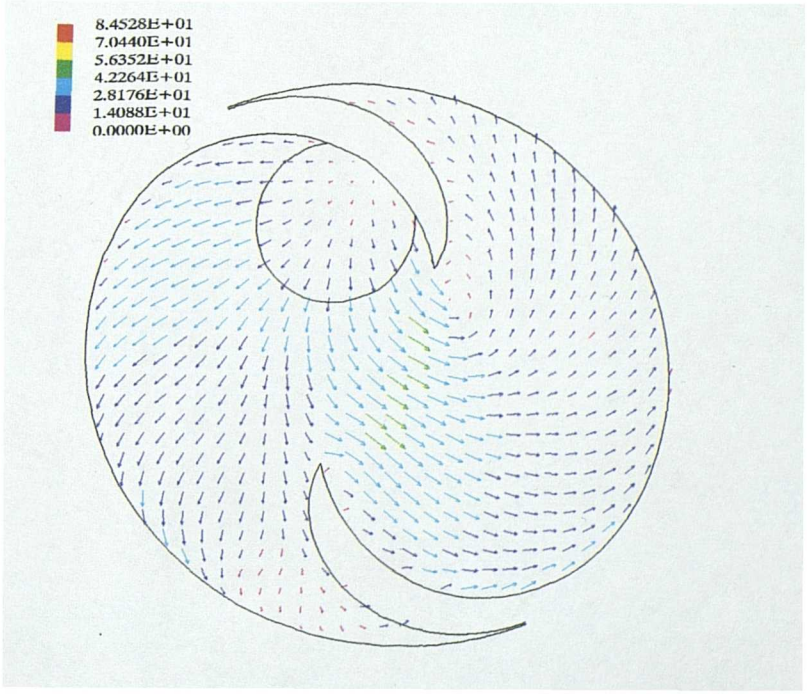

Figure 5.53 Scroll-Expander. Rotational speed 6000 RPM, Speed vectors, Z-plane =-0.018, step=100, 50 degrees (1.389m sec) after suction commences

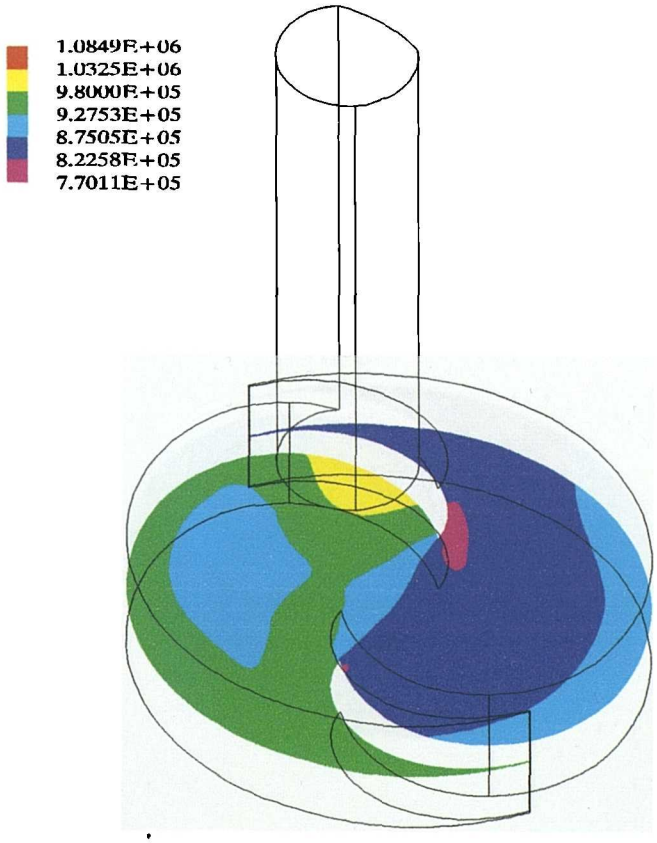

Figure 5.54 Scroll-Expander. Rotational speed 6000 RPM, Pressure contours, Z-plane =-0.1, step=100, 50 degrees (1.389m sec) after suction commences

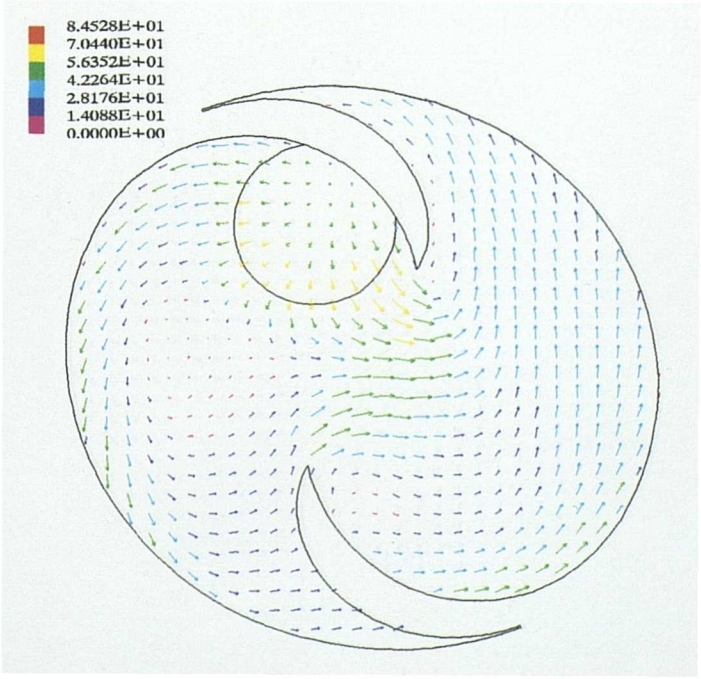

Figure 5.55 Scroll-Expander. Rotational speed 6000 RPM, Speed vectors, Z-plane =-0.1, step=100, 50 degrees (1.389m sec) after suction commences

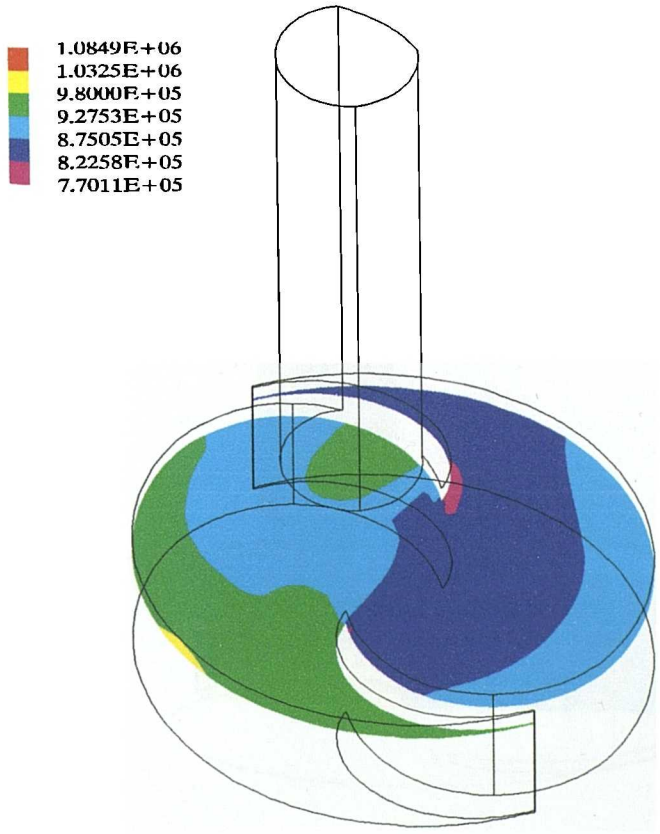

Figure 5.56 Scroll-Expander. Rotational speed 6000 RPM, Pressure contours, Z-plane =-0.0025, step=100, 50 degrees (1.389m sec) after suction commences

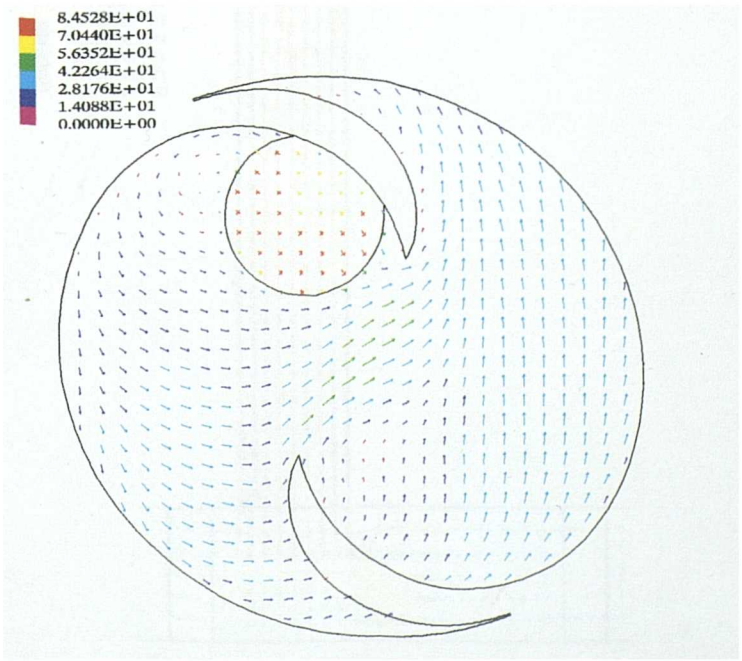

Figure 5.57 Scroll-Expander. Rotational speed 6000 RPM, Speed vectors, Z-plane =-0.0025, step=100, 50 degrees (1.389m sec) after suction commences

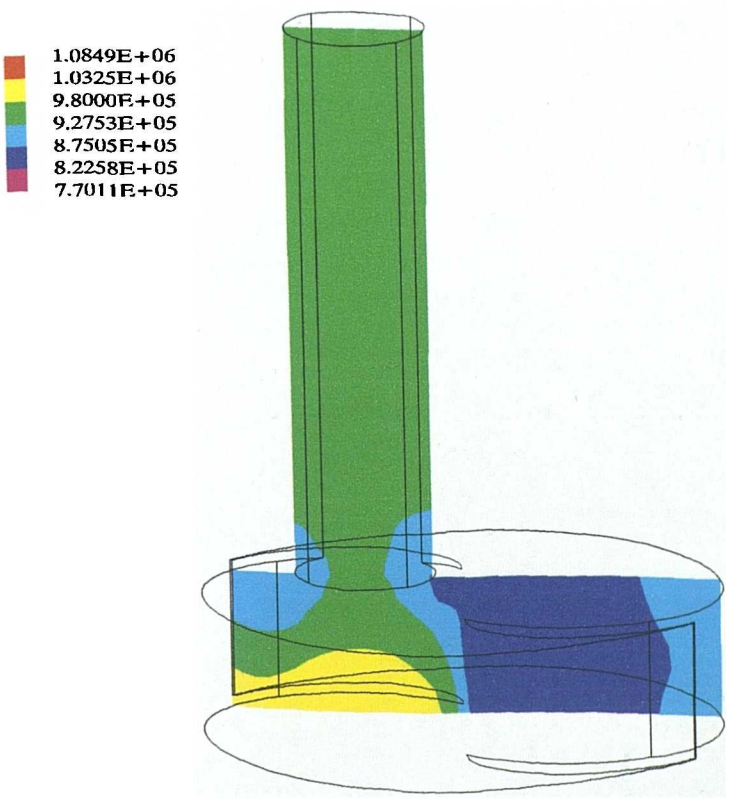

Figure 5.58 Scroll-Expander. Rotational speed 6000 RPM, Pressure contours, Arbitrary plane, step=100, 50 degrees (1.389m sec) after suction commences

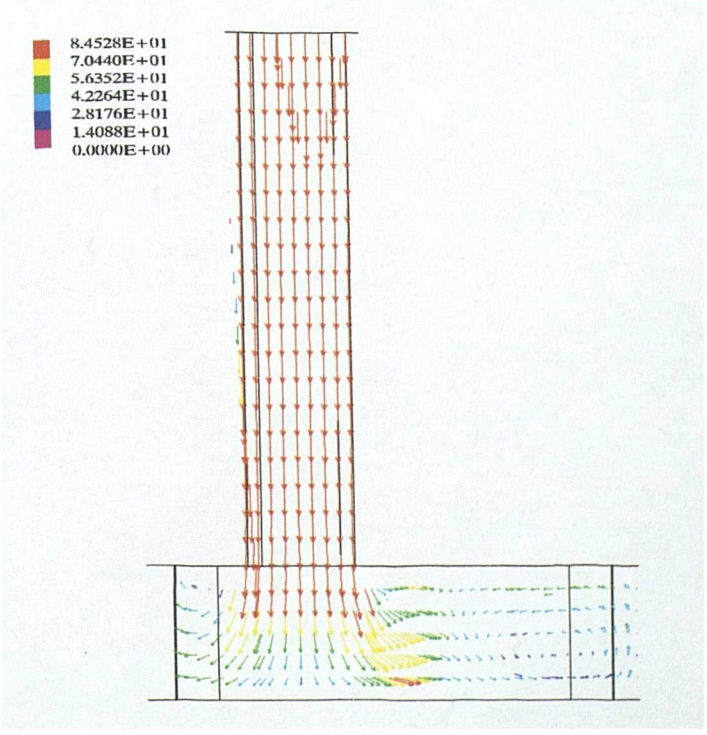

Figure 5.59 Scroll-Expander. Rotational speed 6000 RPM, Speed vectors, Arbitrary plane, step=100, 50 degrees (1.389m sec) after suction commences

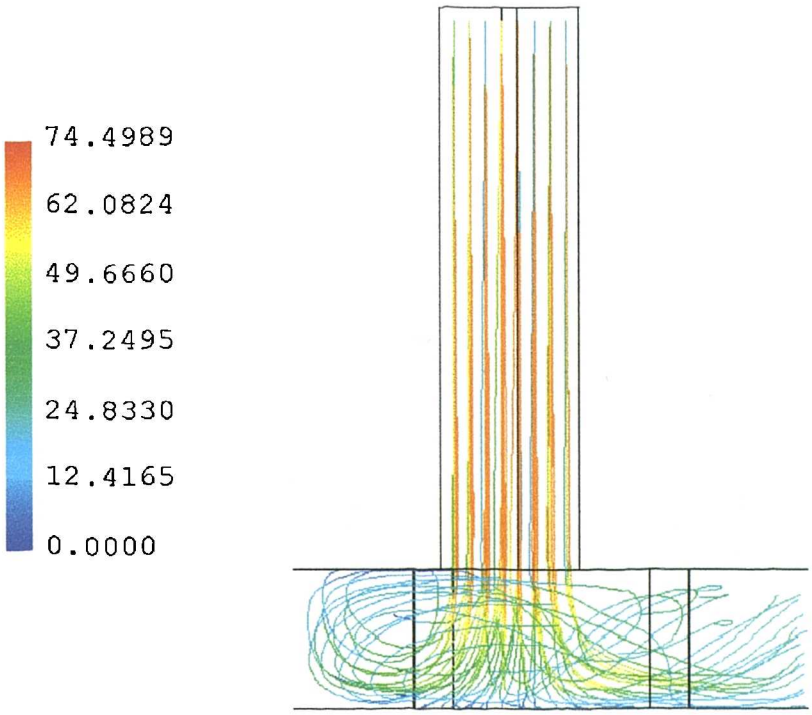

Figure 5.60 Scroll-Expander. Rotational speed 6000 RPM, Stream lines step=100, 50 degrees (1.389m sec) after suction commences

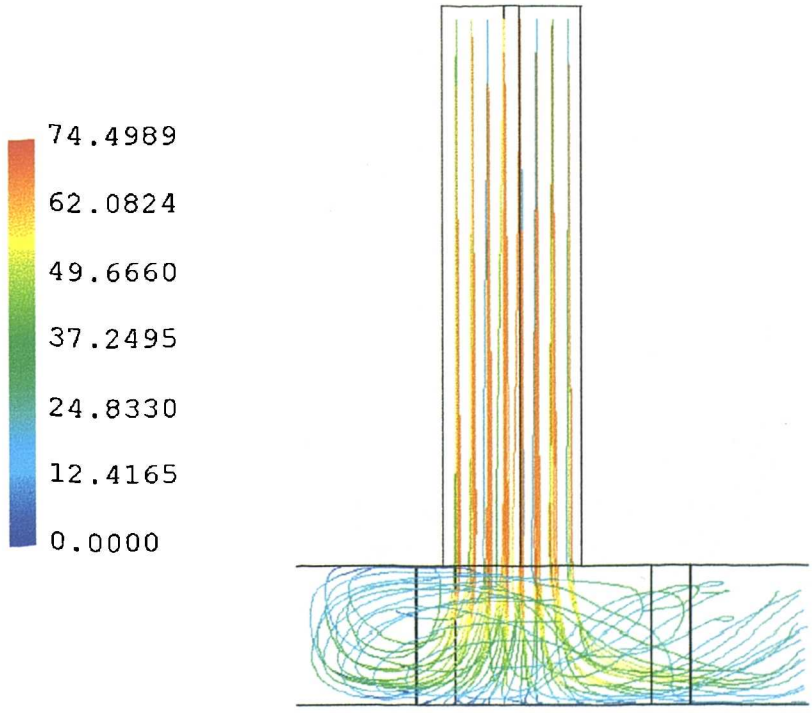

Figure 5.61 Scroll-Expander. Rotational speed 6000 RPM, Stream lines, step=100, 50 degrees (1.389m sec) after suction commences

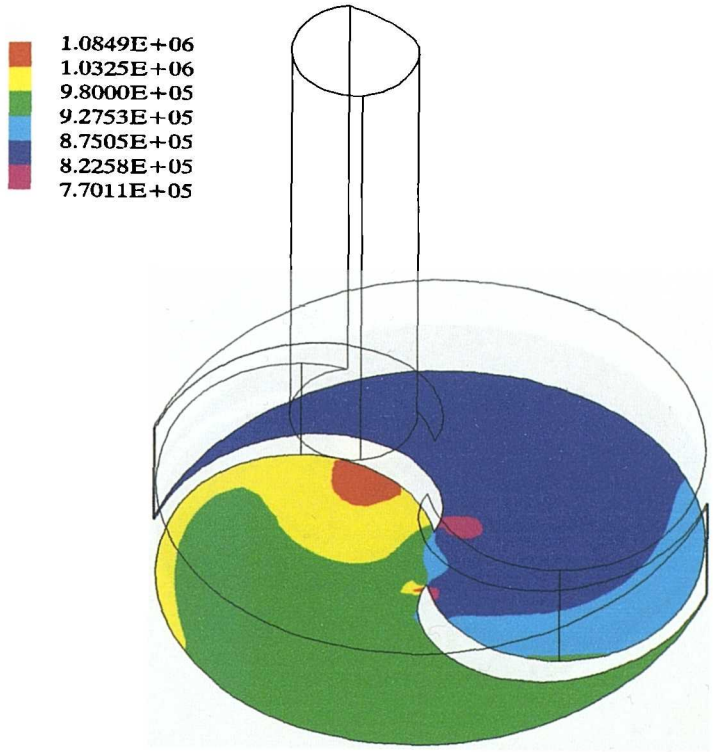

Figure 5.62 Scroll-Expander. Rotational speed 6000 RPM, Pressure contours, Z-plane =-0.2, step=200, 100 degrees (2.778m sec) after suction commences

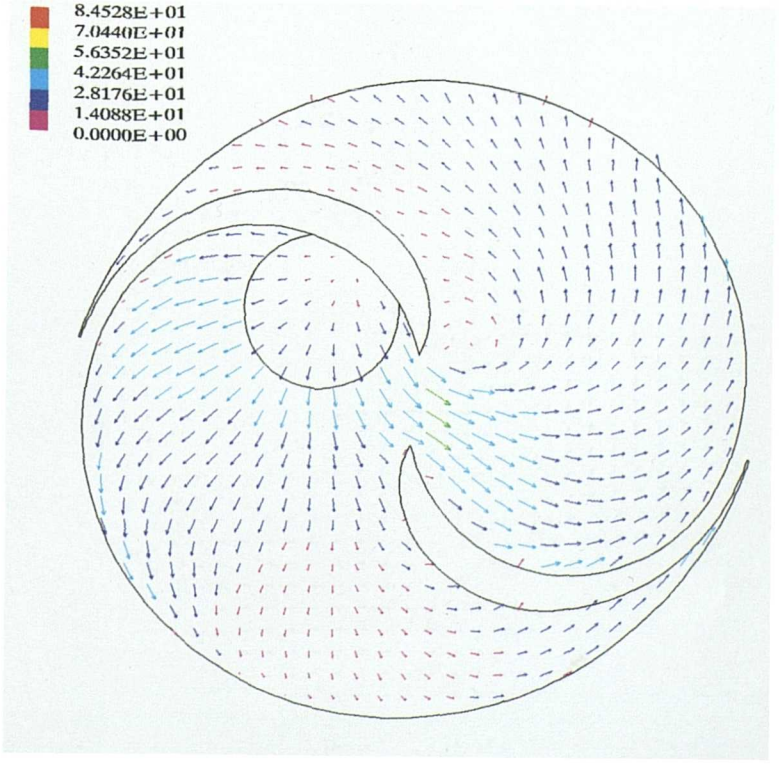

Figure 5.63 Scroll-Expander. Rotational speed 6000 RPM, Speed vectors, Z-plane =-0.018, step=200, 100 degrees (2.778m sec) after suction commences

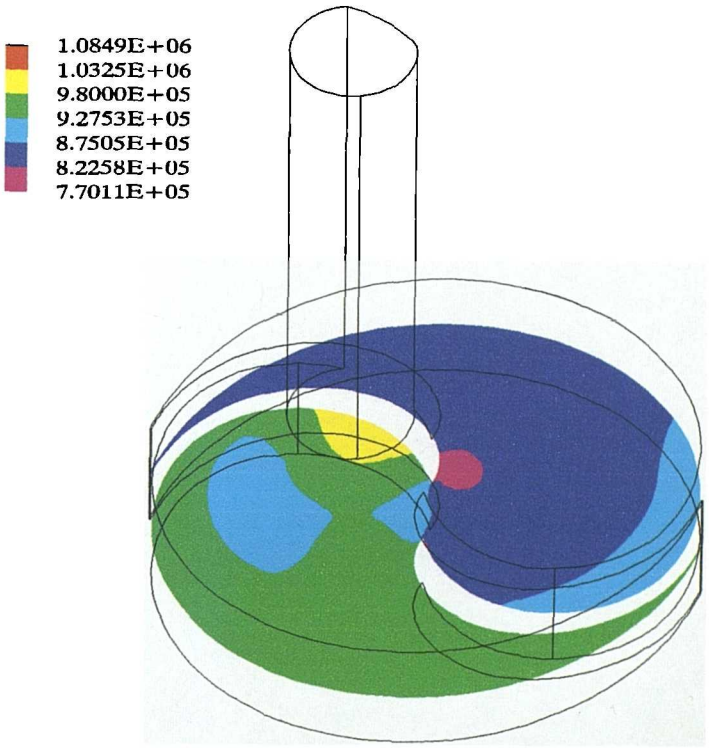

Figure 5.64 Scroll-Expander. Rotational speed 6000 RPM, Pressure contours, Z-plane =-0.1, step=200, 100 degrees (2.778m sec) after suction commences

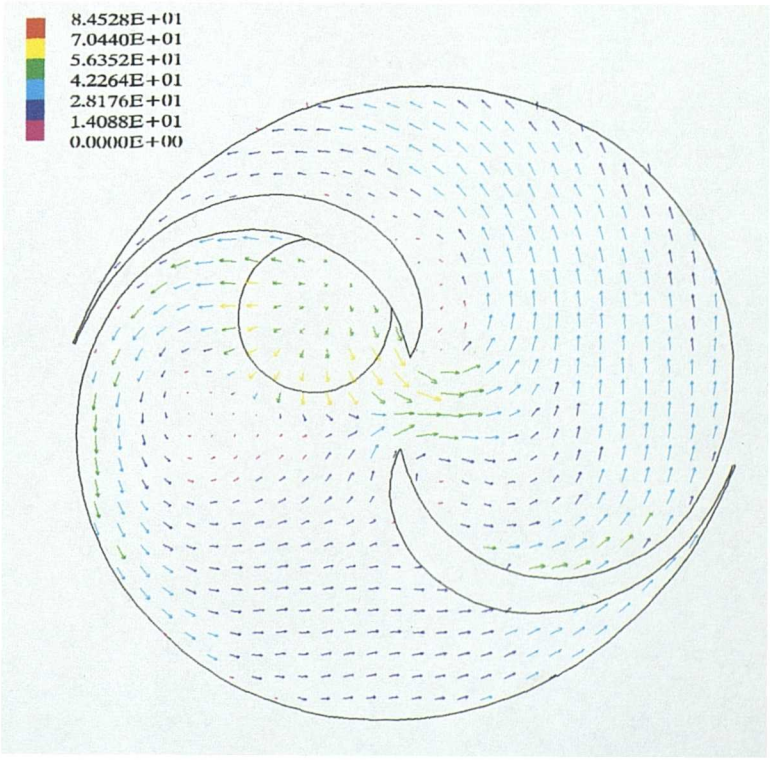

Figure 5.65 Scroll-Expander. Rotational speed 6000 RPM, Speed vectors, Z-plane =-0.1, step=200, 100 degrees (2.778m sec) after suction commences

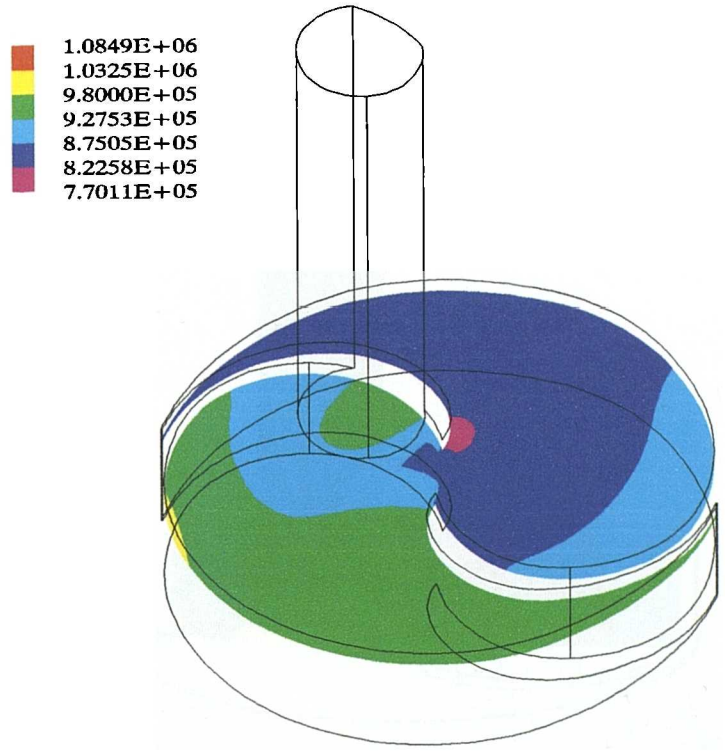

Figure 5.66 Scroll-Expander. Rotational speed 6000 RPM, Pressure contours, Z-plane =-0.0025, step=200, 100 degrees (2.778m sec) after suction commences

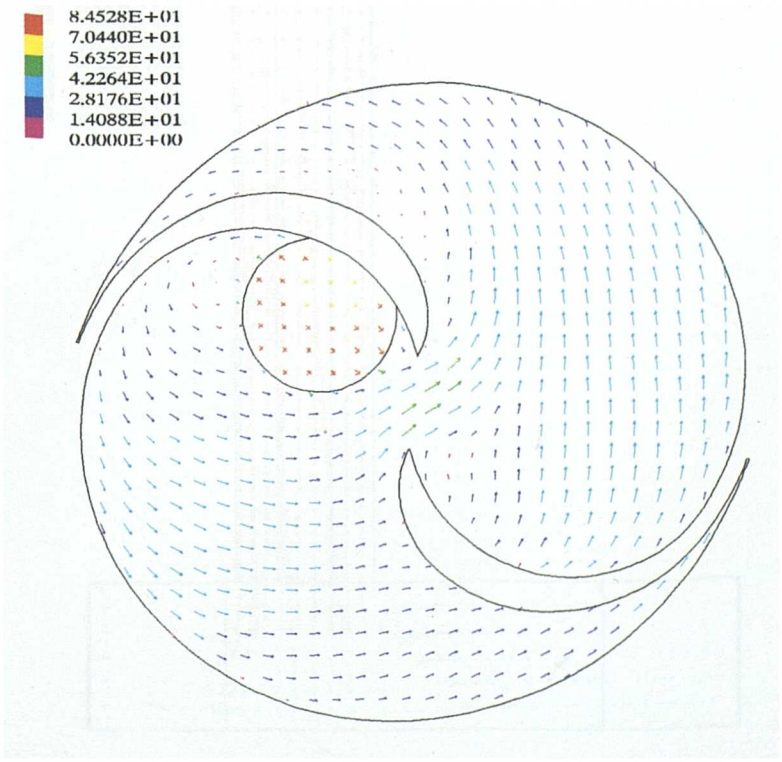

Figure 5.67 Scroll-Expander. Rotational speed 6000 RPM, Speed vectors, Z-plane =-0.0025, step=200, 100 degrees (2.778m sec) after suction commences

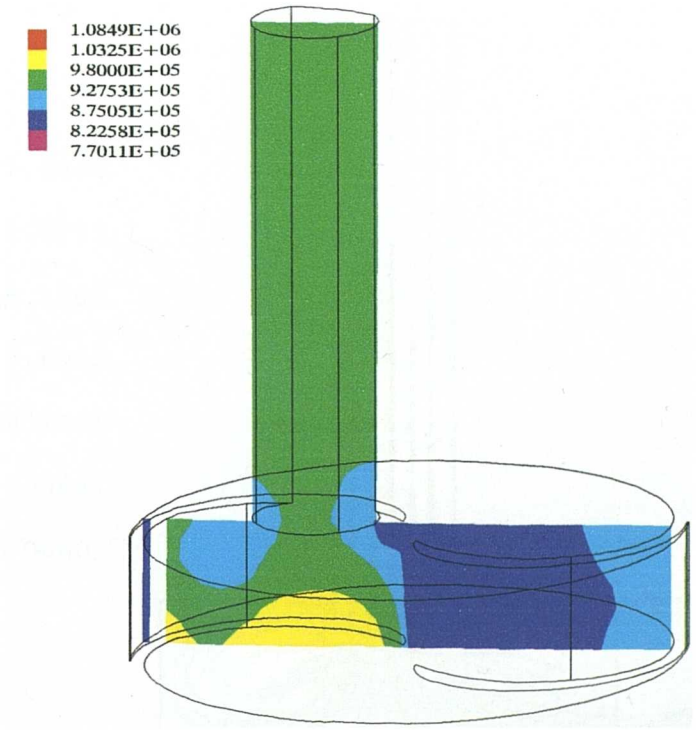

Figure 5.68 Scroll-Expander. Rotational speed 6000 RPM, Pressure contours, Arbitrary plane, step=200, 100 degrees (2.778m sec) after suction commences

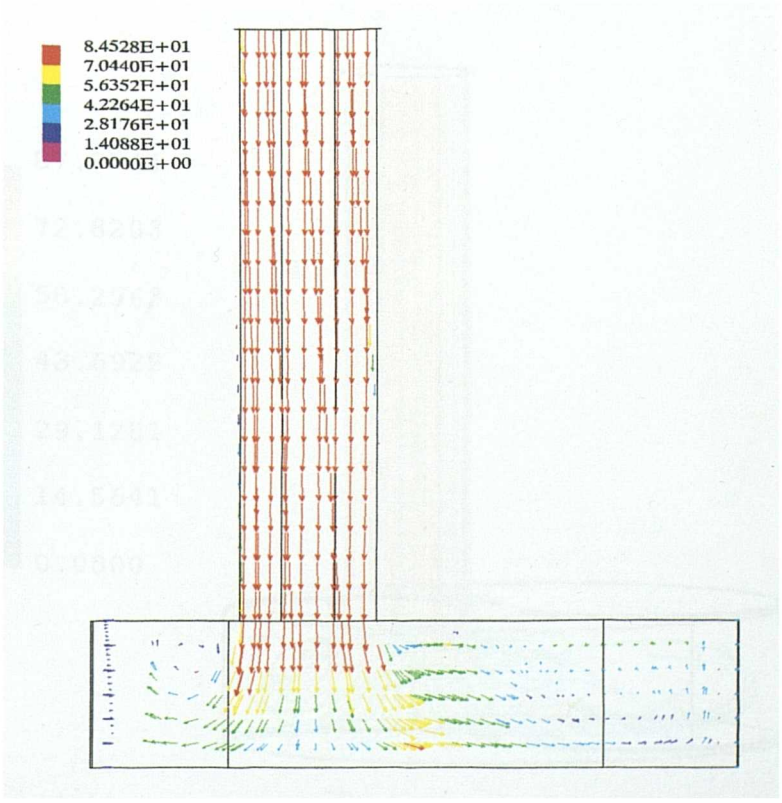

Figure 5.69 Scroll-Expander. Rotational speed 6000 RPM, Speed vectors, Arbitrary plane, step=200, 100 degrees (2.778m sec) after suction commences

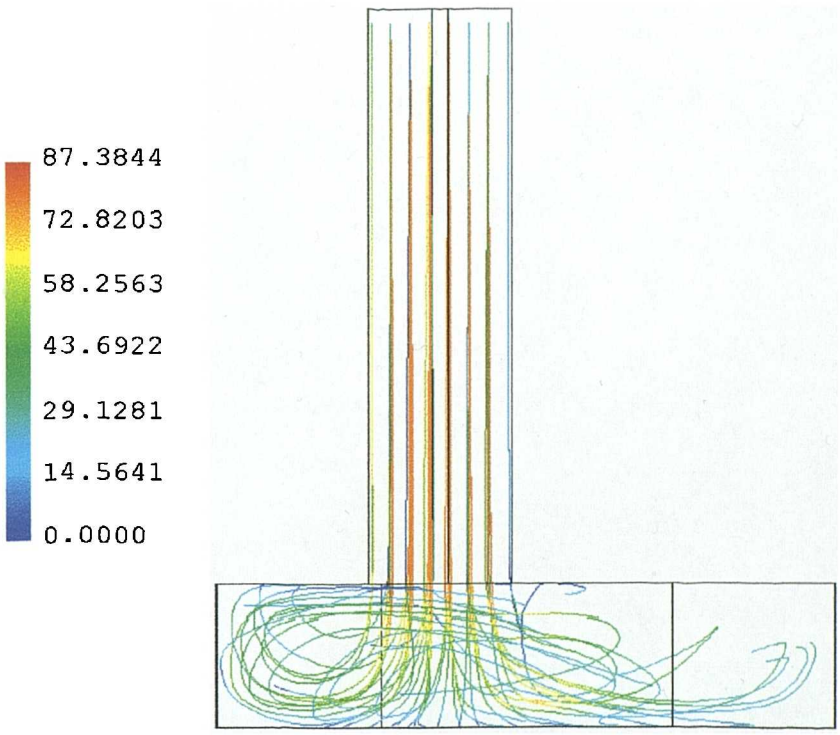

Figure 5.70 Scroll-Expander. Rotational speed 6000 RPM, Stream lines step=200, 100 degrees (2.778m sec) after suction commences

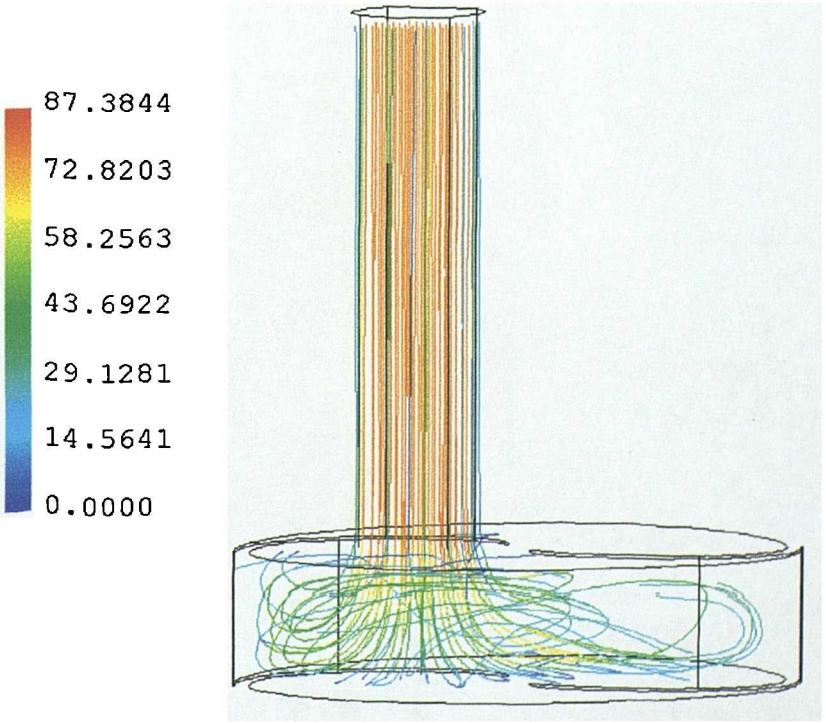

Figure 5.71 Scroll-Expander. Rotational speed 6000 RPM, Stream lines, step=200, 100 degrees (2.778m sec) after suction commences

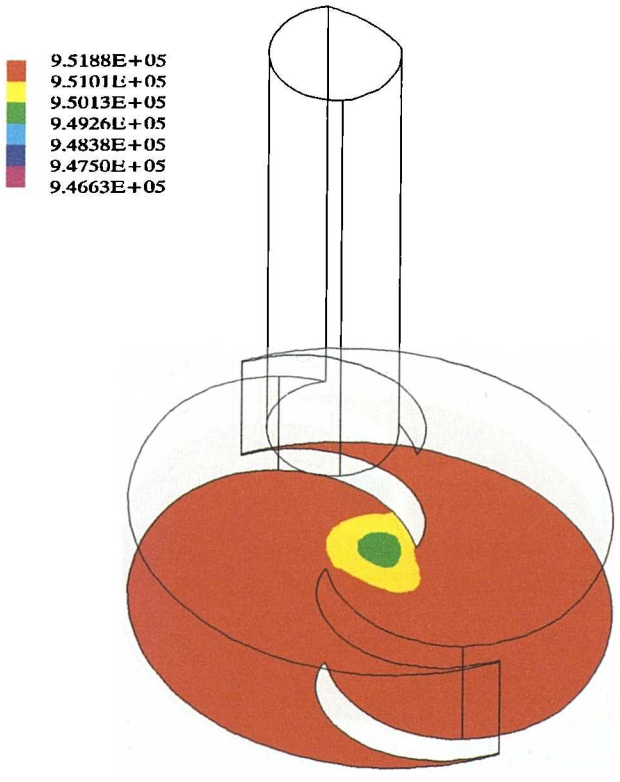

Figure 5.72 Scroll-Compressor. Rotational speed 1000 RPM, Pressure contours, Z-plane =-0.2, step=100, 50 degrees (8.333m sec) after discharge commences

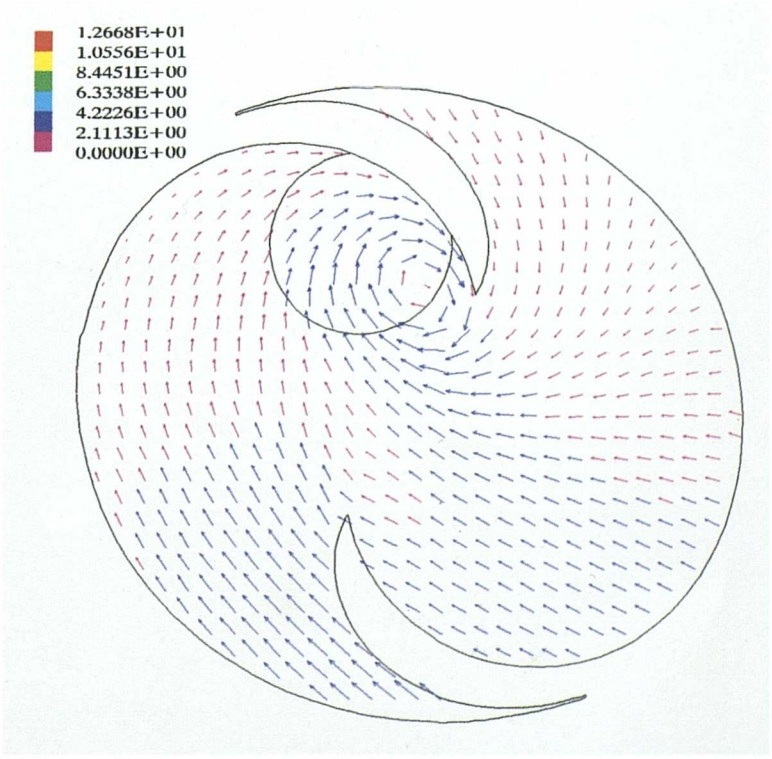

Figure 5.73 Scroll-Compressor. Rotational speed 1000 RPM, Speed vectors, Z-plane =-0.018, step=100, 50 degrees (8.333m sec) after discharge commences

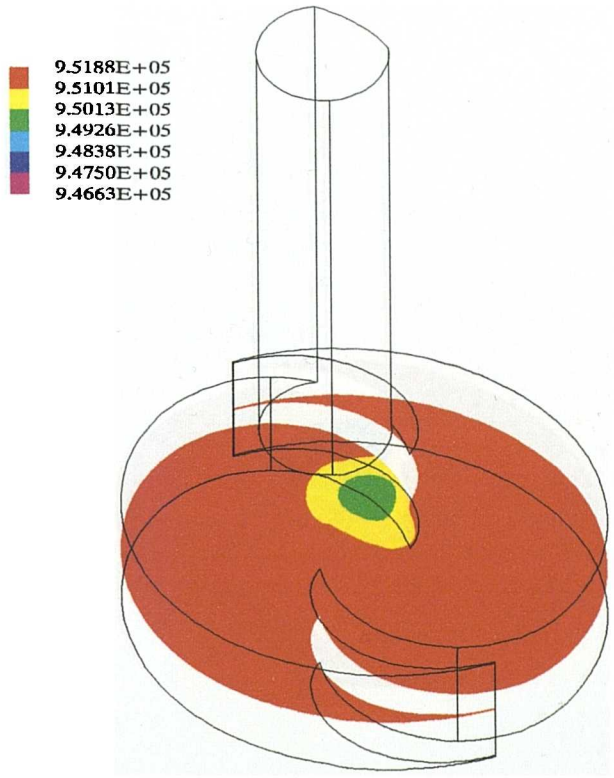

Figure 5.74 Scroll-Compressor. Rotational speed 1000 RPM, Pressure contours, Z-plane =-0.1, step=100, 50 degrees (8.333m sec) after discharge commences

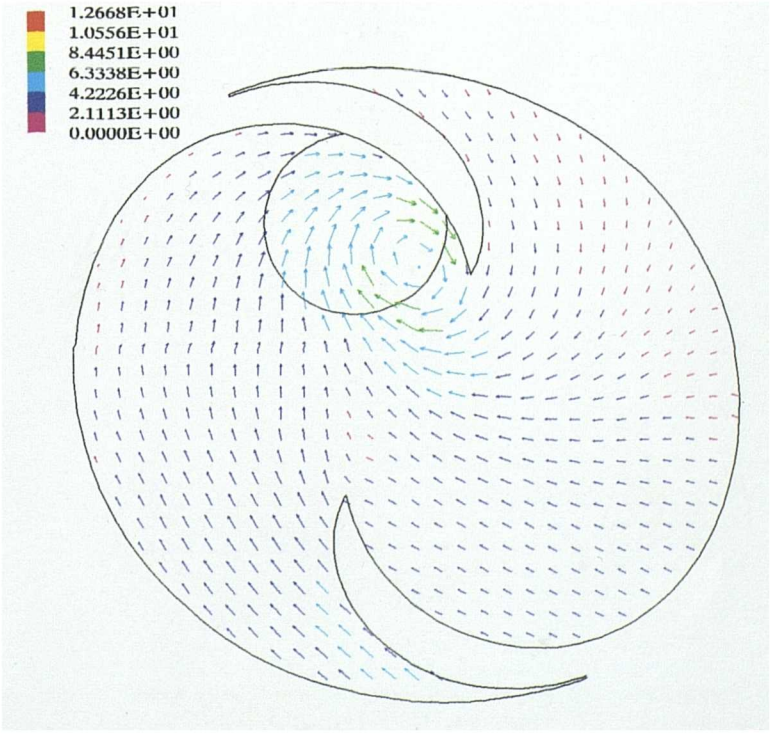

Figure 5.75 Scroll-Compressor. Rotational speed 1000 RPM, Speed vectors, Z-plane =-0.1, step=100, 50 degrees (8.333m sec) after discharge commences

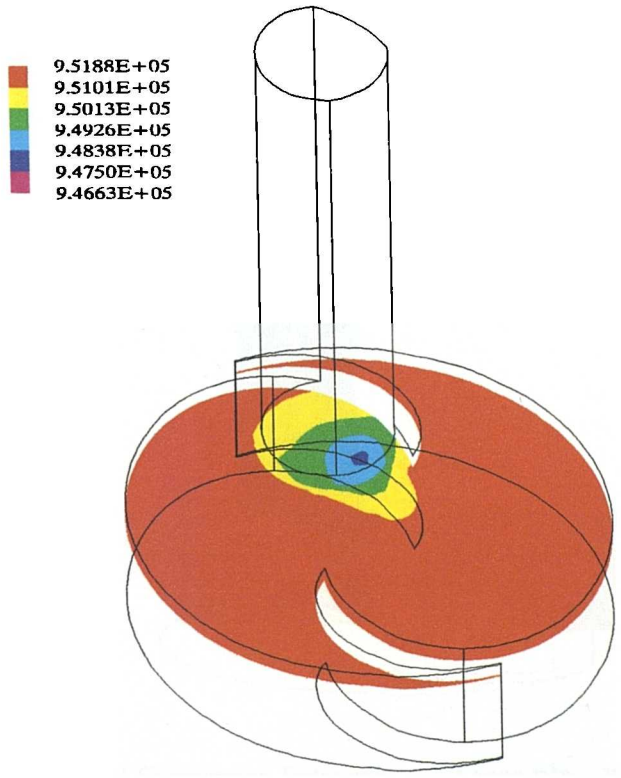

Figure 5.76 Scroll-Compressor. Rotational speed 1000 RPM, Pressure contours, Z-plane =-0.0025, step=100, 50 degrees (8.333m sec) after discharge commences

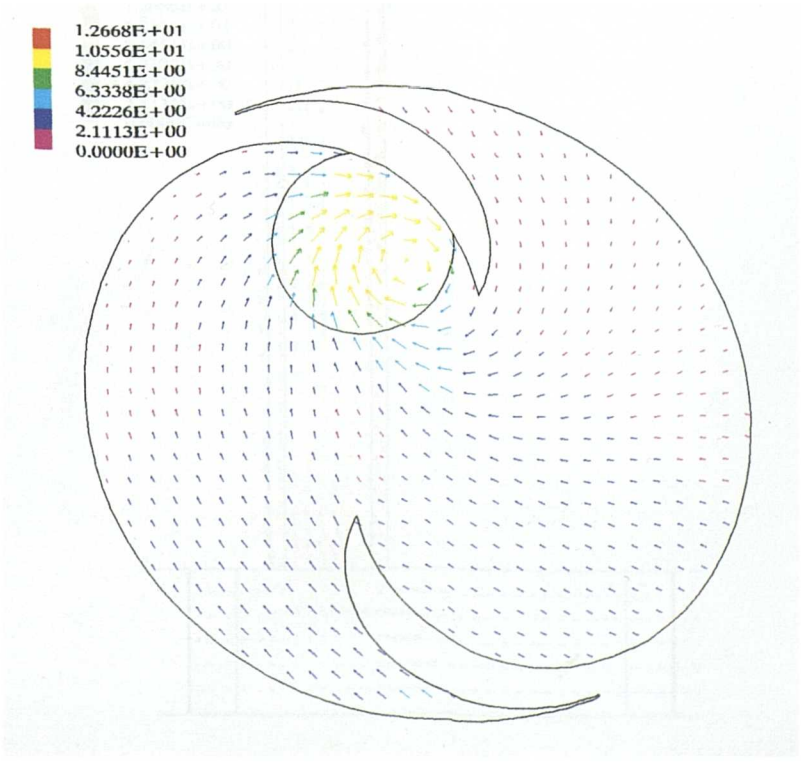

Figure 5.77 Scroll-Compressor. Rotational speed 1000 RPM, Speed vectors, Z-plane =-0.0025, step=100, 50 degrees (8.333m sec) after discharge commences

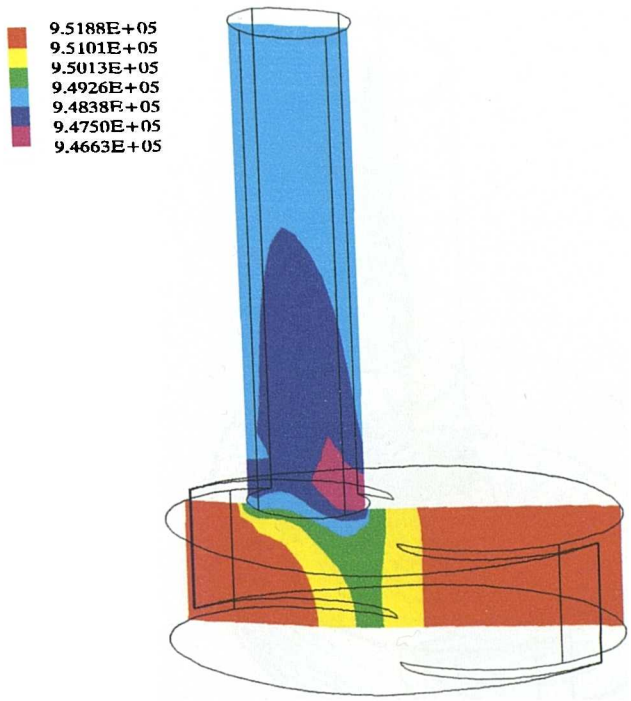

Figure 5.78 Scroll-Compressor. Rotational speed 1000 RPM, Pressure contours, Arbitrary plane, step=100, 50 degrees (8.333m sec) after discharge commences

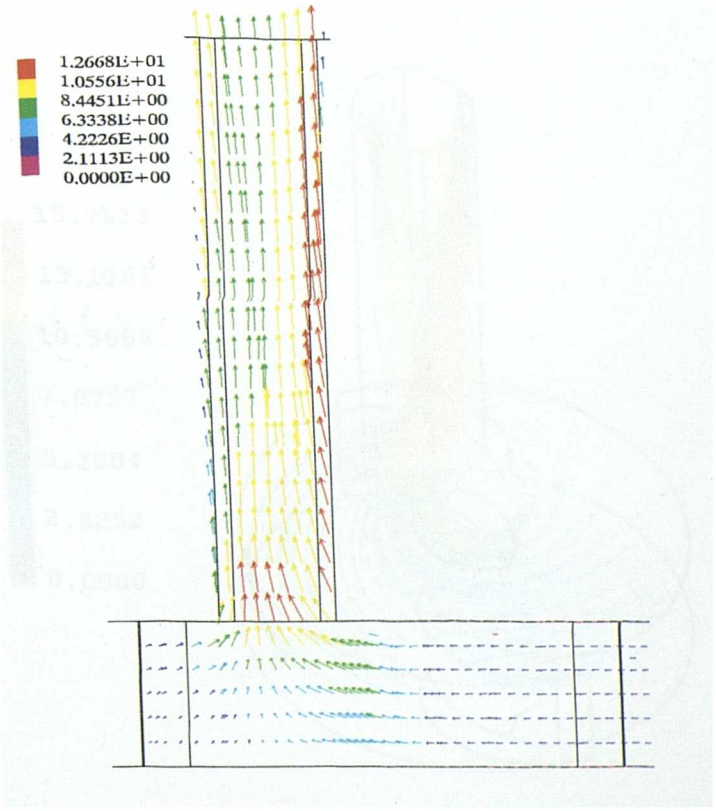

Figure 5.79 Scroll-Compressor. Rotational speed 1000 RPM, Speed vectors, Arbitrary plane, step=100, 50 degrees (8.333m sec) after discharge commences

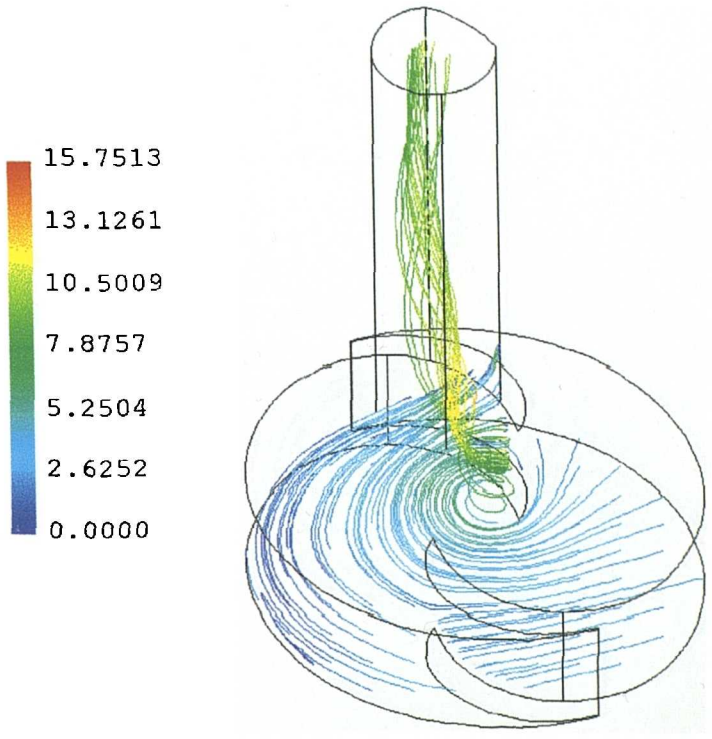

Figure 5.80 Scroll-Compressor. Rotational speed 1000 RPM, Stream lines step=100, 50 degrees (8.333m sec) after discharge commences

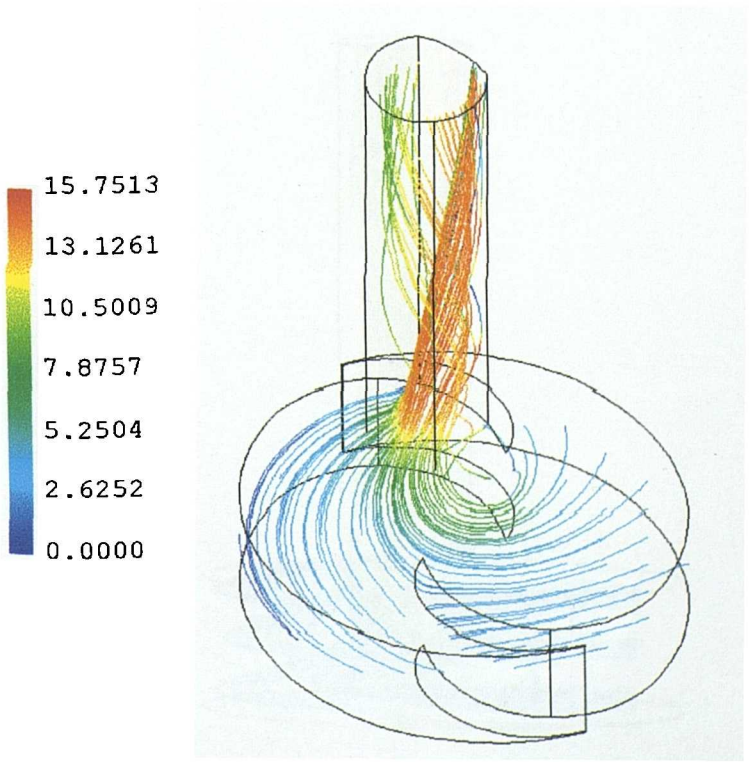

Figure 5.81 Scroll-Compressor. Rotational speed 1000 RPM, Stream lines, step=100, 50 degrees (8.333m sec) after discharge commences

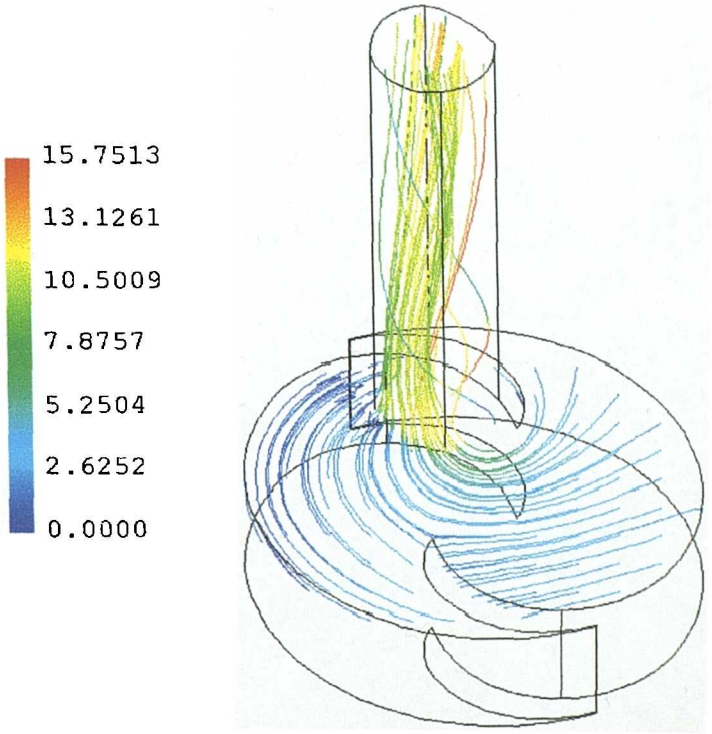

Figure 5.82 Scroll-Compressor. Rotational speed 1000 RPM, Stream lines step=100, 50 degrees (8.333m sec) after discharge commences

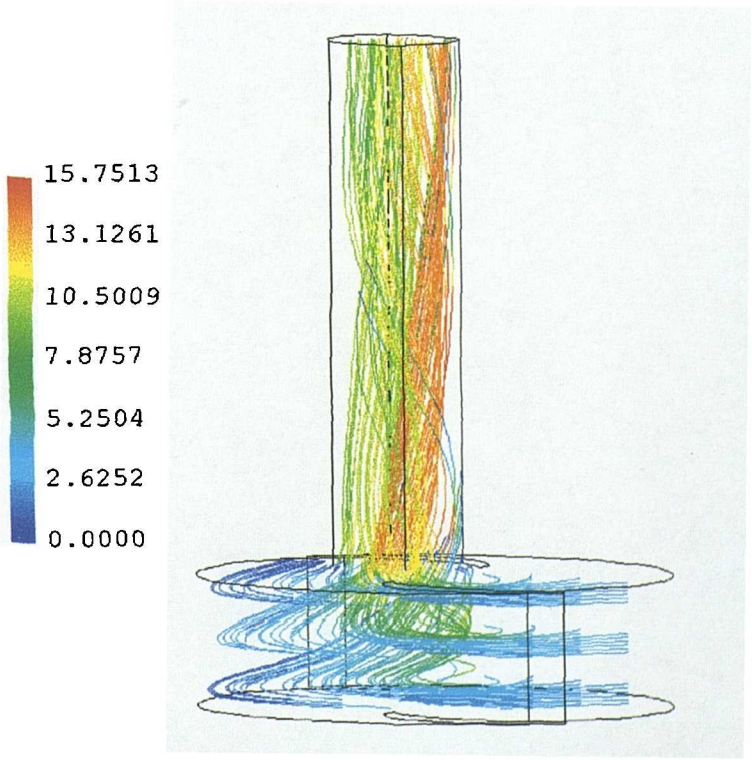

Figure 5.83 Scroll-Compressor. Rotational speed 1000 RPM, Stream lines, step=100, 50 degrees (8.333m sec) after discharge commences

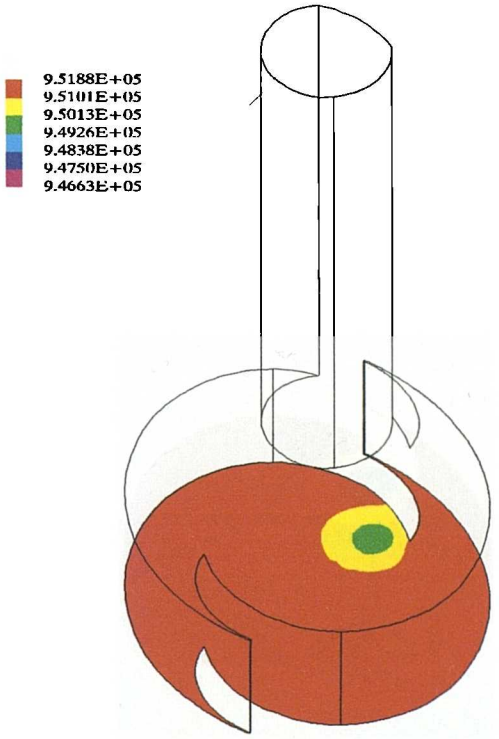

Figure 5.84 Scroll-Compressor. Rotational speed 1000 RPM, Pressure contours, Z-plane =-0.2, step=200, 100 degrees (16.66m sec) after discharge commences

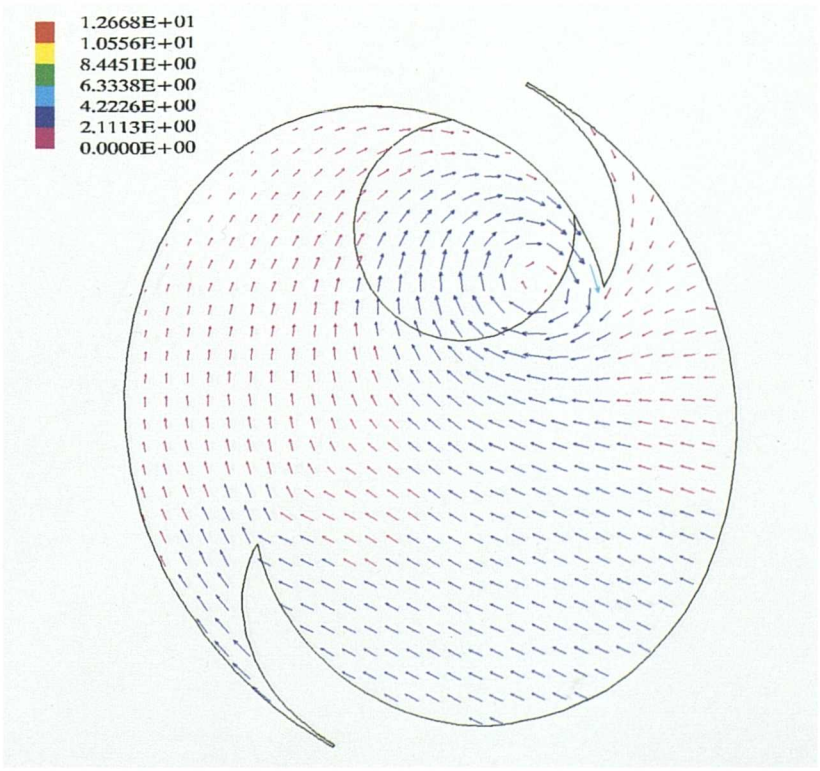

Figure 5.85 Scroll-Compressor. Rotational speed 1000 RPM, Speed vectors, Z-plane =-0.018, step=200, 100 degrees (16.66m sec) after discharge commences

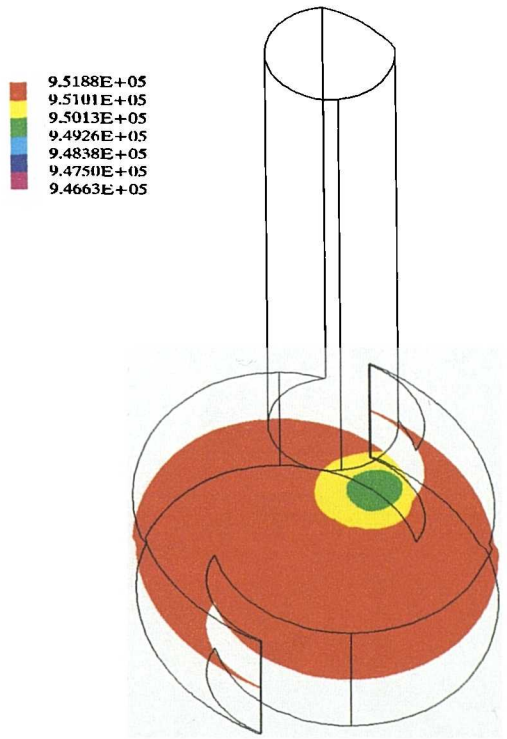

Figure 5.86 Scroll-Compressor. Rotational speed 1000 RPM, Pressure contours, Z-plane =-0.1, step=200, 100 degrees (16.66m sec) after discharge commences

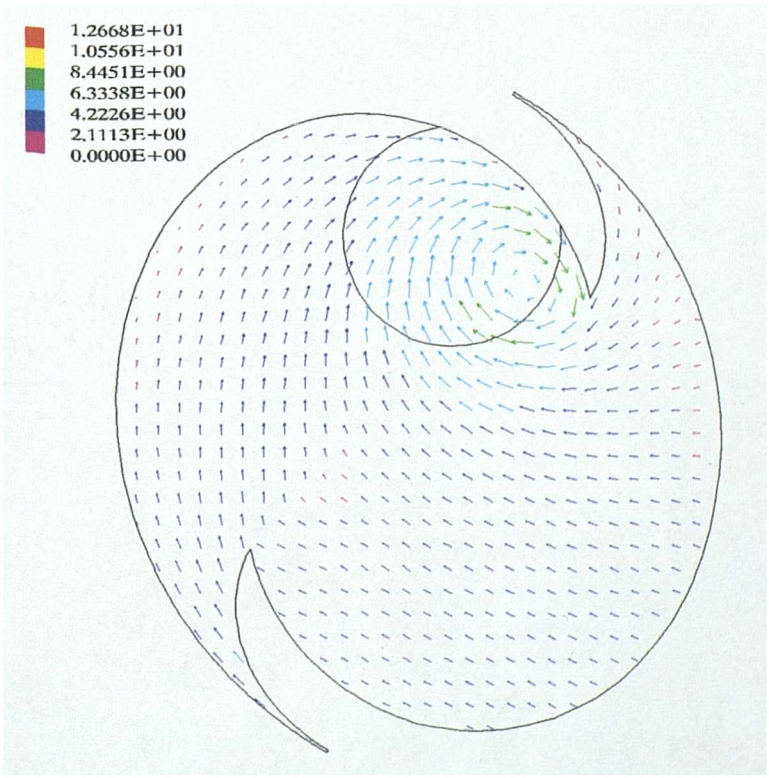

Figure 5.87 Scroll-Compressor. Rotational speed 1000 RPM, Speed vectors, Z-plane =-0.1, step=200, 100 degrees (16.66m sec) after discharge commences

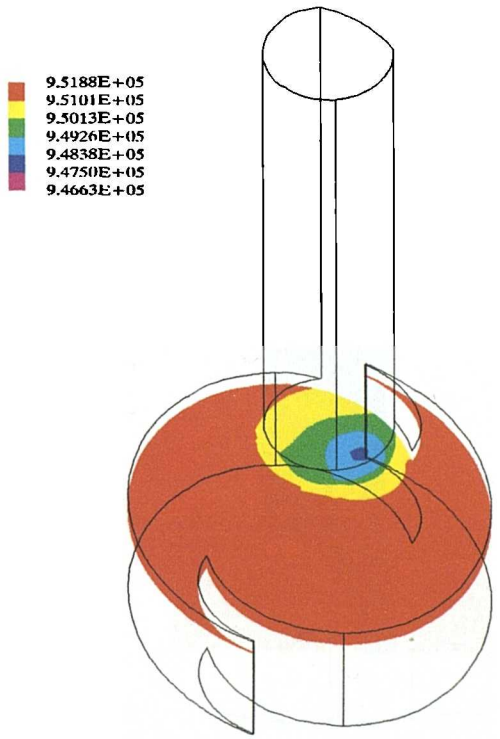

Figure 5.88 Scroll-Compressor. Rotational speed 1000 RPM, Pressure contours, Z-plane =-0.0025, step=200, 100 degrees (16.66m sec) after discharge commences

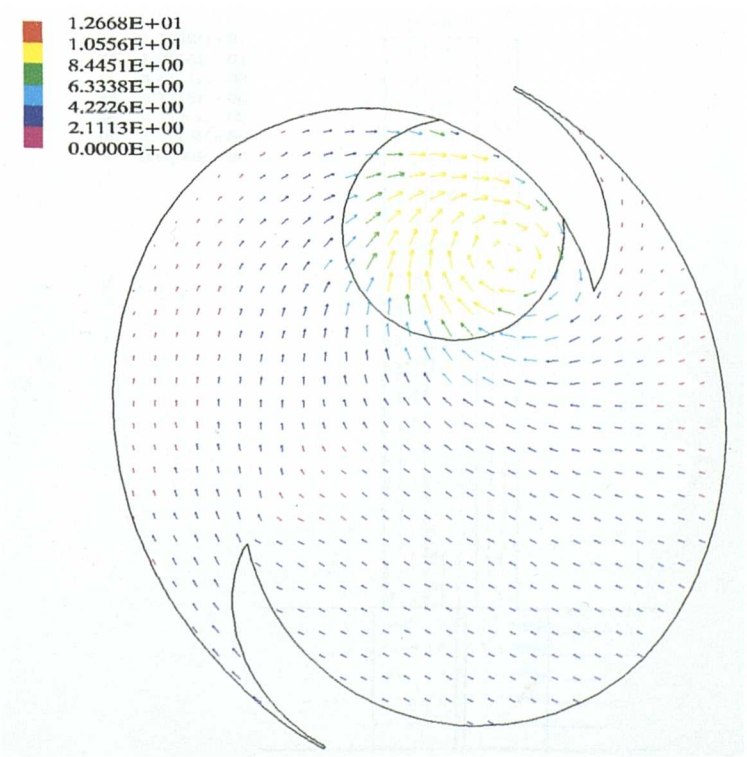

Figure 5.89 Scroll-Compressor. Rotational speed 1000 RPM, Speed vectors, Z-plane =-0.0025, step=200, 100 degrees (16.66m sec) after discharge commences

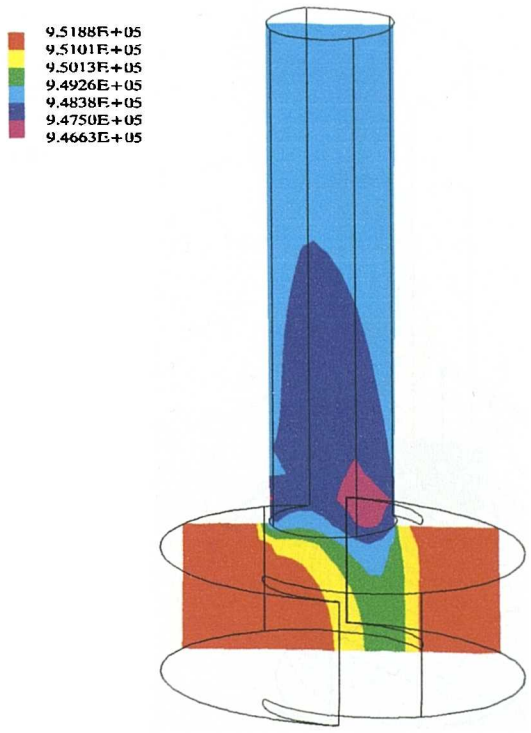

Figure 5.90 Scroll-Compressor. Rotational speed 1000 RPM, Pressure contours, Arbitrary plane, step=200, 100 degrees (16.66m sec) after discharge commences

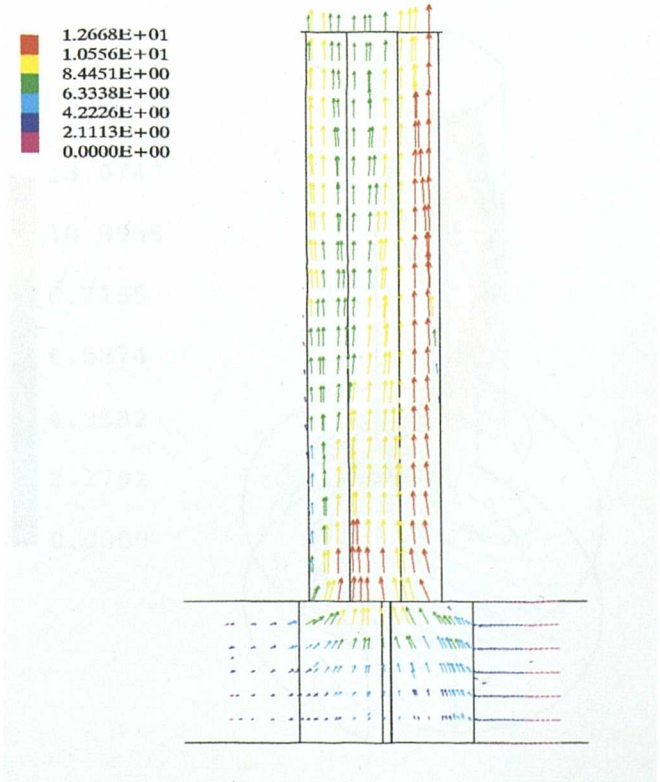

Figure 5.91 Scroll-Compressor. Rotational speed 1000 RPM, Speed vectors, Arbitrary plane, step=200, 100 degrees (16.66m sec) after discharge commences

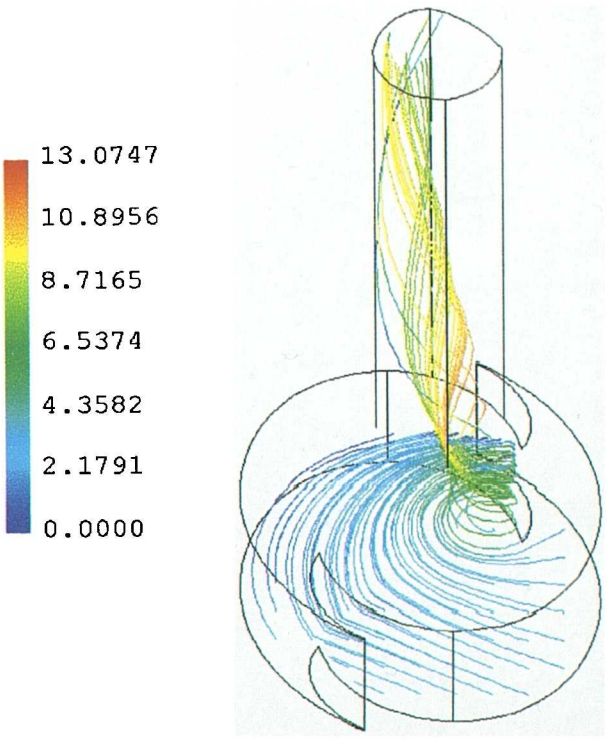

Figure 5.92 Scroll-Compressor. Rotational speed 1000 RPM, Stream lines step=200, 100 degrees (16.66m sec) after discharge commences

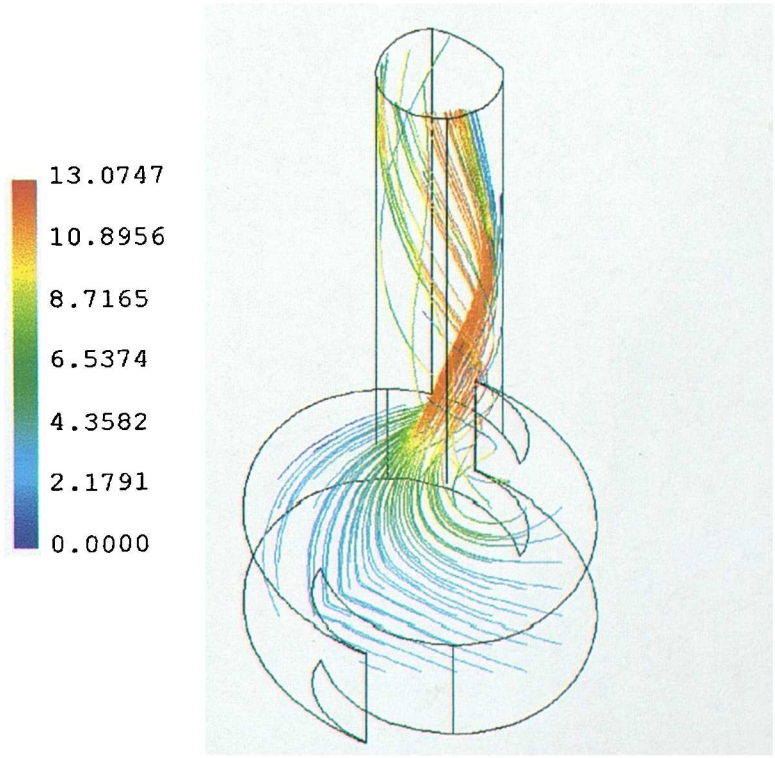

Figure 5.93 Scroll-Compressor. Rotational speed 1000 RPM, Stream lines, step=200, 100 degrees (16.66m sec) after discharge commences

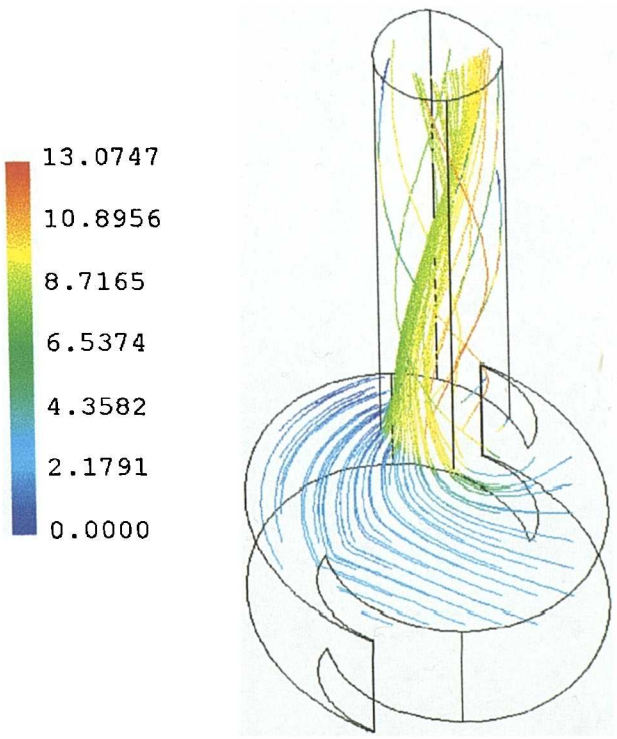

Figure 5.94 Scroll-Compressor. Rotational speed 1000 RPM, Stream lines step=200, 100 degrees (16.66m sec) after discharge commences

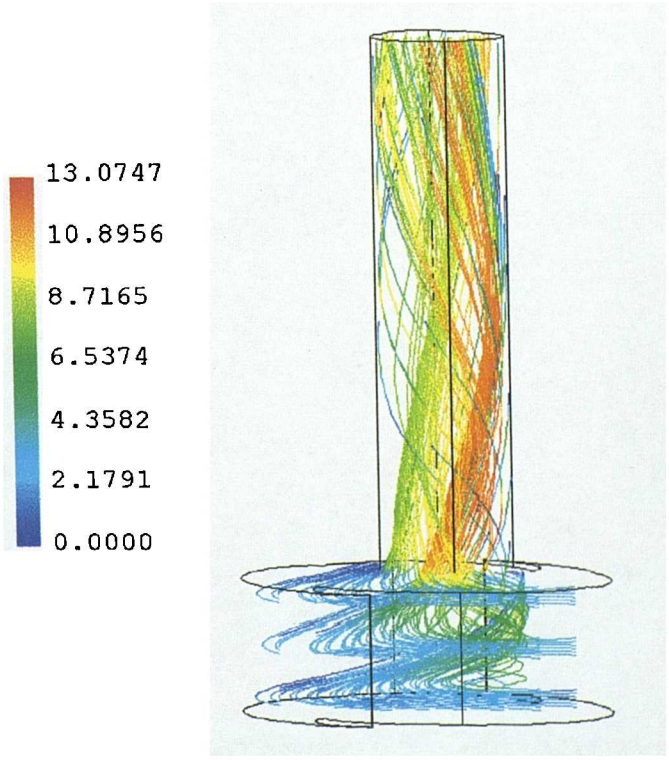

Figure 5.95 Scroll-Compressor. Rotational speed 1000 RPM, Stream lines, step=200, 100 degrees (16.66m sec) after discharge commences

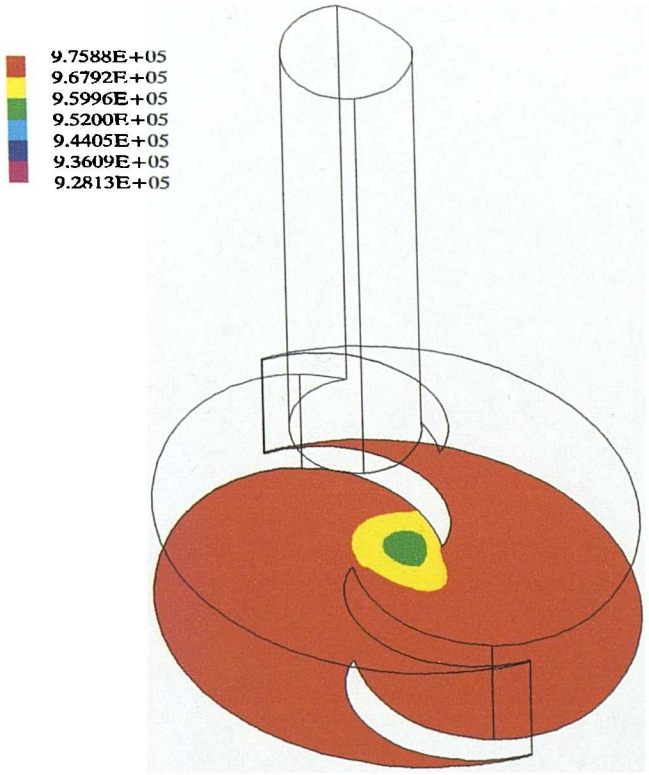

Figure 5.96 Scroll-Compressor. Rotational speed 3000 RPM, Pressure contours, Z-plane =-0.2, step=100, 50 degrees (2.777m sec) after discharge commences

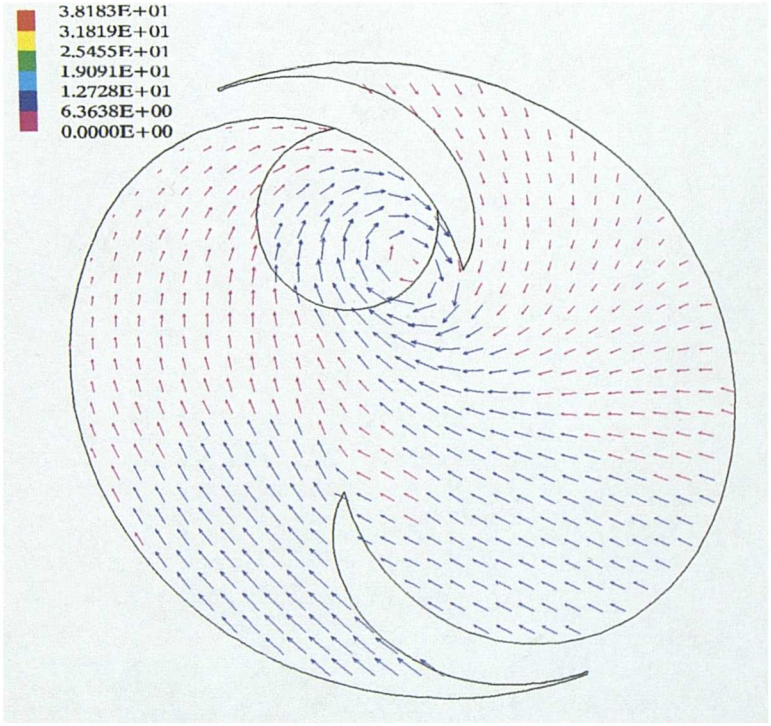

Figure 5.97 Scroll-Compressor. Rotational speed 3000 RPM, Speed vectors, Z-plane =-0.018, step=100, 50 degrees (2.777m sec) after discharge commences

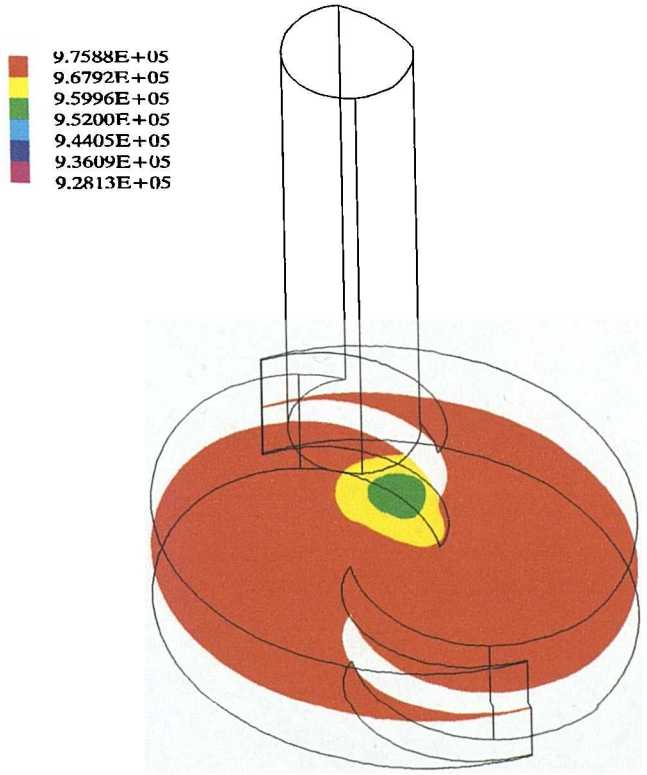

Figure 5.98 Scroll-Compressor. Rotational speed 3000 RPM, Pressure contours, Z-plane =-0.1, step=100, 50 degrees (2.777m sec) after discharge commences

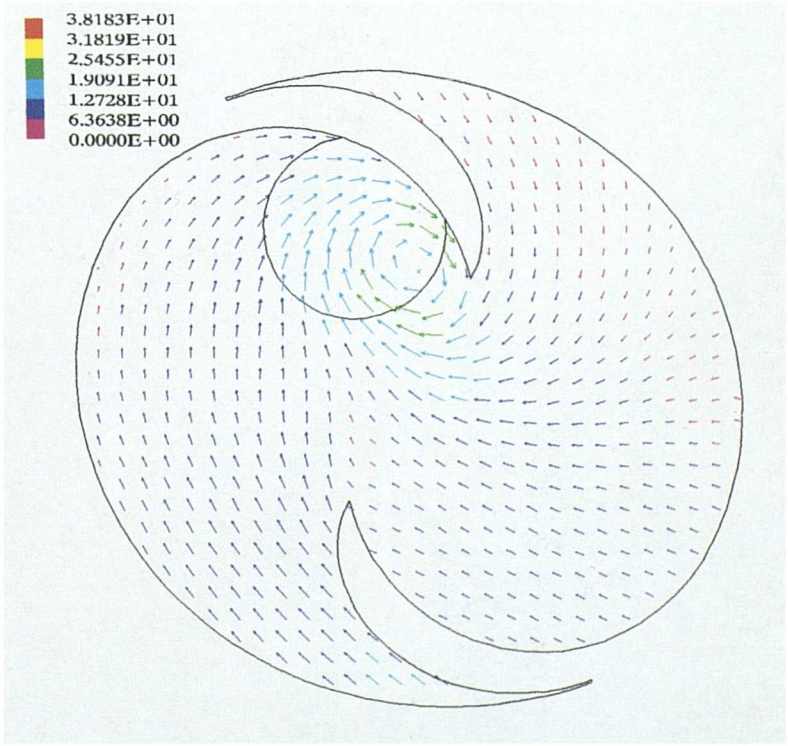

Figure 5.99 Scroll-Compressor. Rotational speed 3000 RPM, Speed vectors, Z-plane =-0.1, step=100, 50 degrees (2.777m sec) after discharge commences

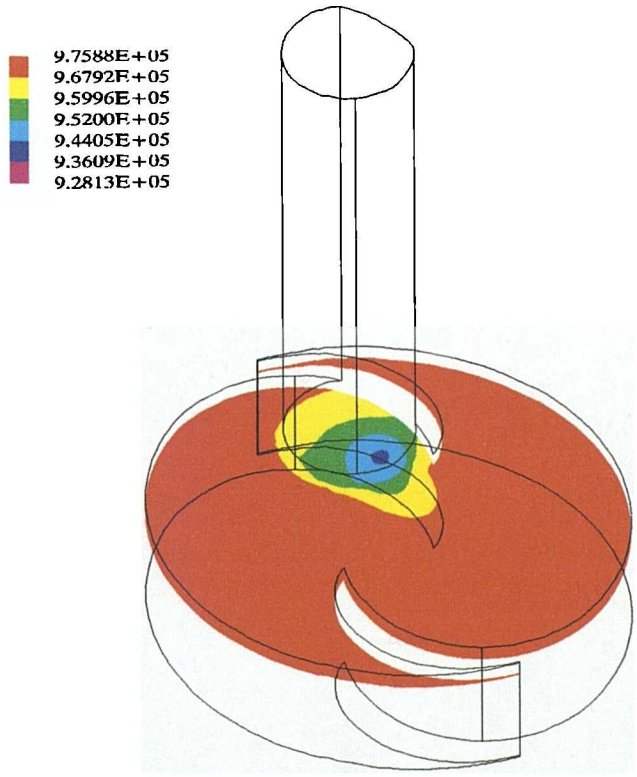

Figure 5.100 Scroll-Compressor. Rotational speed 3000 RPM, Pressure contours, Z-plane =-0.0025, step=100, 50 degrees (2.777m sec) after discharge commences

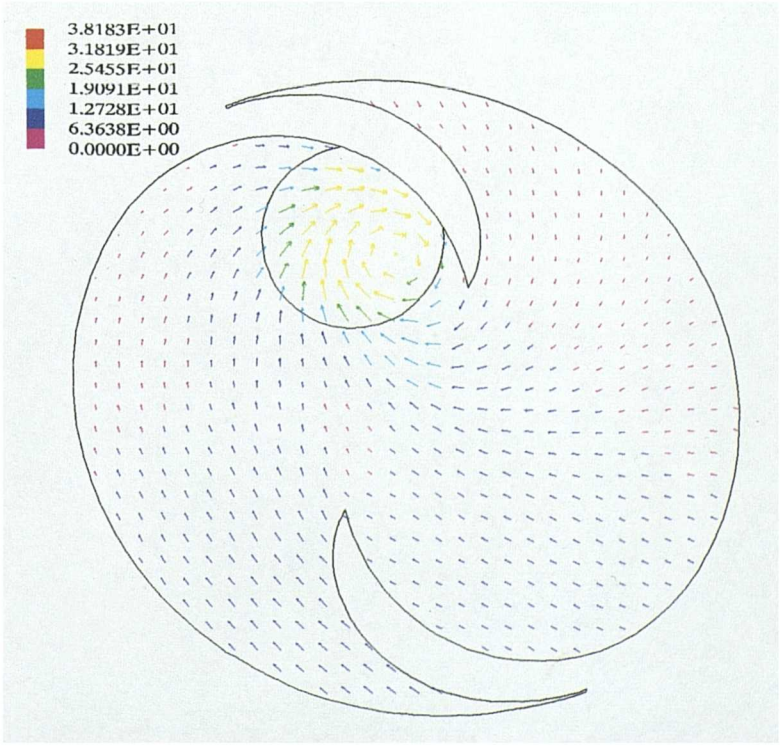

Figure 5.101 Scroll-Compressor. Rotational speed 3000 RPM, Speed vectors, Z-plane =-0.0025, step=100, 50 degrees (2.777m sec) after discharge commences

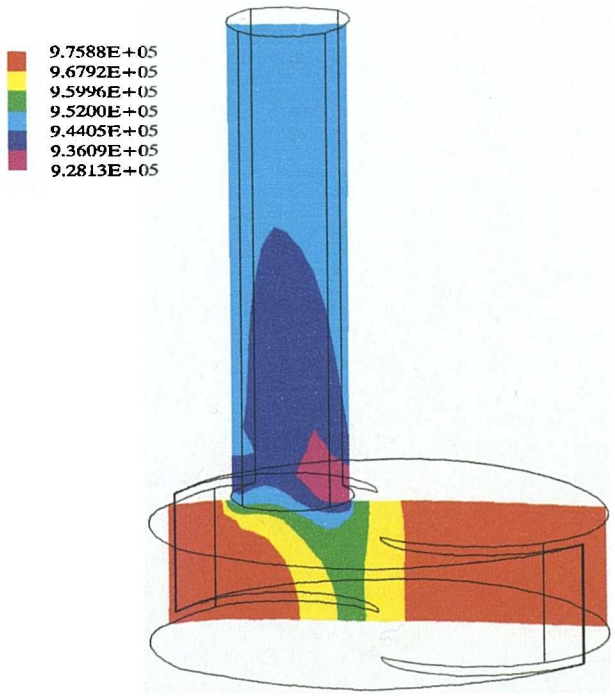

Figure 5.102 Scroll-Compressor. Rotational speed 3000 RPM, Pressure contours, Arbitrary plane, step=100, 50 degrees (2.777m sec) after discharge commences

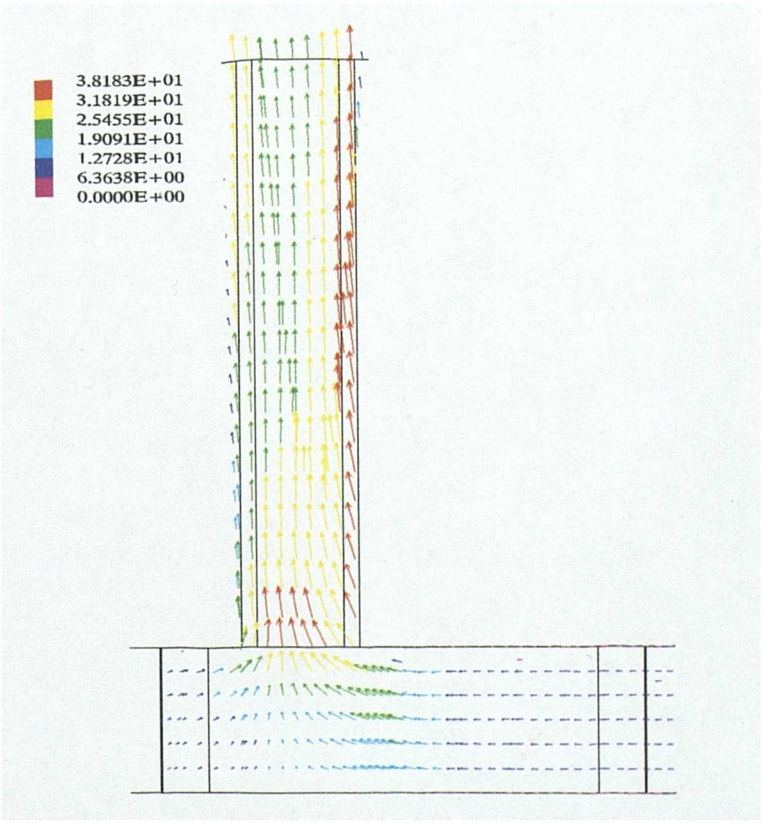

Figure 5.103 Scroll-Compressor. Rotational speed 3000 RPM, Speed vectors, Arbitrary plane, step=100, 50 degrees (2.777m sec) after discharge commences

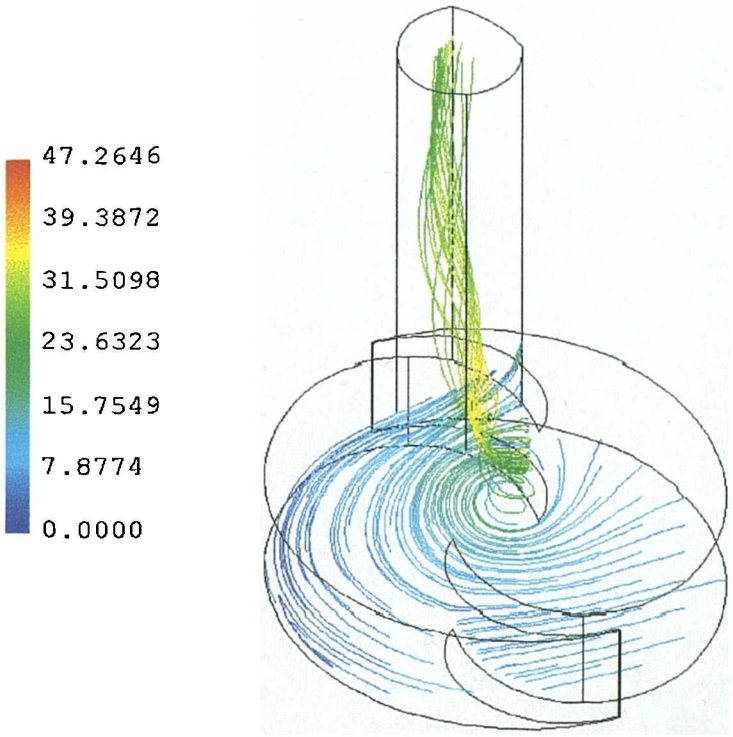

Figure 5.104 Scroll-Compressor. Rotational speed 3000 RPM, Stream lines step=100, 50 degrees (2.777m sec) after discharge commences

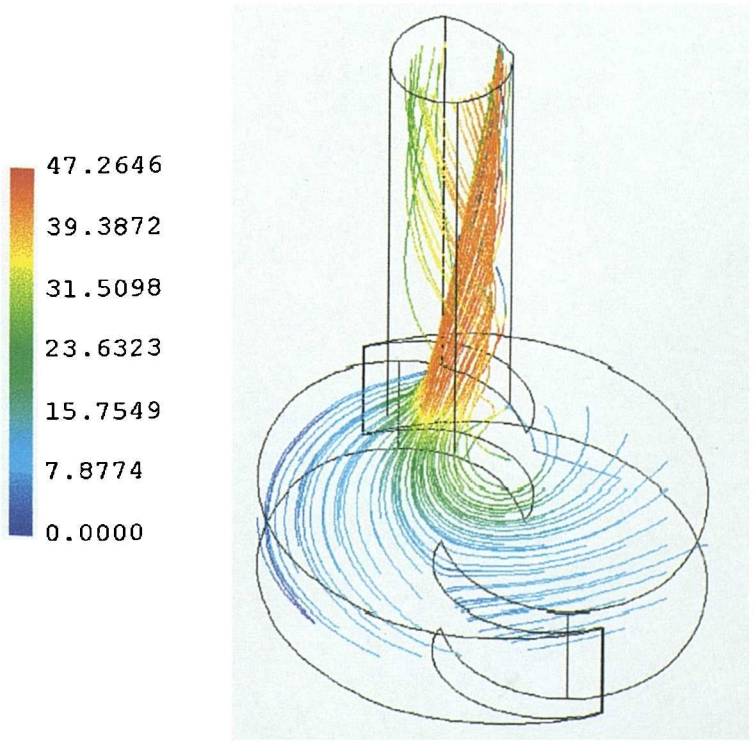

Figure 5.105 Scroll-Compressor. Rotational speed 3000 RPM, Stream lines, step=100, 50 degrees (2.777m sec) after discharge commences

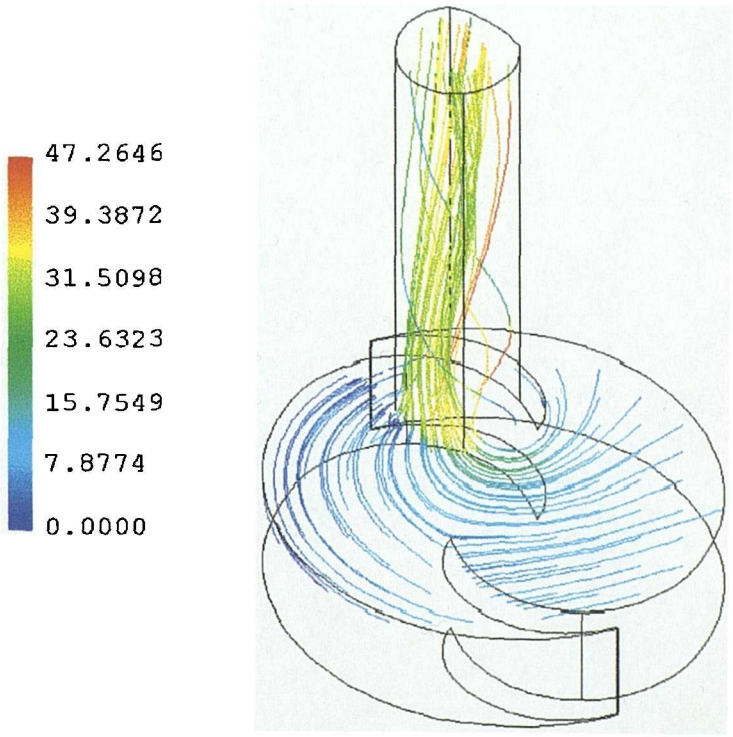

Figure 5.106 Scroll-Compressor. Rotational speed 3000 RPM, Stream lines step=100, 50 degrees (2.777m sec) after discharge commences

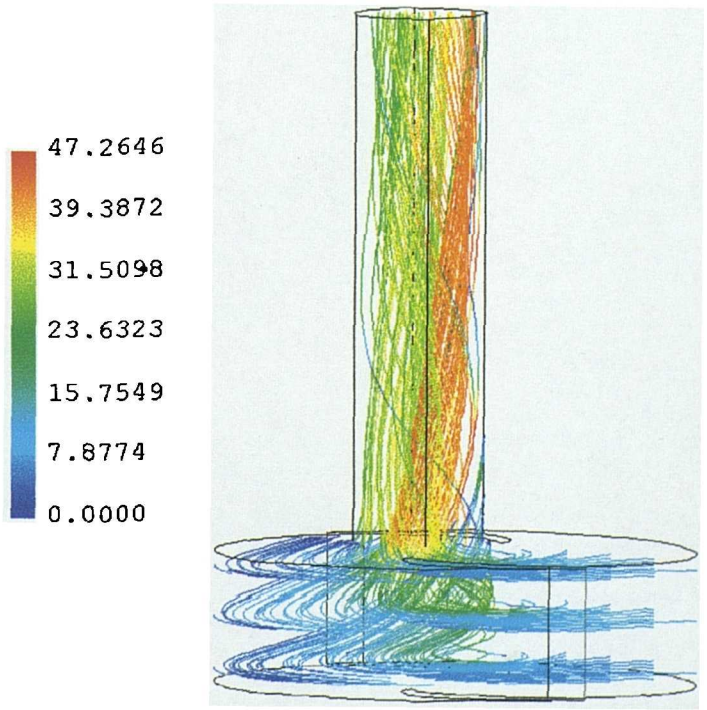

Figure 5.107 Scroll-Compressor. Rotational speed 3000 RPM, Stream lines, step=100, 50 degrees (2.777m sec) after discharge commences

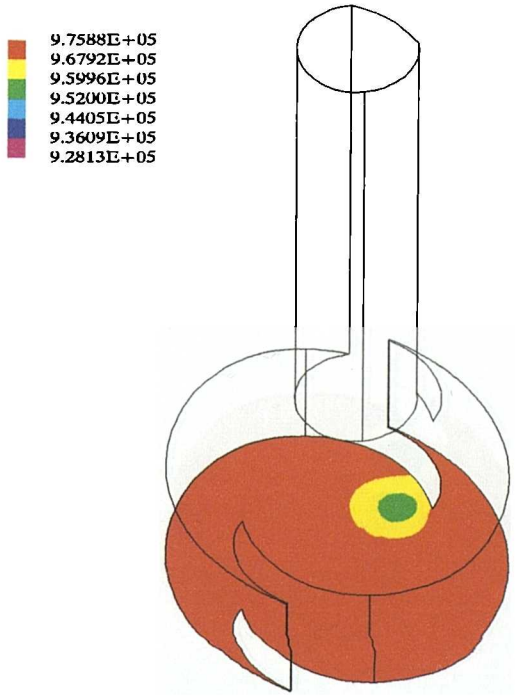

Figure 5.108 Scroll-Compressor. Rotational speed 3000 RPM, Pressure contours, Z-plane =-0.2, step=200, 100 degrees (5.54m sec) after discharge commences

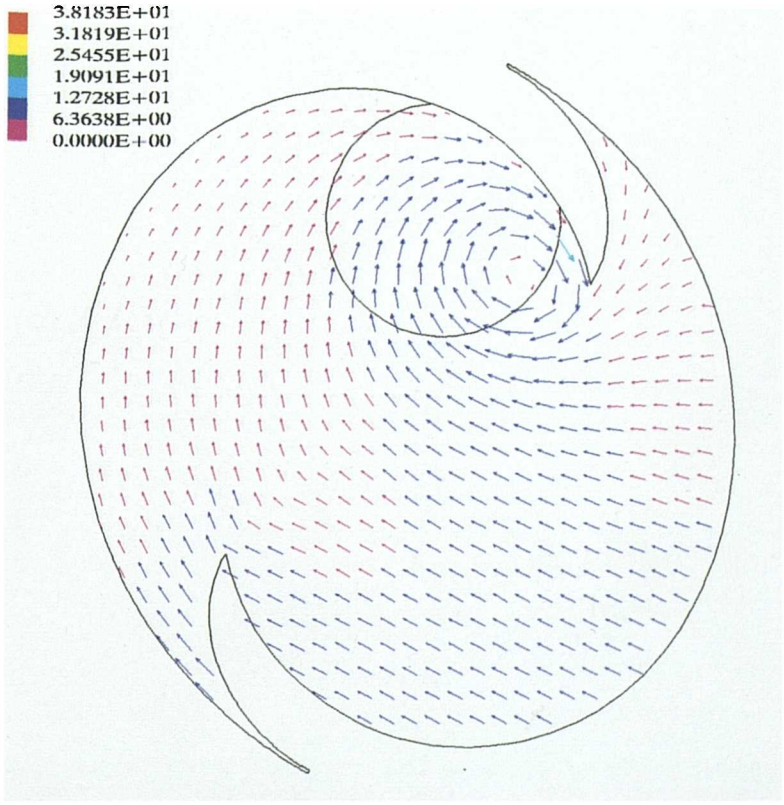

Figure 5.109 Scroll-Compressor. Rotational speed 3000 RPM, Speed vectors, Z-plane =-0.018, step=200, 100 degrees (5.54m sec) after discharge commences

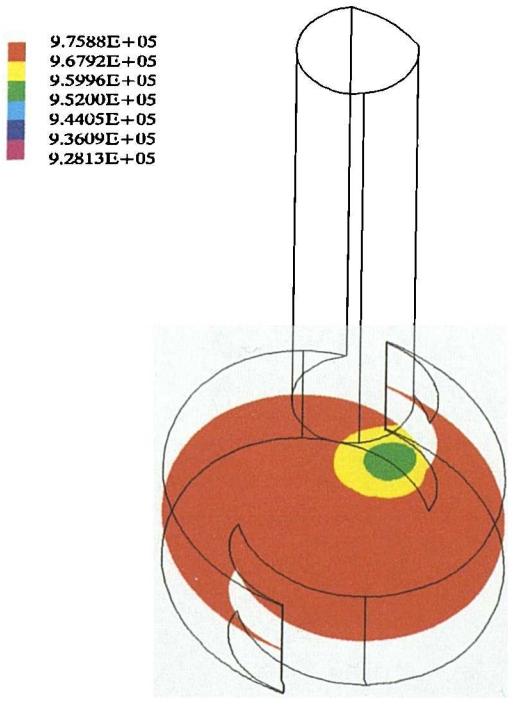

Figure 5.110 Scroll-Compressor. Rotational speed 3000 RPM, Pressure contours, Z-plane =-0.1, step=200, 100 degrees (5.54m sec) after discharge commences

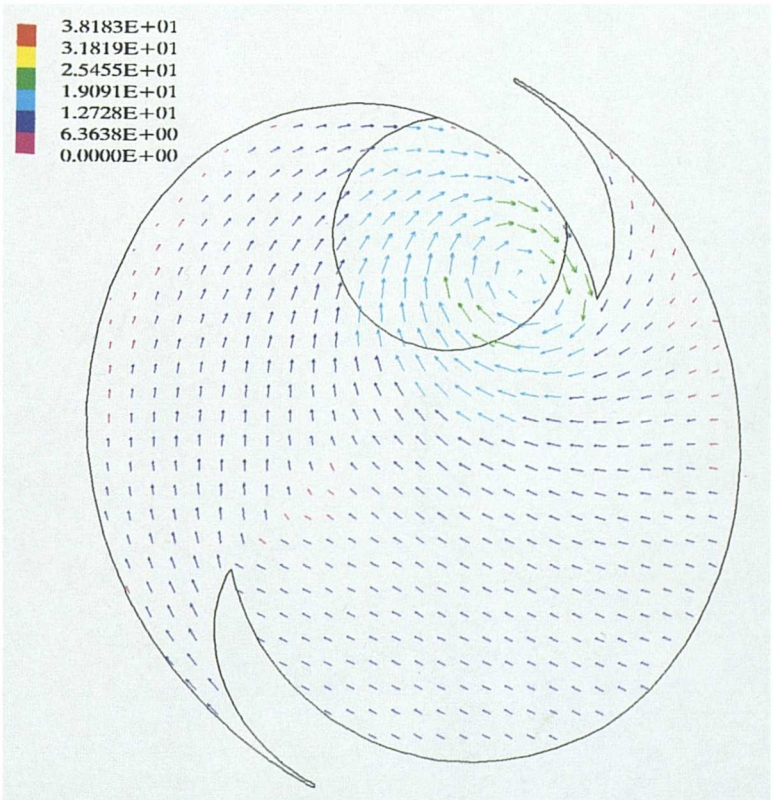

Figure 5.111 Scroll-Compressor. Rotational speed 3000 RPM, Speed vectors, Z-plane =-0.1, step=200, 100 degrees (5.54m sec) after discharge commences

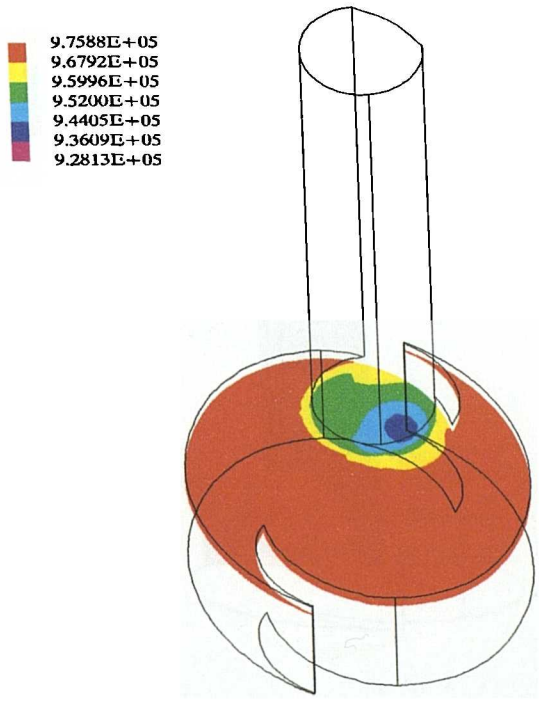

Figure 5.112 Scroll-Compressor. Rotational speed 3000 RPM, Pressure contours, Z-plane =-0.0025, step=200, 100 degrees (5.54m sec) after discharge commences

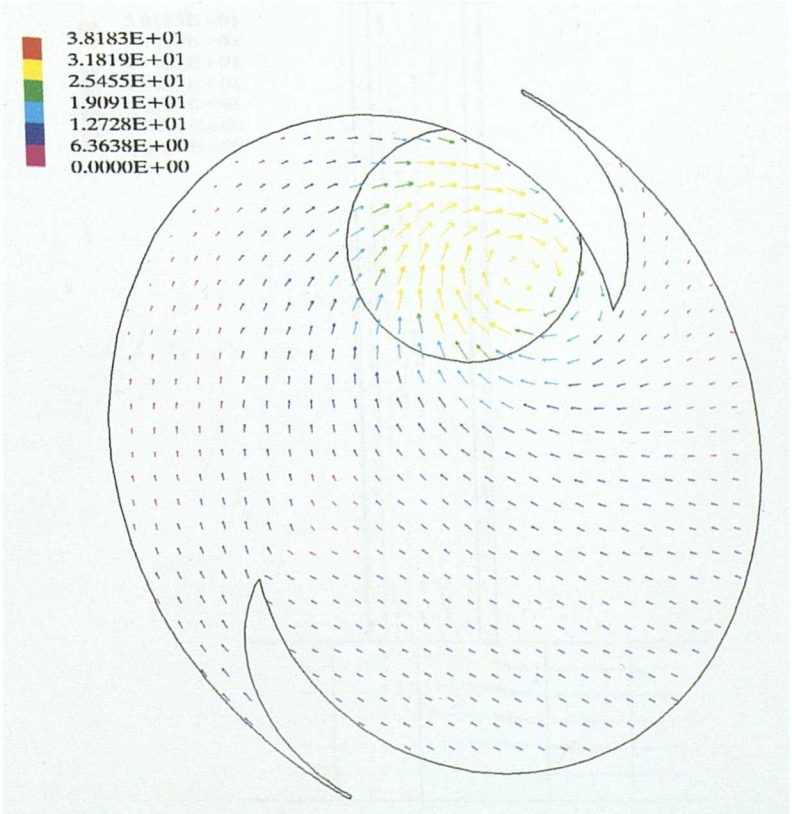

Figure 5.113 Scroll-Compressor. Rotational speed 3000 RPM, Speed vectors, Z-plane =-0.0025, step=200, 100 degrees (5.54m sec) after discharge commences

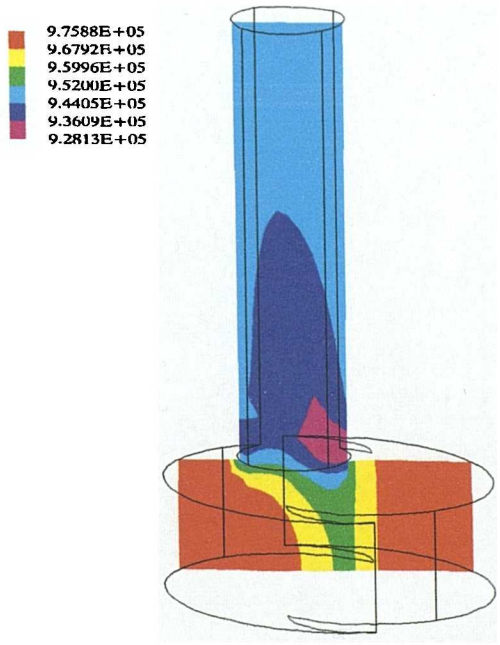

Figure 5.114 Scroll-Compressor. Rotational speed 3000 RPM, Pressure contours, Arbitrary plane, step=200, 100 degrees (5.54m sec) after discharge commences

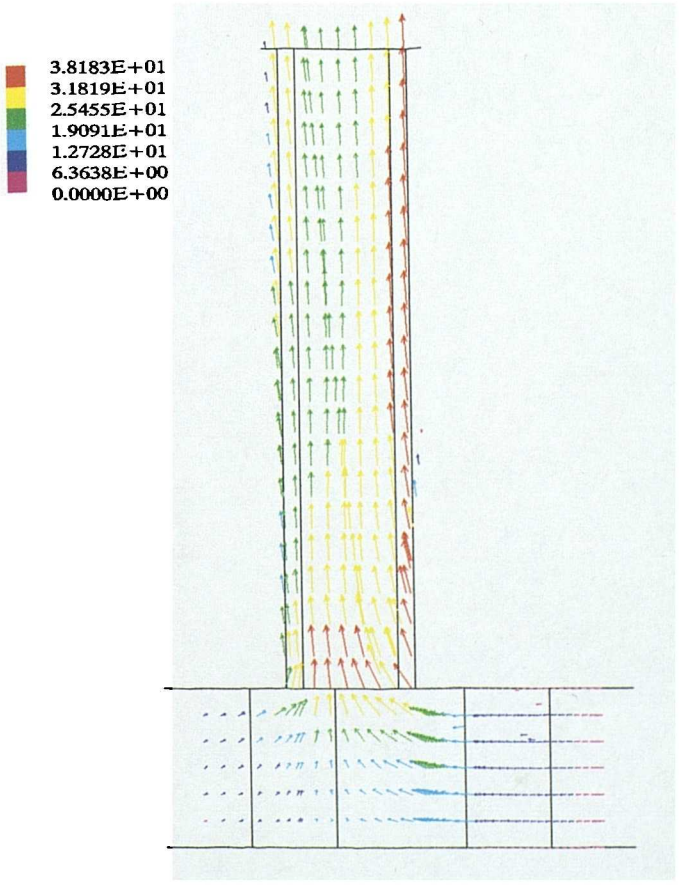

Figure 5.115 Scroll-Compressor. Rotational speed 3000 RPM, Speed vectors, Arbitrary plane, step=200, 100 degrees (5.54m sec) after discharge commences

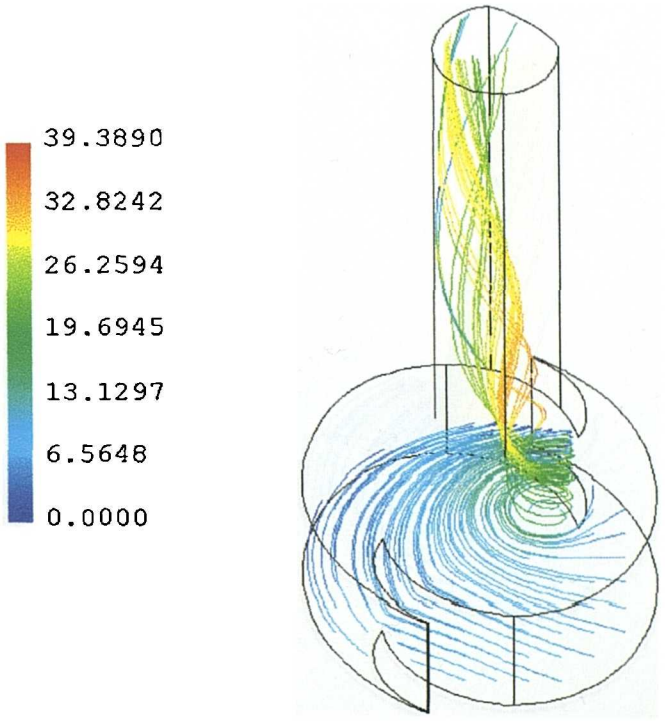

Figure 5.116 Scroll-Compressor. Rotational speed 3000 RPM, Stream lines step=200, 100 degrees (5.54m sec) after discharge commences

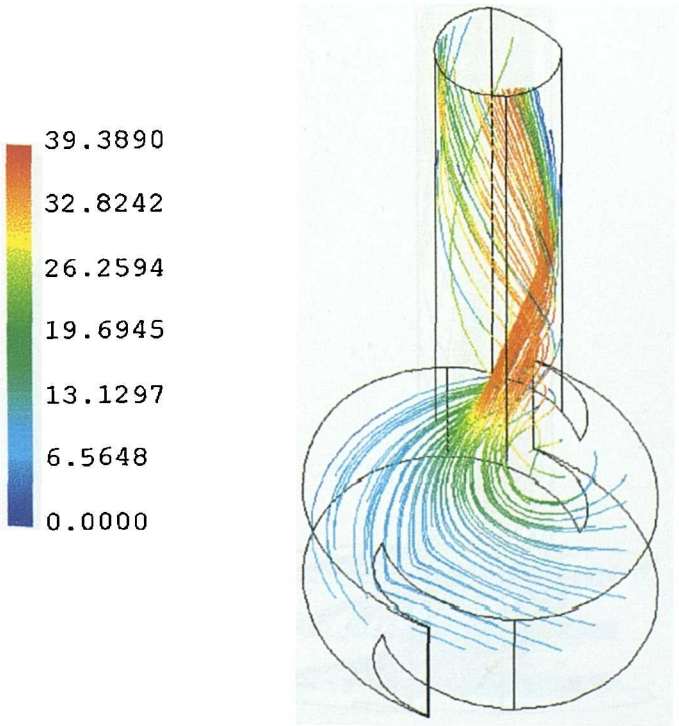

Figure 5.117 Scroll-Compressor. Rotational speed 3000 RPM, Stream lines, step=200, 100 degrees (5.54m sec) after discharge commences

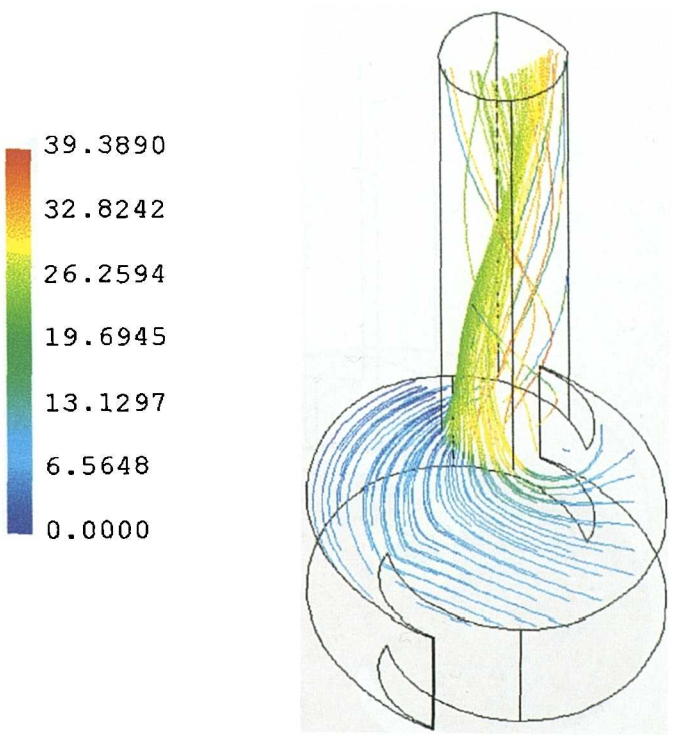

Figure 5.118 Scroll-Compressor. Rotational speed 3000 RPM, Stream lines step=200, 100 degrees (5.54m sec) after discharge commences

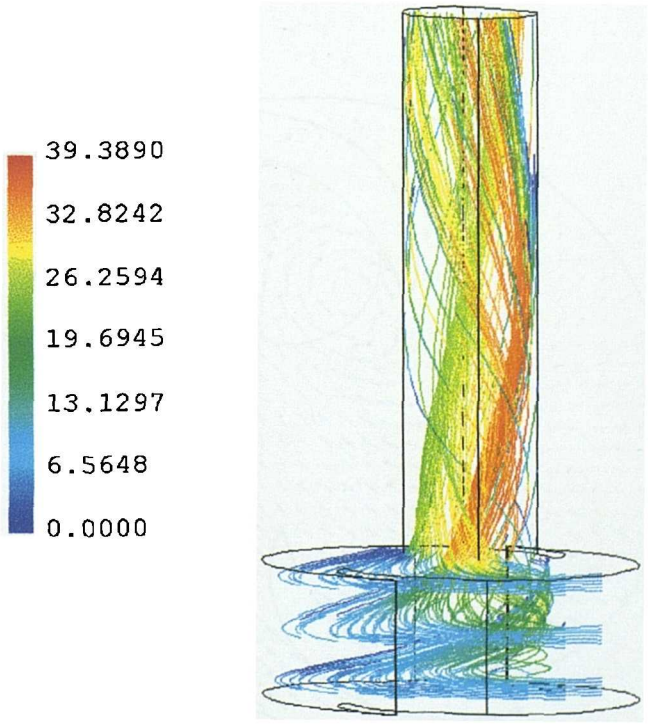

Figure 5.119 Scroll-Compressor. Rotational speed 3000 RPM, Stream lines, step=200, 100 degrees (5.54m sec) after discharge commences

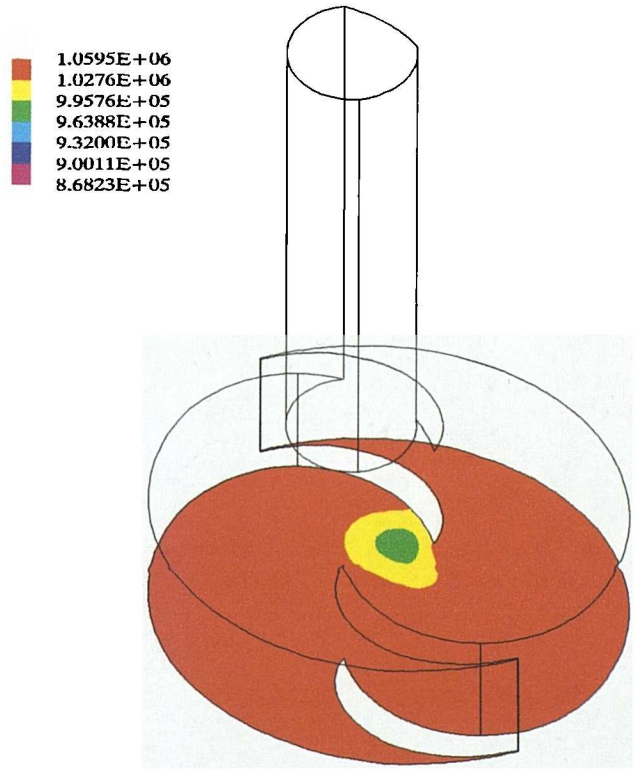

Figure 5.120 Scroll-Compressor. Rotational speed 6000 RPM, Pressure contours, Z-plane =-0.2, step=100, 50 degrees (1.389m sec) after discharge commences

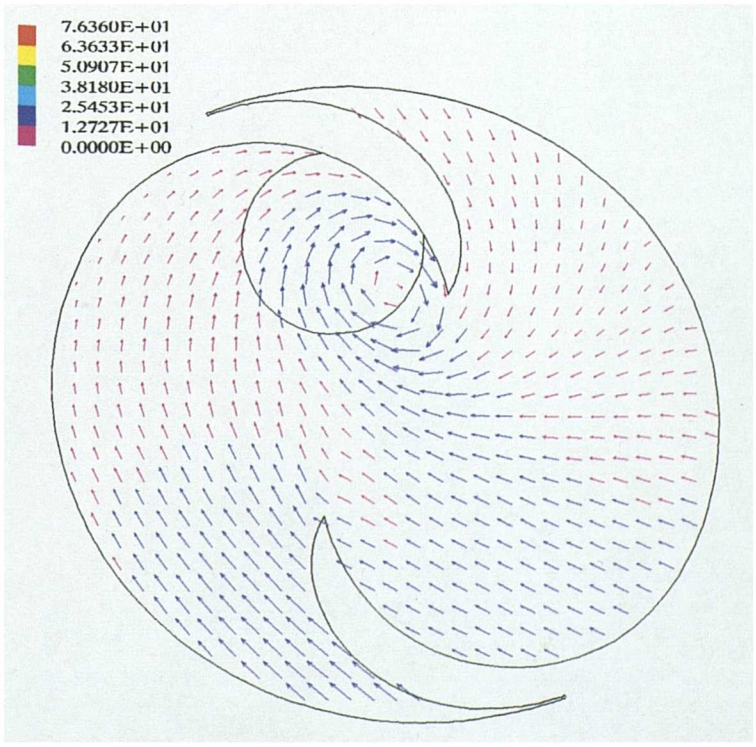

Figure 5.121 Scroll-Compressor. Rotational speed 6000 RPM, Speed vectors, Z-plane =-0.018, step=100, 50 degrees (1.389m sec) after discharge commences

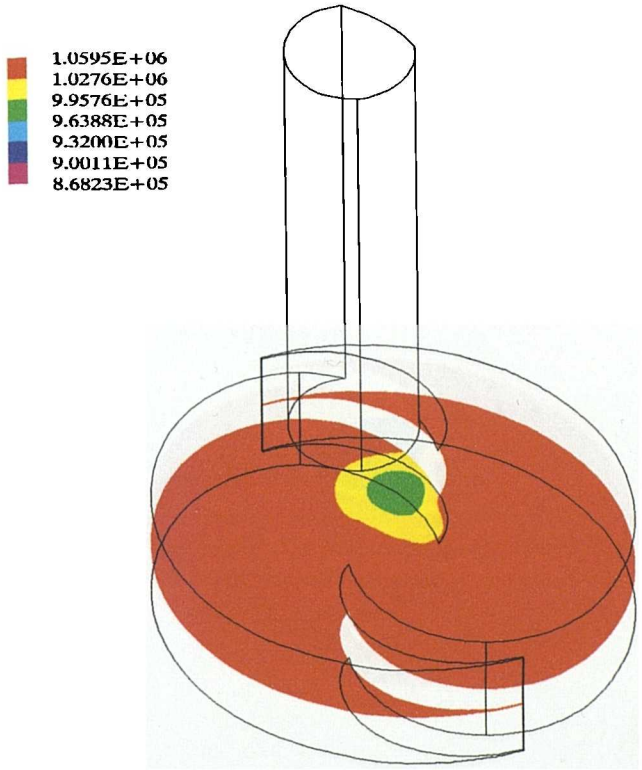

Figure 5.122 Scroll-Compressor. Rotational speed 6000 RPM, Pressure contours, Z-plane =-0.1, step=100, 50 degrees (1.389m sec) after discharge commences

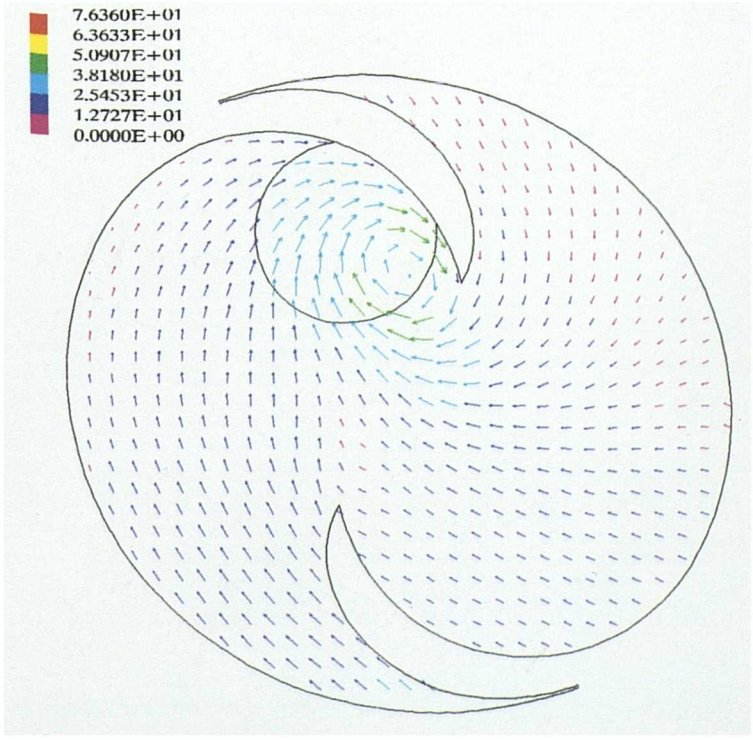

Figure 5.123 Scroll-Compressor. Rotational speed 6000 RPM, Speed vectors, Z-plane =-0.1, step=100, 50 degrees (1.389m sec) after discharge commences

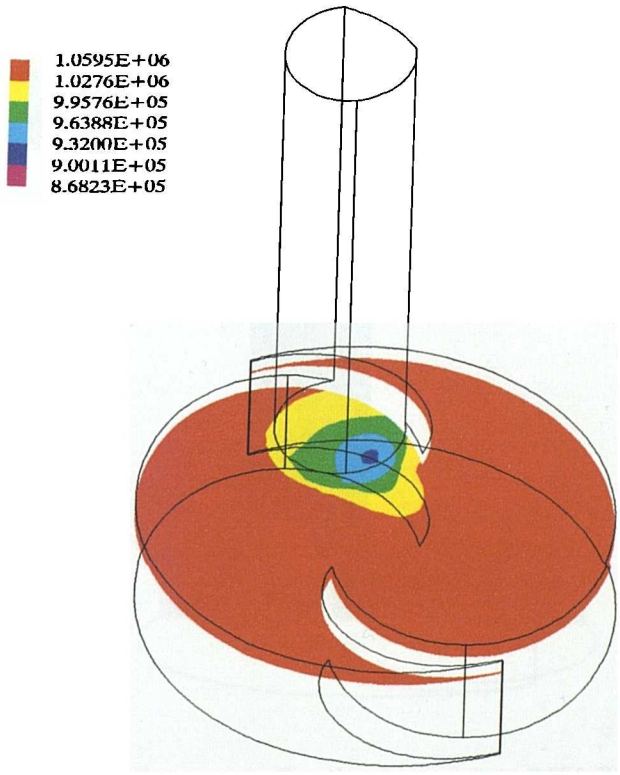

Figure 5.124 Scroll-Compressor. Rotational speed 6000 RPM, Pressure contours, Z-plane =-0.0025, step=100, 50 degrees (1.389m sec) after discharge commences

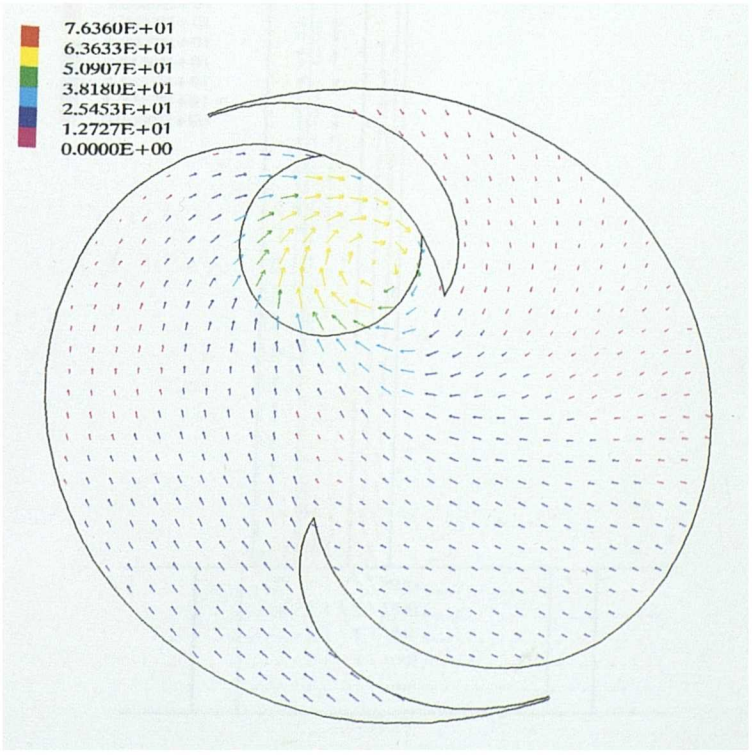

Figure 5.125 Scroll-Compressor. Rotational speed 6000 RPM, Speed vectors, Z-plane =-0.0025, step=100, 50 degrees (1.389m sec) after discharge commences

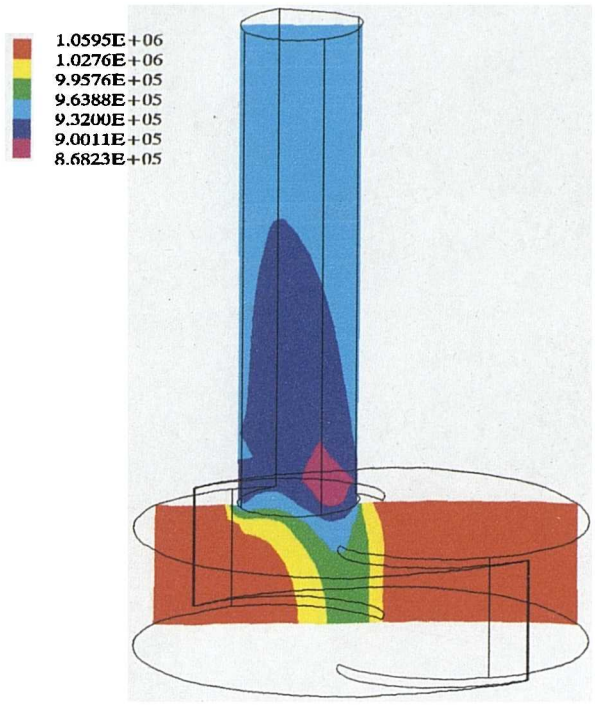

Figure 5.126 Scroll-Compressor. Rotational speed 6000 RPM, Pressure contours, Arbitrary plane, step=100, 50 degrees (1.389m sec) after discharge commences

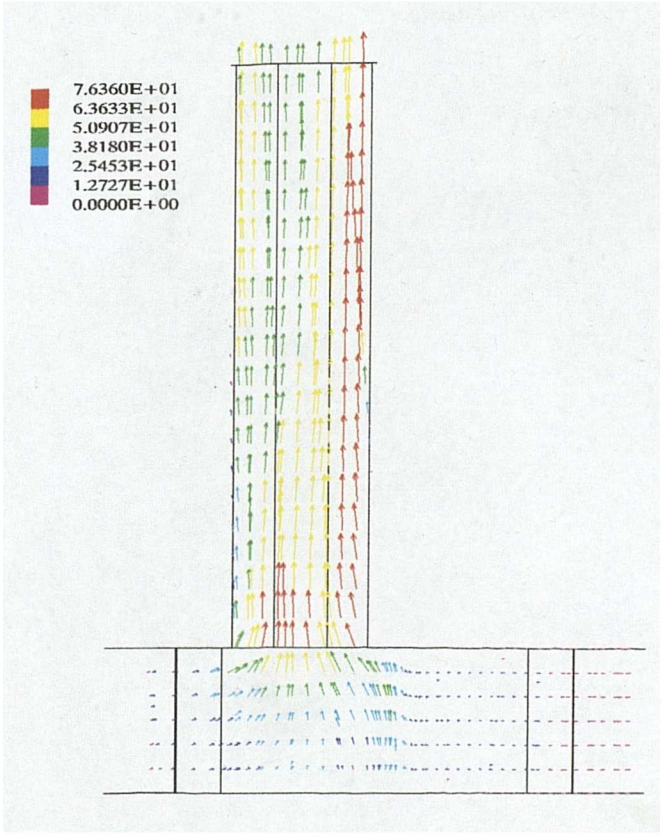

Figure 5.127 Scroll-Compressor. Rotational speed 6000 RPM, Speed vectors, Arbitrary plane, step=100, 50 degrees (1.389m sec) after discharge commences

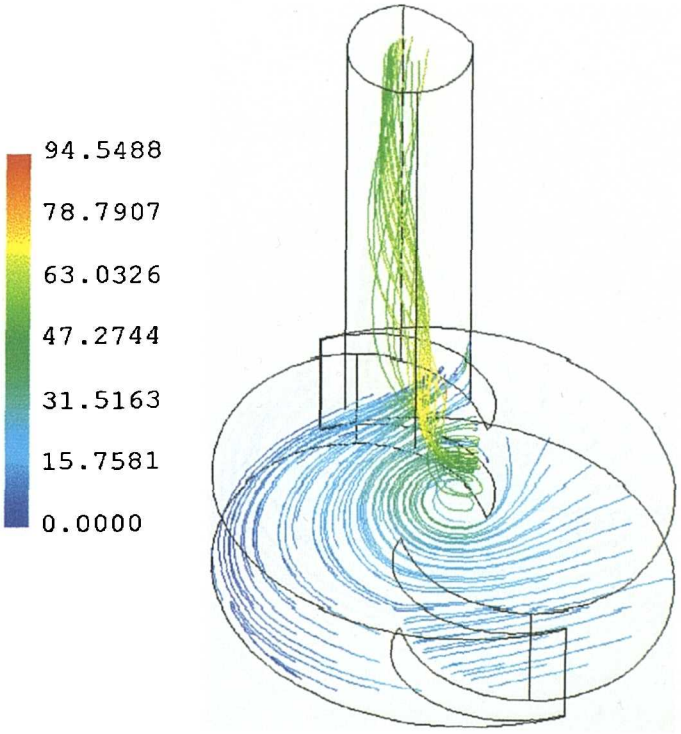

Figure 5.128 Scroll-Compressor. Rotational speed 6000 RPM, Stream lines step=100, 50 degrees (1.389m sec) after discharge commences

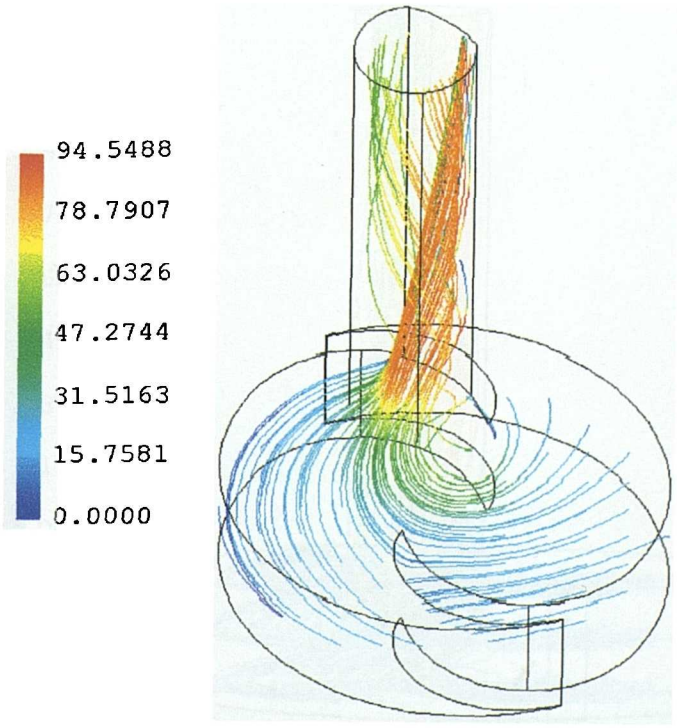

Figure 5.129 Scroll-Compressor. Rotational speed 6000 RPM, Stream lines, step=100, 50 degrees (1.389m sec) after discharge commences

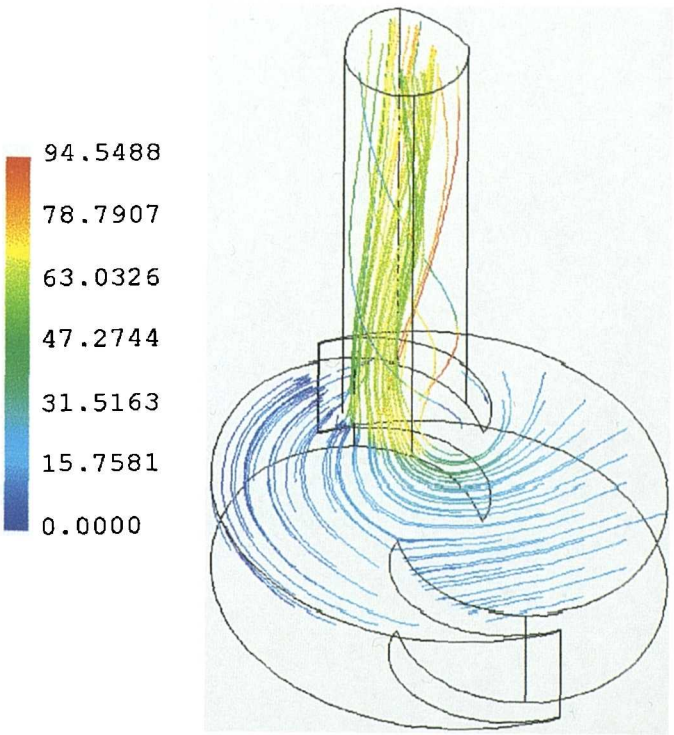

Figure 5.130 Scroll-Compressor. Rotational speed 6000 RPM, Stream lines step=100, 50 degrees (1.389m sec) after discharge commences

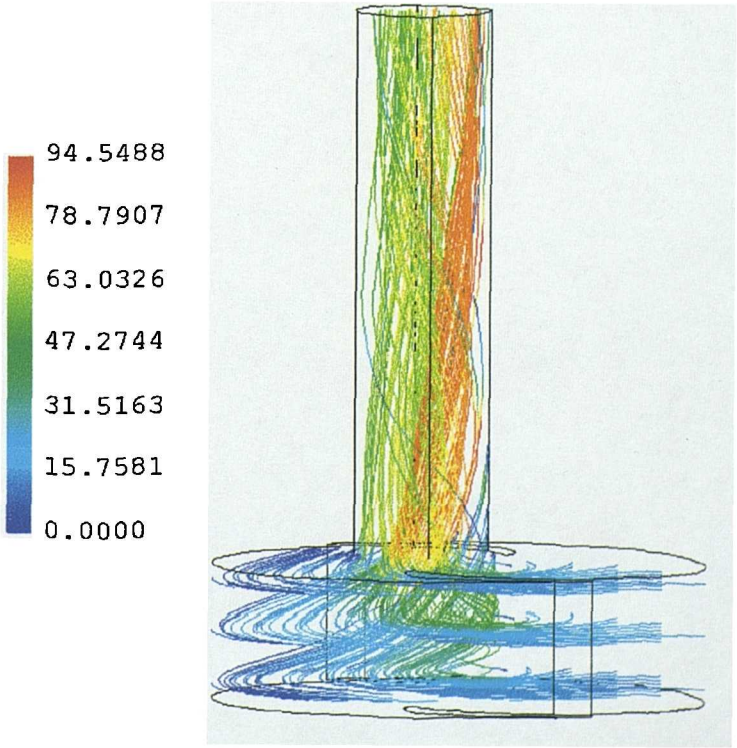

Figure 5.131 Scroll-Compressor. Rotational speed 6000 RPM, Stream lines, step=100, 50 degrees (1.389m sec) after discharge commences

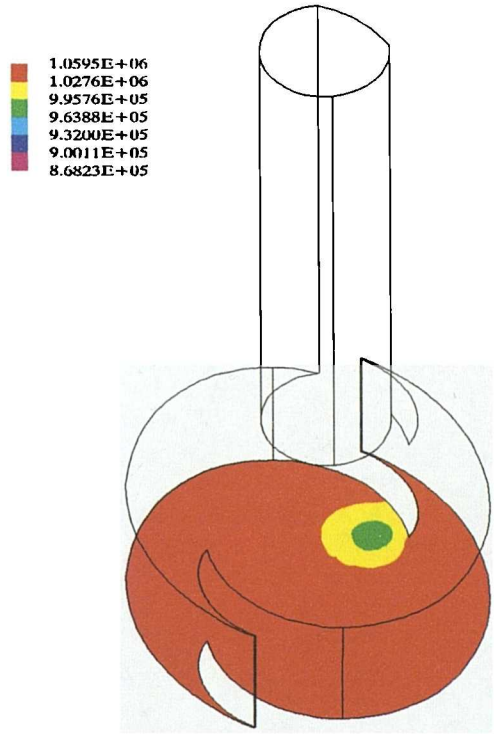

Figure 5.132 Scroll-Compressor. Rotational speed 6000 RPM, Pressure contours, Z-plane =-0.2, step=200, 100 degrees (2.778m sec) after discharge commences

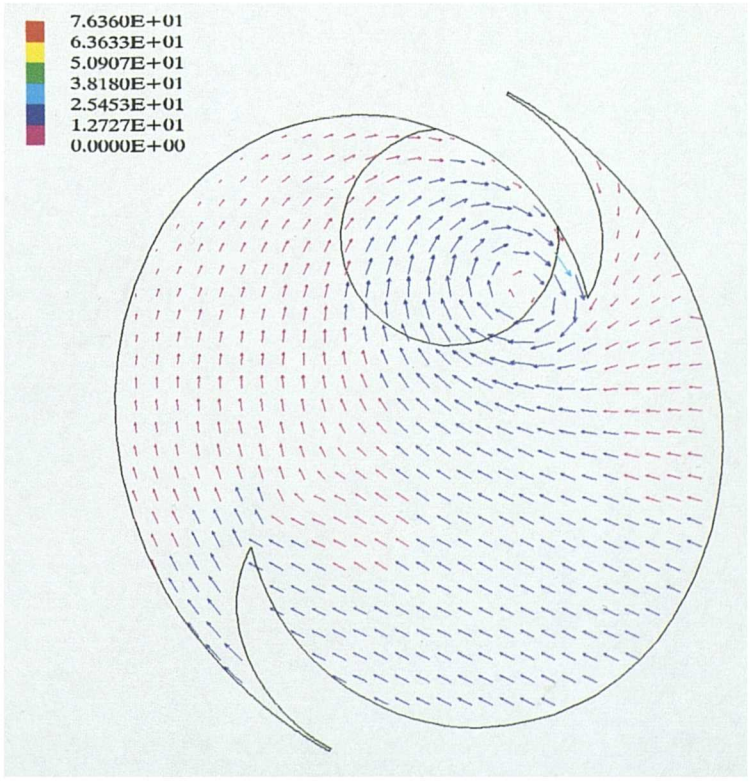

Figure 5.133 Scroll-Compressor. Rotational speed 6000 RPM, Speed vectors, Z-plane =-0.018, step=200, 100 degrees (2.778m sec) after discharge commences

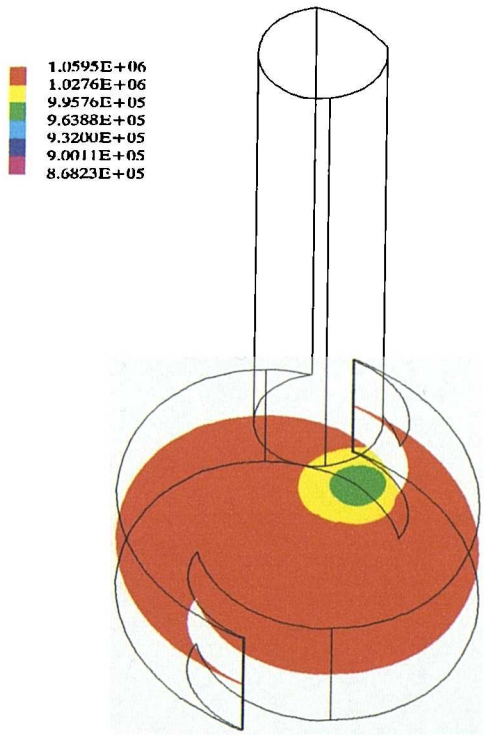

Figure 5.134 Scroll-Compressor. Rotational speed 6000 RPM, Pressure contours, Z-plane =-0.1, step=200, 100 degrees (2.778m sec) after discharge commences

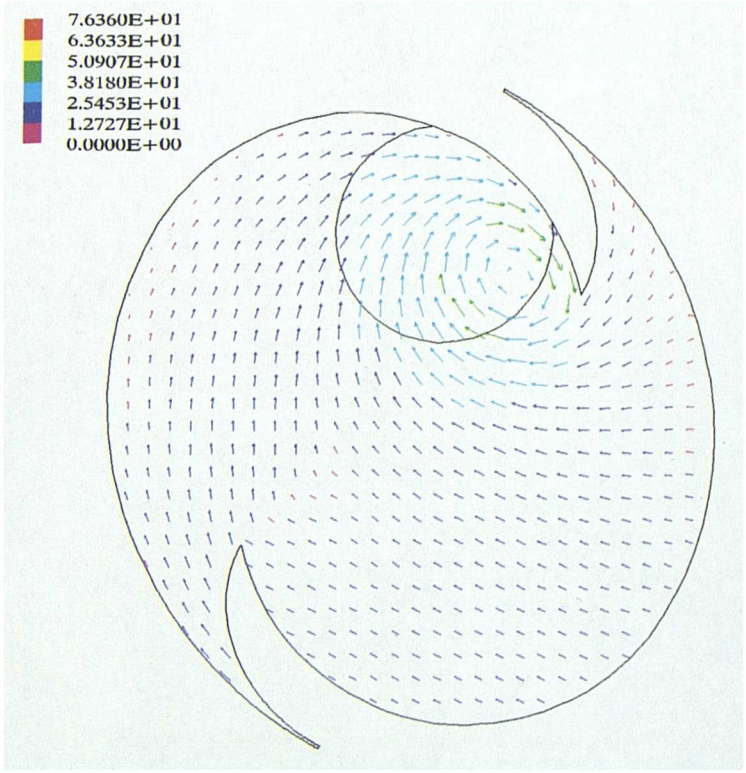

Figure 5.135 Scroll-Compressor. Rotational speed 6000 RPM, Speed vectors, Z-plane =-0.1, step=200, 100 degrees (2.778m sec) after discharge commences

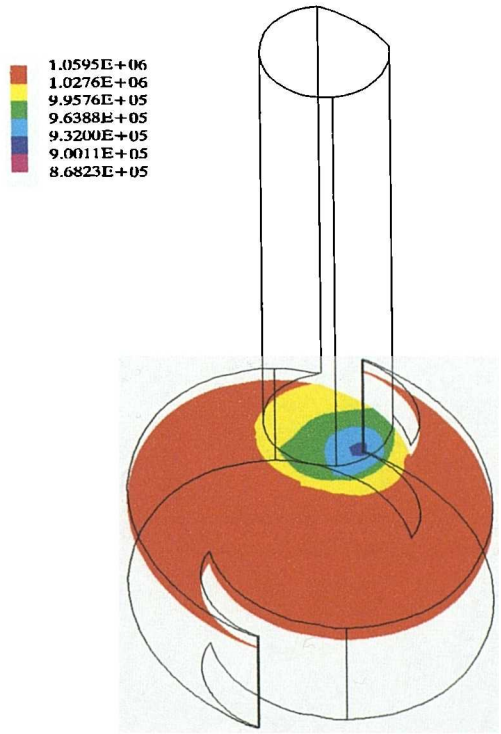

Figure 5.136 Scroll-Compressor. Rotational speed 6000 RPM, Pressure contours, Z-plane =-0.0025, step=200, 100 degrees (2.778m sec) after discharge commences

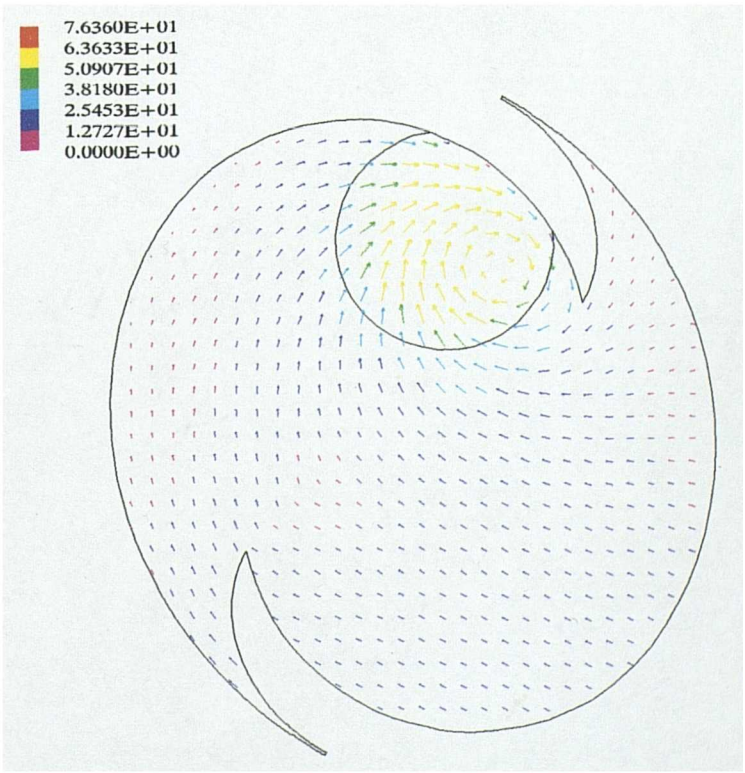

Figure 5.137 Scroll-Compressor. Rotational speed 6000 RPM, Speed vectors, Z-plane =-0.0025, step=200, 100 degrees (2.778m sec) after discharge commences

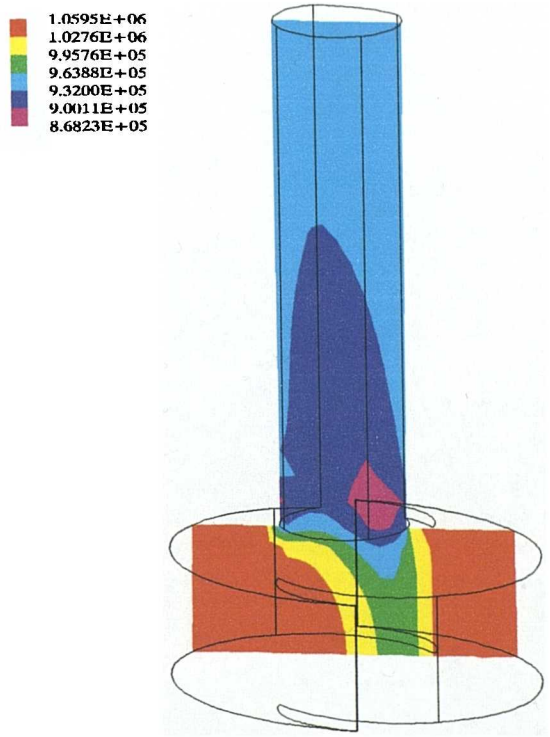

Figure 5.138 Scroll-Compressor. Rotational speed 6000 RPM, Pressure contours, Arbitrary plane, step=200, 100 degrees (2.778m sec) after discharge commences

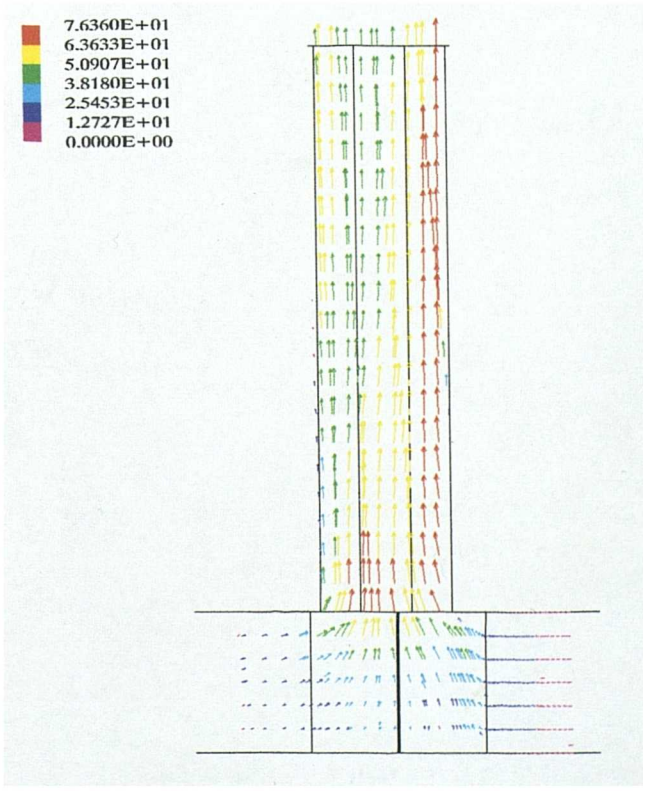

Figure 5.139 Scroll-Compressor. Rotational speed 6000 RPM, Speed vectors, Arbitrary plane, step=200, 100 degrees (2.778m sec) after discharge commences

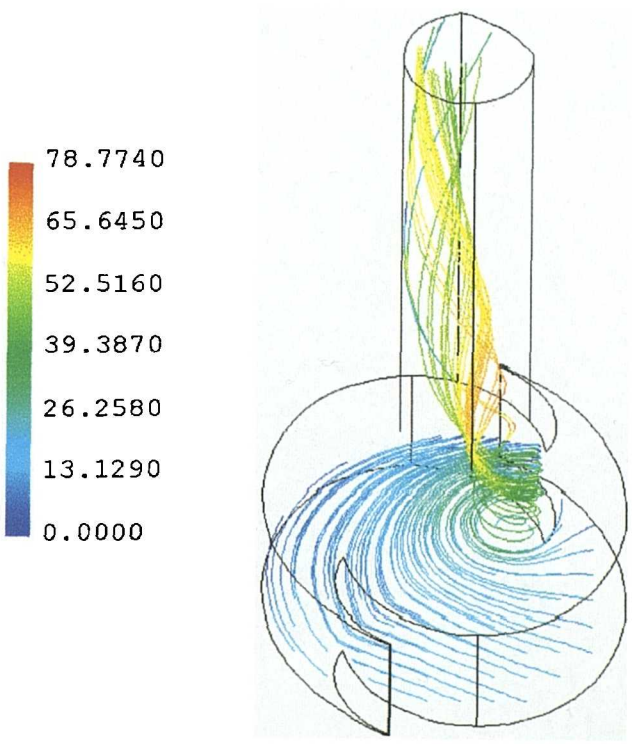

Figure 5.140 Scroll-Compressor. Rotational speed 6000 RPM, Stream lines step=200, 100 degrees (2.778m sec) after discharge commences

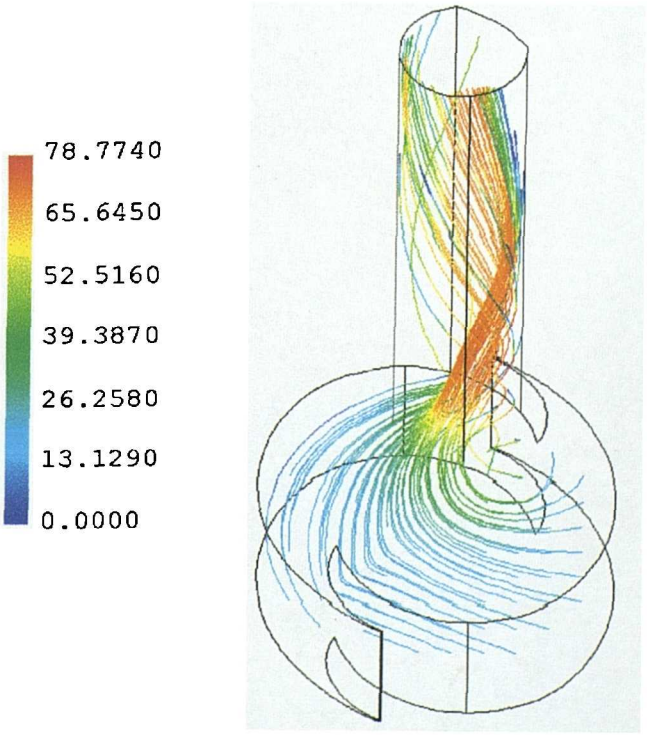

Figure 5.141 Scroll-Compressor. Rotational speed 6000 RPM, Stream lines, step=200, 100 degrees (2.778m sec) after discharge commences

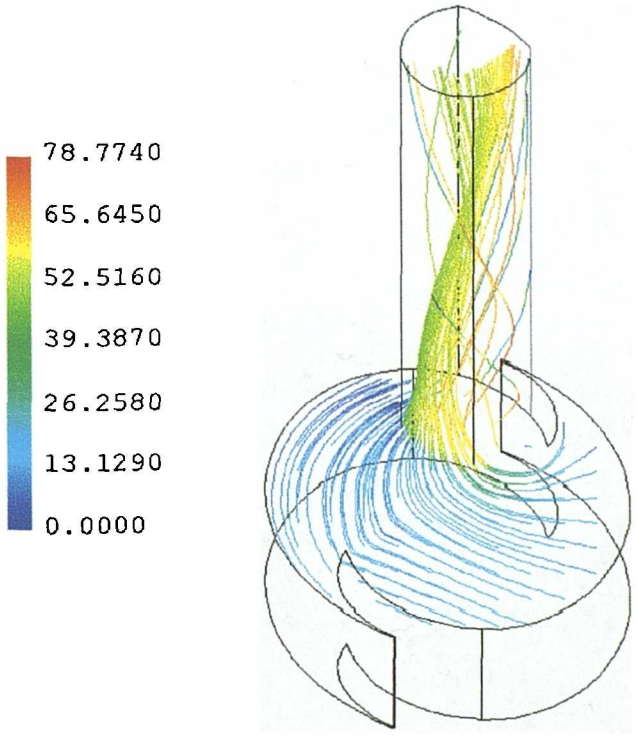

Figure 5.142 Scroll-Compressor. Rotational speed 6000 RPM, Stream lines step=200, 100 degrees (2.778m sec) after discharge commences

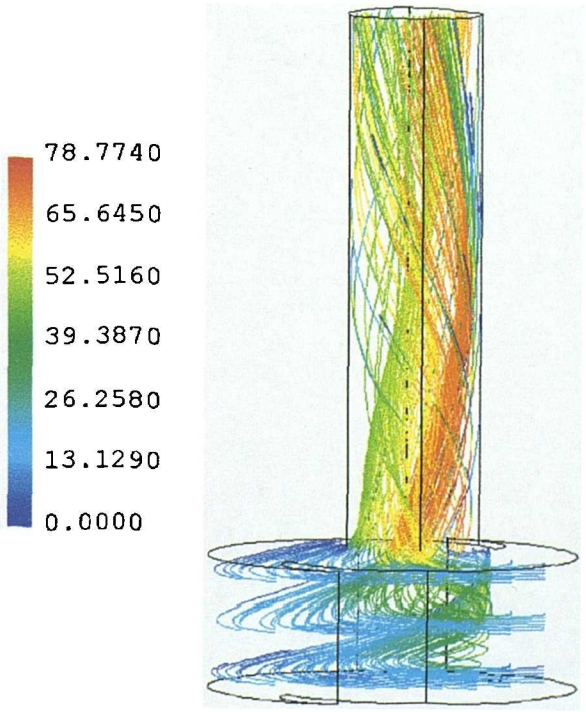

Figure 5.143 Scroll-Compressor. Rotational speed 6000 RPM, Stream lines, step=200, 100 degrees (2.778m sec) after discharge commences

Chapter 6

Conclusions and Future Work

This chapter presents some conclusions which can be drawn from the work done and also a few suggestions for possible future work.

6.1 Conclusions

In this study, an analytical model for the geometry of scroll machines, and a grid generation program with automatic moving mesh capabilities has been developed and used together with a finite volume code to model the flow of a scroll compressor - expander. The geometry was also attached to a package of subroutines developed to analyse compressor and expander thermodynamic characteristics based on a Quasi 1-D modeling approach. The proposed grid generation program developed is capable of resolving the complexity of the rotating working volumes of these machines.

The main findings can be summarised as follows:

1. The importance of the relationship between built-in volume ratio and pressure ratio and the use of the correct pressure ratio is clearly defined. The significant point is that the built-in volume ratio is a constant for any given scroll compressor or expander design whereas the pressure ratio, which is a function of the gas being compressed or expanded is not. Speed also affects the relationship between pressure and volume ratios.

2. A scroll expander driving a scroll compressor in a sealed unit could be used as a throttle valve replacement in large vapour compression chiller systems. Such a device would be stable in operation and increase the Coefficient of Performance.

3. The development of a grid to analyze motion in space and time, and the use of non uniform distribution functions such as the Hyperbolic tangent distribution

together with the transfinite interpolation has produced excellent results. The non uniform distribution gives the flexibility to user to put fewer elements in areas which are not so important or to concentrate elements in crucial areas so as to allow the solver to capture the activity of the fluid with a higher accuracy. Aspect ratio, orthogonality, cell distortion, and smooth distribution, are some of the difficult issues involved in the transient structured body fitted grid generation package developed. All these issues increase the speed of convergence.

4. Flows inside scroll compressors and expanders are turbulent, time dependent, and compressible. The flow inside the scroll expander is two phase as well. Furthermore these flows are driven by the wall motion. An interesting feature of the predicted flow patterns of the scroll expander, is the significant pressure drop which takes place within the flow domain during the filling process and the existence of re-circulation areas. It is clear that at these areas a stagnation point occurs. However the important conclusion from this case is the fact that these re-circulation areas are directly related to the geometry of the machine, the movement of the boundaries, and the direction of the flow.

5. The significant finding for the case of the scroll compressor is that we have approximately uniform pressures within the flow domain. There are also some areas of re-circulation but unlike the case of the expander are related to the discharge pipe. The calculations indicate that the flow passing through the discharge port is not uniform. Another important finding is the swirling that takes place, mainly in the outlet pipe. This swirling appears to be an extension of the re-circulation which is underneath the discharge pipe.

6. From the results presented in Chapter 5, we can conclude that both qualitative and quantitative results were obtained from the numerical predictions. These results have indicated that modern CFD codes, such as CFX4, are probably capable of simulating flows in scroll compressors and expanders. These codes can be used in such a way that they can provide a powerful and reliable comprehensive analysis tool for the design of such machines. However the computational cost of this simulations is something that needs to be taken into consideration.

6.2 Future work

The following areas, arising from the present work, are considered suitable for further investigation:

1. The grid generation code has not been optimised to execute the minimum number of operations. Therefore, further attempts will be necessary in order to make this code more efficient for practical purposes. In this optimisation, one should concentrate on the calculations of the non uniform distribution functions.

2. It may be of interest to adjust the code in such a way that can be used in an adaptive grid strategy in conjunction with the solver. When an adaptive grid is used, the grids are clustered where sharp gradients are present such as in the case of a shock. By concentrating the grids only at the locations where sharp gradients are taking place, one can avoid the use of unnecessary grids at locations where there is no need and therefore save on storage and computational time.

3. A further recommendation would be to put the discharge pipe in different angles. As it was said earlier some swirling is taking place inside the discharge pipe for the case of the compressor. If we examine the flow patterns underneath the pipe and the stream lines inside the pipe we will see that the swirling is due to the direction of the flow underneath the pipe, therefore the use of the discharge pipe in different angles might decrease the presence of this swirling. Another pipe related recommendation would be the modeling of the flow through the discharge pipe when an adjusting pressure valve is fitted on it. This will give us an indication of how the flow underneath will be affected from the pressure valve.

4. Now, after significant progress in both software and hardware technology, it is possible to carry out coupled simulations such as fluid-structure interactions. One way to do this is to solve the governing equations within one code, another approach would be the use of two different codes one to do the fluids and the other to do the structure calculations. The second approach will require a coupling interface as well. The design and development of a scroll compressor - expander require a detailed examination of structural behaviour and fluid dynamics. In this study only the fluid side of the problem was investigated.

Therefore another recommendation would be a fully coupled analysis of fluid structure interaction.

5. Finally, in this thesis 3-D numerical studies have modeled only the fluid dynamics of the suction process of a scroll expander and the discharge process of a scroll compressor. This was due to the prohibitive computational cost. However, the expansion and discharge process of the scroll expander, and the suction and compression process of the scroll compressor are still to be modeled. As it is well known, the biggest and most difficult part of a 3-D Numerical Simulation is the grid generation. In this case the grid generation as well as the setup of the program have been developed, and the remaining task is the provision of powerful computing facilities. Modeling all the processes of the scroll compressor - expander in 'one run' is another recommendation that can be done in the future.

Appendix A

Scroll Compressor-Expander Geometry

A.1 Introduction

In this Appendix the geometry of the scroll compressor-expander is analyzed. The derived equations are general parametric equations which amongst others can be used for

- The design and construction of scroll compressor-expander devices.
- The generation of boundary-fitted, orthogonal, block-structured, transient grids used in CFD analysis.
- The determination of the working volumes of scroll devices as functions of the crank angle θ and the parameters α and N determining the lengths of the devices' spirals.

A.2 Geometry of the Scroll Device

A.2.1 Basic Geometry

In this section the equations defining the inner and outer surfaces of the fixed and orbiting spirals of the compressor are derived. Figure (A-1) depicts the Cartesian system XY which is used in the treatment of the problem. The centre of a generating circle with radius r, is located at the point

$$S=\begin{pmatrix} S_x \\ S_y \end{pmatrix}.$$

The meaning of the term "generating" will become apparent later in this section.

The line segment BP, shown in figure (A-1), is constructed so that it is tangent to the generating circle at the points B, hence perpendicular to the radius SB. Its

length **BP** is equal to the length **GB** of the arc GB, as measured anti-clockwise, that is

$$BP \perp SB, \quad \mathbf{BP} \equiv \mathbf{GB} = r\varphi, \quad \varphi \geq 0, \quad 2\pi > \varepsilon \geq 0, \quad \varepsilon = \text{constant}, \qquad (A.1)$$

where by definition, φ is the angle $G\hat{S}B$ subtended by the chord GB and $\varepsilon \equiv A\hat{S}G$ is a given constant angle in the semi-open range $[0, 2\pi)$. Clearly, the coordinates of the point B are given by

$$B = \begin{pmatrix} r\cos(\varphi+\varepsilon)+S_x \\ r\sin(\varphi+\varepsilon)+S_y \end{pmatrix}, \quad \varphi \geq 0, \quad 2\pi > \varepsilon \geq 0, \quad \varepsilon = \text{constant}. \qquad (A.2)$$

The curve C, also shown in figure (A-1), is defined as the geometric locus of the points P satisfying the relations *(A.1)*. From this definition and the geometry shown in the figure, it is obvious that the parametric equations of the points P and hence the curve C, are

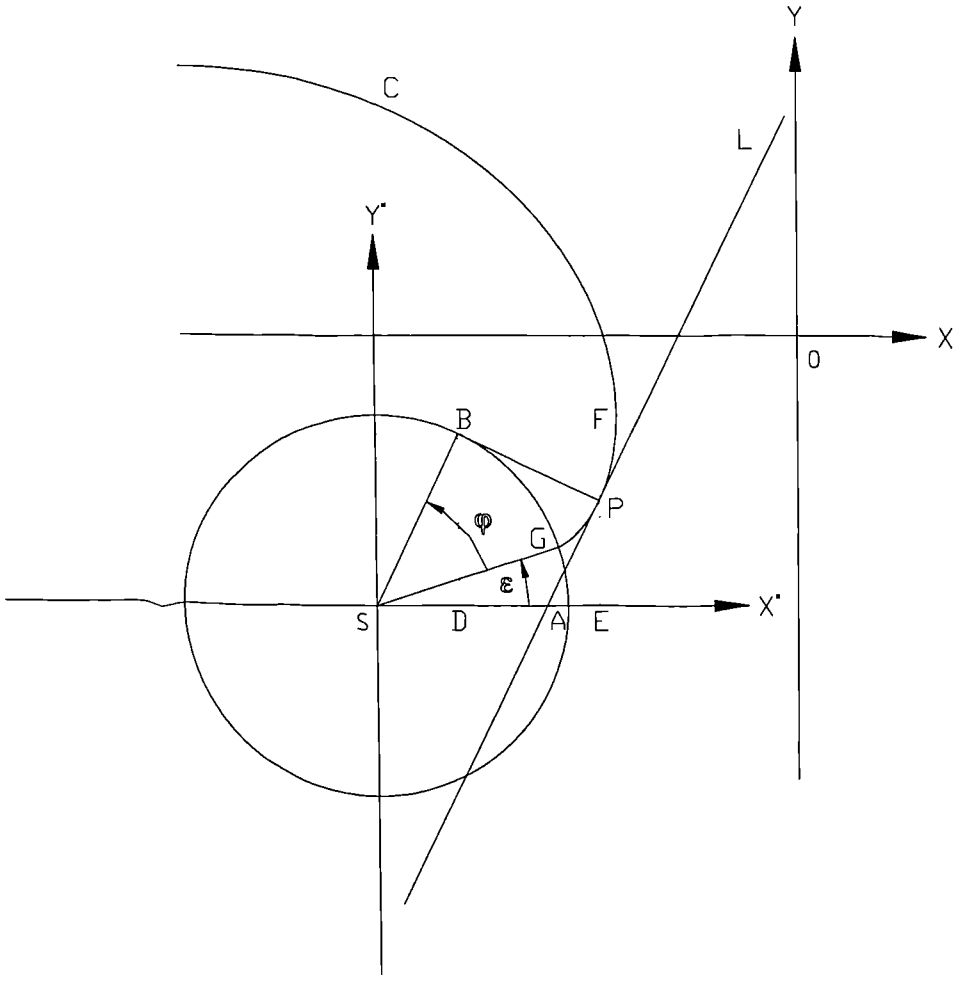

Figure (A-1). General geometry of the involute.

$$C: \begin{pmatrix} x \\ y \end{pmatrix} = \begin{pmatrix} SD + DE \\ EF - PF \end{pmatrix} = \begin{pmatrix} r\cos(\varphi+\varepsilon) + \mathbf{BP}\sin(\varphi+\varepsilon) + S_x \\ r\sin(\varphi+\varepsilon) - \mathbf{BP}\cos(\varphi+\varepsilon) + S_y \end{pmatrix} = \tag{A.3}$$

$$\begin{pmatrix} r\cos(\varphi+\varepsilon) + r\varphi\sin(\varphi+\varepsilon) + S_x \\ r\sin(\varphi+\varepsilon) - r\varphi\cos(\varphi+\varepsilon) + S_y \end{pmatrix}, \quad \varphi \geq \mathbf{0}, \quad 2\pi > \varepsilon \geq \mathbf{0}, \quad \varepsilon = \mathbf{constant}.$$

The starting point G of this curve is obtained form the above equations for $\varphi = \mathbf{0}$. This is the only common point between the curve and the generating circle and its coordinates are

$$G = \begin{pmatrix} x_G \\ y_G \end{pmatrix} = \begin{pmatrix} r\cos(\varepsilon) + S_x \\ r\sin(\varepsilon) + S_y \end{pmatrix}, \quad 2\pi > \varepsilon \geq \mathbf{0}. \tag{A.4}$$

The gradient m of the curve C at any of its points P, can easily be obtained from equation *(A.3)*. Differentiation of this equation once with respect to φ, yields

$$C: \begin{pmatrix} \dfrac{\mathbf{dx}}{\mathbf{d}\varphi} \\ \dfrac{\mathbf{dy}}{\mathbf{d}\varphi} \end{pmatrix} = r\varphi \begin{pmatrix} \cos(\varphi+\varepsilon) \\ \sin(\varphi+\varepsilon) \end{pmatrix}, \quad \varphi \geq \mathbf{0}, \quad 2\pi > \varepsilon \geq \mathbf{0}, \quad \varepsilon = \mathbf{constant}, \tag{A.5}$$

and hence the gradient m is given by

$$m = \tan(\varphi+\varepsilon), \quad \varphi \geq \mathbf{0}, \quad 2\pi > \varepsilon \geq \mathbf{0}, \quad \varepsilon = \mathbf{constant}. \tag{A.6}$$

This is equal to the gradient of the radius SB, a fact obvious from figure (A-1). Consequently, the tangent L to the curve C at the point P is parallel to the radius SB, and according to relations *(A.1)*

The tangent L to the curve C at a point P and the tangent BP to the generating circle are perpendicular, while L is parallel to the radius SB, that is $SB \perp BP$, $L \perp BP$, $SB \parallel L$, *(A.7)*

where the coordinates of the points B and P are given by the relations *(A.2)* and *(A.3)* respectively.

A second Cartesian system X^*Y^* is defined so that its origin is located at the point

$$S = -d\begin{pmatrix} \cos(\theta) \\ \sin(\theta) \end{pmatrix}, \quad d = \mathbf{constant}, \quad \theta \in \Re,$$

and its axes are parallel to the axes of the XY coordinate system as shown in figure (A-1). The symbol $\Re$ denotes the set of the real numbers.

The curves $C_1 \equiv C_{FO}$, $C_2 \equiv C_{FI}$, $C_3 \equiv C_{OO}$ and $C_4 \equiv C_{OI}$, defining the inner and outer surfaces of the fixed and orbiting spirals of the compressor are shown in figure (A-2). The meaning of the subscripts is : FO = Fixed Outer, FI = Fixed Inner, OO = Orbiting Outer, and OI = Orbiting Inner. The analytical expressions for these curves are obtained from equations *(A.1)*, *(A.2)* and *(A.3)* applied for different values of the parameter ε and different locations of the point S. The values of ε and S corresponding to each of these curve are given below

$$
\begin{aligned}
&C_1{=}C_{FO} \;:\; S = \begin{pmatrix}0\\0\end{pmatrix}, && \varepsilon = 0,\\
&C_2{=}C_{FI} \;:\; S = \begin{pmatrix}0\\0\end{pmatrix}, && \varepsilon = \gamma,\quad 0 < \gamma = \text{constant} < \pi/2,\\
&C_3{=}C_{OO} \;:\; S = d\begin{pmatrix}\cos(\pi+\theta)\\ \sin(\pi+\theta)\end{pmatrix}, && \varepsilon = \pi,\\
&C_4{=}C_{OI} \;:\; S = d\begin{pmatrix}\cos(\pi+\theta)\\ \sin(\pi+\theta)\end{pmatrix}, && \varepsilon = \pi+\gamma,\quad 0 < \gamma = \text{constant} < \pi/2,
\end{aligned}
\qquad (A.8)
$$

where by definition, γ is a constant angle, called thickness angle, and

$$
0 < r < d = \text{constant}, \quad \theta \in \Re . \qquad (A.9)
$$

Combining these equations with the relations *(A.3)*, we obtain the equations describing the curves $C_1{=}C_{FO}$, $C_2{=}C_{FI}$, $C_3{=}C_{OO}$ and $C_4{=}C_{OI}$. Thus,

$$
\begin{aligned}
&C_1{=}C_{FO} \;:\; \begin{pmatrix}x_1\\y_1\end{pmatrix} = r\begin{pmatrix}\cos(\varphi)+\varphi\sin(\varphi)\\ \sin(\varphi)-\varphi\cos(\varphi)\end{pmatrix},\\
&C_2{=}C_{FI} \;:\; \begin{pmatrix}x_2\\y_2\end{pmatrix} = r\begin{pmatrix}\cos(\varphi+\gamma)+\varphi\sin(\varphi+\gamma)\\ \sin(\varphi+\gamma)-\varphi\cos(\varphi+\gamma)\end{pmatrix},\\
&C_3{=}C_{OO} \;:\; \begin{pmatrix}x_3\\y_3\end{pmatrix} = -\begin{pmatrix}r(\cos(\varphi)+\varphi\sin(\varphi))+d\cos(\theta)\\ r(\sin(\varphi)-\varphi\cos(\varphi))+d\sin(\theta)\end{pmatrix},\\
&C_4{=}C_{OI} \;:\; \begin{pmatrix}x_4\\y_4\end{pmatrix} = -\begin{pmatrix}r(\cos(\varphi+\gamma)+\varphi\sin(\varphi+\gamma))+d\cos(\theta)\\ r(\sin(\varphi+\gamma)-\varphi\cos(\varphi+\gamma))+d\sin(\theta)\end{pmatrix},
\end{aligned}
\qquad (A.10)
$$

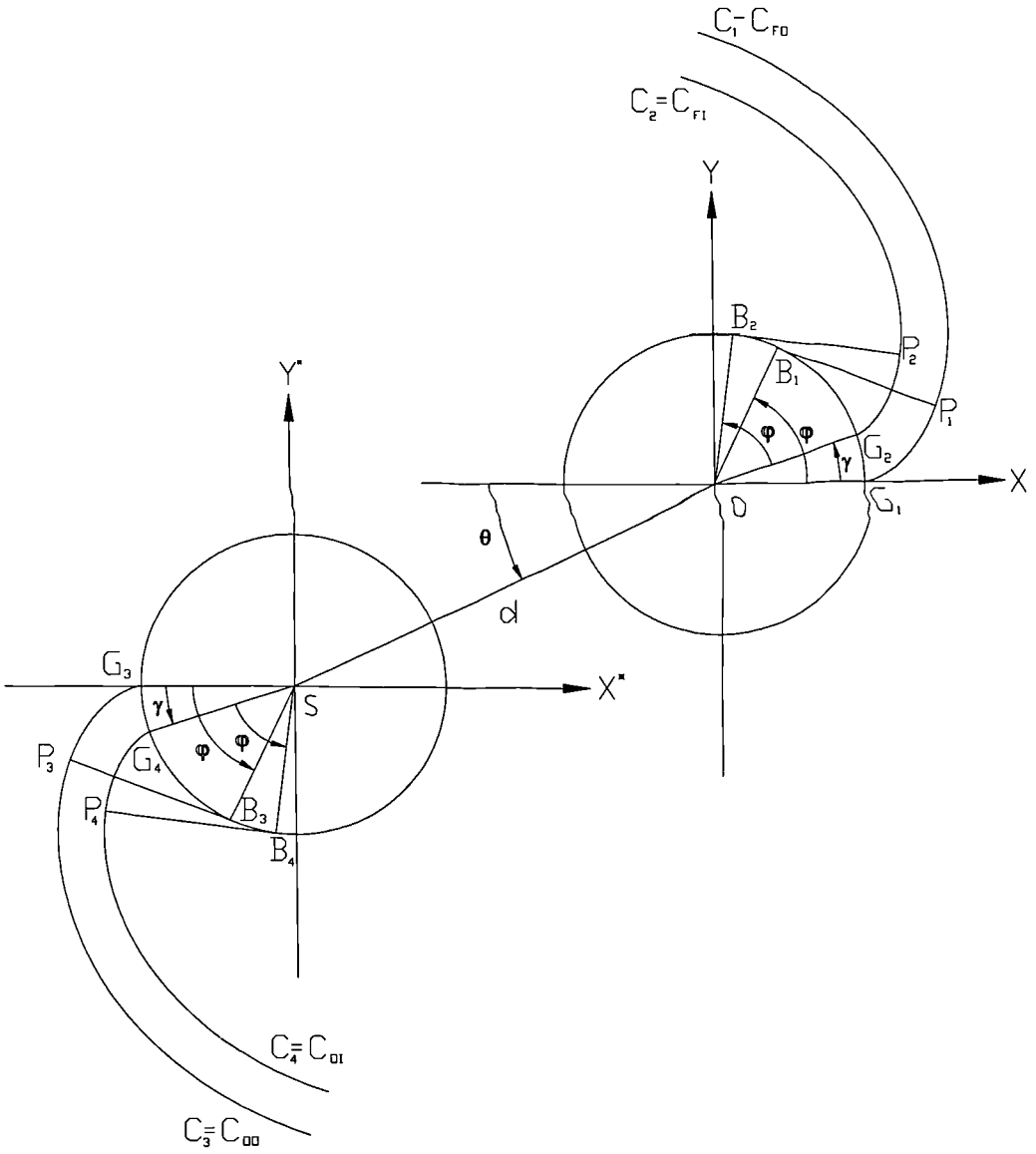

Figure (A-2). Generating circles and involutes.

---

where $\varphi \geq 0$, $0 < \gamma = \text{constant} < \pi/2$, $\theta \in \Re$, $0 < r < d = \text{constant}$.

The starting points of these curves, according to equations *(A.4)* and *(A.8)* are

$$C_1{=}C_{FO}:\ G_1 = \begin{pmatrix} r \\ 0 \end{pmatrix}, \qquad C_2{=}C_{FI}:\ G_2 = r\begin{pmatrix} \cos(\gamma) \\ \sin(\gamma) \end{pmatrix},$$

$$C_3{=}C_{OO}:\ G_3 = -\begin{pmatrix} r + d\cos(\theta) \\ d\sin(\theta) \end{pmatrix}, \quad C_4{=}C_{OI}:\ G_4 = -\begin{pmatrix} r\cos(\gamma) + d\cos(\theta) \\ r\sin(\gamma) + d\sin(\theta) \end{pmatrix}. \tag{A.11}$$

From the relations *(A.8)*, *(A.9)* and *(A.10)* we can easily deduce the following facts, important for the treatment of the present problem. The curves $C_1 = C_{FO}$ and $C_2 = C_{FI}$ are associated with a generating circle whose centre coincides with the origin of the XY Cartesian system, while the curves $C_3 = C_{OO}$ and $C_4 = C_{OI}$ are associated with a second generating circle whose centre is located at the origin of the X^*Y^* Cartesian system. The parameter φ appearing in the definitions *(A.10)* of the curves, is always measured anti-clockwise. However, for the curve $C_1 = C_{FO}$ it is measured from the positive X semi-axis, for the curve $C_2 = C_{FI}$ it is measured from the line OG_2, for the curve $C_3 = C_{OO}$ it is measured from the negative X^* semi-axis and for of the curve $C_4 = C_{OI}$ it is measured from the line SG_4. Finally, the angle θ is measured anti-clockwise from the negative X semi-axis. All these facts are shown in the figure (A-2).

The gradients m_i $(i=1,2,3,4)$ of the curves C_i $(i=1,2,3,4)$ for any given value of the parameter φ, are obtained from equation *(A.6)* upon introduction of the values of the parameter ε given in equations *(A.8)*, thus

$$
\begin{aligned}
&C_1 = C_{FO}: \quad m_1 = \tan\varphi, && \varphi \geq 0, \\
&C_2 = C_{FI}: \quad m_2 = \tan(\varphi + \gamma), && \varphi \geq 0, \quad 0 < \gamma = \text{constant} < \pi/2, \\
&C_3 = C_{OO}: \quad m_3 = \tan\varphi, && \varphi \geq 0, \\
&C_4 = C_{OI}: \quad m_4 = \tan(\varphi + \gamma), && \varphi \geq 0, \quad 0 < \gamma = \text{constant} < \pi/2.
\end{aligned}
\qquad (A.12)
$$

We now proceed with the determination of the distances between the pairs of the curves $C_1 = C_{FO}$, $C_2 = C_{FI}$, and $C_3 = C_{OO}$, $C_4 = C_{OI}$. As it will be shown below, these distances are equal throughout the lengths of the spirals. They are thus independent of the value of the parameter φ.

By construction, the points P_1, P_2, P_3 and P_4, shown in figure (A-3), correspond to the same, arbitrary value of the parameter φ, say ω. The segments B_iP_i $(i=1,2,3,4)$, drawn from these points, are tangents to the generating circles at the points B_i $(i=1,2,3,4)$. The points Q_1 and Q_3 are the intersections of the curves C_1 and C_3 with the produced segments B_2P_2 and B_4P_4. Finally, the lines L_i $(i=1,2,3,4)$, also shown in the figure, are the tangents to the curves C_i $(i=1,2,3,4)$ at the points Q_1, P_2, Q_3, and P_4 respectively.

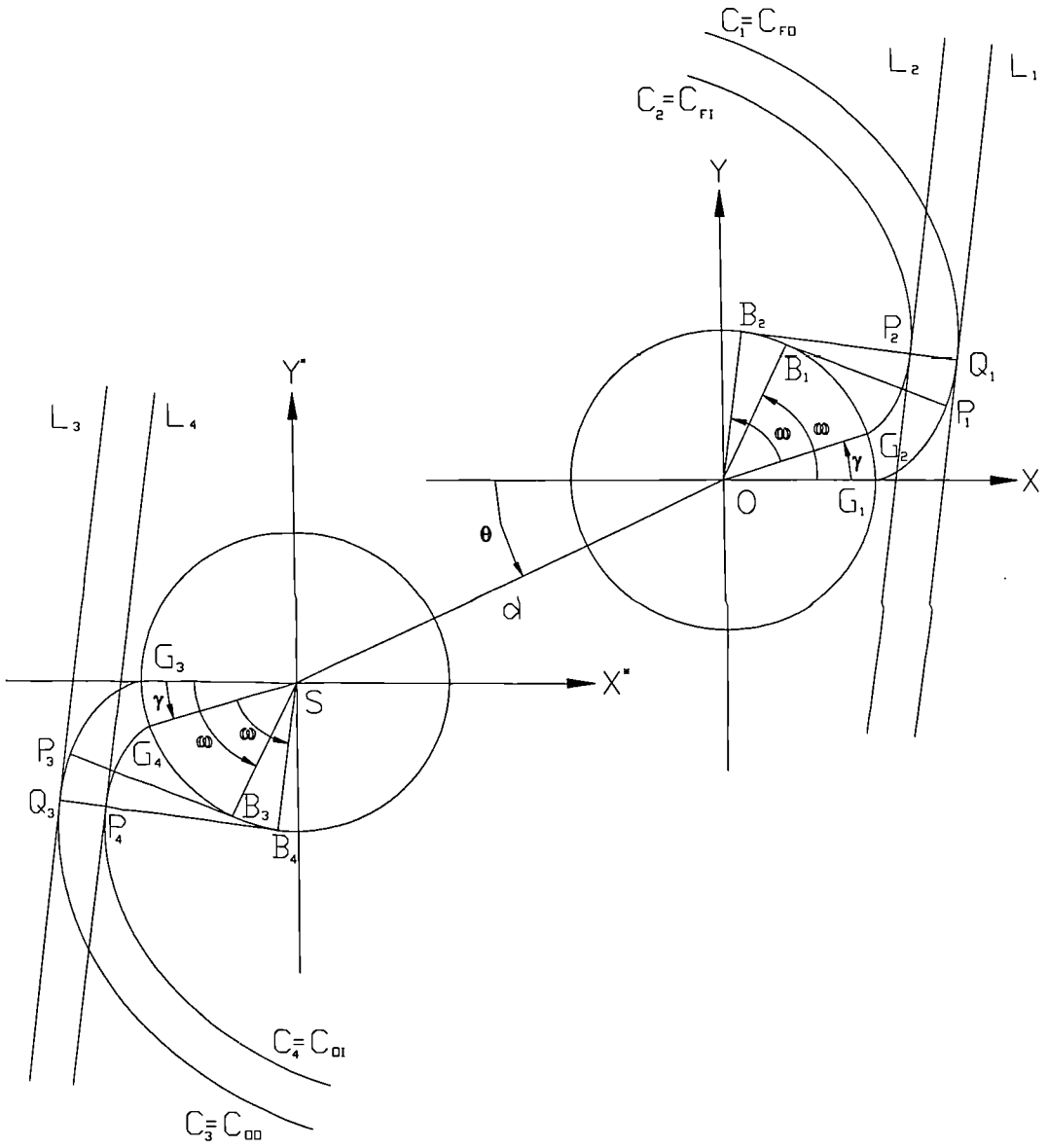

Figure (A-3). Generating circles, involutes and their tangents.

Clearly, the values of the parameter φ corresponding to the points Q_1, P_2, Q_3, and P_4, are given by

$$\begin{aligned} &P_2 \text{ and } P_4 \;:\; \varphi = \omega, \qquad \omega \geq 0\ , \\ &Q_1 \text{ and } Q_3 \;:\; \varphi = \omega + \gamma, \quad \omega \geq 0\,,\ 0 < \gamma = \mathbf{constant} < \pi/2\,. \end{aligned} \tag{A.13}$$

Substitution of these values into equations *(A.10)* yields the coordinates of the

above mentioned points. Hence

$$Q_1 : \begin{pmatrix} x_{Q1} \\ y_{Q1} \end{pmatrix} = r\begin{pmatrix} \cos(\omega+\gamma)+(\omega+\gamma)\sin(\omega+\gamma) \\ \sin(\omega+\gamma)-(\omega+\gamma)\cos(\omega+\gamma) \end{pmatrix}, \quad \varphi = \omega+\gamma,$$

$$P_2 : \begin{pmatrix} x_{P2} \\ y_{P2} \end{pmatrix} = r\begin{pmatrix} \cos(\omega+\gamma)+\omega\sin(\omega+\gamma) \\ \sin(\omega+\gamma)-\omega\cos(\omega+\gamma) \end{pmatrix}, \quad \varphi = \omega, \tag{A.14}$$

$$Q_3 : \begin{pmatrix} x_{Q3} \\ y_{Q3} \end{pmatrix} = -\begin{pmatrix} r(\cos(\omega+\gamma)+(\omega+\gamma)\sin(\omega+\gamma))+d\cos(\theta) \\ r(\sin(\omega+\gamma)-(\omega+\gamma)\cos(\omega+\gamma))+d\sin(\theta) \end{pmatrix}, \quad \varphi = \omega+\gamma,$$

$$P_4 : \begin{pmatrix} x_{P4} \\ y_{P4} \end{pmatrix} = -\begin{pmatrix} r(\cos(\omega+\gamma)+\omega\sin(\omega+\gamma))+d\cos(\theta) \\ r(\sin(\omega+\gamma)-\omega\cos(\omega+\gamma))+d\sin(\theta) \end{pmatrix}, \quad \varphi = \omega,$$

where $\omega \geq 0$.

Furthermore, combining equations *(A.13)* with equations *(A.12)*, it is easy to prove that the lines L_i ($i=1,2,3,4$), OB_2 and SB_4 are parallel, with gradients given by

$$m_1 = m_2 = m_3 = m_4 = \tan(\omega+\gamma),$$

On the other hand, the line segments B_2Q_1 and B_4Q_3 are perpendicular to the radii OB_2 and SB_4 and hence they are also perpendicular to the lines L_i ($i=1,2,3,4$).

From the above discussion it is evident that B_2Q_1 and B_4Q_3 are perpendicular to the curves C_i ($i=1,2,3,4$), at the points Q_1, P_2, Q_3, and P_4. Consequently, P_2Q_1 is the distance between the curves $C_1=C_{FO}$ and $C_2=C_{FI}$, while P_4Q_3 is the distance between the curves $C_3=C_{OO}$ and $C_4=C_{OI}$. These distances, easily derived from equations *(A.14)*, are independent of the parameter φ. They are equal and depend only on the common radius r of the generating circles and the thickness angle γ, that is,

$$\text{Distance between } C_1 \text{ and } C_2 = P_2Q_1 = \sqrt{(x_{P2}-x_{Q1})^2+(y_{P2}-y_{Q1})^2} = r\gamma, \tag{A.15}$$

$$\text{Distance between } C_3 \text{ and } C_4 = P_4Q_3 = \sqrt{(x_{P4}-x_{Q3})^2+(y_{P4}-y_{Q3})^2} = r\gamma,$$

where $0 < \gamma = \text{constant} < \pi/2$, $0 < r < d = \text{constant}$.

It is worth noting that the distance between the curves is equal to the lengths of the arcs G_1G_2 or G_3G_4, to which the thickness angle γ subtends. Furthermore, the curves $C_1=C_{FO}$, $C_2=C_{FI}$, $C_3=C_{OO}$ and $C_4=C_{OI}$ are perpendicular to the generating circles at their starting points.

A.2.2 Contact Conditions

It is now assumed that the curves $C_1=C_{FO}$ and $C_4=C_{OI}$ have been constructed in such a way that they never intersect each other, but there exist points at which they are tangent. The same assumptions are also made for the pair of the curves $C_2=C_{FI}$ and $C_3=C_{OO}$. Two such touching points are illustrated in figure (A-4). Clearly, at these points the touching curves (either C_1 and C_4 or C_2 and C_3) have the same coordinates and the same gradients. However, the value of the parameter φ at these points would be different for each curve. Denoting the values of φ, corresponding to the curves C_i ($i=1,2,3,4$), by φ_i ($i=1,2,3,4$) respectively and introducing equations ***(A.10)*** and ***(A.12)***, the above assumptions for the pair of curves C_1 and C_4 are fully described by the following relations

$$\begin{aligned} r\cos(\varphi_1)+r\varphi_1\sin(\varphi_1) &= -r\cos(\varphi_4+\gamma)-r\varphi_4\sin(\varphi_4+\gamma)-d\cos(\theta), \\ r\sin(\varphi_1)-r\varphi_1\cos(\varphi_1) &= -r\sin(\varphi_4+\gamma)+r\varphi_4\cos(\varphi_4+\gamma)-d\sin(\theta), \\ \tan(\varphi_1) &= \tan(\varphi_4+\gamma), \end{aligned} \qquad (A.16)$$

while the corresponding equations for the pair of the curves C_2 and C_3 are

$$\begin{aligned} r\cos(\varphi_2+\gamma)+r\varphi_2\sin(\varphi_2+\gamma) &= -r\cos(\varphi_3)-r\varphi_3\sin(\varphi_3)-d\cos(\theta), \\ r\sin(\varphi_2+\gamma)-r\varphi_2\cos(\varphi_2+\gamma) &= -r\sin(\varphi_3)+r\varphi_3\cos(\varphi_3)-d\sin(\theta), \\ \tan(\varphi_2+\gamma) &= \tan(\varphi_3). \end{aligned} \qquad (A.17)$$

The above algebraic systems obey the conditions

$$\varphi_i \geq 0 \quad (i=1,2,3,4), \qquad 0<\gamma=\text{constant}<\pi/2, \quad \theta\in\Re,$$
$$0<r<d=\text{constant}. \qquad (A.18)$$

The last of equations ***(A.16)*** and ***(A.17)*** have the following general solutions

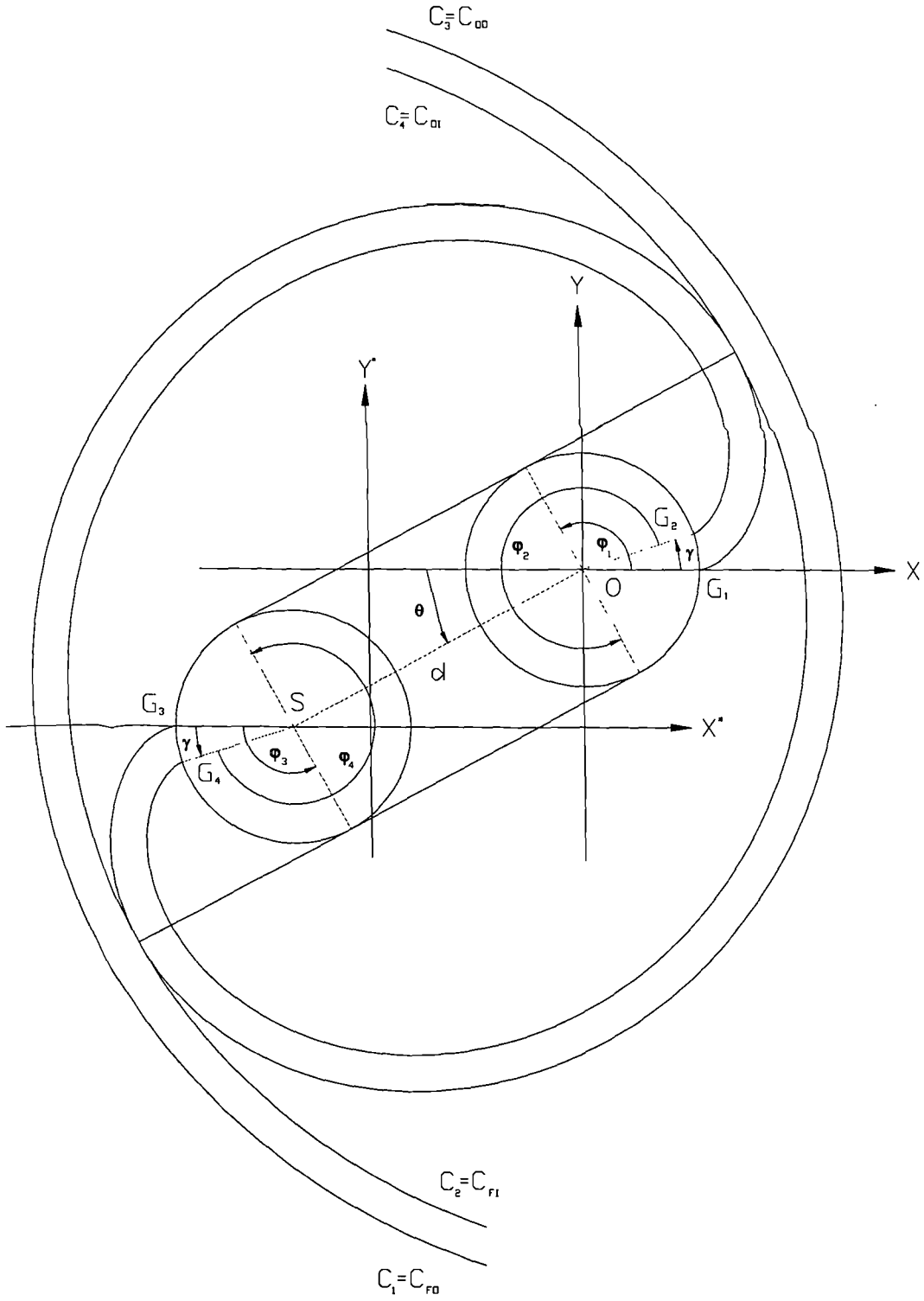

Figure (A-4). Involutes and their innermost touching points.

$$\begin{aligned}
&\varphi_4 = (2k+1)\pi + \varphi_1 - \gamma, && k \in \backslash W, && \varphi_1,\ \varphi_4 \geq 0,\\
&\varphi_4 = 2k\pi + \varphi_1 - \gamma, && k \in \backslash W, && \varphi_1,\ \varphi_4 \geq 0,\\
&\varphi_4 = -(2k+1)\pi + \varphi_1 - \gamma, && k \in \backslash W, && \varphi_1,\ \varphi_4 \geq 0,\\
&\varphi_4 = -2k\pi + \varphi_1 - \gamma, && k \in \backslash W, && \varphi_1,\ \varphi_4 \geq 0,
\end{aligned} \qquad (A.19)$$

and

$$\begin{aligned}
&\varphi_2 = (2k+1)\pi + \varphi_3 - \gamma, && k \in \backslash W, && \varphi_2,\ \varphi_3 \geq 0,\\
&\varphi_2 = 2k\pi + \varphi_3 - \gamma, && k \in \backslash W, && \varphi_2,\ \varphi_3 \geq 0,\\
&\varphi_2 = -(2k+1)\pi + \varphi_3 - \gamma, && k \in \backslash W, && \varphi_2,\ \varphi_3 \geq 0,\\
&\varphi_2 = -2k\pi + \varphi_3 - \gamma, && k \in \backslash W, && \varphi_2,\ \varphi_3 \geq 0,
\end{aligned} \qquad (A.20)$$

where the symbol $\backslash W$ denotes the set of the whole numbers.

Introducing the solutions *(A.19)* into equations *(A.16)* and the solutions *(A.20)* into equations *(A.17)*, squaring and adding the resulting expressions, we obtain the following relations

$$\begin{aligned}
&d = r\left[(2k+1)\pi - \gamma\right], && \varphi_4 = (2k+1)\pi + \varphi_1 - \gamma,\\
& && \varphi_2 = (2k+1)\pi + \varphi_3 - \gamma,\\
&d = r\left[(2k+1)\pi + \gamma\right], && \varphi_4 = \varphi_1 - \gamma - (2k+1)\pi,\\
& && \varphi_2 = \varphi_3 - \gamma - (2k+1)\pi,\\
&d = r\sqrt{4 + \left[2k\pi + 2\varphi_1 - \gamma\right]^2}, && \varphi_4 = 2k\pi + \varphi_1 - \gamma,\\
&d = r\sqrt{4 + \left[2k\pi + 2\varphi_3 - \gamma\right]^2}, && \varphi_2 = 2k\pi + \varphi_3 - \gamma,\\
&d = r\sqrt{4 + \left[2\varphi_1 - \gamma - 2k\pi\right]^2}, && \varphi_4 = \varphi_1 - \gamma - 2k\pi,\\
&d = r\sqrt{4 + \left[2\varphi_3 - \gamma - 2k\pi\right]^2}, && \varphi_2 = \varphi_3 - \gamma - 2k\pi,
\end{aligned} \qquad (A.21)$$

where $\varphi_i \geq 0$ $(i=1,2,3,4)$, $0<\gamma<\pi/2$, $0<r<d$, $k \in \backslash W$.

The restriction imposed upon d from the last of the relations *(A.18)* implies that the last four of the above solutions are unacceptable since they depend on either φ_1 or φ_3 and hence such a d is not constant. In order to select one of the first two solutions, we impose the following "***extra***" condition : the distance d must have the minimum possible value satisfying the relations *(A.16)*, *(A.17)* and *(A.21)*. Under this condition, the first of the above equations for $k=0$ yields

$$d = r(\pi - \gamma),$$

$$\varphi_4 = \pi + \varphi_1 - \gamma, \quad \varphi_2 = \pi + \varphi_3 - \gamma, \qquad (A.22)$$

$$\varphi_i \geq 0 \ (i=1,2,3,4), \quad 0<\gamma = \mathbf{constant} < \pi/2, \quad 0<r<d = \mathbf{constant}.$$

We must of course justify the imposition of the "***extra***" condition mentioned above. Any other constant value of d given by equations *(A.21)*, except the minimum, produces spirals that not only touch but intersect each other as well. For example the second of equations *(A.21)*, for $k=0$ furnishes

$$d = r(\pi + \gamma),$$

$$\varphi_4 = \varphi_1 - \gamma - \pi, \quad \varphi_2 = \varphi_3 - \gamma - \pi,$$

$$\varphi_i \geq 0 \ (i=1,2,3,4), \quad 0<\gamma = \mathbf{constant} < \pi/2, \quad 0<r<d = \mathbf{constant}.$$

This value of d differs from the minimum given by equation *(A.22)* by $2r\gamma$ which according to expressions *(A.15)*, is twice the thickness of the spirals. This increase of d corresponds to a movement of the orbiting spiral away from the origin O by $2r\gamma$. Consequently, for $d = r(\pi + \gamma)$ the spirals touch and intersect each other simultaneously as shown in the figure of next page.

Having found the expression for the distance between the centres of the two generating circles, we proceed with the determination of the relation between the parameters φ and θ at the touching points. Substituting equations *(A.22)* into equations *(A.16)* and *(A.17)*, and after some algebraic calculations, we obtain

$$\tan(\varphi_1) = -\cot(\theta), \quad \tan(\varphi_3) = -\cot(\theta),$$

$$\varphi_4 = \pi + \varphi_1 - \gamma, \ \varphi_2 = \pi + \varphi_3 - \gamma, \ \varphi_i \geq 0 \ (i=1,2,3,4), \quad d = r(\pi - \gamma), \qquad (A.23)$$

$$0<\gamma = \mathbf{constant} < \pi/2, \quad \theta \in \Re.$$

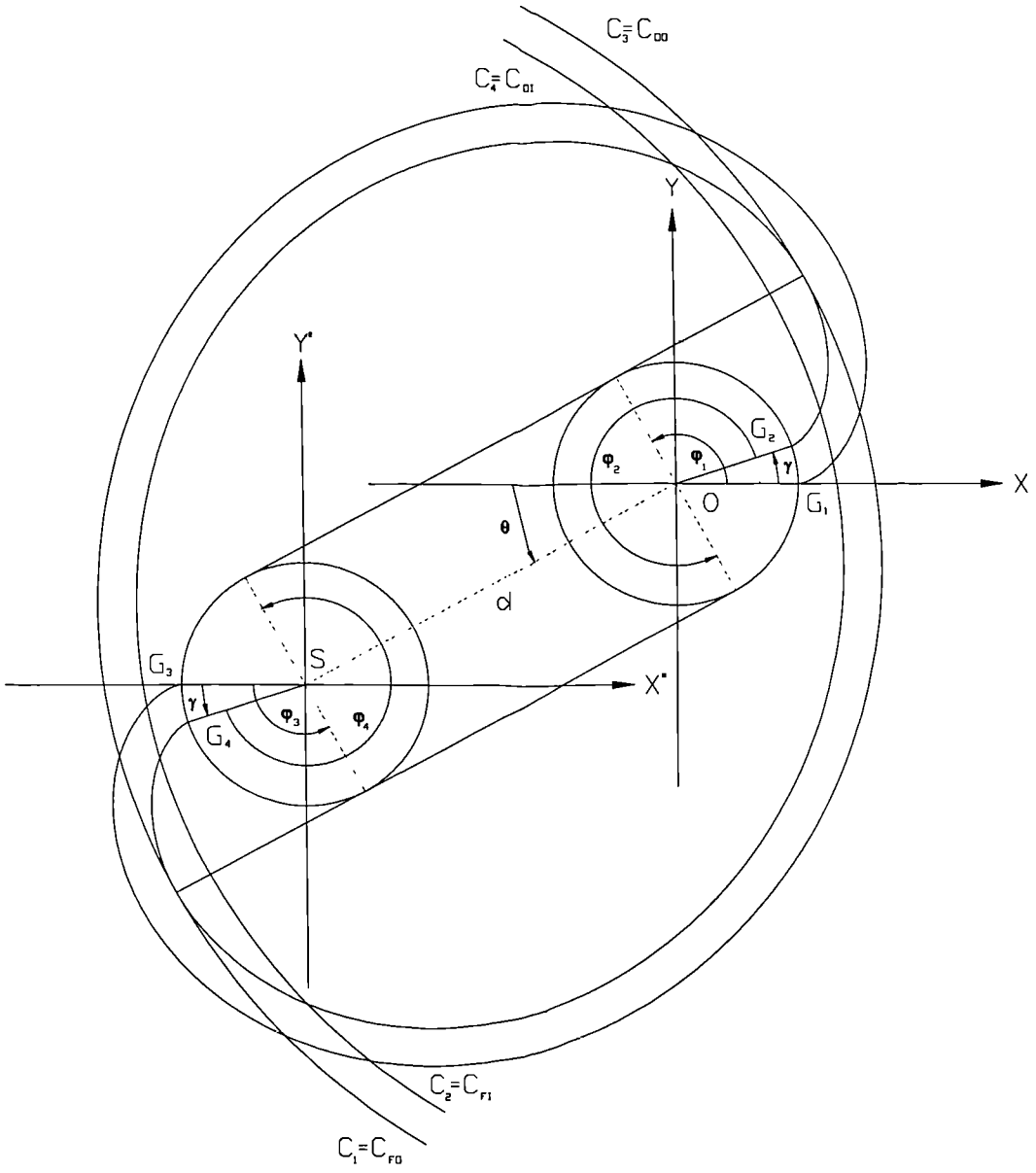

Figure (A-5). The involutes touching internally.

These trigonometric equations have the following general solutions

$$\varphi_1 = 2k\pi + \frac{\pi}{2} + \theta \quad \text{or} \quad \theta = 2k\pi + \frac{\pi}{2} + \varphi_1 \quad \text{or} \quad \theta = (2k+1)\pi + \frac{\pi}{2} + \varphi_1, \tag{A.24}$$

$$\varphi_3 = 2k\pi + \frac{\pi}{2} + \theta \quad \text{or} \quad \theta = 2k\pi + \frac{\pi}{2} + \varphi_3 \quad \text{or} \quad \theta = (2k+1)\pi + \frac{\pi}{2} + \varphi_3.$$

In order to select one of the above solutions, we impose the restrictions implied from the relations *(A.23)* and figure (A-4), that is

$$\theta < \varphi_1 < \varphi_4, \quad \theta < \varphi_3 < \varphi_2, \tag{A.25}$$

and hence at the touching points the following relations hold

$$\varphi_1 = 2k\pi + \frac{\pi}{2} + \theta, \quad \varphi_3 = 2k\pi + \frac{\pi}{2} + \theta,$$

$$\varphi_4 = \pi + \varphi_1 - \gamma, \quad \varphi_2 = \pi + \varphi_3 - \gamma, \quad \varphi_i \geq 0 \ (i=1,2,3,4), \quad d = r(\pi - \gamma), \tag{A.26}$$

$$0 < \gamma = \text{constant} < \pi/2, \quad k \in W, \quad \theta \in \Re.$$

Clearly, the relations between the angles φ_1, φ_4 and θ refer to the touching conditions of the curves C_1=C_{FO} and C_4=C_{OI}, while the relations between the angles φ_2, φ_3 and θ refer to the touching conditions of the curves C_2=C_{FI} and C_3=C_{OO}.

Two other solutions satisfy equations *(A.23)* and the restrictions *(A.25)*, namely

$$\varphi_1 = (2k+1)\pi + \frac{\pi}{2} + \theta, \ \varphi_3 = (2k+1)\pi + \frac{\pi}{2} + \theta, \ \varphi_4 = \pi + \varphi_1 - \gamma, \ \varphi_2 = \pi + \varphi_3 - \gamma.$$

These however correspond to the internal touching points as shown in figure (A-5), and are unacceptable.

A.2.3 Starting Points - Inner Circular Arcs

Under the conditions *(A.22)* and *(A.26)* not only the external curves touch with the internal curves in pairs (C_1 =C_{FO}, C_4 =C_{OI} and C_2=C_{FI}, C_3=C_{OO}), but for a specific value of θ the external curves C_1=C_{FO} and C_3=C_{OO} touch externally as well. This situation is illustrated in the figure (A-6). Clearly at the point of touching these curves have the same coordinates and equal gradients. Denoting the value of the parameter φ at this point by φ_{1S} for the curve C_1=C_{FO} and by φ_{3S} for the curve C_3=C_{OO}, and introducing the relations *(A.10)* and *(A.12)*, the touching conditions are fully described by the following relations

$$\begin{aligned} r\cos(\varphi_{1S}) + r\varphi_{1S}\sin(\varphi_{1S}) &= -r\cos(\varphi_{3S}) - r\varphi_{3S}\sin(\varphi_{3S}) - d\cos(\theta), \\ r\sin(\varphi_{1S}) - r\varphi_{1S}\cos\varphi_{1S}) &= -r\sin(\varphi_{3S}) + r\varphi_{3S}\cos(\varphi_{3S}) - d\sin(\theta), \\ \tan(\varphi_{1S}) &= \tan(\varphi_{3S}). \end{aligned} \tag{A.27}$$

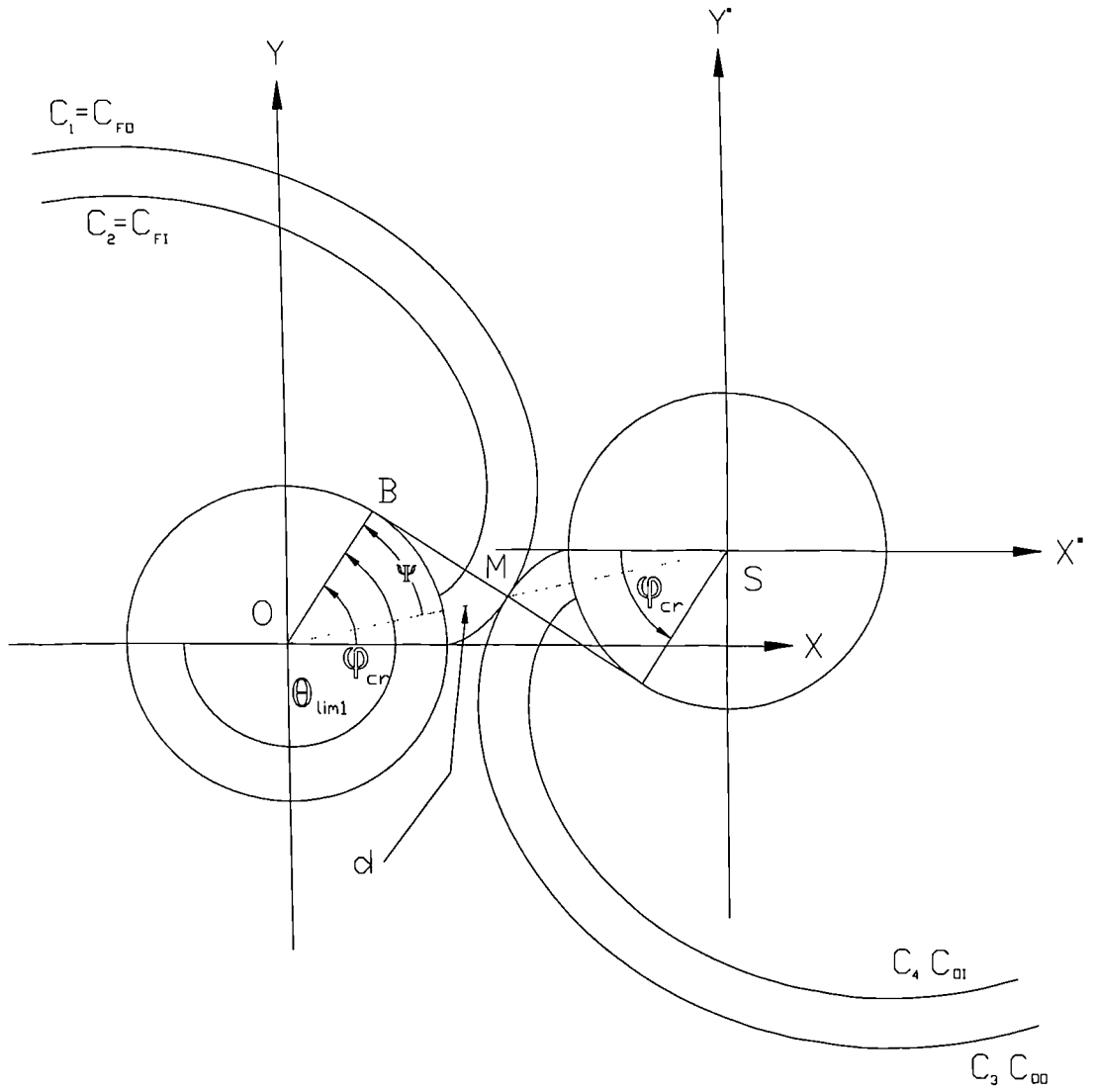

Figure (A-6). The trimming point of the external involutes.

These are, of course, subject to the conditions *(A.18)* and *(A.22)*. That is

$$d = r(\pi - \gamma), \quad \varphi_{1S}, \ \varphi_{3S} \geq 0, \quad 0 < r < d = \text{constant},$$
$$\theta \in \Re, \quad 0 < \gamma = \text{constant} < \pi/2. \tag{A.28}$$

Given that $|\varphi_{1S} - \varphi_{3S}| < 2\pi$, the general solution of the last of *(A.27)* has the form

$$\varphi_{1S} = \varphi_{3S} + \pi, \quad \varphi_{3S} = \varphi_{1S} + \pi, \quad \varphi_{1S} = \varphi_{3S}. \tag{A.29}$$

Substituting any of the first two of these solutions into equations *(A.27)*, squaring and adding the resulting expressions and after some rearrangements, we get

$$d = r\pi\,, \quad \varphi_{1S} = \varphi_{3S} + \pi\,, \quad \varphi_{3S} = \varphi_{1S} + \pi\,.$$

These relations do not agree with the first of the expressions *(A.22)* and they are therefore unacceptable. On the other hand, combining the last of the solutions *(A.29)* with equations *(A.27)* and *(A.28)*, following steps similar to the steps described above and rejecting negative values for φ_{1S} and φ_{3S}, we find that the curves C_1=C_{FO} and C_3=C_{OO} touch externally when

$$\begin{gathered}\varphi_{1S},\ \varphi_{3S} = \sqrt{\left(\frac{d}{2r}\right)^2 - 1}\,, \quad \varphi_{1S} = \varphi_{3S}\,, \\ d = r(\pi - \gamma)\,, \quad \varphi_{1S},\ \varphi_{3S} \geq 0\,, \quad 0 < r < d = \mathbf{constant}\,, \\ \theta \in \Re\,, \quad 0 < \gamma = \mathbf{constant} < \pi/2\,.\end{gathered} \tag{A.30}$$

The first of these relations implies the condition

$$d \geq 2r\,,$$

which is evident from the geometry shown in figures (A-2), (A-3) and (A-4). Note that for $d = r(\pi - \gamma)$, the above inequality furnishes $(\pi - 2) \geq \gamma$. Given that $\pi/2 > \pi - 2$, the condition $0 < \gamma = \mathbf{constant} < \pi/2$ appearing in most of the above equations, must be substituted by

$$0 < \gamma = \mathbf{constant} \leq \pi - 2\,. \tag{A.31}$$

Evidently, for values of the parameter φ less than the critical angle

$$\varphi_{cr} \equiv \sqrt{\left(\frac{d}{2r}\right)^2 - 1} = \sqrt{[(\pi - \gamma)/2]^2 - 1}\,, \quad 0 < \gamma = \mathbf{constant} \leq \pi - 2\,, \tag{A.32}$$

there exist values of the crank angle θ for which the spirals intersect each other. We are therefore forced to introduce one more condition while defining the curves C_i (i=1,2,3,4), namely

$$\varphi \geq \varphi_{cr} = \sqrt{\left(\frac{\pi - \gamma}{2}\right)^2 - 1}\,, \quad 0 < \gamma = \mathbf{constant} \leq \pi - 2\,. \tag{A.33}$$

This condition, being a general one, holds true at the contact points of the curves C_i ($i=1,2,3,4$) as well. Thus, in the case of the curves $C_1=C_{FO}$ and $C_3=C_{OO}$, though equations *(A.26)* imply that the values φ_1 and φ_3 of the parameter φ at the points of touching can lie anywhere in the semi-open interval **[0, ∞)** as the crank angle θ varies in the range $(-\infty, +\infty)$, the above inequality restricts the range of φ_1 and φ_3 to values greater than or equal to φ_{cr}, thus

$$\varphi_1,\ \varphi_3 \geq \varphi_{1S} = \varphi_{3S} = \varphi_{cr} = \sqrt{\left(\frac{\pi-\gamma}{2}\right)^2 - 1}\,, \quad 0 < \gamma = \mathbf{constant} \leq \pi - 2. \qquad (A.34)$$

Similarly, for the curves $C_2=C_{FI}$ and $C_4=C_{OI}$, according to equations *(A.26)* and *(A.34)*, the values φ_2 and φ_4 of the parameter φ at the points of touching satisfy the relation

$$\varphi_2,\ \varphi_4 \geq \varphi_{2S} = \varphi_{4S} = (\varphi_{cr} + \pi - \gamma) = \sqrt{\left(\frac{\pi-\gamma}{2}\right)^2 - 1} + \pi - \gamma\,,$$

$$0 < \gamma = \mathbf{constant} \leq \pi - 2. \qquad (A.35)$$

The above two restrictions must hold regardless of the value of the crank angle θ.

It must be stressed here that for values of φ_2 or φ_4 less than φ_{2S} or φ_{4S}, the curves $C_2=C_{FI}$ and $C_4=C_{OI}$ do not have any contact points, since a drop in the value φ_2 or φ_4 below $\varphi_{2S} = \varphi_{4S} = (\varphi_{cr} + \pi - \gamma)$ implies a drop in the values of φ_1 or φ_3 below φ_{cr}. This of course, according to restriction *(A.34)*, is unacceptable. However, for values of the parameter φ in the closed interval $[\varphi_{cr}, (\varphi_{cr} + \pi - \gamma)]$, we require that -as the moving spiral rotates in a circular orbit round the fixed spiral- the curves $C_2=C_{FI}$ and $C_4=C_{OI}$ are continuously in touch with the starting points G_3 and G_1 of the curves $C_3=C_{OO}$ and $C_1=C_{FO}$ respectively. This is of great importance in the design of the scroll compressor if leakage of the flow from the discharge chamber to the last pair of compression chambers is to be avoided.

The above requirement can be satisfied if and only if the sections of the curves $C_2=C_{FI}$ and $C_4=C_{OI}$, defined for values of φ in the range $\varphi_{cr} \leq \varphi \leq (\varphi_{cr} + \pi - \gamma)$, are replaced by the paths followed by the starting points of the curves $C_1=C_{FO}$ and $C_3=C_{OO}$ as the scroll device is in motion. It will be proved below that these paths are circular arcs. The relevant geometry is shown in figures (A-7a) and (A-7b).

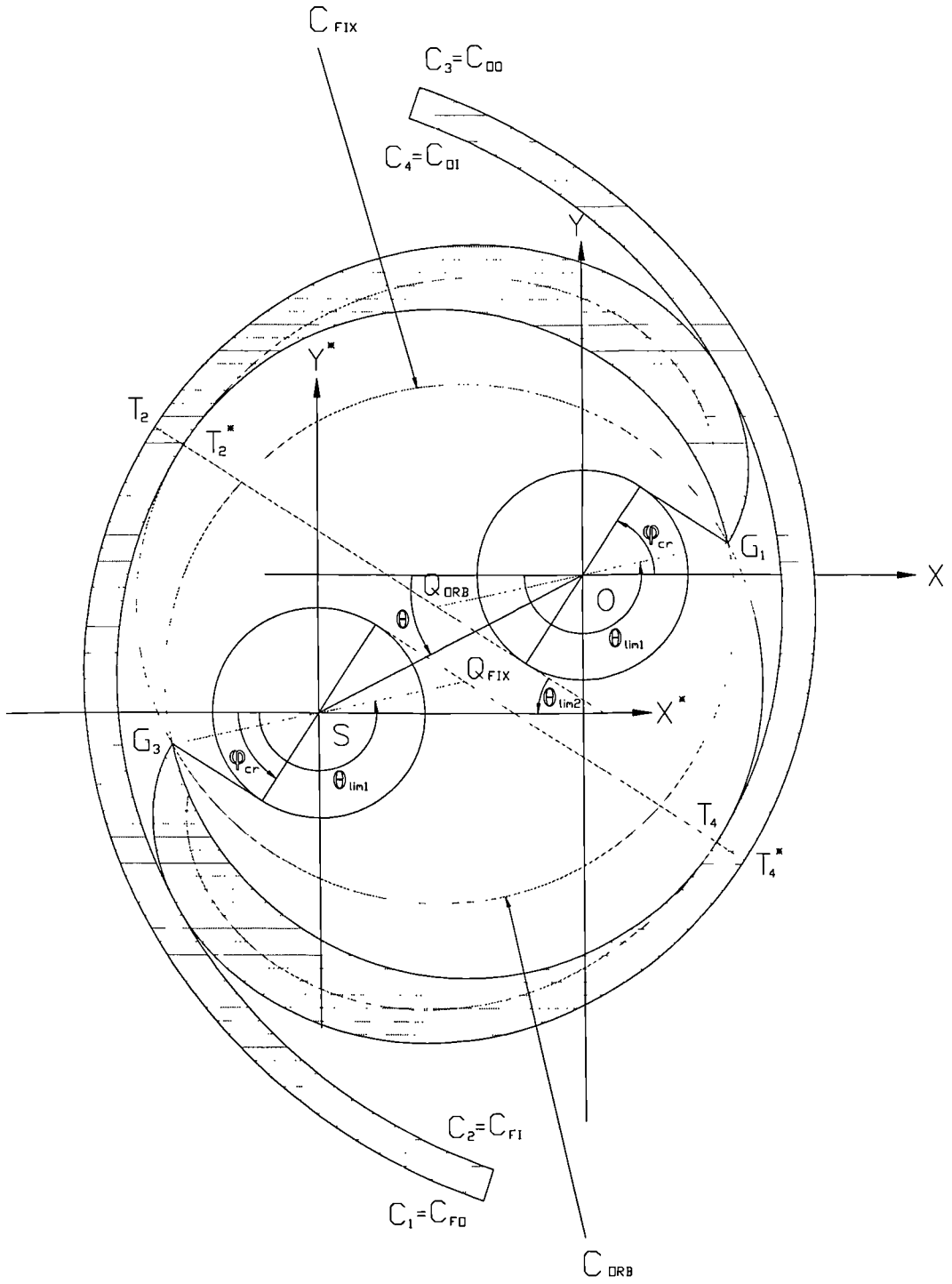

Figure (A-7a). Replacement of internal involutes by circular arcs.

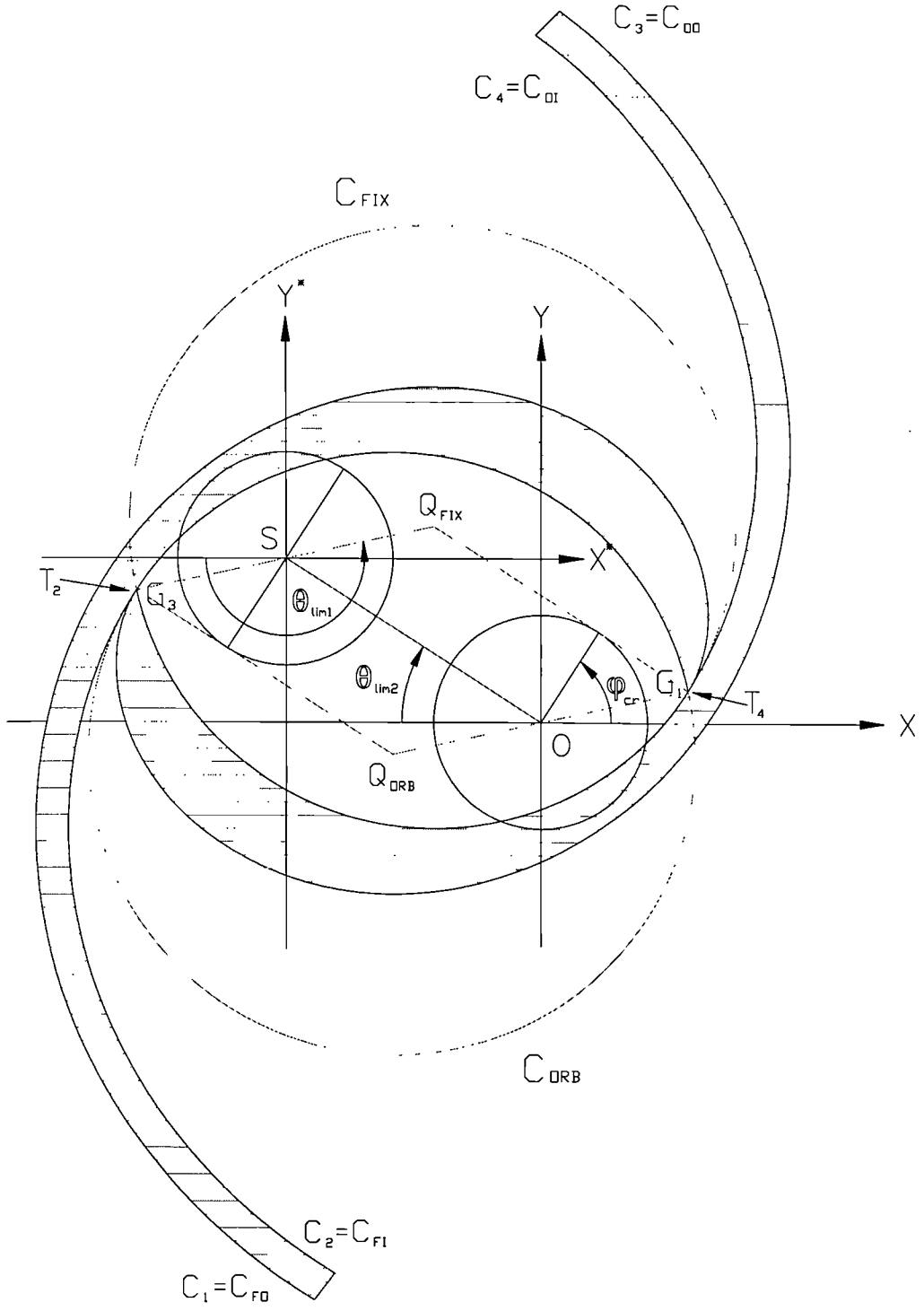

Figure (A-7b). Contact of spiral tips with inner circular arcs.

The condition *(A.33)* alters the starting points of the curves, which are not any more given by equations *(A.11)*. Instead, equations *(A.10)* upon introduction of the critical angle φ_{cr}, yield the starting points or tips G_1 and G_3 of the curves C_1=C_{FO} and C_3=C_{OO} respectively, that is

$$C_1=C_{FO} \;:\; G_1 = r\begin{pmatrix}\cos(\varphi_{cr})+\varphi_{cr}\sin(\varphi_{cr})\\ \sin(\varphi_{cr})-\varphi_{cr}\cos(\varphi_{cr})\end{pmatrix},$$

$$C_3=C_{OO} \;:\; G_3 = \begin{pmatrix}-r(\cos(\varphi_{cr})+\varphi_{cr}\sin(\varphi_{cr}))+d\cos(\pi+\theta)\\ -r(\sin(\varphi_{cr})-\varphi_{cr}\cos(\varphi_{cr}))+d\sin(\pi+\theta)\end{pmatrix}. \qquad (A.36)$$

The starting points G_2 and G_4 of the curves C_2=C_{FI} and C_4=C_{OI} will be discussed later on in this sub-section.

The introduction of the values $\varphi_{2S} = \varphi_{4S} = (\varphi_{cr} + \pi - \gamma)$ into equations *(A.10)* furnishes the coordinates of the points T_2 and T_4 shown in figures (A-7). At these points the tips G_1 and G_3 touch the curves C_2=C_{FI} and C_4=C_{OI} nearest to the generating circles for the first time respectively, thus

$$C_2=C_{FI} \;:\; T_2 = -r\begin{pmatrix}\cos(\varphi_{cr})+(\varphi_{cr}+\pi-\gamma)\sin(\varphi_{cr})\\ \sin(\varphi_{cr})-(\varphi_{cr}+\pi-\gamma)\cos(\varphi_{cr})\end{pmatrix},$$

$$C_4=C_{OI} \;:\; T_4 = \begin{pmatrix}r(\cos(\varphi_{cr})+(\varphi_{cr}+\pi-\gamma)\sin(\varphi_{cr}))+d\cos(\pi+\theta)\\ r(\sin(\varphi_{cr})-(\varphi_{cr}+\pi-\gamma)\cos(\varphi_{cr}))+d\sin(\pi+\theta)\end{pmatrix}. \qquad (A.37)$$

The independent variable describing the motion of the spirals of the machine is the crank angle θ as it varies in the open interval $(-\infty, +\infty)$, Thus, according to the second of equations *(A.36)*, the motion of the tip G_3, is a circle (hereafter called C_{ORB}) with radius **d** and center located at the point Q_{ORB} whose coordinates are

$$\begin{pmatrix}x_{Q,ORB}\\ y_{Q,ORB}\end{pmatrix} = -r\begin{pmatrix}\cos(\varphi_{cr})+\varphi_{cr}\sin(\varphi_{cr})\\ \sin(\varphi_{cr})-\varphi_{cr}\cos(\varphi_{cr})\end{pmatrix}. \qquad (A.38)$$

By construction this circle passes through the points G_1 and T_2, and at the point T_2 its slope is equal to the slope of the curve C_2=C_{FI}. Indeed, subtracting the first of equations *(A.36)* and *(A.37)* from equation *(A.38)*, squaring and adding the resulting expressions, rejecting negative solutions and after some algebraic manipulations, we obtain the distances G_1Q_{ORB} and T_2Q_{ORB}

$$G_1Q_{ORB} = 2r\left(1+\varphi^2{}_{cr}\right)^{1/2}, \quad T_2Q_{ORB} = r\left(\pi-\gamma\right).$$

These expressions, according to equation *(A.22)* and *(A.32)* are equal to the radius d of the circle C_{ORB}, that is

$$G_1Q_{ORB} = T_2Q_{ORB} = d\,,$$

and hence, this circle passes through the points G_1 and T_2.

In order to determine the slope of the circle at the point T_2, we require the value $\theta_{\lim 2}$ of the crank angle θ corresponding to this point. By definition, at T_2 the tip G_3 touches the curve C_2=C_{FI} for the first time and therefore $\varphi_3 = \varphi_{3S} = \varphi_{cr}$ and $\varphi_2 = \varphi_{2S} = (\varphi_{cr} + \pi - \gamma)$. Substituting these values into equation *(A.26)* and introducing equation *(A.32)*, we get

$$\theta_{\lim 2} = \varphi_{cr} - \frac{\pi}{2} = \sqrt{\left(\frac{\pi-\gamma}{2}\right)^2 - 1} - \frac{\pi}{2}, \quad 0 < \gamma = \mathbf{constant} \le \pi - 2. \qquad (A.39)$$

It is worth noting that according to this relation, $\theta_{\lim 2}$ lies in the interval

$$-\frac{\pi}{2} \le \theta_{\lim 2} < \frac{\sqrt{\pi^2-4}-\pi}{2} < 0. \qquad (A.40)$$

The slope of the circle C_{ORB} at any point of its circumference, as derived from the second of equations *(A.36)*, is given by

$$\frac{-1}{\tan(\pi+\theta)}, \quad \text{where} \quad \theta \in \Re.$$

Combining the above expression with the relation *(A.39)*, we obtain the slope of the circle C_{ORB} at the point T_2

$$\text{slope of } C_{ORB} \text{ at } T_2 = \frac{-1}{\tan(\pi+\theta_{\lim 2})} = -\cot\left(\frac{\pi}{2}+\varphi_{cr}\right) = \tan\varphi_{cr}.$$

On the other hand, for the curve C_2=C_{FI} at the point T_2 we have $\varphi = \varphi_{2S} = (\varphi_{cr} + \pi - \gamma)$, and according to equations *(A.12)* the slope of the curve at this point is given by

$$\text{slope of } C_2 \text{ at } T_2 = \tan\left(\varphi_{cr}+\pi\right) = \tan\left(\varphi_{cr}\right).$$

This is equal to the slope of the circle C_{ORB} and guarantees geometric continuity of first order for the circle and the spiral at T_2.

Another useful parameter in the present analysis is the value $\theta_{\lim 1}$ of the crank angle θ, attained when the tips of the curves C_1=C_{FO} and C_3=C_{OO} are just in touch. This situation is illustrated in figure (A-6). From this figure and the above discussion, it is evident that G_1 and G_3 are in touch when $\varphi_1 = \varphi_3 = \varphi_{cr}$ and hence

$$\theta_{\lim 1} = \pi + \varphi_{cr} - \psi ,$$

where ψ is the angle $M\hat{O}B$ easily determined from figure (A-6). Thus

$$\psi = \mathbf{arctan}\left(\frac{r\varphi_{cr}}{r}\right) = \mathbf{arctan}(\varphi_{cr}) .$$

Combining the above two equations and making use of the definition *(A.33)*, we obtain

$$\theta_{\lim 1} = \varphi_{cr} - \mathbf{arctan}\,\varphi_{cr} + \pi = \pi + \sqrt{\left[\frac{(\pi-\gamma)}{2}\right]^2 - 1} - \mathbf{arctan}\left[\sqrt{\left[\frac{(\pi-\gamma)}{2}\right]^2 - 1}\right] . \qquad (A.41)$$

The upper and lower bounds of $\theta_{\lim 1}$ are easily deduced from this equation. Thus,

$$\mathbf{0} < \pi - \mathbf{arctan}\left(\frac{\sqrt{\pi^2-4}}{2}\right) < \theta_{\lim 1} < \pi + \frac{\sqrt{\pi^2-4}}{2} < 3\pi/2 . \qquad (A.42)$$

It is now possible to replace the section of the curve C_2=C_{FI} defined for values of φ in the range $\varphi_{cr} \le \varphi \le (\varphi_{cr} + \pi - \gamma)$, by the minor arc T_2G_1 of the circle C_{ORB}, defined for values of θ in the closed interval $[\theta_{\lim 1}, \theta_{\lim 2} + 2\pi]$ as shown in figures (A-7a) and (A-7b). This replacement guarantees the required continuous touching of the tip G_3 of the moving spiral with the inner surface of the fixed spiral. It also guarantees geometric continuity of the first order (smooth blending) at the point T_2 between the circle C_{ORB} and the curve C_2 as defined by equations *(A.10)* for $\varphi \ge (\varphi_{cr} + \pi - \gamma)$. Finally, the arc T_2G_1 meets the curve C_1 at its starting point G_1 rather smoothly, a prerequisite for the manufacturing of the scroll device. This way G_1 coincides with the starting point G_2 of the inner surface of the fixed spiral.

Before proceeding with the replacement of the innermost part of the curve $C_4=C_{OI}$, it is necessary to obtain the equations of the curves C_i $(i=1,2,3,4)$, when referred to the rotating X^*Y^* Cartesian coordinate system. This is achieved by subtracting the "instantaneous" coordinates

$$\begin{pmatrix} S_x \\ S_y \end{pmatrix} = -d \begin{pmatrix} \cos(\theta) \\ \sin(\theta) \end{pmatrix},$$

of the origin S of the X^*Y^* system from equations ***(A.10)***, which thus take form

$$\begin{aligned}
C_1=C_{FO} &: \begin{pmatrix} x_1^* \\ y_1^* \end{pmatrix} = \begin{pmatrix} r(\cos(\varphi)+\varphi\sin(\varphi))+d\cos(\theta) \\ r(\sin(\varphi)-\varphi\cos(\varphi))+d\sin(\theta) \end{pmatrix}, \\
C_2=C_{FI} &: \begin{pmatrix} x_2^* \\ y_2^* \end{pmatrix} = \begin{pmatrix} r(\cos(\varphi+\gamma)+\varphi\sin(\varphi+\gamma))+d\cos(\theta) \\ r(\sin(\varphi+\gamma)-\varphi\cos(\varphi+\gamma))+d\sin(\theta) \end{pmatrix}, \\
C_3=C_{OO} &: \begin{pmatrix} x_3^* \\ y_3^* \end{pmatrix} = -r \begin{pmatrix} \cos(\varphi)+\varphi\sin(\varphi) \\ \sin(\varphi)-\varphi\cos(\varphi) \end{pmatrix}, \\
C_4=C_{OO} &: \begin{pmatrix} x_4^* \\ y_4^* \end{pmatrix} = -r \begin{pmatrix} \cos(\varphi+\gamma)+\varphi\sin(\varphi+\gamma) \\ \sin(\varphi+\gamma)-\varphi\cos(\varphi+\gamma) \end{pmatrix}.
\end{aligned} \qquad (A.43)$$

Evidently, the definitions of the curves C_i $(i=1,2,3,4)$ are independent of the system of reference and hence the meaning of the parameters φ and θ is not altered in the new system of coordinates. The same is true for the thickness angle γ and the particular values φ_i $(i=1,2,3,4)$, φ_{iS} $(i=1,2,3,4)$, φ_{cr}, θ_{lim1} and θ_{lim2}.

Introduction of the critical value φ_{cr} into the first and third of the equations ***(A.43)*** furnishes the expressions for the tips G_1 and G_3 in the X^*Y^* system of reference. Thus

$$\begin{aligned}
C_1=C_{FO} &: G_1 = \begin{pmatrix} r(\cos(\varphi_{cr})+\varphi_{cr}\sin(\varphi_{cr}))+d\cos(\theta) \\ r(\sin(\varphi_{cr})-\varphi_{cr}\cos(\varphi_{cr}))+d\sin(\theta) \end{pmatrix}, \\
C_3=C_{OO} &: G_3 = -r \begin{pmatrix} \cos(\varphi_{cr})+\varphi_{cr}\sin(\varphi_{cr}) \\ \sin(\varphi_{cr})-\varphi_{cr}\cos(\varphi_{cr}) \end{pmatrix}.
\end{aligned} \qquad (A.44)$$

Similarly, substitution of the values $\varphi_{2S}=\varphi_{4S}=(\varphi_{cr}+\pi-\gamma)$ into equations ***(A.43)***, yields the coordinates of the points T_2 and T_4 in the X^*Y^* coordinate

system, that is

$$C_2=C_{FI} \;:\; T_2 = \begin{pmatrix} -r(\cos(\varphi_{cr}) + (\varphi_{cr} + \pi - \gamma)\sin(\varphi_{cr})) + d\cos(\theta) \\ -r(\sin(\varphi_{cr}) - (\varphi_{cr} + \pi - \gamma)\cos(\varphi_{cr})) + d\sin(\theta) \end{pmatrix},$$

$$C_4=C_{OO} \;:\; T_4 = r\begin{pmatrix} \cos(\varphi_{cr}) + (\varphi_{cr} + \pi - \gamma)\sin(\varphi_{cr}) \\ \sin(\varphi_{cr}) - (\varphi_{cr} + \pi - \gamma)\cos(\varphi_{cr}) \end{pmatrix}. \qquad (A.45)$$

From the first of equations *(A.44)*, it is at once obvious that as the crank angle θ varies the relative motion of the tip G_1 is a circle (hereafter called C_{FIX}) with radius d and centre located at point Q_{FIX}.

$$\begin{pmatrix} x_{Q,FIX} \\ y_{Q,FIX} \end{pmatrix} = r\begin{pmatrix} \cos(\varphi_{cr}) + \varphi_{cr}\sin(\varphi_{cr}) \\ \sin(\varphi_{cr}) - \varphi_{cr}\cos(\varphi_{cr}) \end{pmatrix}. \qquad (A.46)$$

It will be shown below that this circle passes through the points G_3 and T_4 and at the point T_4 its slope is equal to the slope of the curve $C_4 = C_{OI}$. Subtracting the second of equations *(A.44)* and *(A.45)* from equation *(A.46)*, squaring and adding the resulting expressions, rejecting negative values and after some algebraic manipulations, we obtain the distances G_3Q_{FIX} and T_4Q_{FIX}

$$G_3Q_{FIX} = 2r\left(1+\varphi^2_{cr}\right)^{1/2} = d, \quad T_4Q_{FIX} = r(\pi - \gamma) = d.$$

These are equal to the radius d of the circle C_{FIX} and hence, this circle passes through the points G_3 and T_4.

The slope of the circle C_{FIX} at any point of its circumference, as derived from the first of equations *(A.44)*, is given by

$$\frac{-1}{\tan(\theta)}, \quad \text{where} \quad \theta \in \Re.$$

On the other hand, by definition, at T_4 the tip G_1 touches the curve $C_4=C_{OI}$ for the first time and hence $\varphi_1 = \varphi_{1S} = \varphi_{cr}$ and $\varphi_4 = \varphi_{4S} = (\varphi_{cr} + \pi - \gamma)$. Consequently, the corresponding value of the crank angle θ, according to equations *(A.26)* for $k = 0$ is given by

$$\theta = \varphi_{cr} - \frac{\pi}{2} = \theta_{lim2}.$$

Combining the above two relations we get the slope of the circle C_{FIX} at the point T_4, that is

$$\text{slope of } C_{FIX} \text{ at } T_4 = \frac{-1}{\tan(\theta_{\lim 2})} = -\cot\left(\varphi_{cr} - \frac{\pi}{2}\right) = \cot\left(\frac{\pi}{2} - \varphi_{cr}\right) = \tan(\varphi_{cr}).$$

For the curve C_4=C_{OI} at the point T_4 we have $\varphi = \varphi_{4S} = (\varphi_{cr} + \pi - \gamma)$, and according to equations *(A.12)*, the slope of the curve at this point is given by

$$\text{slope of } C_4{=}C_{OI} \text{ at } T_4 = \tan(\varphi_{4S} + \gamma) = \tan(\varphi_{cr} + \pi) = \tan(\varphi_{cr}).$$

The above two equations guarantee that the slope of the curve C_4 at the point T_4 is equal to the slope of the circle C_{FIX} and secures smooth blending between the circle and the curve C_4=C_{OI} at this point.

As in the case of the curve C_2, the section of the curve C_4=C_{OI} defined for values of φ in the range $\varphi_{cr} \le \varphi \le (\varphi_{cr} + \pi - \gamma)$, is replace by the minor arc T_4G_3 of the circle C_{FIX} defined for values of θ in the closed interval $[\theta_{\lim 1}, \theta_{\lim 2} + 2\pi]$ as shown in figures (A-7a) and (A-7b). With this replacement we secure the required continuous touching of the tip G_1 of the fixed spiral with the inner surface of the moving spiral. We also secure geometric continuity of the first order (smooth blending) at the point T_4 between the arc T_4G_3 and the curve C_4=C_{OI} as defined by equations *(A.10)* for $\varphi \ge (\varphi_{cr} + \pi - \gamma)$. Additionally, the minor arc T_4G_3 meets the curve C_3=C_{OO} at its starting point G_3 rather smoothly, a prerequisite for the manufacturing of the spirals of the device. This way G_3 coincides with the starting point G_4 of the inner surface of the moving spiral.

After the replacement of the innermost sections of the curves C_2=C_{FI} and C_4=C_{OI} by the arcs T_2G_1 and T_4G_3 the tips G_1 and G_3 are in continuous touch with these arcs for values of the crank angle θ in the closed interval $[\theta_{\lim 1}, \theta_{\lim 2} + 2\pi]$. In the limiting case when $\theta = \theta_{\lim 1}$, the two tips are in touch as depicted in figure (A-10). At the other limiting case when $\theta = \theta_{\lim 2} + 2\pi$, tips G_1 and G_3 are in touch with the curves C_4=C_{OI} and C_2=C_{FI} at the points T_4 and T_2 respectively as shown in figure (A-7b). Intermediate positions of the tips for values of the crank angle θ in the range $\theta_{\lim 1} < \theta < \theta_{\lim 2} + 2\pi$, are shown in figures (A-11).

A.2.4 Length of Device's Spirals

This section completes the geometry and the design of the scroll compressor used in the numerical investigations of the fluid flows presented elsewhere in this thesis.

The rotation of the orbiting spiral of the compressor is described by the crank angle θ. Hence, the geometry of every chamber completes a full cycle of changes returning to its original configuration, as θ continuously increases (or decreases) by 2π. The innermost touching points of the curves C_i (i=1,2,3,4) as given from equations *(A.26)* when $k = 0$, are

$$\varphi_{i,0} = \frac{\pi}{2} + \theta, \quad \text{i=1,3,} \qquad \varphi_{i,0} = \pi + \frac{\pi}{2} + \theta - \gamma, \quad \text{i=2,4,} \tag{A.47}$$

where by definition, the single-subscript notation of the angles φ_i is related to their double-subscript notation as follows

$$\varphi_{i,j} \equiv \varphi_i\big|_{j=k}, \quad i=1,2,3,4, \quad k \in \backslash W. \tag{A.48}$$

The relations *(A.47)*, upon introduction of the inequalities *(A.34)* and *(A.35)*, become

$$\begin{aligned} \theta &= \varphi_{i,0} - \frac{\pi}{2} \geq \varphi_{cr} - \frac{\pi}{2}, \quad \text{i=1,3,} \\ \theta &= \varphi_{i,0} - \pi - \frac{\pi}{2} + \gamma \geq \varphi_{cr} - \frac{\pi}{2}, \quad \text{i=2,4.} \end{aligned} \tag{A.49}$$

These inequalities can be reduced further using the expression *(A.39)*, that is

$$\theta \geq \theta_{lim2}. \tag{A.50}$$

The maximum value of θ, as suggested by the form of equations *(A.26)* and the above inequality, may not exceed the value of $(\theta_{lim2} + 2\pi)$ and therefore

$$\theta_{lim2} \leq \theta < \theta_{lim2} + 2\pi. \tag{A.51}$$

For the sake of clarity the end, outermost points of the curves C_i (i=1,2,3,4) are denoted by S_i (i=1,2,3,4), while the maximum values of the parameter φ, defining these points are denoted by ω_i (i=1,2,3,4) respectively. The locations of the points S_i (i=1,2,3,4) are shown in the figure below.

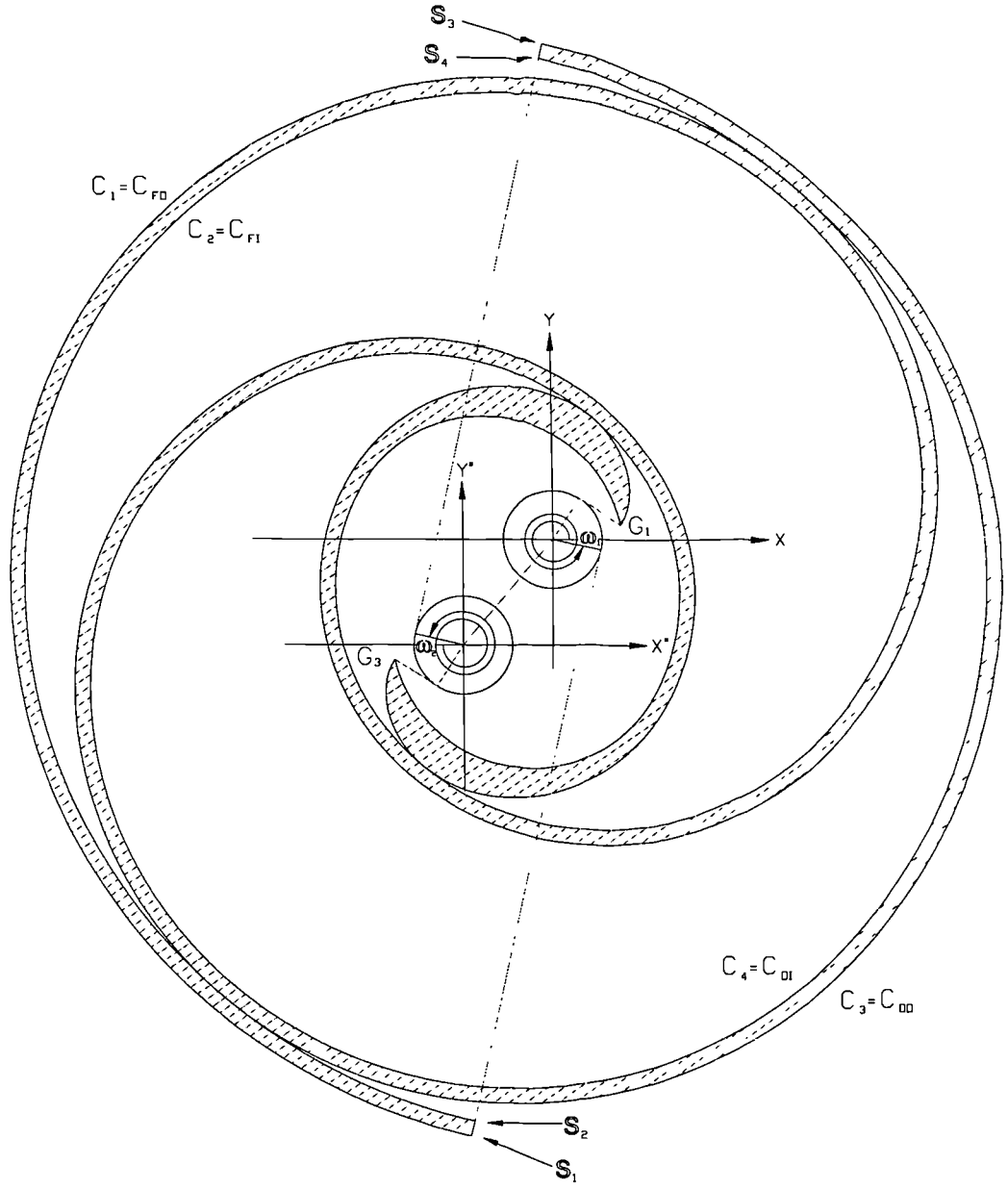

Figure (A-8). The angles ω_i and the location of the points S_i.

Obviously, the angles ω_i $(i=1,2,3,4)$ can be selected arbitrarily and independently of each other and hence the spirals of the machine can have unrelated and arbitrary lengths. However, in practice for self explanatory reasons, the spirals are always constructed to have equal lengths. In the present study, the choice of the maximum angles ω_i $(i=1,2,3,4)$ is based on a specific well defined range of volume ratios. Volume ratios and the reasons for selecting this particular range are discussed

extensively elsewhere in this thesis. The precise values of the angles ω_i $(i=1,2,3,4)$ are determined by another important factor, namely the position of the end points S_i $(i=1,2,3,4)$.

The pairs of the curves C_i, C_{i+1} $(i=1,3)$ describe the geometry of the external and internal surfaces of the compressor's spirals. It is therefore necessary to select such values for ω_i $(i=1,2,3,4)$ that the distances S_1S_2 and S_3S_4 are minimum and equal to the constant thickness of the spirals. According to equations ***(A.15)***, this is achieved when

$$S_1S_2 = S_3S_4 = r\gamma . \qquad (A.52)$$

Equations ***(A.34)*** and ***(A.35)*** and the definition of the angles ω_i $(i=1,2,3,4)$ imply the following relation

$$\varphi_{cr} \le \varphi_{i,j} \le \omega_i , \quad 0 \le j \le k , \quad i=1,3, \quad j,k \in \backslash W , \qquad (A.53)$$

where $\varphi_{i,j}$ are the values of the parameters φ at the various touching points of the curves C_i $(i=1,2,3,4)$. The above condition, upon introduction of equations ***(A.32)*** and ***(A.39)***, take the form

$$\omega_1,\ \omega_3 \ge \frac{\pi}{2} + \theta_{lim2} = \varphi_{cr} > 0 . \qquad (A.54)$$

According to relations ***(A.26)*** and ***(A.51)*** this condition furnish at least one pair of touching points between the spirals as described by equations ***(A.10)***.

In the most general case the angles ω_i $(i=1,3)$ must be allowed to cover all possible values equal to or greater than the above minimum value, hence

$$\omega_1,\ \omega_3 = 2N\pi + \alpha + \left(\frac{\pi}{2} + \theta_{lim2}\right), \qquad (A.55)$$

where by definition N is an arbitrary whole number and the angle α obeys the condition

$$0 \le \alpha < 2\pi . \qquad (A.56)$$

For the sake of convenience, we introduce the parameter β defined by

$$\beta \equiv \alpha + \theta_{lim2} . \qquad (A.57)$$

The range of β is deduced from the range of the parameter α. Given that $0 \le \alpha < 2\pi$, β lies in the semi-open interval

$$\theta_{\lim 2} \le \beta < (\theta_{\lim 2} + 2\pi). \tag{A.58}$$

Combining the definition *(A.57)* with equation *(A.55)*, we obtain

$$\omega_1, \omega_3 = 2N\pi + \frac{\pi}{2} + \beta, \quad \beta \in [\theta_{\lim 2}, \theta_{\lim 2} + 2\pi), \quad N \in \backslash W. \tag{A.59}$$

Assuming that the curves C_2 and C_4 are long enough, there exists a value θ_s of the crank angle θ for which the suction process begins. At this instance the end points S_1 and S_3 come in touch with the curves C_4 and C_2 respectively, and hence equations *(A.26)* and *(A.59)* furnish

$$\omega_1 = \varphi_{1,N}, \quad \omega_3 = \varphi_{3,N},$$

$$\varphi_{1,N} = \varphi_{3,N} = 2N\pi + \frac{\pi}{2} + \beta = 2k\pi + \frac{\pi}{2} + \theta_s,$$

$$\varphi_{2,N} = \varphi_{4,N} = (2N+1)\pi + \frac{\pi}{2} + \beta - \gamma = (2k+1)\pi + \frac{\pi}{2} + \theta_s - \gamma, \tag{A.60}$$

$$k \in \backslash W, \quad N \in \backslash W, \quad 0 < \gamma \le \pi - 2, \quad \theta_{\lim 2} \le \beta, \ \theta_s < (\theta_{\lim 2} + 2\pi).$$

The functionality of the compressor under study is based on the existence of the touching points between its spirals. Hence, the most appropriate choices for the end, outermost points S_2 and S_4 of the curves C_2 and C_4 are the points corresponding to the angles $\varphi_{2,N}$ and $\varphi_{4,N}$ given by equations *(A.60)*. In this case

$$\omega_2 = \omega_4 = (2N+1)\pi + \frac{\pi}{2} + \beta - \gamma = (2k+1)\pi + \frac{\pi}{2} + \theta_s - \gamma, \tag{A.61}$$

$$k \in \backslash W, \quad N \in \backslash W, \quad 0 < \gamma \le \pi - 2, \quad \theta_{\lim 2} \le \beta, \ \theta_s < (\theta_{\lim 2} + 2\pi).$$

If the angles ω_i $(i=1,2,3,4)$ were to be accepted as given by equations *(A.59)* and *(A.61)* it would be impossible to construct the spirals of the compressor due to the considerable difference in the length of their external (C_1, C_3) and internal (C_2, C_4) surfaces. This difficulty can easily be avoided. The lengths of the curves C_1 and C_3 are extended by adding π to the angles ω_1 and ω_3 given by equations *(A.60)*. Then equations *(A.60)* and *(A.61)* yield

$$\omega_1 = \omega_3 = (2N+1)\pi + \frac{\pi}{2} + \beta = (2k+1)\pi + \frac{\pi}{2} + \theta_s,$$

$$\omega_2 = \omega_4 = (2N+1)\pi + \frac{\pi}{2} + \beta - \gamma = (2k+1)\pi + \frac{\pi}{2} + \theta_s - \gamma, \qquad (A.62)$$

$$k \in \backslash W, \quad N \in \backslash W, \quad 0 < \gamma \le \pi - 2, \quad \theta_{lim2} \le \beta, \ \theta_s < (\theta_{lim2} + 2\pi).$$

The end, outermost points S_i (i=1,2,3,4) of the curves C_i (i=1,2,3,4) are obtained from equations *(A.10)* upon introduction of the relations *(A.62)*. After some algebraic manipulations the formulae giving the coordinates of the end points are

$$S_1 = \mathbf{r}\begin{pmatrix} \sin(\beta) - \Phi\cos(\beta) \\ -\cos(\beta) - \Phi\sin(\beta) \end{pmatrix},$$

$$S_2 = r\begin{pmatrix} \sin(\beta) - (\Phi-\gamma)\cos(\beta) \\ -\cos(\beta) - (\Phi-\gamma)\sin(\beta) \end{pmatrix},$$

$$S_3 = -\begin{pmatrix} r(\sin(\beta) - \Phi\cos(\beta)) + d\cos\theta \\ r(-\cos(\beta) - \Phi\sin(\beta)) + d\sin\theta \end{pmatrix}, \qquad (A.63)$$

$$S_4 = -\begin{pmatrix} r(\sin(\beta) - (\Phi-\gamma)\cos(\beta)) + d\cos\theta \\ r(-\cos(\beta) - (\Phi-\gamma)\sin(\beta)) + d\sin\theta \end{pmatrix},$$

$$0 < r \le d/2, \quad 0 < \gamma \le \pi - 2$$

where by definition

$$\Phi \equiv (2N+1)\pi + \pi/2 + \beta. \qquad (A.64)$$

It is worth noting that according to equations *(A.62)*

$$\omega_1 = \omega_3 = \Phi \quad \text{and} \quad \omega_2 = \omega_4 = \Phi - \gamma. \qquad (A.65)$$

The distances S_1S_2 and S_3S_4 obtained from the relations *(A.63)* satisfy the requirement *(A.52)*.

The relation connecting the angles θ_s and β is deduced from equations *(A.62)* as described bellow. The inequalities *(A.51)* and *(A.58)* guarantee that both angles θ_s

and β are defined in the same semi-open interval $[\theta_{\lim 2},\ \theta_{\lim 2}+2\pi)$. On the other hand the relation *(A.40)* implies that the lower and upper bounds of this interval are $-\pi/2$ and $[(\pi^2-4)^{1/2}+3\pi]/2$. These bounds lie well inside the closed interval $[2\pi,\ 2\pi]$, and hence

$$-2\pi < -\pi/2 \le \beta,\ \theta_s < \left(\sqrt{\pi^2-4}+3\pi\right)/2 < 2\pi. \qquad (A.66)$$

As a result of this condition, equations *(A.62)* can be valid if and only if $k = N$, $N \in \backslash W$, thus

$$\theta_s = \beta, \quad \theta_{\lim 2} \le \theta_s,\ \beta < (\theta_{\lim 2}+2\pi), \qquad (A.67)$$

or according to definition *(A.57)*

$$\theta_s = \alpha + \theta_{\lim 2}. \qquad (A.68)$$

If k and N where to be taken different, then either β or θ_s would have been absolutely greater than 2π violating the condition *(A.66)*.

It is important to note that the relation $k = N$ was proved to be true only when $\theta = \theta_s$, and in this case N is the maximum value of k entering equations *(A.26)*. For any other value of θ the maximum value of k, hereafter called K_{max}, is determined from the restriction *(A.53)*. This restriction, when combined with the relations *(A.26)* and *(A.62)*, furnishes

$$2(N-K_{max})\pi \ge (\theta-\theta_s), \quad \theta_{\lim 2} \le \theta_s,\ \theta < (\theta_{\lim 2}+2\pi), \quad K_{max},\ N \in \backslash W. \qquad (A.69)$$

Given that N and K_{max} are whole numbers, the above inequality and the relations *(A.40)*, *(A.51)*, *(A.57)* and *(A.58)* yields the following conditional solutions for K_{max} in terms of N, depending on the value of the crank angle θ

$$\begin{aligned} &K_{max} = N, \quad \theta_s \ge \theta \ge \theta_{\lim 2}, \quad K_{max},\ N \in \backslash W, \\ &K_{max} = N-1, \quad (\theta_{\lim 2}+2\pi) > \theta > \theta_s, \quad K_{max},\ N \in \backslash W. \end{aligned} \qquad (A.70)$$

From the definition of K_{max} it is obvious that at any instance of the scroll device's operation, there exist $2(K_{max}+1)$ pairs of touching points between the curves C_i $(i=1,2,3,4)$. These are obtained from equations *(A.26)* for $k = 0,1,2,\ldots K_{max}$. It must be emphasised that these points do not include the touching points due to the replacement of the innermost sections of the curves $C_2=C_{FI}$ and $C_4=C_{OI}$ by circular arcs as discussed in the previous section.

The value of N is of paramount importance in the design of the scroll compressor-expander. It determines the length of the spirals , the number of the pairs of the touching points, and the number of the working chambers. It also controls together with the angle α the maximum volume of the suction chamber and hence the volume of the trapped fluid. In practice the selection of N is based on volume and pressure ratio considerations as discussed elsewhere and is left to be decided by the designer of the device. The minimum possible value of N is determined by the requirement that the device has long enough spirals to be able to function as a compressor. For $N=1$, even when $\alpha=0$, that is $\beta=\theta_{lim2}$, the device has a pair of touching points given by equations *(A.26)* and it works properly as a compressor. This situation is depicted in figures (A-9) below

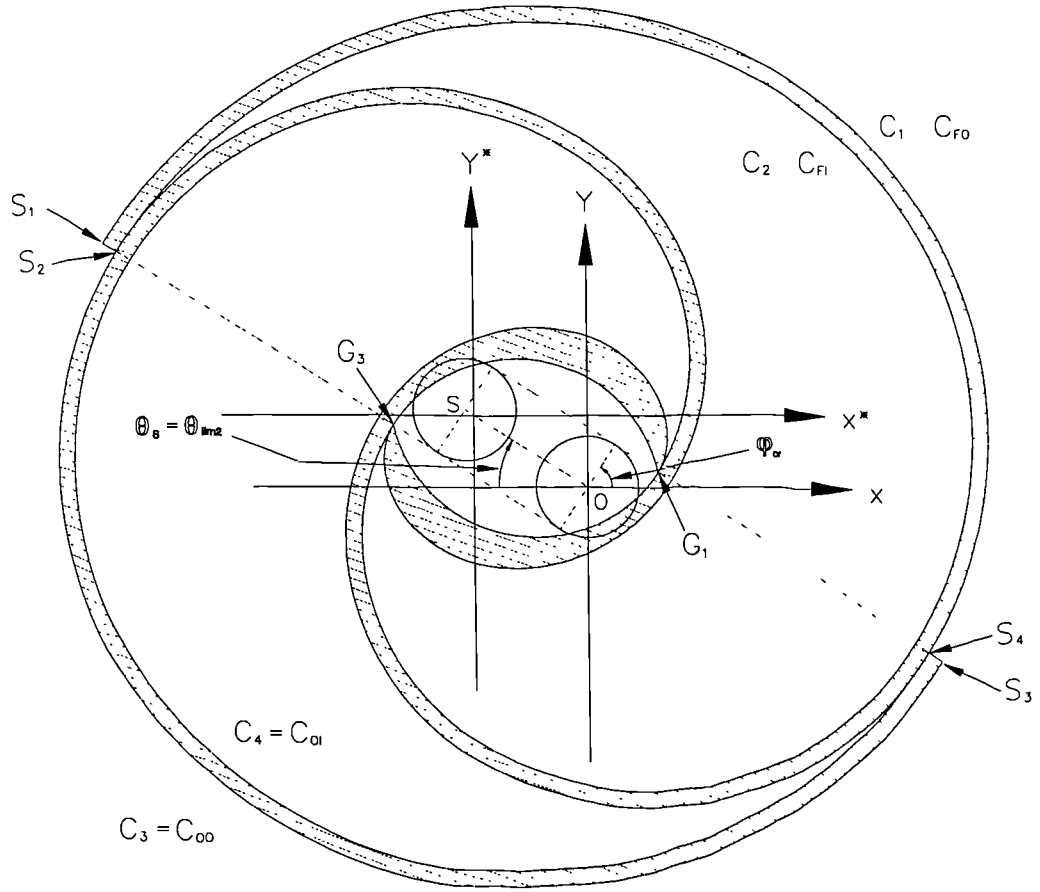

Figure (A-9). Scroll device with $N=1$ and $\alpha=0$ at $\theta=\theta_s=\beta=\theta_{lim2}$.

It will be shown below that even for $N = 0$ the device has long enough spirals to function perfectly well as a compressor if the angle α exceeds a certain minimum value α_{min}. This is due to the replacement of the curves C_2 and C_4 by circular arcs for values of φ in the interval $[\varphi_{cr}, \varphi_{cr} + \pi - \gamma]$ and to the resulting continuous touching of the tips G_1 and G_3 with these arcs for values of the crank angle θ in the closed interval $[\theta_{lim1}, \theta_{lim2} + 2\pi]$. Obviously, the device can function as a compressor if and only if there are two pairs of touching points between the surfaces of its spirals. The limiting case occurs when the two tips G_1 and G_3 are just in touch and the lengths of the spirals are such that there exists one extra pair of touching points between the curves C_i $(i=1,2,3,4)$ as shown in figures (A-10). In this case, by definition $\theta = \theta_{lim1}$ while the angles ω_2 and ω_4 correspond to the outer touching points. Thus, according to equations *(A.26)*, *(A.57)*, *(A.62)* and the definition of θ_s, we have

$$\theta = \theta_s = \theta_{lim1}, \quad \beta = \beta_{min} \equiv \alpha_{min} + \theta_{lim2}, \quad N = 0,$$
$$\omega_2 = \omega_4 = \varphi_{2,0} = \varphi_{4,0} = \pi + \pi/2 + \beta_{min} - \gamma = \pi + \pi/2 + \theta_{lim1} - \gamma. \tag{A.71}$$

The second of these equations becomes

$$\beta_{min} = \theta_{lim1}. \tag{A.72}$$

Combining this equation with the relations *(A.39)*, *(A.41)* and *(A.57)*, we obtain

$$\beta_{min} = \theta_{lim1} = \varphi_{cr} - \arctan \varphi_{cr} + \pi,$$
$$\alpha_{min} = \theta_{lim1} - \theta_{lim2} = \frac{3\pi}{2} - \arctan \varphi_{cr}. \tag{A.73}$$

Note that according to relations *(A.40)*, *(A.42)*, *(A.68)* and *(A.73)*, for $N = 0$ the first of the equations *(A.70)* must be applied and therefore in this particular case $K_{max} = N = 0$.

A direct consequence of the replacement of the innermost sections of the curves C_2=C_{FI} and C_4=C_{OI} by circular arcs, is the increase of the pairs of touching points between the device's spirals for values of the crank angle θ lying in the open interval $(\theta_{lim1}, \theta_{lim2} + 2\pi)$. Obviously, this alters the number of chambers formed by the spirals. Both the total number of touching points (hereafter denoted by T_P) and the total number of chambers (hereafter denoted by C_B) depend on the value of the crank angle θ and the design parameters N and α. The kind of dependency

of the actual values of T_P and C_B on θ, N and α is obtained with the help of equations *(A.39)*, *(A.41)*, *(A.67)* , *(A.68)* and *(A.73)*, and it is given in tabular form below. Using the above mentioned equations, it can be proved that the relation between the angles α_{min} and α dictates the relation between the angles θ_s and θ_{lim1} and vice versa. Thus, the following reciprocal relations hold

$$\alpha > \alpha_{min} \leftrightarrow \theta_s > \theta_{lim1} \leftrightarrow (\theta_{lim2} + 2\pi) > \theta_s > \theta_{lim1} > \theta_{lim2}$$
$$\alpha = \alpha_{min} \leftrightarrow \theta_s = \theta_{lim1} \leftrightarrow (\theta_{lim2} + 2\pi) > \theta_s = \theta_{lim1} > \theta_{lim2}$$
$$\alpha < \alpha_{min} \leftrightarrow \theta_s < \theta_{lim1} \leftrightarrow (\theta_{lim2} + 2\pi) > \theta_{lim1} > \theta_s > \theta_{lim2}$$

These inequalities and the geometry of the scroll device guarantee the validity of the following :

Table (A-1)

If	*and*	*then*
$\alpha > \alpha_{min}$	$\theta_{lim2} \le \theta < \theta_{lim1}$	$K_{max} = N$ $T_P = 2(K_{max} + 1) = 2N + 2$ $C_B = T_P + 1 = 2N + 3$
	$\theta = \theta_{lim1} < \theta_S$	$K_{max} = N$ $T_P = 2(K_{max} + 1) + 1 = 2N + 3$ $C_B = T_P + 1 = 2N + 4$
	$\theta_{lim1} < \theta \le \theta_S$	$K_{max} = N$ $T_P = 2(K_{max} + 1) + 2 = 2N + 4$ $C_B = T_P + 1 = 2N + 5$
	$\theta_S < \theta < (2\pi + \theta_{lim2})$	$K_{max} = N - 1$ $T_P = 2(K_{max} + 1) + 2 = 2N + 2$ $C_B = T_P + 1 = 2N + 3$

If	*and*	*then*
$\alpha = \alpha_{min}$	$\theta_{lim2} \le \theta < \theta_{lim1} = \theta_S$	$K_{max} = N$ $T_P = 2(K_{max} + 1) = 2N + 2$ $C_B = T_P + 1 = 2N + 3$
	$\theta = \theta_{lim1} = \theta_S$	$K_{max} = N$ $T_P = 2(K_{max} + 1) + 1 = 2N + 3$ $C_B = T_P + 1 = 2N + 4$
	$\theta_{lim1} = \theta_S < \theta < (2\pi + \theta_{lim2})$	$K_{max} = N - 1$ $T_P = 2(K_{max} + 1) + 2 = 2N + 2$ $C_B = T_P + 1 = 2N + 3$

If	*and*	*then*
$\alpha < \alpha_{min}$	$\theta_{lim2} \le \theta \le \theta_S$	$K_{max} = N$ $T_P = 2(K_{max} + 1) = 2N + 2$ $C_B = T_P + 1 = 2N + 3$
	$\theta_S < \theta < \theta_{lim1}$	$K_{max} = N - 1$ $T_P = 2(K_{max} + 1) = 2N$ $C_B = T_P + 1 = 2N + 1$
	$\theta = \theta_{lim1}$	$K_{max} = N - 1$ $T_P = 2(K_{max} + 1) + 1 = 2N + 1$ $C_B = T_P + 1 = 2N + 2$
	$\theta_{lim1} < \theta < (2\pi + \theta_{lim2})$	$K_{max} = N - 1$ $T_P = 2(K_{max} + 1) + 2 = 2N + 2$ $C_B = T_P + 1 = 2N + 3$

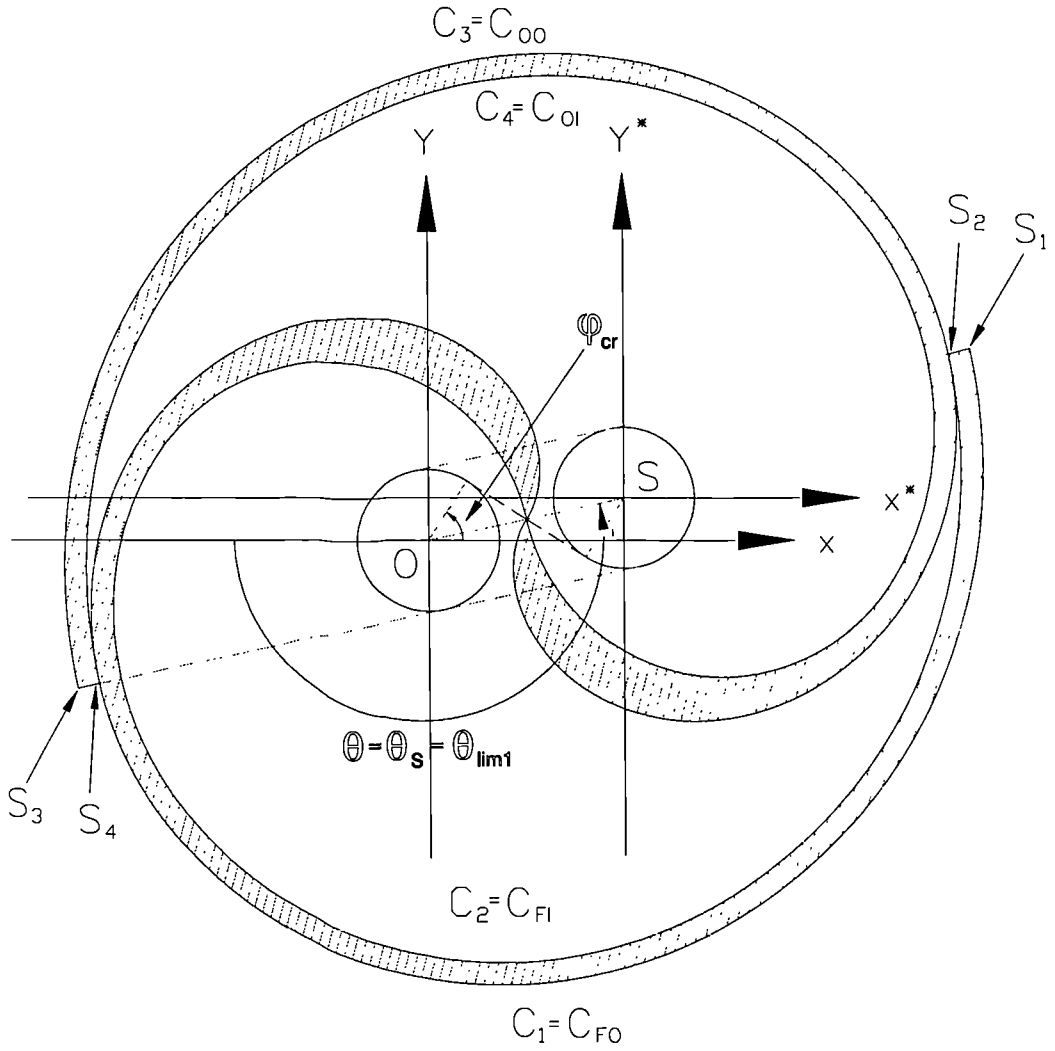

Figure (A-10). *Scroll device with* $N = 0$ and $\alpha = \alpha_{min} = \theta_{lim1} - \theta_{lim2}$ at $\theta = \theta_s = \beta_{min} = \theta_{lim1}$.

The above discussion concludes the necessary details required for the full understanding of the geometry and the touching conditions of the spirals of the scroll compressor-expander.

A.3 Working Chambers and Working Volumes

A.3.1 An Overview

This section gives a detailed account of the geometry of the working chambers of the scroll device -often called pockets- and concludes with the determination of the working volumes as functions of the crank angle θ and the other design parameters such as N, α, γ, etc.

For the sake of clarity and convenience the following definitions are introduced:

$$\textbf{pressure ratio of the compressor} \equiv \frac{\textbf{pressure inside the discharge chamber at the start of disharge cycle}}{\textbf{pressure inside the suction chamber at the end of the suction cycle}}$$

$$\textbf{volume ratio of the compressor} \equiv \frac{\textbf{volume of the suction chamber at the end of the suction cycle}}{\textbf{volume of the discharge chamber at the start of disharge cycle}}$$

As mentioned previously, the angles ω_i $(i=1,2,3,4)$ can be selected arbitrarily and hence the spirals of the machine can have unrelated and arbitrary lengths. However, in practice the spirals are always constructed to have equal lengths which can be determined from the required pressure ratio. When designing scroll compressors-expanders, more often than not, volume ratios are preferred to pressure ratios. This is due to the fact that pressure ratios are sensitive to factors not related to the geometry of the machine, such as the physical properties of the working fluid.

For any value of the crank angle θ the scroll device has rotational symmetry of 180^0 about the mid point of the segment connecting the centres of the two generating circles. This symmetry is apparent in figures (A-11) which show a plan view of a scroll compressor for various values of θ. Furthermore, the geometry of the device changes with period 2π as the orbiting spiral rotates around the centre O of the fixed generating circle. The independent variable describing this periodicity is the crank angle θ. The physical process that describes the motion of the fluid through the device, though essentially periodic, repeats itself only after a number of complete revolutions, say M, $M \in \backslash W$. Clearly, the number M depends on the values of the parameter N and the angle α, introduced by the relations *(A.55)* and *(A.56)*.

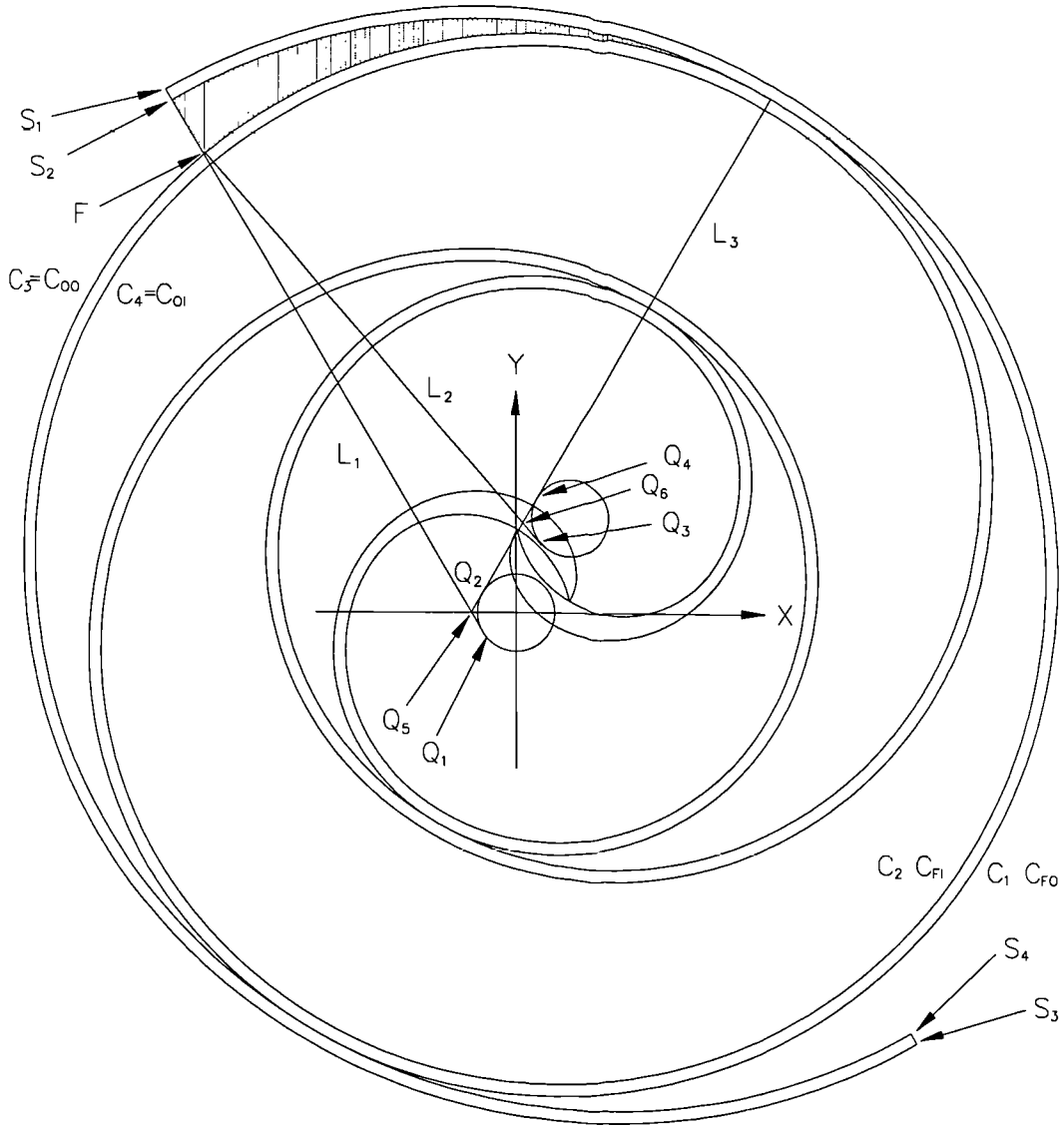

Figure (A-11a). *Scroll device with* $N = 1$ and $\alpha = 300^0 - \theta_{lim\,2}$ at $\theta = \theta_s - 60^0$.

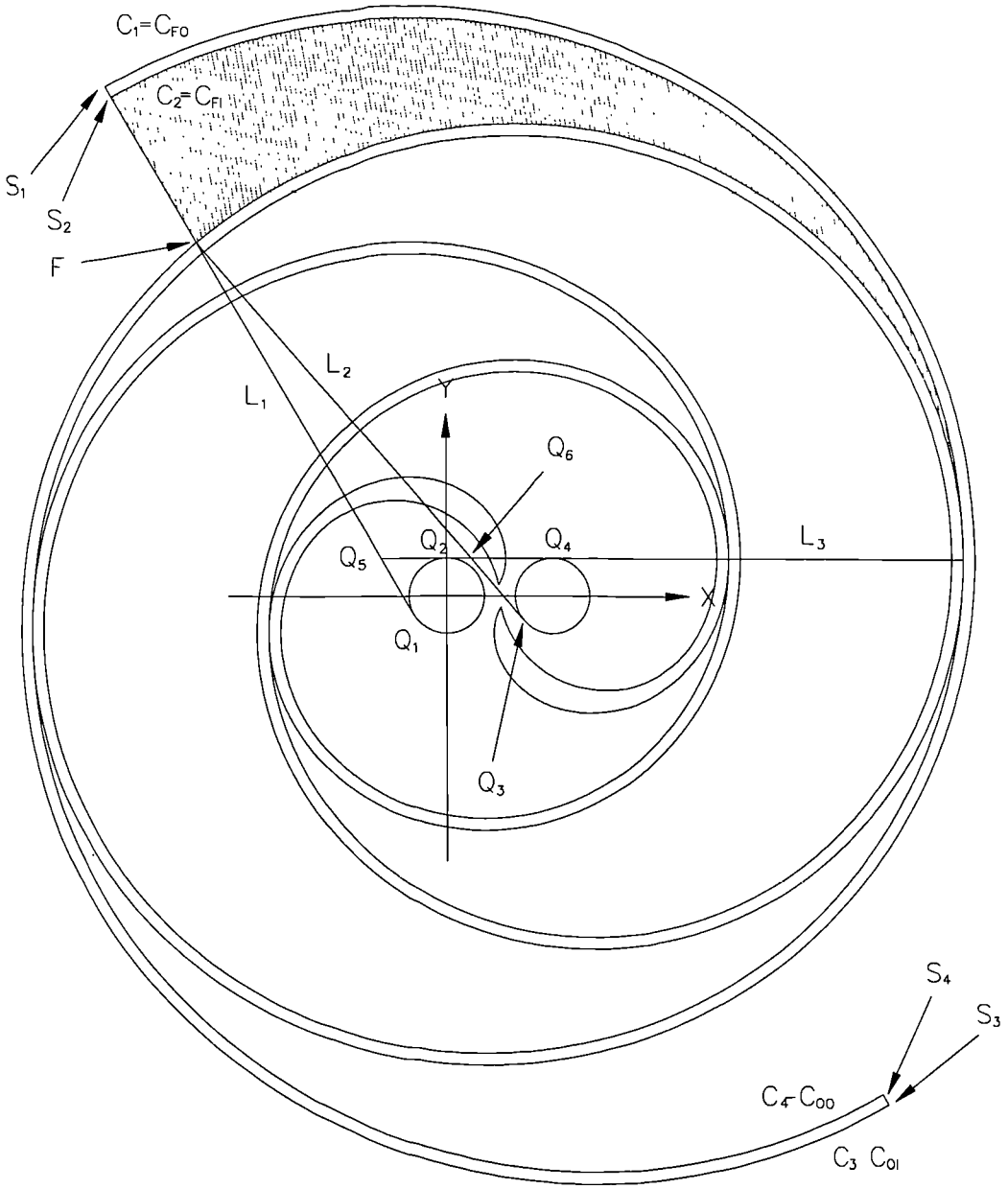

Figure (A-11b). *Scroll device with* $N = 1$ and $\alpha = 300^0 - \theta_{lim2}$ at $\theta = \theta_s - 120^0$.

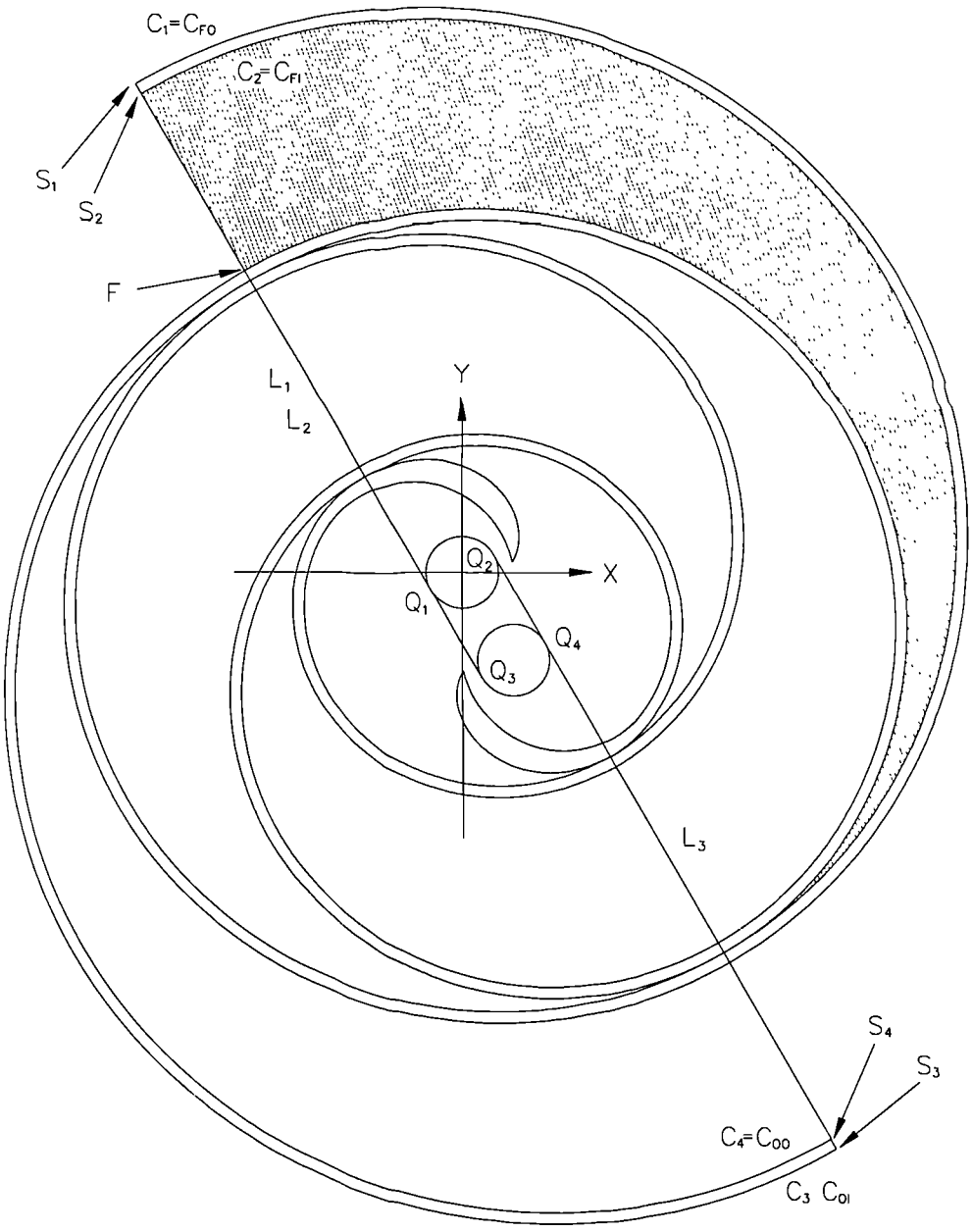

Figure (A-11c). *Scroll device with* $N = 1$ and $\alpha = 300^0 - \theta_{lim2}$ at $\theta = \theta_s - 180^0$.

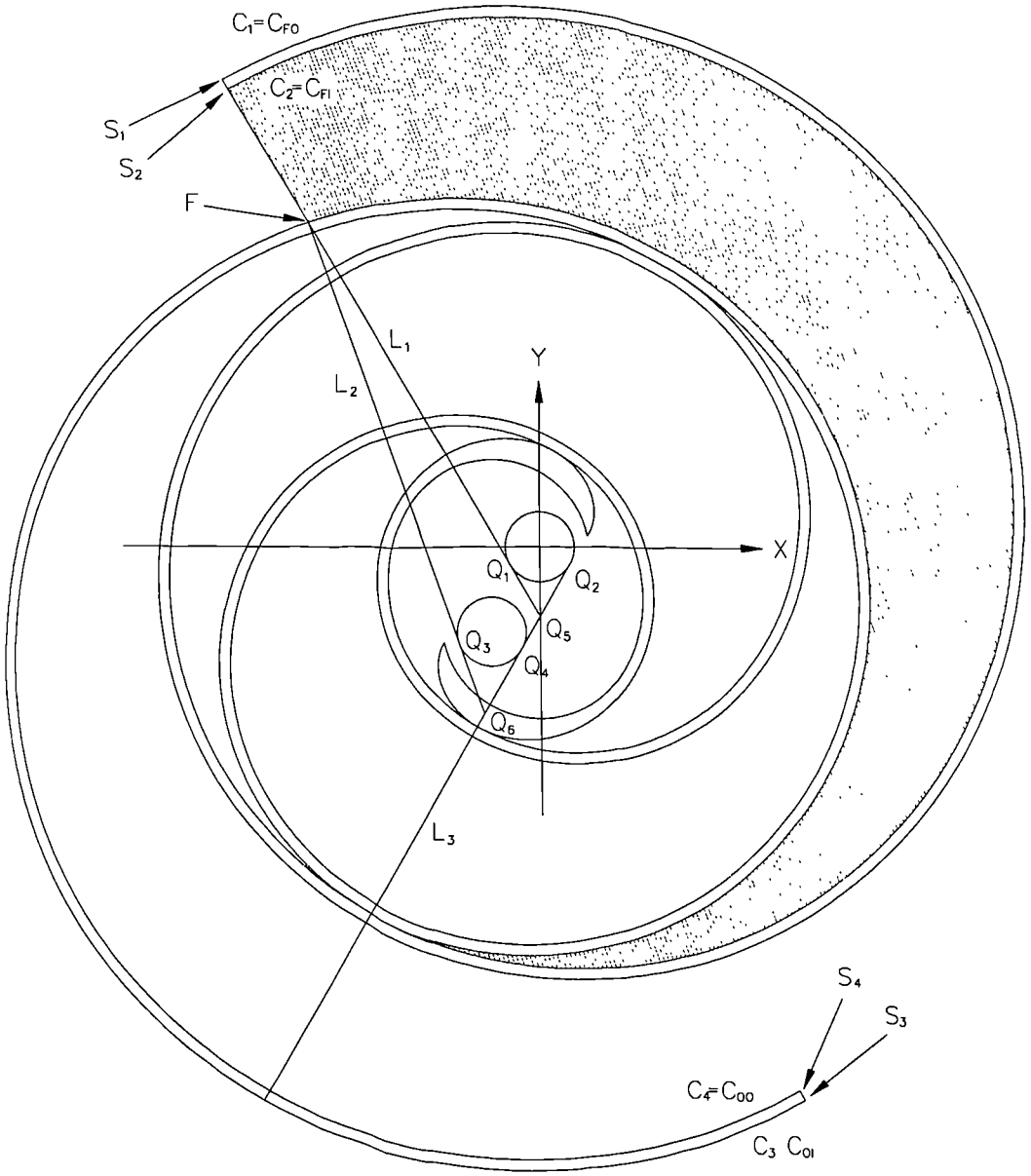

Figure (A-11d). *Scroll device with* $N = 1$ and $\alpha = 300^0 - \theta_{lim\,2}$ at $\theta = \theta_s - 240^0$.

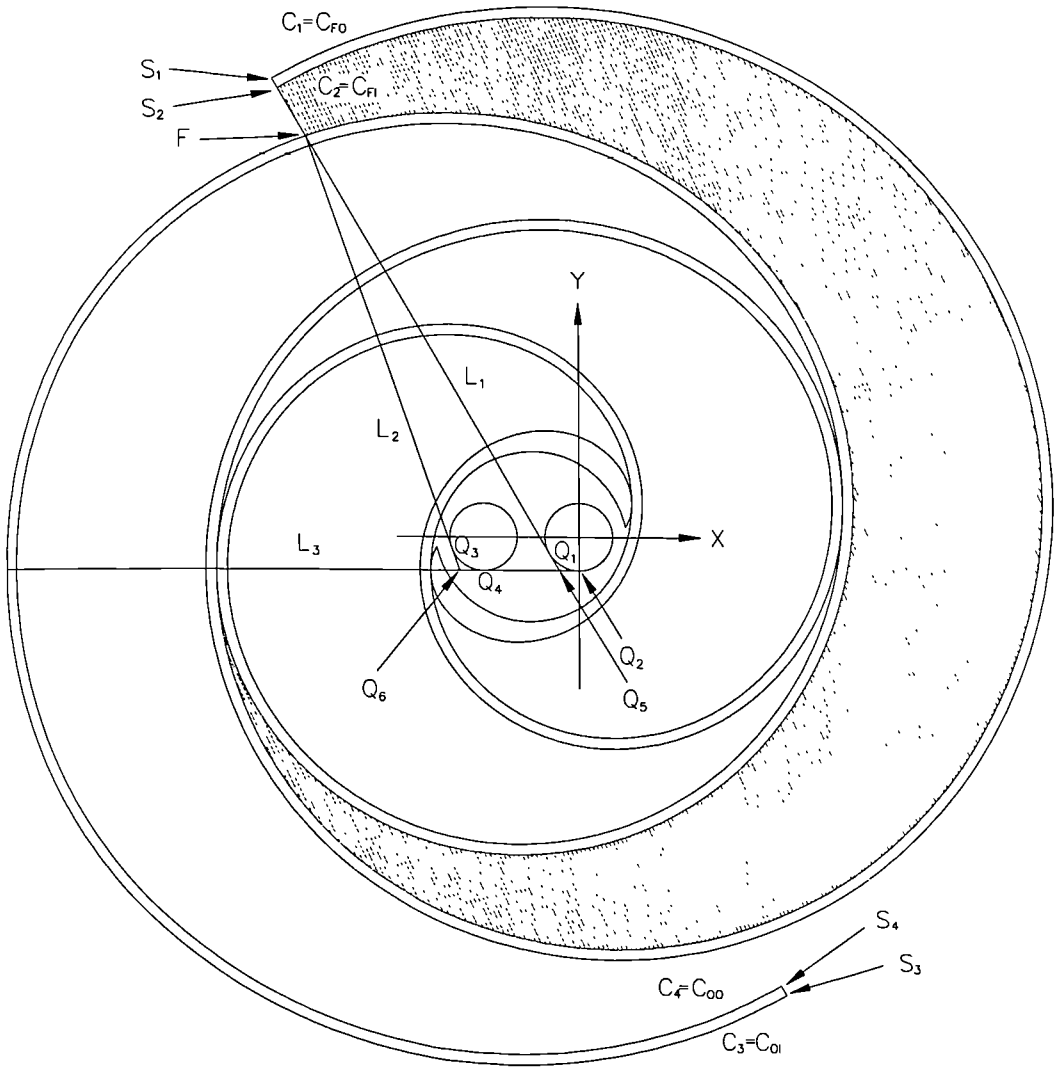

Figure (A-11e). Scroll device with $N = 1$ and $\alpha = 300^0 - \theta_{lim\,2}$ at $\theta = \theta_s - 300^0$.

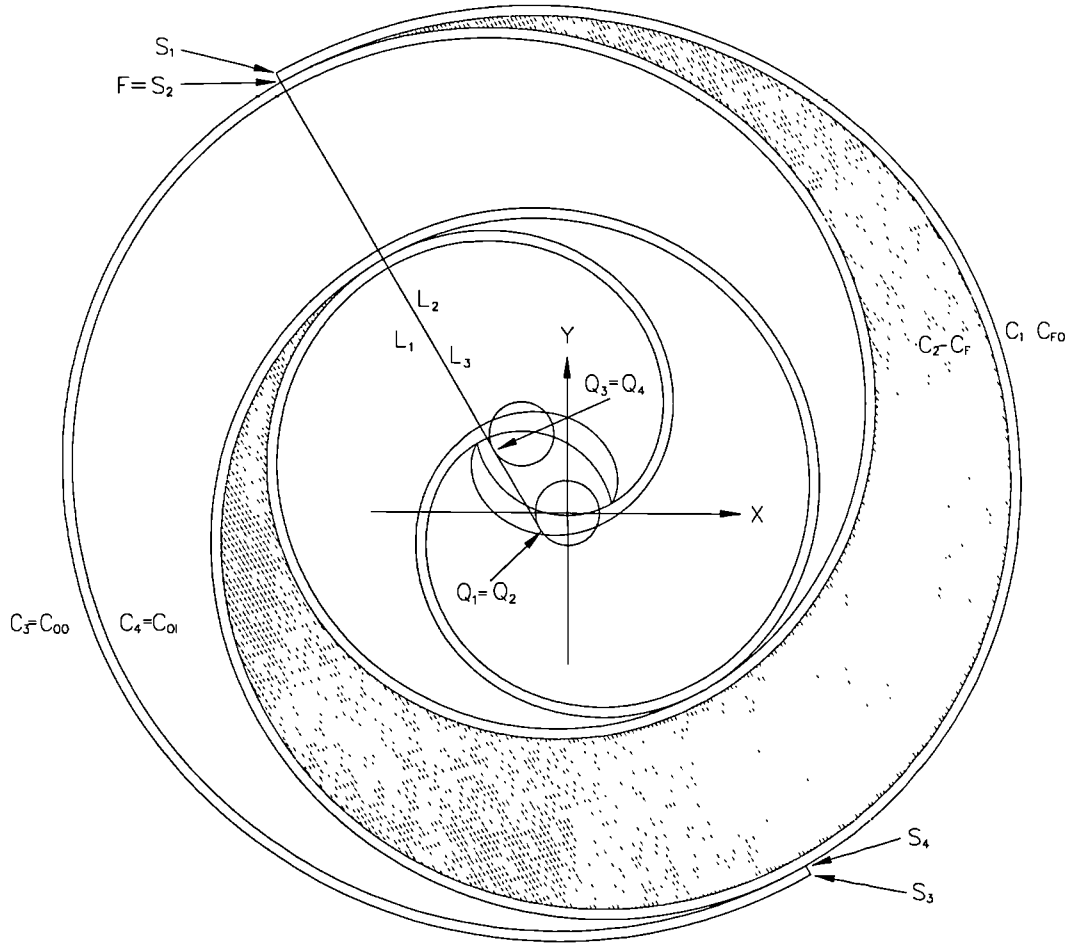

Figure (A-11f). *Scroll device with* $N = 1$ and $\alpha = 300^0 - \theta_{lim\,2}$ at $\theta = \theta_s - 360^0$.

Clearly, the number M depends on the values of the parameter N and the angle α, introduced by the relations *(A.55)* and *(A.56)*.

The geometry described in section A.2 allows the scroll device to operate either as an expander or as a compressor. The selection of the plus or minus sign in the above equation depends on the device's mode of operation. A clockwise rotation means that the device operates as a compressor and equation *(A.74)* should be taken with the minus sign. An anti-clockwise rotation means that the device operates as an expander and equation *(A.74)* should be taken with the plus sign. The two modes of operation can easily be realised from the figures presented in this chapter such as figures (A-11).

In practice it is important to be able to deduce the crank angle θ from the rotation angle Θ. For this purpose two pieces of pseudo-code are given below corresponding to the compressor and expander mode of the scroll device.

Compressor mode

$\theta = \Theta$
while ($\theta < \theta_{lim2}$)
$\{ \theta = \theta + 2\pi \}$

Expander mode

$\theta = \Theta$
while ($\theta \geq \theta_{lim2} + 2\pi$)
$\{ \theta = \theta - 2\pi \}$

A.3.2 Suction Chamber and its Working volume

When the scroll device operates as a compressor, the suction cycle begins at, $\Theta = \theta_s \pm 2n\pi$ and finishes after a full revolution of the moving spiral when $\Theta = \theta_s \pm 2n - 2\pi$, $n \in \backslash W$. The suction is associated with a pair of working chambers, sometimes called suction pockets. The volumes of these chambers increase smoothly from zero at the start of the cycle to a maximum at the end of it. The suction chambers are symmetrical and have the same geometry, shape, volumes, etc. Therefore, without loss of generality, only one of these chambers need to be studied, namely the chamber which is enclosed by the inner surface defined by the fixed spiral C_2 and the outer surface defined by the orbiting spiral C_3, This chamber is clearly marked in figures (A-11). The reason for the selection

of this chamber is simple, its outer wall, associated with the curve C_2, is fixed in space when referred to the XY coordinate system.

The suction chamber under study is completely sealed and its geometry fully defined by the curves C_2 and C_3 only when $\Theta = \theta_s \pm 2n\pi$, $n \in \backslash W$. For any other value of Θ this chamber is open at one end. In this case, in order to define the volume of the trapped fluid, the chamber is notionally sealed with a straight line connecting the end point S_2 with a point F located on the curve C_3, as shown in figures (A-11) and in detail in figure (A-12). The point F is selected in such a way that coincides with the point S_2 when $\Theta = \theta_s \pm 2n\pi$, $n \in \backslash W$ and the suction chamber is fully closed. At this position the points S_1, S_2 and F are collinear. We decide to maintain this condition of collinearity for any value of the angle Θ. Thus F is the point at which the straight line L_1, defined by the points S_1 and S_2, intersects the curve C_3 nearest to the point S_2. From this definition it is evident that the location of the point F on C_3 is not constant but varies slightly with the value of the rotation angle Θ.

The volume of the fluid trapped into the suction chamber when a suction cycle ends and a compression cycle is about to begin, is independent of the shape and the position of the sealing line L_1 as far as the points S_2 and F coincide at this instant when, of course, $\Theta = \theta_s \pm 2n\pi$, $n \in \backslash W$. In fact, just before the sealing of the suction pocket the points S_1, S_2 and F are nearly collinear and hence the straight line $L_1 \equiv S_1S_2$ is the only natural selection. Moreover, this selection facilitates the calculation of the suction volume since the line L_1 is fixed in space and independent of the value of the rotation angle Θ.

Figure (A-12) and equations *(A.26)* and *(A.62)* imply that the values of the parameter φ corresponding to the points S_2 and F when $\Theta = \theta_s \pm 2n\pi$, $n \in \backslash W$, are ω_2 and φ_{seal} respectively, where

$$\omega_2 = (2N+1)\pi + \frac{\pi}{2} + \theta_s - \gamma, \quad \varphi_{seal} \equiv (\omega_3 - \pi) = 2N\pi + \frac{\pi}{2} + \theta_s,$$
$$N \in \backslash W, \quad 0 \le \gamma < \pi - 2, \quad \theta_{lim2} \le \theta_s < (\theta_{lim2} + 2\pi). \qquad (A.75)$$

The value φ_F of the angle φ, defining the position of the point F on the curve C_3 when $\Theta \neq \theta_s \pm 2n\pi$, $n \in \backslash W$, differs only slightly from the value of φ_{seal}. It can therefore be written as

$$\varphi_F = \varphi_{seal} + \delta\varphi_F, \qquad (A.76)$$

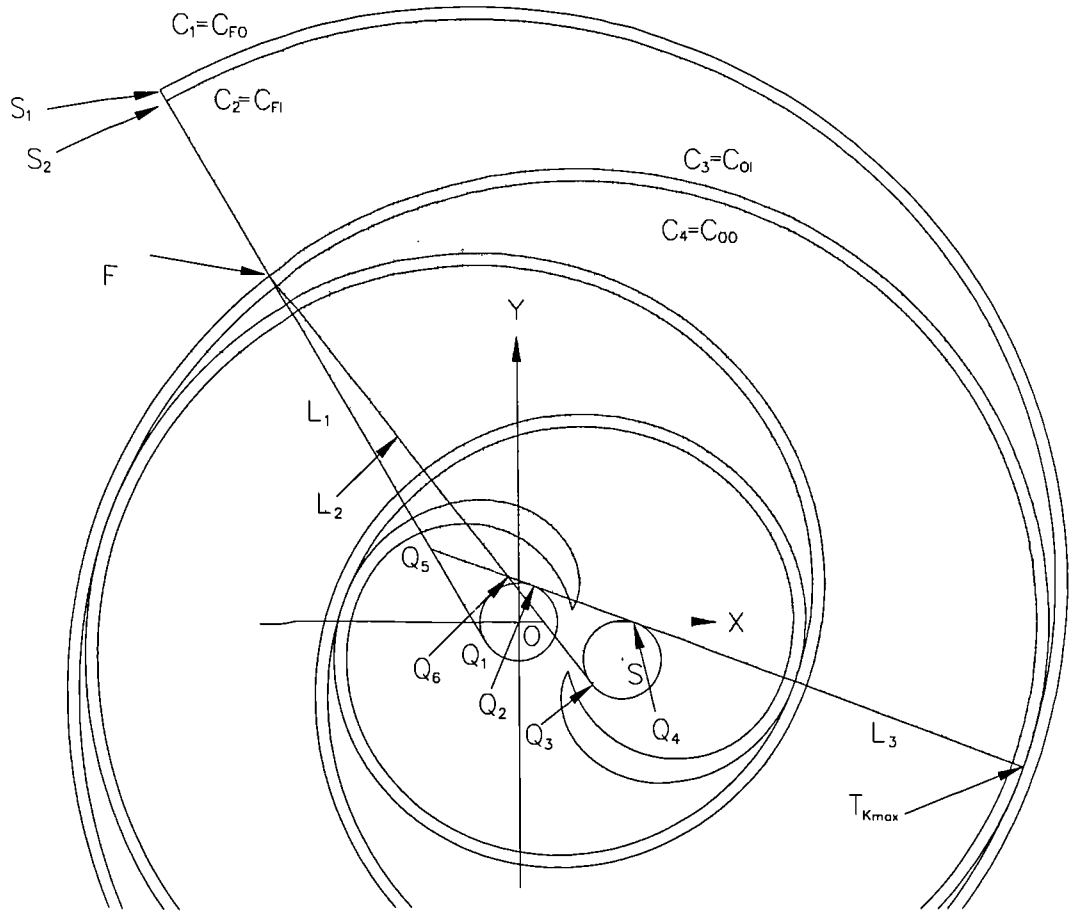

Figure (A-12). Details of suction chamber of a scroll compressor with $N = 1$ and $\alpha = 300^0 - \theta_{lim2}$ at $\theta = \theta_s - 140^0$.

where the correction angle $\delta\varphi_F$ is within few degrees from zero and is a function of the rotation angle Θ.

The analytical expression relating $\delta\varphi_F$ with Θ is obtained from the definition of the point F, as the point of intersection between the line L_1 and the curve C_3. By construction, the line L_1 passes through the points S_1 and S_2 whose coordinates are given by the first two of equations *(A.63)*. It is therefore fairly easy to prove that the equation defining the line L_1 has the form

$$L_1 : \; \mathbf{x}\sin\beta - \mathbf{y}\cos\beta = r, \quad x, y \in \Re, \quad \theta_{lim2} \le \beta < (\theta_{lim2} + 2\pi). \qquad (A.77)$$

The coordinates of the point

$$F \equiv \begin{pmatrix} x_F \\ y_F \end{pmatrix},$$

located on the involute C_3 and the line L_1, satisfy simultaneously the equation *(A.77)* and the third of equations *(A.10)*. Thus,

$$x_F \sin\beta - y_F \cos\beta = r,$$

$$F \equiv \begin{pmatrix} x_F \\ y_F \end{pmatrix} = -\begin{pmatrix} r(\cos\varphi_F + \varphi_F \sin\varphi_F) + d\cos\Theta \\ r(\sin\varphi_F - \varphi_F \cos\varphi_F) + d\sin\Theta \end{pmatrix}. \qquad (A.78)$$

These relations obey the conditions

$$\Theta = \theta \pm 2n\pi, \quad n \in \mathbb{W}, \quad \theta_{lim2} \le \beta < (\theta_{lim2} + 2\pi). \qquad (A.79)$$

Combining equations *(A.78)*, *(A.75)* and *(A.76)*, and after tedious and laborious algebraic manipulations, we obtain the relation between the correction and the rotation angles $\delta\varphi_F$ and Θ in the form

$$F(\delta\varphi_F) = 0,$$

where

$$F(\delta\varphi_F) \equiv r\cos(\delta\varphi_F) + r(2N\pi + \pi/2 + \beta + \delta\varphi_F)\sin\delta\varphi_F + [d\sin(\Theta - \beta) - r], \qquad (A.80)$$

$$\Theta = \theta \pm 2n\pi, \quad n \in \mathbb{W}, \quad \theta_{lim2} \le \beta < (\theta_{lim2} + 2\pi).$$

The roots of this equation cannot be determined analytically. Numerical techniques must therefore be employed in order to solved it with respect to $\delta\varphi_F$. Various fixed point methods (secant, bisection, fixed point iteration) have been tried. However, the Newton-Ralphson iterative algorithm was found to be the fastest and most accurate. This method is based on the formula

$$\delta\varphi_{F,i+1} = \delta\varphi_{F,i} - \left(\frac{F(\delta\varphi_F)}{dF(\delta\varphi_F)/\mathrm{d}\delta\varphi_F} \right)_{\delta\varphi_F = \delta\varphi_{F,i}}, \quad i \in \mathbb{W}, \qquad (A.81)$$

and if a prediction $\delta\varphi_{F,i}$ for the correction angle $\delta\varphi_F$ is available, a better prediction $\delta\varphi_{F,i+1}$ can be computed.

Differentiation of equation *(A.80)* once with respect to $\delta\varphi_F$ and introduction of the resulting expression, together with the function $F(\delta\varphi_F)$, into the above relation

furnishes the formula

$$\delta\varphi_{F,i+1} = \delta\varphi_{F,i} - \frac{r\cos(\delta\varphi_{F,i}) + r(2N\pi + \frac{\pi}{2} + \beta + \delta\varphi_{F,i})\sin(\delta\varphi_{F,i}) + d\sin(\Theta - \beta) - r}{r(2N\pi + \frac{\pi}{2} + \beta + \delta\varphi_{F,i})\cos(\delta\varphi_{F,i})} \qquad (A.82)$$

$$\Theta = \theta \pm 2n\pi\,, \quad i,\ n,\ N \in \mathbb{W}\,, \quad \theta_{lim2} \le \beta,\ \theta < (\theta_{lim2} + 2\pi)\,.$$

The correction angle $\delta\varphi_F$ is small compared to φ_F and its absolute value is very close to zero. Consequently, an obvious selection for the starting value of the iteration is $\delta\varphi_{F,0} = 0$. After $\delta\varphi_F$ is computed to the required accuracy, equations *(A.62)*, *(A.75)*, *(A.76)*, *(A.78)* and *(A.82)* allow the numerical calculation of the coordinates of the point F.

The line L_1, as defined above, is not only passing through the points S_1, S_2 and F, it is also tangent to the fixed generating circle at a point hereafter denoted by Q_1. The coordinates of this point which is fixed in space, are given by

$$Q_1 \equiv \begin{pmatrix} x_{Q1} \\ y_{Q1} \end{pmatrix} = r\begin{pmatrix} \cos(\omega_1) \\ \sin(\omega_1) \end{pmatrix},$$

or, upon introduction of the first of equations *(A.62)*

$$Q_1 \equiv \begin{pmatrix} x_{Q1} \\ y_{Q1} \end{pmatrix} = r\begin{pmatrix} \sin\beta \\ -\cos\beta \end{pmatrix}, \quad \theta_{lim2} \le \beta < (\theta_{lim2} + 2\pi)\,. \qquad (A.83)$$

It can easily be proved by direct substitution that the point Q_1 is located on the line L_1 and the circumference of the fixed generating circle. Furthermore, the gradients of the radius OQ_1 and the line L_1, obtained from equations *(A. 83)* and *(A. 77)*, are equal to $\tan\beta$ and $-\cot\beta$ respectively. Consequently, OQ_1 and L_1 are perpendicular. Hence, L_1 is tangent to the fixed generating circle at Q_1 as shown in figure (A-12).

The equations of two more straight lines, namely L_2 and L_3, are required for the determination of the volume of the suction chamber. Figure (A-12) shows the positions of the lines L_i (i=1,2,3) relative to the generating circles and the curves C_i (i=1,2,3,4).

By definition, the line L_2 passes through F and it is tangent to the orbiting generating circle at a point hereafter denoted by Q_3. Of course, from an external

point two tangents can be drawn to a circle. The ubiquity is resolved by selecting the line L_2 so that it coincide with the line L_1 when the suction chamber is completely sealed at $\Theta = \theta_s \pm 2n\pi$, $n \in \backslash W$. The coordinates of the touching point Q_3 are obtained from the definition of the involutes and the statement *(A.7)*. Since the location of F on the curve C_3 is determined by the angle φ_F, it easily can be shown that

$$Q_3 \equiv \begin{pmatrix} x_{Q3} \\ y_{Q3} \end{pmatrix} = \begin{pmatrix} r\cos(\varphi_F + \pi) - d\cos\Theta \\ r\sin(\varphi_F + \pi) - d\sin\Theta \end{pmatrix} = -\begin{pmatrix} r\cos\varphi_F + d\cos\Theta \\ r\sin\varphi_F + d\sin\Theta \end{pmatrix},$$
$$\Theta = \theta \pm 2n\pi, \quad n \in \backslash W, \quad \theta_{lim2} \le \theta < (\theta_{lim2} + 2\pi), \tag{A.84}$$

Note that the angle φ_F is adjusted by π. With this adjustment the angle defining the point Q_3 on the circumference of the orbiting generating circle is measured anti-clockwise from the positive X semi-axis, as against φ_F which is measured anti-clockwise from the negative X^* semi-axis.

The equation describing the line L_2 is deduced from the coordinates of the points F and Q_3, given by equations *(A.78)* and *(A.84)* respectively. After some calculations it can be shown that

$$L_2: \quad y\sin\varphi_F + x\cos\varphi_F = -(r + d\cos(\varphi_F - \Theta)),$$
$$\Theta = \theta \pm 2n\pi, \quad n \in \backslash W, \quad \theta_{lim2} \le \theta < (\theta_{lim2} + 2\pi). \tag{A.85}$$

The line L_3 is defined by any two pairs of points at which the curves C_2 and C_3 come in contact. It should be emphasised here that all here points are collinear. The values of the parameter φ corresponding to the two outermost pairs of these touching points, are obtained from the relations *(A.26)* and *(A.51)* and the definition of K_{max}. Thus,

$$\varphi_{3,K\,max} = 2K_{max}\pi + \pi/2 + \theta,$$
$$\varphi_{2,K\,max} = (2K_{max} + 1)\pi + \pi/2 + \theta - \gamma,$$
$$\varphi_{3,K\,max-1} = 2(K_{max} - 1)\pi + \pi/2 + \theta,$$
$$\varphi_{2,K\,max-1} = (2K_{max} - 1)\pi + \pi/2 + \theta - \gamma,$$
$$\theta_{lim2} \le \theta < (\theta_{lim2} + 2\pi), \quad 0 \le \gamma < \pi - 2. \tag{A.86}$$

Introducing these equations and equation *(A.22)* into the second and third of the relations *(A.10)*, and after long algebraic manipulations on the resulting coordinates, we obtain the following equation for the line L_3

$$L_3 \ : \ x\sin\Theta - y\cos\Theta = r\,,$$
$$\Theta = \theta \pm 2n\pi\,,\ n \in \backslash W\,,\ \theta_{\lim 2} \le \theta < (\theta_{\lim 2} + 2\pi)\,. \qquad (A.87)$$

This line is tangent to the fixed and orbiting generating circles at two points hereafter denoted by Q_2 and Q_4 respectively. Their geometry is shown in figure (A-12). The coordinates of these points are given by

$$Q_2 \equiv \begin{Bmatrix} x_{Q2} \\ y_{Q2} \end{Bmatrix} = r\begin{Bmatrix} \cos(\varphi_{2,K\max} + \gamma) \\ \sin(\varphi_{2,K\max} + \gamma) \end{Bmatrix},$$

$$Q_4 \equiv \begin{pmatrix} x_{Q4} \\ y_{Q4} \end{pmatrix} = \begin{pmatrix} r\cos(\varphi_{3,K\max} + \pi) - d\cos\Theta \\ r\sin(\varphi_{3,K\max} + \pi) - d\sin\Theta \end{pmatrix}, \qquad (A.88)$$

$$\Theta = \theta \pm 2n\pi\,,\ n \in \backslash W\,,\ \theta_{\lim 2} \le \theta < (\theta_{\lim 2} + 2\pi)\,,\ 0 \le \gamma < \pi - 2\,,$$

or, upon introduction of equation *(A.86)*

$$Q_2 \equiv \begin{pmatrix} x_{Q2} \\ y_{Q2} \end{pmatrix} = r\begin{pmatrix} \sin\Theta \\ -\cos\Theta \end{pmatrix},$$

$$Q_4 \equiv \begin{pmatrix} x_{Q4} \\ y_{Q4} \end{pmatrix} = \begin{pmatrix} r\sin\Theta - d\cos\Theta \\ -r\cos\Theta - d\sin\Theta \end{pmatrix}, \qquad (A.89)$$

$$\Theta = \theta \pm 2n\pi\,,\ n \in \backslash W\,,\ \theta_{\lim 2} \le \theta < (\theta_{\lim 2} + 2\pi)\,.$$

As mentioned above, the points Q_2 and Q_4 are located on the line L_3 and the circumferences of the fixed and orbiting generating circles. This can be proved by direct substitution of equations *(A.89)* into equation *(A.87)* and the equations of the generating circles. Note also that the gradients of the radii OQ_2 and SQ_4, obtained from the foregoing equations, are identical and equal to $-\cot\Theta$. On the other hand, the gradient of the line L_3, as derived from equation *(A.87)*, is $\tan\Theta$. Consequently, OQ_2 and SQ_4 are perpendicular to the line L_3. Hence, L_3 is tangent to the generating circles at the points Q_2 and Q_4 as shown in figure (A-12).

The values of the angles $\varphi_{2,\mathrm{K\,max}}$ and $\varphi_{3,\mathrm{K\,max}}$ entering equations *(A.88)*, have been adjusted by γ and π respectively. With these adjustments the angles defining the points Q_2 and Q_4 are measured anti-clockwise from the positive X semi-axis, as they should.

Two more points are required for the determination of the working volume of the suction chamber, namely the point Q_5, defined by the intersection of the lines L_1 and L_3, and the point Q_6 defined by the intersection of the lines L_2 and L_3. Equations *(A.77)*, *(A.85)* and *(A.87)* form two algebraic systems. These, when solved with respect to x and y, yield the following coordinates for the points Q_5 and Q_6

$$Q_5 \equiv \begin{pmatrix} x_{Q5} \\ y_{Q5} \end{pmatrix} = \left(\frac{r}{\sin(\Theta - \beta)} \right) \begin{pmatrix} \cos\beta - \cos\Theta \\ \sin\beta - \sin\Theta \end{pmatrix},$$

$$Q_6 \equiv \begin{pmatrix} x_{Q6} \\ y_{Q6} \end{pmatrix} = -\frac{1}{\cos(\varphi_F - \Theta)} \begin{pmatrix} \cos\Theta[r + d\cos(\varphi_F - \Theta)] - r\sin\varphi_F \\ \sin\Theta[r + d\cos(\varphi_F - \Theta)] + r\cos\varphi_F \end{pmatrix}, \qquad (A.90)$$

$$\Theta = \theta \pm 2n\pi, \quad n \in \mathbb{W}, \quad \theta_{lim2} \le \theta,\ \beta < (\theta_{lim2} + 2\pi).$$

In order to obtain the instantaneous working volume of the suction chamber as function of the crank angle Θ and the compressor's design parameters, we require the expressions for a number of surface areas. The description of these surface areas and the derivation of their analytical expressions are given below.

From the definition of the points Q_1, Q_2, S_2, T_{Kmax} and the diagram in figure (A-12), it is clear that the section $T_{Kmax}S_2$ of the involute C_2 is defined for values of the parameter φ lying in the closed interval $[\varphi_{2,\mathrm{K\,max}}, \omega_2]$. When constructing this section, the straight line segment Q_2T_{Kmax} moves from its original position to the position Q_1S_2, sweeping an area hereafter denoted by A_F. This area is shown in figure (A-12) hatched with vertical lines. In complete analogy, the section $T_{Kmax}F$ of the involute C_3 is defined for values of the parameter φ in the range $[\varphi_{3,\mathrm{K\,max}}, \varphi_F]$. When constructing this section, the straight line segment Q_4T_{Kmax} moves to the position Q_3F thus sweeping an area hereafter called A_0. This area is shown in figure (A-12) hatched with horizontal lines.

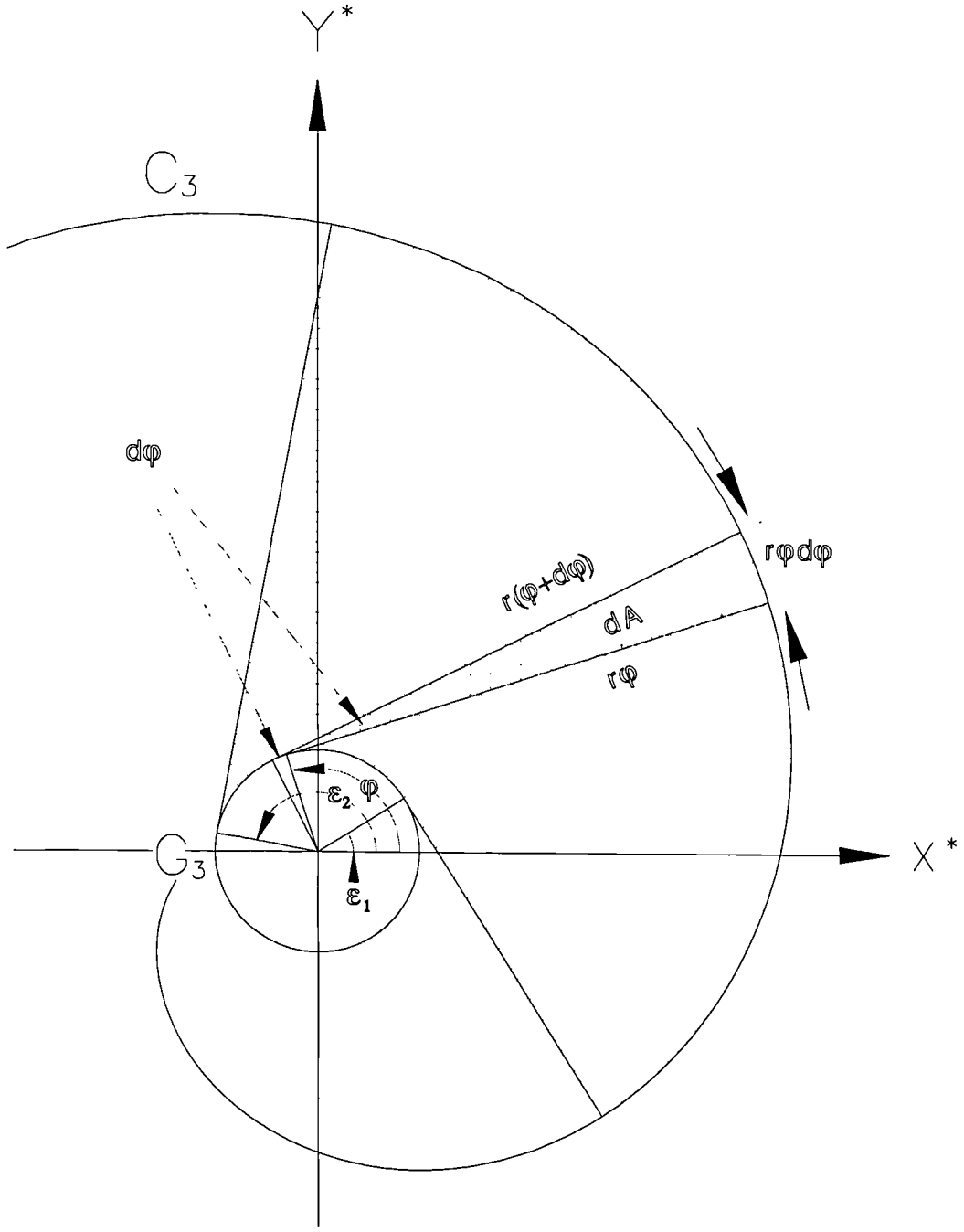

Figure (A-13). Determination of surface area under involute

The determination of the surface areas A_F and A_O is based on the definitions of the curves C_2 and C_3. Figure (A-13) portrays the orbiting generating circle together with a section of the curve C_3 starting from the tip G_3. The differential area dA, also shown in the figure, is swept by a line segment tangential to the generating circle, when the value of the parameter φ changes by $d\varphi$. According to statement *(A.7)*, any line tangential to the generating circle is perpendicular to the curve. Thus, the differential area dA approximated to the second order, is a triangle with base and height equal to $r\varphi d\varphi$ and $r\varphi$ respectively. Consequently

$$dA = \frac{1}{2}(r^2\varphi^2 d\varphi). \tag{A.91}$$

The integration of this relation with respect to φ from an initial angle ε_1 to a final angle ε_2 furnishes the marked area A shown in figure (A-13). Thus

$$A = \frac{1}{2}\int_{\varepsilon_1}^{\varepsilon_2} r^2\varphi^2 d\varphi = \frac{1}{6}r^2\left(\varepsilon_2^3 - \varepsilon_1^3\right). \tag{A.92}$$

The area is completely equivalent to the areas A_F and A_O, the only difference been the range of integration. By definition, integrating over the range $[\varphi_{2,K\max}, \omega_2]$ we obtain the area A_F, while integrating over the range $[\varphi_{3,K\max}, \varphi_F]$ we get the area A_O. Combining equations *(A.62)*, *(A.67)*, *(A.75)*, *(A.76)* and *(A.86)*, these areas can be expressed in the form

$$A_F = \frac{1}{6}r^2\left\{\omega_2^3 - \varphi_{2,K\max}^3\right\} =$$

$$= \frac{1}{6}r^2\left\{\left[(2N+1)\pi + \frac{\pi}{2} + \beta - \gamma\right]^3 - \left[(2K_{\max}+1)\pi + \frac{\pi}{2} + \theta - \gamma\right]^3\right\},$$

$$A_O = \frac{1}{6}r^2\left\{\varphi_F^3 - \varphi_{3,K\max}^3\right\} = \tag{A.93}$$

$$= \frac{1}{6}r^2\left\{\left[2N\pi + \frac{\pi}{2} + \beta + \delta\varphi_F\right]^3 - \left[2K_{\max}\pi + \frac{\pi}{2} + \theta\right]^3\right\},$$

$$N, K_{\max}, n \in \backslash W\ ,\quad \theta_{lim2} \le \theta, \beta < (\theta_{lim2} + 2\pi),\quad 0 < \gamma \le \pi - 2.$$

where $\delta\varphi_F$ is the correction angle obtained from the iterative algorithm *(A.82)*. The relations *(A.67)*, *(A.70)* and *(A.93)* guarantee that equations *(A.93)* always yield non-negative values for the surface areas A_F and A_O. For $\Theta = \theta_s \pm 2n\pi$, $n \in \backslash W$, these areas attain their minimum values $A_F = A_O = 0$. It is worth noting that the angle θ entering the foregoing equations, is the crank angle and not the rotational angle Θ. This is in agreement with what is stated in section A.2, since the areas A_F and A_O are part of the scroll compressor's geometry and only indirectly related to the motion of the fluid through the device.

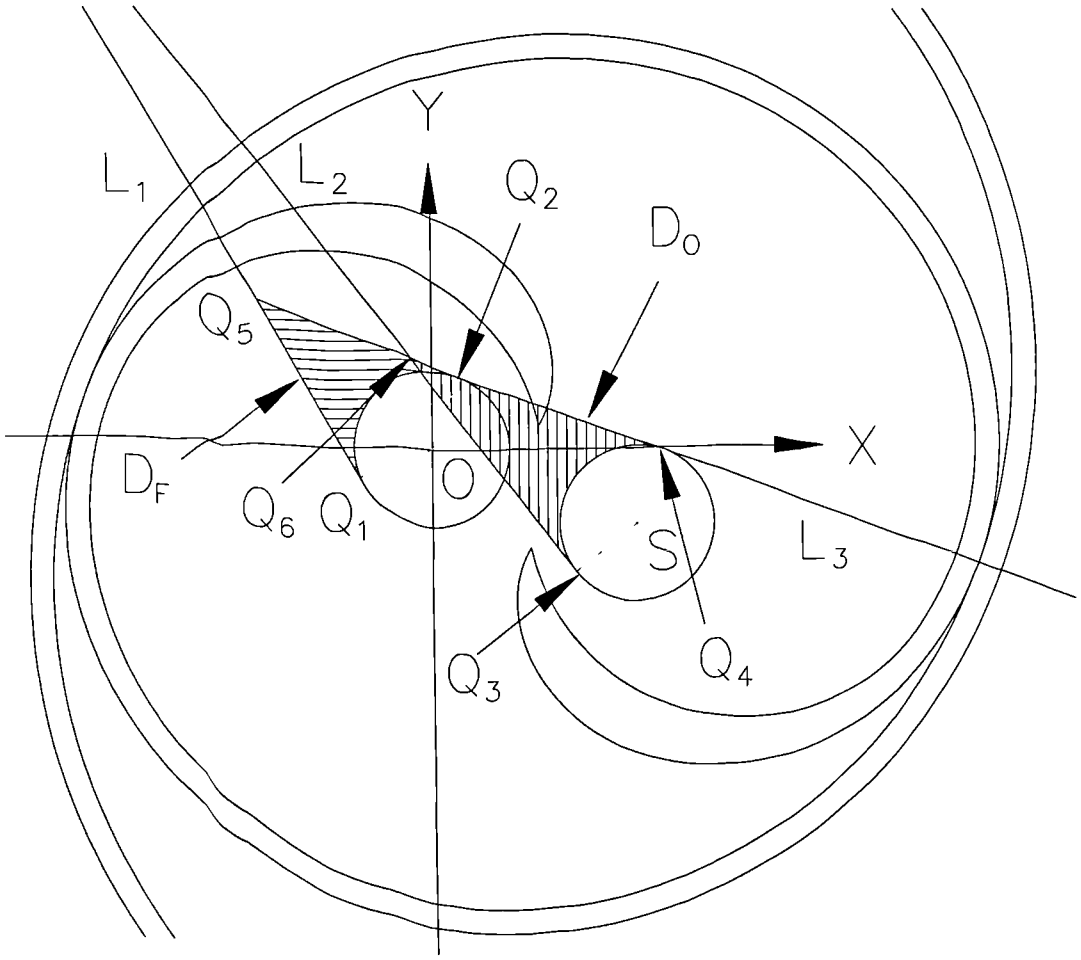

Figure (A-14). Details of the regions D_F and D_O

The determination of the instantaneous volume of the suction chamber cannot be completed without the expressions for the surface areas of three more plane geometric regions. These are, the region D_F bounded by the straight line segments Q_1Q_5, Q_2Q_5 and the minor circular arc Q_1Q_2; the region D_O bounded by the straight line segments Q_3Q_6, Q_4Q_6 and the minor circular arc Q_3Q_4; and finally the triangle FQ_5Q_6. The regions D_F and D_O are shown in figure (A-14), in comparatively large scale.

The area A_T of the triangle FQ_5Q_6 is computed from the formula

$$A_T = \{S(S-a)(S-b)(S-c)\}^{1/2}, \qquad (A.94)$$

where by definition a, b and c are the triangle's sides and S is the triangle's semi-perimeter, that is

$$a \equiv |Q_5Q_6|, \quad b \equiv |FQ_5|, \quad c \equiv |FQ_6|, \quad S \equiv \frac{1}{2}(a+b+c). \qquad (A.95)$$

The lengths a, b and c can be obtained from the coordinates of the points F, Q_5 and Q_6. The resulting expressions are extremely long and they are not be stated here. For computational purposes suffice to state the following

$$a = \left\{(x_{Q5}-x_{Q6})^2 + (y_{Q5}-y_{Q6})^2\right\}^{1/2},$$

$$b = \left\{(x_F-x_{Q5})^2 + (y_F-y_{Q5})^2\right\}^{1/2}, \qquad (A.96)$$

$$c = \left\{(x_F-x_{Q6})^2 + (y_F-y_{Q6})^2\right\}^{1/2}.$$

where the x and y coordinates entering these equations are given by the expressions *(A.78)* and *(A.90)*.

Figure (A-14) implies that the surface area A_{DF} of the region D_F is the difference of the surface areas of the quadrilateral $OQ_1Q_5Q_2$ and the minor circular sector Q_1OQ_2. Hence,

$$A_{DF} = \{\text{area of quadrilateral } OQ_1Q_5Q_2 \text{ - minor circular sector } Q_1OQ_2\}. \qquad (A.97)$$

Regardless of the value of the rotation angle Θ, the quadrilateral $OQ_1Q_5Q_2$ is an inscribed quadrilateral with angles $O\hat{Q}_1Q_5 = O\hat{Q}_2Q_5 = \pi/2$. Consequently,

$$\text{area of quadrilateral } OQ_1Q_5Q_2 = |OQ_1||Q_1Q_5| = r|Q_1Q_5|. \qquad (A.98)$$

The angle $Q_1\hat{O}Q_2$ is easily obtained from the geometry depicted in figure (A-14), thus

$$\text{angle } Q_1\hat{O}Q_2 = 2\arctan\left(\frac{|Q_1Q_5|}{r}\right). \qquad (A.99)$$

By virtue of this equation, the surface area of the minor circular sector Q_1OQ_2 is given by

$$\text{surface area of minor sector } Q_1OQ_2 = r^2\arctan\left(\frac{|Q_1Q_5|}{r}\right). \qquad (A.100)$$

In view of equations *(A.98)* and *(A.100)*, equation *(A.97)* becomes

$$A_{DF} = r\left\{|Q_1Q_5| - r\arctan\left(\frac{|Q_1Q_5|}{r}\right)\right\}. \qquad (A.101)$$

The expressions for the equal distances $|Q_1Q_5|$ and $|Q_2Q_5|$, obtained from the coordinates of the points Q_1, Q_2 and Q_5 given by equations *(A.83)*, *(A.88)* and *(A.90)*, have the form

$$|Q_1Q_5| = |Q_2Q_5| = r\frac{(1-\cos(\Theta-\beta))}{\sin(\Theta-\beta)}. \qquad (A.102)$$

Hence, equation *(A.101)* reduces to

$$A_{DF} = r^2\left\{\frac{1-\cos(\Theta-\beta)}{\sin(\Theta-\beta)} - \arctan\left[\frac{1-\cos(\Theta-\beta)}{\sin(\Theta-\beta)}\right]\right\}. \qquad (A.103)$$

Completely analogous steps furnish the follow relations from which the surface area A_{DO} of the region D_O can be deduced with the help of the geometry shown in figure (A-14)

A_{DO} = {area of quadrilateral $SQ_3Q_6Q_4$ - minor circular sector Q_3SQ_4},

$$\text{area of quadrilateral } SQ_3Q_6Q_4 = |SQ_3||Q_3Q_6| = r|Q_3Q_6|,$$

$$\text{angle } Q_3\hat{S}Q_4 = 2\arctan\left(\frac{|Q_3Q_6|}{r}\right),$$

$$\text{surface area of minor sector } Q_3SQ_4 = r^2 \arctan\left(\frac{|Q_3Q_6|}{r}\right),$$

$$A_{DO} = r\left\{|Q_3Q_6| - r\arctan\left(\frac{|Q_3Q_6|}{r}\right)\right\},$$

$$|Q_3Q_6| = |Q_4Q_6| = r\frac{(1-\cos(\Theta-\beta))}{\sin(\Theta-\beta)},$$

Combing these equations, we obtain the expression for the surface area A_{DO} of the region D_O in the form

$$A_{DO} = r^2\left\{\frac{1-\sin(\varphi_F-\Theta)}{\cos(\varphi_F-\Theta)} - \arctan\left[\frac{1-\sin(\varphi_F-\Theta)}{\cos(\varphi_F-\Theta)}\right]\right\}. \qquad (A.104)$$

Figures (A-11) and (A-12) show plan views of the scroll compressor-expander for various values of the crank angle θ. A careful inspection of these figures reveals that the base area A_S of the suction chamber can be computed using the following formulae

Table (A-2)

If	*then*	*and*
$\theta = \theta_S$	$\Theta = \theta_S \pm 2n\pi$, $n \in \backslash W$	$A_S = A_F - A_O = 0$
$\theta_S < \theta < \theta_P$	$\theta_S \pm 2n\pi < \Theta < \theta_S \pm 2n\pi$ $n \in \backslash W$	$A_S = A_F - A_O - (A_T + A_{DF} - A_{DO})$
$\theta = \theta_P$	$\Theta = \theta_P \pm 2n\pi$, $n \in \backslash W$	$A_S = A_F - A_O + 2rd = 2rd$
$\theta_P < \theta < (\theta_S + 2\pi)$	$\theta_S \pm 2n\pi < \Theta < \theta_P \pm 2n\pi + 2\pi$ $n \in \backslash W$	$A_S = A_F - A_O + (A_T + A_{DF} - A_{DO})$

where, by definition $\theta_P \equiv \theta_S + \pi$. Evidently, the surface areas entering the equations in table (A-2) are given by *(A.93)*, *(A.94)*, *(A.103)* and *(A.104)*.

The terms $\cos(\varphi_F - \Theta)$ and $\sin(\Theta - \varphi_F)$ appearing as denominators in the foregoing expressions vanish for specific values of the rotation angle Θ and they may cause computational problems while calculating the suction volume. Specifically, for $\Theta = \theta_S \pm n\pi$, $n \in \backslash W$ equations *(A.67)*, *(A.75)*, *(A.76)*, and *(A.82)* furnish

$$\sin(\Theta - \beta)\Big|_{\Theta=\theta_s \pm n\pi} = \cos(\varphi_F - \Theta)\Big|_{\Theta=\theta_s \pm n\pi} = 0 \qquad (A.105)$$

This implies infinite values for the distances $|Q_1Q_5|$, $|Q_3Q_6|$, $|Q_5Q_6|$, $|F_3Q_5|$, $|FQ_6|$ and the areas A_{DF} and A_{DO}. However, as the rotation angle Θ approaches the values $\Theta = \theta_S \pm n\pi$, $n \in \backslash W$, the area $(A_T + A_{DF} - A_{DO})$ tends to finite values. Indeed,

$$\lim_{\Theta \to \theta_S \pm (2n+1)\pi} (A_T + A_{DF} - A_{DO}) = 2rd \qquad (A.106)$$

and

$$\lim_{\Theta \to \theta_S \pm 2n\pi} (A_T + A_{DF} - A_{DO}) = 0 \qquad (A.107)$$

A.3.3 Compression Chamber and its Working volume

Following the suction process, the first compression cycle starts when $\theta = \theta_S - 2\pi$, $\Theta = \theta \pm 2n\pi$, $n \in \backslash W$ and completes after a full rotation when $\theta = \theta_S - 4\pi$, $\Theta = \theta \pm 2n\pi - 2\pi$; $n \in \backslash W$. If the design of the scroll device allows for more than one compression cycle, the m^{th}, $m \in {}^+Z$ such cycle starts when $\Theta = \theta \pm 2n\pi - 2m\pi$, $n \in \backslash W$, $m \in {}^+Z$ and completes when $\Theta = \theta \pm 2n\pi - 2(m+1)\pi$, $n \in \backslash W$, $m \in {}^+Z$, where the symbol ${}^+Z$ denotes the set of the positive integers.

Due to the symmetry of the device each compression cycle is associated with a pair of geometrically equivalent chambers. These chambers, regardless of the value of Θ, have the same shape and area. They also have rotational symmetry of 180^0. In the general case of the m^{th}, $m \in {}^+Z$ compression cycle, the first of these chambers is formed by the scroll device's surfaces defined by the curves C_2 and C_3

and it is sealed by two pairs of touching points corresponding to the following values of the parameter φ

$$\varphi_{3,K\,max-m+1} = 2(K_{max} - m + 1)\pi + \pi/2 + \theta,$$

$$\varphi_{2,K\,max-m+1} = 2(K_{max} - m + 1)\pi + \pi + \pi/2 + \theta - \gamma,$$

$$\varphi_{3,K\,max-m} = 2(K_{max} - m)\pi + \pi/2 + \theta, \qquad (A.108)$$

$$\varphi_{2,K\,max-m} = 2(K_{max} - m)\pi + \pi + \pi/2 + \theta - \gamma,$$

$$\theta_{lim2} \le \theta < (\theta_{lim2} + 2\pi), \quad 0 \le \gamma < \pi - 2, \quad m \in {}^{+}Z.$$

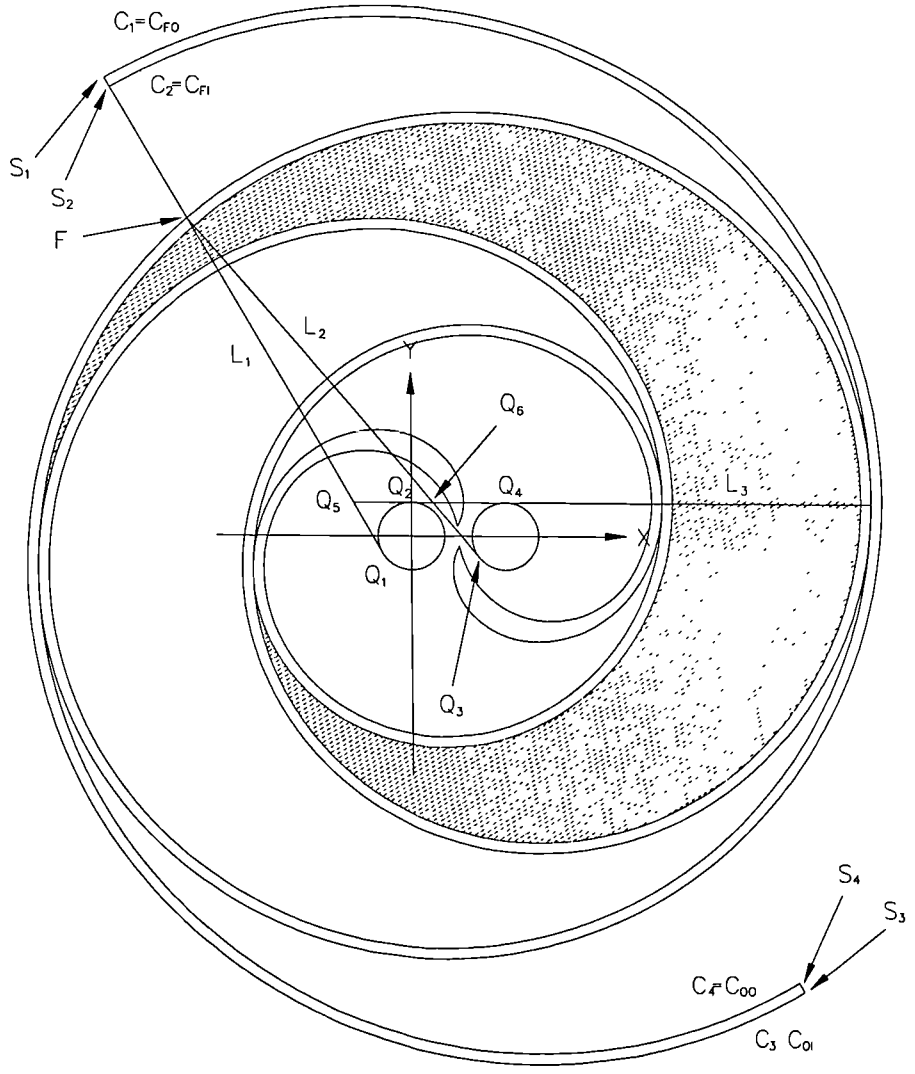

Figure (A-15). Details of a compression chamber

The second chamber is formed by the by the scroll device's surfaces defined by the curves C_1 and C_4 and it is sealed by the touching points associated with the following values of the parameter φ

$$\varphi_{1,K\max-m+1} = \varphi_{3,K\max-m+1}, \qquad \varphi_{4,K\max-m+1} = \varphi_{2,K\max-m+1}$$

$$\varphi_{1,K\max-m} = \varphi_{3,K\max-m}, \qquad \varphi_{4,K\max-m} = \varphi_{2,K\max-m}$$

A plane view of the scroll compressor is shown in figure (A-15), where one of the outermost compression chambers is clearly marked. From these figure as well as figures (A-11) and (A-12), it is clear that following steps similar to the steps leading to equations *(A.93)*, we obtain the expression for the base area $A_{C,m}$ of either of the symmetrical compression chambers of the m^{th}, $m \in {}^{+}Z$ compression cycle. This expression has the form

$$A_{C,m} = \frac{1}{2} r^2 \left\{ \int_{\varphi 2,K\max-m}^{\varphi_{2,K\max-m+1}} \varphi^2 d\varphi - {}^2 \int_{\varphi 3,K\max-m}^{\varphi_{3,K\max-m+1}} \varphi^2 d\varphi \right\} =$$

$$\frac{r^2}{2}\Big\{\big[2(K_{\max}-m+1)\pi+\pi+\pi/2+\theta-\gamma\big]^3 - \big[2(K_{\max}-m)\pi+\pi+\pi/2+\theta-\gamma\big]^3 \qquad (A.109)$$

$$-\big[2(K_{\max}-m+1)\pi+\pi/2+\theta\big]^3 + \big[2(K_{\max}-m)\pi+\pi/2+\theta\big]^3\Big\}$$

$$\theta_{\lim 2} \le \theta, \beta < (\theta_{\lim 2} + 2\pi), \quad 0 < \gamma \le \pi - 2, \quad m \in {}^{+}Z$$

The formulae given above hold only for cases where the compression chambers are formed by surfaces fully described by the curves *(A.10)*. However, there are cases in which parts of the walls are formed by the innermost circular arcs defined by equations *(A.36)*, *(A.38)*, *(A.44)* and *(A.46)*, as shown in figure (A-16). Clearly the equation *(A.109)* cannot be applied. This equation is not valid under the condition $\theta_{\lim 1} \le \theta < (\theta_{\lim 2} + 2\pi)$. In these cases, in order to determine the base area $A_{C,m}$, m^{th}, $m \in {}^{+}Z$, knowledge of the following areas is required :

- The area A_{D1} enclosed by the curve C_1=C_{FO}, the innermost circular arc T_2G_1 and the straight line segment $T_2T_2^*$, shown in figure (A-16). In figure (A-17) this area is hatched with horizontal lines.
- The base area A_{D2}. This is the section of the device's fixed arm, enclosed by the straight line segments $T_2T_2^*$ and AC and the curves C_1=C_{FO} and C_2=C_{FI}. It is shown in figure (A-16) and partially in figure (A-17) hatched with slant lines. By construction, the straight line segment AC is perpendicular to all

curves C_i $(i=1,2,3,4)$, while by definition, the point B is located on this segment and is the first touching point between the curves $C_1=C_{FO}$ and $C_4=C_{OI}$. The values of the parameter φ corresponding to point B are given by equations ***(A.26)*** and have the form $\varphi_1=\varphi_{1,0}=\pi/2+\theta$ and $\varphi_4=\varphi_{4,0}=\pi+\pi/2+\theta-\gamma$.

- The area A_{D3} enclosed by the two generating circles and their external tangents, shown in figure (A-16) cross-hatched.

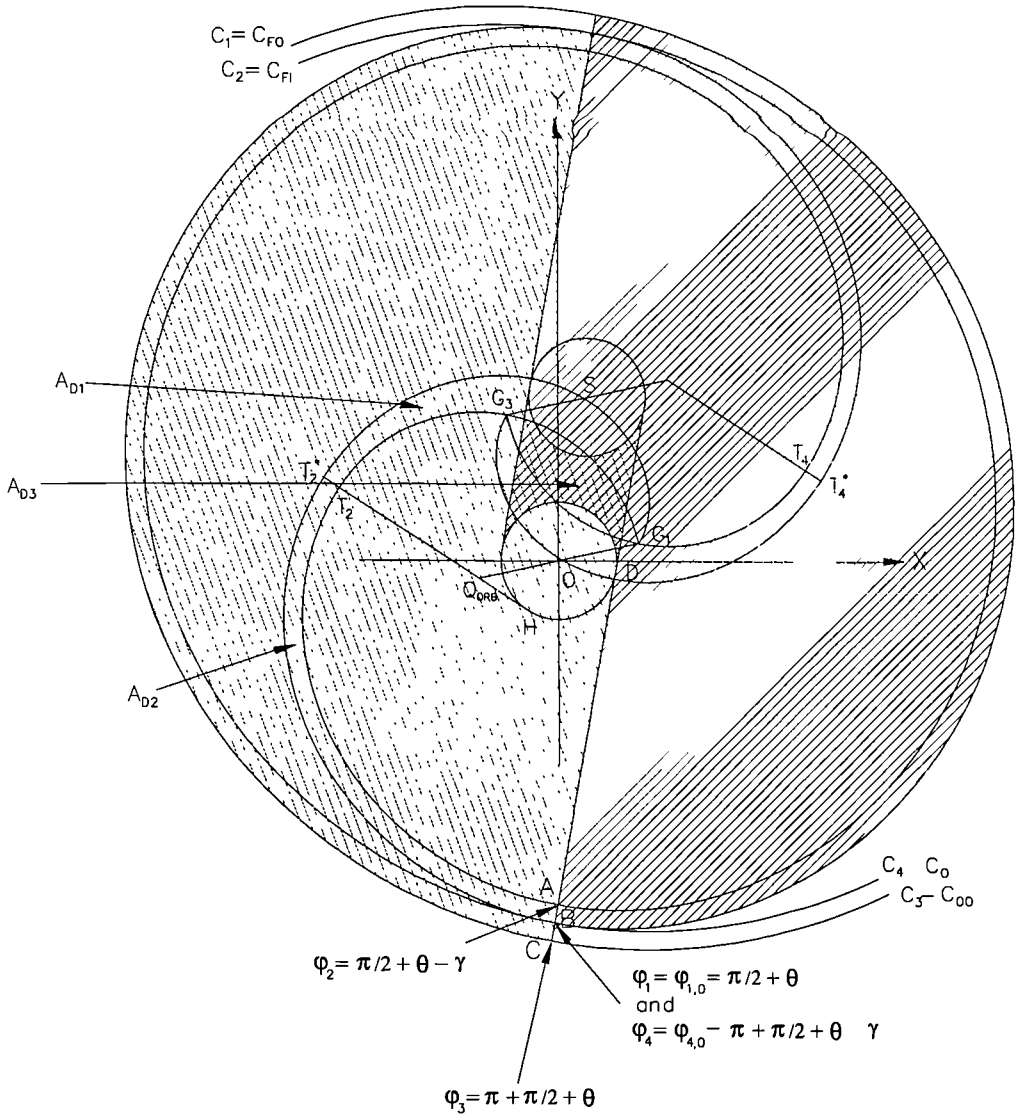

Figure (A-16). Details of a innermost compression chambers.

- The area A_{D4} enclosed by the innermost circular arcs defined by equations *(A.36)*, *(A.38)*, *(A.44)* and *(A.46)*, for various values of the crank angle θ in the semi-open interval $[\theta_{lim1},\ \theta_{lim2}+2\pi)$,.

The determination of the above mentioned areas require knowledge of the sizes of various angles and the lengths of a series straight line segments, which are calculated below.

From figures (A-7a) and (A-17), the definition *(A.36)* of the tip point G_1 and the definition *(A.41)* of the angle θ_{lim1}, it is at once obvious that

$$X\hat{O}F = \varphi_{cr} \quad \text{and} \quad X\hat{O}G_1 = \theta_{lim1} - \pi = \varphi_{cr} - \arctan\varphi_{cr}, \tag{A.110}$$

and hence,

$$G_1\hat{O}F = X\hat{O}F - X\hat{O}G_1 = \arctan\varphi_{cr}. \tag{A.111}$$

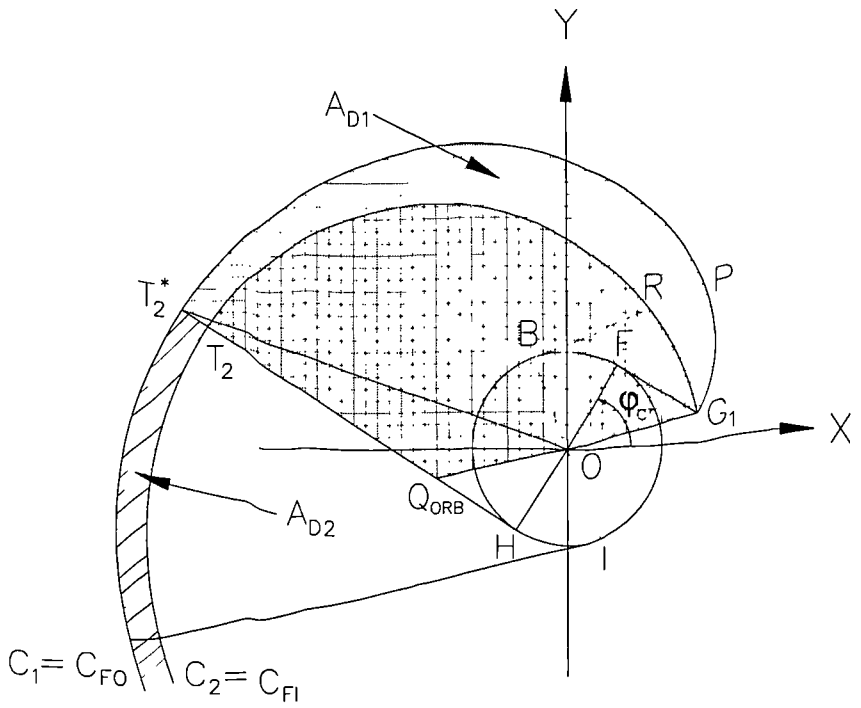

Figure (A-17). The base areas A_{D1} and A_{D2}

On the other hand, according to equations *(A.37)*, the point T_2 is located on the curve C_2=C_{FI} and the corresponding value of the parameter φ is $\varphi_2 = \varphi_{2S} = \pi + \varphi_{cr} - \gamma$. Therefore, as suggested by equations *(A.36)* and *(A.35)*, the value of φ corresponding to the point T_2^*, located on the curve C_1=C_{FO}, is

$$X\hat{O}H = \varphi_{2S} + \gamma = \pi + \varphi_{cr}. \qquad (A.112)$$

This equation and the definition of the curve C_1=C_{FO} furnish

$$HT_2^* = OH(X\hat{O}H) = r(\pi + \varphi_{cr}), \qquad (A.113)$$

consequently,

$$H\hat{O}T_2^* = \arctan\left(\frac{HT_2^*}{OH}\right) = \arctan(\pi + \varphi_{cr}). \qquad (A.114)$$

The coordinates of the point H, obtained form this equation, are given by

$$H = \begin{pmatrix} x_H \\ y_H \end{pmatrix} = r\begin{pmatrix} \cos(\varphi_{cr} + \pi) \\ \sin(\varphi_{cr} + \pi) \end{pmatrix} = -r\begin{pmatrix} \cos\varphi_{cr} \\ \sin\varphi_{cr} \end{pmatrix}. \qquad (A.115)$$

The foregoing equation and equations *(A.37)* and *(A.38)* furnish the slopes of the straight line segments $T_2^*\hat{Q}_{ORB}$ and $\hat{Q}_{ORB}H$. These slopes are identical and equal to $-\cot\varphi_{cr}$. Therefore, the points T_2^*, $\hat{Q}_{ORB}$ and H are collinear. Similarly, from equations *(A.110)* and *(A.112)*, it is evident that the angle $F\hat{O}H$ is a straight angle and thus the points F, O and H are also collinear. Furthermore, combining equations *(A.38)* and *(A.115)*, the distance $H\hat{Q}_{ORB}$ is found to be

$$H\hat{Q}_{ORB} = r\varphi_{cr}, \qquad (A.116)$$

hence

$$H\hat{O}Q_{ORB} = \arctan\left(\frac{HQ_{ORB}}{OH}\right) = \arctan\varphi_{cr}, \qquad (A.117)$$

and

$$O\hat{Q}_{ORB}T_2^* = O\hat{H}Q_{ORB} + H\hat{O}Q_{ORB} = \frac{\pi}{2} + \arctan\varphi_{cr}. \qquad (A.118)$$

From figure (A-17) and equations *(A.111)* and *(A.117)* it is evident that the triangles FOG_1 and HOQ_{ORB} are equal, that is

$$\Delta FOG_1 = \Delta HOQ_{ORB}\,. \qquad (A.119)$$

As a result of this relation, the areas of the plane figures $HFG_1PT_2^*H$ and $Q_{ORB}G_1PT_2^*Q_{ORB}$ are equal and hence figure (A-17) easily yields the following relation

$$A_{D1-F} \equiv \textit{area of}\ \ Q_{ORB}G_1PT_2^*Q_{ORB} = \textit{area of}\ \ HFG_1PT_2^*H = \\ = \textit{area of}\ \ HBFG_1PT_2^*H + \frac{\pi r^2}{2}\,. \qquad (A.120)$$

The area of the plane figure $HBFG_1PT_2^*H$ entering the foregoing equation is swept by the tangent to the fixed generating circle BP, as it moves from the position FG_1 to the position HT_2^*. It can therefore be calculated following steps completely analogous to the steps leading to equation *(A.92)*, where of course $\varepsilon_1 = X\hat{O}F = \varphi_{cr}$ and $\varepsilon_2 = X\hat{O}H = \pi + \varphi_{cr}$. Thus equation *(A.120)* takes the form

$$A_{D1-F} \equiv \textit{area of}\ \ Q_{ORB}G_1PT_2^*Q_{ORB} = \frac{r^2}{6}\left\{(\pi+\varphi_{cr})^3 - \varphi_{cr}^{\,3}\right\} + \frac{\pi r^2}{2}\,. \qquad (A.121)$$

The base area A_{D1}, as figure (A-17) suggests, is obtained by subtracting the area A_{D1-C} of the circular sector $Q_{ORB}G_1T_2$, centered at Q_{ORB}, from the area $A_{D1\,F}$ of the plane figure $Q_{ORB}G_1PT_2^*Q_{ORB}$, that is

$$A_{D1} = A_{D1-F} - A_{D1-C}\,. \qquad (A.122)$$

The area A_{D1-C} of the circular sector, determined with the help of equation *(A.118)*, is given from

$$A_{D1-C} = \pi r^2 \frac{O\hat{Q}_{ORB}T_2^*}{2\pi} = \frac{r^2}{2}\left\{\frac{\pi}{2} + \arctan\varphi_{cr}\right\}. \qquad (A.123)$$

Substitution of the relations *(A.121)* and *(A.123)* into equation *(A.122)* yields

$$A_{D1} = \frac{r^2}{2}\left\{\frac{1}{3}\left[(\pi+\varphi_{cr})^3 - \varphi_{cr}^{\,3}\right] + \frac{\pi}{2} - \arctan\varphi_{cr}\right\}. \qquad (A.124)$$

The determination of the area A_{D2} is again based on the discussion leading to equation *(A.92)*. By definition , the values of the parameter φ corresponding to the points A, B and C shown in figure (A-16), are given by

$$\varphi_{1B} = \varphi_{1,0} = \frac{\pi}{2} + \theta, \qquad \varphi_{4B} = \pi + \frac{\pi}{2} + \theta - \gamma,$$
$$\varphi_{2A} = \varphi_{2,0} = \frac{\pi}{2} + \theta - \gamma, \qquad \varphi_{3C} = \pi + \frac{\pi}{2} + \theta \ . \tag{A.125}$$

On the other hand, according to equation *(A.112)*, the values of the parameter φ corresponding to the points T_2^* and T_2 are

$$\varphi_{1T_2^*} = X\hat{O}H = \varphi_{2S} + \gamma = \pi + \varphi_{cr} \quad \text{and} \quad \varphi_{2T_2} = \varphi_{2S} = \pi + \varphi_{cr} - \gamma \tag{A.126}$$

respectively.

From figure (A-16) it is evident that the area A_{D2} is the difference of the areas swept by the tangents to the fixed generating circle HT_2^* and HT_2 as they move form their original positions to the positions DB and DA. Thus, according to equations *(A.92)*, *(A.125)* and *(A.126)*

$$A_{D2} = \frac{1}{2}\left\{\int_{\pi+\varphi_{cr}}^{\pi/2+\theta} r^2\varphi^2 d\varphi - \int_{\pi+\varphi_{cr}-\gamma}^{\pi/2+\theta-\gamma} r^2\varphi^2 d\varphi\right\} =$$
$$= \frac{r^2}{6}\left\{\left(\frac{\pi}{2}+\theta\right)^3 - \left(\frac{\pi}{2}+\theta-\gamma\right)^3 - (\pi+\varphi_{cr})^3 + (\pi+\varphi_{cr}-\gamma)^3\right\}. \tag{A.127}$$

The base area A_{D3} is the difference between the areas of a parallelogram and a generating circle. The width of the parallelogram is equal to the distance between the centres of the generating circles while its breadth is equal to their common diameter. Thus

$$A_{D3} = r(2d - \pi r) \tag{A.128}$$

The area A_{D4} is the common intersection of two identical circles. From elementary geometry is known that such an area is given by $R^2(\omega - \sin\omega)/2$, where R is the common radius of the intersecting circles and ω is the angle to which the common chord subtends.

The co-ordinates of the point G_3 when referred to a system of axes $X'Y'$ shown in figure (A-18), been parallel to XY and centered at the point Q_{ORB}, are obtained from equations *(A.36)* and *(A.38)*, thus

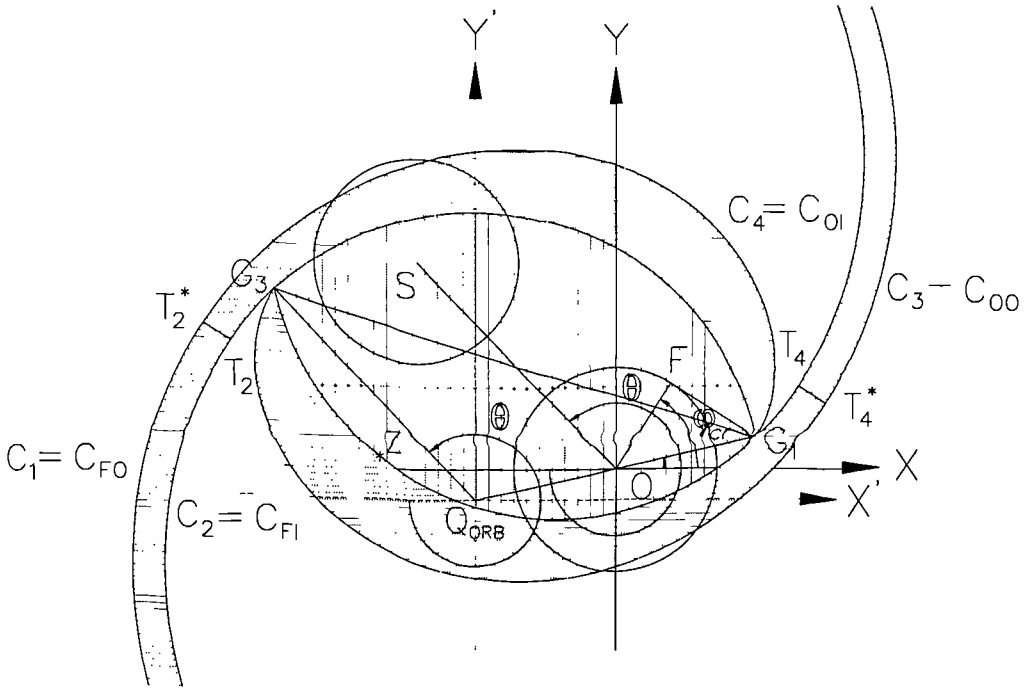

Figure (A-18). Details of the innermost miniscus

$$G_3 = \begin{pmatrix} x_{G_3} \\ y_{G_3} \end{pmatrix} - \begin{pmatrix} x_{Q_{ORB}} \\ y_{Q_{ORB}} \end{pmatrix} = d\begin{pmatrix} \cos(\pi+\theta) \\ \sin(\pi+\theta) \end{pmatrix} = -d\begin{pmatrix} \cos\theta \\ \sin\theta \end{pmatrix}. \qquad (A.129)$$

Consequently, the line segments $Q_{ORB}G_3$ and OS are parallel having the same slope equal to $-\tan\theta$. Referring to equation *(A.41)* and the figures (A-15), (A-16) and (A-17), we have

$$X'\hat{O}G_1 = X\hat{O}G_1 = \varphi_{cr} - \arctan\varphi_{cr} \qquad (A.130)$$

and therefore

$$G_1\hat{O}S = G_1\hat{Q}_{orb}G_3 = \theta - \pi - (\varphi_{cr} - \arctan\varphi_{cr}) = \theta - \theta_{lim1},$$
$$\theta_{lim1} \le \theta \le (\theta_{lim1} + 2\pi). \qquad (A.131)$$

Furthermore equations *(A.37)* and *(A.38)* furnish $Q_{ORB}T_2 = r(\pi - \gamma) = d$ while by definition $OS = d$. Hence

$$Q_{ORB}T_2 = OS = d. \qquad (A.132)$$

Application of the formula $R^2(\omega - \sin\omega)/2$ mentioned above for $R = d$ and $\omega = G_1\hat{Q}_{ORB}G_3 = \theta - \theta_{lim1}$, furnishes

$$A_{D4} = \frac{d^2}{2}\{(\theta - \theta_{lim1}) - \sin(\theta - \theta_{lim1})\}. \qquad (A.133)$$

Having found the expressions for the areas A_{D1}, A_{D2} and A_{D3} it is easy to determine the area $A_{C,m}$, m^{th}, $m \in {}^{+}Z$ of the innermost compression chambers.

$$I = \frac{1}{2}r^2\left\{\int_{\frac{\pi}{2}+\theta-\gamma}^{\pi+\frac{\pi}{2}+\theta-\gamma}\varphi^2 d\varphi\right\} = \frac{1}{6}r^2\left\{\left[\pi + \frac{\pi}{2} + \theta - \gamma\right]^3 - \left[\frac{\pi}{2} + \theta - \gamma\right]^3\right\} \qquad (A.134)$$

$$\theta_{lim1} \le \theta < (\theta_{lim2} + 2\pi)$$

Therefore,

$$A_{C,m} = \frac{(2I - A_{D3}) - 2A_{D2} - 2A_{D1} - A_{D4}}{2} = I - \frac{A_{D3}}{2} - A_{D2} - A_{D1} - \frac{A_{D4}}{2} \qquad (A.135)$$

A.3.4 Discharge Chamber and its Working volume

Following the compression process, the discharge cycle starts when $\Theta = \theta \pm 2n\pi - 2(m+1)\pi$, $n \in \backslash W$, $m \in {}^{+}Z$, where the symbol ${}^{+}Z$ denotes the set of the positive integers, and completes when $\Theta = \theta \pm 2n\pi - 2(m+2)\pi$.

For values of the parameter θ in the range $\theta_{lim1} \le \theta < (\theta_{lim2} + 2\pi)$ the working volume is given by equation

$$A_D = \frac{d^2}{2}\{(\theta - \theta_{lim1}) - \sin(\theta - \theta_{lim1})\}. \qquad (A.136)$$

Where as for the rest of the discharge process is given by the formulae

$$A_D = (2I - A_{D3}) - 2A_{D2} - 2A_{D1} \qquad (A.137)$$

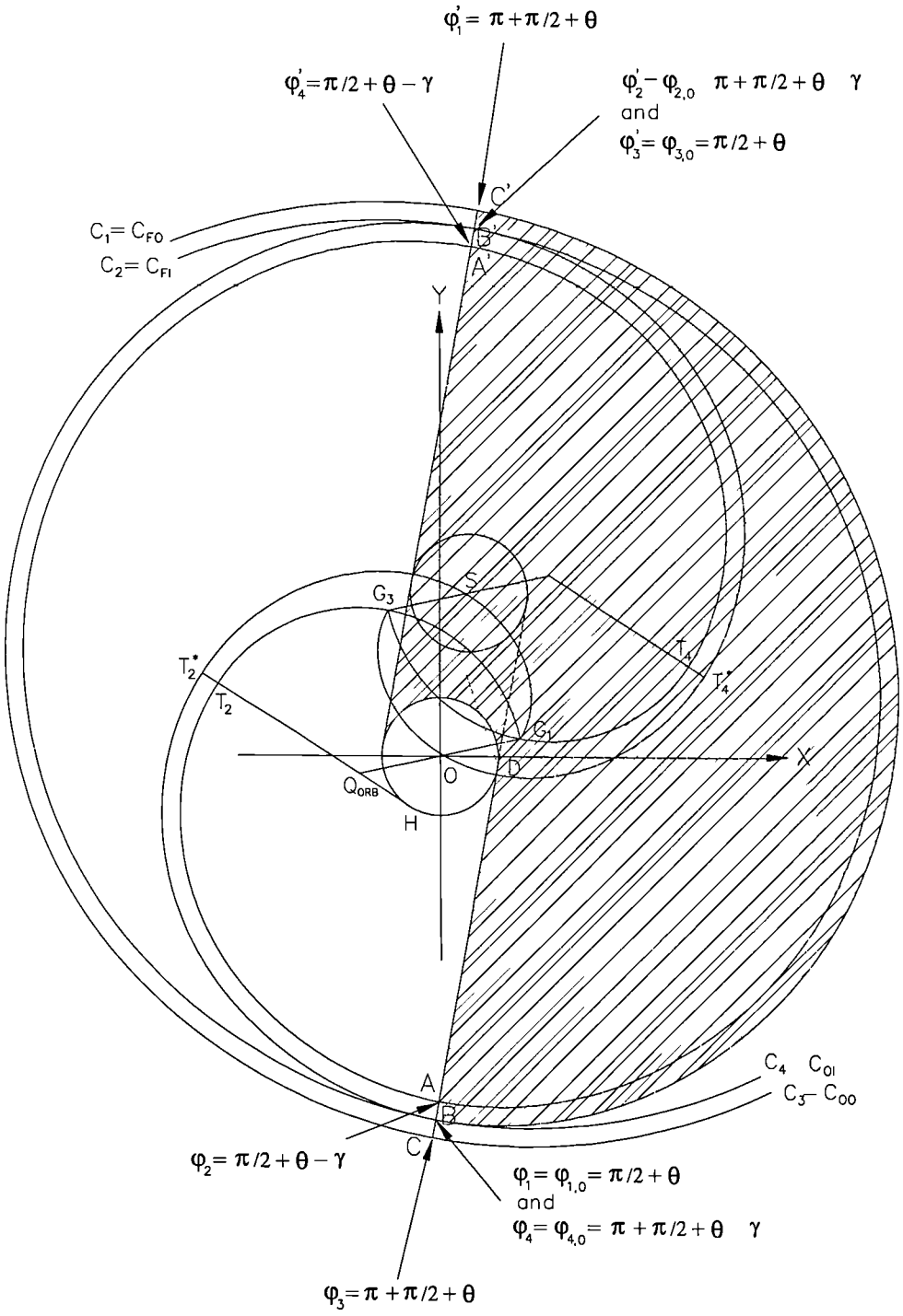

Figure (A-18). Determination of area of innermost chambers

Appendix B

Governing Equations

B.1 The Continuity Equation

Physical principle: mass is conserved

Consider the flow model shown on figure B.1 , namely, an infinitesimally small element fixed in space, with the fluid moving through it. Here, for convenience we adopt a Cartesian coordinate system, where the velocity and density are functions of (x,y,z) space and time t. Fixed in this (x,y,z) space is an infinitesimally small element of sides dx, dy, and dz, (figure B.1). there is a mass flow through this fixed element, as shown in figure B.1. Consider the left and right faces of the element which are perpendicular to the x axis. The area of these faces is $dy\ dz$. The mass flow through the left face is $(\rho u)\ dy\ dz$. Since the velocity and density are functions of spatial location, the values of the mass flux across the right face will be different from that across the left face; indeed, the difference in mass flux between the two faces is simply $[\partial(\rho u)/\partial x]\ dx$. Thus the mass flow across the right face can be expressed as $\{\rho u + [\partial(\rho u)/\partial x]\ dx\ \}\ dy\ dz$. The mass flow across both the left and the right faces is shown in figure B.1. In a similar vein the mass flow through both the bottom and the top faces, which are perpendicular to the y axis, is $(\rho v)\ dx\ dz$ and $\{\rho v + [\partial(\rho v)/\partial y]dy\}\ dx\ dz$, respectively. The mass flow through both the front and back faces, which are perpendicular to the z axis is $(\rho w)dxdy$ and $\{\rho w + [\partial(\rho w)/\partial z]dz\}\ dx\ dz$, respectively. Note that u, v, and w are positive, by convection, in the positive x, y, and z directions, respectively. Hence the arrows in figure B.1. Show the contributions to the inflow and outflow of mass through the sides of the fixed element. If we denote a net outflow of mass as a positive quantity, then from figure B.1 we have

Net outflow in x *direction:*

$$\left[\rho u + \frac{\partial(\rho u)}{\partial x} dx\right] dy\, dz - (\rho u)\, dy\, dz = \frac{\partial(\rho u)}{\partial x} dx\, dy\, dz$$

Net outflow in y *direction:*

$$\left[\rho v + \frac{\partial(\rho v)}{\partial y} dy\right] dx\, dz - (\rho v)\, dx\, dz = \frac{\partial(\rho v)}{\partial y} dx\, dy\, dz \qquad (B.1)$$

Net outflow in z *direction:*

$$\left[\rho w + \frac{\partial(\rho w)}{\partial z} dz\right] dx\, dy - (\rho w)\, dx\, dy = \frac{\partial(\rho w)}{\partial z} dx\, dy\, dz$$

Hence, the net mass flow out of the element is given by

$$\text{Net mass flow} = \left[\frac{\partial(\rho u)}{\partial x} + \frac{\partial(\rho v)}{\partial y} + \frac{\partial(\rho w)}{\partial z}\right] dx\, dy\, dz \qquad (B.2)$$

The total mass of fluid in the infinitesimally small element is $\rho\ (dx\ dy\ dz)$; hence the time rate of increase of mass inside the element is given by

$$\text{Time rate of mass increase} = \frac{\partial \rho}{\partial t}(dx\, dy\, dz) \qquad (B.3)$$

The physical principle that mass is conserved, when applied to the fixed element in figure B.1, can be expressed in words as follows: the net mass flow out of the element must equal the time rate of *decrease* of mass inside the element. Denoting the mass decrease by a negative quantity, the statement can be expressed in terms of equations (B.2) and (B.3) as

$$\left[\frac{\partial(\rho u)}{\partial x} + \frac{\partial(\rho v)}{\partial y} + \frac{\partial(\rho w)}{\partial z}\right] dx\, dy\, dz = -\frac{\partial \rho}{\partial t}(dx\, dy\, dz) \qquad (B.4)$$

or

$$\frac{\partial \rho}{\partial t} + \left[\frac{\partial(\rho u)}{\partial x} + \frac{\partial(\rho v)}{\partial y} + \frac{\partial(\rho w)}{\partial z}\right] = 0$$

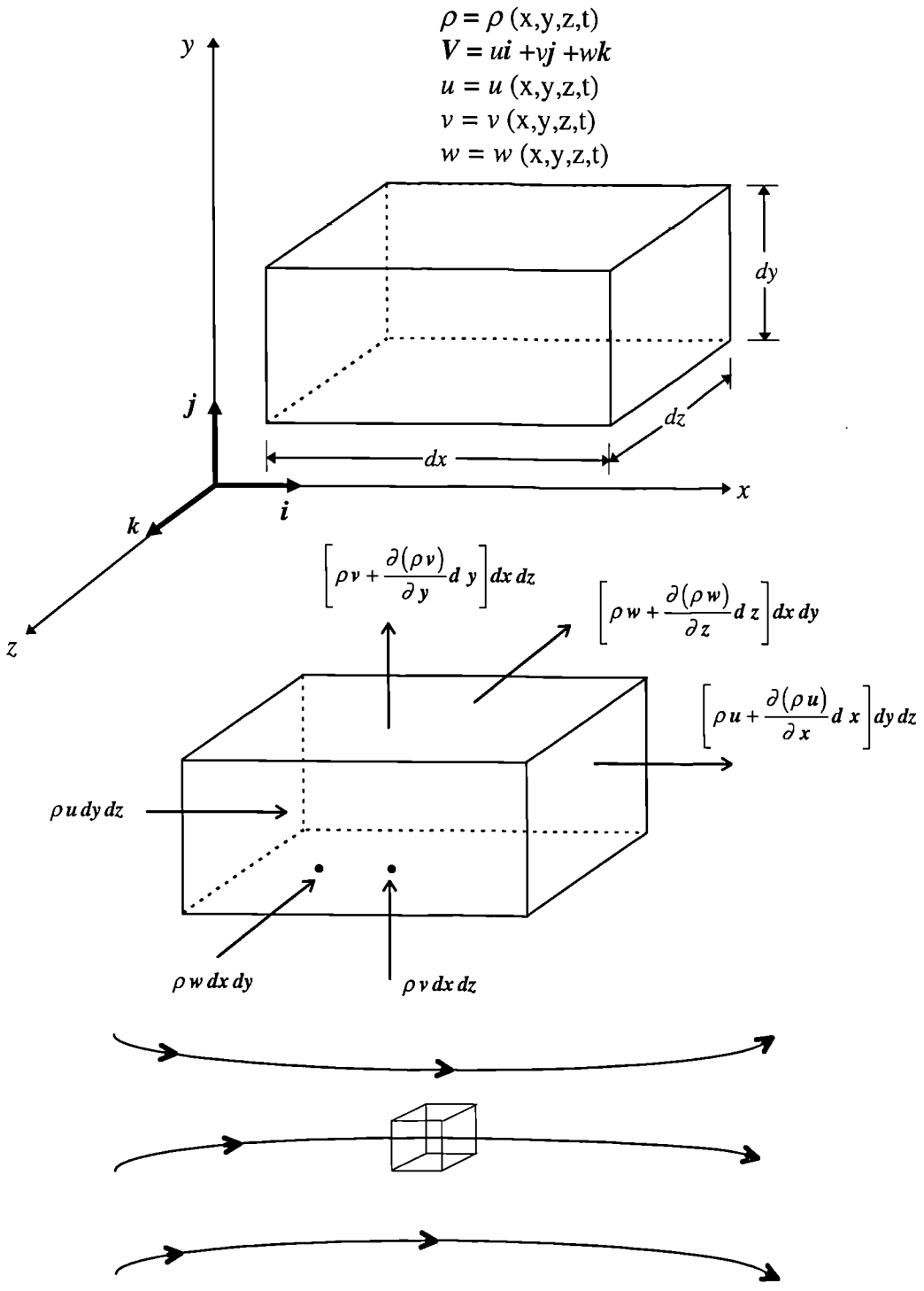

Figure B.1 Model of the infinitesimally small element fixed in space and a diagram of the mass fluxes through the various faces of the element-for a derivation of the continuity equation.

In equation (B.4) the term in brackets is simply $\nabla \cdot (\rho \mathbf{V})$. Thus equation (B.4) becomes

$$\frac{\partial \rho}{\partial t} + \nabla \cdot (\rho V) = 0 \qquad (B.5)$$

Equation (B.5) is a partial differential equation form of the *continuity equation.* It was derived on the basis of an infinitesimally small element fixed in space. The infinitesimally small aspect of the element is why the equation is obtain directly in partial differential equation form. The fact that the element was fixed in space leads to the specific differential form given by equation (B.5), which is called the *conservation form.* The forms of the governing flow equations that are directly obtained from a flow model which is fixed in space are, by definition, called the conservation form.

B.2 The Momentum Equation

In this section, we apply another fundamental physical principle to a model of the flow namely:

Physical principle: $F = ma$ (Newton's second law)

The resulting equation is called the *momentum equation.* Unlike the derivation of the continuity equation, where the model of an infinitesimally small element fixed in space was used, here we will apply a different model. We will utilize the moving fluid element model shown in figure B.2 because this model is particularly convenient for the derivation of the momentum equations as well as the energy equation (to be consider in section B.3). Momentum and energy equations can be derived using the other model of flow shown in figure B.1, each different model of flow leads directly to a different form of the equations.

Newton's second law, expressed above, when applied to the moving fluid element in figure B.2, says that the net force on the fluid element equals its mass times its acceleration of the element. This is a vector relation, and hence can be split into three scalar relations along the x, y, and z axes. Let us consider only the x component of Newton's second law,

$$F_x = ma_x \qquad (B.6)$$

where F_x and a_x are the scalar x components of the force and acceleration respectively.

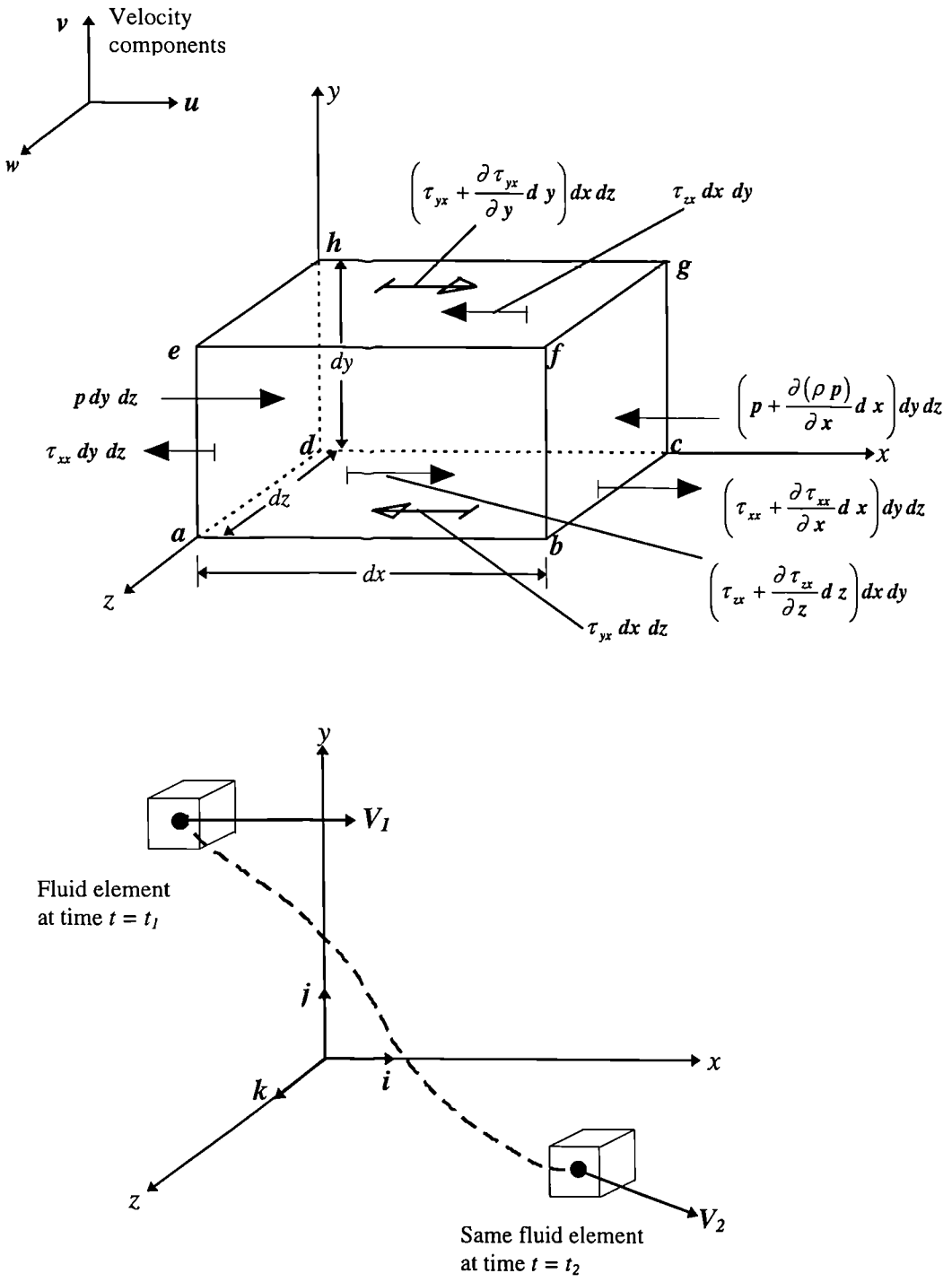

Figure B.2 Infinitesimally small, moving fluid element. Only the forces in the x direction are shown. Model used for the derivation of the x component of the momentum equation.

First, consider the left side of equation (B.6). We say that the moving fluid experiences a force in the x direction. There are two sources of this force:

1. *Body forces*, which act directly on the volumetric mass of the fluid element. These forces "act at a distance"; examples are gravitational, electromagnetic, centrifugal, and Coriolis forces.
2. *Surface forces*, which act directly on the surface of the fluid element. They are due to only two sources: (a) the pressure distribution acting on the surface, imposed by the outside fluid surrounding the fluid element, and (b) the shear and normal stress distributions acting on the surface, also imposed by the outside fluid "tugging" or "pushing" on the surface by means of friction.

Let us denote the body force per unit mass acting on the fluid element by $\mathbf{f}$, with f_x as its x component. The volume of the fluid element is $(dx\,dy\,dz)$; hence,

$$\text{Body force on fluid element acting in } x \text{ direction} = \rho f_x (dx\,dy\,dz) \qquad (B.7)$$

The shear and normal stresses in a fluid are related to the time rate of change of the deformation of the fluid element, as sketched in figure B.3 for just the xy plane. The shear stress denoted by τ_{xy} in figure B.3a, is related to the time rate of change of the shearing deformation of the fluid element, whereas the normal stress, denoted by τ_{xx} in figure B.3b, is related to the time rate of change of volume of the fluid element. As a result, both shear and normal stresses depend on velocity gradients in the flow. In most viscous flows, normal stresses (such as τ_{xx}) are much smaller than shear stresses and many times neglected. Normal stresses (say τ_{xx} in the x direction) become important when the normal velocity gradients (say $\partial u/\partial x$) are very large, such as inside a shock wave.

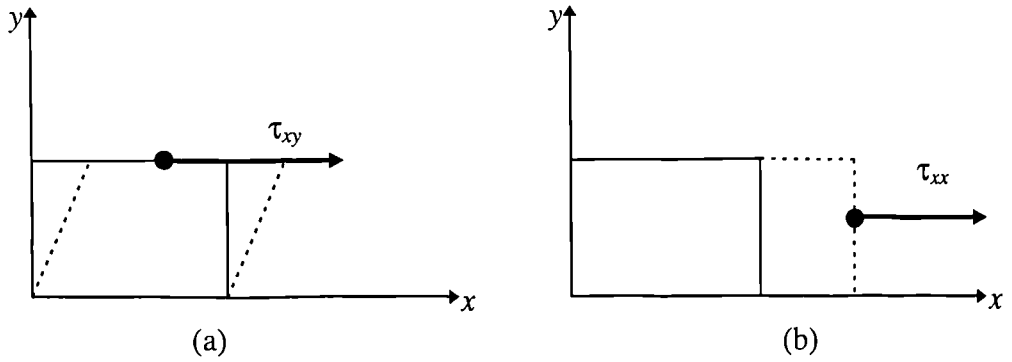

Figure B.3 Illustration of (a) shear stress and (b) normal stress

The surface forces in the x direction exerted on the fluid element are sketched in figure B.2. The convention will be used here that τ_{ij} denotes a stress in the j direction exerted on a plane perpendicular to the i axis. On the face ***abcd***, the only force in the x direction is that due to shear stress, τ_{yz} ***dxdz***. Face ***efgh***, is a distance ***dy*** above face ***abcd***; hence the shear force in the x direction on face ***efgh*** is $[\tau_{yx}+(\partial\tau_{yx}/\partial y)dy]dxdz$. Note the direction of the shear force on the faces ***abcd*** and ***efgh***; on the bottom face, τ_{yx} is to the left (the negative x direction), whereas on the top face, $\tau_{yz}+(\partial\tau_{yx}/\partial y)dy$ is to the right (the positive x direction). These directions are consistent with the convention that positive increases in all three components of velocity, u, v, and w, occur in the positive direction of the axes. For example, in figure B.2, u increases in the positive y direction. Therefore, concentrating on the face ***efgh***, u is higher just above the face than on the face; this causes a "tugging" action which tries to pull the fluid element in the positive x direction (to the right) as shown in figure B.2. In turn, concentrating on face ***abcd***, u is lower just beneath the face than on the face; this causes a retarding or dragging action on the fluid element, which acts in the negative x direction (to the left) as shown in figure B.2. The directions of all the other viscous stresses shown in figure B.2 including τ_{xx}, can be justified in a like fashion. Specifically on face ***dcgh***, τ_{zx} acts in the negative x direction, whereas on face ***abfe***, $\tau_{zx} + (\partial\tau_{zx}/\partial z)dz$ acts in the positive x direction. On face ***adhe***, which is perpendicular to the x axis, the only forces in the x direction are the pressure force $p\ dy\ dz$, which always acts in the direction into the fluid element, and $\tau_{xx}\ dy\ dz$, which is in the negative x direction. In figure B.2, the reason why τ_{xx} on face ***adhe*** is to the left hinges on the convention mentioned earlier for the direction of increasing velocity. Here, by convention, a positive increase in the u just to the left face of ***adhe*** is smaller than the value of u on the face itself. As a result, the viscous action of the normal stress acts as a "suction" on face ***adhe***; i.e. there is a dragging action toward the left that wants to retard the motion of the fluid element. In contrast, on face ***bcgf***, the pressure force $[p + (\partial p/\partial x)dx]dy\ dz$ presses inward on the fluid (in the negative x direction). And because the value of u just to the right of the face ***bcgf*** is larger than the value of u on the face, there is a "suction" due to the viscous normal stress which tries to pull the element to the right (in the positive x direction) with a force equal to $[\tau_{xx} + (\partial\tau_{xx}/\partial x)dx]dy\ dz$.

With the above in mind, for the moving fluid element we can write

$$\text{Net surface force in } x \text{ direction} = \left[p - \left(p + \frac{\partial p}{\partial x}dx\right)\right]dy\,dz + \left[\left(\tau_{xx} + \frac{\partial \tau_{xx}}{\partial x}dx\right) - \tau_{xx}\right]dy\,dz + \left[\left(\tau_{yx} + \frac{\partial \tau_{yx}}{\partial y}dy\right) - \tau_{yx}\right]dx\,dz + \left[\left(\tau_{zx} + \frac{\partial \tau_{zx}}{\partial z}dz\right) - \tau_{zx}\right]dx\,dy \qquad (B.8)$$

The total force in the x direction F_x, is given by the sum of equations (B.7) and (B.8). Adding, and canceling terms, we obtain

$$F_x = \left[-\frac{\partial p}{\partial x} + \frac{\partial \tau_{xx}}{\partial x} + \frac{\partial \tau_{yx}}{\partial y} + \frac{\partial \tau_{zx}}{\partial z}\right]dx\,dy\,dz + \rho f_x\,dx\,dy\,dz \qquad (B.9)$$

Equation (B.9) represents the left-hand side of equation (B.6). Considering the right-hand side of equation (B.6), recall that the mass of the fluid element is fixed and is equal to

$$m = \rho\,dx\,dy\,dz \qquad (B.10)$$

Also recall that the acceleration of the fluid element is the time rate of change of its velocity. Hence, the component acceleration in the x direction, denoted by a_x, is simply the time rate of change of u; since we are following a moving fluid element, this time rate of change is given by its substantial derivative. Thus,

$$a_x = \frac{Du}{Dt} \qquad (B.11)$$

Combining equations (B.6) and (B.9) to (B.11), we obtain

$$\rho\frac{Du}{Dt} = -\frac{\partial p}{\partial x} + \frac{\partial \tau_{xx}}{\partial x} + \frac{\partial \tau_{yx}}{\partial y} + \frac{\partial \tau_{zx}}{\partial z} + \rho f_x \qquad (B.12a)$$

Which is the x component of the momentum equation for a viscous flow. In a similar fashion, the y and z components can be obtained as

$$\rho\frac{Dv}{Dt} = -\frac{\partial p}{\partial y} + \frac{\partial \tau_{xy}}{\partial x} + \frac{\partial \tau_{yy}}{\partial y} + \frac{\partial \tau_{zy}}{\partial z} + \rho f_y \qquad (B.12b)$$

$$\rho\frac{Dw}{Dt} = -\frac{\partial p}{\partial z} + \frac{\partial \tau_{xz}}{\partial x} + \frac{\partial \tau_{yz}}{\partial y} + \frac{\partial \tau_{zz}}{\partial z} + \rho f_z \qquad (B.12c)$$

Equations (B.12a) to (B.12c) are the x, y, and z components respectively, of the momentum equation. Note that they are partial differential equations obtained directly from an application of the fundamental physical principle to an infinitesimal fluid element. Moreover, since this fluid element is moving with the flow, equations (B.12) are in *non conservation form.* They are scalar equations and are called the *Navier - Stokes equations* in honor of two men, the Frenchman M.Navier and the Englishman G. Stokes, who independently obtain the equations in the first half of the nineteenth century.

The Navier - Stokes equations can be obtained in conservation form as follows. Writing the left-hand side of equation (B.12a) in terms of the definition of a substantial derivative we have

$$\rho\frac{Du}{Dt} = \rho\frac{\partial u}{\partial t} + \rho V\cdot\nabla u \qquad (B.13)$$

Also, expanding the following derivative,

$$\frac{\partial(\rho u)}{\partial t} = \rho\frac{\partial u}{\partial t} + u\frac{\partial \rho}{\partial t}$$

and rearranging, we have

$$\rho\frac{\partial u}{\partial t} = \frac{\partial(\rho u)}{\partial t} - u\frac{\partial \rho}{\partial t} \qquad (B.14)$$

Recalling the vector identity for the divergence of the product of a scalar times a vector, we have

$$\nabla\cdot(\rho u V) = u\nabla\cdot(\rho V) + (\rho V)\cdot\nabla u$$

or

$$\rho V\cdot\nabla u = \nabla\cdot(\rho u V) - u\nabla\cdot(\rho V) \qquad (B.15)$$

Substituting equations (B.14) and (B.15) into equation (B.13).

$$\begin{aligned}\rho\frac{Du}{Dt} &= \frac{\partial(\rho u)}{\partial t} - u\frac{\partial \rho}{\partial t} - u\nabla\cdot(\rho V) + \nabla\cdot(\rho u V)\\ &= \frac{\partial(\rho u)}{\partial t} - u\left[\frac{\partial \rho}{\partial t} + \nabla\cdot(\rho V)\right] + \nabla\cdot(\rho u V)\end{aligned} \qquad (B.16)$$

The term in brackets in equation (B.16) is simply the left-hand side of the continuity equation, hence the term in brackets is zero. Thus equation (B.16) reduces to

$$\rho\frac{Du}{Dt}=\frac{\partial(\rho u)}{\partial t}+\nabla\cdot(\rho uV) \qquad (B.17)$$

Substitute equation (B.17) into (B.12a).

$$\frac{\partial(\rho u)}{\partial t}+\nabla\cdot(\rho uV)=-\frac{\partial p}{\partial x}+\frac{\partial\tau_{xx}}{\partial x}+\frac{\partial\tau_{yx}}{\partial y}+\frac{\partial\tau_{zx}}{\partial z}+\rho f_x \qquad (B.18a)$$

Similarly, equations (B.12b) and (B.12c) can be expressed as

$$\frac{\partial(\rho v)}{\partial t}+\nabla\cdot(\rho vV)=-\frac{\partial p}{\partial x}+\frac{\partial\tau_{xy}}{\partial x}+\frac{\partial\tau_{yy}}{\partial y}+\frac{\partial\tau_{zy}}{\partial z}+\rho f_y \qquad (B.18b)$$

and

$$\frac{\partial(\rho w)}{\partial t}+\nabla\cdot(\rho wV)=-\frac{\partial p}{\partial z}+\frac{\partial\tau_{xz}}{\partial x}+\frac{\partial\tau_{yz}}{\partial y}+\frac{\partial\tau_{zz}}{\partial z}+\rho f_z \qquad (B.18c)$$

Equations (B.18) are the Navier - Stokes equations in *conservation form.* In the late seventeenth century, Isaac Newton stated that shear stress in a fluid is proportional to the time rate of strain, i.e., velocity gradients. Such fluids are called *Newtonian fluids.* (fluids in which τ is not proportional to the velocity gradients are non Newtonian fluids). For Newtonian fluids, Stokes in 1845 obtained

$$\tau_{xx}=\lambda(\nabla\cdot V)2\mu\frac{\partial u}{\partial x} \qquad (B.19a)$$

$$\tau_{yy}=\lambda(\nabla\cdot V)2\mu\frac{\partial v}{\partial y} \qquad (B.19b)$$

$$\tau_{zz}=\lambda(\nabla\cdot V)2\mu\frac{\partial w}{\partial z} \qquad (B.19c)$$

$$\tau_{xy}=\tau_{yx}=\mu\left[\frac{\partial v}{\partial x}+\frac{\partial u}{\partial y}\right] \qquad (B.19d)$$

$$\tau_{xz}=\tau_{zx}=\mu\left[\frac{\partial u}{\partial z}+\frac{\partial w}{\partial x}\right] \qquad (B.19e)$$

$$\tau_{yz} = \tau_{zy} = \mu\left[\frac{\partial w}{\partial y} + \frac{\partial v}{\partial z}\right] \qquad (B.19f)$$

where μ is the molecular viscosity coefficient and λ is the second viscosity coefficient. Stokes made the hypothesis that

$$\lambda = -\frac{2}{3}\mu$$

which is frequently used but which has still not been definitely confirmed to present day. Substituting equations (B.19) into (B.18), we obtain the complete Navier - Stokes equations in conservation form.

B.3 The Energy Equation

Physical principle: Energy is conserved

In keeping with our derivation of the Navier - Stokes equations (i.e. the momentum equation) in section B.2 we will use again the flow model of an infinitesimally small fluid element moving with the flow (as shown in figure B.2). The physical principle stated above is nothing more than the first law of thermodynamics. When applied to the flow model of a fluid element moving with the flow, the first law states that

Rate of change of energy inside fluid element	=	Net flux of heat into element	+	Rate of work done on element due to body and surface forces	*(B.20)*
A	=	B	+	C	

where A, B, and C denote the respective terms above.

Let us first evaluate C; that is. Let us obtain an expression for the rate of work done on the moving fluid element due to body and surface forces. It can be shown that the rate of doing work by a force exerted on a moving body is equal to the product of the force and the component of velocity in the direction of force. Hence the rate of work done by the body force acting on the fluid element moving at a velocity V is

$$\rho \mathbf{f} \cdot V(dx\,dy\,dz)$$

With regard to the surface forces (pressure plus shear and normal stresses), consider just the forces in the x direction shown in figure B.2. The rate of work done on the moving fluid element by the pressure and shear forces in the x direction shown in figure B.2 is simply the x component of velocity u, multiplied by the forces; e.g. on face ***abcd*** the rate of work done by $\tau_{yx}\, dx\, dz$ is $u\tau_{yx}\, dx\, dz$, with similar expressions on the other faces. To emphasize these energy considerations, the moving fluid element is redrawn in figure B.4, where the rate of work done on each face by surface forces in the x direction is shown explicitly. To obtain the net rate of work done on the fluid element by the surface forces, note that forces in the positive x direction do positive work and that forces in the negative x direction do negative work. Hence, comparing the pressure forces on face ***adhe*** and ***bcgf*** in figure B.4, the net rate of work done by pressure in the x direction is

$$\left[up - \left(up + \frac{\partial(up)}{\partial x}dx\right)\right]dy\,dz = -\frac{\partial(up)}{\partial x}dx\,dy\,dz$$

Similarly, the net rate of work done by the shear stresses in the x direction on faces ***abcd*** and ***efgh*** is

$$\left[\left(u\tau_{yx} + \frac{\partial(u\tau_{yx})}{\partial y}dy\right) - u\tau_{yx}\right]dx\,dz = -\frac{\partial(u\tau_{yx})}{\partial y}dx\,dy\,dz$$

Considering all the surface forces shown in figure B.4, the net rate of work on the moving fluid element due to these forces is simply

$$\left[-\frac{\partial(up)}{\partial x} + \frac{\partial(u\tau_{xx})}{\partial x} + \frac{\partial(u\tau_{yx})}{\partial y} + \frac{\partial(u\tau_{zx})}{\partial z}\right]dx\,dy\,dz$$

The above expression considers only surface forces in the x direction. When the surface forces in the y and z directions are also included, similar expressions are obtained. In total, the net rate of work done on the moving fluid element is the sum of the surface force contributions in the x, y, and z directions, as well as the body force contribution. This denoted by C in equation B.20 and is given by

$$C = -\left[\left(\frac{\partial(up)}{\partial x}+\frac{\partial(vp)}{\partial y}+\frac{\partial(wp)}{\partial z}\right)+\frac{\partial(u\tau_{xx})}{\partial x}+\frac{\partial(u\tau_{yx})}{\partial y}+\frac{\partial(u\tau_{zx})}{\partial z}\right.$$
$$+\frac{\partial(v\tau_{xy})}{\partial x}+\frac{\partial(v\tau_{yy})}{\partial y}+\frac{\partial(v\tau_{zy})}{\partial z} \qquad (B.21)$$
$$\left.+\frac{\partial(w\tau_{xz})}{\partial x}+\frac{\partial(w\tau_{yz})}{\partial y}+\frac{\partial(w\tau_{zz})}{\partial z}\right]dx\,dy\,dz+\rho\mathbf{f}\cdot V\,dx\,dy\,dz$$

Note in equation (B.21) that the first three terms on the right-hand side are simply $\nabla\cdot(\rho V)$.

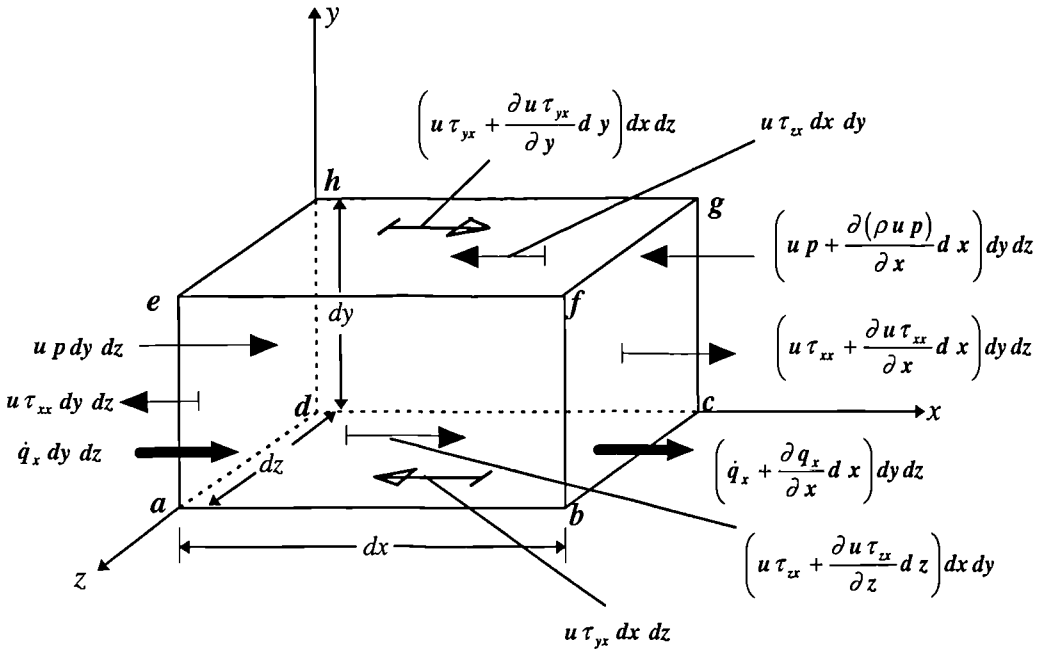

Figure B.4 Energy fluxes associated with an infinitesimally small, moving fluid element. For simplicity, only the fluxes in the x direction ere shown. Model used for the derivation of the energy equation.

B is the net flux of heat into the element. This heat flux is due to (1) volumetric heating such as absorption or emission or radiation and (2) heat transfer across the surface due to temperature gradients, i.e. thermal conduction. Define $\dot{q}$ as the rate of volumetric heat addition per unit mass. Noting that the mass of the moving fluid element in figure B.4 is $\rho\,dx\,dy\,dz$, we obtain

$$\text{Volumetric heating of element} = \rho\dot{q}\,dx\,dy\,dz \qquad (B.22)$$

In figure B.4, the heat transfer by thermal conduction into the moving fluid element across face ***adhe*** is $\dot{q}_x\, dy\, dz$, where $\dot{q}_x$ is the heat transferred in the x direction per unit time per unit area by thermal conduction. (The heat transfer in a given direction, when expressed in dimensions of energy per unit area perpendicular to the direction is called the *heat flux* in that direction.) The heat transfer out of the element across face ***bcgf*** is $\left[\dot{q}_x + (\partial \dot{q}_x / \partial x)dx\right] dy\, dz$. Thus, the net heat transfer in the x direction into the fluid element by thermal conduction is

$$\left[\dot{q}_x - \left(\dot{q}_x + \frac{\partial \dot{q}_x}{\partial x} dx\right)\right] dy\, dz = -\frac{\partial \dot{q}_x}{\partial x} dx\, dy\, dz$$

Taking into account heat transfer in the y and z directions across the other faces in figure B.4 we obtain

$$\begin{array}{l}\text{Heating of} \\ \text{fluid element by} \\ \text{thermal conduction}\end{array} \quad = -\left(\frac{\partial \dot{q}_x}{\partial x} + \frac{\partial \dot{q}_y}{\partial y} + \frac{\partial \dot{q}_z}{\partial z}\right) dx\, dy\, dz \qquad \textit{(B.23)}$$

The term B in equation (B.20) is the sum of equations (B.22) and (B.23).

$$B = \left[\rho \dot{q} - \left(\frac{\partial \dot{q}_x}{\partial x} + \frac{\partial \dot{q}_y}{\partial y} + \frac{\partial \dot{q}_z}{\partial z}\right)\right] dx\, dy\, dz \qquad \textit{(B.24)}$$

The heat flux due to thermal conduction, from Fourier's law of heat conduction, is proportional to the local temperature gradient:

$$\dot{q}_x = -k\frac{\partial T}{\partial x} \qquad \dot{q}_y = -k\frac{\partial T}{\partial y} \qquad \dot{q}_z = -k\frac{\partial T}{\partial z}$$

where k is the thermal conductivity. Hence equation (B.24) can be written

$$B = \left[\rho \dot{q} + \frac{\partial}{\partial x}\left(k\frac{\partial T}{\partial x}\right) + \frac{\partial}{\partial y}\left(k\frac{\partial T}{\partial y}\right) + \frac{\partial}{\partial z}\left(k\frac{\partial T}{\partial z}\right)\right] dx\, dy\, dz \qquad \textit{(B.25)}$$

Finally the term A in equation (B.20) denotes the time rate of change of energy of the fluid element. The fluid element has two contributions to its energy:

1. The internal energy due to random molecular motion, e (per unit mass). This is the physical significance of the internal energy that appears in the first law of

thermodynamics.

2. The kinetic energy due to translational motion of the fluid element. The kinetic energy per unit mass is simply $V^2/2$.

Hence, the moving fluid element has both *internal* and *kinetic* energy; the sum of these two is the "*total*" energy. In equation (B.20), the energy in the term A is the total energy, i.e. the sum of the internal and kinetic energies. The total energy is $e+V^2/2$. Since we are following a moving fluid element, the time rate of change of the total energy per unit mass is given by the substantial derivative. Since the mass of the fluid element is $\rho\, dx\, dy\, dz$, we have

$$A=\rho\frac{D}{Dt}\left(e+\frac{V^2}{2}\right)dx\,dy\,dz \tag{B.26}$$

The final form of the energy equation is obtained by substituting equations (B.21), (B.25), and (B.26) into (B.20)

$$\begin{aligned}\rho\frac{D}{Dt}\left(e+\frac{V^2}{2}\right)&=\rho\dot{q}+\frac{\partial}{\partial x}\left(k\frac{\partial T}{\partial x}\right)+\frac{\partial}{\partial y}\left(k\frac{\partial T}{\partial y}\right)+\frac{\partial}{\partial z}\left(k\frac{\partial T}{\partial z}\right)\\&-\frac{\partial(up)}{\partial x}-\frac{\partial(vp)}{\partial y}-\frac{\partial(wp)}{\partial z}+\frac{\partial(u\tau_{xx})}{\partial x}+\frac{\partial(u\tau_{yx})}{\partial y}+\frac{\partial(u\tau_{zx})}{\partial z}\\&+\frac{\partial(v\tau_{xy})}{\partial x}+\frac{\partial(v\tau_{yy})}{\partial y}+\frac{\partial(v\tau_{zy})}{\partial z}+\frac{\partial(w\tau_{xz})}{\partial x}+\frac{\partial(w\tau_{yz})}{\partial y}+\frac{\partial(w\tau_{zz})}{\partial z}+\rho\mathbf{f}\cdot V\end{aligned} \tag{B.27}$$

This is the *non conservation* form of the energy equation; also note that it is in terms of the *total energy* $e+V^2/2$. Once again, the non conservation form results from the application of the fundamental physical principle to a moving fluid element.

The left-hand side of the equation (B.27) involve the substantial derivative of the total energy $D\left(e+V^2/2\right)/Dt$. This is just one of the many different forms of the energy equation; it is the form that comes directly from the principle of conservation of energy applied to a moving fluid element. This equation can be readily modified in two respects as follows;

1. The left-hand side can be expressed in terms of the internal energy e alone, or the static enthalpy h alone, or the total enthalpy $h_0=\left(h+V^2/2\right)$ alone.

2. For each of the different forms of the energy equation mentioned above, there are both non conservation as well as conservation forms.

Note that the manipulations required to change the non conservation form to the conservation form change only the left-hand side of the equations; the right-hand side remains the same. Equation (B.28) below is the *conservation* form of the energy equation written in terms of total energy $e+V^2/2$.

$$\begin{aligned}&\frac{\partial}{\partial t}\left[\rho\left(e+\frac{V^2}{2}\right)\right]+\nabla\cdot\left[\rho\left(e+\frac{V^2}{2}\right)V\right]=\rho\dot{q}+\frac{\partial}{\partial x}\left(k\frac{\partial T}{\partial x}\right)+\frac{\partial}{\partial y}\left(k\frac{\partial T}{\partial y}\right)\\&+\frac{\partial}{\partial z}\left(k\frac{\partial T}{\partial z}\right)-\frac{\partial(up)}{\partial x}-\frac{\partial(vp)}{\partial y}-\frac{\partial(wp)}{\partial z}+\frac{\partial(u\tau_{xx})}{\partial x}+\frac{\partial(u\tau_{yx})}{\partial y}+\frac{\partial(u\tau_{zx})}{\partial z}\\&+\frac{\partial(v\tau_{xy})}{\partial x}+\frac{\partial(v\tau_{yy})}{\partial y}+\frac{\partial(v\tau_{zy})}{\partial z}+\frac{\partial(w\tau_{xz})}{\partial x}+\frac{\partial(w\tau_{yz})}{\partial y}+\frac{\partial(w\tau_{zz})}{\partial z}+\rho f\cdot V\end{aligned}\qquad (B.27)$$

B.4 The Equation Of State

The motion of a fluid in three dimensions is described by a system of five partial differential equations: mass, three momentum equations, and energy. In these equations there are seven unknowns ρ, p, e, T, u, v, w. In order to close the system of fluid dynamic equations it is necessary to establish relations between the thermodynamic variables ρ, p, e, T as well as to relate the transport properties μ, k to the thermodynamic variables. It is obvious that two additional equations are required. These two additional equations can be obtained by determining relations that exist between thermodynamic variables. Relations of this type are known as equations of state. According to the state principle of thermodynamics, the local thermodynamic state is fixed by any two independent thermodynamic variables, provided that the chemical composition of the fluid is not changing owing to diffusion or finite-rate chemical reactions. (John C Tannehill page 258).

A perfect gas is defined as a gas whose intermolecular forces are negligible. A perfect gas obeys the perfect gas equation of state,

$$p=\rho RT \qquad (B.28)$$

where R is the gas constant. The intermolecular forces become important under conditions of high pressure and relatively low temperature. For these conditions,

the gas no longer obeys the perfect gas equation of state, and an alternatively equation must be used. An example is the compressibility factor Z (equation (3.23) section 3.2.5), another example is the Van der Waals equation of state,

$$\left(p + a\rho^2\right)\left(\frac{1}{\rho} - b\right) = RT \qquad (B.29)$$

where a and b are constants for each type of gas.

For problems involving a perfect gas at relatively low temperatures, it is possible to also assume a *calorically perfect gas.* A calorically perfect gas is defined as a perfect gas with constant specific heats. In a calorically perfect gas, the specific heat at constant volume c_v, the specific heat at constant pressure c_p, and the ratio of specific heats γ all remain constant, and the following exists:

$$e = c_v T \qquad h = c_p T \qquad (B.30)$$

For fluids that can not be considered calorically perfect, the required state relations can be found in the form of tables, charts, or curve fits.

The coefficients of viscosity and thermal conductivity can be related to the thermodynamic variables using the kinetic theory. For example, Sutherland's formulas for viscosity and thermal conductivity are given by

$$\mu = C_1 \frac{T^{3/2}}{T + C_2} \qquad k = C_3 \frac{T^{3/2}}{T + C_4}$$

where C_1 - C_4 are constants for a given gas. The Prandtl number

$$Pr = \frac{c_p \mu}{k}$$

is often used to determine the coefficient of thermal conductivity k once μ is known. This is possible because the ratio c_p/Pr, which appears in the expression below is approximately constant for most gases.

$$k = \frac{c_p}{Pr}\mu$$

Appendix C

Program Listing

C.1 Hyperbolic Tangent Distribution

```
************************************************************************
*              SUBROUTINE HYPERBOLIC TANGENT                           *
*                        DECEMBER 1996                                 *
* This routine MUST be called ONLY when the argument BETA is LESS than *
* one.  In this case  the hyperbolic functions are used. See reference *
* Thompson                                                             *
* ARGUMENTS :                                                          *
* NSUBDIV  = INTEGER*4. On entry specifies the number of subdivisions  *
*        which is one less than the number of nodes. Unchanged on      *
*        exit.                                                         *
* ALPHA                                                                *
* BETA     = REAL*8. On entry specify the parameters defined by eqs    *
*        (A.6) and (A.7) respectively. Unchanged on exit.              *
*        Note that in the cases ICASE=2 or ICASE=3, ALPHA is not       *
*        used and can have any REAL*8 value                            *
* ICASE    = INTEGER*4. On entry has one of the following values and   *
*        corresdponding meanings :                                     *
*        1 (one) if both initial and final division are specified.     *
*        See equationS (A.9) and (A.10).                               *
*        2 if only the initial division is specified. See equation     *
*        (A.13) and finally                                            *
*        3 if only the final division is specified. See equation       *
*        (A.14).                                                       *
* IERROR   = INTEGER*4. On exit has one of the following values        *
*        0 (zero) = no error in subroutine                             *
*        1 (one) = BETA passed to routine is greater or equal to 1     *
*        or ICASE has a value different than  1, 2 or 3                *
*        2 Denominator in N-R method to small.                         *
*        3 No convergence achieved while solving for delta             *
************************************************************************
      SUBROUTINE HYPERB(NSUBDIV,BETA,ALPHA,
     ^             ICASE,IERROR)
      IMPLICIT DOUBLE PRECISION (D)
C     IMPLICIT REAL*4(A-H,O-Z), INTEGER*4(I-N)
      PARAMETER(MAXITERP=1000,EFZEROP=1.0D-18,TOLP=1.0D-03,
     ^IDPHIP=1000,ONE=1.0D+00)
      COMMON /ARRAY/ SXI(IDPHIP)
*
      WRITE(*,*)'SUBROUTINE HYPERBOLIC TANGENT'
      IERROR=0
      IF(ICASE.LT.1 .OR. ICASE.GT.3) THEN
```

```
      IERROR=1
      RETURN
    ENDIF
    IF(BETA.GE.ONE) THEN
      IERROR=1
      RETURN
    ENDIF
*
*   Solution of eq (A.8) with respect to delta, using Newton-Raphson
*   method. Original value obtained by expanding hyperbolic sine.
*   Correction is the -(Function/Derivative of Function)
    ITER=0
    CORRECTION=1.0D+10
    DELTA=DSQRT(6.0D+00*(ONE-BETA)/BETA)
    DO WHILE(CORRECTION.GT.TOLP.AND.ITER.LE.MAXITERP)
      DERIV=BETA*DCOSH(DELTA)-ONE
      IF(DABS(DERIV).LE.EFZEROP)THEN
        IERROR=2
        RETURN
      ENDIF
      CORRECTION=-(BETA*DSINH(DELTA)-DELTA)/DERIV
      DELTA=DELTA+CORRECTION
      ITER=ITER+1
    END DO
    IF(ITER.GE.MAXITERP) THEN
      IERROR=3
      RETURN
    ENDIF
*
    SUBDIV=FLOAT(NSUBDIV)
    PARONOM=DTANH(0.5D+00*DELTA)
    DO KSI=0,NSUBDIV
      RATIO=FLOAT(KSI)/SUBDIV
      IF(ICASE.EQ.1) THEN
        UKSI=DTANH(DELTA*(RATIO-0.5D+00))
        UKSI=0.5D+00*(ONE+UKSI/PARONOM)
        SKSI=UKSI/(ALPHA+(ONE-ALPHA)*UKSI)
      ELSE IF(ICASE.EQ.2) THEN
        SKSI=DTANH(0.5D+00*DELTA*(RATIO-ONE))
        SKSI=ONE+SKSI/PARONOM
      ELSE
        SKSI=DTANH(0.5D+00*DELTA*RATIO)
        SKSI=SKSI/PARONOM
      ENDIF
*     Array starts from one and not zero. Dimensions
*     are  1 to (NSUBDIV+1)  and not  0 to NSUBDIV
      SXI(KSI+1)=SKSI
    END DO
*
    RETURN
    END
```

C.2 Trigonometric Tangent Distribution

```
**********************************************************************
*              SUBROUTINE TRIGONOMERTRIC TANGENT                     *
*                          DECEMBER 1996                             *
* This routine MUST be called ONLY when the argument BETA is GREATTER *
* than one. In this case  the hyperbolic functions are used. See ref. *
* Thompson                                                           *
* ARGUMENTS :                                                        *
* NSUBDIV  = INTEGER*4. On entry specifies the number of subdivisions *
*        which is one less than the number of nodes. Unchanged on    *
*        exit.                                                       *
* ALPHA                                                              *
* BETA     = REAL*8. On entry specify the parameters defined by eqs  *
*        (A.6) and (A.7) respectively. Unchanged on exit.            *
*        Note that in the cases ICASE=2 or ICASE=3, ALPHA is not     *
*        used and can have any REAL*8 value                          *
* ICASE    = INTEGER*4. On entry has one of the following values and *
*        corresponding meanings :                                    *
*        1 (one) if both initial and final division are specified.   *
*        See equations (A.9) and (A.10).                             *
*        2 if only the initial division is specified. See equation   *
*        (A.13) and finally                                          *
*        3 if only the final division is specified. See equation     *
*        (A.14).                                                     *
* IERROR   = INTEGER*4. On exit has one of the following values      *
*        0 (zero) = no error in subroutine                           *
*        1 (one) = BETA passed to routine is less or equal to 1      *
*        or ICASE has a value different than  1, 2 or 3              *
*        2 Denominator in N-R method to small.                       *
*        3 No convergence achieved while solving for delta           *
**********************************************************************
      SUBROUTINE TRIGON(NSUBDIV,BETA,ALPHA,
     ^            ICASE,IERROR)
      IMPLICIT DOUBLE PRECISION (D)
C     IMPLICIT REAL*4(A-H,O-Z), INTEGER*4(I-N)
      PARAMETER(MAXITERP=1000,EFZEROP=1.0D-18,TOLP=1.0D-03,
     ^IDPHIP=1000,ONE=1.0D+00)
      COMMON /ARRAY/ SXI(IDPHIP)
*
      WRITE(*,*)'SUBROUTINE TRIGONOMETRIC TANGENT'
      IERROR=0
      IF(ICASE.LT.1 .OR. ICASE.GT.3) THEN
        IERROR=1
        RETURN
      ENDIF
      IF(BETA.LT.ONE) THEN
        IERROR=1
        RETURN
      ENDIF
*
*     Solution of eq (A.8) with respect to delta, using Newton-Raphson
*     method. Original value obtained by expanding hyperbolic sine.
*     Correction is the  -(Function/Derivative of Function)
      ITER=0
      CORRECTION=1.0D+10
```

```
      DELTA=DSQRT(6.0D+00*(BETA-ONE)/BETA)
      DO WHILE(CORRECTION.GT.TOLP.AND.ITER.LE.MAXITERP)
        DERIV=BETA*DCOS(DELTA)-ONE
        IF(DABS(DERIV).LE.EFZEROP)THEN
          IERROR=2
          RETURN
        ENDIF
        CORRECTION=-(BETA*DSIN(DELTA)-DELTA)/DERIV
        DELTA=DELTA+CORRECTION
        ITER=ITER+1
      END DO
      IF(ITER.GE.MAXITERP) THEN
        IERROR=3
        RETURN
      ENDIF
*
      SUBDIV=FLOAT(NSUBDIV)
      PARONOM=DTAN(0.5D+00*DELTA)
      DO KSI=0,NSUBDIV
        RATIO=FLOAT(KSI)/SUBDIV
        IF(ICASE.EQ.1) THEN
          UKSI=DTAN(DELTA*(RATIO-0.5D+00))
          UKSI=0.5D+00*(ONE+UKSI/PARONOM)
          SKSI=UKSI/(ALPHA+(ONE-ALPHA)*UKSI)
        ELSE IF(ICASE.EQ.2) THEN
          SKSI=DTAN(0.5D+00*DELTA*(RATIO-ONE))
          SKSI=ONE+SKSI/PARONOM
        ELSE
          SKSI=DTAN(0.5D+00*DELTA*RATIO)
          SKSI=SKSI/PARONOM
        ENDIF
*       Array starts from one and not zero. Dimensions
*       are  1 to (NSUBDIV+1)  and not  0 to NSUBDIV
        SXI(KSI+1)=SKSI
      END DO
*
      RETURN
      END
```

C.3 Transfinite Interpolation

```
**********************************************************************
*      SUBROUTINE PREPARE FOR TRANSFINITE INTERPOLATION              *
*                              MARCH 1996                            *
* This routine MUST be called ONLY when the definition of the edges is known and *
* the distribution of the vertices along the edges completed. (SEE common block)  *
* ARGUMENTS :                                                        *
* IMAX  = INTEGER*4. On entry specifies the number of subdivisions   *
*         which is one less than the number of nodes on the I-Direction.  *
*         Unchanged on exit.                                         *
* JMAX  = INTEGER*4. On entry specifies the number of subdivisions   *
*         which is one less than the number of nodes on the J-Direction.  *
*         Unchanged on exit.                                         *
* XXX   = 2-Dimensional Array.                                       *
*         On exit has the X-values of the boundaries of the BLOCK    *
* YYY   = 2-Dimensional Array.                                       *
*         On exit has the Y-values of the boundaries of the BLOCK    *
**********************************************************************
C
      SUBROUTINE PREPARE_FOR_TRANS (XXX,YYY,IMAX,JMAX)
      PARAMETER (NI=100,NJ=100)
C
      IMPLICIT DOUBLE PRECISION (D)
C     IMPLICIT REAL*4(A-H,O-Z), INTEGER*4(I-N)
C
      COMMON /ARRAY/ X_EDGE1(NI),Y_EDGE1(NI),X_EDGE2(NI),Y_EDGE2(NI),
     ^               X_EDGE3(NI),Y_EDGE3(NI),X_EDGE4(NI),Y_EDGE4(NI)
C
      DIMENSION XXX(NI,NJ)
      DIMENSION YYY(NI,NJ)
C
      IMIN=1
      JMIN=1
C
      DO 230 J=JMIN,JMAX
        XXX(IMIN,J)=X_EDGE4(J)
        YYY(IMIN,J)=Y_EDGE4(J)
 230  CONTINUE

      DO 235 J=JMIN,JMAX
        XXX(IMAX,J)=X_EDGE2(J)
        YYY(IMAX,J)=Y_EDGE2(J)
 235  CONTINUE

      DO 240 I=IMIN,IMAX
        XXX(I,JMIN)=X_EDGE1(I)
        YYY(I,JMIN)=Y_EDGE1(I)
 240  CONTINUE

      DO 245 I=IMIN,IMAX
        XXX(I,JMAX)=X_EDGE3(I)
        YYY(I,JMAX)=Y_EDGE3(I)
 245  CONTINUE
      RETURN
      END
```

```
**************************************************************************
*                  SUBROUTINE TRANSFINITE INTERPOLATION                  *
*                                MARCH 1996                              *
* This routine CAN be called ONLY from the subroutine PREPARE_FOR_TRANS  *
* ARGUMENTS :                                                            *
* IMAX  = INTEGER*4. On entry specifies the number of subdivisions       *
*         which is one less than the number of nodes on the I-Direction. *
*         Unchanged on exit.                                             *
* JMAX  = INTEGER*4. On entry specifies the number of subdivisions       *
*         which is one less than the number of nodes on the J-Direction. *
*         Unchanged on exit.                                             *
* XX    = 2-Dimensional Array.                                           *
*         On entry has only the X-values of the vertices along the       *
*         boundaries of the BLOCK                                        *
*         On exit has all the X-values of the vertices of the BLOCK      *
* YY    = 2-Dimensional Array.                                           *
*         On entry has only the Y-values of the vertices along the       *
*         boundaries of the BLOCK                                        *
*         On exit has all the Y-values of the vertices of the BLOCK      *
**************************************************************************
C
    SUBROUTINE TRANS (XX,YY,IMAX,JMAX)
    PARAMETER (NI=100,NJ=100)

    DIMENSION xx(NI,NJ),yy(NI,NJ)
    DIMENSION xx1(NI,NJ),yy1(NI,NJ),xx2(NI,NJ),yy2(NI,NJ)


 400  DO 410 I=1,IMAX
       DO 410 J=1,JMAX
        RI1=FLOAT(I-1)/FLOAT(IMAX-1)
        RI2=FLOAT(IMAX-I)/FLOAT(IMAX-1)
        xx1(I,J)=RI1*XX(IMAX,J)+RI2*XX(1,J)
        yy1(I,J)=RI1*YY(IMAX,J)+RI2*YY(1,J)
 410  CONTINUE
c
     DO 420 I=1,IMAX
      DO 420 J=1,JMAX
       RJ1=FLOAT(J-1)/FLOAT(JMAX-1)
       RJ2=FLOAT(JMAX-J)/FLOAT(JMAX-1)
       XX2(I,J)=RJ1*(XX(I,JMAX)-XX1(I,JMAX))+RJ2*(XX(I,1)-XX1(I,1))
       YY2(I,J)=RJ1*(YY(I,JMAX)-YY1(I,JMAX))+RJ2*(YY(I,1)-YY1(I,1))
 420  CONTINUE
c
     DO 430 I=1,IMAX
      DO 429 J=1,JMAX
       XX(I,J)=XX1(I,J)+XX2(I,J)
       YY(I,J)=YY1(I,J)+YY2(I,J)
 429  CONTINUE
 430  CONTINUE
     RETURN
     END
```

C.4 Geometry

```
(' GEOMETRY-WORKING VOLUMES-SEALING LINES- PEPRENDICULAR ');
(' CIRCULAR ARCS OF SCROLL MACHINES-WITH RESPECT TO CRANK ANGLE');
fidx0=fopen('x0','wt+');
fidy0=fopen('y0','wt+');
fidx1=fopen('x1','wt+');
fidy1=fopen('y1','wt+');
fidx2=fopen('x2','wt+');
fidy2=fopen('y2','wt+');
fidx3=fopen('x3','wt+');
fidy3=fopen('y3','wt+');
fidx4=fopen('x4','wt+');
fidy4=fopen('y4','wt+');
fidx5=fopen('x5','wt+');
fidy5=fopen('y5','wt+');
fidXk=fopen('Xk','wt+');
fidYk=fopen('Yk','wt+');
fidXk1=fopen('Xk1','wt+');
fidYk1=fopen('Yk1','wt+');

ZOOM ON

rb=0.75;
theta=-27.0*pi/9;
a=theta;
c=0.026;
g=0.3;
l=(pi-g).*rb;
l=l-c;
Pos=sqrt(((pi-g).^2./4)-1);
Pis=pi+sqrt(((pi-g).^2./4)-1)-g;
M=5.5;
Pof=M*pi;
Pif=(M*pi)-g;

if theta >-2.0*pi
  ('SUCTION');

  ('starting and finishing angles for the working volumes');
  f1f=4.0*pi+pi/2.0;
  f4f=f1f+pi-g;
  f1s=f1f+theta;
  f4s=f4f+theta;

  f4f=(M.*pi)-g;
  f4s=f4f+theta;
  f1s=f4s-pi+g;
  f1f=(M-1)*pi;

  ('starting and finishing angles for the outer spirals');
  Pos=f1s;
  Pof=f1f;
  ('starting and finishing angles for the inner spirals');
  Pis=f4s;
  Pif=f4f;
```

```
  ('starting and finishing angles for the mid planes');
  Posm=f1s;
  Pofm=(4.5.*pi+f1f)/2;
end

if theta <-2.0*pi
  ('COMPRESSION-DISCHARGE');
  Xos=rb.*(cos(Pos)+Pos.*sin(Pos));
  Yos=rb.*(sin(Pos)-Pos.*cos(Pos));
  Xis=rb.*(cos(Pis+g)+Pis.*sin(Pis+g));
  Yis=rb.*(sin(Pis+g)-Pis.*cos(Pis+g));
  Yoo1=(((Xos-Xis).^2)-((2.*(Xos-Xis).*tan(Pos).*Yis))+(Yos).^2.-(Yis).^2);
  Yoo2=2.*(Yos-Yis-(Xos-Xis).*tan(Pos));
  Yoo=Yoo1/Yoo2;
  Xoo=Xis-tan(Pos).*(Yoo-Yis);
  r=((Xis-Xoo).^2.+(Yis-Yoo).^2).^0.5;
  Xfc=Xis:0.01:Xos;
  Yfc=((r.^2.-(Xfc-Xoo).^2).^0.5)+Yoo;
  Yoc=-Yfc-l.*sin(a);
  Xoc=-Xfc-l.*cos(a);
end

('OUTER SPIRALS');
p=Pos:0.1:Pof;
('p=0:0.01:Pof');
x0=rb.*(cos(p)+p.*sin(p));
y0=rb.*(sin(p)-p.*cos(p));
x1=-rb.*(cos(p)+p.*sin(p))-l.*cos(a);
y1=-rb.*(sin(p)-p.*cos(p))-l.*sin(a);

('INNER SPIRALS');
p=Pis:0.1:Pif;
('p=0:0.01:Pif');
x2=rb.*(cos(p+g)+p.*sin(p+g));
y2=rb.*(sin(p+g)-p.*cos(p+g));
x3=-rb.*(cos(p+g)+p.*sin(p+g))-(l.*cos(a));
y3=-rb.*(sin(p+g)-p.*cos(p+g))-(l.*sin(a));


('MID PLANE 1 FIXED OUTER - ORBITING INNER');
p=Pos:0.1:(M-1).*pi;
('p=0.0:0.01:(M-1).*pi;');

('THIS SECTION IS TO PLOT THE MID PLANE');
GPI=pi;
RGEN=rb;
GAMMA=g;
CLEARAN=c;
PHI=p;
THETA=a;
GPIGAM=(GPI-GAMMA)/2.0;
DCENTR=(RGEN*(GPI-GAMMA)-CLEARAN);
COSPHI=cos(PHI);
SINPHI=sin(PHI);
XMP=RGEN*(COSPHI+(PHI+GPIGAM).*SINPHI)-DCENTR*cos(THETA)/2.0;
YMP=RGEN*(SINPHI-(PHI+GPIGAM).*COSPHI)-DCENTR*sin(THETA)/2.0;
x4=XMP;
```

```
y4=YMP;
('THIS SECTION IS TO FIND THE ANGLE PHI_FO');
('PEPPENDICULAR TO FIXED OUTER');
('CHOOSE A POINT ON THE MID PLANE');
p=7.0*pi/9;
ppp=p;
PHI=p;
COSPHI=cos(PHI);
SINPHI=sin(PHI);
XMP1=RGEN*(COSPHI+(PHI+GPIGAM).*SINPHI)-DCENTR*cos(THETA)/2.0;
YMP1=RGEN*(SINPHI-(PHI+GPIGAM).*COSPHI)-DCENTR*sin(THETA)/2.0;
xmm=XMP1;
ymm=YMP1;

('!--->3');
RMP1=sqrt(XMP1*XMP1+YMP1*YMP1);
COS_OMEGA=YMP1/RMP1;
if COS_OMEGA>0.999999
  COS_OMEGA =1.0;
end
if COS_OMEGA<-0.999999
  COS_OMEGA=-1.0;
end
OMEGA=acos(COS_OMEGA);
if XMP1<0.0
  OMEGA=2.0*GPI-OMEGA;
end
('!--->4');
SINALPHA=RGEN/RMP1;
if SINALPHA>0.999999
  SINALPHA =1.0;
end
if SINALPHA<-0.999999
  SINALPHA=-1.0;
end
ALPHA=asin(SINALPHA);
('!--->5');
PHI_FO=GPI-(OMEGA+ALPHA);

while PHI_FO>0.0
    PHI_FO=PHI_FO-2.0*GPI;
end
while PHI_FO<0.0
    PHI_FO=PHI_FO+2.0*GPI;
end

SINPHI_FO=sin(PHI_FO);
COSPHI_FO=cos(PHI_FO);
XFO=RGEN*(COSPHI_FO + PHI_FO*SINPHI_FO);
YFO=RGEN*(SINPHI_FO - PHI_FO*COSPHI_FO);
RFO=sqrt(XFO*XFO + YFO*YFO);
('!--->6');

while RFO<RMP1
    PHI_FO=PHI_FO + 2.0D+00*GPI;
    SINPHI_FO=sin(PHI_FO);
    COSPHI_FO=cos(PHI_FO);
```

```
    XFO=RGEN*(COSPHI_FO + PHI_FO*SINPHI_FO);
    YFO=RGEN*(SINPHI_FO - PHI_FO*COSPHI_FO);
    RFO=sqrt(XFO*XFO + YFO*YFO);
end
(' IF(RFO .NE. RMP1)i dont know how to do it in matlab');
PHI_FO=PHI_FO - 2.0*GPI;
phi=PHI_FO;
('!') ;
XFO=RGEN*(COSPHI_FO + PHI_FO*SINPHI_FO);
YFO=RGEN*(SINPHI_FO - PHI_FO*COSPHI_FO);

xstep=(xmm-XFO);
ystep=(ymm-YFO);
xplot=XFO:xstep:xmm;
yplot=YFO:ystep:ymm;

('THIS SECTION IS TO FIND THE ANGLE PHI_OI');
('PEPPENDICULAR TO ORBITING INNER');
('!--->7');

XMP1=XMP1+DCENTR*cos(THETA);
YMP1=YMP1+DCENTR*sin(THETA);

('!--->3');
RMP1=sqrt(XMP1*XMP1+YMP1*YMP1);
COS_OMEGA=YMP1/RMP1;
if COS_OMEGA>0.999999
  COS_OMEGA =1.0;
end
if COS_OMEGA<-0.999999
  COS_OMEGA=-1.0;
end
OMEGA=acos(COS_OMEGA);
if XMP1<0.0
  OMEGA=2.0*GPI-OMEGA;
end
('!--->4');
SINALPHA=RGEN/RMP1;
if SINALPHA>0.999999
  SINALPHA =1.0;
end
if SINALPHA<-0.999999
  SINALPHA=-1.0;
end
ALPHA=asin(SINALPHA);
('!--->8');
PHI_OI=-(OMEGA+ALPHA+GAMMA);

while PHI_OI>0.0
    PHI_OI=PHI_OI-2.0*GPI;
end
while PHI_OI<0.0
    PHI_OI=PHI_OI+2.0*GPI;
end

SINPHI_OIG=sin(PHI_OI+GAMMA);
COSPHI_OIG=cos(PHI_OI+GAMMA);
```

```
XOI=-RGEN*(COSPHI_OIG + PHI_OI*SINPHI_OIG);
YOI=-RGEN*(SINPHI_OIG - PHI_OI*COSPHI_OIG);
ROI=sqrt(XOI*XOI+YOI*YOI);

while ROI< RMP1
    PHI_OI=PHI_OI + 2.0*GPI;
    SINPHI_OIG=sin(PHI_OI+GAMMA);
    COSPHI_OIG=cos(PHI_OI+GAMMA);
    XOI=-RGEN*(COSPHI_OIG+PHI_OI*SINPHI_OIG);
    YOI=-RGEN*(SINPHI_OIG-PHI_OI*COSPHI_OIG);
    ROI=sqrt(XOI*XOI+YOI*YOI);
end

PHI_OI=PHI_OI;
phi1=PHI_OI;
XOI=-RGEN*(COSPHI_OIG+PHI_OI*SINPHI_OIG)-DCENTR*cos(THETA);
YOI=-RGEN*(SINPHI_OIG-PHI_OI*COSPHI_OIG)-DCENTR*sin(THETA);
xstep1=(xmm-XOI);
ystep1=(ymm-YOI);
xplot1=XOI:xstep1:xmm;
yplot1=YOI:ystep1:ymm;

('SUBROUTINE THREE_POINT_ARC');
X11=XOI;
Y11=YOI;
X22=xmm;
Y22=ymm;
X33=XFO;
Y33=YFO;

IVERTIC12_YESP=1;
IVERTIC12_NOP=2;
IVERTIC13_YESP=10;
IVERTIC13_NOP=20;
('!--->3');
    X12=0.5D+00*(X11+X22);
    Y12=0.5D+00*(Y11+Y22);
    X13=0.5D+00*(X11+X33);
    Y13=0.5D+00*(Y11+Y33);
('!--->4');
    IAUX=IVERTIC12_YESP;
    AUX=abs(Y11-Y22);
    if AUX>0.0
     IAUX=IVERTIC12_NOP;
    end
    IAUX1=IVERTIC13_YESP;
    AUX=abs(Y11-Y33);
    if AUX> 0.0
      IAUX1=IVERTIC13_NOP;
    end
    IAUX=IAUX+IAUX1;
('!--->5');
    AUX=IVERTIC13_NOP+IVERTIC12_NOP;
    gnk1=IVERTIC13_NOP+IVERTIC12_YESP;
    gnk2=IVERTIC13_YESP+IVERTIC12_NOP;
    if IAUX == AUX;
        GRAD12 =-(X22-X11)/(Y22-Y11);
```

```
        C12   =Y12-GRAD12*X12;
        GRAD13 =-(X33-X11)/(Y33-Y11);
        C13   =Y13-GRAD13*X13;
        AUX=abs(GRAD12-GRAD13);
        if AUX<=0.0
          ANGLE=GPI;
          ('RETURN')
        end
        XO=-(C12-C13)/(GRAD12-GRAD13);
        YO=-(C12*GRAD13-C13*GRAD12)/(GRAD12-GRAD13);
    elseif IAUX==gnk1
        GRAD13 =-(X33-X11)/(Y33-Y11);
        C13   =Y13-GRAD13*X13;
        XO=X12;
        YO=GRAD13*XO+C13;
    elseif IAUX==gnk2
        GRAD12 =-(X22-X11)/(Y22-Y11);
        C12   =Y12-GRAD12*X12;
        XO=X13;
        YO=GRAD12*XO+C12;
    else
    ('All points on straight AND horizontal line')
       ANGLE=GPI;
    end

('!--->6');
    X1O=X11-XO;
    Y1O=Y11-YO;
    X3O=X33-XO;
    Y3O=Y33-YO;
    RADIUS2=X1O*X1O+Y1O*Y1O;
    RADIUS=sqrt(RADIUS2);
    ANGLE=acos((X1O*X3O+Y1O*Y3O)/RADIUS2);
('!--->7');
    X12=X11-X22;
    Y12=Y11-Y22;
    X32=X33-X22;
    Y32=Y33-Y22;
    gnk4=X12*Y32-X32*Y12;
    if gnk4> 0.0
      ANGLE=-ANGLE;
    end
('!--->8');
    GONIA_A=asin(abs(Y1O)/RADIUS);
    X1OY1O=X1O*Y1O;
    if X1OY1O<0.0
      GONIA_A = -GONIA_A;
    end
    if X1O<0.0
      GONIA_A =GPI+GONIA_A;
    end
    if GONIA_A<0.0
      GONIA_A =2.0D+00*GPI+GONIA_A;
    end
    gpi2=GPI/2.0;
    if GONIA_A==gpi2
      if Y1O<0.0
```

```
        GONIA_A=GPI+GONIA_A;
      end
    end

gnkangle=ANGLE;
gnkgonia_a=GONIA_A;
aktina=RADIUS;
step=ANGLE/10.0;
ANGLEC=GONIA_A+ANGLE;
deltaphi=GONIA_A:step:ANGLEC;

Xk=RADIUS*cos(deltaphi)+XO;
Yk=RADIUS*sin(deltaphi)+YO;

Xk1=-Xk-DCENTR*cos(THETA);
Yk1=-Yk-DCENTR*sin(THETA);

('MID PLANE 2 ORBITING OUTTER FIXED INNER');
p=Pos:0.01:(M-1).*pi;
('p=0.0:0.01:(M-1).*pi;');
('x5=((rb.*(cos(p+pi)+(p+pi-g).*sin(p+pi)))+(-rb.*(cos(p)+(p).*sin(p))-(l.*cos(a))))/2;');
('y5=((rb.*(sin(p+pi)-(p+pi-g).*cos(p+pi)))+(-rb.*(sin(p)-(p).*cos(p))-(l.*sin(a))))/2;');
x5=-x4-DCENTR*cos(THETA);
y5=-y4-DCENTR*sin(THETA);


p=ppp;
xmm=((rb.*(cos(p+pi)+(p+pi-g).*sin(p+pi)))+(-rb.*(cos(p)+(p).*sin(p))-(l.*cos(a))))/2;
ymm=((rb.*(sin(p+pi)-(p+pi-g).*cos(p+pi)))+(-rb.*(sin(p)-(p).*cos(p))-(l.*sin(a))))/2;

('PEPPENDICULAR TO ORBITING OUTER');
p=phi;
xm55=-rb.*(cos(p)+p.*sin(p))-l.*cos(a);
ym55=-rb.*(sin(p)-p.*cos(p))-l.*sin(a);
xstep5=(xmm-xm55);
ystep5=(ymm-ym55);
xplot5=xm55:xstep5:xmm;
yplot5=ym55:ystep5:ymm;

('PEPPENDICULAR TO FIXED INNER');
p=phi1;
xm66=rb.*(cos(p+g)+p.*sin(p+g));
ym66=rb.*(sin(p+g)-p.*cos(p+g));
xstep6=(xmm-xm66);
ystep6=(ymm-ym66);
xplot6=xm66:xstep6:xmm;
yplot6=ym66:ystep6:ymm;

Yoo=0;
Xoo=0;

('FIXED CIRCLE');
Xfc11=-rb:0.01:rb;
Yfc11=((rb.^2.-(Xfc11-Xoo).^2).^0.5)+Yoo;
Yfc22=-((rb.^2.-(Xfc11-Xoo).^2).^0.5)+Yoo;

('ORBITING CIRCLE');
```

```
Xoc11=-Xfc11-l.*cos(a);
Yoc11=-Yfc11-l.*sin(a);
Yoc22=-Yfc22-l.*sin(a);

('GRANK CIRCLE');
r=l;
Xgc=-r:0.01:r+0.0054;
Ygc=((r.^2.-(Xgc-Xoo).^2).^0.5)+Yoo;
Ygc1=-((r.^2.-(Xgc-Xoo).^2).^0.5)+Yoo;

('saveabcde x0 y0 x1 y1');
('saveabcde x0 y0 x1 y1 -ascii -double -tabs');

('IF YOU WANT TO PRINT INTO FILES THE COORDINATES OF THE');
('PERPENDICULAR STRAIGHT LINES PUT PRINTLINES=1 OTHERWISE 0');
('NOTE ALSO THAT THE COORIDINATES WILL BE STORED IN THE FILES');
('x0,y0 and x1,y1 RESPECTIVELY');
PRINTLINES=2;
if PRINTLINES==1
  fprintf(fidx0,'%10.4f\n',xplot);
  fprintf(fidy0,'%10.4f\n',yplot);
  fprintf(fidx0,'%10.4f\n',xplot1);
  fprintf(fidy0,'%10.4f\n',yplot1);
  fprintf(fidx1,'%10.4f\n',xplot5);
  fprintf(fidy1,'%10.4f\n',yplot5);
  fprintf(fidx1,'%10.4f\n',xplot6);
  fprintf(fidy1,'%10.4f\n',yplot6);
end

fprintf(fidx0,'%10.4f\n',x0);
fprintf(fidy0,'%10.4f\n',y0);
fprintf(fidx1,'%10.4f\n',x1);
fprintf(fidy1,'%10.4f\n',y1);

fprintf(fidx2,'%10.4f\n',x2);
fprintf(fidy2,'%10.4f\n',y2);
fprintf(fidx2,'%10.4f\n',Xfc);
fprintf(fidy2,'%10.4f\n',Yfc);

fprintf(fidx3,'%10.4f\n',x3);
fprintf(fidy3,'%10.4f\n',y3);
fprintf(fidx3,'%10.4f\n',Xoc);
fprintf(fidy3,'%10.4f\n',Yoc);

fprintf(fidx4,'%10.4f\n',x4);
fprintf(fidy4,'%10.4f\n',y4);
fprintf(fidx5,'%10.4f\n',x5);
fprintf(fidy5,'%10.4f\n',y5);
fprintf(fidXk,'%10.4f\n',Xk);
fprintf(fidYk,'%10.4f\n',Yk);
fprintf(fidXk1,'%10.4f\n',Xk1);
fprintf(fidYk1,'%10.4f\n',Yk1);
fclose(fidx0);
fclose(fidy0);
fclose(fidx1);
fclose(fidy1);
fclose(fidx2);
```

```
fclose(fidy2);
fclose(fidx3);
fclose(fidy3);
fclose(fidx4);
fclose(fidy4);
fclose(fidx5);
fclose(fidy5);
fclose(fidXk);
fclose(fidYk);
fclose(fidXk1);
fclose(fidYk1);

s=1;
if s>2
('WORKING VOLUME SPIRALS, GENERATING CIRCLES, CRANK CIRCLE');
plot(x0,y0,x1,y1,x2,y2,x3,y3,Xfc,Yfc,Xoc,Yoc,Xfc11,Yfc11,Xfc11,Yfc22,Xoc11,Yoc11,Xoc11,Y
oc22,Xgc,Ygc,Xgc,Ygc1)
axis([-13,13,-13,13])
axis('equal')
end

s=3;
if s>2
('WORKING VOLUME SPIRALS, MIDPLANES PERPENDICULAR STRAIGHT LINES');
plot(x0,y0,x1,y1,x2,y2,x3,y3,x4,y4,x5,y5,Xfc,Yfc,Xoc,Yoc,xplot,yplot,xplot1,yplot1,xplot5,yplot5,
xplot6,yplot6)
axis([-13,13,-13,13])
axis('equal')
end

s=3;
if s>2
('WORKING VOLUME SPIRALS, MIDPLANES PERPENDICULAR CIRCULAR ARCS');
plot(x0,y0,x1,y1,x2,y2,x3,y3,x4,y4,x5,y5,Xfc,Yfc,Xoc,Yoc,Xk,Yk,Xk1,Yk1)
axis([-13,13,-13,13])
axis('equal')
end

s=1;
if s>2
('WORKING VOLUME SPIRALS, GENERATING CIRCLES,');
('MIDPLANES PERPENDICULAR STRAIGHT LINES');
plot(x0,y0,x3,y3,x1,y1,x2,y2,x4,y4,x5,y5,Xfc11,Yfc11,Xfc11,Yfc22,Xoc11,Yoc11,Xoc11,Yoc22,x
plot,yplot,xplot1,yplot1,xplot5,yplot5,xplot6,yplot6)
axis([-13,13,-13,13])
axis('equal')
end

if theta >-2.0*pi
  ('COMPRESSION - DISCHARGE');
  ('SPIRALS, GENERATING CIRCLES,');
  ('MIDPLANES PERPENDICULAR STRAIGHT LINES');

plot(x0,y0,x3,y3,x1,y1,x2,y2,x4,y4,x5,y5,Xfc,Yfc,Xoc,Yoc,Xfc11,Yfc11,Xfc11,Yfc22,Xoc11,Yoc
11,Xoc11,Yoc22,xplot,yplot,xplot1,yplot1,xplot5,yplot5,xplot6,yplot6)
  axis([-14,14,-14,14])
  axis('equal')
end
```

C.5 Command Language (CFX4)

```
/*************************************************************/
/* SCROLL EXPANDRER                                          */
/* TRANSIENT GRID  COMPRESSIBLE, TURBULENT FLOW  */
/*************************************************************/
>>CFXF3D
  #CALC
    NI1=60;
    NJ1=20;
    NK1=6;
    NI2=20;
    NJ2=20;
    NK2=6;
    NI3=60;
    NJ3=20;
    NK3=6;
    NI4=20;
    NJ4=20;
    NK4=6;
    NI5=10;
    NJ5=10;
    NK5=20;
  #ENDCALC
   >>SET LIMITS
    TOTAL INTEGER WORK SPACE 5000000
    TOTAL REAL WORK SPACE 15000000
    MAXIMUM NUMBER OF BLOCKS 5
    MAXIMUM NUMBER OF PATCHES 50
    MAXIMUM NUMBER OF INTER BLOCK BOUNDARIES 30
    END
 >>OPTIONS
  THREE DIMENSIONS
  TURBULENT FLOW
  HEAT TRANSFER
  COMPRESSIBLE FLOW
  TRANSIENT FLOW
  TRANSIENT GRID
  END
 >>USER FORTRAN
  USRGRD
  USRTRN
  END
>>MODEL TOPOLOGY
 /*****************/
 /* CREATE BLOCKS */
 /*****************/
 >>CREATE BLOCK
    BLOCK NAME 'BLOCK-1'
    NUMBER OF I CELLS #NI1
    NUMBER OF J CELLS #NJ1
    NUMBER OF K CELLS #NK1
    END
 >>CREATE BLOCK
    BLOCK NAME 'BLOCK-2'
    NUMBER OF I CELLS #NI2
```

```
    NUMBER OF J CELLS #NJ2
    NUMBER OF K CELLS #NK2
    END
>>CREATE BLOCK
    BLOCK NAME 'BLOCK-3'
    NUMBER OF I CELLS #NI3
    NUMBER OF J CELLS #NJ3
    NUMBER OF K CELLS #NK3
    END
>>CREATE BLOCK
    BLOCK NAME 'BLOCK-4'
    NUMBER OF I CELLS #NI4
    NUMBER OF J CELLS #NJ4
    NUMBER OF K CELLS #NK4
    END
>>CREATE BLOCK
    BLOCK NAME 'BLOCK-5'
    NUMBER OF I CELLS #NI5
    NUMBER OF J CELLS #NJ5
    NUMBER OF K CELLS #NK5
    END
/*****************/
/* CREATE PATCH  */
/*****************/
>>CREATE PATCH
  BLOCK NAME 'BLOCK-1'
  PATCH NAME 'PATCH-1.1'
  PATCH TYPE 'INTER BLOCK BOUNDARY'
  LOW I
  END
>>CREATE PATCH
  BLOCK NAME 'BLOCK-1'
  PATCH NAME 'PATCH-1.2'
  PATCH TYPE 'WALL'
  HIGH J
  END
>>CREATE PATCH
  BLOCK NAME 'BLOCK-1'
  PATCH NAME 'PATCH-1.3'
  PATCH TYPE 'WALL'
  HIGH I
  END
>>CREATE PATCH
  BLOCK NAME 'BLOCK-1'
  PATCH NAME 'PATCH-1.4'
  PATCH TYPE 'WALL'
  LOW J
  END
>>CREATE PATCH
  BLOCK NAME 'BLOCK-1'
  PATCH NAME 'PATCH-1.5'
  PATCH TYPE 'WALL'
  LOW K
  END
>>CREATE PATCH
  BLOCK NAME 'BLOCK-1'
  PATCH NAME 'PATCH-1.6'
```

```
 PATCH TYPE 'WALL'
 HIGH K
 END

>>CREATE PATCH
 BLOCK NAME 'BLOCK-2'
 PATCH NAME 'PATCH-2.1'
 PATCH TYPE 'WALL'
 LOW J
 END
>>CREATE PATCH
 BLOCK NAME 'BLOCK-2'
 PATCH NAME 'PATCH-2.2'
 PATCH TYPE 'WALL'
 HIGH I
 END
>>CREATE PATCH
 BLOCK NAME 'BLOCK-2'
 PATCH NAME 'PATCH-2.3'
 PATCH TYPE 'INTER BLOCK BOUNDARY'
 HIGH J
 END
>>CREATE PATCH
 BLOCK NAME 'BLOCK-2'
 PATCH NAME 'PATCH-2.4'
 PATCH TYPE 'INTER BLOCK BOUNDARY'
 LOW I
 END
>>CREATE PATCH
 BLOCK NAME 'BLOCK-2'
 PATCH NAME 'PATCH-2.5'
 PATCH TYPE 'WALL'
 LOW K
 END
>>CREATE PATCH
 BLOCK NAME 'BLOCK-2'
 PATCH NAME 'PATCH-2.6'
 PATCH TYPE 'WALL'
 HIGH K
 END

>>CREATE PATCH
 BLOCK NAME 'BLOCK-3'
 PATCH NAME 'PATCH-3.1'
 PATCH TYPE 'INTER BLOCK BOUNDARY'
 LOW I
 END
>>CREATE PATCH
 BLOCK NAME 'BLOCK-3'
 PATCH NAME 'PATCH-3.2'
 PATCH TYPE 'WALL'
 HIGH J
 END
>>CREATE PATCH
 BLOCK NAME 'BLOCK-3'
 PATCH NAME 'PATCH-3.3'
 PATCH TYPE 'WALL'
```

```
 HIGH I
 END
>>CREATE PATCH
 BLOCK NAME 'BLOCK-3'
 PATCH NAME 'PATCH-3.4'
 PATCH TYPE 'WALL'
 LOW J
 END
>>CREATE PATCH
 BLOCK NAME 'BLOCK-3'
 PATCH NAME 'PATCH-3.5'
 PATCH TYPE 'WALL'
 LOW K
 END
>>CREATE PATCH
 BLOCK NAME 'BLOCK-3'
 PATCH NAME 'PATCH-3.6'
 PATCH TYPE 'WALL'
 HIGH K
 END

>>CREATE PATCH
 BLOCK NAME 'BLOCK-4'
 PATCH NAME 'PATCH-4.1'
 PATCH TYPE 'WALL'
 LOW J
 END
>>CREATE PATCH
 BLOCK NAME 'BLOCK-4'
 PATCH NAME 'PATCH-4.2'
 PATCH TYPE 'WALL'
 HIGH I
 END
>>CREATE PATCH
 BLOCK NAME 'BLOCK-4'
 PATCH NAME 'PATCH-4.3'
 PATCH TYPE 'INTER BLOCK BOUNDARY'
 HIGH J
 END
>>CREATE PATCH
 BLOCK NAME 'BLOCK-4'
 PATCH NAME 'PATCH-4.4'
 PATCH TYPE 'INTER BLOCK BOUNDARY'
 LOW I
 END
>>CREATE PATCH
 BLOCK NAME 'BLOCK-4'
 PATCH NAME 'PATCH-4.51'
 PATCH TYPE 'WALL'
 LOW K
 PATCH LOCATION 1 5  1 20  1 1
 END
>>CREATE PATCH
 BLOCK NAME 'BLOCK-4'
 PATCH NAME 'PATCH-4.52'
 PATCH TYPE 'WALL'
 LOW K
```

```
 PATCH LOCATION 6 15  11 20  1 1
 END
>>CREATE PATCH
 BLOCK NAME 'BLOCK-4'
 PATCH NAME 'PATCH-4.53'
 PATCH TYPE 'WALL'
 LOW K
 PATCH LOCATION 16 20  1 20  1 1
 END
>>CREATE PATCH
 BLOCK NAME 'BLOCK-4'
 PATCH NAME 'PATCH-4.54'
 PATCH TYPE ' INTER BLOCK BOUNDARY'
 LOW K
 PATCH LOCATION 6 15  1 10  1 1
 END
>>CREATE PATCH
 BLOCK NAME 'BLOCK-4'
 PATCH NAME 'PATCH-4.6'
 PATCH TYPE 'WALL'
 HIGH K
 END
>>CREATE PATCH
 BLOCK NAME 'BLOCK-5'
 PATCH NAME 'PATCH-5.1'
 PATCH TYPE 'WALL'
 LOW J
 END
>>CREATE PATCH
 BLOCK NAME 'BLOCK-5'
 PATCH NAME 'PATCH-5.2'
 PATCH TYPE 'WALL'
 HIGH I
 END
>>CREATE PATCH
 BLOCK NAME 'BLOCK-5'
 PATCH NAME 'PATCH-5.3'
 PATCH TYPE 'WALL'
 HIGH J
 END
>>CREATE PATCH
 BLOCK NAME 'BLOCK-5'
 PATCH NAME 'PATCH-5.4'
 PATCH TYPE 'WALL'
 LOW I
 END
>>CREATE PATCH
 BLOCK NAME 'BLOCK-5'
 PATCH NAME 'PATCH-5.5'
 PATCH TYPE 'INTER BLOCK BOUNDARY'
 HIGH K
 END
>>CREATE PATCH
 BLOCK NAME 'BLOCK-5'
 PATCH NAME 'INLET'
 PATCH TYPE 'PRESSURE BOUNDARY'
 LOW K
```

```
 END

/*****************/
/* GLUE PATCHES  */
/*****************/
 >>GLUE PATCHES
    FIRST PATCH NAME 'PATCH-1.1'
    SECOND PATCH NAME 'PATCH-2.3'
    ORIENTATION CHANGE 'HIGH J' 'HIGH I' 'HIGH K'
    END
 >>GLUE PATCHES
    FIRST PATCH NAME 'PATCH-2.4'
    SECOND PATCH NAME 'PATCH-4.4'
    ORIENTATION CHANGE 'LOW I' 'LOW J' 'HIGH K'
    END
 >>GLUE PATCHES
    FIRST PATCH NAME 'PATCH-3.1'
    SECOND PATCH NAME 'PATCH-4.3'
    ORIENTATION CHANGE 'HIGH J' 'HIGH I' 'HIGH K'
    END
 >>GLUE PATCHES
    FIRST PATCH NAME 'PATCH-4.54'
    SECOND PATCH NAME 'PATCH-5.5'
    END

>>MODEL DATA
 >>TITLE
  PROBLEM TITLE 'SCROLL EXPANDER R134a'
  END
 >>PHYSICAL PROPERTIES
  >>FLUID PARAMETERS
   VISCOSITY 0.206E-4
   END
 >>COMPRESSIBILITY PARAMETERS
  WEAKLY COMPRESSIBLE
  UNIVERSAL GAS CONSTANT 8314.0
  FLUID MOLECULAR WEIGHT 102.03
  REFERENCE PRESSURE 9.489E+05
  END
 >>HEAT TRANSFER PARAMETERS
  FLUID SPECIFIC HEAT 1020.0
  THERMAL CONDUCTIVITY 0.0211
  ENTHALPY REFERENCE TEMPERATURE 288.0
  END
 >>TRANSIENT PARAMETERS
   TIME STEPS 200*8.333E-5
   END

>>SOLVER DATA
 >>PROGRAM CONTROL
  MAXIMUM NUMBER OF ITERATIONS 100
  OUTPUT MONITOR BLOCK 'BLOCK-4'
  OUTPUT MONITOR POINT 10 5 3
  MASS SOURCE TOLERANCE 1.0E-5
  END
 >>DEFERRED CORRECTION
  EPSILON START 101
```

```
  EPSILON END 101
  K START 101
  K END 101
  END

>>CREATE GRID

>>MODEL BOUNDARY CONDITIONS
 >>SET VARIABLES
   #CALC
    UINL=40.0;
    TEINL=0.002*UINL*UINL;
    CH=0.02;
    EPSINL=TEINL**1.5/(0.3*CH);
    #ENDCALC
   PATCH NAME 'INLET'
   PRESSURE     9.489E+05
   TEMPERATURE   310.0
   END

>>OUTPUT OPTIONS
 >>DUMP FILE OPTIONS
   U VELOCITY
   V VELOCITY
   W VELOCITY
   PRESSURE
   GEOMETRY DATA
   TIME STEP 10
   END
 >>DUMP FILE OPTIONS
   U VELOCITY
   V VELOCITY
   W VELOCITY
   PRESSURE
   GEOMETRY DATA
   TIME STEP 20
   END
 >>DUMP FILE OPTIONS
   U VELOCITY
   V VELOCITY
   W VELOCITY
   PRESSURE
   GEOMETRY DATA
   TIME STEP 30
   END
 >>DUMP FILE OPTIONS
   U VELOCITY
   V VELOCITY
   W VELOCITY
   PRESSURE
   GEOMETRY DATA
   TIME STEP 40
   END
 >>DUMP FILE OPTIONS
   U VELOCITY
   V VELOCITY
   W VELOCITY
```

```
 PRESSURE
 GEOMETRY DATA
 TIME STEP 50
 END
>>DUMP FILE OPTIONS
 U VELOCITY
 V VELOCITY
 W VELOCITY
 PRESSURE
 GEOMETRY DATA
 TIME STEP 60
 END
>>DUMP FILE OPTIONS
 U VELOCITY
 V VELOCITY
 W VELOCITY
 PRESSURE
 GEOMETRY DATA
 TIME STEP 70
 END
>>DUMP FILE OPTIONS
 U VELOCITY
 V VELOCITY
 W VELOCITY
 PRESSURE
 GEOMETRY DATA
 TIME STEP 80
 END
>>DUMP FILE OPTIONS
 U VELOCITY
 V VELOCITY
 W VELOCITY
 PRESSURE
 GEOMETRY DATA
 TIME STEP 90
 END
>>DUMP FILE OPTIONS
 U VELOCITY
 V VELOCITY
 W VELOCITY
 PRESSURE
 GEOMETRY DATA
 TIME STEP 100
 END
>>DUMP FILE OPTIONS
 U VELOCITY
 V VELOCITY
 W VELOCITY
 PRESSURE
 GEOMETRY DATA
 TIME STEP 110
 END
>>DUMP FILE OPTIONS
 U VELOCITY
 V VELOCITY
 W VELOCITY
 PRESSURE
```

```
 GEOMETRY DATA
 TIME STEP 120
 END
>>DUMP FILE OPTIONS
 U VELOCITY
 V VELOCITY
 W VELOCITY
 PRESSURE
 GEOMETRY DATA
 TIME STEP 130
 END
>>DUMP FILE OPTIONS
 U VELOCITY
 V VELOCITY
 W VELOCITY
 PRESSURE
 GEOMETRY DATA
 TIME STEP 140
 END
>>DUMP FILE OPTIONS
 U VELOCITY
 V VELOCITY
 W VELOCITY
 PRESSURE
 GEOMETRY DATA
 TIME STEP 150
 END
>>DUMP FILE OPTIONS
 U VELOCITY
 V VELOCITY
 W VELOCITY
 PRESSURE
 GEOMETRY DATA
 TIME STEP 160
 END
>>DUMP FILE OPTIONS
 U VELOCITY
 V VELOCITY
 W VELOCITY
 PRESSURE
 GEOMETRY DATA
 TIME STEP 170
 END
>>DUMP FILE OPTIONS
 U VELOCITY
 V VELOCITY
 W VELOCITY
 PRESSURE
 GEOMETRY DATA
 TIME STEP 180
 END
>>DUMP FILE OPTIONS
 U VELOCITY
 V VELOCITY
 W VELOCITY
 PRESSURE
 GEOMETRY DATA
```

```
  TIME STEP 190
  END
 >>DUMP FILE OPTIONS
  U VELOCITY
  V VELOCITY
  W VELOCITY
  PRESSURE
  GEOMETRY DATA
  TIME STEP 200
  END

 >>DUMP FILE FORMAT
  UNFORMATTED
  END

>>STOP
```

References And Bibliography

Alderton J.H., Wilkes N.S. (1988): Some applications of New Finite Difference Schemes for Fluid Flow Problems. Harwell Report AERE-R 13234

Anderson D.A., Tannehill J.C., Pletcher R.H. (1986): Computational Fluid Mechanics and Heat Transfer. McGraw-Hill Book Company

Anonymous (1990a): STAR-CD Manual, Computational Dynamics, London, 1990
Anonymous (1990b): The PHOENICS Reference Manual. Report CHAM/TR/100. CHAM Ltd, London 1990.

Anonymous (1990c): Harwell-FLOW3D, Release 2.3: User Manual, Harwell Laboratory, 1990

Anonymous (1991a): User guide to FEAT. Engineering Analysis Centre, Nuclear Electric Plc, UK

Anonymous (1991b): FLOW3D, Release 2.4: User Manual. AEA Ind-Tech, Harwell-Laboratory, Oxfordshire U.K., 1991

Anonymous (1992): FLOW3D, Release 3.1.2: User Manual. AEA Ind-Tech, Harwell-Laboratory, Oxfordshire U.K., 1992

Anonymous (1993): FLOW3D, Release 3.2: User Manual. AEA Ind-Tech, Harwell-Laboratory, Oxfordshire U.K., 1993

Anonymous (1994a): FLOW3D, Release 3.3: User Manual. AEA Ind-Tech, Harwell-Laboratory, Oxfordshire U.K., 1994

Anonymous (1994b): ENVIROMENT User Guide Release 1.5: User Manual. AEA Ind-Tech, Harwell-Laboratory, Oxfordshire U.K., 1994

Babuska I., Aziz A.K. (1972): Survey lectures on the mathematical foundation of the finite element method. In: Mathematical Formulation of the Finite Element Method. Ed. A.K. Aziz. Academic Press, New York

Baker A.J. (1983): Finite Element Computational Fluid Mechanics. McGraw-Hill

Baker A.J. (1984): Finite Element Penalty Algorithm for the Parabolic Navier-Stokes Equations for Turbulent Three Dimensional Flows. Computer Methods in Applied Mechanics and Engineering Vol. 46 pp. 277-93

Baliga B.R., Patankar S.V. (1980): A New Finite Element Formulation for Covection-

Diffusion Problems. Num. Heat Transfer Vol.3 pp. 393-409

Baliga B.R., Patankar S.V. (1993): A Control Volume Finite Element Method for Two Dimensional Fluid Flow and Heat Transfer. Num. Heat Transfer Vol.6 pp. 245-61

Brooks A.N., Hughes T.S.R. (1982): Streamline Upwind/Petrov-Galerkin Formulations for Convection Dominated Flows with Particular Emphasis on the Incompressible Navier Stokes Equations. Comp. Mech. Appl. Mech. Eng. Vol.32 pp. 199-259

Burns A.D., Wilkes N.S. (1987): A Finite Difference Method for the Computation of Fluid Flows in Complex Three-Dimensional Geometries. UKAEA Report AERE-R 12342
Burns A.D., Wilkes N.S., Jones I.P., Kightley J.R. (1996): FLOW3D: Body-Fitted Co-ordinates. AERE-R 12262

Bush W.B., Cailat J.L., Seibel M.S. (1986): Dimensional Optimization of Scroll Compressors. 8th Int. Compressor Eng. Conf. Pardue Univ.

Canuto C., Hussaini M.Y., Quarteroni A., Zang T.A. (1987): Spectral Methods in Fluid-Dynamics. Berlin. Springer-Verlag

Cebeci T., Hirsh R.S., Keller H.B., Williams P.G (1981): Studies of Numerical Methods for the Plane Navier-Stokes Equations. Computer Methods in Applied Mechanics and Engineering Vol.27 pp. 13-44

Chen C.J., Chen H.C (1984): Finite analytic numerical method for unsteady two-dimensional Navier-Stokes Equations. J. Comp. Physics Vol.53 pp. 209-226

Chen C.J., Naseri-Neshat H., Ho K.S. (1981): Finite Analytical Numerical Solution of Heat Transfer in Two-Dimensional Cavity Flow. Numerical Heat Transfer Vol.4 pp. 179-97

Chorin A.J. (1967): A Numerical Method for Solving Incompressible Viscous Flow Problems. J. Comput. Phys. Vol.2 pp. 12-26

Ciofalo M. (1992): Large-Eddy Simulation of Turbulent Flows with Heat Transfer in Simple and Complex Geometries. Ph.D. Thesis, Dept of Mechanical Engineering and Aeronautics, City University, London, U.K.

Ciofalo M., Collins M.W. (1989): κ-ε Predictions of Heat Tranfer in Turbulent Recirculating Flows using an Improved Wall Treatment. Numerical Heat Transfer, Part B Vol.15 pp. 21-47

Courant R., Isaacson E., Rees M. (1952): On the solution of Non-Linear Hyperbolic Differential Equations by Finite differences. Comm. Pure Appl. Math. Vol.5 p. 243

DeBlois R.L., Cutts D.G., Drost R.T. (1990): Lubrication System for a Low-Side Horizontal Scroll Compressor. 10th Int. Compressor Eng. Conf. Pardue Univ.

Demirdzic I., Peric M. (1988): Space conservation law in finite volume calculations of fluid flow. Intern. J. Numerical Methods in Fluids Vol.88 pp. 1037-58

Demirdzic I., Peric M. (1990): Finite Volume Method prediction of fluid in arbitrarily shaped domains with moving boundaries. Intern. J. Numerical Methods in Fluids Vol.88 pp. 771-790

Douglas R.W., Ramshaw J.D (1994): Future Research Directions in Computational Fluid-Dynamics. J. Fluids Eng. ASME Vol.116 pp. 212-5

Eiseman P.R., Eriebacher G. (1982): Grid Generation for the Solution of Partial Differential Equations. NASA Contract Report 178365

Eisman P. (1979): A Multi -Surface Method of Coordinate Generation. J. Comp. Phys. Vol.33 pp. 118-150

Etemad S., Nieter J. (1988): Computational Parametric Study of Scroll Compressor Efficiency, Design, and Manufacture. . 9th Int. Compressor Eng. Conf. Pardue Univ.

Fearn R.M., Mullin T., Cliffe K.A. (1990): Nonlinear flow phenomena in a symmetric sudden expansion. J. Fluid Mech. Vol.211 pp.595-608

Finlayson B.A. (1972): The Method of Weighted Residuals and Variational Principles. Academic Press, New York

Fletcher D.F., McCaughey m., Hall R.W. (1993): Numerical Simulation of A Laminar Jet Flow- A Comparison of 3 CFD Models. Computer Physics Communications Vol.78 n.1-2 pp.113-20

Folkow B., Neil E (1971): Circulation. Oxford University Press, New York

Forsey C.R., Billing C.M. (1988): Some Experiences with Grid Generation on Gurved Surface using Variational and Optimmization Techniques. In: Numerical Grid Generation Methods for Fluid Dynamics (3). Ed. By K.W. Morton and M.J. Baines, Oxford University Press.

Frankel S.P. (1950): Convergence Rates of Iterative Treatments of Partial Differential Equations. Mathematical Tables and other Aids to Computation Vol.4 pp. 65-75

Galiat J.L., Ni S., Daniels M. (1988): A Computer Model For Scroll Compressors. 9th Int. Compressor Eng. Conf. Pardue Univ.

Gentry R.A., Martin R.E., Daly B.J. (1996): An Eulerian Differencing Method for Unsteady Compressible Flow Problems. J. Comput. Phys. Vol.1 pp.87

Glass J., Rodi W. (1982): A Higher Order Numerical Scheme for Scalar Transport. Comput. Mech. Appl. Mech. Engin. Vol.3 pp. 37-58

Glowinski R., Pironneau (1992): Finite Element Methods for Navier-Stokes Equations. Ann. Rev. of Fluid Mechanics Vol.24 pp.

Gosman A.D., Peric M. (1985): A Flux Bendin Sceme for Redusing Numerical Diffuesion in Convective Transport, Mech. Eng. Dept. Report, Imperial College, London

Gosman A.D., Pun W.M. (1974): Lecture Notes for a Course Entitled "Computation of Recirculating Flows". Heat Transfer Sec. Report HTS/74/2, Imperial College, London, 1974

Gosman A.D., Pun W.M., Runchal A.K., Spalding D.B., Wolfshtein M. (1969): Heat and Mass Transfer in Recirculating Flows. Academic, New York

Graham D.I., Jawes P.W., Jones T.E.R., Davies J.M., Delo E.A (1992): Measurement and Prediction of Surface Shear-Stress in Annular Flume. J. of Hydraulic Enginnering ASCE VOL.118 n.9 pp. 1270-86

Greox Leon (1905): U.S. Patent 801,182

Gresho P.A. (1984): A Modified Finite Element Method for Solving the Time-Dependent Incompressible Navier-Stokes Equations. Part I: Theory. Int. J. Mathematics in fluids Vol.4 pp. 557-98

Gresho P.M., Lee R.L., Sani R.L. (1980): On the Time Dependent Solution for the Incompressible Navier-Stokes Equations in two and three Dimensions In: Recent Advances in Num. Methods in Fluids. Eds. C. Taylor and K. Morgan. Pineridge Press, Swansea Vol.1

Grunwald S., Beagle W. (1990): Check Valve Movement in a Scroll Compressor. 10th Int. Compressor Eng. Conf. Pardue Univ.

Hall M.G. (1981): Computational Fluid Dynamics - A Revolutionary Force in Aerodynamics. AIAA Paper 81-1014, Palo Alto, California

Hassan Y.A., Rice J.G., Kim J.H. (1983): A Stable Mass-Flow-Weighted two-dimensional Skew Upwind Sceme. Num. Heat Transfer Vol.6 pp. 395-408

Hawkins I.R., Wilkes N.S. (1991): Moving Grids in Harwell FLOW3D. UKAEA Report AEA-Im Tech-0608

Hayano M., Sakata H., Nagamoto S., Murasaki H. (1988): An Analysis of Loses in Scroll Compressors. . 9th Int. Compressor Eng. Conf. Pardue Univ.

Hayano Makoto et al. (1986): Performance Analysis of Scroll Compressor for Air Conditioners. . 8th Int. Compressor Eng. Conf. Pardue Univ.

Hedberg P.K.M. (1989): NONDIF: A Method to Avoid Numerical Diffusion and over- and under-shoots. Proc. 6th Int. Conf. Num. Meth. Lam. Turb. Flow. Swansea UK, 11-15 July 1989 Ed. By C. Taylor, P. Gresho, P.L. Sani and J. Hauser. Pineridge Press, Swansea pp. 193-202

Henry F.S., Pearcey H.H (1994): Numerical Model of Boundary-Layer Control using Air-Jet Generated Vortices. AIAA J. Vol.32 n.12 pp. 2415-25

Hindman R.G., Spencer J (1983): A New Approach to Truly Adaptive Grid Generation. AIAA Paper 83-0450, Reno Nevada

Hirano T., Matsumura N. (1988): Development of High Efficiency Scroll Compressors for Air Conditioners. . 9th Int. Compressor Eng. Conf. Pardue Univ.

Huiqing L., Disheng W., Huanran W., Penggao C. (1992): Research of oil-injected Scroll Compressor Working Process. 11th Int. Compressor Eng. Conf. Pardue Univ.

Hussaini M.Y., Zang T.A. (1987): Spectral Methods in Fluid-Dynamics. Ann. Review Fluid Mech. Vol.19 pp. 339-67

Hutton A.G., Smith R.M., Hickmott S. (1987): The Computattion of Turbulent Flows of Industrial Complexity by the Finite Element Method- Progress and Prospects. Int. J. for Numerical Methods in Fluids Vol.& pp. 1277-98

Ishi N., Yamamura M., Muramatsu S., Yamamoto S., Sakai M. (1990): Mechanical Efficiency of a Variable Speed Scroll Compressor. 10th Int. Compressor Eng. Conf. Pardue Univ.

Ishi Noriaki et al. (1986): A Study on Dynamic Behavior of a Scroll Compressor. 8th Int. Compressor Eng. Conf. Pardue Univ.

Issa R.I. (1985): Solution of Implicitly Discretised Fluid Flow Equations by Operator Splitting. J. Computational Physics Vol.61 pp.40

Jeff J.N., Douglas P.G. (1992): Analytical modeling of Discharge flow dynamics in scroll compressors. 11th Int. Compressor Eng. Conf. Pardue Univ.

Jones I.P.(1991): CFDS Software- Vlidation Report: Part I: AEA-In Tech Report Harwell Laboratory, Nov 1991

Jones I.P., Kightley J.R., Thompson C.P., Wilkes N.S. (1985): FLOW3D, a Computer Code for the Prediction of Laminar and Turbulent Flow and Heat Transfer Release 1. Harwell Report AERE -R 11825, 1985

Jones I.P., Kightley J.R., Thompson C.P., Wilkes N.S. (1986): FLOW3D Release 1: User Manual. Harwell Report AERE -R 11893, 1986

- Kazutaka S., Masao S., Kenji T. (1992): Performance Analysis of Hermetic Scroll Compressors. 11th Int. Compressor Eng. Conf. Pardue Univ.

- Kenji Tojo et al. (1984): A Scroll Compressor For Air Conditioners. . 7th Int. Compressor Eng. Conf. Pardue Univ.

- Kenji Tojo et al. (1986): Computer modeling of scroll compressor with self adjusting back-pressure mechanism. 8th Int. Compressor Eng. Conf. Pardue Univ.

Kobayashi M.H., Pereira J.C.F. (1994): A computational method for solving arbitary two-dimensional physiological flows. ASME J. Biomechanical Engineering Vol.116 pp. 315-7
Latimer B.R., Pollard A. (1989): Comparison of Pressure-Velocity Coupling Algorithms. Num. Heat Transfer Vol.8 pp. 635-52

Leonard B.P. (1979): A Stable and Accurate Convective Modeling Procedure based on Quadratic Upstream Interpolation. Comp. Meth. Appl. Mech. Eng. Vol.19 pp.59-98

Levine R.D. (1982): Supercomputers. Sc. Am. Vol.246 pp.118-135

- Liansheng L., Yongzhang Y. (1990): The Theoretical Analysis and Experimental Research for A Refrigerating Scroll Compressor. 10th Int. Compressor Eng. Conf. Pardue Univ.

Lillington J.N. (1981): A Vector Upstream Differencing Scheme for Problems in Fluid Flow involving Significant Source Term in Steady-Linear Systems. Int. J. Num. Meth. Fluids Vol.1 pp. 3-6

Lin A. (1985): The Parameterized Strongly Implicit Method for Solving Elliptic Difference Equations. Int. J. Num. Meth. In Fluids Vol.1 pp. 3-6

Lohner R. (1987): Finite Elements in CFD: What lies Ahead?. Int. J. Numer. Meth. Engng. Vol.24 pp.1741-56

- Lysholm A. (1967): Screw Rotor Machine. U.S. Patent No. 3,314,598

McDonough J.M., Catton I. (1982): A mixed Finite difference-Galerkin Procedure for Two Dimensional Convection in A square Box. Int. J. Heat and Mass Transfer Vol.25 pp. 1137-46

Moin P., Kim J. (1982): Numerical Investigation of Turbulent Channel Flow. J. Fluid Mech. Vol.118 pp. 341-77

Morishita E., Kitora Y., Nishida M. (1992): Basic Study of Engine with Scroll Compressor and Expander. 11th Int. Compressor Eng. Conf. Pardue Univ.

Morishita Etsuo et al. (1984): Scroll Compressor Analytical Model. 7th Int. Compressor Eng. Conf. Pardue Univ.

Nieter J. (1988): Dynamics of Scroll Suction Process. . 9th Int. Compressor Eng. Conf. Pardue Univ.

Patankar S.V. (1980): Numerical Heat Transfer and Fluid Flow. McGraw-Hill Book Company

Patankar S.V. (1981): A Calculation Procedure for Two Dimensional Elliptic Situations. Numerical Heat Transfer Vol.4 pp.409-25

Patankar S.V. (1988): Recent Developments in Computational Heat Transfer. ASME J. Heat Transfer Vol.110 pp. 1037-45

Patankar S.V., Spalding D.B. (1972): A Calculation Procedure for Heat, Mass and Momentum Transfer in Three Dimensional Parabolic Flows. Int. J. Mass Transfer Vol.15 pp. 1787-1806

Patera A.T. (1984): A Spectral Method for Fluid Dynamics: Laminar Flow in a Channel Expansions. J. Comp. Phys. Vol.54 pp.468-88

Pedley T.J. (1985): Flow along a channel with a time-dependent indentation in one wll: the generation of vorticity waves. J. Fluid Mech. Vol.160 pp. 337-367

Peraire J., Morgan K., Peiro J.(1990): Unstructured mesh methods for CFD. Von Karman Institute for Fluid Dynamics. "Numerical Grid Generation" Lecture Notes

Peric M. (1987): Efficient Semi-Implicit Solving Algorithm for Nine-Diagonal Coefficient Matrix. Numerical Heat Transfer Vol.11 pp.251-79

Proceedings of the First CFDS International User Conference 6-7 May 1993, Eynsham Hall. Oxford

Puttre'M. (1991): FEA programs band together. ASME Mech. Engng Vol.113 pp.77-80
Rai M.M., Anderson D.A. (1982): Application of Adaptive Grids to Fluid Flow Problems with Asymptotic Solutions. AIAA J. Vol.20 pp.496-502

Raithby G.D. (1976): Skew Upwind Differencing Schemes for Problems involving Fluid

Flow. Comp. Meth. Appl. Mech Eng. Vol9 pp.153-65

Reddy J.N. (1982): On Penalty Function Methods in the Finite Element Analysis of Flow Problems. Int. J. Num. Metho. In Fluids Vol.2 pp.151-71

Rhie C.M. (1981): A Numerical Study of the Flow Past an Isolated Airfoil with Separation. Ph.D. Thesis Dept. Mech. And Industrial Engineering University of Illinois at Urbana-Champaign

Rhie C.M., Chow W.L. (1983): Numerical Study of the Turbulrnt Flow Past an Airfoil with Trailing Edge Separation. AIAA J. Vol.21 pp. 1527-32

Rizzi A. Erikson L.E. (1981): Transfinite Mesh Generation and Damped Eulerian Equation Algorithm for Transonic Flow around Wing-Body Configurations. Proc. AIAA 5th Computational Fluid Dynamics Conference, Palo Alto, California pp. 43-69

Roache P.J. (1972): Computational Fluid Dynamics. Hermosa Publishers

Rogers R.J., Wagner T.C. (1990): Scroll Compressors Flow Modeling: Experimental and Computational Investigation. 10th Int. Compressor Eng. Conf. Pardue Univ.

Ronald T.D., Quesada J.F. (1992): Analytical and Experimental Investigation of a Scroll Compressor Lubrication System. 11th Int. Compressor Eng. Conf. Pardue Univ.

Runchal A.K. (1987): CONDIF: A Modified Central-Difference Scheme for Convective Flows. Int. J. Num. Meth. Eng. Vol.24 pp.1593-608

Smith I.K (1985): "PROJECT SPHERE: An Assessment of the Practicability of the Trilateral Wet Vapour Cycle for Recovery of Power from Low Grade Heat Sources", Thermo-Fluids Engineering Research Centre Report, The City University

Smith I.K. (1986): "A Comparison of Three Surface Plant Options for the Conversion of Geothermal Energy From HDR", IRD 86/17

Smith I.K. (1993): Development of the Trilateral Flash Cycle System: 1 Fundamental Considerations. J. of Power and Energy, Proc IMechE Vol.207 pp. 179-194

Smith I.K., Aldis C.A (1990): Lysholm Screw Expanders in place of throttle valves in large heat pump and refrigeration systems. Proc. Meeting of Commission E2, Stockholm, Aug 29-31

Smith I.K., Pitanga Marques da Silva R. (1994): Part 2: Increasing power output with working fluid mixtures. J. of Power and Energy, Proc. IMechE Vol.208 pp. 135-144

Smith I.K., Stosic N., Aldis C.A. (1994): Lysholm twin screw machines as two-phase

expanders. 12th Int. Compressor Engineering Conf. Pardue Univ. July

Smith I.K., Stosic N., Aldis C.A. (1995): Development of the Trilateral Flash Cycle System: Part 3: The Design of High Efficiency Two-phase Screw Expanders. J. of Power and Energy Proc. IMechE

Spalding D.B. (1970): A Novel Finite Difference Formulation for Differential Expressions Involving both First and Second Derivatives. Int. J. Num. Meth. Eng. Vol.4 pp.551-9

Spalding D.B. (1972): Mathematical Modeling of Fluid Mechanics, Heat Transfer and Mass Transfer Processes. Imperial College, London, Mech. Eng. Dept. Rep. N. HTS/80/1

Sprankle R.S. (1973): Electrical Power Generating Systems. U.S. Patent 3,751,673, August 1973

Sprankle R.S. (1976): Throttling Means for Geothermal Stream. U.S. Patent 3,977,818

Starius G. (1977): Construction of Orthogonal Curvilinear Meshes by solving Initial Values Problems. Num. Math. Vol.28 pp.25-48

Steidel R.F., Weiss H., Flower J.E. (1982): Characteristics of the Lysholm Engine as Tested for Geothermal Applications in the Imperial Valey. J. Eng. For Power Vol.104 pp. 231-240

Stone H.L. (1968): Iterative Solution of Implicit Approximations of Multi-Dimensional Partial Differential Equations. SIAM J. Num. Anal. Vol.5 pp. 530-58

Stosic N., Hanjalic K. (1994): Development and optimization of screw engine rotor pairs on the basis of computer modeling. 12th Int. Compressor Eng. Conf. Pardue Univ. July

Stosic N., Milutinovic L., Hanjalic K., Kovacevic A.(1992): Investigation of oil injection influence upon the screw compressor working process. Int j. Refrig. Vol.15 pp. 206-220

Syed S., Chiappeta L. (1985): Finite Difference Methods For Reducing Numerical Diffusion in TEACH-type Calculations. AIAA Paper 85-0056

Taniguchi H. (1988): Analytical and Experimental Investigation of Two-Phase Flow Screw Expanders for Power Generation. Tran. Os ASME, J. of Eng. For Gas Turbines and Power, Vol.110

Thompson J.F. (1984): A Survey of Dynamically-Adaptive Grids in the Numerical Solution of Partial Differential Equations. J. of Numerical Mathematics

Thompson J.F. (1984): Grid Generation Techniques in Computational Fluid Dynamics.

AIAA Journal Vol.22 n.11 pp. 1505-23

Thompson J.F. (1988): A Composite Grid Generation Code for General 3_D Regions. The Eagle Code. AIAA J. Vol.26 pp. 271-2

Thompson J.F., Thames F.C., Mastin C.W. (1974): Automatic Numerical Generation of Body-Fitted Curvilinear Coordinate System for Field Containing Any Number Arbitrary Two Dimensional Bodies. J. Computational Physics Vol.15 pp. 299-319

Thompson J.F., Warsi Z.u., Mastin C.W. (1982): Boundary Fitted Coordinate Systems for Numerical Solution of Partial Differential Equations - A Review. J. Comp. Phys. Vol.47 pp. 1-108

Thompson J.F., Warsi Z.U., Mastin C.W. (1985): Numerical Grid Generation. Elsevier Science Publishing

Thompson J.F., Warsi Z.U.A. (1983): Three Dimensional Grid Generation from Elliptic Systems. AIAA -83-1905. AIAA 6th Computational Fluid Dynamics Conference, Danvers, Massachusetts

Thompson J.F., Wilkes N.S. (1982): Experiments with Higher-Order Finite Difference Formulae. AERE 10493

Tsutomu Inaba et al. (1986): A scroll compressor with sealing means and low side shell. 8th Int. Compressor Eng. Conf. Pardue Univ.

Van Doormal J.P., Rairhby G.D. (1984): Enhancements of the SIMPLE Method for predicting Incopressible Fluid Flow. Heat Transfer Vol.7 pp. 147-63

Wang Zongyan (1992) A New Type of Curve Used in the Wrap Design of the Scroll Compressor. 11th Int. Compressor Eng. Conf. Pardue Univ.

Weatherill N.C., Forsey C.R. (1984): Grid Generation and Flow Calculations for Complex Aircrafts Geometrics using a Multiblock Scheme. AIAA -84-1665. AIAA 17th Fluid Dynamics, Plasma Dynamics, and Lasers Conference, Snowmass, Co

Wong H.H., Raithby G.D. (1979): Improved Finite Difference Methods Based on a Critical Evaluation of the Approximation Errors. Num. Heat. Transfer Vol.2 pp. 139-63

Yamamura M., et al. (1990): Compact Type Scroll Compressor for Air Conditioners. 10th Int. Compressor Eng. Conf. Pardue Univ.

Yanagisawa T. et al. (1990): Optimum Operating Pressure Ratio For Scroll Compressors. 10th Int. Compressor Eng. Conf. Pardue Univ.

Yogzhang Y., Yuhua X., Lianheng L. (1992): The Mechanical Analysis of a Scroll Compressor. 11th Int. Compressor Eng. Conf. Pardue Univ.

Yong H. (1994): Leakage Calculation Through Clearances. 12th Int. Compressor Eng. Conf. Pardue Univ.

Zaneli R., Favrat D. (1994): Experimental Investigation of a Hermetic Scroll Expander-Generator. 12th Int. Compressor Eng. Conf. Pardue Univ.

Zhang H., Reggio M., Trepanier J.Y., Camarero R. (1993): Discrete Form of the CGL for Moving Meshes and its Implementation in CFD schemes. Computers Fluids Vol.22 N.1 pp. 9-23

Zhenquan L., Guirong D., Shicai Y., Mingzhi W. (1992): The Grapjics Method Of Modified Wrap Of Scroll Compressor. 11th Int. Compressor Eng. Conf. Pardue Univ.

Zhu J., Wang D. (1990): A research of scroll compressor working process computer simulation and testing. 10th Int. Compressor Eng. Conf. Pardue Univ.

Zienkiewicz O.C. (1977): The Finite Element Method. Third Edition, McGraw-Hill

Zienkiewicz O.C., Cheung Y.K. (1965): Finite Elements in the Solution of Field Problems. The Engineer pp. 507-10